

# AGARD

ADVISORY GROUP FOR AEROSPACE RESEARCH & DEVELOPMENT

7 RUE ANCELLE, 92200 NEUILLY-SUR-SEINE, FRANCE

**AGARD REPORT 812**

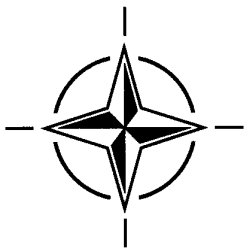
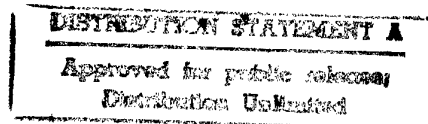
**Special Course**

**on**

**Advances in Cryogenic Wind Tunnel  
Technology**

(les Avancées en technologie des souffleries cryogéniques)

*The material assembled in this report was prepared under the combined sponsorship of the AGARD Fluid Dynamics Panel, the Consultant and Exchange Program of AGARD, and the von Kármán Institute (VKI) for Fluid Dynamics. It contains the papers presented at a Special Course held in Köln, Germany, 20-24 May 1996.*

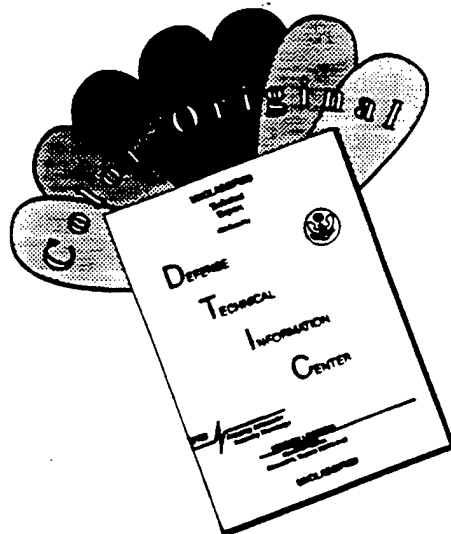


**NORTH ATLANTIC TREATY ORGANIZATION**

Published February 1997

*Distribution and Availability on Back Cover*

# DISCLAIMER NOTICE



THIS DOCUMENT IS BEST QUALITY AVAILABLE. THE COPY FURNISHED TO DTIC CONTAINED A SIGNIFICANT NUMBER OF COLOR PAGES WHICH DO NOT REPRODUCE LEGIBLY ON BLACK AND WHITE MICROFICHE.

# AGARD

ADVISORY GROUP FOR AEROSPACE RESEARCH & DEVELOPMENT

7 RUE ANCELLE, 92200 NEUILLY-SUR-SEINE, FRANCE

---

**AGARD REPORT 812**

**Special Course**

**on**

**Advances in Cryogenic Wind Tunnel  
Technology**

(les Avancées en technologie des souffleries cryogéniques)

The material assembled in this report was prepared under the combined sponsorship of the AGARD Fluid Dynamics Panel, the Consultant and Exchange Program of AGARD, and the von Kármán Institute (VKI) for Fluid Dynamics. It contains the papers presented at a Special Course held in Köln, Germany, 20-24 May 1996.



North Atlantic Treaty Organization  
*Organisation du Traité de l'Atlantique Nord*

DTIC QUALITY INSPECTED 4

---

19970225 054

# The Mission of AGARD

According to its Charter, the mission of AGARD is to bring together the leading personalities of the NATO nations in the fields of science and technology relating to aerospace for the following purposes:

- Recommending effective ways for the member nations to use their research and development capabilities for the common benefit of the NATO community;
- Providing scientific and technical advice and assistance to the Military Committee in the field of aerospace research and development (with particular regard to its military application);
- Continuously stimulating advances in the aerospace sciences relevant to strengthening the common defence posture;
- Improving the co-operation among member nations in aerospace research and development;
- Exchange of scientific and technical information;
- Providing assistance to member nations for the purpose of increasing their scientific and technical potential;
- Rendering scientific and technical assistance, as requested, to other NATO bodies and to member nations in connection with research and development problems in the aerospace field.

The highest authority within AGARD is the National Delegates Board consisting of officially appointed senior representatives from each member nation. The mission of AGARD is carried out through the Panels which are composed of experts appointed by the National Delegates, the Consultant and Exchange Programme and the Aerospace Applications Studies Programme. The results of AGARD work are reported to the member nations and the NATO Authorities through the AGARD series of publications of which this is one.

Participation in AGARD activities is by invitation only and is normally limited to citizens of the NATO nations.

The content of this publication has been reproduced  
directly from material supplied by AGARD or the authors.

Published February 1997

Copyright © AGARD 1997  
All Rights Reserved

ISBN 92-836-1047-4



*Printed by Canada Communication Group  
45 Sacré-Cœur Blvd., Hull (Québec), Canada K1A 0S7*



# **Advances in Cryogenic Wind Tunnel Technology**

## **(AGARD R-812)**

### **Executive Summary**

This report is a compilation of the edited proceedings of the Special Course on "Advances in Cryogenic Wind Tunnel Technology" held at the DLR Research Center, Köln, Germany, 20-24 May 1996.

The development and use of cryogenic wind tunnels represents a major advance in aerodynamics testing. One advantage of cryogenic tunnels is their ability to achieve full-scale values of Reynolds number in tunnels of moderate size at reasonable operating pressures. Another important advantage is the ability to independently vary temperature, pressure and speed, which lets one separate the effects of Reynolds number, aeroelasticity and Mach number.

This series of lectures, supported by the AGARD Fluid Dynamics Panel and the von Kármán Institute, incorporated a brief review of the development and early uses of cryogenic tunnels, and reports on current operational cryogenic facilities. It then covered the theory and advantages of cryogenic wind tunnels, as well as the special considerations required in their design, construction, and use. Subjects included cryogenic systems, thermal insulation, facility and model design and construction, strain-gage balances, pressure instrumentation, flow visualization, data accuracy, safety, and productivity.

# **Les avancées en technologie des souffleries cryogéniques**

**(AGARD R-812)**

## **Synthèse**

Ce rapport est une compilation des travaux du Cours spécial sur «les avancées en technologies des souffleries cryogéniques» tenu au DLR Research Center, à Köln, en Allemagne du 20 au 24 mai 1996.

Le développement et l'utilisation des souffleries cryogéniques représente un progrès considérable pour les essais aérodynamiques. L'un des avantages des souffleries cryogéniques réside dans les possibilités offertes pour générer des nombres de Reynolds en vraie grandeur dans des souffleries de dimensions moyennes à des pressions d'utilisation raisonnables. Un autre avantage important est représenté par les possibilités de variation indépendante de température, pression et vitesse, ce qui permet de séparer les effets du nombre de Reynolds, de l'aéroélasticité et du nombre de Mach.

Ce cycle de conférences, organisé conjointement par le Panel AGARD de la dynamique des fluides et l'Institut von Kármán, a inclu un bref résumé du développement et des premières applications des souffleries cryogéniques, ainsi qu'un certain nombre de rapports sur différentes installations cryogéniques en exploitation. La conférence a examiné ensuite la théorie et les avantages des souffleries cryogéniques, ainsi que les considérations particulières régissant leur conception, leur construction et leur utilisation. Les sujets suivants ont été abordés: les souffleries cryogéniques, l'isolation thermique, la conception et la construction des installations et des maquettes, les extensomètres, l'instrumentation de pression, la visualisation des écoulements, la précision des données, la sécurité et la productivité.

# Contents

	Page
<b>Executive Summary</b>	iii
<b>Synthèse</b>	iv
<b>Recent Publications of the Fluid Dynamics Panel</b>	vii
<b>Special Course Staff</b>	ix
	Reference
<b>Introduction to Cryogenic Wind Tunnels</b> by M.J. Goodyer	1
<b>Cryogenic Engineering and Materials</b> by D.A. Wigley	2
<b>Materials for Use in Cryogenic Wind Tunnels</b> by D.A. Wigley	3
<b>Cryogenic Model Systems</b> by C.P. Young, Jr.	4
<b>Instrumentation for Cryogenic Tunnels</b> by M. Bazin, C. Blanchet and F. Dupriez	5
<b>Force Testing with Internal Strain Gage Balances</b> by K. Hufnagel and B. Ewald	6
<b>Fundamental Considerations for Testing in Cryogenic Tunnels</b> by A. Mignosi	7
<b>The Cryogenic Ludwig-Tube Tunnel at Göttingen</b> by H. Rosemann	8
<b>T2 Transonic Cryogenic Wind Tunnel at Toulouse</b> by A. Seraudie and J.P. Archambaud	9
<b>The Concept of the Kryo-Kanal-Köln (KKK)</b> <b>Operational Experience, Flow Quality, Model Handling and</b> <b>Half Model Testing Technique</b> by G. Viehweger	10
<b>Development of Correction Procedure for Signals of Cryogenic Balances</b> by R. Rebstock	11
<b>Model Dynamics</b> by C.P. Young, Jr.	12
<b>An Overview of Test Capabilities at ETW</b> by I. Price and D. Schimanski	13

<b>Cryogenic Internal Balance Calibration at ETW</b> by L.M. Badet	<b>14</b>
<b>The National Transonic Facility (NTF) Operational Status</b> by J.S. Hill	<b>15</b>
<b>Other Cryogenic Wind Tunnel Projects</b> by R.A. Kilgore	<b>16</b>

# Recent Publications of the Fluid Dynamics Panel

## **AGARDOGRAPHS (AG)**

### **Turbulent Boundary Layers in Subsonic and Supersonic Flow**

AGARD AG-335, July 1996

### **Computational Aerodynamics Based on the Euler Equations**

AGARD AG-325, September 1994

### **Scale Effects on Aircraft and Weapon Aerodynamics**

AGARD AG-323 (E), July 1994

### **Design and Testing of High-Performance Parachutes**

AGARD AG-319, November 1991

### **Experimental Techniques in the Field of Low Density Aerodynamics**

AGARD AG-318 (E), April 1991

### **Techniques Expérimentales Liées à l'Aérodynamique à Basse Densité**

AGARD AG-318 (FR), April 1990

### **A Survey of Measurements and Measuring Techniques in Rapidly Distorted Compressible Turbulent Boundary Layers**

AGARD AG-315, May 1989

### **Reynolds Number Effects in Transonic Flows**

AGARD AG-303, December 1988

## **REPORTS (R)**

### **Aerothermodynamics and Propulsion Integration for Hypersonic Vehicles**

AGARD R-813, Special Course Notes, October 1996

### **Parallel Computing in CFD**

AGARD R-807, Special Course Notes, October 1995

### **Optimum Design Methods for Aerodynamics**

AGARD R-803, Special Course Notes, November 1994

### **Missile Aerodynamics**

AGARD R-804, Special Course Notes, May 1994

### **Progress in Transition Modelling**

AGARD R-793, Special Course Notes, April 1994

### **Shock-Wave/Boundary-Layer Interactions in Supersonic and Hypersonic Flows**

AGARD R-792, Special Course Notes, August 1993

### **Unstructured Grid Methods for Advection Dominated Flows**

AGARD R-787, Special Course Notes, May 1992

### **Skin Friction Drag Reduction**

AGARD R-786, Special Course Notes, March 1992

### **Engineering Methods in Aerodynamic Analysis and Design of Aircraft**

AGARD R-783, Special Course Notes, January 1992

### **Aircraft Dynamics at High Angles of Attack: Experiments and Modelling**

AGARD R-776, Special Course Notes, March 1991

## **ADVISORY REPORTS (AR)**

### **Cooperative Programme on Dynamic Wind Tunnel Experiments for Manoeuvring Aircraft**

AGARD AR-305, Report of WG-16, October 1996

### **Hypersonic Experimental and Computational Capability, Improvement and Validation**

AGARD AR-319, Vol. I, Report of WG-18, May 1996

### **Aerodynamics of 3-D Aircraft Afterbodies**

AGARD AR-318, Report of WG-17, September 1995

### **A Selection of Experimental Test Cases for the Validation of CFD Codes**

AGARD AR-303, Vols. I and II, Report of WG-14, August 1994

### **Quality Assessment for Wind Tunnel Testing**

AGARD AR-304, Report of WG-15, July 1994

### **Air Intakes of High Speed Vehicles**

AGARD AR-270, Report of WG-13, September 1991

**Appraisal of the Suitability of Turbulence Models in Flow Calculations**  
AGARD AR-291, Technical Status Review, July 1991

**Rotary-Balance Testing for Aircraft Dynamics**  
AGARD AR-265, Report of WG11, December 1990

**Calculation of 3D Separated Turbulent Flows in Boundary Layer Limit**  
AGARD AR-255, Report of WG10, May 1990

**Adaptive Wind Tunnel Walls: Technology and Applications**  
AGARD AR-269, Report of WG12, April 1990

**CONFERENCE PROCEEDINGS (CP)**

**Progress and Challenges in CFD Methods and Algorithms**  
AGARD CP-578, April 1996

**Aerodynamics of Store Integration and Separation**  
AGARD CP-570, February 1996

**Aerodynamics and Aeroacoustics of Rotorcraft**  
AGARD CP-552, August 1995

**Application of Direct and Large Eddy Simulation to Transition and Turbulence**  
AGARD CP-551, December 1994

**Wall Interference, Support Interference, and Flow Field Measurements**  
AGARD CP-535, July 1994

**Computational and Experimental Assessment of Jets in Cross Flow**  
AGARD CP-534, November 1993

**High-Lift System Aerodynamics**  
AGARD CP-515, September 1993

**Theoretical and Experimental Methods in Hypersonic Flows**  
AGARD CP-514, April 1993

**Aerodynamic Engine/Airframe Integration for High Performance Aircraft and Missiles**  
AGARD CP-498, September 1992

**Effects of Adverse Weather on Aerodynamics**  
AGARD CP-496, December 1991

**Manoeuvring Aerodynamics**  
AGARD CP-497, November 1991

**Vortex Flow Aerodynamics**  
AGARD CP-494, July 1991

**Missile Aerodynamics**  
AGARD CP-493, October 1990

**Aerodynamics of Combat Aircraft Controls and of Ground Effects**  
AGARD CP-465, April 1990

**Computational Methods for Aerodynamic Design (Inverse) and Optimization**  
AGARD CP-463, March 1990

**Applications of Mesh Generation to Complex 3-D Configurations**  
AGARD CP-464, March 1990

**Fluid Dynamics of Three-Dimensional Turbulent Shear Flows and Transition**  
AGARD CP-438, April 1989

**Validation of Computational Fluid Dynamics**  
AGARD CP-437, December 1988

**Aerodynamic Data Accuracy and Quality: Requirements and Capabilities in Wind Tunnel Testing**  
AGARD CP-429, July 1988

**Aerodynamics of Hypersonic Lifting Vehicles**  
AGARD CP-428, November 1987

**Aerodynamic and Related Hydrodynamic Studies Using Water Facilities**  
AGARD CP-413, June 1987

**Applications of Computational Fluid Dynamics in Aeronautics**  
AGARD CP-412, November 1986

# Special Course Staff

## Special Course Director

R.A. Kilgore  
C.E.S. - Hampton  
359 Marlfield Circle  
Hampton Virginia  
23669-1733  
United States

## LECTURERS

L. Badet  
European Transonic Wind Tunnel  
P.O. Box 906116  
Ernst-Mach-Str.  
51127 Köln  
Germany

M. Bazin  
ONERA BP 72  
Avenue de la Division Leclerc  
92322 Châtillon Cedex  
France

C. Blanchet  
BERTIN  
144 rue Louis Arnaud  
BP 22000/Z.I. les Milles  
13791 Aix-en-Provence Cedex 3  
France

F. Dupriez  
ONERA/IMFL  
5, BLD. Paul Painlevé  
France

M.J. Goodyer  
University of Southampton  
Dept. of Aeronautics  
10 Randall Road/Chandler Ford  
Hampshire SO5 1AL  
United Kingdom

H. Rosemann  
DLR-Inst. of Fluid Mechanics  
SM-SK-HGA  
Bunsenstrasse 10  
37073 Göttingen  
Germany

D. Schimanski  
European Transonic Wind Tunnel  
P.O. Box 906116  
Ernst-Mach-Str.  
51127 Köln  
Germany

A. Seraudie  
ONERA-CERT  
BP 4025  
2 av. E. Belin  
31055 Toulouse Cedex  
France

J.S. Hill  
NASA Langley Research Center  
Hampton, Virginia  
23681-0001  
United States

K. Hufnagel  
Technical Univ. of Darmstadt  
Windkanal  
Flughafenstr. 19  
64347 Griesheim  
Germany

A. Mignosi  
ONERA/CERT  
BP 4025  
2 av. E. Belin  
31055 Toulouse Cedex  
France

I. Price  
European Transonic Wind Tunnel  
P.O. Box 906116  
Ernst-Mach-Str.  
51127 Köln  
Germany

R. Rebstock  
Kryo Kanal Köln  
DLR Research Center  
Postfach 906058  
5000 Köln  
Germany

G. Viehweger  
Kryo Kanal Köln  
DLR Research Center  
Postfach 906058  
5000 Köln  
Germany

D.A. Wigley  
C.M. & M. Consultants  
17 Basset Wood Drive  
Bassett, Southampton SO16 3PT  
United Kingdom

C.P. Young  
VIGYAN Inc.  
30 Research Drive  
Hampton, Virginia  
23666-1325  
United States

## INTRODUCTION TO CRYOGENIC WIND TUNNELS

M J Goodyer  
 Professor of Experimental Aerodynamics  
 Department of Aeronautics and Astronautics  
 The University  
 Southampton SO17 1BJ  
 England

### SUMMARY

The situation which existed in the era which spawned the cryogenic wind tunnel, the early 1970's, is first explained. The background includes the strong desire felt at that stage to raise Reynolds number in transonic testing, together with the response in the form of the expensive solutions then under consideration. Some paper studies describing the benefits of changing test temperature did exist, mostly older and obscure, but had been ignored up to this time. This situation coincided with the contemporary state of maturity of cryogenic engineering.

The cryogenic wind tunnel evolved in this environment as the way to increase Reynolds number while avoiding undue increase of wind tunnel size or operating pressure. The paper describes the theoretical principles, showing the way in which it achieves its aim. Some cryogenic wind tunnel practice is included, also a description of beneficial features additional to achieving high test Reynolds numbers. These are a rather important reduction of motor power in the case of fan-driven tunnels and the ability for the first time in wind tunnel testing to isolate the separate effects of changes in Reynolds number, Mach number and dynamic pressure. Finally there is an outline of the way in which cryogenic operation affects some representative types of tunnel.

### SYMBOLS

a	speed of sound
A	flow area, reference area
c	reference length, wing mean chord
m	mean molecular weight
M	Mach number
n	index in $\mu \propto T^n$
P, P <sub>0</sub>	static, stagnation pressure
q	dynamic pressure $\frac{1}{2}\rho U^2$
R	gas constant
R <sub>0</sub>	universal gas constant
Re	Reynolds number
Re <sub>c</sub>	Reynolds number based on length c
T, T <sub>0</sub>	static, stagnation temperature
U	reference velocity
V	specific volume
Z	compressibility factor
$\alpha$	incidence = angle of attack
$\gamma$	ratio of specific heats
$\lambda$	drive power constant of proportionality
$\mu$	viscosity
$\rho$	density

### 1 BACKGROUND

In any attempt to justify the expenditure of considerable manpower and effort on a project such as that forming the subject of this Course it is appropriate to reflect for a moment on the underlying reasons for the work, which I will first attempt to do. The root cause of us being here is the fundamental weakness of classical mathematics: despite the undoubted brilliance of mathematicians past and present they have not been able to give us the means to forecast by calculation, and with certainty, the behaviour of real life devices such as the products of aerospace industries. This failure reveals inadequacy in the discipline and not in the practitioners. A quotation specifically about our business of aerodynamics is as follows: "The disparity between the designer's need for aerodynamic prediction and the power of his analytic methods seems to be so vast as almost to defy description"(Ref 1). This statement was published by a very experienced aircraft designer in September 1971, close to the time of the beginning of construction of the first cryogenic wind tunnel (Ref 2). Since then the two avenues of endeavour, empirical and theoretical, have advanced in healthy competition with improvement in each, which is a recognition that the former was not without weakness.

The birth of the cryogenic wind tunnel was preceded by a 20 year period spawning almost all of the transonic wind tunnels now in use. During this period the need to provide for the needs of experimental aerodynamics in a reasonably economic way followed the pattern already set, that of matching the required Mach number but in most cases not the required Reynolds number. The reason for this is because Mach number effects were known to be strong, particularly at speeds near the speed of sound, while it was felt that the effects of Reynolds number on performance were rather weak and perhaps systematic and predictable. If the same circumstances existed now and we had to choose between the two parameters there is no doubt that we would still pick Mach number for proper matching. It is perhaps fortunate that background research in Japan and the U.S.A. in the 1930's led to the development of the ventilated test section for transonic testing, allowing the immediately most pressing needs to be satisfied at reasonable cost. Had Reynolds number effects seemed more important there is no knowing what solutions might have emerged, but possibly the cryogenic wind tunnel because the necessary information and most of the technology was around and the route to full scale Reynolds number by more conventional means is inordinately expensive.

It should be mentioned that throughout almost the whole time of aerodynamic testing, the position with regard to Reynolds number was not accepted without question. The needs of the low speeds of the early days of flight were



satisfied with large unpressurised wind tunnels which were just economically feasible, reaching full scale Reynolds numbers, but the situation became more difficult with the progressive increases in flight speed and aircraft size. To anyone who begins to design a wind tunnel for flight values of Reynolds number at normal values of tunnel pressure and temperature it soon becomes apparent that the cost will be very high. To circumvent this problem searches were made, from about 1920 onwards, for test gases alternative to air which would inherently provide such flows at reasonable size and cost. Pozniak (Ref 3) gives a comprehensive summary and list of references. The searches revealed some gases which were not too toxic and which would provide useful increases in Reynolds number, by factors of up to 4 when compared with air at otherwise the same conditions. However these gases were polyatomic with ratios of specific heats  $\gamma$  much lower than in air and it was felt that in tests at compressibility speeds their behaviour might not always be close enough to that of a diatomic gas. It is no use replacing one system which occasionally and unpredictably gives wrong answers (that is air at low Reynolds number) with another which might do the same but for a different reason. Mixtures of gases having  $\gamma \approx 1.4$  gave too small rewards.

On at least two occasions the prospects were discussed for the use of low temperatures in aerodynamic testing. Margoulis (Refs 4,5) in 1920 in open literature, and Smelt (Ref 6) in 1945 in a classified report, gave predictions of the advantages, but the possibilities were largely ignored although from time to time in reports from the period various authors again drew attention to the idea. It is likely that the motivation for producing high Reynolds number flows was not strong enough to encourage facing the practical problems, more serious then because tonnage cryogenics was in its infancy.

While errors can be made of either sign in the prediction of aircraft performance, the cases which cause concern are those where full scale performance is worse than expectation by too large a margin. In the U.S.A. and Europe during the above period there were examples of aircraft projects which performed rather too badly in comparison with predictions based on wind tunnel data. The consensus was that mismatch in Reynolds number was the likely cause. It was decided to reduce the disparity because the state of the art of corrections did not allow their application with confidence. These experiences prompted campaigns on both sides of the Atlantic to provide transonic wind tunnels with Reynolds number capabilities closer to those experienced in flight, and there began considerable activity.

AGARD, through its Fluid Dynamics Panel, set up the High Reynolds Number Working Group (HIRT) in 1969 which in September 1970 offered some solutions to the transonic needs of NATO countries. Following this the same panel set up the Large Wind Tunnels Working Group (the LaWs Group) in 1971 to examine broader needs of aerodynamic testing but including those of transonic testing, and to evaluate the options, although the option of the cryogenic wind tunnel was not evaluated (Ref 7). These activities represent an interim period, ending in about 1973, during which a variety of designs was actively pursued based on

the use of normal temperatures, often in otherwise unconventional tunnels.

The procedure followed was first to define requirements and then identify possible solutions. On the subject of requirements it should be mentioned that other inadequacies in flow simulation had also become apparent in the meantime, additional to that simply of low Reynolds number. Notable was the realisation that other measures of flow quality including non-uniformity, noise and turbulence, were often unsatisfactory and would need to be reduced in any new wind tunnel. On the subject of the requirement for Reynolds number there were differences of opinion on the extent to which it was necessary to bridge the existing tunnel-to-flight gap. Some (mostly in Europe) felt that there was a level below which there could be expected to be seen changes in data and above which there would be no significant change. Others (mostly in the USA) felt that tunnels should match flight Reynolds number if at all possible.

There was also disagreement over the minimum practical run time for the new tunnels, but the consensus was that around 10 seconds would suffice for most kinds of test. However in retrospect there is no doubt that such compromises were driven to some extent by what was considered economically possible rather than being based on sound technical merit.

The transonic tunnel specifications which emerged included minimum run time, Mach number bands, maximum pressure and of course Reynolds number. It was recognised in Europe that this would need to be a multi-national collaborative project because of the capital cost. Several competing schemes emerged for evaluation (Ref 7). A tunnel was separately proposed for construction in the U.S.A. which also had several competing schemes (Refs 8-10).

The projected cost of a tunnel varies strongly with its size and therefore all steps are taken to minimise size, including the use of the maximum practical pressure, but there are limits to the pressure than can be used. It is easy to show that in the case where the structure of an aircraft is modelled as well as the aerodynamic envelope, the bending stresses in the wind tunnel model, say in the wing root, in relation to those in the aircraft in flight are factored by the two ratios, tunnel-to-flight, of the static pressures and lift coefficients. The tunnels which offered highest Reynolds numbers used static pressures several times those experienced in transonic cruising flight. Further, particularly in the case of transport aircraft, the range of lift coefficient required to be explored in the tunnel could be much wider than structurally acceptable in the aircraft. The net effect is that models are designed for high loads which demand the use of high strength materials (for example maraging steels) coupled with the use of a much more substantial model construction compared with the aircraft, to the extent that many model components are solid. With increases in pressure there is an increasing problem from support interference. While these comments are on the subject only of stresses, aeroelastic considerations may be even more demanding in terms of model and support stiffness. It

became clear that there was insufficient scope for raising Reynolds number, to the levels required, by the sole action of raising the test pressure.

The outcome was a set of designs featuring less than full scale Reynolds number, large test sections (typically 5m, 16 feet) across operating at pressures up to 5 atmospheres or more, with various kinds of intermittent drives. The combination of size and pressure resulted in tunnels projected at rather high cost and requiring also large and expensive models.

At about this stage (in fact in September and October 1971) a small group of engineers at NASA Langley Research Center was faced with a similar kind of problem in relation to a wind tunnel magnetic suspension system, that is much too low a Reynolds number. They proposed the use of a low temperature gas as a means to raise the value. A low speed tunnel was immediately built which served to dispel the most elementary misgivings over the concept and also to draw the attention of the teams working on the large transonic tunnel projects to this alternative approach. In due course the proposals for large transonic tunnels on both sides of the Atlantic narrowed to just cryogenic wind tunnels, fan driven and therefore nominally continuous, capable of reaching full scale flight Reynolds numbers with moderate tunnel size and pressure.

The cryogenic wind tunnel evidently was born out of the needs of transonic testing, but is finding wider application as we will hear in this Special Course. For example achieving full scale Mach and Reynolds numbers in high lift/low speed wind tunnel testing is also important.

The decision to proceed with an investigation of the cryogenic approach for transonic high Reynolds number testing opened up many new lines of endeavour additional to that of just proving the novel aerodynamics. There were the subjects to address of tunnel design and control, cooling, thermal insulation, instrumentation, real gas effects, safety, materials and model making. These and more were first taken on by NASA in relation to the fan driven tunnel. Other organisations have extended the range of tunnel drives as we will hear later, covering intermittent options.

The aims of the remaining parts of this paper are to establish requirements in terms of Reynolds number, to examine briefly the normal-temperature air option, and to introduce the principles of the cryogenic wind tunnel in its practical form. But firstly it is appropriate to discuss some Reynolds number effects.

## 2 MODELS AND REYNOLDS NUMBER EFFECTS.

The use of small models and therefore low Reynolds numbers raises the question of how the development of the boundary layers affects performance. Boundary layer growth over the model is non-linear and at low Reynolds numbers is disproportionately rapid. Therefore, even when other factors in a tunnel test which might affect performance are correct, such as the model's shape and the airspeed, the boundary layers will not have the correctly scaled thickness or even perhaps the correct character in terms of laminar or

turbulent flow, or separations. The force experienced by the model, the net effect of skin friction and pressure distribution, is likely to be incorrect and contain a source of systematic error which cannot be detected whatever the accuracy of the measuring instruments.

Only if an error in a wind tunnel test is large enough will its existence be revealed in subsequent flight tests. Take the example of the Wright brothers. Among the huge amount of work which they did most successfully leading to manned powered flight, work which included learning how best to control and fly several gliders and the design, construction and development of their own engine, they built and used a low speed wind tunnel. This because they had learned from experience not to trust the aerodynamic data of others. Based on their own wind tunnel results they correctly used a high aspect ratio wing planform but incorrectly chose a thin aerofoil section as better aerodynamically compared to thick. This conclusion was a result, it is believed (Ref 11), of using very small models of order 6 inches span compared with the 44 feet span of the aircraft. However the difference in performance between thick and thin did not prevent them from achieving their aim in 1903: the flights did not reveal any significant error even though the Reynolds number of their wind tunnel tests was low by about two orders of magnitude.

In open commercial competition very small differences of performance are now important, often decisively affecting sales and the fortunes of large sections of industry.

In recognising the influence of scale, organisations built as large tunnels as they could reasonably afford during the 60 years or so following the Wright brothers flight, with the largest allowing low speed testing of full scale smaller aircraft such as fighters and light training aircraft as has been mentioned. However as the cost of a tunnel rises with airspeed partly because of a sharp increase in tunnel drive power, no wind tunnel has ever been built to accommodate complete full scale aircraft at transonic or supersonic speeds, speed ranges which became of interest from about 1940 on.

Wind tunnel test data, in the form of dimensionless force and moment coefficients, are functions of a lengthy list of tunnel/model parameters of various levels of importance in terms of their influence on aerodynamic behaviour. Some have been mentioned. Singled out as being of particular relevance to the subject matter of this Course are the three parameters of model shape and the Mach and Reynolds numbers. The wind tunnel test must reproduce closely the environment of flight in these and in other respects.

It is so obvious a requirement to correctly reproduce the shape of the aircraft that it might seem fair to question its inclusion in the above list. However the issue is not simple. The word shape is used here to include all geometric factors, some subtle in nature, which can influence the pattern of airflow around the model. Subtleties include surface finish, pressure tappings, small gaps through which air can or should flow, the deflections of parts of the model under load and the modification of the external flow by engine flows. A more obvious way in which a model can differ from the aircraft is any alteration to accommodate a

mechanical support. The alteration can take two forms: alteration of the shape of the model for the support, while the support itself can disturb airflow and interfere with the model, modifying its aerodynamic behaviour. Once the question of shape is examined in detail it is seen to become a complex issue.

Assuming that all else in a test is correct then reproducing the flight Mach number ensures that compressibility effects are modelled properly. Reproducing the Reynolds number should ensure proper modelling of viscous effects.

It is usual now to derive Reynolds number using dimensional analysis although Osborne Reynolds (Ref 12) used just physical reasoning to derive the group which is, with his symbols,

$$\frac{c\rho U}{\mu} \text{ ---- (1)}$$

where  $c$  is an appropriate length scale,  $\rho$ ,  $U$  and  $\mu$  are respectively fluid density, speed and viscosity.

It is common practice to evaluate Reynolds number in relation to aircraft by using the mean chord of the wing as the length scale  $c$ , while the fluid's properties are evaluated at its undisturbed state. For an aircraft in flight the appropriate state is the ambient air density and viscosity at that altitude, and the flight speed. In the tunnel test these properties are estimated from airflow measurements in the entrance region of the test section reasonably far upstream of the model, away from the strongest effects of its disturbances.

Table 1 allows comparisons between the requirements of cruising flight with the Reynolds number capabilities of tunnels each side of the Atlantic. A representative selection of transport aircraft is shown. They all cruise in the Mach number band 0.7 to 0.9. It is apparent that flight requirements are above tunnel capability by large factors, a

Table 1. Reynolds numbers of a variety of aircraft and projects of the 1960's compared with the capabilities of contemporary tunnels.

*Reynolds numbers (millions) based on wing mean chord and cruising flight:*

Boeing 737-200: 23.	Boeing 727-200: 38.
Airbus A300B: 41.	Lockheed L-1011: 49.
Lockheed C-141: 50.	DC 10-10: 54.
Lockheed C-5A: 63.	Boeing 747: 71.

*Transonic tunnel maximum capabilities for tests on complete transport aircraft models at Mach 0.9 in*

Europe:  
B.Ae. (Warton) 1.2m tunnel, DRA 8 foot, and ONERA Modane S1, ~8.5 millions  
the USA:  
typically NASA Ames 11' and AEDC 16T, ~10 millions.

situation which was only likely to get worse with the passage of time. Reynolds number needed to be raised to around 70 millions in the wind tunnel to match large transports in cruise, perhaps more to allow for future needs. Therefore about a ten-fold increase in capability was needed from the new facilities, bearing in mind the likelihood of long lifetimes.

As far as the speed requirement of the new tunnel was concerned it will be noticed that the band of cruising speed of the aircraft listed, as indicated by Mach number, is rather narrow. This is because for aircraft such as these, which are required to cruise efficiently, there is in effect a barrier inhibiting the use of slightly higher flight speeds. Of course this is not an absolute speed barrier but one of economics: drag rises sharply when Mach number is allowed to rise from these general levels.

The shortfall in Reynolds number needs to be linked with indications of some effects of Reynolds number on aerodynamic behaviour in order to begin to form a picture of possible consequences. The first examples are the classic cases of low speed flow around a circular cylinder and a sphere. In each case the pressure distribution and drag vary widely with Reynolds number, with particularly strong variations in one rather narrow Reynolds number band. Figure 1 shows empirical data on the dependence of drag, in its non-dimensional form drag coefficient, on Reynolds number. It is seen that the coefficient rises by a large factor on moving down through Reynolds numbers around  $10^5$ .

Clearly a test carried out at the wrong Reynolds number on a shape which had a similarly strong sensitivity to Reynolds number could yield very misleading results. Extrapolating

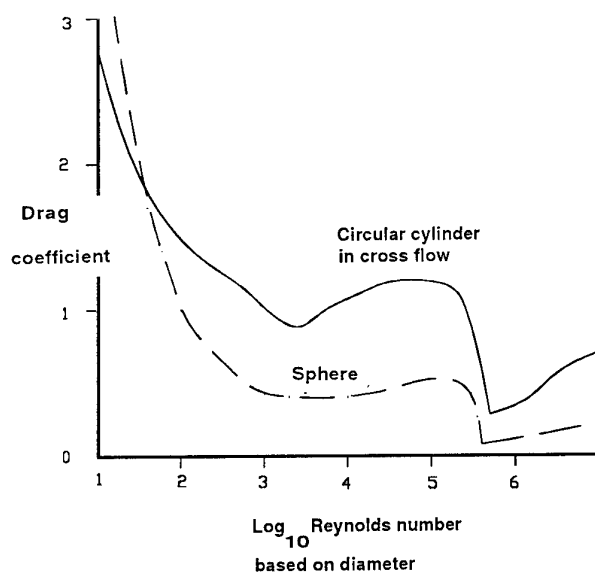


Fig 1. Drag coefficients of a sphere and circular cylinder in cross flow. Reynolds number is based on diameter.

data which was obtained in one range of Reynolds number for use at another can be unsafe. Examples of flows around aircraft which have a general similarity to that of a cylinder in cross flow include high incidence flows around rear fuselages of almost any aircraft and across the noses of fighters, and flows across undercarriage components.

The next three examples relate to two-dimensional aerofoil tests. Figure 2 shows lift coefficient for one section as a function of angle of incidence, measured at two values of Reynolds number at low speeds. At low incidences there is little difference between the two data sets. However the maximum lift coefficient is very sensitive to Reynolds number.

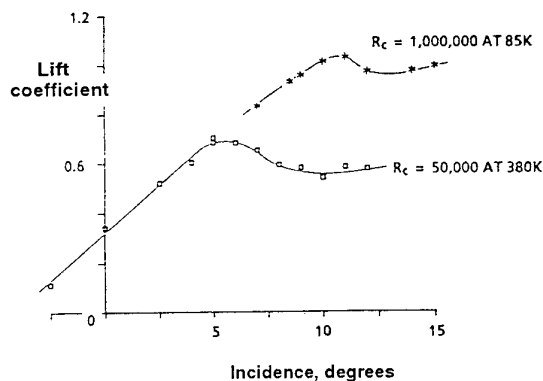


Fig 2. Illustration of the sensitivity of the maximum lift of an aerofoil to Reynolds number.

Therefore the dependence on Reynolds number varies from little to large depending on incidence, but the importance of using the correct Reynolds number for the correct overall picture is very apparent. The Reynolds numbers in this

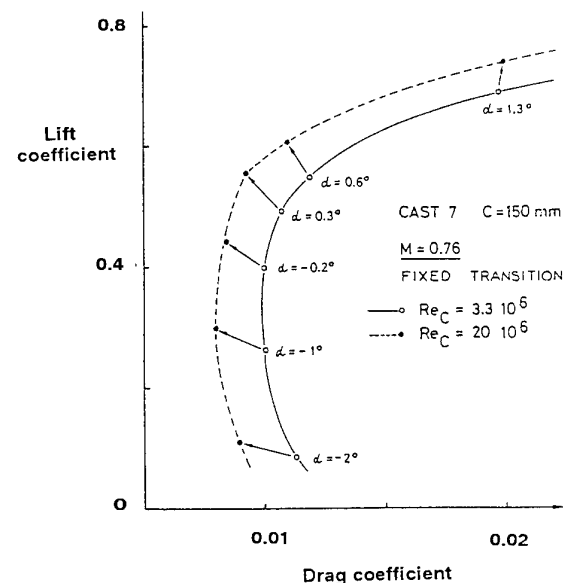


Fig 3. Polars from transonic aerofoil tests showing Reynolds number effects on lift and drag.

example are very low for the flight of normal aircraft although the higher value, 1 million, corresponds roughly to that of a glider's wing at stalling speed. There is plenty of empirical evidence showing that maximum lift coefficient can continue to rise (Refs 13-15) with further increase in Reynolds number.

Figure 3 shows experimental data, taken by ONERA (Ref 16) in a cryogenic wind tunnel which will be described in a later lecture, for an aerofoil section at Mach 0.76. Lift and drag coefficients are shown as functions of angle of incidence for two values of Reynolds number. The lower value is typical of those used in much aerodynamic testing in the past. The higher value approaches those experienced in some transport aircraft. Through the incidence range there is seen to be a varying dependence of lift and drag (in magnitude and sign) on Reynolds number, effects large and different enough to be of definite concern to planemakers. One measure of the aerodynamic effect of change of Reynolds number is the ratio of lift to drag. The maximum values differ by about 28% in this case.

Finally an example of Reynolds number effects in data taken by NASA in their 0.3m Transonic Cryogenic Tunnel (Ref 17) on an aft-loaded section also over a band of Reynolds numbers spanning those attainable in conventional tunnels and, in this case, the flight of a fairly large aircraft. Near the design Mach number and lift coefficient the drag coefficient is shown to decrease by about 18% on raising Reynolds number from about 7 millions to about 48 millions, with the trend evidently continuing.

In summary, the evidence available to aerodynamicists on Reynolds number effects, derived from wind tunnel tests such as in the examples above and also from tunnel-flight comparisons, led the wind tunnel community to seek new generations of tunnel which could solve the problem. They were uneasy making such large extrapolations and corrections as typified by these examples. The disparity in Reynolds number was greatest for large transonic transports because of their size and speed. When the needs of all types of aerospace products are taken into account, the speed range of concern could extend from the low range associated with takeoff and landing, upwards at least to supersonic flight. This range is covered by a variety of designs of wind tunnel, but there was a firm opinion held that the need for bridging the Reynolds number gap was felt most strongly in the aerodynamics of flight at transonic speeds. Therefore attention became focused on the search for a high Reynolds number transonic wind tunnel. According to the data in table 1 and the discussion following, the need was for roughly a tenfold increase in the highest wind tunnel Reynolds number capability in order to cover anticipated flight values. Some designs of tunnel which were receiving serious consideration before the emergence of the cryogenic option in the early 1970's are now reviewed, partly to highlight some of the appeal of the cryogenic tunnel but also to remind researchers of what they might now have been preparing to use, in other circumstances, for their high Reynolds number tests.

### 3. Raising Reynolds number by conventional methods

The shortfall in Reynolds number can be bridged in several ways. Equation (1) shows that the options for change are through the properties of the test gas, namely its density, speed or viscosity, and by changing  $c$  the length scale of the model. The options are made clearer in the context of aerodynamic testing by substituting

(i) for density using the ideal gas equation of state

$$\rho = \frac{P}{RT} = \frac{Pm}{R_0 T} \text{ ----- (2)}$$

where  $P$  and  $T$  are the reference static pressure and temperature of the test gas,  $R$  and  $R_0$  are the particular and universal gas constants respectively and  $m$  is the mean molecular weight,

(ii) for the velocity  $U$  as the product Mach number and speed of sound now written for convenience as

$$U = Ma = M \sqrt{\gamma R_0 \frac{T}{m}} \text{ ----- (3)}$$

where  $\gamma$  is the ratio of specific heats and  $a$  the speed of sound,

(iii) finally for the viscosity of the gas as a function of temperature  $\mu(T)$ .

These are combined in (1) to give

$$\text{Reynolds number } Re = \frac{Pm}{\mu(T)} \sqrt{\frac{m\gamma}{R_0 T}} \text{ ----- (4)}$$

an expression which shows all options available for influencing Reynolds number.

First consider increasing  $c$  by using larger complete models, with the same wind tunnel gas properties as at present. As the model cannot be increased in size significantly relative to the tunnel, in order to satisfy the Reynolds number needs established in section 2 both the model and tunnel would be scaled up linearly by a factor of 10 relative to the largest existing transonic tunnels. Implications in terms of costs are immediately available. Firstly tunnel fan drive power. To a first order the power is proportional to the flux of kinetic energy in the air passing through the test section

$$\text{Power} = \lambda \frac{1}{2} \rho U^3 A \text{ ----- (5)}$$

where  $A$  is the flow area of the test section,  $U$  and  $\rho$  are flow reference values of velocity and density, and  $\lambda$  is an empirically determined proportionality factor usually in the region of 1/3. Similar substitutions in this expression may be made giving

$$\text{Power} = \frac{\lambda}{2} P m^3 \gamma^{1.5} \sqrt{\frac{R_0 T}{m}} A \text{ ----- (6)}$$

A tunnel 10 times larger than the largest would have a flow area  $A$  100 times larger and absorb 100 times the power.

This becomes around 20 million horsepower.

Secondly the cost of the shell of the tunnel. Various sources relate the cost approximately to its surface area which again varies as the square of the scale. Therefore the two major components of capital cost, motors and structure, would be higher by a factor of around 100 than the largest transonic wind tunnels. Further considerations would be the time and cost of making models upwards of 100ft, 30m span.

Difficulties are apparent.

The expressions for Reynolds number (1) and power (5) show each increasing in proportion to density. One way of raising density is by pressurisation, an idea probably first published by Margoulis (Refs 4,5) and put into practice by Munk (Ref 18). A tunnel providing full scale Reynolds number would have to withstand a pressure differential of more than 10 atmospheres and therefore would be expensive. However the indications are that this might be a more economical option than that of just increasing size, partly because, from (6), pressurisation would raise the drive power by a factor of only 10 compared with existing wind tunnels.

The aerodynamic loads acting on a model in a particular attitude relative to the airflow vary to a first order with the dynamic pressure  $q = \frac{1}{2} \rho U^2$  which increases directly with pressure. Models of transport aircraft can experience very high loads when tested at transonic speeds as was established in section 1, dominated by the lift force component. Opinions vary, but studies (Refs 7,19) have set the maximum stagnation pressure at around 6 atmospheres for complete models of transport aircraft, the limit being influenced also by considerations of the size of the model's support sting. Existing high Reynolds number tunnels operate at 1 atmosphere or above, therefore it was not possible to advocate increased pressure alone to bridge the Reynolds number gap. When confined to using normal air temperatures, moderately higher pressure must be combined with increased size. Within these constraints the tunnel would have a test section about 40 feet, 12m across, operate at up to 6 atmospheres stagnation pressure and for transonic speeds would require about 3 million horsepower for its fan.

The costs, capital and running, were still too high to contemplate and the designers resorted to compromise. Among the options for economy were (additional to the use of alternative gases), designing for values of Reynolds numbers below full scale and the use of a variety of different tunnel drive systems all exploiting intermittent operation of the tunnel in contrast to the continuous operation available with a motor driven fan. The latter compromises are now discussed briefly.

The temptation to design for sub-full-scale Reynolds numbers was strong because with the other factors held constant the power and construction costs vary strongly with the targeted Reynolds number (Ref 20). Engineers studied the possibility of aiming low because of the rewards for even modest reductions, and came up with justifications. Both in the USA and Europe the targeted Reynolds number based on mean-wing-chord was set at around 40 millions

(Refs 7,21), low by a factor of about 2 compared with the full scale requirements even of large contemporary aircraft, and by a larger but unknown factor in relation to future needs. A supporting argument was that the variation of aerodynamic performance at Reynolds numbers beyond these compromise values would be small, systematic and predictable.

Wind tunnel capital costs can be further reduced if the run-time is restricted. Opinions were again divided but the consensus was that times of 2 to 10 seconds were adequate. The tunnel would then remain idle for a period before another run, for example to allow compressed air to be stored. These run-time and Reynolds number figures were adopted and quite a variety of design schemes emerged under this influence on both sides of the Atlantic (Refs 8-10,22-29). These included various drive schemes including induction, blowdown, the Ludweig tube, hydraulics and more. Just two are selected for illustration and brief description in order to show what might have been in use if cryogenics had not come along.

The projects shared an operating envelope like that shown on figure 4, because of an almost-common specification. In constructing this figure it has been assumed that the minimum operating pressure would have been atmospheric although technically it could have been lower in some designs.

The highest Reynolds number boundary on the figure is given by the maximum pressure, 6 atmospheres in this example. This envelope boundary would extend across to the maximum Mach number of the wind tunnel, here 1.4, had sufficient power been available. The peak power demand is in the top right corner. The minimum Mach number might be set by fan speed or difficulties in resolving small forces or pressures. Lines of constant dynamic pressure  $q$  are superimposed, along with broad arrows showing examples of two test sweeps which are possible with this type of tunnel. One, Y, at constant Mach number where Reynolds number is varied, is aimed at showing

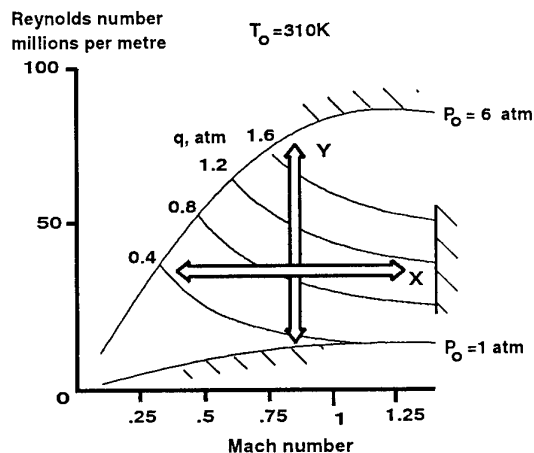


Figure 4. A representative operating envelope of the normal temperature pressure tunnels being considered before the advent of the cryogenic wind tunnel.

Reynolds number effects, while sweep X is intended to show just Mach number effects. In both cases the arrows cross iso-dynamic-pressure lines showing variations of aerodynamic load with the possibility that varied aeroelastic distortion of the model might corrupt its aerodynamic performance.

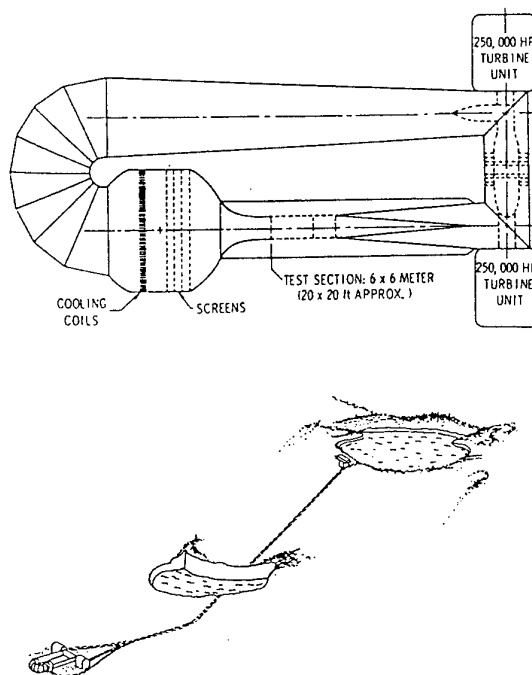


Figure 5. A NASA project where the power demands of the large tunnel would be met hydraulically by a pumped storage scheme.

Figure 5 is a sketch of one NASA normal-temperature project (Ref 8) of the early 1970's. An outline of the tunnel, comprising a closed circuit around which the pressurised air would be driven by a fan, is in the upper half of the figure. This was a transonic tunnel project for speeds up to just over the speed of sound and the tunnel demanded considerable drive power for the fan. Two motors are shown totalling half a million horsepower. Usually electric motors are used in fan-driven tunnels but in this project it was proposed to avoid the cost of building and feeding such large motors and instead site the tunnel in the mountainous region of West Virginia where a pumped water storage scheme could be built to supply hydraulic turbines coupled to the fans. In the site layout, below, the wind tunnel is on the left. The tunnel operators would drain water relatively quickly during a run, then smaller electric motors would pump back the water over a much longer period. Altogether this was a large mechanical and civil engineering project, but capable only of reaching the compromise value of Reynolds number.

An example of a European project of the same era (Refs 28,29) is shown on figure 6. For capital economy this project used the Ludweig Tube principle, in which stored compressed air, approximately at normal temperature in this case, is released by a quick-acting valve to flow for a period through the test section. The tunnel also would have reached

the compromise Reynolds number for a 10 second run. Its most striking feature is its length: over 2½ miles, 4.1 km.

There were many other design schemes but these two will serve as illustrations. Quite clearly the capital costs of such projects were high but it is almost certain that two would have been built. Agreement to proceed was close when the successful demonstration of the small cryogenic wind tunnel (Ref 2) introduced the alternative method of raising Reynolds number, avoiding the need to build these very large conventional temperature tunnels. In the intervening years the cryogenic wind tunnel has been further researched, then brought into mainstream transonic aerodynamic testing with, in the cases of the largest facilities, Reynolds number capabilities somewhat above those of the normal temperature alternate schemes which they have displaced.

#### 4. Cryogenic wind tunnels - introduction.

The cryogenic wind tunnel emerged because of the powerful effect of air temperature on Reynolds number. The relevant background comprises the early studies by Margoulis and Smelt (Refs 4-6), and the mix of experimental/theoretical cryogenic tunnel project work at NASA Langley Research Center in 1971/2. An incubation period spanning 50 years.

Cooling the test gas raises its density and reduces its viscosity, both of which contribute to an increase in Reynolds number as is clear from equation (1). In the case of transonic testing we are not free to change Mach number in assessing the effect of temperature. Probably this is also true in typical low speed testing in aeronautics. This restraint results in the velocity of the gas varying as the square root of temperature which, on cooling, is an effect which reduces Reynolds number.

Smelt carried out a comprehensive review of the effects of temperature and choice of test gas and showed in some cases very substantial advantages in terms of tunnel size and drive power. From among the diatomic gases cryogenic hydrogen showed the best promise with a size of 6.3% and a power demand of 0.5% of a normal temperature air tunnel. Aside from any safety issues, the use of hydrogen gas is now judged questionable because of a real-gas behaviour rather far removed from the nearly ideal-gas behaviour of atmospheric air (Ref 30).

The best of the remaining diatomic gases for use in a cryogenic wind tunnel are nitrogen, carbon monoxide and air, offering tunnel sizes in the order of 25% to 30% of that of normal temperature air. Because of the small differences

the choice of working fluid is dictated by practical issues and the most commonly used working fluid has become nitrogen.

In comparing the cryogenic wind tunnel with conventional tunnels it is useful to take the Reynolds number expression (4) a stage further with the approximation that viscosity varies with temperature according to

$$\mu \propto T^n \text{ ----- (7)}$$

where for nitrogen  $n \approx 0.9$ . Adopting this value and omitting constants

$$\text{Reynolds number} \propto \frac{1}{T^{1.4}} \text{ ----- (8)}$$

for particular values of Mach number and pressure. This shows more clearly the effect of temperature on Reynolds number and is illustrated on figure 7.

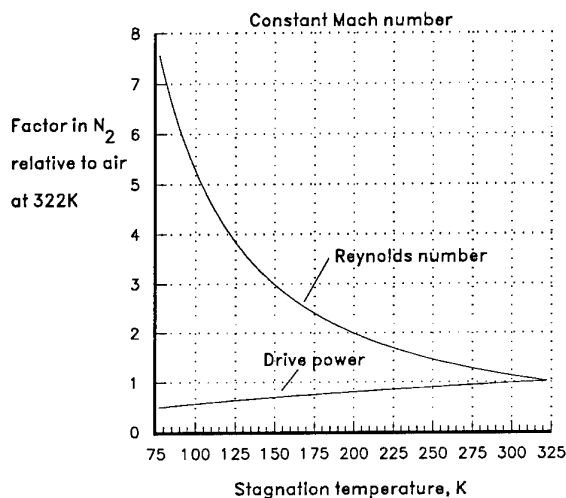


Figure 7. The influence of temperature on the test Reynolds number and tunnel drive power in a nitrogen wind tunnel compared with air at a normal temperature.

Also shown on this figure is tunnel drive power which, from (6), actually falls in these circumstances with the increase in Reynolds number. Not shown is that dynamic pressure is invariant as is clear from its expression  $q = \frac{1}{2} \rho U^2 = \frac{1}{2} \gamma P M^2$ . This is an example of one important aerodynamic parameter,

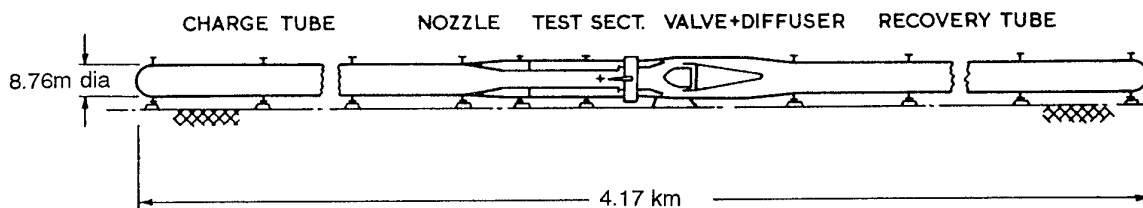


Figure 6. A European proposal for reaching full-scale Reynolds number at normal temperature

in this case the Reynolds number, being varied over a wide range by means of a change in temperature while both Mach number and dynamic pressure both are constant, a test not possible in a normal temperature variable pressure tunnel. The curves on figure 7 are taken down to 77K but the question arises immediately as to the minimum permissible operating temperature because of the advantageous slopes of both curves at low temperature. One limit is set by the need to avoid any effects of liquefaction of the test gas. The equilibrium saturation boundary is first reached at the point in the tunnel where the pressure and temperature are lowest. While this could be in the region of the fan inlet or over its rotor blades, the prime concern is condensation affecting the model. The saturation boundary is reached first where the Mach number is locally the highest which will be somewhere close to the model's surface, likely regions being the outer edge of a boundary layer or close to the core of a vortex. Take for example a test at about Mach 1. The highest local Mach number probably would not exceed about 1.7 and for this example the minimum pressure existing in a tunnel operating at 1 atmosphere stagnation pressure would be about 0.2 atmospheres. Figure 8 is the saturation curve for nitrogen from which it is seen that a minimum static temperature of 66K is permissible. This leads to a minimum stagnation temperature of 104K for such a test.

From figure 7 it is seen that at 104K the Reynolds number advantage in comparison with normal tunnels is about 5, an advantage insufficient in itself to satisfy the needs of the high Reynolds number transonic wind tunnel. It is still necessary to use elevated pressure. For the test conditions adopted in the paragraph above and the stagnation pressure limit of 6 atmospheres the minimum stagnation temperature becomes 125K where the Reynolds number advantage attributable to low temperature reduces to 3.8. More generally applicable data is that shown on figure 9 where the minimum useable temperature (giving the maximum Reynolds number) is shown as a function of the local maximum Mach number and stagnation pressure.

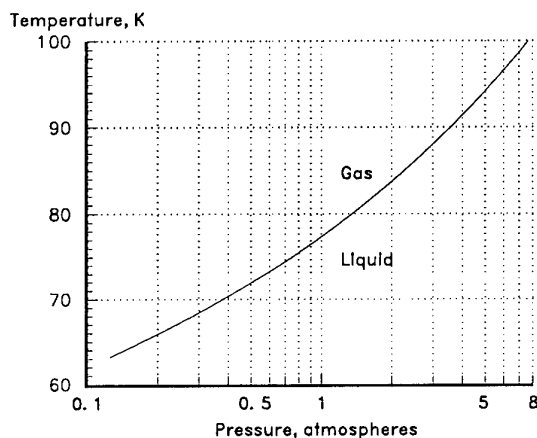


Figure 8. The liquid-gas saturation curve for nitrogen.

The impact of the smaller factor, 3.8, on the full-scale Reynolds number tunnel discussed in section 3 is still quite profound: the required size of the test section is reduced to

about 10.8ft, 3.3m, smaller than many existing high speed tunnels. The full scale Reynolds number transonic tunnel was no longer necessarily an impossibly large tunnel.

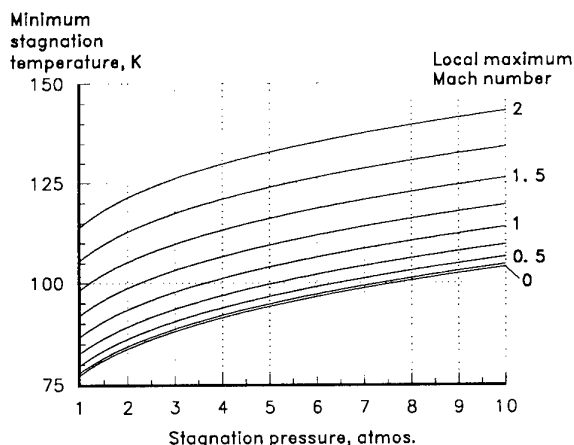


Figure 9. The minimum operating temperature of a cryogenic nitrogen tunnel set by isentropic expansion of the gas from stagnation conditions to the local minimum pressure/maximum Mach number.

Following the demonstration of the low speed atmospheric pressure cryogenic wind tunnel and the associated studies NASA immediately constructed the 0.3-meter Transonic Cryogenic Tunnel, an excellent wind tunnel which quickly yielded some very important experimental results. Among these were demonstrations (Refs 31,32) that the flow could in some circumstances be taken over the saturation boundary leading to supercooling. On occasion the tunnel could be operated with the saturation point being reached in the free stream ahead of the model without affecting performance to any detectable extent. The advantages in terms of Reynolds number, drive power and operating cost were predicted to be up to 22%.

Further, it was also almost immediately realised that the cryogenic wind tunnel offered a unique testing capability. The cryogenic pressure tunnel can be considered to have the three controllable parameters of speed, pressure and temperature. These are each variable over a usefully wide range and can be used to control independently the test Mach number, Reynolds number and dynamic pressure. This versatility is not available in any other tunnel. The significance is that for a model in a given attitude, each of these parameters can affect aerodynamic performance (through Mach number, Reynolds number or aeroelastic effects) but the cryogenic pressure tunnel allows each to be independently varied and their individual effects determined.

As any new high Reynolds number transonic wind tunnel would be required to set new standards in terms of the test environment, this unique test feature of the cryogenic pressure tunnel may have been decisive in its adoption as the preferred solution.



## 5. Operating envelopes for cryogenic wind tunnels.

### 5.1 Atmospheric-pressure cryogenic tunnels.

Guidelines for the minimum operating temperature of a cryogenic nitrogen tunnel have now been established. The maximum temperature is probably unimportant but will depend on the cooling method used near room temperature, the power of the tunnel and the temperature tolerance of its structure and is usually somewhat above ambient. In the general charts which follow a fixed maximum of 310K has been assumed as being fairly representative of maximum temperatures attained in typical tunnels over a wide band of Mach number.

The first chart shows the operating envelope of a subsonic cryogenic wind tunnel designed to operate only at ambient stagnation pressure. The chart, figure 10, applies to the original cryogenic wind tunnel (Refs 2,33,34) as well as to several current types (Ref 35) in most respects except coverage of Mach number. Unit Reynolds number is shown as a function of Mach number for the available temperature range using a nitrogen test gas.

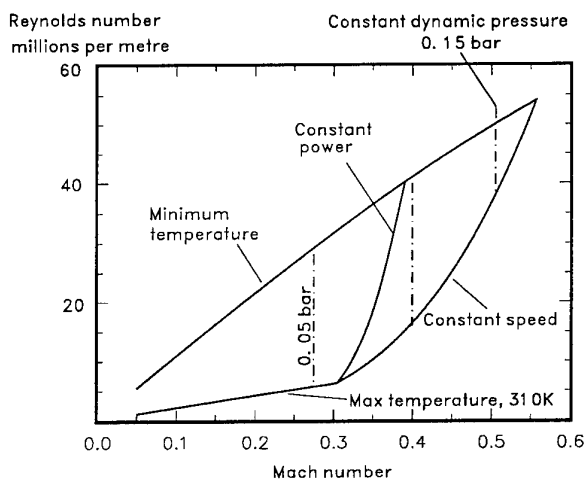


Figure 10. The operating envelope of subsonic cryogenic nitrogen wind tunnels operating at atmospheric pressure.

Lines of constant dynamic pressure are superimposed at intervals of 0.05 bar and are seen to be vertical which shows that traverses may be made in Reynolds number at constant Mach number without affecting dynamic pressure or therefore, to a first order for a model at fixed attitude, affecting aerodynamic loads and therefore model shape. A traverse at constant Reynolds number does involve variations of dynamic pressure. However they are less than experienced in normal temperature pressure tunnels. At Mach 0.3 the derivative  $\partial q/\partial M = 0.375$  bar in the ambient pressure cryogenic wind tunnel at all available Reynolds numbers. The derivative is about half of that which would exist in normal temperature pressure tunnels at similar conditions. In the latter case, for example at Mach 0.3 and a unit Reynolds number of 20 millions per metre, the derivative is 0.62 bar.

Two of the boundaries comprise the maximum temperature (310K stagnation) and a minimum temperature which here is set at 95.7K by reaching saturation in an isentropic expansion to Mach 1.4 which is a representative local high Mach number for subsonic testing. With this type of wind tunnel a variety of factors can restrict the right-hand boundary, depending on how the tunnel is driven and what limits speed. Arbitrary examples are shown here, of power and fan rotational speed limits for the case of a motor and fan drive.

Figures 2 and 10 serve to highlight another feature of the atmospheric pressure cryogenic wind tunnel, that is the wide dynamic range of Reynolds number which is available without change of model. The data of figure 2 was taken in such a tunnel and the ratio of maximum to minimum Reynolds number is seen to be 20:1 in this example. This is rather a wide range, obtained by combining the useable band of airspeed, similar to that available in any wind tunnel, with the effects of change of temperature. In the case of a fan-driven tunnel the speed band is determined by the maximum speed of the fan and the minimum practical dynamic pressure at which aerodynamic data can be obtained with acceptable resolution. The ratio of maximum to minimum Reynolds number given by this band is multiplied in the case of the cryogenic wind tunnel by the ratio of maximum to minimum Reynolds number conferred by change of temperature, which is the temperature-dependent factor shown on figure 7.

### 5.2 The cryogenic pressure tunnel.

This tunnel is more complex because of the pressure variable and therefore it is regarded as having an operating volume. A universal operating volume may be constructed in the form of a three-dimensional figure having axes of test dynamic pressure, Mach number and Reynolds number. This is shown on figure 11 for nitrogen. It has six faces and is drawn for the following operational limits:

- stagnation pressure range 1 to 6 atmospheres. The minimum pressure in a cryogenic tunnel is limited to about 1 atmosphere by the frequent need to exhaust gas from the tunnel and it is convenient, in that it saves on plant costs, to have the tunnel at least slightly pressurised,
- Mach numbers 0.2 to 1.4. This represents typically the range covered by transonic wind tunnels,
- temperatures from 310K to the minimum reached in isentropic expansions to local Mach numbers varying from 1.4 to 1.85 depending on free stream Mach number according to the "High maximum local Mach number" on figure 3 of reference 33.

The viewpoint of the operating volume on figure 11 places a vertical Mach 1.4 plane close to the reader and the vertical Mach 0.2 plane at the far end. The left and right vertical boundaries are curved in single curvature and represent tunnel operation at stagnation pressures of 1 and 6 atmospheres respectively. The remaining boundaries at the top and bottom represent the minimum temperature and 310K stagnation temperature respectively. The tunnel may

be operated anywhere inside the volume which serves to highlight the freedom to vary test parameters in isolation or, if desired, in combination to follow a flight locus. There is particular freedom for manoeuvre within the volume at the higher Mach numbers, say 0.5 upwards. The top right corner of the volume will be clipped in the case of a power-limited fan driven tunnel.

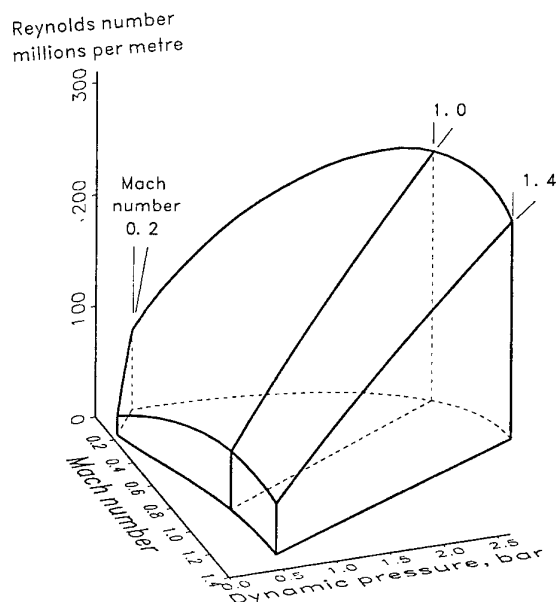


Figure 11. The generalised operating volume of a transonic cryogenic pressure tunnel.

The point on the operating volume, figure 11, where the maximum unit Reynolds number is reached is not clear. It can be seen to lie on the minimum temperature/maximum pressure line but at an indistinct Mach number. In the case of constant stagnation pressure and temperature the product  $\rho U$  in the Reynolds number expression, equation (1), is a maximum precisely at Mach 1 as in nozzle flow. However the viscosity is falling steadily with increase of Mach number and this postpones the peak in the value of unit Reynolds number  $\rho U/\mu$  to a Mach number above 1. From (4) and for a given gas the Reynolds number varies with Mach number as

$$Re \propto M \left( 1 + \frac{\gamma-1}{2} M^2 \right)^{\frac{n-\gamma+1}{2(\gamma-1)}}$$

where  $n$  is the index in the temperature-viscosity relationship equation (7). For diatomic gases and  $n=0.9$  this reduces to

$$Re \propto \frac{M}{(1+0.2M^2)^{2.1}}$$

which, on differentiation, shows a maximum unit Reynolds number at Mach 1.25.

## 6 COOLING THE CRYOGENIC WIND TUNNEL

While mechanical refrigeration to the desired temperatures is possible in principle, the plant costs are too high. In place of this method there appear to be two other methods available for cooling a wind tunnel, each intermittent in its own way.

One is the near-isentropic expansion of a gas from high pressure storage to the test stagnation pressure. Demonstrations have shown that cryogenic temperatures can be reached at expansion pressure ratios above about 20:1 (Refs 36-38).

The second and most common method comprises cooling by means of injecting liquid nitrogen  $LN_2$  directly into the circuit as a coolant which then becomes also part or all of the test gas. Nitrogen is used because it is relatively cheap and has low levels of contaminants. This cooling method is also intermittent in that the liquid is produced in continuously-running plant, stored and used relatively rapidly during wind tunnel tests.

The liquid, on evaporating in the tunnel, cools by latent and sensible heat absorption and on doing so reduces or displaces, for induced flow or fan-driven tunnels respectively, the air contents of the tunnel circuit. This reduces or removes oxygen,  $CO_2$  and water vapour with advantage in each case. The cooling capacity of  $LN_2$  is well established (Ref 39) and is dissipated in several ways. There is a requirement to absorb fan power or, in the case of the induced flow tunnel, to cool the inducing air. There is also the need to account for cooling at least a proportion of the tunnel structure, the proportion depending on the thermal insulation scheme and on run time. The exchange rate, expressed as the ratio of the mass of  $LN_2$  to mass of cooled structure, in cooling from 300K to 100K is about 0.25 for steels.

Additional coolant is required to absorb heat inflow through the thermal insulation. The quantity required is strongly design-dependent and it is difficult to provide very general information. However the proportion of  $LN_2$  consumption quoted as attributable to heat inflow ranges from 1½% up to 10% of the total  $LN_2$  flow under typical steady running conditions at 100K.

While the requirements of a cryogenic wind tunnel for coolant and therefore cooling power depend on its design and operating cycle, studies have shown that the total energy consumption of a well insulated fan driven cryogenic wind tunnel (taking into account fan drive power and the power to generate the  $LN_2$ ) is appreciably less than that required for a conventional tunnel compared on the basis of equal pressure, Mach and Reynolds numbers. Other factors in determining the coolant costs are the times required to get the tunnel to an operating condition and be held there during a test, which are pointers to the need for efficient operating procedures, instrumentation and controls.

The exhausting gas needs careful treatment except perhaps for the smallest tunnels where all that may be required is to exhaust outdoors away from people. Pure nitrogen gas must

not be allowed to accumulate as could easily happen if the cold gas was simply allowed to discharge at ground level. Typically in large tunnels the cold gas is mixed with air in a ratio which renders the mixture very safe in terms of oxygen content while warming it to reduce the tendency of the plume to fall. The mixture is discharged to the atmosphere (from whence it came in the liquefaction plant) using a chimney.

## 7 REAL GAS EFFECTS

Analyses of flows and the test data from wind tunnels usually assume the working fluid to behave as a perfect gas, that is one obeying the equation of state for an ideal gas while having constant specific heats. Examples of departures from perfect gas behaviour are: (1) a thermal imperfection where, in the equation of state  $PV = ZRT$ , the compressibility factor  $Z$  is not unity ( $V$ =specific volume), (2) a caloric imperfection where the ratio of specific heats  $\gamma$  departs from the ideal diatomic gas value of 1.4.

Each varies several percent from its value at room temperature for the ranges of pressure and temperature experienced in cryogenic wind tunnels. These were thought to introduce more stringent restrictions to operating temperatures than set by liquefaction (Refs 2,33) in a tunnel required to behave as air at room temperature. The effects were examined by Kilgore, Adcock, Albone and Johnson (Refs 34,40-43), analytically and by experiment in the 0.3m Transonic Cryogenic Tunnel. Representative isentropic, shock and boundary layer flows were studied. The conclusion was that a cryogenic wind tunnel can be operated at conditions very close to saturation without these real gas effects becoming apparent, a very useful discovery.

Another real gas effect is condensation, mentioned already in connection with the choice of operating temperature.

## 8 REVIEW

The aim of this final section is to describe some of the broad impacts which cryogenic operation has on tunnels with drives other than the fan, and to highlight some general reference sources. Cryogenic techniques might be applied to most types of tunnel drive, for all speeds up to supersonic, with a view to raising unit Reynolds number and in most cases there are authoritative accounts in lectures to follow. The hypersonic tunnel is an inappropriate application of cryogenic technology because of the low static temperature which already exists in the test section under normal circumstances.

The Cryogenic Ludweig Tube. A reduction of the temperature of the gas stored in the Ludweig Tube results in increases both of Reynolds number and run time. Run time varies approximately inversely with  $\sqrt{T_0}$ . The permissible temperature reductions from normal are modified by the reduction of stagnation temperature which occurs during the passage of the expansion wave along the tube, a feature of this tunnel drive. Model precooling generally would be required. By injecting a cryogenic fluid directly into the tube for the purpose of cooling, the pressure recharging process might be simplified and

shortened.

The Cryogenic Induced-Flow Tunnel. The cryogenic mode of operation is applicable to the closed-circuit induced-flow facility. The inducing gas must be cooled in order to maintain a constant test temperature. Precooling of the model could be carried out simultaneously with the tunnel, depending on the design and method of operation of the tunnel (but please note the different technique used by ONERA and described later). If a test in air was deemed desirable then suitable proportions of liquid oxygen and  $LN_2$  could be evaporated within the circuit or inducing airstream.

The Cryogenic Blowdown Tunnel. One mode of operation of this tunnel might be to store air at normal temperature, to precool the model, and during a run to hold a constant test temperature by injecting and evaporating coolant in the region of the settling chamber. As an example of some of the changes to facility design which would result from operation at cryogenic temperatures, a comparison can be made between a normal-temperature blowdown-tunnel and an equivalent cryogenic tunnel which operates at the same Reynolds number, stagnation pressure (3 atmospheres) and transonic Mach number. The test section of the cryogenic tunnel would be about 24% of the size of that for the normal tunnel when designed for the minimum practical temperature in a nitrogen-air mix. When operating from the same-sized air storage bottles the cryogenic tunnel would run 20 times as long. However the consumption of  $LN_2$  is high, comprising almost half of the gas flow rate through the test section, and therefore this type of tunnel must be considered only for intermittent operation.

To close, I recommend references 35,44 and 45 as sources which the reader might consult for more detailed and specialised information on cryogenic wind tunnel and related technologies, in many cases the citations supplementing the material of this Course.

## 9 REFERENCES

1. Allen, J.E. "The Future of Aeronautics - Dreams and Realities." *The Aeronautical Journal*, Vol 75, No 729, pp587-609, September 1971.
2. Goodyer, M.J., Kilgore, R.A. "The high Reynolds number cryogenic wind tunnel." *AIAA paper 72-995*, 7th Aerodynamic Testing Conference, September 1972.
3. Pozniak, O.M. "Investigation into the use of Freon 12 as a working medium in a high speed wind-tunnel." *College of Aeronautics Note 72*, 1957.
4. Margoulis, W. "Nouvelle Methode d'essai de Modeles en Souffleries Aerodynamiques." *Comptes Rendus Acad Sci.*, vol 171, 1920.
5. Margoulis, W. "A new method of testing models in wind tunnels." *NACA TN-52*, 1921.
6. Smelt, R. "Power economy in high speed wind tunnels by the choice of working fluid and temperature." *R.A.E Report Aero 2081*, 1945.

7. LaWs Working Group. "The need for large wind-tunnels in Europe." AGARD Advisory Report 60, December 1972.
8. Baals, D.D., Stokes, G.M. "A facility concept for high Reynolds number testing at transonic speeds." Paper 28, Facilities and techniques for aerodynamic testing at transonic speeds and high Reynolds number. AGARD CP 83, 1971.
9. Whitfield, J D. et al. "Higher Reynolds Number Transonic Tunnels - Blowdown or Ludweig Tube?" Paper 29, AGARD CP83, April 1971.
10. Schueler, C.J. "Experimental studies in a Ludweig tube transonic tunnel." AGARD Report 615, December 1973.
11. R. T. Jones. "Highlights from the history of airfoil development." Sport Aviation, June 1978.
12. Reynolds O. "An experimental investigation of the circumstances which determine whether the motion of water shall be direct or sinuous, and the law of resistance in parallel channels." The Philosophical Transactions of the Royal Society, 1883.
13. Abbott, I. H. and Von Doenhoff, A. E. "Theory of wing sections." Dover, 1959.
14. J. L. Jones. "Problems of flow simulation in wind tunnels." AIAA paper 69-660, June 1969.
15. Hoerner, B. "Fluid dynamic lift." Hoerner Fluid Dynamics.
16. Dor, J-B. "The T2 cryogenic induction tunnel in Toulouse." Paper 9, Special Course on cryogenic technology for wind tunnel testing, AGARD Report no. 722, 1985.
17. Jenkins, R V. "Reynolds Number Tests of an NPL 9510 Airfoil in the Langley 0.3-Meter Transonic Cryogenic Tunnel." NASA TM 85663, 1983.
18. Munk, M.M., Miller, E.W. "The Variable-Density Wind Tunnel of the National Advisory Committee for Aeronautics." NACA TR 227, 1926.
19. Evans, J.Y.G., Taylor, C.R. "Some factors relevant to the simulation of full-scale flows in model tests and to the specification of new high Reynolds number transonic testing." Paper 31 in AGARD CP 83, 1971.
20. Heppe, R.R., O'Laughlin, B.D., Celniker, L. "New Aeronautical Facilities-We Need Them Now." Aeronautics and Astronautics, March 1968, AIAA.
21. Igoe W. B., Baals D. D. "Reynolds number requirements for valid testing at transonic speeds." Paper 5-1, AGARD Cp 83, April 1971.
22. Agard report number 603. "Aerodynamic test simulation: lessons from the past and future prospects." Editor J.Lukasiewicz. December 1972.
23. "Facilities and techniques for aerodynamic testing at transonic speeds and high Reynolds number." AGARD CP 83, Göttingen, 1971.
24. Schueler, C.J. "Experimental studies in a Ludweig tube tunnel. Paper 3, Large Windtunnels: Required Characteristics and the Performance of Various Types of Transonic Facility." AGARD-R-615, 1974.
25. Nelander, C., Overby, B. "Application of the gasometer storage concept to a transonic windtunnel meeting the Laws specification." Paper 4, Large Windtunnels: Required Characteristics and the Performance of Various Types of Transonic Facility. AGARD-R-615, 1974.
26. Evans, J.Y.G. "A scheme for a quiet transonic flow suitable for model testing at a high Reynolds number." RAE Technical Report 71112, 1971.
27. Pugh, P.G., Beckett, W.A., Gell, T.G. "The ECT drive system : a demonstration of its practicability and utility." Paper 2, Windtunnel Design and Testing Techniques, AGARD-CP-174, 1976.
28. Ludweig, H., Grauer-Carstensen, H., Lorenz-Meyer, W. "Project study of a large European transonic Ludweig tube windtunnel." Paper 2, Problems of Wind Tunnel Design and Testing, AGARD Report R-600, 1973.
29. Ludweig, H., Grauer-Carstensen, H., Lorenz-Meyer, W. "The Ludweig tube - a proposal for a high Reynolds number transonic windtunnel." Paper 3, Windtunnel Design and Testing Techniques, AGARD-CP-174, 1976.
30. Haut, R.C. "Evaluation of Hydrogen as a Cryogenic Wind Tunnel Gas." NASA CR-145186, April 1977.
31. Hall, R.M., Ray, E.J. "Investigation of minimum operating temperatures for cryogenic wind tunnels." AIAA paper 76-89, 14th Aerospace Sciences Meeting, Washington, 1976.
32. Hall, R.M. "Studies of Condensation Effects on Airfoil Testing in the Langley 0.3 Meter Transonic Cryogenic Tunnel." NASA TP 2509, 1986.
33. Kilgore, R.A., Goodyer, M.J., Adcock, J.B., Davenport, E.E. "The cryogenic wind-tunnel concept for High Reynolds number testing." NASA TN D-7762, 1974.
34. Kilgore, R.A. "The Cryogenic Wind Tunnel for High Reynolds Number Testing." Southampton University, Ph.D. Thesis, 1974.
35. Kilgore, R.A. (editor). "CRYO Newsletter", PO Box 4006, Hampton, VA 23664-0006, U.S.A.
36. Stollery, J.L., Murthy, A.V. "An Intermittent High-Reynolds Number Wind Tunnel." Aeronautical

Quarterly, vol. 28, 1977.

37. Hutt, G.R., East, R.A. "Preliminary Studies of a Free Piston Expander for an Intermittent Cryogenic Wind Tunnel." Paper 8, First International Symposium on Cryogenic Wind Tunnels, Southampton University, 1979.

38. Edmundson, I.C. The generation of cryogenic temperatures by high pressure expansion." Paper 12, First International Symposium on Cryogenic Wind Tunnels, Southampton University, 1979.

39. Kilgore, R.A., Adcock, J.B. "Specific Cooling Capacity of Liquid Nitrogen." NASA TM-X-74015, 1977.

40. Adcock, J.B. "Real-Gas Effects Associated With One-Dimensional Transonic Flow of Cryogenic Nitrogen." NASA TN D-8274, 1976.

41. Albone, C.M. "An investigation into the real gas effects of cryogenic nitrogen in inviscid homentropic flow." Paper 17, First International Symposium on Cryogenic Wind Tunnels, Southampton University, 1979.

42. Adcock, J.B., Johnson, C.B. "A Theoretical Analysis of Simulated Transonic Boundary Layers in Cryogenic-Nitrogen Wind Tunnels." NASA TP-1631, 1980.

43. Johnson, C.B., Adcock, J.B. "Measurements of Recovery Temperature on an Airfoil in the Langley 0.3-m Transonic Cryogenic Tunnel." AIAA Thermophysics Conference, Palo Alto, June 1981.

44. Goodyer, M.J., "The Cryogenic Wind Tunnel." Progress in Aerospace Sciences, vol 29 no 3, 1992.

45. Tuttle, M.H., Kilgore, R.A., Moore, D.L. "Cryogenic Wind Tunnels. A Comprehensive, Annotated Bibliography." NASA TM 4273, 1991.

# CRYOGENIC ENGINEERING AND MATERIALS.

David. A. Wigley.  
Cryogenic, Marine and Materials Consultants Ltd  
17 Bassett Wood Drive, Bassett,  
Southampton, SO16 3PT, UK

## SUMMARY

The following aspects of cryogenic engineering and basic properties of materials are considered:

- The oxygen-nitrogen binary phase diagram and the formation of liquid oxygen in unsealed insulation systems.
- The large liquid/gas volume expansion and the dangers inherent in the pressure created in closed containers.
- Nucleate and film boiling in liquid nitrogen, the different heat transfer rates in between solid/liquid and solid/gas, operation of liquid nitrogen level sensors and of electric immersion heaters used to evaporate liquid nitrogen.
- Safe working practices for handling liquid nitrogen, the physiological effects of oxygen deficiency, anoxia and asphyxiation, the use of oxygen monitors, breathing apparatus, condensation clouds and nitrogen concentration, escape routes and victim rescue.
- The cause and avoidance of cold burns by good working practice and the use of protective clothing.
- Storage of liquid nitrogen and its transfer using bare and insulated transfer lines over long and short distances.
- Selection of materials for their LOX compatibility and for the avoidance of moisture desorption.
- Thermal contraction of metals and non-metals, problems caused by temperature gradients and the use of materials with mis-matched expansion coefficients.
- Thermal conductivity and insulation, heat capacity, thermal response times and thermal shock.

## 1. INTRODUCTION

This paper might well be described as a "foundation level" course on those aspects of cryogenic engineering and materials technology that underlie the design and operation of High Reynolds' Number Cryogenic Wind Tunnels (abbreviated in this paper as HRNCWTs). There are parallels with the foundations of a building in that both are often taken for granted, but necessary in order to give a solid base for the subsequent structure. In particular, an understanding of the safe use and handling of liquid nitrogen is of extreme importance if accidents are to be avoided. Cold burns or asphyxiation are just two of the hazards that needed to be prevented, while a working knowledge of the storage and transfer of liquid nitrogen is essential for those handling this cryogenic fluid. Control of moisture desorption important to maintain very low dew point atmospheres needed to avoid formation of ice on the surface of a cold model. An understanding of physical properties such as thermal contraction is important for the correct design of equipment operating at cryogenic temperatures, while an appreciation of thermal conductivities can avoid unnecessary heat influxes.

## 2. GENERAL PROPERTIES OF LIQUID AIR, ARGON, NITROGEN AND OXYGEN

The basic properties of liquid air and its constituents are given in Table 1 and discussed in the next few paragraphs.

Table 1. Properties of Liquid Nitrogen, Air, Argon and Oxygen.

Property	Nitrogen	Air	Argon	Oxygen
Molecular Weight	28	28.8	40	32
Critical Pressure (Atm.)	33.5	38.7	48.3	50.1
Critical Temperature (K)	126	132	151	154
Normal Boiling Point (K)	77.4	Bubble 78.8 Dew 81.8	87.3	90.2
Freezing Point (K)	63.2	-	84	54.8
Liquid Density @ Normal Boiling Pt, (kg/m <sup>3</sup> )	808	876	1402	1138
Specific Gravity of Gas at 288 K and 1 Atm.	0.97	1	1.38	1.10
Vol.Gas @ 288 K, 1 Atm./Unit Vol.Gas @ B.P.	683	730	823	843
Latent Heat of Vaporisat'n (kJ/kg)	199	205	161	213
Specific Heat of Liquid, C <sub>p</sub> , (J/kg.K)	2.038	1.967	1.138	1.699
Liquid Viscosity, (microPascal.sec)	158	163	256	188
Paramagnetism	None	Oxygen / 5	None	Strong
Colour	Colourless	Light blue	Colourless	Blue
Oxidising Power	None	Moderate	None	High

## 2.1 Binary Phase Diagram for Oxygen-Nitrogen Mixtures.

For simplicity, gaseous air is assumed to contain 21% oxygen and 79% nitrogen, neglecting the minor constituents such as argon, neon, krypton and carbon dioxide. The binary phase diagram between pure oxygen, boiling point 90.3 K (-183 °C) and pure nitrogen, boiling point 77.3 K (-196 °C), is shown in Figure 1.

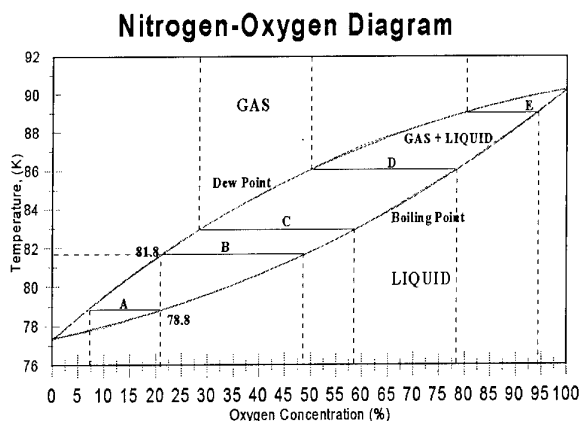


Figure 1. Nitrogen/Oxygen Binary Phase Diagram.

The dew point temperature is the temperature at which droplets of liquid start to condense from saturated vapour. For air this is 81.8 K (-191.4 °C), as may be seen from the vertical dashed line at a composition of 21% oxygen. The bubble point temperature of air, where bubbles of gas start to form from the saturated liquid, is 78.8 K (-194.4 °C). Consider now the horizontal tie line, A, drawn at 78.8 K, the bubble point temperature of liquid air. It can be seen that the evaporating gas contains only about 7% oxygen and 93% nitrogen, thus the gas is enriched in nitrogen. In commercial air separation this composition difference between the liquid and gas is exploited by arranging a series of trays in the column on which the liquid is re-evaporated. The liquid descends and becomes progressively richer in oxygen, while the gas rising up the column contains more and more nitrogen.

A similar mechanism gives rise to inadvertent liquid oxygen formation where air can come into contact with a surface cooled by liquid nitrogen, as indicated schematically in Figure 2. This assumes that air can migrate through the insulation and condense on the surface at its dew point of 81.8 K. As can be seen from tie line B, the liquid that condenses is enriched to a concentration of almost 50% oxygen. The droplets of liquid then fall into the insulation and the liquid warms up in the temperature gradient within the insulation. The composition of the evaporating gas is given by the dew point line and that of the gas by the bubble line. Thus, when the droplet is at position C and a temperature of 83 K the evaporating gas will contain 29% oxygen and the remaining liquid 58% oxygen. At 86 K, position D, the liquid contains 78% oxygen, while at position E, 89 K, it is enriched to about 95%. Depending on the actual conditions within the insulation it is possible that almost pure liquid oxygen will be created within the insulation, or even drip from it.

It is this mechanism that gives rise to potential hazards if combustible material such as grease, most plastics and

even some metals come into contact with the liquid oxygen or oxygen-enriched gas.

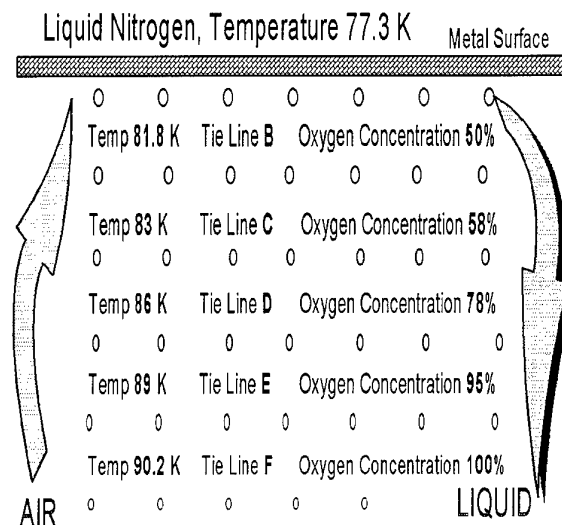


Figure 2. Schematic View of the Mechanism of Liquid Oxygen Enrichment

## 2.2 Liquid-Gas x 683 Volume Increase.

As may be seen from Table 1, when unit volume of liquid nitrogen evaporates at 77 K, it produces 683 unit volumes of gas at atmospheric pressure at room temperature. As  $PV = RT$ , the volume of gas at 77 K is  $683 \times 77 / 288 = 183$  unit volumes. Thus 1 cc of liquid at 77 K evaporates to give 183 cc of gas at 1 atmosphere pressure at 77 K. Alternatively, if the liquid is unable to evaporate freely, a large pressure is generated in the trapped volume. Thus,

**NEVER CLOSE A PIPE OR ENCLOSURE CONTAINING LN, UNLESS IT IS FITTED WITH A PRESSURE-RELIEF SYSTEM!**

By law, all vessels operating at pressures above  $\frac{1}{2}$  an atmosphere must be fitted with relief valves and bursting disks. The effective operation of relief valves must be checked periodically.

## 2.3 Effect of Pressure on Boiling Point.

Figure 3 shows the Vapour Pressure - Temperature relationship for nitrogen. The triple point, at which liquid, solid and gas co-exist is at a temperature of 63.2 K and a pressure of 0.012 MPa. Although unlikely to be of much interest for HRNCWT applications, in research laboratories temperatures between 77.3 K and 63.2 K are obtained by pumping off the evaporating gas using rotary pumps and thus lowering the boiling point.

In contrast, if the pressure over the liquid is increased, the boiling point is increased up to the Critical point, where there is no distinction between liquid and gas. This occurs at a temperature of 126 K and a pressure of 33.5 Atm. (~3.4 MPa). If high pressure nitrogen gas is cooled to below 126 K, liquid can be created by expansion through a small orifice, the so-called Joule-Thompson effect.

The effect of increasing the pressure over liquid nitrogen can be demonstrated using an un-silvered glass Dewar and covering the top with a balloon. If the balloon is compressed to raise the pressure, gas bubble formation ceases as boiling is quenched.

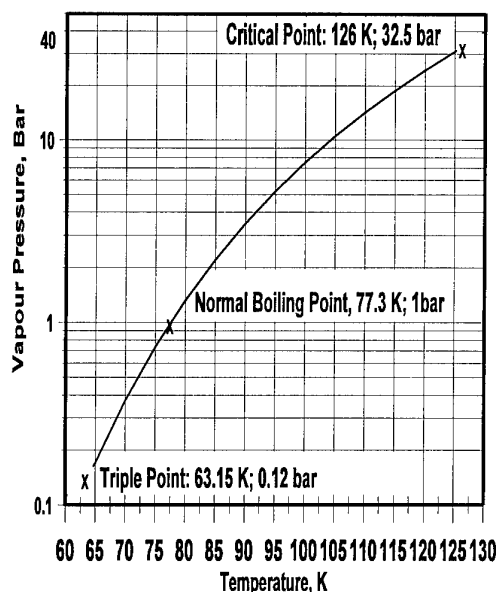


Figure 3. Vapour Pressure-Temperature Curve for Nitrogen

## 2.4 Heat Transfer in Liquid and Gaseous Nitrogen.

### 2.4.1 Difference Between Heat Transfer Rates in Liquid and Gas.

Heat can be transferred at a much greater rate between a solid and a surrounding liquid than between a solid and surrounding gas. This effect can be used to make a simple liquid nitrogen level detector by attaching a thermocouple junction to a small electric resistor through which a current is passed. When immersed in liquid nitrogen, the power dissipated in the resistor is set to give a thermocouple reading a few degrees above the liquid temperature of 77 K. If the resistor is then raised above the liquid, its temperature will rise quite rapidly and stabilise a temperature that can be sustained by heat transfer to the cold gas. Thus, when immersed in liquid,  $\Delta T$  is a few K, surrounded by gas  $\Delta T$  is 10's of K. This effect is shown in Figure 4.

A relevant example of the restriction on power dissipation in  $\text{LN}_2$  by the onset of film boiling is that of heaters used to evaporate liquid nitrogen. Commercially available water heaters, rated at 3 kW were tested in liquid nitrogen and it was found that a maximum of 720 W could be dissipated by nucleate boiling. This was equivalent to a dissipation rate of about  $3 \text{ W/cm}^2$ , significantly lower than the  $10 - 12 \text{ W/cm}^2$  obtained under ideal conditions. At the maximum rate of heat transfer, the temperature of a thermocouple taped to the surface of the heater coil showed a  $\Delta T$  of a few K above the liquid temperature. The tests also showed that the surface temperature of the upper heater coil increased very rapidly as soon as the liquid nitrogen level dropped to allow it to be partially uncovered by the boiling nitrogen, a further indication of the much lower heat transfer rate between the heated surface and gaseous nitrogen.

It is also possible to demonstrate the effect of surface condition by comparing the time for bubble formation to stop on a series of otherwise identical specimens of copper, lead or aluminium that are polished, tarnished, and coated with a clear lacquer, white, or black paint. The most striking result is that the lacquer-coated specimen

cools most rapidly, as the insulating effect of the lacquer layer allows nucleate boiling and its characteristically high heat-transfer rate to be established more rapidly.

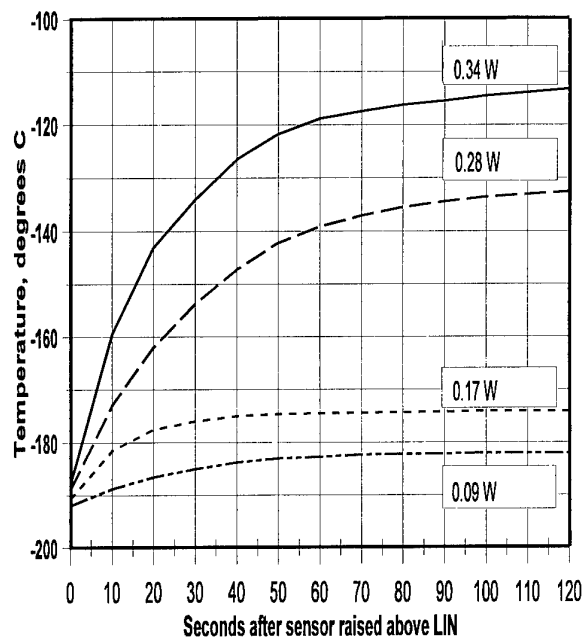


Figure 4. Temperature of Thermocouple / Heater After Removal from Liquid Nitrogen.

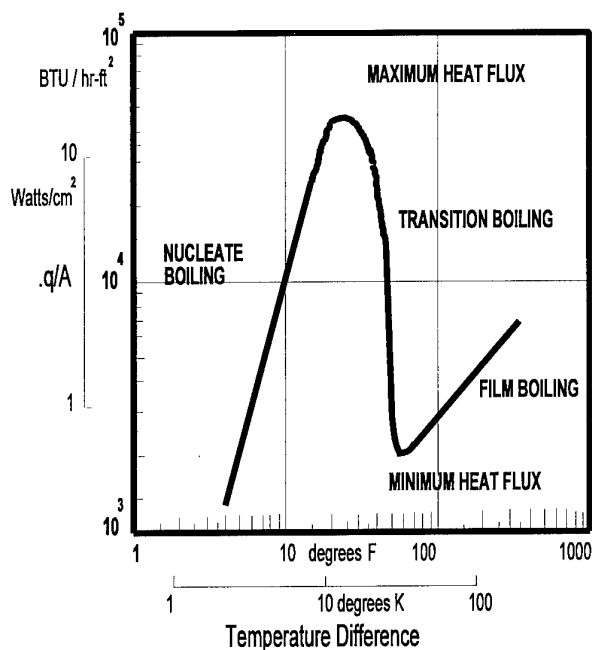


Figure 5. Typical Pool Boiling Characteristic Curve.

## 3. SAFETY: OXYGEN DEFICIENCY, ANOXIA, ASPHYXIATION.

Safe handling of cryogenic fluids and solids is discussed in the British Cryogenics Council "Cryogenics Safety Manual - A Guide To Good Practice". Suitable training in these topics should form a natural part of training of operatives by the contractor. Advice and assistance is also available from suppliers of cryogenic liquids.



### 3.1 Physiological Effects of Nitrogen.

Liquid nitrogen evaporates to produce a gas that is potentially liable to cause asphyxiation. It is only necessary for the oxygen content of air to fall a few percent below its normal value of about 20% for bodily functions, both mental and physical, to be adversely affected. Gradual asphyxiation occurs if the oxygen concentration decreases slowly. Reduction of the oxygen level towards about 14% causes anoxaemia, characterised by an increase in pulse rate, laboured breathing and difficulty in concentration. At oxygen levels between 14 and 10% the victim is still conscious but muscular effort causes rapid fatigue and mental processes such as co-ordination and judgement deteriorate.

When the oxygen concentration falls below 10% there is a severe risk of asphyxiation and possibly permanent brain damage. By the time the victim realises that something is wrong it may be too late for him to save himself as his muscles will be unable to function and allow his escape. If the oxygen level falls below 6% death is virtually inevitable - apparently painless, but nonetheless permanent! These effects are summarised in Table 2.

Table 2. Signs and Symptoms of Gradual Asphyxiation.

O <sub>2</sub> % at 1 Atm. Press.	Victim at rest, signs and symptoms of O <sub>2</sub> deficiency
12-14	Respiration deeper, pulse faster, coordination poor
10 - 12	Giddiness, poor judgement, lips blue.
8 - 10	Nausea, vomiting, unconsciousness, ashen face
6 - 8	After 8 min., 100% die; 6 min., 50% die and 50% recover with treatment; 4 - 5 min., all recover with treatment.
4	Coma in 40 sec., convulsions, respiration ceases

Sudden asphyxia occurs by inhalation of a gas that contains little or no oxygen and the victim often falls as if struck by a blow on the head. It is surprisingly easy to produce such low oxygen levels. Inhaling just a few breaths, or even one deep breath of pure nitrogen, or any other inert gas, can flush the oxygen out of the lungs and the loss of muscle function can prevent them refilling even if the victim is removed from the inert atmosphere. Death can occur in a few minutes and some form of rapid resuscitation is necessary to restore oxygen to the lungs and allow possible recovery. A typical scenario for such an accident is where someone opens an inspection hatch in a nitrogen-purged vessel, puts his head inside to "take a quick look" and collapses within a few seconds because his lungs have become filled with nitrogen. Unlike the gradual loss of breathable air that takes place in a sealed volume when the oxygen is not replaced, little or no warning is given by the body of this form of anoxia. Use of liquid nitrogen in, or near, pits and ducts is particularly hazardous as cold gases tend to sink and accumulate at low levels. Positive air flow is required to prevent dangerously low levels of oxygen in such locations.

One of the few fatal accidents involving liquid nitrogen

that have occurred in the UK involved pipe freezing in a pit. One operator went down to investigate a leak in the freezing jacket and collapsed due to anoxia. Unfortunately, he was not wearing a safety harness or rope, neither was a colleague who attempted to rescue him. When he also collapsed, a third colleague also attempted rescue, also without wearing appropriate equipment. Ultimately, the first two operatives died, while the third recovered. There are a number of ways in which the effects of anoxia can be avoided, including ensuring a supply of fresh air and the use of oxygen monitors, both of which are discussed in paragraph 3.1.3.

#### 3.1.1 Rescue of the Victim and Treatment of Oxygen Deficiency and Anoxia.

If a serious accident is not to be compounded into a tragedy, rescue personnel must ensure that they are adequately equipped with breathing apparatus, air line, etc. **before** entering the zone in which the victim of an oxygen-deficient incident lies. As noted earlier, it was the failure to observe this precaution that increased the number of casualties in the pipe freezing related incident. The victim should be removed immediately to a normal atmosphere. If he is not breathing it is vitally important to start artificial respiration at the first opportunity, preferably by the use of an automatic resuscitator employing oxygen gas, or alternatively by the mouth or other unaided method.

#### 3.1.2 Oxygen Monitors

In order to avoid anoxia, it is necessary to be able to detect the presence, and extent, of regions of low oxygen concentration. Oxygen monitors are used for this purpose and used correctly they are invaluable. There are a number of types of monitor available, but the most useful are the small portable types. Care is needed in the appropriate placing of oxygen monitors. If, for example, they are placed too high up they will not register a dangerous loss of oxygen at working head height. Placed directly over a nitrogen vent or on the floor below an outlet they will trigger prematurely. Such false alarms are likely to lead to distrust or complacency that could prevent operatives from reacting to a truly dangerous situation. Small, portable monitors can be worn high up on the body to give a rapid warning if the head is moved into a potentially dangerous location. It is important that oxygen monitors are serviced and re-calibrated regularly, as their efficiency decreases over periods of about 6 to 12 months.

#### 3.1.3 Safe Methods of Working with Liquid Nitrogen.

##### Fresh Air Supply

When using liquid nitrogen it is essential to maintain a flow of fresh air to prevent the build up of an inert gas. Often this is simply a matter of opening appropriate doors and windows, in other cases it is necessary to provide air movers to ensure an adequate air flow.

##### Condensation Clouds

When a cold gas comes into contact with moist air, water vapour is condensed to form a cloud, the conditions for which depend on factors such as the temperature of the gas and the dew point of the air. It should be assumed that the fog could contain a high proportion of nitrogen gas and a correspondingly low amount of oxygen. It should, therefore, not be entered. It is also possible for the clear air beneath a cloud to be oxygen deficient as the cold nitrogen gas will sink to the lowest level. A dense cloud can cause a loss of visibility and create a hazard to personnel in the area, especially in the event of a large spillage.

### Escape Routes

It is particularly important that an advance evaluation is made of the likely mode and extent of a possible spillage and the measures that should be taken to minimise its effect. For example, evacuation routes should be marked and kept clear. Breathing equipment and other safety equipment should be kept handy and personnel properly trained in its use so that they could reach safety and/or effect rescue even in the event of a large spillage and severe nitrogen build-up. Alternatively, the availability of a breathing set could allow someone to remain safely in the affected area and carry out rapid remedial action that could prevent a small incident from becoming a major accident.

### Breathing Apparatus

Suitable portable breathing equipment should always be readily available for emergency use in the event of an accident. As with any safety equipment, much of the value of such equipment is, however, lost if it is not available for immediate use when needed. Thus, having the equipment in a van 200 metres away is no substitute for having it within a few metres. Similarly, personnel need appropriate training in the use of BA sets. Such training may be provided by the employer, the equipment supplier, or as part of a more comprehensive training course. Furthermore, BA sets need regular and correct maintenance. Schedules for such maintenance are usually laid down by their suppliers.

### **Summary: Stay Alive!**

*- Limit the amount of LN<sub>2</sub> used in enclosed spaces and store it in robust, narrow-necked containers that need pressurisation or external pumps to decant the liquid.*

*- Always ensure that there is a plentiful supply of fresh air either by opening windows, by boosting the installed ventilation air flow or by bringing in an air mover.*

*- Ensure that there are alternative exits and that the way out is un-obstructed.*

*- Work in pairs, or make certain someone else knows where you are and checks frequently.*

*- Wear a personal oxygen monitor and place other monitors at suitable positions.*

*- In the event of a spillage, keep your head at the highest possible level.*

### **3.2. Safety: Cold Burns.**

Despite the apparent contradiction in terminology, the physiological effect of the exposure of human flesh to cryogenic temperatures is similar to that of a thermal burn. The affected tissue dies. In a controlled form this effect is used in cryosurgery to destroy growths and cancers.

A severe cold burn can be caused if moist, bare flesh is held in contact with a very cold surface, for example an un-insulated pipe carrying liquid nitrogen. The moisture on the skin is frozen hard to the surface and it may be impossible to release the skin without tearing or cutting off the frozen layer. This may, unfortunately, be the only course of action in the event of such a cold burn is to be minimised and the thermal mass of the cold surface is too great to allow rapid warming. Another typical situation is when liquid nitrogen soaks into clothing, for example a sock if nitrogen is spilled into a shoe. In this case, it may

be better to leave the sock frozen to the foot until it has been thawed out. Wet clothing should be avoided, as it is more likely to freeze in contact with the skin if liquid nitrogen is spilt. Frozen tissues have a waxy appearance, a pallid colour and while frozen, there is little or no sensation of pain. They become painful, swollen and very prone to infection when thawed.

#### **3.2.1 Treatment for Cold Burns.**

Under most circumstances, it is recommended that the affected area be thawed as rapidly as possible. This should preferably be done using flowing tepid water. Do NOT, however, apply any form of direct heat, such as hot water, air or radiant heat.

Any clothing that may restrict blood flow to the affected area should be loosened. Thawing may take, typically, from 15 to 50 minutes and should be continued until the skin has returned to a pink or red colour. Morphine and tranquillises may need to be given during thawing to control the pain and this should be done under professional medical supervision. Thus, if the accident takes place remote from a hospital and no drugs are available, it may be preferable to allow the affected area to thaw naturally in order to minimise the pain involved. If, however, the frozen part of the body has thawed by the time medical attention has been obtained, no re-warming should be carried out. The affected areas should be covered with dry sterile dressing with a large protective covering. A tetanus booster should be administered after hospitalisation. In severe cases, when there has been a massive exposure to very cold conditions, the general body temperature (core temperature) may become lowered. The patient should then be re-warmed by total immersion in a bath of warm water. Shock may occur during re-warming. Alcohol and smoking decrease the flow of blood to the frozen tissue and they should therefore be avoided.

#### **3.2.2 Treatment of Frost-bite.**

Frost-bite is the result of continued exposure of naked or inadequately insulated flesh to low temperatures. It is usually accompanied by pain in the affected areas during freezing and this gives an adequate warning to alert the potential victim. If frost-bite does occur, re-warming to temperatures of about 22 to 24 °C should normally be all that is required to prevent injury. A subsequent medical check up is advisable.

#### **3.2.3 Personal Safety Equipment and Actions.**

The selection and issue of appropriate personal safety equipment is normally considered the responsibility of the employer. Its proper use and maintenance in good condition is, however, the responsibility of the operative. Misuse should be considered a violation of company safety procedures and dealt with accordingly. At all times an operative should act in such a manner as to maximise his own safety and that of others who might be affected by the consequences of his actions.

### Eye Protection, Face Masks and Goggles.

Eye tissue is much more sensitive than ordinary flesh and it can easily be damaged by exposure to cold gasses, and in particular, to splashing liquid nitrogen. Eye protection should thus always be used when transferring liquid cryogenics, especially into warm vessels. There are two types of eye protection commonly used, the choice of which depends on the specific circumstances and operator preference. Where splashing is likely, the full-face visor is usually preferred. At other times safety goggles with side protection are adequate.

### Gloves

Gloves should be dry, non-absorbent and loose-fitting so that they could be removed rapidly if liquid should get inside. Natural materials such as leather are preferred by many operatives as they do not embrittle when used to handle cold transfer hoses and other equipment. Rubber and some plastics embrittle when cooled to low temperatures and can crack when in use. Where prologued exposure to low temperatures is expected two layers of gloves should be used. An inner thin rubber surgical glove is worn to provide a "detachable second skin" and to prevent surface moisture on the fingers from reaching the colder parts of the outer glove. The insulated outer glove is replaced by a new pre-warmed glove as soon as the operator starts to feel cold.

### Clothing

Clothing worn when handling cryogenic liquids should be non-absorbent to avoid any spilled liquid from soaking in and creating a cold spot. Leather or rubber aprons are recommended for use where liquid splashing could occur. Clothing should also be dry, as wet clothing can freeze to the body and cause a cold burn. In general, a number of thin layers of clothing are preferable to fewer, thicker layers. There is also a preference for clothing made from natural fibres such as wool or cotton as many man-made fibres suffer from electro-static charging.

### Shoes and Socks

When transferring cryogenic liquids, care must be taken to ensure that any spilled liquid cannot be trapped inside shoes and trousers should be long enough to prevent liquid from getting into a shoe. Sandals should not be worn when handling cryogenic liquids. If liquid splashing is likely to be severe, some form of gaiter is recommended if such an event is foreseen.

### Head Cover

Where safety helmets are not mandatory, some other form of head covering should be considered where there is the possibility of liquid nitrogen falling downwards.

## **4. STORAGE AND TRANSPORT OF LIQUID NITROGEN.**

Storage vessels for cryogenic liquids such as nitrogen are not designed to be full of liquid. About 10% of the total volume, called the ullage space, is left above the liquid surface. This space also allows liquid to separate out and settle as the vessel is filled and typically, once vessel is about 90% full, liquid appears in the gas stream venting from the vessel, indicating that transfer is complete.

### **4.1 High Pressure Vessels**

Liquid nitrogen can be stored under relatively high pressures, up to about 200 psi. High pressure storage is used when the main requirement is for low volume storage of a source of high-pressure gas, e.g. where large volumes of nitrogen gas are required for purging or inerting. Storage under high pressures is not, however, recommended when supply of liquid at atmospheric pressure is the main objective. When liquid nitrogen stored under high pressure is de-pressurised for low pressure transfer, 'flashing' occurs, that is large volumes of gas are produced suddenly. The net amount of liquid nitrogen available under these conditions is much lower than when transfer is carried out at low pressures.

### **4.2 Low Pressure Vessels**

Low pressure storage vessels are most suitable for liquid storage for HRNCWT applications. Common sizes are:

25, 50, 100, 160, 200, 300, and 500 litres. In general, storage vessels of over 1000 litres are too large and heavy to be positioned close to the point of use and they are used for local storage of liquid. They are commonly hired from, and / or maintained by, the liquid supplier and specific operating procedures must be followed when withdrawing liquid nitrogen from such storage vessels.

The 200, 300 and 500 litre vessels are often mounted on wheels or casters and are thus more mobile, especially for use indoors and where there are lifts. The 50, 100 and 160 litre sizes are the most commonly used as they are large enough to hold a reasonable supply of liquid while being capable of being moved along narrow passages, down into ducts or up onto scaffolding. Most types, especially those with carbon steel outer shells, are also robust enough to withstand such treatment. The 25 litre vessels are usually un-pressurised and used to transfer small quantities of liquid nitrogen where access is too limited to permit use of a transfer line.

It is essential that storage vessels are well maintained and that their pressure relief valves are checked periodically. Any double skinned vessel must be fitted with a bursting disk to prevent a pressure building up in the space between the two skins. This space is usually evacuated and loss of vacuum lowers the insulation of the vessel.

## **5 TRANSFER OF LIQUID NITROGEN.**

### **5.1 Removal of Liquid Nitrogen from a Storage Vessel**

There are three principle methods used to remove liquid from a storage vessel (1) self pressurisation of the inner vessel, (2) external gas pressurisation, (3) pump transfer. The liquid flow rates obtainable with self pressurisation are relatively low and this technique is usually used for smaller sized vessels up to about 500 litres. Some of the liquid is removed from the storage vessel and passed through an external vaporising coil where it evaporates, expands and causes the pressure to increase. This warm gas is fed back into the storage vessel through the diffuser which, together with stratification in the gas prevents the warm gas flowing directly into contact with the liquid and re-condensing. Problems can sometimes arise with icing up of the vaporising coil if small quantities of liquid are withdrawn continuously over a long period.

External pressurisation can utilise either the same gas as that liquefied in the storage vessel, or a separate, often non-condensable gas. Considerably higher transfer rates, together with rapid response times, can be achieved by external pressurisation. This technique is, however, rarely used except for specialised applications. Pumps are used to transfer liquid from large [thousands of litres] storage vessels, usually to smaller, more easily transportable storage vessels, e.g. 160 litre vessels. For very large static storage tanks the pumps are often mounted inside the vessel and are cooled and lubricated by the liquid nitrogen. For most transportable vessels, the pumps are mounted externally in the transfer line. It should be noted that a Net Positive Suction Head (NPSH) must be maintained at the pump inlet if cavitation is to be avoided.

### **5.2 Insulated Transfer Lines**

For intermediate and longer lengths and permanent installations transfer lines should invariably be insulated to minimise losses. Vacuum-insulated, double-walled transfer lines, with or without powder or superinsulation, are usually favoured for the larger and longer permanent lines. Some form of expansion joint has to be provided in

these lines to prevent the build up of tensile stresses on the inner pipe during cool-down. Vacuum-insulated transfer lines are initially more expensive to instal, but their lower loss rates usually make them cost effective if used regularly and / or for long periods. Flexible foams, with suitable vapour barriers to prevent liquid oxygen condensation are frequently used for intermediate lengths.

### 5.3 Short Un-insulated Transfer Lines

Structures with low thermal mass cool more rapidly and evaporate less cryogenic liquid than those with larger thermal masses. This factor has to be taken into consideration in deciding whether to insulate transfer lines or to leave them bare. When liquid nitrogen is passed through an un-insulated pipe, frost builds up on the outside and this tends to insulate it by preventing convective cooling by the air. If the cold surface is visible and covered with frost, its temperature is too high to condense liquid air. If it looks wet and free of frost it is probably because the condensing liquid air has washed any frost away. Short, un-insulated flexible transfer lines are used to transfer liquid nitrogen to small storage vessels, and from a storage vessel to the application, as they are cheaper and less cumbersome than insulated lines. Losses become excessive, however, in un-insulated lines over a few metres long. Care must be taken to prevent contact with the surface as this could cause the 'cold burns' discussed in paragraph 3.2. Suitable gloves should always be used when handling cold transfer lines.

### 5.4 Long Transfer Lines

In a perfectly insulated, pre-cooled pipe cryogenic fluid would be transferred as a single phase liquid, but in most cases some degree of two phase flow is usually present. This can take many forms depending on the horizontal or vertical orientation of the pipe, the mass flow rate, the pressure drop across the line and the heat inleak. In general, stratified flow occurs at low flow rates, with the liquid at the bottom of a horizontal pipe and vapour above. At higher flow rates, shear between gas and liquid sets up waves or plugs which completely fill the pipe with liquid.

### 5.5 Fanno Flow.

During initial cool-down the first liquid introduced into a warm pipe evaporates on contact with the warm sides. This gas then flows ahead of the advancing liquid front pre-cooling the walls as it progresses towards the outlet, a process that can often take a surprisingly long time. Such a situation exists in some HRNCWT applications where cool-down of long transfer lines can take about an hour. Increasing the liquid delivery pressure can speed up the process, but this is expensive and not very effective, as less of the sensible heat of the gas is used in pre-cooling the pipe. In extreme cases liquid may never be obtained from the end of the pipeline. The evaporated gas occupies a much greater volume than the liquid, gas velocities can be very high and frequently the flow is choked at the exit during practically the entire cool-down and it leaves at sonic velocity. If the flow resistance in the pipe is large it may be impossible to make the liquid front advance more than partially along the pipe and liquid never emerges from the other end, thus producing a zero delivery condition. One solution to such a problem is to modify the line by installing sufficient intermediate venting points to allow the liquid front to be advanced progressively by venting from these intermediate points until liquid emerges and then moving on sequentially to the next vent.

### 5.6 Condensation and Moisture Pick-up.

A cold surface, such as one cooled by the presence or

transfer of liquid nitrogen, can condense moisture from air because the surface temperature is below the Dew point. This effect is utilised in Cold Panels, surfaces cooled by liquid nitrogen used to cryopump moisture, carbon dioxide and other impurities from air supplies.

Moisture pick-up has a number of implications for HRNCWT applications.

- The ends of a pipe used to transfer liquid nitrogen should be capped after use to prevent moisture condensing on their inside surfaces. Subsequent use of a transfer line containing condensed moisture could lead to pick up of ice during transfer and to contamination of the liquid nitrogen. This happened in the storage tanks for the 0.3 m TCT at NASA Langley.

- There are some areas, such as the Dry Air Hall and the VTCRs at ETW that are maintained at a very low Dew point of about -55 to -60°C. A surface cooled by liquid nitrogen will be below this dew point temperature and any residual moisture will condense on the surface. During transport of a cold model between the test section and QCR residual moisture will condense on the coldest surface, the model and sting.

### 5.7 Selection of Materials to Minimise Water Vapour Desorption.

After the NTF was completed it became apparent that a large amount of water vapour was contained in its internal PU foam insulation and that this water desorbed during subsequent operation at ambient and moderately low temperatures. The tunnel atmosphere thus had a relatively high dew point and at low operating temperatures ice formed on the surface of the model. The NTF now has to be purged extensively before use and elaborate precautions have to be taken to prevent moisture ingress during model changes. Forewarned of this problem, the ETW PU foam insulation system incorporated fully vapour-barriered panels and moisture desorption is negligible. However, the ETW also has a large Dry Air Hall through which a cold model is transported en route to the VTCRs and the dew point of the air in these rooms has to be maintained below about -65°C.. This provided a greater challenge that providing a low dew point atmosphere in the tunnel itself, partly due to the large number of separate contractors responsible for the various work packages in these areas.

All concrete surfaces had to be covered with primary and secondary vapour barriers as even small uncoated penetrations could give rise to large sources of desorbable moisture. All insulation systems, load-bearing supports, cables, fixtures and contents of these areas had either to have inherently low moisture desorption rates or to be covered with a vapour barrier. The large areas of painted surface on the transfer lock doors were a potentially large source of moisture. Many different paint systems were screened before choosing an aluminium powder loaded lacquer than has a moisture desorption rate between 10 and 50 times smaller than other candidate paints.

### 6. LOX COMPATIBILITY OF MATERIALS.

All hydrocarbon-based solids, liquids and gases are incompatible with Liquid OXygen (LOX) and the greatest care should be taken to avoid their presence in an oxygen-enriched atmosphere. Despite its low temperature, liquid oxygen is an extremely efficient oxidising agent and many materials, including some metals, will burn violently if ignited in its presence. Particularly reactive metals such as titanium and magnesium are a hazard even in the bulk form, while ferritic and austenitic steels,

aluminium and zinc will burn fiercely when in the finely divided form of dust or fibres. All hydrocarbons, including ordinary clothing, human hair and tissue as well as many plastic foams and fibres used in insulation systems are LOX incompatible materials.

## 7. MATERIALS: MECHANICAL PROPERTIES.

### 7.1 Metals.

For application in load-bearing structures operating at cryogenic temperatures, metallic materials have to be both strong and tough enough to fulfil their required duties. In general, austenitic stainless steels, aluminium- and copper-based alloys are preferred for such applications as their strengths increase at low temperatures and their toughnesses do not decline significantly. For applications requiring high working loads, the choice of materials becomes more difficult as the fracture toughness many such materials decreases at low temperatures. These topics are dealt with in our next lecture.

### 7.2 Non-metals:

Most polymeric materials embrittle at low temperatures, particularly at high strain rates and in the presence of sharp notches. In particular, nylon, perspex, PVC, polyethylene and rubbers become very brittle at liquid nitrogen temperature. In contrast PTFE and PCTFE retain some ductility, while polycarbonate and mylar can still be used in some applications.

## 8. MATERIALS: PHYSICAL PROPERTIES.

### 8.1 Thermal Contraction.

This is probably the most important of the physical properties because the stresses set up in components by differential thermal expansion can very easily cause severe distortion or, at the worst, failure. The total linear contraction of a number of representative materials is shown as a function of temperature in Figure 6. It can be seen from the figure that the total linear contraction at 77 K varies from about 0.05% for Invar and Pyrex glass to over 2% for some thermosetting resins. It is not surprising, therefore, that problems can arise when materials are used together without adequate forethought.

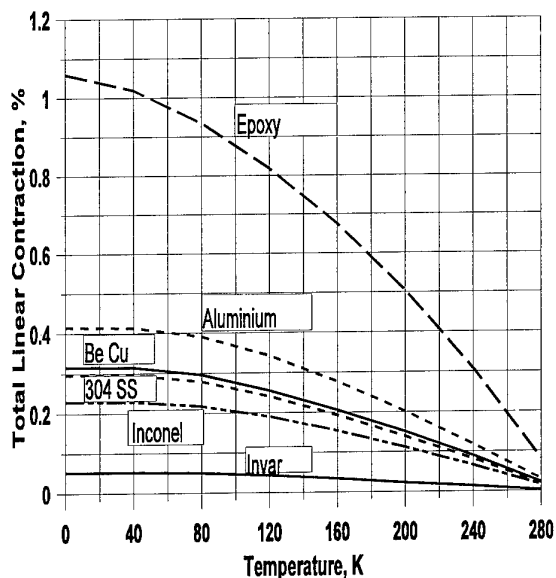


Figure 6. Total Linear Contraction as a Function of Temperature.

Problems can, in practice, usually be resolved into two basic categories:

- i) those in which only one type of material is involved and where differential contraction is a result of temperature gradients,
- ii) those in which the same temperature gradient is applied across two or more materials having different expansion coefficients.

Considering first the case of dissimilar materials, a common mercury in glass thermometer uses the large differences in expansion coefficients between the two components, but no stresses are set up as the mercury is free to move inside the glass tube. In contrast, a bi-metallic strip consists of two metals firmly fixed together and when the temperature decreases the free end moves towards the side containing the metal with the higher expansion coefficient. If the end were not free to move the metal with the higher expansion coefficient would be put into tension and the other metal into compression. A further example is an externally-insulated, closed-circuit cryogenic tunnel. When cold the tunnel contracts relative to its warm mountings and, as one end is effectively clamped by the fan shaft bearing, the other end must be able to move to prevent thermally-induced stressing on cooldown. In the NASA LaRC 0.3-m TCT this is accomplished by supporting the tunnel on a PTFE pad placed on stainless steel supports.

Differential contraction between the inner and outer walls is also a common design problem in transfer lines for cryogenic fluids and some form of expansion joint has to be built into the system. It was noted earlier that the total linear contraction of Invar from 300 to 77 K was very much smaller than other alloys, about 1/6th of that of austenitic stainless steels and 1/8th of that of aluminium alloys. Thus a transfer line with the inner wall made from Invar would need only 1/6th or 1/8th as many expansion joints as it would if made from stainless steel or aluminium alloy respectively and the savings thus achieved are sometimes more than enough to offset Invar's higher material and fabrication costs.

An example of mismatched materials is a flanged joint between aluminium alloy and stainless steel pipes. Aluminium alloys contract more than stainless steels and if an aluminium alloy bolt were used its load would be increased as it contracted more rapidly than the stainless steel flange. It is possible that the bolt might in fact fail on cooling: if not it would yield and stretch so that on warming to room temperature it would now be too long to compress the gasket adequately and a room temperature leak would be created. The use of a stainless steel bolt would also cause problems because on cooling it would contract less rapidly than the aluminium flange and so be unable to keep the same compressive stress on the gasket - the likely outcome being a low temperature leak which would then seal itself up when the joint were rewarmed to ambient temperature. One elegant solution to this problem is to have a long stainless steel bolt pass through the centre of a Monel compensating sleeve as well as through the two flanges. The length of the Monel sleeve is calculated to compensate exactly for the lower contraction in the bolt.

The whole question of fits and clearances at low temperatures has to be kept very much in mind. Most of us are familiar with the practice of heating a gear wheel before placing it onto a shaft so that it will shrink to a tight fit on cooling. Some will also be aware that the same

operation is sometimes carried out by cooling the shaft with liquid nitrogen prior to fitting the gear so that the required fit is obtained when the shaft expands on rewarming to room temperature. These examples should be remembered when constructing models, balances or other fittings where there are close fits and small clearances. On cooling these clearances could either decrease and cause a seizure, or increase and lead to looseness and possible leakage. This can also manifest itself in changes in the clamping force applied to models which could decrease on cooling and allow the model to vibrate loose, or increase and possibly cause damage. These problems are likely to be particularly severe if non-metallic materials are used as their total linear contractions are so large.

## 8.2 Thermal Conductivity.

Pure metals are good conductors of heat and their thermal conductivities often increase as the temperature falls. They are used where thermal gradients have to be minimised and where large heat fluxes are required. High purity copper is a very good conductor of heat, but its strength is too low for many applications. Beryllium copper can be precipitation-hardened to moderately high strengths while still maintaining a thermal conductivity that is higher than other copper alloys. In contrast, the conductivities of strongly alloyed and cold-worked metals are low and they decrease further at low temperatures. However, as it is impossible to recognise whether a material has been cold worked by looking at its surface and, as the physical and mechanical history of the sample is rarely well documented, uncertainties can arise in using thermal conductivity data from the literature. Austenitic stainless steels combine reasonably high strengths with low thermal conductivities and they have long been used for load-bearing, thermally-isolating applications.

Amorphous or micro-crystalline non-metals have very low thermal conductivities, but variations in their density, structure and processing history can change their thermal conductivities by about an order of magnitude as well as causing considerable anisotropy, so care has to be taken in extracting suitable values from the literature. Even lower conductivities may be obtained by increasing the number of interfaces crossed by the heat flux. The combination of many fine glass filaments with a thermo-setting plastic matrix (G.R.P) gives a material with the highest known ratio of tensile or compressive strength to thermal conductivity. GRPs are often used for thermally-insulating supports which are loaded in either compression or tension. Their use to separate the inner and outer skins of modern vessels for storing cryogenic liquids is, in a large measure, responsible for the low boil-off rates.

Fibres and foams of non-metallic materials are the most commonly used thermal insulators for large cryogenic structures such as storage tanks and transfer lines. Polyurethane foam has been used for the internal insulation in both the NTF and ETW.

## 8.3 Thermal Shock.

Non-metals with amorphous or microcrystalline structures are very efficient thermal insulators, but many of them also become embrittled at low temperatures, especially if in the bulk form. They have low thermal conductivities and high expansion coefficients and, together with the embrittlement, these three factors can cause thermal shock if a structure is cooled rapidly. This can be particularly severe if the materials are present in thick sections and/or cool-down rates are high.

## 8.4 Heat Capacity and Specific Heat

Information on the specific heat of materials used in cryogenic equipment is needed to calculate the energy needed to cool them to the operating temperature. Structures with the highest heat capacities require the largest amount of cooling and this has to be supplied by the latent heat of the evaporating liquid or by the sensible heat of the cold gas. For structures which have to undergo frequent cooling and warming cycles, it is important to minimise the total thermal mass to achieve both low liquid boil-off rates during cool-down and also short cooling times. For equipment that rarely warms up once it is cooled, low heat capacities are not so important. A relevant example of the effect of thermal mass is the NASA 0.3-m TCT tunnel, insulated on the outside of the 6061-T6 aluminium alloy pressure shell. A large thermal mass of metal is cooled down to the working temperature and its thermal inertia evens out fluctuations in the gas temperature that would otherwise be created by changes in the liquid nitrogen injection rate. In contrast, the mild steel pressure shell of the tunnel at Tsukuba, Japan, is internally insulated and the inner liner is thin and has a low thermal mass. The gas is thus unable to absorb much heat without its temperature rising and the liquid nitrogen injection control system has to work much harder to achieve temperature stability. Changes in operating temperature are achieved more rapidly in this tunnel.

Extensive cold work may cause a slight decrease in the specific heat of metals, but they are largely unaffected by the normal range of conditions found in metals. Specific heats of alloys at room temperature are given approximately by the Kopp-Newman rule of mixtures in which the specific heat of a metallic solution is given by the sum of the products of specific heat and molar fraction for each constituent element. Although the rule gets less applicable at low temperatures, in the absence of alternative data it gives an acceptable first approximation.

The specific heats of non-crystalline and amorphous materials cannot be described theoretically and there is no alternative to measured values for amorphous ceramics, glasses, polymers, elastomers, composites and adhesives. When considered on a unit mass basis most of these materials have high heat capacities compared to metals, but this discrepancy is reduced if they are considered on a unit volume basis. For heat balance calculations the enthalpy,

$H = \int C_p dT$ , is of most direct use and in Reference 2 tabulated values of the enthalpy relative to 0K are given together with the specific heat at constant pressure,  $C_p$ , for a range of metals and non-metals.

## 9. ACKNOWLEDGEMENTS.

The author would like to acknowledge with gratitude the use in this paper of material previously prepared for ETW and the assistance received over many years from colleagues at NASA, ETW and other organisations.

## 10. REFERENCES.

1. Corruccini, R.J. and Gniewick, J.J., "Thermal Expansion of Technical Solids at Low Temperatures." NBS Monograph 29. U.S. Department of Commerce, Washington, D.C. (1961)
2. Corruccini, R.J. and Gniewick, J.J., "Specific Heats and Enthalpies of Technical Solids at Low Temperatures." NBS Monograph 21. U.S. Department of Commerce, Washington, D.C. (1960)

# MATERIALS FOR USE IN CRYOGENIC WIND TUNNELS.

David. A. Wigley.

Cryogenic, Marine and Materials Consultants Ltd  
17 Bassett Wood Drive, Bassett,  
Southampton, SO16 3PT, UK

## SUMMARY

The basic concepts of yield, plastic deformation, toughness and crack propagation are discussed in the context of those alloys likely to be used in cryogenic wind tunnels. The mechanical and physical properties of the major alloys used for model construction are discussed and summarised. Dimensional instability in 15-5PH and 17-4PH stainless steels makes them unsuitable for use, but 304L, A286, Nitronic 40 and PH13-8Mo have been used successfully. 200 grade 18 nickel maraging steel has been extensively used for constructing models and stings, but for large diameter forged bars the Charpy impact energy,  $C_v$ , at 77K falls well below the required value of 34 J. An empirical relationship between bar diameter and  $C_v$  at 77K is demonstrated for samples cut in the AR, RR and RA orientations, the orientation effect being most marked between diameters of 150 and 400 mm. The use of 250 grade 18 Ni maraging steel and beryllium copper for balances is also considered. Fabrication techniques are discussed with particular reference to the dimensional changes induced by different machining operations and the implications for the fabrication of high-accuracy components. Non-conventional machining methods and various joining techniques are also discussed. The availability of information in a form suitable for use in model design and stress calculations is discussed in the light of the recent publication of the ETW Materials Guide and the data compilations in its appendices.

## 1. INTRODUCTION

In preparation for this paper, the author has reviewed the information presented at the three previous AGARD Lecture Series on Cryogenic Wind Tunnel Technology. In 1980, the NTF was being built by NASA and a large amount of information was presented from design studies for the NTF and on the results obtained from smaller cryogenic wind tunnels in the USA and Europe. By 1985 the NTF was operational and the lecture series contained details of the models used and the initial results obtained. The information available on the materials and techniques for model construction was collated by this author into tabular format and included in his 1985 lecture. Final design of the ETW was nearing completion and an increasing amount of work was reported from European organisations developing their experience of the various technologies needed to carry out tests in the ETW. By 1989 construction of the ETW was underway and the focus of the lecture series was the need to inform its contractors of the many factors involved in the design, construction and operation of a large cryogenic wind tunnel. Information was also presented by NASA and other organisations on some of the innovative technologies that had been developed to construct and instrument complex wind tunnel models.

Now, in 1996, the ETW is operational and information from its initial use will be given in this lecture series. The NTF is still running but information on its use has slowed to a trickle compared with the comparative flood in previous years. Indeed it has been difficult to find in the

literature much, if any, post-1990 information on materials and techniques for model construction. There are now model shops in US and each of the ETW supporting nations that are capable of making models for high Reynolds' number cryogenic wind tunnels. (Abbreviated to HRNCWTs in the rest of this paper). Due to the economic competition between these organisations, many of the details of their fabrication techniques are considered commercially confidential. It would appear that the subject has reached a state of maturity and that now the priority is consolidation of the existing pool of knowledge for the use of those now designing and fabricating the next generation of models. The closure of groups such as the Experimental Techniques Branch at NASA, retirements, job changes and other factors, have all contributed to loss of knowledge and experience from this pool. Furthermore, the more commercial attitude now prevalent seems to have limited the generation of new information. Due to rationalisation of the steel suppliers, the availability of many of the materials used in model construction is no better, and often worse than in the 1980s, especially as materials for cryogenic use is still a very limited market.

Feedback received from the tables created for our 1985 paper showed that such compilations were widely appreciated and they have now effectively been updated. The recently published ETW Materials Guide contains Appendices that give data suitable for the initial design of models, stings and other equipment for HRNCWTs. It also brings together information on the mechanical and physical properties of materials and the analyses necessary to ensure that models can be tested safely in the ETW. It is available to potential ETW clients and their suppliers.

This paper sets out to summarise the basic properties of materials at low temperatures, to present salient features of the materials most used for HRNCWTs and to illustrate some of the problems encountered in obtaining suitable information for the design of a typical large component for a HRNCWT. The choice of subject matter reflects the authors perceived views on the current requirements of those entering or already working in the field. Inevitably, it also reflects to some extent those areas of technology in which he has been personally involved.

## 2. THE CHALLENGE OF DESIGNING MODELS FOR USE AT CRYOGENIC TEMPERATURES.

The advent of large, pressurised, high Reynolds number cryogenic wind tunnels such as the NTF and the ETW has created many challenges for the designers of models. Optimization of the choice of material and fabrication technique calls for fine judgement, as many of the properties required are near the limits obtainable with state-of-the-art technology.

In many cases improvements in one direction seem inevitably to be accompanied by losses in others. Thus, for example, the material has to have a yield stress high enough to carry the imposed aerodynamic loadings, yet be tough enough to operate safely at low temperatures. It has



to be capable of being fabricated using available machining and joining techniques to give a model with a precisely known shape and a high quality surface finish which is able to retain dimensional stability during thermal cycling between ambient and at cryogenic operating temperatures. It has either to be intrinsically resistant to, or capable of being protected from, corrosion and degradation and, if it is to be of maximum use as an aerodynamic test facility, it has to be furnished with a complex array of orifices, tubes, sensors, heaters and other components needed for data gathering.

While many of these requirements have been familiar to generations of experimental aerodynamicists, it is the high Reynolds number requirement and, in particular, the added cryogenic dimension that has raised the designers' challenge to its present level.

## **2.1 Strength and Toughness of Materials at Low Temperatures**

One of the principal design requirements of any piece of equipment is that it should have adequate stiffness, strength and toughness to withstand safely any load or stress that may be applied to it. In many alloys high strengths are associated with low toughness and, as virtually all materials are both stiffer and stronger at low temperatures than at ambient, the requirement for adequate toughness at the operating temperature is one of the most important design considerations.

Furthermore, some materials embrittle at low temperatures and it is of critical importance to select materials with strengths and toughness adequate for their intended duty. A load-bearing structure must, therefore, be able to cope with not only the static and dynamic stresses which can be predicted for normal operation, but also the thermal shocks it may be subjected to on cool down, the thermal stresses induced by differential expansion during warming and cooling cycles, as well as the accidental overstresses or impact loads that it may receive in the presence of the scratches and dents it is liable to suffer during service.

## **2.2 Dimensional Stability**

In order to fabricate a model to high levels of dimensional accuracy, the material from which it is made must be completely stable. Unfortunately, some iron-based alloys are not metallurgically stable and they can undergo a partial transformation to a more stable phase on cooling below room temperature. Some austenitic stainless, semi-austenitic and martensitic stainless steels can become dimensionally unstable as a result of such transformations and care must be taken to avoid their use for HRNCWT models and components.

## **2.3 Thermal Effects**

In the design and construction of a model it is necessary to bear in mind the extra constraints that cryogenic operation will introduce. Thus, for example, all materials contract to a greater or lesser extent when they are cooled and one of the essential aspects of the successful design of cryogenic equipment lies in avoiding the problems created by differential contraction. One main cause of thermal stresses is the juxtaposition of dissimilar materials, as might occur if the wing were made from a different material to the body, or where a non-metallic component has to fit closely to a metallic part. The other principal causes of thermal stresses are the temperature gradients set up when thin, light structures cool down more rapidly than adjacent heavy sections. For example, the thinner

wings of a model have a lower thermal mass and a faster thermal response than the body of the model with its larger thermal mass. In order to carry out an analysis of thermal stresses it is necessary to have reliable data on the thermal conductivity and diffusivity, the heat capacity and the thermal expansion of the material(s) concerned.

Another thermally important part of a model is the balance. If it is to operate at ambient temperature in a cryogenic tunnel, heaters must be used to warm the appropriate regions and low conductivity materials have to be used to provide the necessary heat breaks between warm and cold regions. In contrast, the use of high conductivity materials such as beryllium copper can reduce temperature gradients where they are undesirable. Alternatively, if the balance is to operate at low temperatures, the variations in the gauge constants brought about by changes in the electrical resistivity of the metallic films or wires have to be compensated. Adequate moisture proofing is also essential.

## **2.4 Use of Data From Reference Manuals**

At this stage it should be noted that care needs to be exercised in the use of data taken from compilations and reference manuals as some properties are more "structure sensitive" than others. For example, the electrical and thermal conductivities, strength, ductility and toughness of materials are properties that are highly dependent on the microstructural and chemical condition of the material. In contrast, the specific heat, thermal expansion and elastic moduli are relatively unaffected by the presence of structural defects. Thus, although it is possible to apply data taken from the literature for the structure-insensitive group of properties, it would be unwise, and even dangerous, to use uncritically the values given for the defect sensitive properties. They should be used for guidance only and if at all possible, they should be backed up by data obtained experimentally on material obtained from the suppliers of the batch of material to be used. In the absence of such experimental verification, generous safety margins should be applied to the literature data.

# **3. BASIC CONCEPTS OF YIELD, PLASTIC DEFORMATION, TOUGHNESS AND CRACK PROPAGATION IN METALS**

## **3.1 Elastic Properties**

Most materials are designed to operate within their elastic limits and typical stress and deflection formulae require the use of appropriate values for the elastic constants such as the Young's, Shear and Bulk moduli and Poisson's ratio. Fortunately, the elastic constants are relatively insensitive to structure variations such as changes in grain size, the degree of cold working, heat treatment and small variations in composition etc.. Furthermore, decreasing the temperature in general increases Young's modulus by about 10% between 300 K and 80 K. Accuracies greater than about 1% are rarely required in the calculations normally used to avoid buckling failure (elastic instability) or excessive elastic deformation and thus values taken from the literature can be used with a reasonably high degree of confidence. The design problems created at ordinary temperatures by the relatively low moduli of aluminium alloys when compared to either austenitic or ferritic steels are also encountered at low temperatures when stiffness is important. For example, where shell bending is a significant design limitation, as in a column subject to lateral air flow loading, the higher modulus materials allow the use of either a stiffer structure for the same section or a thinner section for the same stiffness.



### 3.2 Yield and Plastic Deformation

The austenitic stainless steels, aluminium-, copper- and nickel-based alloys have face-centred-cubic structures. In these alloys yield is a gradual process and the yield stress increases only moderately as the temperature decreases. The strain hardening rate (slope of the stress-strain curve after yield), the ultimate tensile stress (maximum point in the curve) and the total plastic elongation all increase as the temperature falls. Thus these alloys become both stronger and more ductile at low temperatures, essentially because they are able to accommodate a greater degree of strain hardening before the onset of necking (plastic instability). It is the combination of increase in ductility and tensile strength, together with the relative temperature-insensitivity of the yield stress that is the definitive characteristic of face-centred-cubic metals and alloys which makes them so eminently suitable for use at low temperatures. However, in the highest strength alloys, particularly the high-strength precipitation-hardened aluminium alloys, the ability to slip and deform to prevent the build-up of high stress concentrations at the tips of cracks and flaws becomes impaired and they can fail in a low energy shear mode at low temperatures.

### 3.3 Ductile and Brittle Fracture

Although ferritic steels are never used in the construction of wind tunnel models, they are the most well-known materials that undergo a ductile-to-brittle transformation. The transformation, due basically to an increasing probability of cleavage rather than shear failure, is observed as a sharp decrease in the tensile elongation that occurs at the transition temperature. However, a much more realistic indication is the tough-brittle transformation measured by the decrease in the impact energy absorbed in Charpy V notch tests carried out over the transition temperature range. For a plain carbon steel the toughness transition takes place at or above room temperature, whereas the ductility transition occurs at some 220°C below. About half of this drop is due to the very much higher strain rates involved in an impact test, as ferritic steels are highly strain rate sensitive. The remainder of the decrease is due to the stress concentration at the notch root, an indication of the importance of avoiding sharp corners and minimising stress concentrations.

In general most metallurgical factors which strengthen a steel, cold work, increased alloy additions, precipitation hardening, etc., also lower its toughness. The only exception to this rule is the action of grain refinement as this increases both the strength and the toughness. Indeed grain refinement is one of the most important methods of obtaining toughness in ferritic steels at low temperatures.

### 3.4 Charpy Impact Tests

The sharp V notch cut into a Charpy specimen ensures that most of the energy absorbed during fracture is that needed to propagate the advancing crack. Thus, although Charpy tests were originally used to determine the shear-to-cleavage transition in ferritic steels, they are now used more widely as a simple and inexpensive means of measuring the toughness of a material. Indeed, many specifications use the Charpy test as a quality control to ensure that a particular batch of material is up to standard. Furthermore, as the toughness of rolled plate or forged bar varies according to whether the crack propagates along or across the rolling or forging axis, Charpy specimens cut from different orientations can measure the relative difficulty of propagating a crack in these directions and thus the toughness in the longitudinal and transverse, or axial and radial directions.

In order to obtain the maximum of information from Charpy tests, it is important that the orientations of specimens are specified and recorded.

### 3.5 Fracture Mechanics

In most materials the presence of a notch or flaw has an embrittling effect due to the stress concentrating effect at its tip. Modern theories of Linear Elastic and General Yielding Fracture Mechanics (LEFM) and (GYFM) relate the fracture strength and flaw size to the Fracture Toughness of the material,  $K_{Ic}$ . The basic relationship is:

$$\sigma_F = \alpha K_{Ic} / [a + 0.5(K_{Ic} / \sigma_y)^2]^{1/2} \quad \text{.....(1)}$$

where  $\sigma_F$  is the fracture stress,  $\alpha$  is a flaw shape factor,  $K_{Ic}$  the fracture toughness,  $\sigma_y$  is the yield stress and  $a$  is the critical crack length. Note particularly the term  $(K_{Ic} / \sigma_y)^2$ , as it gives an indication of the amount of plastic deformation that takes place in the material ahead of the advancing crack. If  $\sigma_y$  is small,  $(K_{Ic} / \sigma_y)^2$  is large and there is a large plastic zone ahead of the crack tip. Relatively large amounts of energy are absorbed in tearing through this zone and crack propagation is therefore made more difficult. In contrast, if  $\sigma_y$  is large,  $(K_{Ic} / \sigma_y)^2$  is relatively small, the plastic zone size is also small and little energy is absorbed by shear deformation. Furthermore, the yield stresses of many alloys increase quite rapidly as the temperature falls and thus to maintain the same relationship between fracture strength and critical crack size the fracture toughness would have to increase in proportion to the yield stress. This does not happen in many high strength alloys and as a result the critical crack size decreases and they become increasingly notch brittle.

Unfortunately the fracture toughness of a material is not only highly dependent on its physical and mechanical condition but also on its thickness and even sample width. Plastic constraint is greatest in thick sections and the fracture toughness falls to its lowest value, the plane strain fracture toughness,  $K_{Ic}$ . For high strength materials such as the 18 nickel maraging steels, plane strain conditions exist for thicknesses over a few mm.

A simplified form of the basic fracture toughness relationship is given by,

$$K_{Ic} = \text{shape factor} \times \sigma_F \sqrt{\pi a_c} \quad \text{.....(2)}$$

Figure 1 illustrates the relationship between applied stress and  $a_c$  for constant values of  $K_{Ic}$ . Considering first the lowest curve for a material with the smallest fracture toughness, the dashed horizontal line from the stress  $\sigma$  intersects the  $K_{Ic}$  curve at the appropriate value of  $a_c$ , as indicated by the vertical dashed line. If  $K_{Ic}$  were larger, the horizontal line from stress  $\sigma$  would intersect one of the higher curves and give a larger value of  $a_c$ . The dotted line bending in towards the stress axis implies that  $K_{Ic}$  can not exceed the yield stress of the material.

Application of the concepts of fracture mechanics have provided a better understanding of fracture behaviour in high strength alloys and a firmer basis for design to prevent low energy absorbent fracture. It is convenient to divide materials according to the value of the ratio of the tensile modulus to the yield strength,  $E/\sigma_y$ .

-If  $E/\sigma_y$  is greater than 300 the material has such a low strength and good ductility that only those bcc metals such as ferritic steels that fail by cleavage lack toughness.

-If  $E/\sigma_y$  is less than 150 the material has such a high strength that critical flaw sizes are low and load-bearing structures must be designed using fracture toughness analyses. Medium strength materials falling between these limits at room temperature can become effectively high strength materials at low temperatures because of the rise in their yield stresses. Fracture mechanics analyses need to be carried out for many of the high strength materials used in various cryogenic wind tunnel applications including the support stings, balances, models and other components that are highly stressed at cryogenic temperatures.

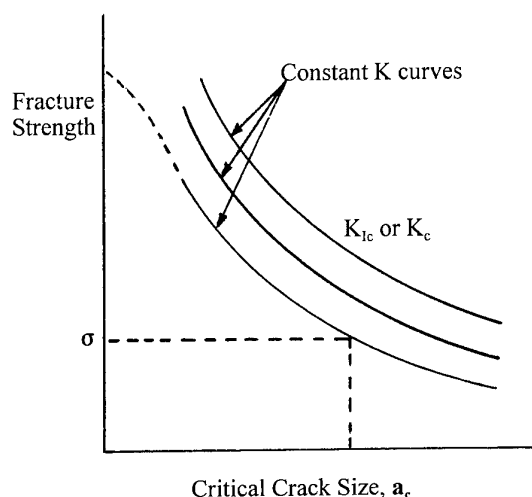


Figure 1 Schematic Relationship Between Applied Stress and Critical Flaw Size for Different  $K_{Ic}$  Values.

### 3.6 The Barsom-Rolfe Relationship Between $K_{Ic}$ and $C_v$

One problem frequently encountered in carrying out fracture mechanics analyses, is the difficulty in obtaining appropriate data, especially values of  $K_{Ic}$ . This problem is eased somewhat, if material for such components is obtained from a well-certified source of supply and if they have already been used for HRNCWTs. However, measurements of  $K_{Ic}$  are expensive and time consuming and in particular values of  $K_{Ic}$  at cryogenic temperatures are rare. It is thus often necessary to infer a value of  $K_{Ic}$  from more readily available Charpy impact data. The following relationship, known as the Barsom-Rolfe relationship<sup>1</sup>, is often used to relate the two parameters;

$$K_{Ic} = [2E (C_v)^{3/2}]^{1/2} \dots\dots\dots(3)$$

where E is the Young's modulus.

This relationship is strictly only true for certain types of ferritic steel, but it is also widely used for other materials, such as aluminium alloys, that do not undergo a classical toughness transition. It is essentially an empirical relationship, not one based on fracture theory.

Care is needed in using the relationship as it is not a rigorous, dimensionally-correct, algebraic formula. Thus, in S.I. units, the LHS when squared has dimensions  $N^2.m^{-3}$ , while the dimensions of the RHS when squared are  $N^{5/2}.m^{-1/2}$ . Furthermore, it only works in the form given above when the fracture toughness is measured in  $ksi.in^{1/2}$ , the modulus is in millions of psi and the Charpy energy is in ft-lb.

Table 1 presents the relationship in numerical form for Young's moduli of 181.3 GPa, the modulus of 200 grade 18 nickel maraging steel at room temperature and 190.3 GPa, its modulus at 77K.

Table 1. Use of the Barsom-Rolfe Relationship to Relate Charpy Impact Energy and Fracture Toughness.

Youngs' Modulus		26.3 Mpsi	181.3 GPa	27.6 Mpsi	190.3 GPa
Charpy Energy		Fracture Toughness			
Ksi√in	MPa√m	Ksi√in	MPa√m	Ksi√in	MPa√m
10.0	13.6	40.8	44.9	41.8	46.0
20.0	27.1	68.6	75.5	70.3	77.3
<b>25.0</b>	<b>33.9</b>	<b>81.1</b>	<b>89.2</b>	<b>83.1</b>	<b>91.4</b>
30.0	40.7	93.0	102.3	95.2	104.8
40.0	54.3	115.4	126.9	118.2	130.0
50.0	67.9	136.4	150.0	139.7	153.7
60.0	81.4	156.4	172.0	160.2	176.2
70.0	95.0	175.5	193.1	179.8	197.8
80.0	108.6	194.0	213.4	198.7	218.6

### 3.7 The Generic Relationship Between Strength and Toughness in Metallic Alloys

The need for high strength while still retaining adequate toughness for safe operation places severe limits on the number of alloys that can be considered for the construction of models for the HRNCWTs. Thus, for example a typical model will call for a yield strength at room temperature of about 1000 MPa and the minimum acceptable fracture toughness at the lowest operating temperature in the ETW is 93.5 MPa√m. When applied together these two design requirements reduce drastically the range of candidate materials. Basically, this is because most metallurgical techniques that increase the yield stress also reduce the fracture toughness. Furthermore, as the critical flaw size in a structure is related to the crack size factor,  $(K_{Ic}/\sigma_y)$ , an increase in yield stress without a corresponding increase in the fracture toughness will lower the resistance of the material to unstable, low-energy crack propagation. This toughness-strength trend for structural materials is illustrated in Figure 2. Most materials fall between the two trend lines, those at the upper boundary having the highest toughness for a given yield stress. Considerable effort has gone into producing materials with properties which lie above the upper trend line, largely in an effort to find materials for the large superconducting magnets used in the atomic fusion programme. Two main approaches have been used:

- increasing the strength of intrinsically tough materials, as in the high-nitrogen, high-manganese austenitic stainless steels, and,
- increasing the fracture toughness without losing strength in ferritic steels by the use of multiple stage heat-treatment through the austenite / austenite + ferrite phase transformation region. This approach was used by Rush<sup>2</sup> to improve the toughness of some heats of 18Ni maraging steel and other ferritic alloys.

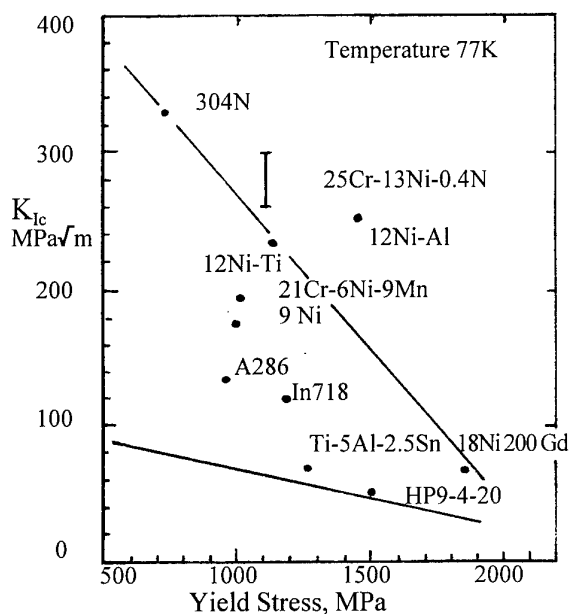


Figure 2. Generic Toughness versus Strength Relationship for Metallic Alloys at 77K.

In practice, however, few of these improvements have reached the stage where they can be applied directly to material purchased for making models and the initial promise of grain-refined 200 grade 18 nickel maraging steels has not been consolidated. Nevertheless, improvements in modern melting, casting and forging practices have made it possible to produce cleaner materials with better properties.

One further fundamental metallurgical characteristic has had a serious impact on achieving the required levels of toughness in thick sections of materials such as the 200 grade 18 nickel maraging steels. Manufacture of stings for the ETW has required the use of forgings up 480 mm in diameter and this has allowed very little working down from the original cast ingot of about 600 mm diameter. The original as-cast structure is not adequately broken up and the average grain size is large. As a consequence the fracture toughness, particularly at low temperatures, is much lower than that obtained on small-diameter, well-forged bars. This problem becomes less severe as the bar diameter or plate thickness decreases, but it is still difficult to obtain 200 grade maraging steel which meets the toughness requirement of 93.5 MPa√m at 77K in the 100-150 mm thick plate needed for the wing, or the 150 mm diameter bar needed for the fuselage of a model. This problem is discussed further in section 4.2.

### 3.8 Fatigue in Uncracked Components

Fatigue failure occurs in flaw-free materials subjected to cyclic or fluctuating stresses and it must be considered as a possible failure mode in wind tunnel models. There is a strong correlation between the fatigue and tensile strengths of most metals as both are increased by those metallurgical factors that increase the ability of a material to work harden. The ultimate tensile stresses of all the alloys of interest for HRNCWTs increase at low temperatures and their fatigue lives show corresponding increases. Indeed, experiments have shown that in many metals the ratio of the endurance limit at  $10^5$  cycles to the ultimate tensile stress is virtually independent of the testing temperature.

If free expansion and contraction is restricted by external constraints during thermal cycling, or if there are large temperature gradients, the resultant high stresses and strains can cause thermal fatigue. In this type of low-cycle, high-strain fatigue, small amounts of plastic deformation take place during each loading cycle and cumulatively lead to failure.

Pre-existing flaws, notches, cracks, badly radiused corners and other surface defects have a strong influence on fatigue lives, causing them to drop sharply at all temperatures even in materials which are not normally considered to be notch sensitive. This is usually a result of the increase in stress intensity brought about by the sharp fatigue cracks and it is particularly severe in some high-strength aluminium alloys, titanium, and stainless steels which are known to be notch sensitive.

### 3.9 Fatigue Crack Propagation Rates

It is possible to apply the concepts of fracture mechanics to crack growth under cyclic applied stresses. The relationship between crack growth rate,  $da/dN$ , and the stress intensity factor range,  $\Delta K$ , is given by the Paris equation:

$$da/dN = C (\Delta K)^n \dots\dots\dots (4)$$

Many data compilations give the constant  $C$  and the exponent  $n$  in the Paris equation. Predicted component lives are then obtained by calculating how many cycles are required to increase the flaw size from its initial to the critical value. Use of the Paris equation and the alternative Forman's equation are discussed in more detail later.

In general, fatigue crack growth rates decrease at low temperatures for most metals normally used for the construction of cryogenic equipment. In contrast they increase for ferritic steels at temperatures below the ductile-brittle transition.

### 3.10 Corrosion and Embrittlement

As has been shown, the fracture stress of a material is strongly influenced by the presence of cracks and flaws. There are three principle mechanisms by which such cracks may form or intensify during service: (1) fatigue, (2) corrosion (especially-stress corrosion and corrosion-fatigue), and (3) hydrogen embrittlement. None of these is a specifically low-temperature phenomenon, indeed the rates at which most corrosion reactions take place drop rapidly as the temperature falls. Rather they increase the probability of unstable failure under service conditions which would normally be considered satisfactory. Their effect is the result of one or more of the following factors: (a) they lower the toughness of the material, (b) they provide a mechanism whereby a crack sharpens and increases the degree of stress concentration, or (c) they allow a sub critical crack to grow at stresses below the gross yield stress until it reaches the critical length required for unstable propagation.

Both corrosion and hydrogen embrittlement are mechanisms by which failure can occur without warning long after the initial application of the stress and they can cause failure at low temperatures even though the actual corrosion or embrittlement is more likely to have taken place at or above room temperature. Stress-corrosion resulting from internal residual stresses is liable to occur in brass, aluminium, magnesium, titanium, and steel as well as some non-metals. It is usually prevented by annealing at a temperature high enough to remove the residual stresses without weakening the material.

#### 4. MATERIALS FOR CONSTRUCTING MODELS, BALANCES AND STINGS

##### 4.1 Stainless Steels.

###### 4.1.1 Metallurgical and Dimensional Stability

In order to fabricate a model to high levels of dimensional accuracy, the material from which it is made must be completely stable. The face-centred-cubic austenitic (gamma) phase of iron is normally only stable at high temperatures, but the addition of alloying elements such as nickel, manganese, carbon and nitrogen can suppress the gamma-alpha transformation and enable the gamma phase to be retained to below room temperature. The austenite structure is, however, only metastable and machining-induced and other stresses and/or cooling can cause a partial transformation to martensite to take place in some of the less highly alloyed steels. The martensite gives an increase in strength but loss of toughness in the transformed state. Furthermore, the transformation is accompanied by a volume expansion which can cause warpage in asymmetric sections such as model wings and spoil the fit of accurately machined components. Martensite is ferromagnetic and this allows the presence of martensite to be detected in otherwise austenitic stainless steels

The stability of 300 series stainless steels can be deduced from their chemical composition by calculating their martensite start,  $M_s$ , temperatures using the Eichelmann-Hull equation:

$$M_s (K) = 1578 - 1667(C+N) - 61.1(Ni) - 41.7(Cr) - 33.3(Mn) - 27.8(Si) - 36.1(Mo) \dots\dots(7)$$

where (Ni) is the wt% nickel etc.

The most stable steels are those with the lowest  $M_s$  temperatures. For example, the high (20%) nickel content of type 310 gives it a calculated  $M_s$  of about -2000K and makes it the most stable member of the 300 series stainless steels. The equation also emphasises the very strong austenite-stabilizing action of carbon and nitrogen and explains why the so-called 'Hi-proof' grades, 304N, 316N and 347N, which contain 0.2% nitrogen to increase their yield strengths by about 70 MPa, are also very much more resistant to martensite transformation than the normal grades. Similarly, it also explains the problems associated with older batches of type 304L which had nickel contents only just above the minimum allowable values and low carbon contents to prevent weld decay. Martensitic transformation occurred because small variations in the carbon and nitrogen content had a large influence on the austenite stability. The problem has been overcome in modern European grades, such as Werkstoff Nr. 1.4306, (the German version of 304L) that have minimum nickel contents of 10% to ensure complete stability at low temperatures. Thus, the European composition type 304L is suitable for most low-strength HRNCWT applications and, if it can be obtained in the required product forms, the high-nitrogen type 304LN (Werkstoff Nr. 1.4311) provides higher yield strengths. Finally, if some martensitic transformation does occur in a particular batch of 300 series stainless steel, and if a partially martensitic material is not a drawback for a particular application which demands good dimensional stability, it is sometimes possible to ensure that transformation is complete before final machining. This may be achieved by cycling repeatedly between 300 K and 77 K, if necessary taking measurements after each few cycles, until no further significant dimensional changes occur.

Dimensional stability is an even more serious problem in the semi-austenitic stainless steels such as 17-7PH and PH 15-7Mo, where unstable retained austenite can revert to martensite, and these steels are not recommended for use in HRNCWT models. Similarly, there is also a severe problem in the use of the medium-strength, precipitation-hardened 15-5PH martensitic stainless steel. It is too brittle to be used with the stable martensitic structure produced by the H900 and H925 heat-treatments. However, if the toughness is increased by using the higher temperature heat-treatments, in particular the H1150M condition that gives adequate toughness at 77K, the microstructure contains significant amounts of unstable, reformed austenite which transforms to martensite on cooling below room temperature. 15-5PH is therefore also not recommended for use in HRNCWT models.

It is, however, possible to use the higher strength precipitation-hardened martensitic stainless steel PH13-8 Mo for HRNCWT models if it is heat-treated to give it a stable microstructure. The use of PH13-8Mo is discussed further in paragraph 4.1.5. Inconel 718 and other nickel based alloys, beryllium copper and other copper-based alloys, aluminium alloys and titanium alloys likely to be considered for cryogenic wind tunnel models have stable metallurgical structures and so not suffer from dimensional instability. Finally, it is sometimes found that there is a very small amount of apparent dimensional instability in the 18Ni maraging steels after rough machining. This is discussed further in paragraph 4.2.2.

###### 4.1.2 300 Series Stainless Steels

300 series stainless steels have only moderate yield strengths, typically about 250 to 300 MPa at room temperature and 450 to 700 MPa at 77K. Ultimate tensile strengths are typically 550 to 650 MPa at 300K and 1300 to 1600 MPa at 77K. Due to these low strengths, the 300 series stainless steels are only suitable for low-stress applications and for HRNCWTs this limits their use to those parts of a model which do not experience high aerodynamic loads. Charpy V notch impact energies are typically above 150 Joules and  $K_{Ic}$  values are above 300 MPa/m even at 77K. There are no toughness problems even at the lowest operating temperatures. It should, however, be noted that 300 series steels can become sensitised if they are held for a significant time in the temperature range 590 to 920°C. Carbides and sigma phase are precipitated at the grain boundaries and this causes a serious loss of toughness at low temperatures and enhanced inter-granular corrosion at ambient temperature.

300 series stainless steels are relatively poor conductors of heat and they are used in thin sections as heat-breaks. Thermal conductivities are about 15 W/m.K at 300K, falling to about 8 W/m.K at 77K. Specific heats at room temperature are about 480 J/kg.°C, dropping to about 220 J/kg.°C at 77K. Expansion coefficients at room temperature are about  $16 \times 10^{-6}$  m/m.K, falling to about  $13 \times 10^{-6}$  m/m.K at 77K. The total linear contraction between 300K and 77K is about 0.285%. The similarity between their expansion coefficients and those of the higher-strength precipitation-hardened stainless steels, such as A286 and PH13-8Mo, makes it possible to combine 300 series steel with the stronger varieties. Fabrication of the 300 series stainless steels is relatively straightforward. Their machining characteristics are well known and should not present problems for a competent machine shop. Similarly, joining techniques, such as welding, brazing and soldering are well established.

#### 4.1.3 Nitronic 40 Stainless Steel

Nitronic 40 is the Armco name for the 21-6-9 type of nitrogen-strengthened austenitic stainless steel with the composition 21% chromium, 6% nickel, 9% manganese and up to 0.4% nitrogen. It has a completely stable austenitic structure and, although manganese is not so efficient as nickel in stabilising the austenite phase, it allows more nitrogen to go into solid solution, thus both increasing the stability and raising its yield strength. The yield strength of Nitronic 40 is about 480 MPa at room temperature and 1030 MPa at 77K, while its ultimate tensile strength is about 760 MPa at 300K and 1380 MPa at 77K. Charpy V notch impact energies are typically above 80 Joules and  $K_{Ic}$  values above 180 MPa $\sqrt{m}$  even at 77K. There are thus no toughness problems with the use of un-sensitised Nitronic 40 even at the lowest HRNCWT operating temperatures. Its physical properties are similar to those of the 300 series stainless steels.

Nitronic 40 was used for fabrication of the fuselage, the empennage and the instrumented wing of the full scale Pathfinder model for the NTF. Some delta ferrite was present in the thick plate used for the wing but this did not appear to have any significant adverse effects. The Nitronic 40 used for Pathfinder 1 had been furnace cooled through the critical temperature range between 590 and 929°C and its microstructure had carbide precipitates in the grain boundaries. This sensitisation can cause intergranular corrosion due to the lowering of the chromium content in the adjacent regions and it also has serious adverse effects on the toughness at low temperatures. As Charpy impact energies measured at 103K were only just above the required minimum of 34 J, measurements were made of the fracture toughness in this condition.<sup>3</sup> It was found that, even at 103K,  $K_{Ic}$  values estimated by the equivalent energy technique were about 400 MPa $\sqrt{m}$ . There was therefore no correlation between these measurements of  $K_{Ic}$  and the values determined using the Barsom-Rolfe relationship and the low Charpy impact energies measured on the same material.

Fabrication of Nitronic 40 is basically similar to the 300 series stainless steels, but care has to be taken to ensure plentiful cooling as Nitronic 40 work-hardens rapidly. This increases machining costs due to the extra time and tool costs involved. The Pathfinder 1 mode for the NTF was shaped by CNC machining using ball-ended milling cutters and hand finished. Brazing was used to insert orifice plugs and pressure tubes into the pressure wing.

#### 4.1.4 A286 Precipitation-Hardening Stainless Steel

The composition of A286 is 25Ni-14Cr-2.2Ti-1.5Mn-1.2Mo-1.5Mn-0.5Si-0.2V-0.2Al and it has a completely stable austenitic structure. The titanium, vanadium and aluminium additions go into solution during solution-annealing at 900 or 980°C which puts the material into condition A. Hardening occurs when precipitates form during heat-treatment at 720°C to give the STA condition. The yield strength of A286 in condition STA is about 650 to 770 MPa at room temperature and 830 to 930 MPa at 77K, while its ultimate tensile strength is about 850 to 1050 MPa at 300K and 1320 to 1480 MPa at 77K. The lower strengths are associated with thicker sections. Charpy V notch impact energies are typically above 70 Joules and  $K_{Ic}$  values above 120 MPa $\sqrt{m}$  even at 77K. There are thus no toughness problems even at the lowest HRNCWT operating temperatures. A286 was used for fabrication of the reference model for the ETW as well as for numerous NTF models including models of the space shuttle.

The physical properties of A286 are similar to those of the 300 series stainless steels.

One of the main disadvantage to the use of A286 for models is the difficulty encountered during machining. It work-hardens very rapidly and severe tool wear can occur if milling, turning and drilling conditions are not optimised. Although rough machining can be carried out in the solution-annealed condition, it is normally considered advisable to carry out intermediate and finish machining on material in the hardened STA condition. High quality modern machining techniques and tools are required if A286 is to be machined cost-effectively. Furthermore, very large surface stresses can be induced during machining and if hold-down and release procedures are incorrect, warpage can occur when the model is released from its supports after final machining.

Electron-beam welding has been used to assemble small model parts and brazing used to install pressure tubes. Vacuum brazing was used to assemble stacks of 1 mm thick sheets of A286 containing chemically milled channels into a model of the X29 canard containing a high density of pressure orifices in a thin aerofoil section.<sup>4</sup>

#### 4.1.5 PH13-8Mo Precipitation-Hardening Stainless Steel

The nominal composition of PH13-8Mo is 13Cr-8Ni-1.1Al-2.2Mo. Its microstructure and properties depend critically on the heat-treatment temperature used for aging. After aging at the lowest temperature of 900°F (482°C) the microstructure is completely martensitic and the material is far too brittle for use at low temperatures. Aging at 1400°F (760°C) for 2 hours and then at 1150 F (621°C) for 4 hours increases the toughness by producing a microstructure of overaged martensite and austenite which is almost completely stable. After this H1150 M heat-treatment the yield stress at room temperature is about 590 MPa and at 77K it is about 1000 MPa. The ultimate tensile stress increases from about 900 MPa at 300K to about 1200 MPa at 77K. NASA specified the H1150 M heat-treatment for the PH13-8Mo used to fabricate the half-scale Pathfinder 1 model, the force wing for the full-scale Pathfinder and other NTF models as this heat-treatment gives the maximum toughness at 77K.

In contrast, the PH13-8Mo used to fabricate the TST demonstrator model utilised the H1125 (608°C) heat-treatment. In this condition the yield stress is about 900 MPa at room temperature and at 120K it varies from 1000 to 1250 MPa. At room temperature the ultimate tensile stress is about 1070 MPa and this increases to about 1300 MPa at 120K. A development programme<sup>5</sup> proved that the material had a Charpy V notch energy higher than the required 34 J in the transverse direction at the lowest operating temperature of 120K (-153°C). Any small amounts of metastable austenite could be forced to transform to martensite by cycling from room temperature to liquid nitrogen three times before final machining. The material is then completely dimensionally stable. Its physical properties are similar to those of the 300 series stainless steels.

PH13-8Mo is considered easier to machine than either Nitronic 40 or A286, but not as easy as the 300 series stainless steels. Rough machining may be carried out in the solution-annealed condition, but, due to the rather large contraction of up to 0.0035 mm/mm that can occur during age hardening, final machining should be carried out after age hardening.

## 4.2 18 Nickel Maraging Steels

Unlike conventional high-strength steels in which martensite is a hard and brittle phase, maraging steels are basically low-carbon, iron-nickel-cobalt-molybdenum alloys in which age-hardening of the soft martensite occurs by the precipitation of titanium and aluminium intermetallics. They are easy to machine in the solution-annealed condition, dimensional changes during ageing at the relatively low temperature of 480°C are small and predictable and components can be finish-machined before ageing. 18Ni maraging steels are not stainless steels, as they contain no chromium, but they do not corrode under normal cryogenic wind tunnel operating conditions if handled correctly.

There are four grades of maraging steel generally available in the USA and Europe, 200, 250, 300 and 350, the grades being denoted by their nominal yield strengths in psi  $\times 10^3$ . Only the 200 and 250 grades are suitable for HRNCWT applications as the fracture toughness of the 300 and 350 grades are too low. In the UK, 200 grade is known as G90 and 250 grade as G110, from the values of their yields strength in tonf/in<sup>2</sup>. In France, two other maraging steels with slightly different compositions are available. Marvel 18 has a yield strength of about 1690 MPa at room temperature and it has been used to make models and balances for cryogenic wind tunnels. Marvel 18H with a yield strength of 1970 MPa has a fracture toughness too low for use at low temperatures. The 200 grade of 18Ni maraging steel has been used for the manufacture of more models for the NTF than any other material. It has also been used for models tested in the ETW and the KKK. The 250 grade has been used to make balances for both the ETW and the NTF.

### 4.2.1 200 Grade

The nominal mechanical properties of 200 grade 18Ni maraging steel at 300K and 77K are shown in Table 2.

Table 2. Properties of 200 Grade 18Ni

Property	At 300K	At 77K
Yield, MPa	1413	1862
UTS, MPa	1448	1931
Charpy, J	48	34
$K_{Ic}$ , MPa/m	187	92

It can be seen that at 77K the Charpy impact energy and the fracture toughness,  $K_{Ic}$ , are on the borderline of the required values of 34 J and 93.5 MPa/m. In practice, the matter is even more serious as even these values can only be obtained in small diameter bars and thin plates. Care must be taken to ensure that the best possible steel making procedures are used in its manufacture if the highest possible toughness is to be obtained.

Some of the most relevant data on the properties of maraging steels at low temperatures has been published by Wagner.<sup>6,7</sup> As well as giving data on tensile properties, Charpy impact energy and  $K_{Ic}$  at 293K and 103K, he carried out an analysis of the fracture surfaces. Observations at high magnification showed that the distinguishing feature of low toughness specimens was the significantly greater number of large angular particles,

identified by microprobe analysis as primary titanium nitrides. Many of the particles were fragmented, suggesting that they had failed in a brittle manner before nucleating the linear voids that were a feature of the ductile-dimple fracture surfaces.

Wagner also carried out the grain-refining treatments originated by Rush<sup>2</sup>, but without achieving significant improvement in the toughness at low temperatures. He concluded that grain-refining only improves the toughness in relatively low quality 18Ni maraging steels and that similar improvements cannot be expected from modern higher-quality steels.

ETW now has much experience in the use of large diameter forged bars of 200 grade 18Ni maraging steel at cryogenic temperatures. This has shown that the impact energy of Charpy samples for 420 mm diameter forged bar can be as low as 16 J and that even for 200 mm forged bar the impact energy is only just over 25 J at 77K. These trends are due to the metallurgical structure of the material. When it is cast into about 600 mm diameter billets, a relatively coarse as-cast grain structure is produced and any second phase particles are relatively large. During hot forging, the large grains are broken up and smaller recrystallised grains are formed during cooling. The second phase particles are also reduced in size and dispersed through the material. During forging to 420 mm diameter, only relatively small amounts of grain reduction and particle size distribution are possible and the transverse ductility and toughness are reduced, especially at cryogenic temperatures. However, further forging to smaller diameters improves the metallurgical structure and there is a corresponding improvement in toughness.

Toughness is highly dependent on the orientation of the specimen. In a forged bar the grains are elongated in the axial direction and the inclusions tend to be located in bands also oriented axially. Cracks are more difficult to propagate in the radial direction as they are deflected around these inclusions. Charpy specimens that are machined with their 55 mm length along the axis and the notch cut in a radial direction, so-called AR or LR specimens, give the highest impact energies as the crack front has to propagate along this tough direction. In contrast, specimens machined with the 55 mm length along a radius and with the notch cut in an axial direction, RA or RL specimens, give the lowest impact energies as the cracks propagate between the inclusions. In the RR specimen the long axis lies along a radial direction and the crack propagates in an orthogonal radial direction. Two types of RR specimen can be identified: specimens cut from near the surface with their long axis oriented along a radius and with the crack propagating along a chord are identified as RC specimens, while those with their long axis oriented along a chord and with the crack propagating along a radius are identified as CR specimens.

The data generated from the fabrication of many large diameter components for ETW has allowed a quantitative relationship to be found for the relationship between diameter and Charpy V energy at 77K.<sup>8</sup> This is shown diagrammatically in Figure 3. It must be emphasized that this analysis can not be considered as a rigorous scientific test programme as it has not been possible to use data obtained from material with a common metallurgical origin. Rather, it should be seen as an attempt to collate and to rationalise available data within its limitations and as an aid to the prediction of realistic values for the toughness of large diameter forged bars.

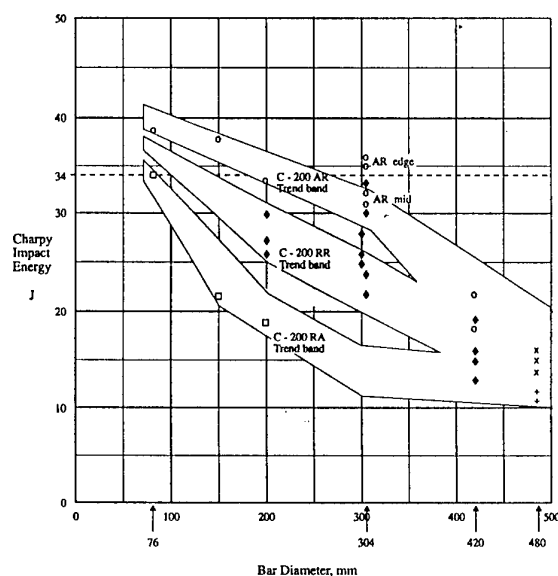


Figure 3. Bar Diameter vs  $C_v$  Relationship

The Figure shows three trend bands: The upper is for the toughest AR direction in which the cracks have to propagate across the axially oriented gains and inclusion stringers. The lowest is for the weakest RA and CA directions in which the cracks run parallel to the axial grains. The intermediate band is for the RR, CR or RC directions in which the crack propagates in a nominally radial direction. In the case of the 480 mm diameter bar only CR and CA specimens were available from the ~20 mm thick slice cut from one end of the forging. For the CA direction the average  $C_v$  energy was almost 12 J at 80K, while for the CA direction the average  $C_v$  energy was 15 J. Due to the small reduction in thickness, there is relatively little grain orientation in such large diameter bars and the three trend bands overlap. Charpy energies at 77K lie between about 10 and 20 J for all orientations.

As the bar diameter is further reduced, the grains and inclusions become oriented axially and at about  $\phi 300$  mm there is the greatest difference between the RA / CA oriented specimens, which have  $C_v$ s of about 12 to 15 J, and the AR oriented specimens, where  $C_v$  can reach about 35 J. The  $C_v$ s of AR specimens taken from near the edge of the bar are also significantly larger than those from near the centre of the bar. Further reduction down to about  $\phi 200$  mm causes a marked improvement in the transverse properties, with  $C_v$ s of the RA / CA specimens lying between about 17 and 22 J. After further reduction to  $\phi 100$  mm, the average  $C_v$  of the RA / CA specimens has risen to about 30 J. These improvements in transverse toughness are probably due to the breaking up of the banded inclusions and the formation of a finer grain structure. The axial properties also improve as the bar diameter decreases, but not so strongly. Thus, the average  $C_v$  for the AR specimens rises from ~32 J at  $\phi 300$ , to ~35 J at  $\phi 200$  and ~38 J at  $\phi 100$  mm. The trend band for the RR / CR / RC orientations lies approximately mid-way between the other two trend bands for all bar diameters.

To date, the toughness of all material with diameter or thickness above about 100 mm has failed to achieve the required 34 J at 77K in a Charpy test. Fracture toughness analyses should thus be carried out on all 18 Ni maraging steel components above this diameter. Critical crack sizes can be kept small enough if stress concentrations are minimised and working stresses are kept below UTS/4.

Fatigue and crack propagation analysis should also be carried out to show that the working life is acceptable.

**In essence, the successful use of 200 grade 18Ni maraging steel at low temperatures requires that the working stresses are kept below a limit determined by the toughness that can be achieved from the diameter of material available.**

The 18 Ni maraging steels have a density of 7920 kg/m<sup>3</sup>. They are relatively poor conductors of heat, with thermal conductivities of about 21 W/m.K at 300K and falling to lower values at 77K. Similarly their electrical conductivities are relatively low, resistivities typically being about 65 micro-ohm.cm in the solution-annealed state and about 0.4 micro-ohm metres in the aged condition at room temperature. The specific heat is about 450 J/kg.°C at 300K. Expansion coefficients at room temperature are about  $9 \times 10^{-6}$  m/m.K, falling to about  $6 \times 10^{-6}$  m/m.K at 77K. It should also be noted that during maraging at 482°C, 200 grade undergoes a contraction of 0.0006 mm/mm after 6 hours and 0.0007 mm/mm after 9 hours. For 250 grade the contractions are 0.0009 and 0.0011 mm/mm after 6 and 9 hours, respectively.

#### 4.2.2 Fabrication

Wherever possible, large maraging steel items should be forged as closely as possible to the final shape. Firstly, the toughness is improved by forging and, as the most highly stressed regions are usually at the smallest diameters, forging enables the best metallurgical structure to be produced in the highly stressed region. Secondly, the basic material cost of 18Ni maraging steel, is quite high and forging costs are relatively low. Thus the net cost of a forged billet can be lower than that of a constant-section, large-diameter bar, as the cost of forging is often more than offset by reduction in the amount of material needed. Furthermore, there are additional savings to be realised in the machining costs, as less work has to be carried out on machining the forged component to its final shape.

Maraging steels are machined most easily in the annealed condition where their machinability is comparable to steels of the same hardness level, 30 to 33 Rc, such as 4340. They can also be machined in the aged condition, hardness 43 Rc for 200 grade and 50 Rc for 250 grade, but the choice of cutting tools and machining conditions become very important. In particular, rigid equipment and firm tool supports are essential and the tools should receive a plentiful stream of cutting fluid especially at their cutting edges. Small problems with machining-induced dimensional changes the model can be avoided by cryocycling into liquid nitrogen 3 times before final machining as this triggers off the transformation of any small amounts of austenite into stable martensite.

18Ni maraging steels can be ground in both the annealed and aged conditions. Grinding is similar to ordinary construction steels when using highly sulphurised oil or heavy duty water-soluble grinding fluid as employed with stainless steels. The use of heavy duty grinding fluid is essential as wheel wear is about ten times greater when ordinary water soluble oil is used. Maraging steels are not completely corrosion resistant and it is important that fresh grinding fluid is used when grinding maraging steel as there are indications that corrosion may be caused either by the use of old fluids or by bi-metallic reaction with particles of other metals that have not been completely removed by the filters.



### 4.3 Nickel-Chromium Alloys.

Inconel 718 is a precipitation-hardenable nickel-based superalloy with a fully stable fcc structure and a nominal composition Ni-18.6Cr-18.5Fe-5.1(Nb&Ta)-3.1Mo-0.9Ti-0.4Al. The metallurgy of superalloys is complex, VIM/VAR melting of the cast ingot is essential and good quality control is necessary during processing and fabrication. Mechanical properties for Inconel 718 in the solution-treated and double aged, STDA, condition vary considerably, depending on the product form, its thickness and the source of the data. For example, yield strengths range from about 1040 to 1170 MPa at room temperature and 1200 to 1350 MPa at 77K, while ultimate tensile strengths range from about 1270 to 1400 MPa at 300K and from 1620 to 1730 MPa at 77K. Values for the fracture toughness also vary considerably, but most sources show that  $K_{Ic}$  increases as the temperature falls. For example, one source gives values of about 90 MPa $\sqrt{m}$  at 300K, rising to about 110 MPa $\sqrt{m}$  at 77K. The combination of high yield stress and moderate fracture toughness indicate that a full fracture mechanics analysis should be carried out for highly loaded models.

Difficulties in machining Inconel 718 arise basically from its high work hardening rate. A stressed layer of deformed metal is formed in the surface of the metal and this hard layer retards further machining, causes rapid tool wear and can lead to distortion if the surface stresses are uneven. Inconel 718 was considered for construction of Pathfinder 1 for the NTF, but at that time the alloy was considered too difficult to machine. However, advances in tooling technology for conventional machining operations, such as milling, and other machining techniques, such as chemical milling, electro-discharge machining, etc., have now made Inconel 718 and other nickel-chromium and iron-nickel alloys serious contenders for models.

### 4.4 Aluminium Alloys

Aluminium alloys have been used to construct simple, lightly-loaded models for large cryogenic wind tunnels such as the NTF. In particular, alloy 6061 in the T6 condition was used to make a series of six solids of revolution having the same size and shape as the bodies of models tested in the NTF. Aluminium alloys are easy to machine but their elastic moduli and strengths are too low for use in more heavily loaded components such as aerofoils. Complications can also arise if aluminium and steel components are mixed in the same model as the two materials have very different expansion coefficients.

### 4.5 Copper Alloys

Copper and its alloys such as brass have been used for many conventional cryogenic applications, but they have limited application for models due to their relatively low strengths. The only exception is the precipitation hardened beryllium copper (BeCu) whose yield strength can reach 1000 MPa, while still retaining a high thermal conductivity when compared to other materials used for models. For example, the high thermal conductivity made it possible to maintain nearly uniform surface temperatures in a 2 dimensional BeCu aerofoil fabricated by the Douglas Aircraft Company and tested in the 0.3 m TCT. Liquid nitrogen was ducted through the model which was used to validate the use of hot film transition detectors. D.A.C. also considered the use of ½ hard Beryllco-25 for the wing of a DC10 model for their cryogenic blow-down tunnel. Beryllium copper has also been considered for use in balances where its high thermal conductivity can minimise thermal gradients.

However, one severe limitation on its use is its low toughness, especially when heavily work hardened and aged.

Due to its low atomic mass, the beryllium content is about 12-14 atomic %, which is greater than the solubility limit. During the aging heat-treatment, the excess is precipitated as Cu-Be intermetallics which harden the copper matrix. The greatest response to aging occurs in the cold rolled hard temper. Much of the available information on the cryogenic properties of beryllium copper is on Beryllco 25. This alloy contains 1.8% Be, 0.2% Co and 0.1%Al, which conforms to the composition of a C17200 alloy. A very wide range of yield and tensile strengths are available from different combinations of solution treatment, cold work and precipitation hardening. Room temperature yield strengths are typically up to 690 after age-hardening and up to 1350 MPa after cold working and aging.

The Charpy impact energy depends on the degree of hardening and there is a clear correlation between increasing yield strengths and decreasing Charpy impact energies. For the solution-treated and aged AT condition and the ½ HT solution-treated, cold-worked and aged condition the impact energies are very low, typically increasing from about 6 J at room temperature to 9 J at 77K. In order to achieve higher toughness, the material has to be used in one of the lower tempers, possibly ½ H, with significantly lower yield and tensile strengths. Furthermore, much of the data availability is from small diameter bar and there are reports that Charpy energies from larger diameter bar and thicker plate are significantly lower.

**Thus, although initial design may be carried out using data from the literature, final acceptance will be based on the values measured on the actual material from which the model or balance is manufactured. It is essential that the tensile and Charpy specimens are taken from suitable locations in the material and that they receive identical solution annealing, cold work and heat-treatments to those received by the model.**

Beryllium coppers have good fatigue characteristics, with fatigue lives increasing significantly at low temperatures and one traditional use of BeCu alloys is for springs. Nevertheless, the low toughness of beryllium copper in the condition required to achieve the desired strength levels makes it essential that a full fracture mechanics analysis is carried out to establish critical flaw sizes and fatigue crack growth rates.

The Young's modulus of Beryllco 25 in the STA condition increases from 123 GPa at 293K to 134 GPa at 77K. In the ½ hard and aged condition it rises from 126 GPa at 293K to 133GPa at 77K.

The density of Beryllco 25 is 8230 kg/m<sup>3</sup>. Its expansion coefficient at 293K is about  $17.0 \times 10^{-6}$  mm/mm.K and the total linear contraction between 293K and 77K is about 0.3%. The specific heat at room temperature is about 419 J/kg, dropping to about half this value at 77K. The thermal conductivity of Beryllco 25 ranges from about 84 to 105 W/m.K at room temperature depending on the temper, with the lowest conductivities in the full hard condition. It drops to about half these values at 77K.

In the solution-treated condition the alloy can be machined and formed easily. After precipitation hardening it is more difficult to machine.



## 5. FABRICATION TECHNIQUES

### 5.1 Machining.

Fabrication of models for cryogenic wind tunnels involves long and often costly machining processes and much time and money can be lost if the machining parameters are not optimised correctly. For example, incorrect tool speeds, feed rates, types of lubrication and other parameters can cause excessively high tool wear rates during CNC milling and consequent additional costs for tool bits and operator down time. In extreme cases tool wear could be so severe, and the model so over-size, after the final cut that it could not be hand-worked to the required final dimensions. It is thus not surprising that such details are regarded as commercially sensitive information that can give one fabricator a decisive edge over competitors.

Probably the most important machining operation in the fabrication of a model for cryogenic wind tunnels is CNC milling of the external contours of the body and the aerofoil sections, such as wings and vertical and horizontal stabilisers. Correct machining parameters must be used for both rough and final CNC machining if the induced surface stresses in the model and the wear rates of the cutting tools are both to be minimised.

### 5.2 Machining-Induced Dimensional Instability

Of all the materials of interest for fabrication of models for cryogenic wind tunnels discussed in Section 4, A286 is the most susceptible to dimensional changes induced by machining and it gives a good insight into the dimension changes that are induced during conventional machining operations. A286 was one of the materials studied during a NASA sponsored investigation of dimension stability using stepped specimens. 200 grade 18Ni maraging steel, PH13-8Mo and HP 9-4-20 were also investigated and the results are reported in reference 9. The results obtained demonstrated the main facets of the behaviour of machining-induced deformation in these materials.

#### Milling

Milling induced large compressive surface stresses in all four materials studied in the stepped specimen programme. There were not enough specimens in the NASA programme to enable the effects of even the most basic processing variables to be studied independently, but there were definite indications that larger stresses were induced by heavier cuts. It is normal practice when using ball-ended cutters under CNC control to try to have the desired shape and size defined by the bottoms of the scalloped cuts. The high points are then subsequently removed by hand working to produce the model profile and required surface finish. Such finishing is unlikely to relieve the milling-induced stresses and thus the finished model should retain the compressive surface stresses that would improve its fatigue performance.

#### Grinding

None of the samples in the stepped specimen programme were machined by grinding alone. However, in all cases where grinding followed a previous milling step which had induced compressive stresses, grinding caused a large reduction in the previous deflection. For some specimens net tensile surface stresses were set up, strongly suggesting that grinding does indeed produce tensile surface stresses.

#### Dimensional Changes During Cryocycling

After the 6 mm and 3 mm steps had been machined, the specimens were cycled between room and liquid nitrogen

temperatures three times and then re-validated. There were essentially no dimensional changes induced by cryocycling A286 and this confirms other evidence that it is dimensionally stable during cryocycling. Significant dimensional changes were, however, measured during the initial NASA tests in samples of PH13-8Mo, due to the transformation of small amounts of metastable austenite to martensite. In general, maraging steel samples were found to be almost as dimensionally stable as A286, but during the first series of tests there were indications that a little movement had taken place in some samples. Longer samples and more realistic machining schedules were utilised in later tests, together with a very reproducible measuring system with a sensitivity limit of about 5 microinches. Very little movement was detected when the samples were re-measured after the first cryocycle, or after many subsequent cryocycles.

Thus the deflections induced in 18Ni maraging steel by cryocycling appear to be negligible for small items such as the stepped specimens. Furthermore, co-ordinate checks on models made for the NTF before and after test campaigns at cryogenic temperatures failed to reveal any significant dimensional changes. However, there are recent indications that there may be a problem in long, slender components. As the microstructure of an aged maraging steel is believed to be very stable, any small changes induced by cryocycling are probably caused by re-arrangement of stresses within the material, particularly its surface layers. This effect occurs in many alloys, especially steels, and it is exploited commercially in processes such as "cryo-toughening" which are believed to improve the life and wear-resistance of cutting tools.

### 5.3 Optimisation of Machining Parameters

The long term aim of the NASA stepped specimen was to use the modified (120 mm long) stepped specimen to compare the deformation induced by machining a variety of materials and using a range of machining parameters. For the most important materials, larger and/or more contoured specimens were then to be used to scale up towards the dimensions of actual wings and other model parts<sup>10</sup>. Gross and Lück<sup>5</sup> investigated machining-induced deformation in PH13-8Mo using three different types of specimen: the modified NASA-standard stepped specimen, a similar sized specimen in which the steps were replaced by a gradual wedge-shaped machined section and a three dimensional model ( 50% scale ) of the inner portion of the TST model wing. Initial tests were carried out to optimise the quality of the milled surface, with the aim of avoiding deep scratches and thus minimising the amount of handwork needed to obtain a good surface finish. The tests involved varying the kind and size of the spherical cutters, their cutting speeds, their axes of rotation as well as the rotation direction, their cutting depths, the track distances and the type of cooling fluid used for lubrication. These tests also showed that the best combination of machining parameters gave the lowest surface stresses and minimum consequent warpage. For example, the authors state that a 0.9 mm tip deflection of an early specimen was caused by "bad" manufacturing procedures and that avoidance of these faults gave a much lower tip deflection of 0.09 mm in a later specimen. They conclude that their tests demonstrated that a knowledge of optimal material processing is essential for the manufacture of extremely accurate models.

Maraging steels, which are usually machined in the annealed condition, are considered relatively easy to machine using conventional practices.

#### 5.4 Fabrication of High Accuracy Components

From the results described in the previous paragraphs, it is clear that very large stresses can be induced in components fabricated from A286 and other alloys by milling and grinding. In order to fabricate components such as wind tunnel models to a high dimensional accuracy, particularly wings and other parts with thin, non-symmetrical sections, there are a number of precautions that must be taken. One of the most important is the rigid support of the workpiece during machining operations. Induced stresses will then be opposed by the restraining action of the support and the workpiece will not deform. This is normally achieved either by bonding the complete lower surface of the workpiece to a baseplate using an adhesive that can subsequently be removed, or by bonding the lower surface to a series of strong rails that are then bolted to the baseplate or machine bed.

Once the top surface has been rough machined, and while the lower surface is still bonded to the baseplate, the rough-machined surface is bonded to a second baseplate or set of rails. The first baseplate is then released but, as the workpiece is now restrained by the second baseplate, the workpiece does not deform. The lower surface of the workpiece is then machined using exactly the same tools and process variables as were used for the first side. If the material had a homogenous structure and if the machining conditions were indeed the same on both sides, the induced surface stresses should be identical and should balance out. When the workpiece is released from the baseplate it should not deform. In particular, both sides should be milled, or both ground, if the surface stresses are to balance. Thus, in theory, subsequent machining stages proceed in pairs so that the induced surface stresses remain balanced. After each stage the workpiece is released and any deformation caused by un-balanced stresses is allowed for in the next stage. In practice, however, life is rarely that simple, particularly in asymmetrical workpieces.

The other essential is to use sharp tools and to keep the workpiece well cooled and lubricated. This is particularly important in alloys such as A286 that work harden rapidly, as induced stresses can be minimised if the alloy is prevented from work-hardening more than necessary. When milling or turning, sharp tools and the correct down- and cross-feed rates are required to keep the chips coming away from the cutting edge and to prevent the tool from getting clogged. Cutting speeds should not be too high as this encourages the tool to skid over the workpiece and cause work-hardening.

Finally, it is important that the dimensions are checked after each machining stage. Should deformation occur during one of the early machining stages it can sometimes be recovered by mechanical means or by re-defining the co-ordinates to fit within the envelope of the deformed workpiece. There is also the possibility of modifying the machining schedule to use the fact that grinding induces tensile surface stresses while milling induces compressive stresses. If there were only enough material to allow machining on one surface of a wing, grinding this surface with the workpiece free to move up or down would cause the work surface to move upwards, while milling would make it move downwards.

#### 5.5 Surface Finish

It is normally considered that a surface finish of better than 10 microinches is required for cryogenic wind tunnel models and values below 4 microinches have been

claimed for some NTF models. Handwork of the highest quality is needed to obtain such finishes on A286, Nitronic 40 and 300 series stainless steels and, once they are obtained, very careful handling is necessary to avoid scratching and other forms of degradation.

Finally, under the normal type of handling procedures to be expected of models and other wind tunnel components, A286, Nitronic 40 and 300 series stainless steels are basically corrosion-resistant and this is one of the principal reasons for their use. Nevertheless, for the very high standards of finish required for the aerodynamic surfaces of a model, even stainless steels must be treated with care. For example, clean gloves must be used when handling a model or when touching its surface. There are indications that the moisture, acids and greases that are present in the surface layers of skin can cause blemishes that might affect the airflow over the model. Furthermore, as noted earlier, 18Ni maraging steels are not corrosion-resistant and they need to be treated with care to avoid degradation of their surface finish.

#### 5.6 Electro-discharge machining, EDM

Because alloys such as A286 are difficult to machine by the conventional machining processes of turning, milling, drilling, grinding, etc., various non-traditional machining processes are used to carry out specific operations. EDM has been used in the fabrication of models for cryogenic wind tunnels. One important aspect of electro-discharge machining is that it is essentially a stress-free process when considered on a macroscopic scale. Indeed, residual stresses created by previous mechanical deformation can be released during machining. However, the arc strikes on the workpiece surface create a damaged layer which is between 0.01 and 0.13 mm thick. In tool steels, the damaged zone is often known as a "white" layer from its metallurgical etching characteristics. This surface layer is under a tensile stress and it contains microcracks that degrade the fatigue performance of the component. Various techniques are used to remove the surface layer or to mitigate its adverse effect. On externally contoured surfaces, especially those that have had a final light cut and where the damage is about 0.01 mm deep, the layer is usually removed during hand finishing using abrasives. Alternatively, the damaged layer is removed by chemical milling or electrochemical milling.

**Plunge EDM** is one of the oldest forms of the EDM technique, familiar in many workshops for the removal of broken drills and taps. In its more developed form as used a typical model application, a shaped tool would be used to produce a recess in the workpiece. For example, plunge EDM can be used to form the cavity in a wing to accommodate pressure tubes, etc., or to form the webs of a balance. The tool can be given the radius of curvature required at the bottom of the cavity and thus ensure that stress concentrations are minimised.

**EDM Wire Cutting** is a more recent development that essentially produces components or apertures that have complex shapes in 2 dimensions and linear, or conical, symmetry in the third. The electrode is a wire that moves continuously across the workpiece. Typical uses in model manufacture are to "slab" form the initial bar or plate and thus avoid the need for large amounts of rough machining. It is also used to cut complex shapes either on the external surface of the workpiece or to form internal cavities. EDM wire cutting has been used to fabricate 2 D aerofoils with spans up to 16 inches (400 mm).<sup>4</sup>

**Rotary EDM**, originally developed for forming a matrix of very fine, dimensionally-accurate holes for inkjet printer heads, has also been evaluated for the formation of very small diameter pressure orifices in models.

### 5.7 Welding

Conventional fusion welding is rarely, if ever, used for model construction. However, **Electron** and **Laser Beam** welding have been used to join together load-bearing sections of model fuselage, to attach cover plates to wings, to eliminate joint gaps in aerofoil surfaces and to secure retaining pins, etc. EB welding was used by NASA for welding model parts and aerofoils made of precipitation-hardened stainless steels. EB welding was also used in the manufacture of a half model of a transport aircraft for testing in the ONERA T2 cryogenic tunnel.<sup>11</sup> In particular, it was used to join together the two parts of the Marvel 18 maraging steel wing after installation of the on-board instrumentation. Problems can be caused by excessive heat build-up and during welding of the wing halves copper masses were placed close to the weld line in order to aid heat dissipation. Due to these problems, EB welding has now been generally superseded by Laser Beam Welding.

One advantage of **Laser Beam Welding** over EB welding is the ability to dispense with the need for vacuum chambers associated with EB welding. The laser beam can be varied from about 0.02 to 2 mm diameter and the heat is concentrated locally in the joint, thus minimising the annealed area. Dissimilar metals can be welded but the joint must be a close fit to achieve a good weld. No filler wires are used and a minor depression, approximately 0.1 mm deep, is created along the path of the weld. If the welding is carried out while the component is oversized this depression can be removed during hand finishing. Alternatively, the surfaces adjacent to the weld line can be left with an additional 0.2 mm thickness to provide a reservoir of molten metal to compensate for evaporation and shrinkage.

### 5.8 Brazing

Flux-less brazing techniques are almost universally employed for high quality applications such as wind tunnel models. In stainless steels the chromium oxide layer that forms the corrosion resistant surface also inhibits wetting and has to be removed. Fortunately at high temperatures and under high vacuum, the oxide is dissociated and atomically clean surfaces are made available for the molten braze alloy to wet. Vacuum brazing has been used extensively by NASA for many aspects of model fabrication, including bonding together the upper and lower halves of a wing, installation of orifice plugs, assembly of small components, etc.

Furthermore, complex assemblies can be sequentially brazed using filler alloys with successively lower brazing temperatures. For example, orifice plugs can be brazed to stainless steel plugs using a copper-based fillers such as AWS BCu1 at a temperature of about 2050°F (1120°C). After assembling the plugs into the aerofoil surface, the use of a gold-nickel alloy such as AWS BAu4 and a brazing temperature of 1825°F (996°C) forms a load-bearing joint between plug and wing without disturbing the initial plug-tube joint. Further brazed joints could subsequently be made using the silver based fillers such as AWS BA9 13 (brazing range 1575 to 1775°F, 857 to 968°C) and AWS BA93 (brazing range 1175 to 1400°F, 635 to 760°C).

The **Isothermally Solidifying Brazing Alloys** contain boron and silicon additions which depress the melting point of the filler alloy. However, once the filler has melted and wetted the bonding surfaces these small, mobile atoms diffuse into the parent metal their concentration in the molten filler alloy decreases and its melting temperature increases until the brazing alloy solidifies isothermally. These alloys are available in the form of thin foils of metallic glass (an amorphous metal alloy that is made by quenching at a rate of about  $10^5$  to  $10^6$  °C/second.) Foils of AWS BNi2 (MBF20) from Metglas Products, New Jersey, USA. made it possible to develop a thin, highly instrumented thin aerofoil by vacuum brazing thin sheets of A286 to form a laminated block containing integral pressure channels<sup>4</sup>. Other fillers commonly used include the nickel-based alloys AWS BNi 1, 2, 3 or 7, (AMS 4776, 4777 and 4778) with brazing temperature from 1800 to 2200°F (980 to 1210°C).

### 5.9 Soldering

Stainless steels can be soldered if an aggressive flux is used to remove the chromium oxide surface layer and allow the molten metal to wet the bonding surface. Orthophosphoric acid, or a commercial equivalent such as Eutector flux 157, is suitable for this purpose, but it is an aggressive flux and it has to be removed completely after soldering to prevent subsequent corrosion or other problems. The choice of alloy composition is important as, although high-tin alloys are strong and they have good wetting characteristics, they embrittle at low temperatures and they may be affected by a phase transformation known as "tin pest". High lead compositions remain ductile at low temperatures but they are much softer, which creates problems in obtaining a good surface finish, and their wetting characteristics are poor. After testing many compositions, NASA chose 50% Tin, 49.5% Lead, 0.5% Antimony as their preferred alloy for use in the installation of pressure tubes, repair of surface imperfections and other applications on cryogenic wind tunnel models. This solder was used to attach the large number of short length of stainless steel tubing to the pressure channels that outcropped at the root of the thin, laminated A286 aerofoil whose construction is described in reference 4.

Woods metal and Cerrobend, are low melting point solders that contain about 50% bismuth, 25% lead, 12.5% cadmium and 12.5% tin. They melt at temperatures between about 62°C and 69°C and can thus be used to make joints near to existing lead-tin soldered joints without causing remelting. Woods metal joints have, however, lower strengths than lead-tin solders. One other use for these low melting point solders is for support during tube bending as they can easily be removed by melting once the bending operation is over.

### 5.10 Adhesive Bonding

It is possible to use some adhesives for bonding together model components, for example orifice plugs, coverplates and other small parts. It is important to match the expansion coefficient of the adhesive to that of the metals being joined and to keep the glue line as thin as possible. Furthermore, although some joints can support loads, high safety factors should be used during design calculations and stress raisers should be avoided. There are very few specific references in the open literature to the adhesives used for use with cryogenic models and the details of their use is regarded as commercially sensitive information that can give one fabricator a decisive edge over competitors.

## 6. AVAILABILITY OF SUITABLE INFORMATION FOR DESIGN AND STRESS CALCULATIONS.

### 6.1 Designing for Operation down to 100K

The following paragraphs set out in a somewhat oversimplified way the sequence of analyses necessary for the design of a large, load-bearing piece of equipment for use in a HRNCWT.

#### 6.1.1 Basic analysis

##### Elastic Deformation

The limiting allowable elastic deflection is determined by the appropriate modulus, usually Young's modulus. As the modulus will increase as the temperature decreases below ambient, the worst case will occur at the highest operating temperature. Elastic moduli are not structure sensitive and thus "standard handbook" values will be adequate and probably readily available.

##### Strength

Operating stresses are kept well below the yield strength of the material, and the required safety factor will be given in the Design Handbook of the facility in which the equipment is to operate or be tested. Safety factors of 3 on the yield stress or 4 on the ultimate tensile stress are commonly used for normally stressed components. For all of the materials used in HRNCWTs, both yield and ultimate stresses increase as the temperature falls below ambient and thus the worst case will occur at the highest operating temperature. Both yield and ultimate tensile stresses should be given on the materials test certificate at room temperature and at either 77K or the lowest operating temperature.

##### Toughness

The toughness of a material determines its resistance to crack propagation in a low energy-absorbing mode. It is either measured by the Charpy V notch impact energy,  $C_v$ , or preferably, but less frequently, by measurement of the plane strain fracture toughness,  $K_{Ic}$ . In most of the higher strength materials both of these values decrease as the temperature falls and the worst case thus occurs at the lowest operating temperatures. For both the NTF and the ETW, the average Charpy impact energy,  $C_v$ , must be at least 34 J (25 ft-lb), while the fracture toughness,  $K_{Ic}$ , must be at least 93.5 MPa $\sqrt{m}$  (85 ksi $\sqrt{in}$ ). Charpy impact test values at the lowest operating temperature should be available from the materials test certificate. In their absence, appropriate tests will be needed.

#### 6.1.2 Critical crack size analysis

In order to calculate the critical crack size,  $a_{crit}$ , values of  $K_{Ic}$  are needed down to the lowest operating temperatures. Often, however, only  $C_v$  values are available and it is then necessary to use the Barsom-Rolfe relationship to obtain values for  $K_{Ic}$ . Calculations should be made for  $a_{crit}$  using a range of stresses and temperatures and for flaw shapes with  $a/2c = 0.23$  and 0.1. The calculated values of  $a_{crit}$  should be very significantly larger than the minimum flaw size that can be detected by available NDT techniques. This will allow for the possibility of sub-critical sized flaws remaining undetected and also give a safety factor against crack growth in service. NDT of the most critically loaded regions should be performed before the equipment enters into service.

#### 6.1.3 Fatigue analysis.

For all materials the fatigue lives of flaw-free components are shortest at room temperature. However, if long periods of service under oscillating loads are to occur at

lower temperatures, S-N curves are needed both at ambient and lower temperatures. For most materials adequate fatigue data is available for room temperature, but data at lower temperatures is harder to obtain. The stress ratio,  $R$ , of the applied load should be checked to see whether the S-N data is applicable.

#### 6.1.4 Crack rate propagation analysis

For a component with a pre-existing flaw it is first necessary to determine the threshold value of the cyclic stress intensity range,  $\Delta K$ , for which crack propagation can occur. If a crack can propagate it is then necessary to use plots of crack growth rate  $da/dN$  as a function of  $\Delta K$  to calculate the rate of crack growth under the assumed cyclic loading pattern. Such plots are reasonably available for all of the main materials used for HRNCWTs at room temperature for a range of  $R$  values. However, it is much more difficult to obtain such data at cryogenic temperatures for all materials in their various heat-treatments and for a range of  $R$  values.

Wagner, from NASA LaRC, has published data for the most widely used material, 200 grade 18 nickel maraging steel, for a range of  $\Delta K$ s that cover most of the stress intensities likely to be encountered<sup>7</sup>. Wagner's data has been re-worked and extended to form the basis for an ETW work sheet, whose use is recommended to their clients for crack propagation analyses. The rationale behind its use is to provide standardised data for these calculations that will allow comparison of the predicted crack growth rates for ETW models and equipment.

Constants for use with the Paris equation have also been derived from Wagners data to allow numerical calculation of crack growth rates. Furthermore, as the Paris equation does not take account of the appropriate values of  $R$  and  $K_{Ic}$ , Wagners fatigue data has been combined with his measurements of  $K_{Ic}$  made on the same batch of 200 grade 18Ni steel to derive constants for the Foreman equation, which does take account of the effects of  $R$  and  $K_{Ic}$ . Again, the use of these "standard" values for the Paris and Foreman equations should enable crack growth rate calculations to be more easily compared.

Crack rate propagation data for most of the other materials used for HRNCWT equipment is reasonably available at room temperature, although for PH13-8Mo stainless steel it is difficult to obtain it for the H1125 and H1150M heat-treatments. The basic plots of crack growth rate  $da/dN$  as a function of  $\Delta K$  for cryogenic temperatures are, however, more difficult to find.

### 6.2 Help for the Designer, The ETW Materials Guide.

As noted earlier, ETW have recently published their "Materials Guide"<sup>8</sup> which is intended to bring together much of the information needed by the designer of models and other equipment for use in the ETW. It contains Appendices which summarise the characteristics of the main materials used for HRNCWT applications together with information on their mechanical and physical properties. The following materials are included:

- 304L, 304LN, Nitronic 40, A286 and PH13-8Mo stainless steels.
  - C200 grade, C250 grade and Marvel 18 18 nickel maraging steels.
  - Inconel 718, aluminium alloy 6061, Berylco 25 beryllium copper and Ti-5Al-2.5Sn titanium alloy.
- Information is also given on:
- Glass transition temperatures and LOX Compatibilities of Common Polymers.

- Total linear contractions, specific heats and enthalpies of various materials.

A copy of appendix A5 is shown to illustrate the scope of the data included for this important material. It can be seen that there are still a number of gaps to be filled, especially on physical properties. For example, there are only two entries shown for the expansion coefficient, and these came from different sources, a room temperature value of  $9 \times 10^{-6}$  m/m and a 77K value of  $6 \times 10^{-6}$  m/m. Data for the expansion coefficient for the whole of the operating temperature range is essential for calculations of the stresses produced by differential contraction when dissimilar materials are used together. A relevant example would be the use of a maraging steel screw to fasten one part made from maraging steel to another made from A286. Reliable data for the expansion coefficients of both materials is needed to determine whether the safe operating stress for the screw would be exceeded, or whether adequate torque would be maintained.

It is hoped that the first edition of the Materials Guide will prove useful to designers of equipment for high Reynolds' number cryogenic wind tunnels. Feedback, and hopefully offers of additional information, from users of the Guide would help to make any subsequent editions more comprehensive and useful.

## 7. CONCLUSIONS.

Where do we go from here? In the author's opinion we are now at a critical stage in the development of techniques for high Reynolds' number cryogenic wind tunnels and the models to be tested therein. Either interested parties continue to disclose information of common interest so that the pool of knowledge in the public domain increases, or each party considers that information that it generates is confidential. If the latter view prevails, courses such as this will become mere seminars in which the basic technologies are taught to newcomers to the field. If, however, the more outward looking view prevails, we can continue to look forward to attending future courses to learn more from our colleagues about recent developments in this fascinating field of technology.

## 8. ACKNOWLEDGEMENTS.

The author would like to acknowledge with gratitude the use in this paper of material previously prepared for ETW and the assistance received over many years from colleagues at NASA, ETW and other organisations.

## 9. REFERENCES.

1. Barsom, J.M. and Rolfe, S.T., "Correlations Between  $K_{Ic}$  and Charpy V-Notch Test Results in the Transition Temperature Range". Impact Testing of Metals, ASTM STP 466, pp 281-302 (1970).
2. Rush, H.F. Jr., "Grain-Refining Heat-Treatments to Improve Cryogenic Toughness of High Strength Steels". NASA TM 85816 (August 1984).
3. Domack, M.S., "Fracture Toughness and Flaw Growth in Nitronic 40 at Cryogenic Temperatures". NASA TP 2312 (1984).
4. Wigley, D.A., "Technology for Pressure-Instrumented Thin Airfoil Models". NASA CR-4173 (Sept 1988).
5. Gross, U. and Lück, H., "Design and Manufacture of a Cryogenic Wind Tunnel Model". Proc. 2nd ETW Cryogenic Technology Review Meeting, (June 1988).
6. Wagner, J.A., "Correlation of Mechanical Properties with Metallurgical Structure for 18 Ni 200 Grade Maraging Steels at Room and Cryogenic Temperatures". Cryogenics, Vol 31, pp 780-785 (Sept 1991).
7. Wagner, J.A., "Mechanical Behaviour of 18Ni 200 Grade Maraging Steel at Cryogenic Temperatures". J. Aircraft, Vol 23, No 10 pp 744-749 (1986).
8. European Transonic Windtunnel GmbH, Köln, Germany. "The ETW Materials Guide". ETW/D/95005. (1995).
9. Wigley, D.A., "The Dimensional Stability Analysis of Seventeen Stepped Specimens of 18Ni 200 Grade, PH13-8Mo and A286". NASA CR-172168 (1983).
10. Wigley, D.A., "Machining-Induced Deformation in Stepped Specimens of PH13-8Mo, 18 Ni Maraging Steel Grade 200Ti and Grain-Refined HP 9-4-20". NASA CR-172450 (1984).
11. Dupriez, F., Geofroy, G. and Outtier, G. "Half Transport Aircraft Cryogenic Model for T2 Wind Tunnel". 2nd Cryogenic Technology Review meeting, Köln/Portz (June 1988).

**A.5 18 Nickel Maraging Steels: Composition, Structure, Heat-Treatment, Properties.**

Grade	200 Condition Solution-Treated and Aged											
Composition	Cr	Co	Mo	Ti	Al	Si	Mn	C	S	P	Zr	Ca
Range, %.	17.0/ 19.0	8.0/ 9.0	3.0/ 3.5	0.15 0.25	0.05 0.15	0.01 max	0.10 max	0.03 max	0.01 max	0.01 max	0.20 max	.05 max
Density	7920 kg/m <sup>3</sup>											
Metallurgical Characteristics..												
Structure.	Low-carbon martensitic											
Strengthening.	Precipitation hardening by titanium and aluminium intermetallics											
Stability.	Completely stable											
Corrosion.	Not stainless and will corrode if not protected. Careful handling needed.											
Heat-Treatment.												
Sol <sup>n</sup> . Anneal	800 to 830°C (1475 to 1525°F) for 1 hour minimum plus 1 hour per 25 mm thickness.											
Recrystaliz <sup>n</sup> .	Above 995°C. (1820°F).											
Sensitisation.	Does not sensitize.											
Ageing.	3 to 6 hours at 482°C (900 to 925°F) then air cool.											
Contraction.	0.0006 mm/mm during ageing.											
Stress Relief.	Heat to 815°C (1500°F), hold for 1 hour and air cool.											
Fabrication: Machining and Joining.												
Milling.	Good in solution annealed condition, reasonable when aged using correct tools, etc.											
Grinding.	Good. Use heavy duty grinding fluid or highly sulphurised oil. Beware corrosion!											
Finishing.	Can be drilled and tapped in aged condition. Good quality surface by hand finishing.											
Welding.	Good. Electron-beam preferred for models and balances.											
Brazing	Reasonable under vacuum, avoid temperatures > 995°C due to grain growth.											
Soldering.	Reasonable if aggressive flux used, but thorough cleaning essential after soldering.											
Specification, Availability and Suppliers.												
Specifications	ASTM A579, Grade 71: MIL Spec. S-46850D, type IV.											
Availability.	Good, but demand is small and occasional long delivery times.											
Suppliers.	Special Melted Products, Teledyne Allvac.											
Comments.												
1.												
2.												

**A.5 18 Nickel Maraging Steels: Physical and Mechanical Properties.**

Grade	200	Condition	Solution-Treated and Aged					
Temperature	K	293	260	220	180	140	100	77
	°C	20	-13	-53	-93	-133	-173	-196
Physical Properties								
Exp <sup>n</sup> , α, 10 <sup>6</sup> (dL/dT)/L <sub>293</sub>	deg <sup>-1</sup> .K	9						6
Cont <sup>n</sup> ., 10 <sup>5</sup> (L <sub>293</sub> -L <sub>T</sub> )/L <sub>293</sub>	-							
Specific Heat, C <sub>p</sub> .	J/kg.K	460						
Thermal Diffusivity.	m <sup>2</sup> /s*10 <sup>-5</sup>	0.567						
Thermal Conductivity, K.	W/m.K	21						
Electrical Resistivity,ρ.	μΩ.cm	Solution annealed: 60 to 70. Maraged: 35 to 50 at room temp.						
Mechanical properties: Elastic.								
Young's Modulus, E.	GPa	181.3	182.7	184.4	186.0	187.6	189.4	190.3
Shear Modulus, G.	GPa	68	70	73	75	76	77	78
Poisson's Ratio, ν.	-	0.264						
Mechanical properties: Plastic Deformation.								
Yield Stress, σ <sub>y</sub> , σ <sub>0.2</sub> .	MPa	1430	1485	1550	1615	1680	1770	1830
Tensile Stress, UTS, σ <sub>t</sub>	MPa	1495	1555	1627	1698	1770	1866	1930
Elongation, ΔL / L <sub>gauge</sub> .	%	13						11
Reduction of Area, R.A.	%	65						64
Mechanical properties: Toughness.								
Charpy V Energy, C <sub>v</sub> .	J	46	43	41	38	35	30	25
Fracture Toughness, K <sub>Ic</sub> .	MPa√m	115	110	105	100	93	83	71
a <sub>c</sub> (S = UTS / 4, a/c=0.23).*	mm	34.9	29.5	24.5	20.4	16.3	11.7	8.0
Mechanical properties: Toughness., Effect of Bar Diameter.								
Bar Diameter	mm	480	420	400	300	200	150	76
C <sub>v</sub> at 293 K, RR orient'n.	J	31	40		55	62	68	70
C <sub>v</sub> at 77K , RR orient'n.	J	14	16		25	28	30	37
Mechanical properties: Fatigue and Crack Propagation.								
Endurance Limit, 10 <sup>6</sup> cs.	MPa	690 MPa (100 ksi) @ 295K			1035 MPa (150 ksi) @ 103K			
ΔK Limit for C & n.	MPa√m	ΔK <sub>293</sub> < 15		ΔK <sub>293</sub> > 15		ΔK <sub>103</sub> < 16.5		ΔK <sub>103</sub> > 16.5
Paris Equation, const. C.	m/cycle	1.2 x 10 <sup>-12</sup>		2.2 x 10 <sup>-11</sup>		6.3 x 10 <sup>-13</sup>		1.3 x 10 <sup>-11</sup>
Paris Equation expn <sup>t</sup> n.	-	n <sub>295</sub> = 3.85		n <sub>295</sub> = 2.80		n <sub>103</sub> = 3.85		n <sub>103</sub> = 2.80

## Cryogenic Model Systems

Clarence P. Young, Jr.  
ViGYAN, Inc.  
30 Research Drive  
Hampton, VA 23666-1325, U.S.A.

### SUMMARY

This lecture presents current information on cryogenic model design requirements, developmental model design studies, design and fabrication experience, recent surface finish and pressure orifice studies, and current practices for filler materials and fastener applications. In addition, results of advanced model support system studies are presented along with composite model designs for cryogenic application, and information relating to cost factors for cryogenic models versus conventional models. Finally, some future development needs are suggested for cryogenic model systems.

### 1.0 INTRODUCTION

Much has been learned in recent years with regard to design, fabrication and test experience for cryogenic model systems. In particular, the NASA Langley National Transonic Facility (NTF) has conducted a large number of high Reynolds number tests for a variety of commercial transport, fighter, and Space Shuttle models as well as a submarine model. Also, a number of models have been tested in the NASA Langley 0.3 Meter Transonic Cryogenic Tunnel (TCT). Each type of test whether production, developmental or research in nature has usually offered different kinds of challenges from a model design, fabrication and wind-tunnel testing point of view.

The special course lectures in 1985 on design and construction of cryogenic models are documented in references 1 and 2. Significant studies and advances in state-of-the-art and test technology have been accomplished in recent years. Although cryogenic model design criteria and material requirements have not changed significantly, significant experience has been gained in the areas of developmental model design studies, employing different fabrication methods, and design of advanced model support systems. Also, composite models have been fabricated and successfully tested in cryogenic wind tunnels.

The purpose of this lecture is to report on advances in the state-of-the-art for design, development, fabrication and testing of wind tunnel model systems.

### 2.0 CURRENT DESIGN REQUIREMENTS FOR CRYOGENIC MODELS

Design requirements for cryogenic models have remained basically unchanged since the NTF was commissioned in 1984. This section highlights current requirements.

#### 2.1 Design Criteria

The design criteria of reference 3 are used for design of NTF and 0.3M TCT cryogenic model systems. Although the document was revised in 1992, no significant changes were made that affect model design requirements.



## 2.2 Analyses

Most models are being designed using handbook analysis methods with safety factors of 3 on yield or 4 on ultimate whichever is greater. Because of high loads on some models, and for risk reduction purposes, more rigorous analyses are performed using finite element methods. Some NTF model systems have been divergence critical, i.e., tested up to the maximum dynamic pressure allowed by reference 3 which requires a safety factor of 2 on divergence. Although model systems are still required to meet the flutter criteria of reference 3, rigorous flutter analyses are no longer being performed. Generally the flutter evaluation is done by an on-site NTF engineer. A word of caution is in order for flutter evaluation since past analyses have been done by modeling clean wing configurations. With the addition of large nacelles, (e.g., twin nacelle configurations) it has been found that theoretical clean wing flutter speeds may be reduced significantly by including the nacelles/pylons in the flutter math models.

## 2.3 Preferred Materials

The preferred material for models and stings is the 18 Ni grade 200 maraging steel. The excellent strength properties coupled with acceptable fracture toughness and good machineability has made this the material of choice. However, long leadtimes (6 months or more) and relatively high costs (approximately 12 U. S. dollars per pound for plate material) has posed problems. A-286 stainless steel material is being used primarily for large sting components. The fastener materials are primarily A-286 and Nitronic 60 stainless steel, with some made of 18 Ni grade 200 maraging steel. Long lead times have been a problem for A-286 screws.

Grain refinement of 18 Ni maraging steel has been studied extensively (ref. 4) and shown to be an effective way of increasing fracture toughness with slight improvement in strength properties and improved machineability. However, grain refinement is generally not used except for cases where toughness enhancement is desired.

### 2.3.1 Inspection

Material inspection specification requirements are basically unchanged. All critical (highly loaded) components receive a Class AAA ultrasonic inspection, i.e., screening defect size is a 1/64 inch diameter flat bottom hole, (see ref. 5). In cases where the model, balance or, sting have been subjected to high dynamic loads, special post-test inspections may be performed. Typically, surface inspections are performed using dye penetrant inspection methods.

### 2.4.1 Testing

Material properties that meet specifications are generally acceptable. For critical applications, material chemical composition and mechanical properties verification are generally required. These tests are usually performed at the NASA Langley Research Center.

In recent years modal (vibration testing) has been done on many of the model systems tested in the NTF. A-priori knowledge of model system natural modes and frequencies are essential for dynamic testing (ref. 6), and for analysis of dynamic behavior if significant vibrations are encountered during the test. Also, correction of the inertial angle-of-attack sensor bias due to model vibration requires pre-test vibration testing, (see references 7 and 8). It is preferable to perform the modal testing of the model system installed in the test section.

Experience at the NTF has revealed some change in natural frequencies of the model system installed in the test section versus the assembly bay. These changes are attributable to different boundary conditions, therefore it is important to understand the influence of the model support structure flexibility on the model system natural vibration modes.

### 3.4 Developmental Cryogenic Models

A number of co-operative programs were initiated to develop new concepts for NTF model design. These models were designed to be tested in the NTF for tunnel-to-tunnel and/or flight data correlation.

#### 3.4.1 F-111 TACT (FAVOR) Model

A contract was awarded in 1983 to the Boeing Company for the design, fabrication and calibration of a 1/20 scale model of the F-111 TACT for testing in the NASA Langley NTF. The model was to be tested at conditions that would allow a match at all significant flight test data points in order to correlate flight data with tunnel data. Aeroelastic deformation was to be measured using light emitting diodes mounted on the wings and body.

##### 3.4.1.1 Design and Fabrication

All external contours were obtained from the actual airplane drawings and lofted on the Boeing Computer Aided Design System. The biggest challenge was to design the aeroelastic wing to match the actual airplane wing stiffness properties by applying stiffness scale factors and then sizing the structure to match the requirements. This proved to be a difficult requirement since the wing had to pivot (similar to the actual airplane) in order to test at two different sweep angles.

The F-111 model components are illustrated in figure 1, while the instrumentation requirements are shown in figure 2. The wing carry through pivot joint is illustrated in figure 3. The wing was originally attached to the carry through structure with 3 tapered fasteners in a radial pattern and a single pivot fastener to allow for variable sweep locations. The carry through flexure proved to be highly non-linear and initially failed to meet strength and stiffness requirements. After extensive finite element analyses (figure 4) and structural testing, the carry through structure was redesigned. The redesign resulted in modification of the flexure shape and development of a cone type fastener design.

The aeroelastic wing was fabricated from 18 Ni grade 200 maraging steel with an upper and lower piece for the right and left wing panels. Both numerically controlled milling and electric discharge machining were used to fabricate the wing section. Final wing shapes are depicted in figure 5. The wing and tubes were nickel-plated to improve the braze joints quality. The pressure tubes were brazed in place and the wing assembly was brazed together as indicated in figure 6. The design essentially met all requirements however, the final assembled wing shapes had slight ripples in the skin and slight braze defects at points on the leading edges. However, it should be pointed out that the F-111 TACT wing was the first application of brazing as a primary joining technique for an NTF model. As of this date the model has not been tested in the NTF.

#### 3.4.2 X-29A Model

The X-29A model was designed and built by Grumman Aerospace Corporation. The X-29A 6.25 percent scale model was to be used for tunnel to flight correlation. The model was manufactured from 18 Ni 200

grade maraging steel and is shown in figure 7. The locations for the 74 pressure taps on the model were taken from the actual aircraft which had 184 wing pressures. Configuration variables included wing flaps, strake flaps, canards, rudder, with nose boom, vertical tail and canards on and off. Pressure taps are indicated in figure 8.

The model design utilized a one piece wing fuselage construction approach due to problems related to attaching the wing to a very thin fuselage. Electron beam welding was used extensively. A separate wing pressure insert was fabricated and welded in place (see fig. 9). Pressure orifices were 0.010 inch diameter with 0.040 pressure tubing brazed and routed internally through the wing into the fuselage as indicated in figure 9.

Because of the complex design and multiple brazing operations required, the model components were shipped to NASA Langley for the brazing operation. At that time, work was ongoing at Langley to develop suitable materials and procedures for brazing. The braze cycles had to be carefully controlled in order not to affect the maraging steel mechanical properties (due to possible grain growth) but still assure good braze joints. The model was cycled 5 times to temperatures between 1600 - 1800°F before a successful braze was acquired. Due to extensive heat cycles, a moderate amount of warpage occurred in the aft fuselage region. The distortion problem was addressed by a structured heat management approach. In order to minimize temperature gradients, shielding was built around the model assembly prior to brazing. During the brazing process, temperatures in several locations on the model were monitored and maintained within 50°F. Despite the concentrated effort, repetitive brazing cycles were required because of poor braze joints.

The aft fuselage section was reconfigured to meet the requirements and the model has been successfully tested in the NTF. The X-29A design and fabrication experience is documented in reference 9.

The experience gained in the brazing process for the X-29A and the aforementioned F-111 TACT formed the basis for subsequent brazing techniques. Enhancement of brazing by Nickel plating, and thermal management, by experienced personnel were determined to be essential factors for obtaining good braze joints. Braze alloy process and strength characterization is discussed in a subsequent section of this paper.

### 3.4.3 Semi-Span Models

The NTF now has semi-span test capability with semi-span testing having been done over the past two years. An example test installation is illustrated in figure 10. The NTF sidewall balance used for semi-span testing is made from 18 Ni grade 200 maraging steel. The one piece NASA Langley balance is 16 inches in diameter and 25.75 inches in length. Full scale design values are: 6100 lbs. normal force, 1000 lbs. axial force, pitching moment 70,000 inch-lbs., roll moment 350,000 inch-lbs., yaw moment of 76,000 inch-lbs. and side force of zero lbs.

## 4.0 SURFACE FINISH , FILLER MATERIALS, BRAZE ALLOYS, AND ORIFICE QUALITY STUDIES FOR CRYOGENIC MODELS

Current requirements as well as recent studies of surface finish effects, advances in filler materials, braze process and strength characterization and research on orifice quality are presented in this section.

#### 4.1 Surface Finish

Since the boundary layer thickness decreases as Reynolds number increases, cryogenic models must have extremely smooth surface finishes. A schematic illustrating a model surface profile is illustrated in figure 11, along with the mathematical definition for arithmetic average and rms deviation used to characterize surface finish. A surface finish of approximately 10  $\mu$  in. rms (or less) has typically been specified which is costly to fabricate and may be smoother than actually needed. The question of what the surface finish requirements should be for high Reynolds number models still has not been answered completely. The most recent studies of surface finish effects on an airfoil at high Reynolds number is documented in reference 10. Experimental work was conducted on a twelve-percent-thick supercritical airfoil model in the NASA Langley 0.3 Meter Transonic Cryogenic Wind Tunnel at chord Reynolds numbers up to 40 million. The airfoil had been previously tested in the same facility with the model having a surface finish of 10  $\mu$  in. rms. The model was then tested with a surface finish of 32  $\mu$  in. rms, which was found to be the roughest surface that resulted from typical model fabrication techniques.

Unfortunately the research program described in reference 10 does not provide any firm conclusions regarding the maximum allowable surface finish which induces no roughness penalty. Further testing with smoother surface finishes applied to the model is required. One of the more interesting observations with respect to the surface character from this study can be seen in figure 12 taken from reference 10. In the figure, examples of a perpendicular trace, which corresponds to the spanwise direction of the model, is compared with a parallel trace, which is in alignment with the

flow direction. Note that the parallel trace appears smoother and more uniform than the perpendicular trace. For this model the arithmetical average roughness  $R_a$ , in the perpendicular direction was approximately 21  $\mu$  in. on the upper surface and 24  $\mu$  in. on the lower surface. Parallel to the lay the upper surface average was 19  $\mu$  in. The variation is explained by small differences between finish direction and direction of profilometer movement. This suggests that if models are typically polished so that the lay is parallel to the flow, then the surface roughness seen by the flow may be significantly less than the surface finish specification would indicate.

A comparison between a machined and polished metal surface and a sand grain roughness is provided in figure 13 taken from reference 10. The emery paper was found to have an arithmetical average roughness height of about 200  $\mu$  in. versus a value of 21  $\mu$  in. for the model surface. The two traces are plotted on similar scales. Note that the sand roughness has a much higher frequency of peaks and valleys than the polished surface. Also the sand roughness is characterized by very steep surface slopes and sharp peaks and valleys. In contrast, the metal surface generally has shallow roughness slopes with occasional deep grooves cut into the surface by the polishing grit. These illustrations show that the character of sand grain roughness is significantly different from that of a polished surface. Therefore, the equivalent sand roughness correlation may not be valid for general extension to polished surfaces, although such correlations are widely used. Models currently being tested in the NTF are usually specified to have a surface roughness of about 4-10  $\mu$  in. rms on leading edges and 16  $\mu$  in. rms elsewhere. It should be noted that a 2-D composite model used for flow visualization tests in the 0.3 M TCT had a

measured surface roughness average of 4  $\mu$  in. rms. The very smooth surface finish on the composite model was obtained by hand finishing the surface. The work reported in reference 10 would require additional tests of the model with surface finishes of 16 and 8  $\mu$  in. rms in order to experimentally determine the maximum allowable surface finish which induces no roughness penalty.

The most recent high speed research model (HSR) being tested in the NTF specified a 10  $\mu$  in. roughness average on leading edges and 4 inches back on the fuselage, with 16  $\mu$  in. over the remainder. Contour tolerance on HSR was  $\pm 0.003$  inch and utilized 0.010 inch orifices near the leading edge and .015 inch orifices elsewhere.

Although very smooth surface finishes are specified for cryogenic models, accurate measurement of surface finish remains questionable. The study of reference 9 points out that the National Bureau of Standards has developed optical techniques and hardware that can accurately map surface roughness of the order of 4 microinches. A 3-D stylus profilometer is used at NASA Langley to measure roughness.

Surface finish requirements for cryogenic models need further investigation. In particular, large cost factors are associated with hand finishing to very smooth surfaces. Current cost estimates by model engineers at NASA Langley place the labor hours cost of going from a 16  $\mu$  in. to 8  $\mu$  in. surface finish as being increased by a factor of 4. In a similar manner, a cost increase factor of 4 is placed on going from a surface finish to 8  $\mu$  in. to 4  $\mu$  in. This suggests that new technology is needed to obtain much smoother surface finishes by machining methods which becomes very difficult to do on airfoil shapes.

It should be pointed out also that smooth surface finishes over filled areas on the models are difficult to achieve. With the new filler materials being used at NASA Langley it is believed up to 8  $\mu$  in. rms can be obtained over filled areas as compared to 50  $\mu$  in. measured on some of the older filler materials. Another issue with regard to leading edge surface finish is how the surface finish may change due to the presence of foreign particles in the airstream which impact the model. Conceivably, the surface finish could change considerably during testing if the tunnel is not clean.

#### 4.3 Filler Materials

Reference 1 and 12 document initial development and tests of filler materials that have been used for NTF cryogenic models. The criteria for NTF filler materials have remained essentially constant, i.e., (1) the filler material must closely match coefficients of expansion for metals used in model construction; (2) be easily hand-worked and readily removable for model changes on maintenance; (3) provide a smooth high quality finish (at least 15-20  $\mu$  in. rms or less) over the NTF temperature ranges; and (4) remain structurally intact during thermal and structural load cycling.

Various systems studied were conducted on specimens such as the one illustrated in figure 14 and the simulated wing panel in figure 15. Various filler system/substructure combinations studied early in the development program are listed in Table I. The best performing and most commonly used filler at NTF has been the EA 9309 epoxy mixed with carbon spheres (1:1 weight ratio). The EA 9309 has proven to be the best performer for large trenches, critical holes or surfaces. The major drawback is the cure time which is up to 24 hours at 77°F for highly loaded deep areas

such as wing grooves, whereas for lightly loaded areas such as bolt holes 8 hours at 77°F is usually adequate. Some fast setting epoxies are used in less critical applications (e.g., Hartman 5-minute epoxy) and in fastener holes requiring frequent removal.

Recently, a new filler material has been developed by NASA which works extremely well and cures very fast. Cure times have been reduced by orders of magnitudes. This new filler material provides for much faster turn-around on model changes during cryogenic test operations, thereby improving productivity. Also very smooth surface finish ( $\sim 10 \mu$  in. rms) can be obtained with this filler.

#### 4.4 Braze Alloy Process and Strength Characterization Studies for 18 Ni Grade 200 Maraging Steel

A comprehensive study of braze alloy selection process and strength characterization with application to wind-tunnel models is presented in reference 13. The applications for this study include the installation of stainless steel pressure tubing in model airfoil sections made of 18 Ni grade 200 maraging steel and the joining of wing structural components by brazing. Acceptable braze alloys for these applications are identified along with process, thermal braze cycle data and thermal management procedures. Shear specimens are used to evaluate comparative shear strength properties for the various alloys at both room and cryogenic (-300°F) temperatures and include the effects of electroless nickel plating.

An illustration of a brazed assembly used for shear test specimens is given in figure 16. The specimens were placed in the furnace as shown in figure 17. The test results for all the braze alloys studied are summarized in

figure 18. The results showed that the shear strength of the braze materials increase at -300°F (cryo temperature) when compared to room temperature results. Also with the exception of the BAU-4 material (which had excellent indicated shear strength with or without plating after grain refinement), the electroless nickel plating improved the joint shear strength. The BAU-4 was by far, the strongest braze material. The BA-8 produced the lowest strength joint.

The work documented in reference 13 found that a number of braze alloys are suitable for wind tunnel models constructed of 18 Ni 200 grade steel. Electroless nickel plating of the surfaces to be brazed significantly enhanced both wettability and shear strength properties. The shear strength properties given in the reference provides a basis for determining design allowable values.

Thermal management of vacuum furnace brazing cycles is needed to assure more uniform heating of model parts having significant differences in thermal mass, thereby enhancing the braze process. Also brazing cycles should be established such that the use of high temperature braze alloys will not significantly alter the microstructure of the parent material which can lead to reductions in strength and stiffness properties.

#### 4.5 Orifice Quality

The issue of orifice-induced pressure measurement error is more critical for high Reynolds number testing due to thinner boundary layers. Recent investigations of orifice induced error and techniques for reducing the error are documented in references 14 and 15. Initial studies on a flat plate model were conducted at the NASA Langley 7- by 10-Foot High-Speed Tunnel at Reynolds numbers up to  $3.4 \times 10^6$

per foot (ref. 14). The results indicated that as orifice size increased, the pressure error also increased but that a porous metal (sintered metal) plug inserted in an orifice could greatly reduce the orifice-induced error. Test orifice geometry is illustrated in figure 19. Figure 20 illustrates the porous metal plug orifice. A follow-on wind-tunnel investigation was conducted in the NASA Langley 0.3 Meter Transonic Cryogenic Tunnel to study the effects of the porous plug orifices on orifice induced static-pressure measurement error at high Reynolds number. Tests were conducted at Mach numbers from 0.60 to 0.80 at Reynolds numbers from  $6 \times 10^6$  to  $40 \times 10^6$  per foot. Data were obtained from the porous plug orifices and from conventional orifices with diameters of 0.010 in. to 0.040 in. A schematic of the test airfoil is shown in figure 21, and orifice placement and cross section of orifice construction for the first tunnel entry are shown in figure 22. Orifice location and model construction for the second tunnel entry is given in figure 23. The results of this investigation showed that the porous plug orifice could be a viable method of reducing pressure error. Also the data obtained for 0.010 in diameter orifices were very close to measurements obtained with a 0.040 in. diameter orifice over much of the airfoil, and that downstream of the shock, orifice size was not critical. The benefits of the porous plug in reducing the static pressure error were noticeable only on about 10 percent of the airfoil chord after which the differences in the static pressure error between the porous plug orifice and the conventional 0.010 in. orifice was negligible. However, the porous plug would also be beneficial in eliminating errors induced by holes that are out-of-round, have burrs or are chambered. It should be noted that the surface finish on the model was specified to be 16  $\mu$  in. rms on the upper surface and 32  $\mu$  in. on the lower surface.

The porous plug orifices were made by diffusion bonding the porous (sintered) metal in the end of a 347 stainless steel tube which had an inner diameter of .040 in. and outer diameter of 0.060 inch. The tube was then attached to the model with an adhesive. The sintered metal for the porous plug was manufactured from 347 stainless steel for thermal compatibility. The porous plugs were later modified and cut from 316 stainless steel, on a slight taper and pressed into the holes lightly filled to make them flush with the model surface, (fig. 23). It should be noted that porous plug orifices have not been incorporated on any cryogenic models up to the present time.

## 5.0 ADVANCED MODEL SUPPORT SYSTEMS STUDIES

The model support (sting) is a critical component of the model support system. The design is often faced with the tradeoff of minimizing sting size, thereby compromising model and facility safety, against a large sting with the associated problems of sting interference effects and possible distortion of configuration geometry. This is true for conventional tunnels but is even more critical for high pressure cryogenic tunnels such as NTF and the European Transonic Wind Tunnel (ETW). The potential for limited test envelopes due to sting divergence or strength limitations is very real. The ETW model design study of reference 16 pointed out that for high dynamic pressure test conditions, angle of attack and Reynolds number were likely to be sting limited. The dynamic problems experienced in the NTF (references 17 and 18) often involve sting bending modes at low frequencies (6-10 Hz) being excited due to pitch or stall buffet or yaw induced vibrations. The associated dynamic loads can be quite severe and may threaten model/sting integrity. Ideally, the aerody-

namacist would like to have an infinitely small and infinitely stiff sting.

It was recognized in the early 80's that advanced model support systems may be needed to fully utilize the NTF test capability. A study of advanced model support system concepts was conducted by General Dynamics and is reported in reference 19. Elements of this study are presented in this section along with discussion of an unconventional aerovane concept, and studies of structural damping response of sting supported models at cryogenic temperatures.

### 5.1 Advanced Support System Design Approach

A primary goal of the reference 19 study was to obtain a 25 percent improvement over the 18 Ni grade 200 maraging steel in both ultimate strength and Young's modulus. Also, because of the cryogenic test environment, fracture toughness had to be maintained by requiring charpy v-notch toughness ( $C_{VN}$ ) of 25 ft-lb at -320°F (ref. 3). Three approaches were studied to find a suitable material and configuration. The three approaches were: (1) conventional material sting, (2) advanced composites and (3) hybrid configurations.

#### 5.1 Conventional Sting Material Approach

A number of high performance metallic material systems were studied. Of these MP 35 Ni alloy offered promise for meeting the design goal illustrated in figure 24. MP 35 Ni has a yield strength of 285 ksi and Young's modulus of 34.8 million lbs per square inch at room temperature. Charpy V notch strength at -320°F was 16 ft-lbs (less than the 25 ft-lb goal).

Although the MP 35 Ni looked promising and machined well, small sizes were needed to cold work the material. The higher strength values were proportional to cold working. For example, 2 inch round bar stock could obtain ultimate strength up to 220 ksi, whereas a 3 inch round bar would be reduced to about 185 ksi.

Several concepts were studied for using MP 35 Ni which included spiral winding very thin MP 35 Ni strips around a tube of the same material. However, such an approach would require a large developmental program. Another approach was to fabricate a rectangular sting utilizing available plate material keyed together on a vertical centerline and welded. However, the material stock required length (4 to 5 feet) was not available at that time, and proof-of-concept testing would be required.

#### 5.1.2 Advanced Composites

A number of composites were considered. An advanced composite system high modulus prepreg combined with carbon fibers and a proprietary epoxy offered the desired properties. However, research into a design/fabrication concept was discontinued based on a structural/material analysis, and in particular the lack of compressive strength.

#### 5.1.3 Hybrid Configurations

One concept studied combined a high stiffness tungsten alloy outer shell of Kennametal with an A-286 stainless steel center core. However, manufacturing the Kennametal to the desired size was a problem, primarily due to degradation of properties with increased size. Another idealized sting concept is shown in figure 25. Such a sting design would combine the best available materials as shown in the



figure. However, a common problem with the idealized sting was differing coefficients of thermal expansion which result in undesired thermal stresses. Also, the very stiff Kennametal (modulus of elasticity =  $90 \times 10^6$  msi) became too highly stressed.

Another hybrid composite concept is illustrated in figure 26. This concept would employ a 18 Ni grade 200 metal core, and use high modulus composite on the tension side with a containment overwrap. However heaters would be required to control thermal stress differentials at the metal to composite interface.

Various concepts were studied using Kennametal as the baseline material. One of the more interesting concepts is illustrated in figure 27. This floating stiffener concept employs a concentric inner rod made of Kennametal with the outer member made of 18 Ni grade 200 maraging steel (or equivalent). Such a concept would get around the joining problem (e.g., brazing or bonding Kennametal to maraging steel) and minimize thermal effects due to coefficient of thermal expansion differentials. Proof-of-concept tests were conducted on this concept with results illustrated in figure 28. A definite improvement in stiffness to strength ratio was demonstrated, but the viability of this concept requires further development.

#### 5.1.4 Recommended Configurations

The configurations recommended for further study were: (1) MP 35 Ni - laser weld/diffusion weld; (2) 18 Ni grade 200 with high modulus composite strip on tension side; and (3) 18 Ni grade 200 with Kennametal insert (floating stiffener).

The study of reference 20 clearly showed that there are no simple solutions. The high stiffness, high strength and toughness

coupled with material availability, and fabrication issues still exist. However, with recent advances in superalloys and composite materials development it is likely that viable designs could be developed which could result in sting stiffness improvements up to 50 percent or more with acceptable strength and toughness properties. However, there doesn't seem to be a strong driver to do further development work. Currently, stings being used in the NTF are conventional designs and most utilize 18 Ni grade 200 maraging steel and/or A-286 stainless steel.

#### 5.2 Vane Support System (VSS)

The present methods of supporting wind tunnel models is by sting/strut combined with internal/external strain gage balance. The wind tunnel model shapes and aerodynamic flow are often compromised by the support system. Also, test envelopes may be restricted by either the support system, sting dynamics or balance limits.

An unconventional approach for supporting wind tunnel models was proposed by Griffin, et al, in reference 20. The concept is to remove the sting and support the model by attaching to both ends of the balance. The concept uses a two-shell balance where the inner rod (nonmetric) is the outer center of the balance. The outer shell is the metric portion of the balance and is the model attachment as shown in figure 29. Vanes/cables are attached to the forward/aft ends of the force balance. Four vanes are positioned above/below the model. The vanes are inclined fore and aft to carry the axial loads and inclined to take out the side loads. The vanes are also offset from the center to take rolling moment and can be shaped for minimum flow disturbance over the model. Vane shapes include a segmented airfoil which floats at 0 angle of

attack around a circular vane (see fig. 29). Other concepts include airfoils and simple circular sections. One end of each vane is attached to the balance while the other end is attached outside the tunnel to one end of a load cell. This in turn is connected to a tensioning device as shown in figure 30. A preload is applied to each vane to ensure that there is always minimum tension.

Pitch is accomplished by using a structural ring/turntable in the flow/ceiling or walls of the tunnel as illustrated in figure 31. The vane, load cells, and tensioning device are attached to the ring. Yaw and roll can be obtained by changing vane lengths. Size of the vanes is minimized by designing for a pin joint at each end, to allow for rotation. Instrumentation leads to the balance are carried through the vanes. The six-component balance on the balance now acts as a beam simply supported at each end by four vanes. (The vanes can be composite pultrusions). The load cell directly monitors the load in each vane. For safety, limits can be established and the system interlocked to rapidly decrease the loads. Seals are required at the model/vane juncture. The vanes are non-metric such that the balance reads model loads plus the forces created by flow disturbances over the vanes. If the vane design is optimized such that they create zero delta force, an interference-free support system may be possible.

### 5.2.1 Vane Concept Evaluation

Various tests were performed to evaluate the concept. A static balance calibration test gave accuracies as good as a sting supported balance (0.1 to 0.3 percent). Tests designed to evaluate vane interference were performed in the General Dynamics Low Speed tunnel at San Diego, California, using a fighter model. The test results were promising for large diameter vanes (5/32 in. dia.). Smaller

vanes deflected and vibrated too much to evaluate accuracy.

A demonstration test was performed at the aforementioned facility to understand the implications and suitability of the VSS. Tests were conducted for the fighter supported on the VSS and in a sting-mounted configuration at angles of attack from -2 to +65 degrees.

Observations from the test indicated a significant difference in the model response to unsteady aerodynamics. The vane supported model was nearly rigid in the tunnel while the sting mounted model vibrated with dynamic data amplitudes approximately 75 percent larger than the static data. The lift and drag data compared very well for both the VSS and sting mounted configuration with 3 - 4 percent drop-off in VSS data, which was consistent with initial static testing of vane interference. Significant reduction in angle of attack corrections were noted for VSS configuration. Other corrections which may be eliminated or significantly reduced would include sting blockage and base pressure corrections.

The VSS is an innovative idea for the new-generation model support system. The VSS may represent a significant improvement in dynamic testing, provide unlimited angle of attack capability, and could greatly reduce or eliminate the flow disturbance. Although the tests and analyses reported in reference 20 are limited, they are very encouraging. Improved accuracy of wind tunnel data has become increasingly important in high Reynolds number cryogenic facilities and for CFD code validation. A real need exists for innovative ideas for model support systems. The vane support system appears to be a candidate for a next generation support system and provides an alternative to the

standard sting/strut arrangement. However, additional development and testing at various speed ranges are needed.

### 5.3 An Approach For Reduction of Angle-of-Incidence and Increasing Aeroelastic Divergence Pressure

A study that was conducted to investigate the effect of increased flexibility of the forward portion of force balances on divergence pressure of wing-tunnel models is reported in reference 21. In the reference study, two design parameters of the forward portion of the balance forward portion are varied. These are the balance diameter and model attachment point.

Wind tunnel models are usually designed such that the attachment to the balance is forward of the aerodynamic center of the model, and the moment center is at or close to the aerodynamic center. A representative mode shape for examining the effect on divergence is shown in figure 32 taken from reference 21. At the model attach point, the moment induced by the lift force tends to rotate the balance in a direction opposite that of the lift force. Note from figure 32, that this gives a pitch down effect on a representative divergence mode shape. Therefore, making the portion the force balance forward of the center of pressure more flexible, tends to pitch the model nose down further and increase the divergence pressure. Also by increasing the length between the balance moment center and model attachment, a similar effect is exhibited.

In a similar manner, Taylor (ref. 16) noted that incidence amplification can be reduced by using a slightly longer sting, with the balance positioned further forward in the model. This approach may have an additional advantage of reducing the gap

needed between the sting and inside wall of the model base (e.g., fuselage). However, as pointed out by Taylor, space in the model nose is at a premium due to the need for instrumentation such that this option may not be available.

Several concerns arise from the flexibility modifications studied in reference 21. Analyses would need to be performed to account for change in deflection and clearance between the model and sting to assure that fouling does not occur. Increase in balance flexibility may result in stress limitations due to operating at a higher dynamic pressure, and angle of attack may be limited. Lengthening of balance or sting (as previously mentioned) may be limited. Finally, dynamic response and/or dynamic instabilities may result due to flexibility changes. It is known (ref. 18) that balance flexibility can significantly affect natural modes and frequencies of the model system. Structural resonance and buffet response therefore become additional issues.

## 6.0 COMPOSITE MODELS

Full utilization of the high Reynolds number capability provided by cryogenic tunnels requires extension of state-of-the-art in model design and fabrication. Based on the success at the NASA Langley Research Center with the use of composite materials for the NTF fan blades (E-glass/epoxy) and early aerodynamic testing of a 2-D composite airfoil in the 0.3 Meter Transonic Cryogenic Tunnel (TCT) (ref. 9), it appeared the model designs utilizing composite materials may have significant fabrication advantages over all-metallic designs. Composite materials are routinely used for wind tunnel models as non-primary structural components e.g., nose section or fuselage components and are heavily relied upon for aeroelastically tailored models (e.g.,

flutter models). This section describes design and fabrication of instrumented airfoils for a cryogenic model (ref. 22) and experience in testing a 2-D composite airfoil in the 0.3 M TCT.

### 6.1 Instrumented Composite Horizontal and Vertical Stabilizers Designed for The Pathfinder I Generic Transport Model

Instrumented composite vertical and horizontal tails were designed and built for testing on the NTF Pathfinder I generic transport model shown in figure 33. The purpose of this research was to demonstrate the feasibility of design and fabrication of cryogenic models and/or model components utilizing conventional and/or advanced composite materials.

#### 6.1.1 Design Requirements

The structural design requirements for the Pathfinder I composite horizontal and vertical stabilizers were identical. The horizontal and vertical stabilizer attachments are illustrated in figure 34. The maximum aerodynamic loads were 255 lbs for the horizontal stabilizer and 513 lbs for the vertical stabilizer. Tolerances specified for the airfoil surface contour were plus or minus .002 inch with relative tolerance variation between ordinates not to exceed .001 inch. Target surface finish was 16  $\mu$  in rms. Each tail was to contain 32 surface pressure taps (orifices having a diameter of 0.010 inch) and be free of imperfections. The stabilizers were designed to meet the requirements of reference 3.

#### 6.1.2 Horizontal Stabilizer Fabrication

Because of the complexity of the breechlock type of attachment (see fig. 35) for the horizontal tails, a metal core with a composite overwrap was chosen. The core

was fabricated of 18 Ni grade 200 maraging steel. This concept offers a high strength, high stiffness design. The steel airfoil core was machined to 0.030 in. undersize and contained all pressure tube grooves. A major fabrication advantage with this concept is that tube grooves can be cut in the core, eliminating the need for using groove filler material. After tubing installation the core was overwrapped with approximately 0.080 in. thick E-glass/epoxy. After curing, a final undersize contour was machined. After final machining, hand polishing and fitting to the fuselage, the airfoil was coated with a gel coat of resin approximately .002 - .003 in. thick. Further handworking was completed, orifices drilled, and final validation of airfoil shape and orifice locations were made. One of the completed horizontal stabilizers is shown in figure 36.

#### 6.1.3 Vertical Stabilizer Fabrication

The fabrication process for the vertical stabilizer was quite similar to the horizontal tail. The core, however, was made of E-glass/epoxy material. (See ref. 23 for typical properties). The fuselage attachment was a simple design (fig. 34) which allowed traditional fabrication methods to be used. The core was machined undersize (same as horizontal tail) and overwrapped with 0.080 in thick E-glass and cured. Stainless steel tubing .030 in. O.D. by 0.02 I. D. was used in both the horizontal and vertical tails. The completed vertical stabilizer is illustrated in figure 37.

#### 6.1.4 Special Procedures

Special procedures were required during fabrication of the instrumented stabilizers. The procedures relative to machining tube grooves, applying the E-glass/epoxy overwraps to the steel, and E-glass/epoxy

spars and machining to finished contour are described in reference 20.

#### 6.1.5 Proof-of-Concept Testing

Proof-of-concept and aerodynamic testing for similar airfoil designs have been reported in references 2 and 9. Both the horizontal and vertical tails were proof load tested. The steel core design was dynamically tested to three times the expected loads which developed a peak stress of 100 ksi in the metal spar. Cyclic loads were applied at temperature ranges from room temperature to -300°F, with no failures or evidence of fatigue damage. The composite stabilizers are shown attached to the Pathfinder fuselage in figure 38.

As previously mentioned, a 2-D carbon fiber reinforced epoxy airfoil was aerodynamically tested in the Langley 0.3 M TCT. The models' performance was excellent with the aerodynamic data comparing very well with an all metal airfoil of the same geometry. This model is shown in figure 39. The research results for the 2-D composite model are reported in reference 9.

#### 6.1.6 Composite Instrumented Stabilizers Study Results

The study demonstrated that use of conventional and/or advanced composite materials for cryogenic models is quite feasible. Fabrication advantages, issues, and costs are discussed in the following section.

##### 6.1.6.1 Fabrication Advantages

The principal advantages afforded by composite concepts when compared to conventional (all metal) models as reported in reference 22 are:

- (a) Models can be more easily recovered from damage during fabrication.
- (b) Location and drilling of orifices is much easier when compared to conventional designs.
- (c) The airfoils are much easier to work to final contour.
- (d) The airfoils have excellent dimensional stability during machining and cryo cycling. Major fabrication difficulties encountered were:
  - (a) Very smooth surface finishes ( $\approx 16$  RMS) were more difficult to achieve with fiberglass than with all metal airfoils.
  - (b) Orifice hole quality was less than desired and needs to be improved.

Significant fabrication cost savings can be achieved. Based on this limited experience it is estimated that an overall fabrication cost savings of approximately 50 percent is achievable for the metal spar design (horizontal stabilizers) when compared to all metal conventional airfoils. An even greater fabrication cost savings can be achieved for the E-glass/epoxy core and overwrap design.

#### 7.0 COST FACTORS FOR CRYOGENIC MODELS VERSUS CONVENTIONAL MODELS

Increased costs for cryogenic models has been an issue from the beginning of testing at the NASA 0.3 M TCT and NTF. At the VKI lecture series in 1985 a data base had

been established for estimating fabrication cost factors for different metals based on experience at that time. These data are given in Table II taken from reference 2.

The cryogenic design and fabrication costs were last addressed via a panel discussion which is documented in reference 9. At that time the cost factors related to fabrication varied from 1.1 to 1.4 among industry and government agency participants, while design and analysis cost factor estimates varied from approximately 1.15 to 1.5.

In recent years, design and fabrication of cryogenic models for NTF have become more routine. Materials being used for cryogenic models are routinely used for non-cryogenic models. The analyses requirements are being routinely met for most models with standard handbook approaches, and with large safety factors. Good thermal design practices are being employed such that thermal loads rarely become a driver on the design (see refs. 24 and 25). Flutter analyses are no longer a firm requirement for NTF models. A judgement is made by on-site structural analyst as to whether a flutter analysis is needed based on parametric or empirical methods. Also with the advent of newer more efficient structural design and analysis codes the design and analysis cycle time has been greatly reduced such that the use of rigorous analytical tools can provide a more optimal design for about the same cost. Current work at NASA and industry is focused on new design tools and techniques which can greatly reduce cycle time for both conventional and cryogenic models.

The fact that each model is different suggests that cost factors will vary from model to model depending on the requirements. Fabrication costs can be reduced or minimized by interaction between

designers and fabricators, more innovative designs (for example hybrid or composite designs) can achieve lower costs. Also, as mentioned earlier the very smooth surface finish requirements can drive the fabrication costs due to hand finishing requirements. Whereas total cost factors for cryogenic models versus conventional models were estimated to be as high as 2 some 10 years ago it is now believed that the total cost factor most likely varies from 1.4 to 1.6 (depending on model complexity) with potential for being reduced even further. Currently, the engineering design and analysis cost factor is estimated to be about 1.3 due primarily to additional analysis requirements, longer interaction time with customers and quality control issues. Risk reduction, surface finish, and model tolerances continue to be the major drivers for NTF models.

## 8.0 FUTURE DEVELOPMENT NEEDS

Although significant advances have been made in development, design and fabrication of cryogenic model systems, many problems or challenges remain to be addressed. Some of the future development needs from the author's perspective are discussed in this section.

### 8.1 Force Balances

Currently work is ongoing at NASA Langley to conduct finite element analyses of NTF type one piece force balances. Although the Langley cryogenic strain-gage force balances have an excellent track record, the actual detail stress fields have been unknown. Also, recent work at the Boeing Company has been done on modeling force balances using the finite element code "Mechania". The Boeing study gave excellent correlation between calculated and measured force balance stress/strain response under load.

Although this work was inspired by the high load requirements of the recently cancelled "National Wind Tunnel Complex Program," finite element analyses are now considered feasible and practical for force balance design, optimization and stress analysis. Although finite element analyses and design optimization of force balances have been done in Europe for quite some time, these are the first known applications in the United States.

Another problem currently being addressed at the NTF is bringing the force balances to thermal equilibrium for cryogenic testing. Times required to thermally condition the balance in the cryogenic mode can be up to 1 hour. Active cooling of the force balance is now being implemented which is expected to cut conditioning time from 1 hour to about 5 minutes. Previous proposals have been to heat the balance to maximum thermal equilibrium.

Full cryogenic balance calibration at NASA Langley Research Center currently takes from 2 to 4 weeks and is done manually. Although automated balance calibration machines are in use throughout the world, only recently have initiatives been undertaken to evaluate and purchase automated balance calibration machines in the United States. Automated balance calibration machines are capable of full calibration in 2 shifts of operation or about 16 hours. This capability is needed for the NTF.

Force balances being used in NTF need to be stiffer, particularly in the yaw direction. Four component balance designs should be considered for NTF where drag polars are the primary test objectives. Studies have shown that increased stiffness can in some cases detune model/balance vibration modes from model support modes thereby avoiding

or minimizing structural resonance problems.

## 8.2 Model/Model Support Dynamics

Current work on analysis and attenuation of model/model support vibration problems in the NTF should be accelerated. Lack of a focused and concentrated effort to alleviate these problems have basically limited testing of large models to about 3000 lb/ft<sup>2</sup> dynamic pressure.

The problem should be attacked from all fronts including model dynamic design, structural dampers or feedback devices/systems to limit vibration amplitude, aerodynamic problems related to separated flow and possible redesign of the model support system using dynamic criteria to minimize vibration problems.

## 8.3 Surface Finish and Contour

The surface finish and model tolerance issues with respect to what is really needed for accurate high Reynolds number testing needs to be resolved. The test program initiated by Al Saadi (ref. 10) needs to be continued. Consensus on surface finish and contour accuracy requirements are needed in order to standardize surface finish requirements. This could result in significant model fabrication cost savings and at the same time assure that high quality high Reynolds number data are obtained. Also, machining technology needs to be advanced so that much smoother finishes can be obtained on airfoils before hand finishing, thereby leading to significant reductions in fabrication cost and time.

## 8.4 Orifices and Pressure Tubes

Further work is needed to better understand orifice quality needs and improved methods for pressure tube installation. Studies

reported in references 14 and 15 point to accuracy improvements obtained by using porous plug orifices yet it appears that conventional orifices are still being used with even smaller orifices (0.005) and pressure tubes sometimes being specified. The questions as to the needed size and location (e.g., in high pressure gradient areas) are being addressed, but specifications vary from model to model. For example, why go to a 0.005 orifice (which can be plugged by dust particles) when a 0.10 orifice may very well give the desired accuracy if space allows. Also, fabrication expertise in terms of pressure orifices and tube installation techniques (e.g., brazing, soldering, etc. (ref. 13)), has been lost due to experienced personnel retirements at NASA Langley.

#### 8.5 Critical Design and Fabrication Skills

With the loss of so many engineers and technicians at NASA Langley due to retirement, much of the expertise in cryogenic model design and fabrication no longer exists. Although virtually all of the cryogenic model technology development work was documented (e.g., ref. 9 and 24) oftentimes, the information is not used by technicians, engineers, etc., and may result in re-inventing the wheel so to speak or encountering problems for which known solutions exist. The point of addressing this issue is that cryogenic model design and fabrication expertise needs to be maintained by the performing organizations. Documentation and training are critical to maintaining such skills.

#### 8.6 Reduced Design, Fabrication, and Testing Cycle Time

With the current emphasis on faster, better, and cheaper design and fabrication cycle time has become a major productivity issue

for cryogenic models. With the recent advances in computed aid design and machining, and advanced analytical tools, the time is near when the design and fabrication process time can be reduced significantly.

With increased emphasis on tunnel productivity, model design issues related to tunnel testing are becoming more and more important. For example, reduction of time installing, making configuration changes, and removing a model should be a design consideration. Model configuration changes are becoming more of a productivity issue. Work is needed to develop remote actuators that can be incorporated in cryogenic model design, and will work at cryogenic temperatures. Although, some work was done on remote actuators for an NTF shuttle model (ref. 26), nothing has been done in this area since that time. Basically, cryogenic model technology development activities ceased at NASA Langley after 1985, but should be resumed to address current issues with model design and testing.

### 9.0 CONCLUDING REMARKS

Cryogenic model design, fabrication and testing technology has advanced significantly in recent years. Cryogenic model design requirements are basically unchanged for the NASA Langley facilities, however; cryogenic model design and fabrication has become more routine and less costly. Current practices relating to surface finish, pressure orifices, filler and braze materials and fastener applications are reviewed. Although some work has been done on surface finish requirements, the surface finish needed for different parts of the model are still aerodynamic data quality and fabrication cost issues. Further development work is needed in this area. New plug type orifices have been developed and studies



made to investigate orifice size effects on data quality.

Much has been learned from cryogenic model development, design and build cooperative efforts between NASA and industry. Advanced model support system studies have resulted in promising concepts and a new innovative concept has been proposed in which the sting is replaced by aerovanes. Composite models have been built and successfully tested in cryogenic facilities. Composite models may offer distinct fabrication advantages over all metallic models. Reduced cost of cryogenic models when compared with conventional models has been effected by more efficient design and fabrication practices coupled with test experience.

Future development needs are judged to be in the area of force balances design optimization (stronger, stiffer, elimination of thermal gradient, etc. without accuracy penalty) and automated calibration. Model/model support dynamics remain as a limiting factor for testing models in the NTF. Further work is needed to attenuate NTF model/model support vibration. Surface finish, and fabrication requirements along with orifice size and type need further development work. These are tunnel productivity and data quality issues which need to be resolved. Clearly there is a need to put more resources into cryogenic model design and fabrication technology as well as resolving data quality issues and improving tunnel productivity.

## 10 ACKNOWLEDGEMENT

The author would like to thank Mrs. Doris Vandever for her proficiency in typing the manuscript and layout of the illustrations.

## 11. REFERENCES

1. Young, C. P., Jr.: Design and Construction of Models for the National Transonic Facility. I. Presented at an AGARD Special Course at the Von Karman Institute, Rhode-Saint-Genese, Belgium, April 22-26, 1985. Published in AGARD 722, pages 4-1 through 4-17.
2. Young, C. P., Jr.: Design and Construction of Models for the National Transonic Facility. II. Presented at an AGARD Special Course at the Von Karman Institute, Rhode-Saint-Genese, Belgium, April 22-26, 1985. Published in AGARD 722, pages 5-1 through 5-16.
3. Anon. Wind-Tunnel Model Systems Criteria. NASA Langley Research Center LHB 1710.15. May 1992.
4. Rush, Homer F.: Grain-Refinishing Heat treatments to Improve Cryogenic Toughness of High Strength Steels. NASA TM 85816, August 1984.
5. Berry, Robert F., Jr: Fabrication Division Ultrasonic Inspection Specification For Critically Stressed Components. NASA TM 84625. February 1983.
6. Young, C. P., Jr.; Hergert, Dennis W.; Butler, Thomas W. and Herring, Fred M.: Buffet Test in the National Transonic Facility. NASA Contractor Report 191420. February 1993.

7. Young, C. P., Jr.; Buehrle, R. D.; Balakrishna, S. and Kilgore, W. A.: Effects of Vibration on Inertial Wind-Tunnel Model Attitude Measurement Devices. NASA TM 109083. July 1994.
8. Buehrle, R. D. and Young, C. P., Jr.: Modal Correction Method for Dynamically Induced Errors in Wind-Tunnel Model Attitude Measurements. 13th International Modal Analysis Conference. February 1995.
9. Young, Clarence P., Jr.; Gloss, Blair B.: Second Workshop on Cryogenic Wind-Tunnel Models. NASA CP-3010. 1988.
10. Al-Saadi, Jassim A.: Surface Finish Effects On An Airfoil At High Reynolds Number. M. S. Thesis North Carolina State University. 1987.
12. Rush, H. F., Jr. and Firth, G. C.: Initial Investigation of Cryogenic Wind Tunnel Filler Materials. NASA TM 86363. January 1985.
13. Bradshaw, James F.; Sandefur, Paul G., Jr.; and Young, Clarence P., Jr.: Braze Alloy Process and Strength Characterization Studies for 18 Nickel Grade 200 Maraging Steel with Application to Wind Tunnel Models. NASA TM 104075, May 1991.
14. Plentovich, E. B.: The Application to Airfoils of A Technique for Reducing Orifice Induced Pressure Error at High Reynolds Number. NASA Technical Paper 2537. January 1986.
15. Plentovich, E. B. and Gloss, B. B.: Orifice-Induced Pressure Error Studies in Langley 7- by 10-Foot High Speed Tunnel. NASA TP 2545. February 1986.
16. Taylor, C. R.: The Use of ETW For Tests At High Reynolds Number. Wind Tunnels and Wind Tunnel Test Techniques Conference. Royal Aeronautical Society. pp. 20.1 - 20.12. September 1992.
17. Young, C. P., Jr.; Popernack, T. G.; and Gloss, B. B.: National Transonic Facility Model and Model Support Vibration Problems. AIAA Paper No. 90-1416, 1990.
18. Buehrle, R. D.; Young, C. P., Jr.; Balakrishna, S.; and Kilgore, W. A.: Experimental Study of Dynamic Interaction Between Model Support Structure and a High Speed Research Model in the National Transonic facility. AIAA Paper No. 94-1623, 1994.
19. Griffin, S. A.; McClain, A. A., et al: Design Study of Advanced Model Support Systems for the National Transonic Facility. General Dynamics Report No. GDC-CRAD-86-004. December 1986.
20. Griffin Stan.; Crooks, Richard S., and Mole, Phillip J.: Vane Support System (VSS) A New Generation Wind Tunnel Model Support System. AIAA Paper No. 91-0398, January 1991.

21. Edwards, R. W.: An Approach For Increasing Aeroelastic Divergence Dynamic Pressure of Wind-Tunnel Models. AIAA Paper No. 92-4002, July 1992.
22. Young, Clarence P., Jr; et al: Design and Fabrication of Instrumented Composite Airfoils for a Cryogenic Wind Tunnel Model. NASA TM 102740.
23. Young, C. P., Jr. and Wallace, John W.: Mechanical Properties of the Fiberglass Prepreg System Used for the National Transonic Facility Replacement Blade Set. NASA TM 102756. February 1991.
24. Carlson, Ann B.: Thermal Analysis of Cryogenic Wind Tunnel Models. AIAA Paper No. 84-1802, 1984.
25. Rash, Larry C.: Finding Realistic Thermal Stress. Machine Design pp. 76-78, April 1993.
26. Young, C. P., Jr, et al: Cryogenic Wind-Tunnel Model Technology Development Activities at the NASA Langley Research Center. AIAA Paper No. 84-0586, 1984.

Table I. Filler Materials/Shear Strength

Material	Shear Strength, psi	
	Room Temp.	Cryo
EA 9309	2500	4500
EA 9309/C 1:1	3000	4500
EA 9309/C 1:2	1000	2300
Super Metal	2900	2700
Fast Set/C 1:2	2000	3300

Table II. Estimated Fabrication Cost Factors

Model material	Machining cost factor	Increase due to		*Total cost factor
		8-10 rms finish	±.002 tolerance	
Nitronic 40	1.50	.040	.120	1.66
A-286	1.50	.040	.120	1.66
PH 13-8 1150 M	1.25	.030	.090	1.37
18 Ni grade 200	1.00	.025	.075	1.10
18 Ni grade 200 (grain refined)	.75	.025	.075	0.85
6061 T-6 AL	0.50	.010	.030	0.54

\*Cost factor of 1.0 would correspond to a non-cryogenic model fabricated from 17-4 PH stainless steel with a 32rms finish and ±.005 tolerance

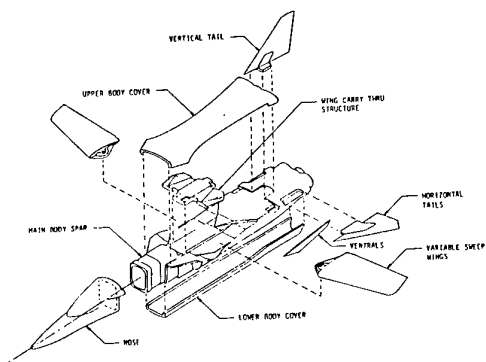


Figure 1.- F-111 Cryogenic Model Components.

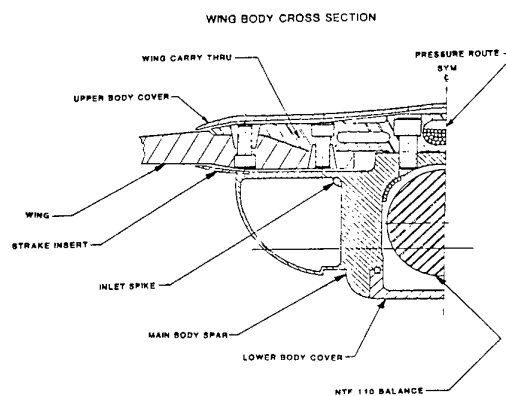
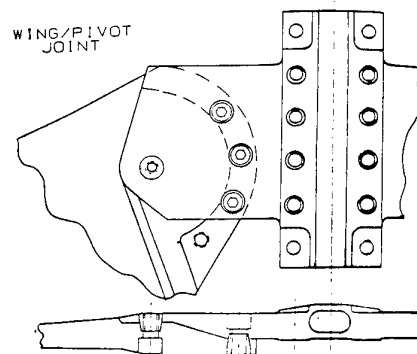


Figure 3.- F-111 Wing/Pivot Joint Design.

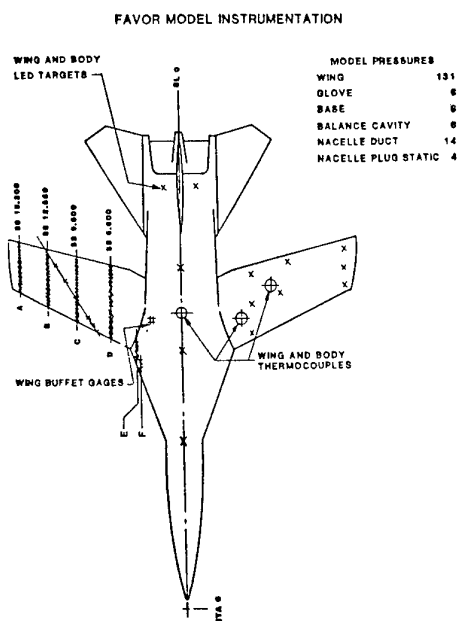


Figure 2.- F-111 Cryogenic Model Instrumentation.

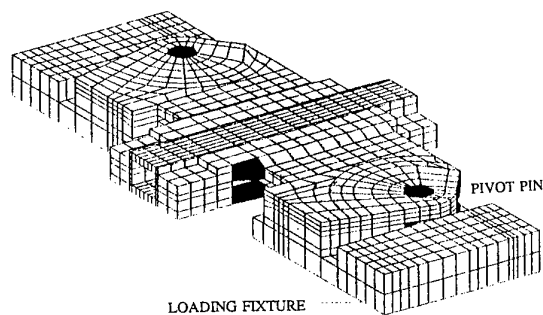


Figure 4.- Finite Element Model of F-111 Carry-Thru Fixture.

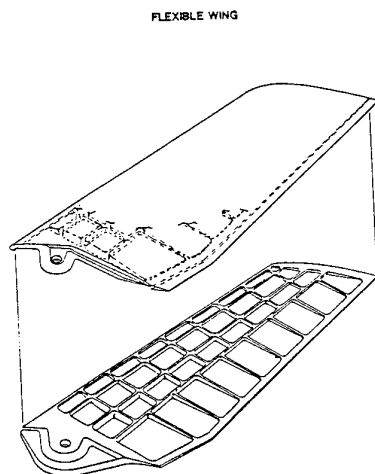


Figure 5.- F-111 Wing Design.

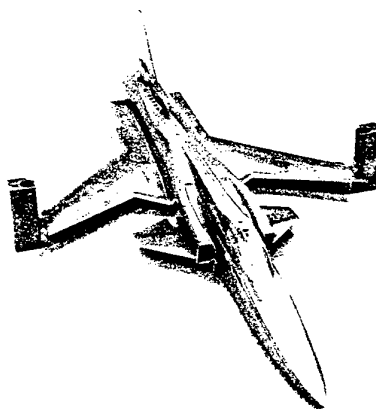


Figure 7.- X-29A Cryogenic Model.

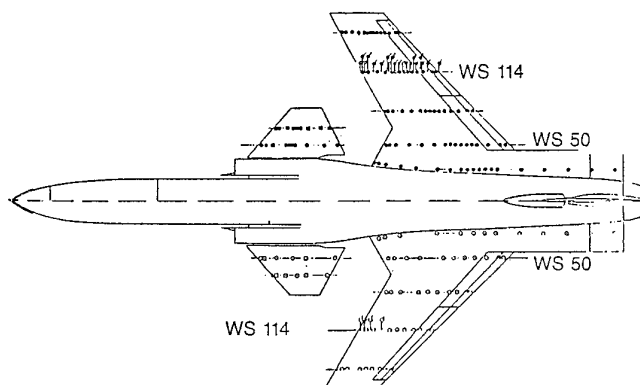


Figure 8.- X-29A Cryogenic Model Instrumentation.

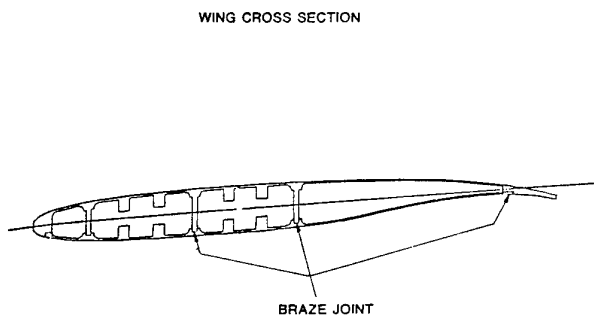


Figure 6.- F-111 Wing Cross Section Illustrating Braze Joints.

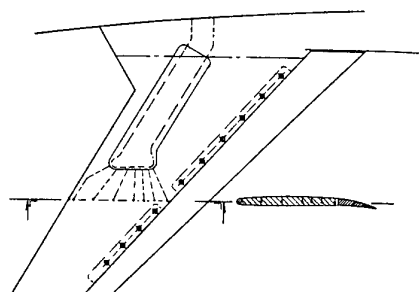


Figure 9.- X-29A Wing Orifice Tubing Illustration.

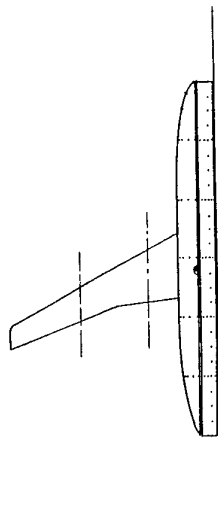
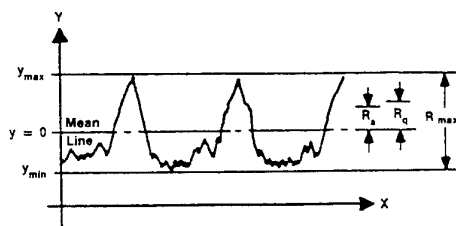
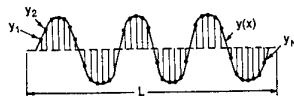


Figure 10.- Planform View of Semi-Span Model  
Illustrating Stand-Off Geometry

#### SCHEMATIC SURFACE PROFILE



#### SCHEMATIC DIAGRAM ARITHMETIC AVERAGE AND RMS DEVIATION



- $R_a$  = Average Deviation of Profile  $y(x)$  from the mean Line  
= Total Shaded Area /  $L$   
=  $\frac{1}{L} \int_0^L |y(x)| dx \approx \frac{1}{N} \sum |y_i|$
- $R_q$  = rms Deviation ...  
=  $\sqrt{\frac{1}{N} \sum y_i^2}$

Figure 11.- Schematic Surface Profile and Diagram  
illustrating Calculation of Arithmetic  
Average and RMS Deviation.

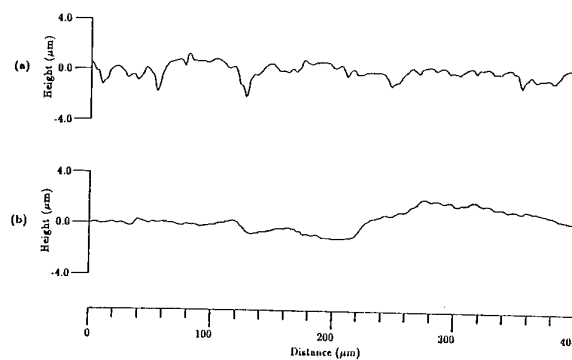


Figure 12.- Profilometer Traces of Model Surface  
(a) Perpendicular to Lay  
(b) Parallel to Lay.

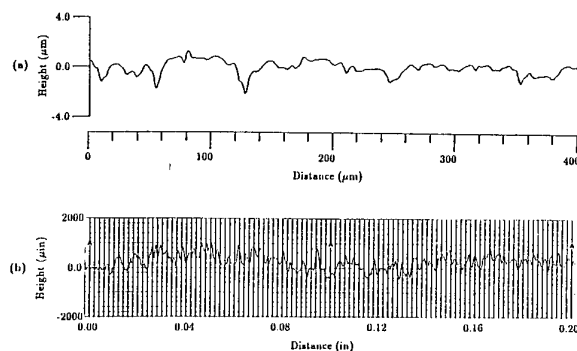


Figure 13.- Profilometer Traces of Model Surface  
and Sand Roughness (a) Model  
Surface Perpendicular to Lay  
(b) 600-Grit Emery Paper.

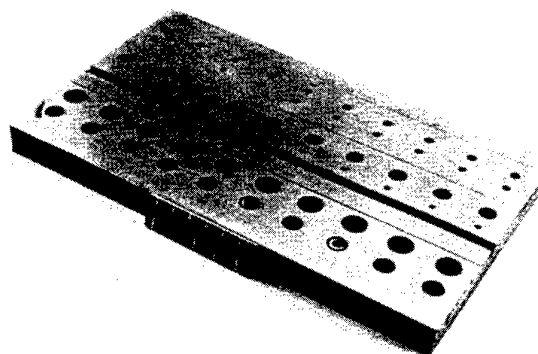


Figure 14.- Filler Test Specimen.

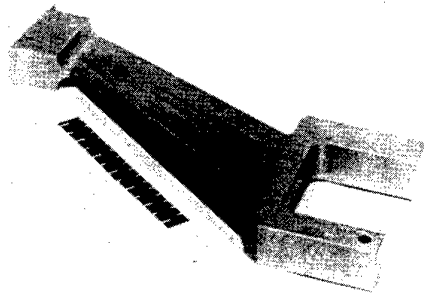


Figure 15.- Wing Spar Filler Test Specimen.

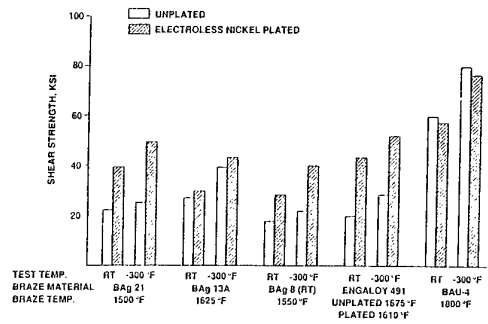


Figure 18.- Shear Strength Properties for 18 Ni Grade 200 Steel Braze Specimens.

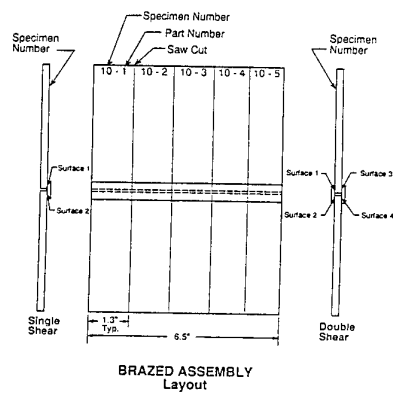


Figure 16.- Illustration of Braze Assembly Used for Shear Test Specimens.

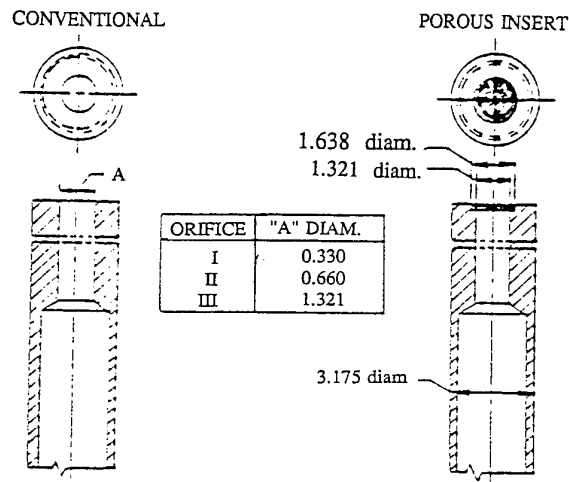


Figure 19.- Test Orifice Geometry (All Dimensions are in Centimeters.).

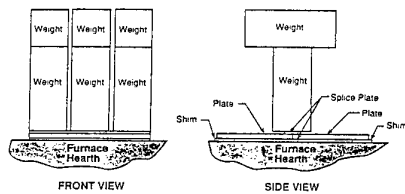


Figure 17.- Illustration of Placement of Braze Specimens In Furnace.

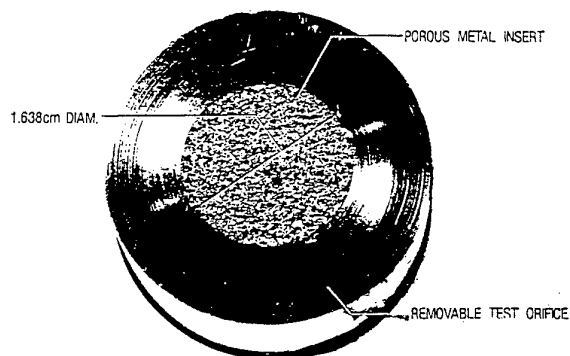


Figure 20.- Porous Metal Plug Orifice.

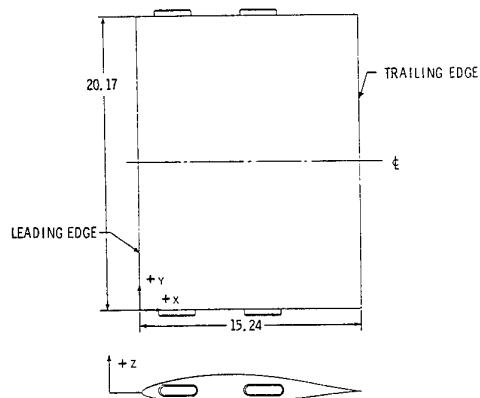
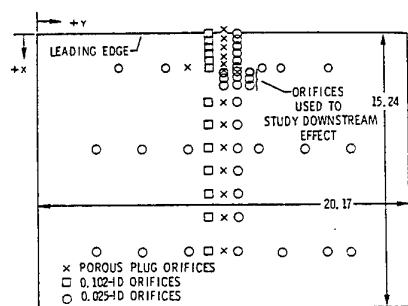
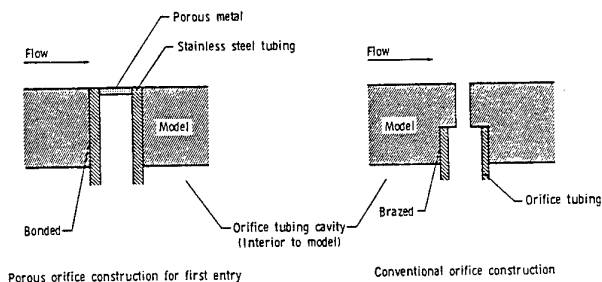


Figure 21.- Schematic Drawing of Orifice Test Model  
(All Dimensions are in Centimeters.).

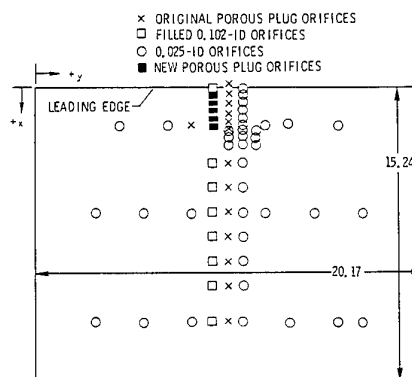


(a) Placement of orifices on upper surface of model.  
(All dimensions are in centimeters.)

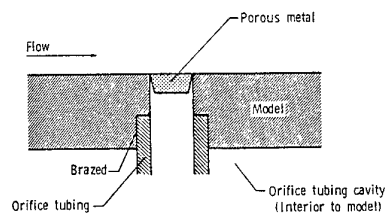


(b) Cross section of orifice construction (not drawn to scale).

Figure 22.- Model Construction for First Tunnel Entry.



(a) Placement of orifices on upper surface of model.  
(All dimensions are in centimeters.)



(b) Cross section of porous plug orifice construction  
for second entry (not drawn to scale).

Figure 23.- Model Construction for Second  
Tunnel Entry.

#### UNBRACED PROPOSED STING MATERIALS

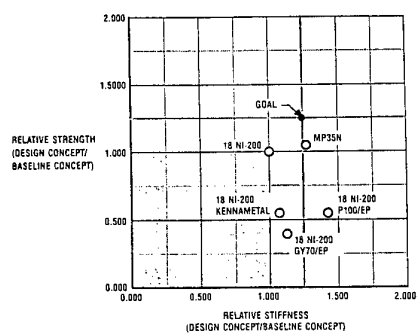


Figure 24.- Design Goal for Advanced Metallic  
Sting.



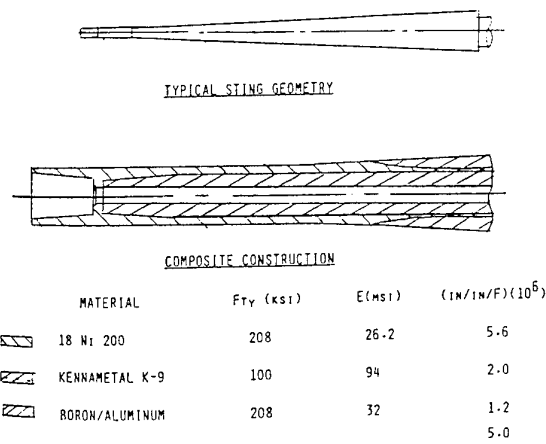


Figure 25. Composite Sting Design Concept.

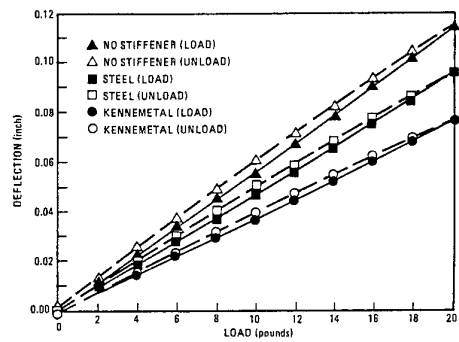


Figure 28.- Floating Stiffner Concept Experimental Data.

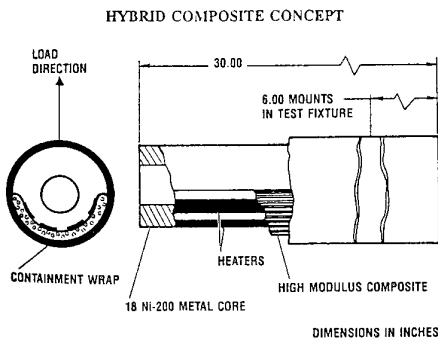


Figure 26.- Hybrid Composite Sting Concept.

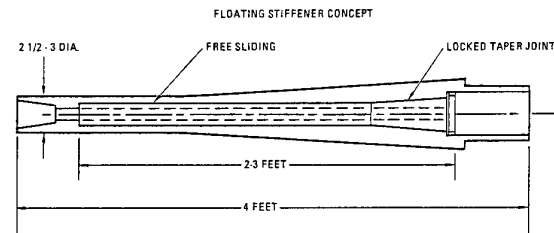
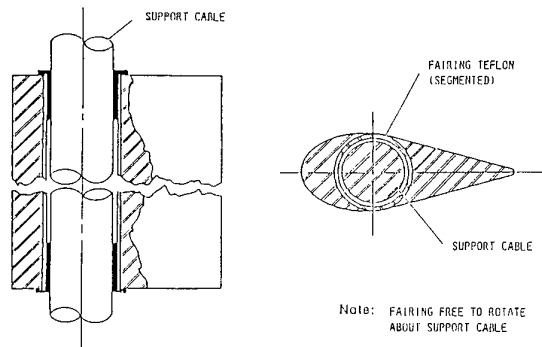


Figure 29.- Aerovane Concept Illustration of Aerovane and Attachment to Balance.

Figure 27.- Floating Stiffner Sting Concept.  
Conventional Steel (18 Ni-200) with  
Kennametal Inner Rod.

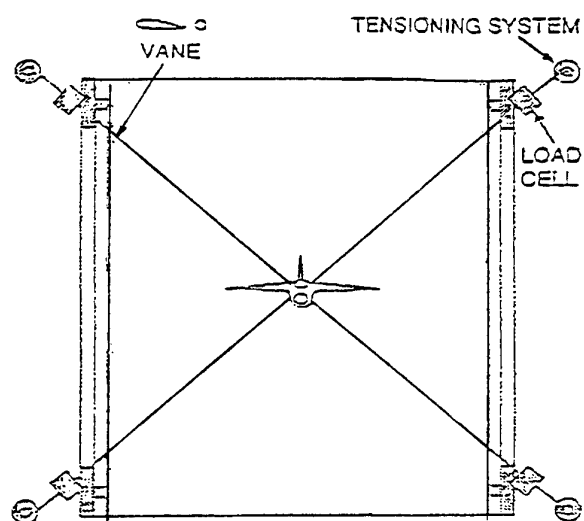


Figure 30.- Aerovane Support System - Front View.

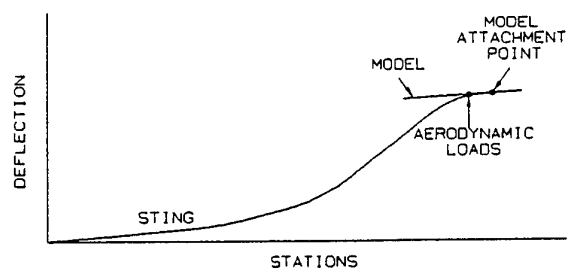


Figure 32.- Representative Divergence Mode Shape.

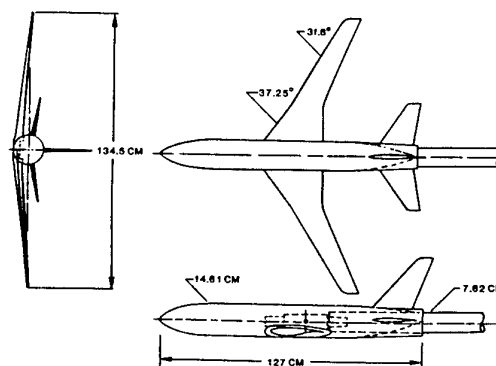


Figure 33.- Pathfinder I Model.

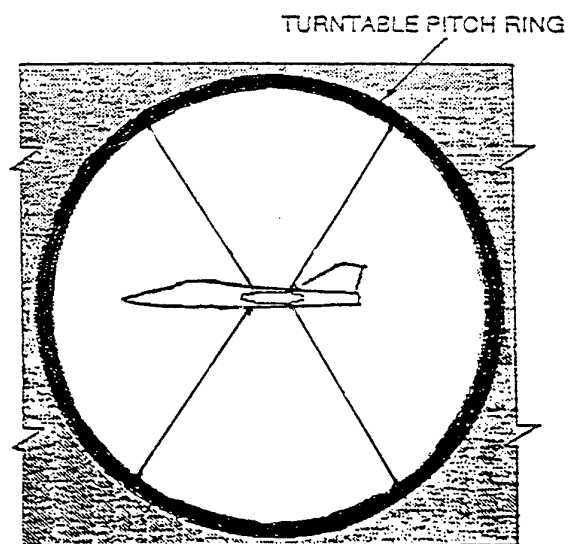


Figure 31.- Aerovane Support System - Side View.

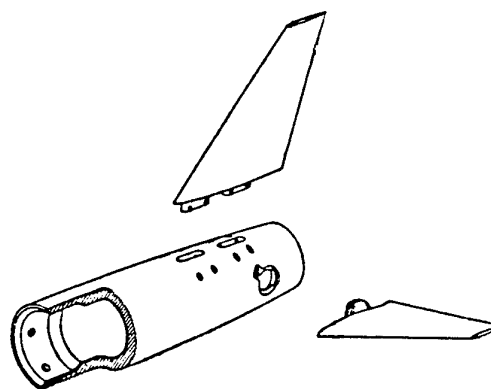


Figure 34.- Illustration of Horizontal and Vertical Stabilizer Attachment for Pathfinder I.

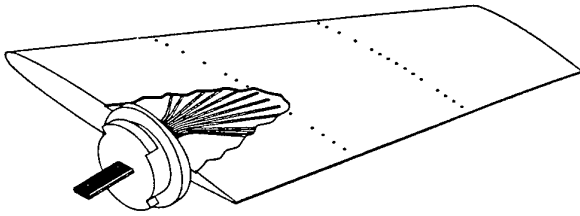


Figure 35.- Pathfinder I Horizontal Stabilizer Composite Design Illustrating Breech-Lock Attachment.

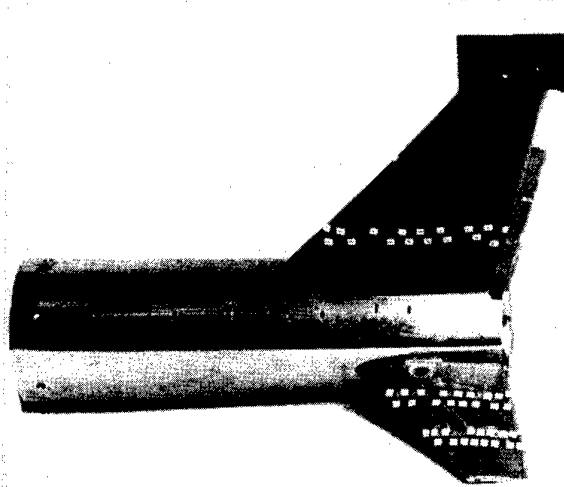


Figure 38.- Composite Horizontal and Vertical Stabilizers Fitted to Pathfinder Fuselage.

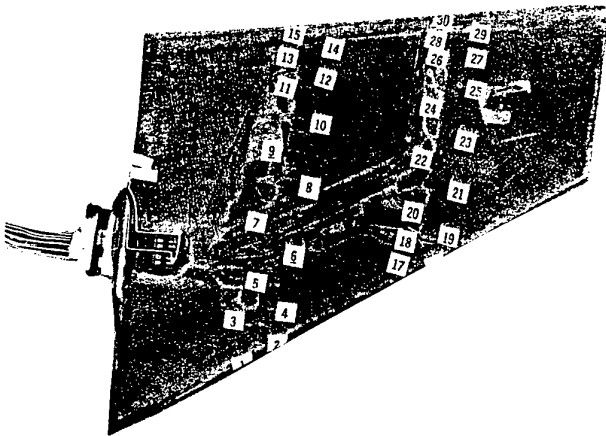


Figure 36.- Pathfinder I Composite Horizontal Stabilizer.

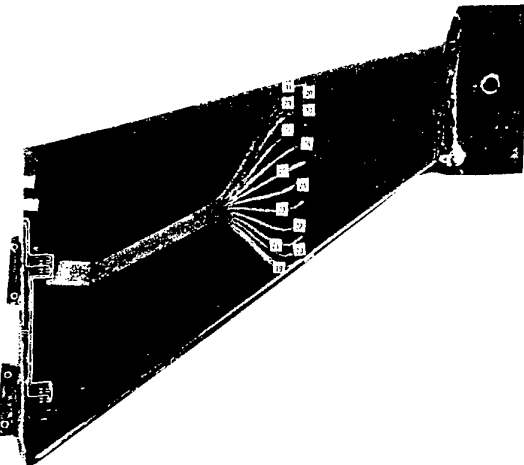


Figure 37.- Pathfinder I Composite Vertical Stabilizer.

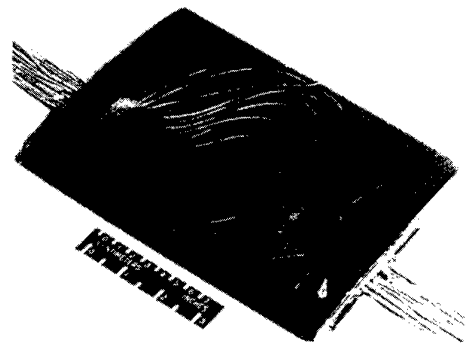


Figure 39.- Composite Airfoil Tested in the NASA Langley 0.3 M TCT.

# Instrumentation for Cryogenic Tunnels

M. Bazin, *Onera/GME*, C. Blanchet, *Bertin*, F. Dupriez, *Onera/IMFL*,  
BP 72, Avenue de la Division Leclerc  
92322 Châtillon Cedex, France

## ABSTRACT

A few examples are given of recent work on the European Wind Tunnel (ETW): the sting balance, which is insensitive to temperature and to thermal gradients; qualification of the transition Reynolds number in the flow; determination of the transition position on models (coating, artificial triggering, and low-temperature infrared camera); optical measurement of the model attitude; and design and construction of a civil aircraft model.

## 1 - INTRODUCTION

Some of the work done in Europe on the periphery of the ETW project was presented in the Special Courses held by the VKI in 1985 and 1989 on cryogenic tunnel technologies. This work, which was essentially on feasibility studies, was coordinated by the WG1 cryogenic technology working group associated with the tunnel project team.

Now that construction is completed, the European group WG1 is no longer operational, and the few subjects presented hereafter concern the work now continuing in France, either under ETW contract or to allow future users to "break into" the facility under the best conditions with proper models. The subject is therefore what is to be constructed for the use of the tunnel.

This is by no means an exhaustive description of all the research under way in the French context, but rather a selection of current activities, with the emphasis on essential and/or original construction.

## 2 - STING BALANCE FOR CIVIL AIRCRAFT

After a request for proposal, the ETW awarded Onera the manufacture of one of the balances used for weighing civil aircraft models in cruising configuration.

The balance design was based largely on previous work to qualify structural and gage bridge materials, including thermal compensation techniques for a cryogenic environment [1], and on the results obtained in the CERT's T2 cryogenic tunnel on the 24 mm diameter probative balance [5, 6].

While the size alone of the 100 mm balance does not directly affect its mechanical design — the rules of similitude apply to the stresses and strains [4] —, increasing the balance dimensions by a ratio of nearly four with respect to the T2 probative balance seriously increases the problems related to the thermal fluxes in the balance structure. Preliminary finite element computations including thermal loadings have shown that satisfactory behavior could be expected for under less favorable conditions than those of the ETW, *i.e.* with a longitudinal gradient of 20 K, of which 10 K in the central portion (5 K over a length of 400 mm for the ETW).

The objective was still to achieve a balance insensitive to any thermal effects in the 100 to 300 K range, with the above thermal gradient. The capacities, outer dimensions, and attachment requirements were set by the ETW:

- 100 mm diameter;
- 450 mm between brackets;
- 490 mm total length.

The balance is a single piece, machined by electro-erosion (Fig.1).

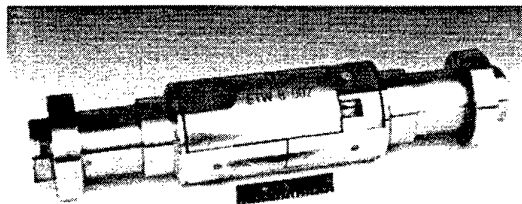


Fig.1 - ONERA balance for ETW.

Its central portion includes the drag dynamometer and the decoupling blades. Special care was taken in designing this

portion for compactness, rigidity, and with symmetries to minimize the thermomechanical effects. The drag dynamometer consists of two beams arranged side by side, vertically head to foot. The end of each beam is connected to the weighted and unweighed parts of the structure by longitudinal link rods with axial thinning, to transmit the axial force and decouple the other forces. The drag dynamometer is framed and effectively decoupled by four groups of three vertical blades of variable heights for homogeneous stresses.

This push-pull arrangement minimizes the thermal gradient effects and provides good sensitivity to the axial force. This type of design has been in use for a very long time for Onera's balances (developed by the Physics Department in the sixties), both for dynamometric elements operating in tensile-compressive, in shear, and, as in the present case, in bending mode. The symmetries of the "decoupled" system make it insensitive to the general temperature level and, under the effect of a temperature gradient, the beams deform in opposition with respect to the "in phase" deformation under an axial load (Fig. 2). All that remains is a  $1 \times 10^{-4}$  in the extreme longitudinal gradient conditions, reported to the maximum stress.

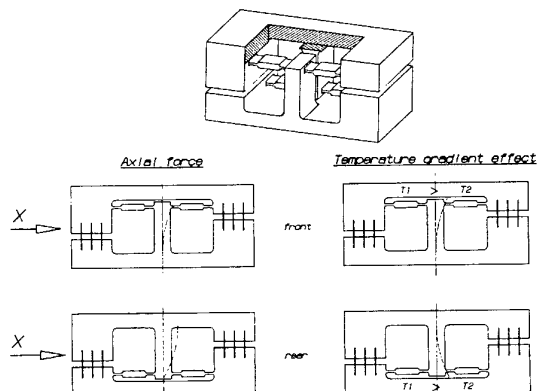


Fig.2 - Bending push pull arrangement.

The other dynamometers — lift, pitching, lateral, yaw, and roll — are simple four-face rings with machined recesses for bonding the gages. They exhibit high rigidity, and allow the thermal fluxes to pass easily through to the center of the balance. The distance to the attachment clamps avoids any clamping

effect. The clamp dimensions and bolt tightening torque were determined by a computation using a specific program (Cobra/Cetim).

The structure is made of Maraging E Z2 NKD 18 steel, treated at 1800 MPa, with little oxidation sensitivity, and protection. A safety device secures the weighed part if ever there is an accidental breakage of the central portion, and immobilizes the assembly during shipping and installation.

The capacities were determined from simultaneous loadings defined by the ETW. The dynamic capacity corresponds to 110 % of the static loads, and the safety coefficients vary from 3 in tensile-compressive and bending to 6 in shear, with a maximum stress on the gage of 200 MPa:

X	1920 N	drag
Y	27300 N	side
Z	28000 N	lift
L	1960 mN	roll
M	3550 mN	pitch
N	1020 mN	yaw

The finite element computation results are re-formatted for input to a program that monitors the balance automatically during testing with consideration of combined efforts to determine maximum local stresses.

The balance is equipped with six main gage bridges (X, M1, M2, N1, N2, and L) supplied with 8 V dc. As a precaution, an  $X_L$  bridge was placed on the internal blades to provide for one last thermal correction [2], but no use was made of this.

Considering the steel used, the gages are nickel-chrome,  $K = 2.1$ , index 09, R of 350 and  $1000 \Omega$ . The protection is M CoatB and M43. The protective cover also serves to improve the thermal properties.

PT 100 temperature probes are provided as required for measurements during testing. They have been used for checks during calibration. There are also heating resistors to create a temperature gradient during the thermal property verification phases.

The gage bridge zero and sensitivity thermal compensation methods were specially

developed at ONERA to deal with the nonlinearities observed at low temperatures. These iterative operations are long and costly, and the painstaking process was therefore interrupted as soon as the contract specifications were reached, without trying to achieve perfection. The results presented show minimum residue.

Before delivery to the ETW, the balance was calibrated in an atmospheric environment by applying unit loads in succession, and then combined loads, on ONERA's calibration stand at the Modane test center. Verifications were then made at five temperature level ranging from 100 to 350 K in a cryogenic chamber in which loads could be applied (Fig. 3). While this is not a true calibration, it was nonetheless possible to check the insensitivity to temperature effects: zero drift, sensitivity variation and gradient effects in the balance's utilization domain. A few examples of results are given in figures 4 and 5 to illustrate the instrument thermal quality.

The pressure insensitivity was also verified between 20,000 and 300,000 Pa, in a pressurized chamber.

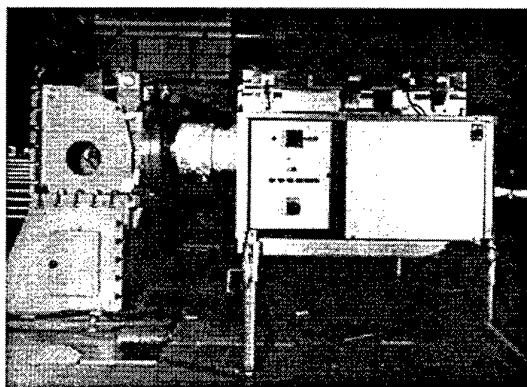


Fig. 3 - Control under effort in cryogenic environment.

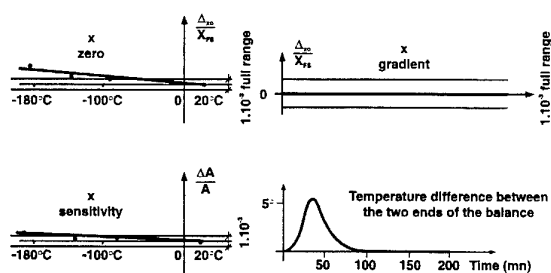


Fig. 4 - Calibration results: Drag.

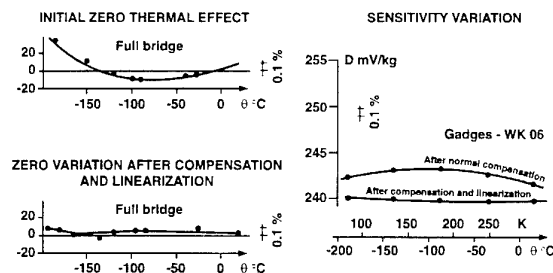


Fig. 5 - Thermal compensation of bridge.

The creep and relaxation properties were found to be very small, at less than  $1 \times 10^{-3}$  of the measured signal.

The mean quadratic differences obtained on the main signals in calibration integrate all of the causes of imprecision, and are less than 0.1 % of the measurement range. A very good agreement was also observed between the computed predictions and all the results.

The instrument delivered to the ETW was therefore deemed to be in conformity with the customer's specifications, and also satisfied ONERA's additional requirements, *i.e.* the possibility of use in the full 100-300 K domain, with a gradient of up to 10 K, with a single matrix. What remained to be done was to observe its behavior under real wind tunnel conditions.

It is understandable that putting a tunnel like the ETW into service and calibrating is a gradual, delicate, exacting process. Perfecting the automatic calibration stand with its temperature adjustment down to 100 K was also a long and difficult phase, during which ONERA's balance served somewhat like a reference. The results on tunnel tests using the balance are not already published by the ETW. "Satisfactory" tests have indeed been performed, but it seems that customers' priorities have not required that the most be made of this balance's thermal insensitivity. The tests have been conducted the same way as with other balances, with precautions being taken primarily to ensure the best quality for wind tunnel calibration, by arranging for long periods of setup thermal stabilization (2 K), to the detriment of operating cost, for the time being.

The calibration stand development phase has generated data with a bridge supply of 5 V rms at 600 Hz, which is different from the

compensation and calibration conditions adopted at Modane. Results are available for nine loading sequences at 11 temperature levels between 100 and 315 K. Each sequence includes six individual forces at 50 and 100 % of capacity, and 15 two-by-two combinations. For each matrix associated with each temperature level, the errors between the load applied and the result generated by the balance are determined for 1500 points.

The differences are in all cases less than 0.1 % (0.03 % in X, 0.01 % in Z, 0.02 % in M), except for a calibration at room temperature (0.17 % in Y), which is currently taken to be an outlying figure.

The repeatability of these calibrations is remarkable: the maximum zero drift in six months has been 20  $\mu$ V, and no variation in the sensitivity.

Onera has conducted a further analysis of the data returned by the ETW, in order to determine the error that would result from using a single matrix, as is possible with this balance, or the error that might result from a difference between the temperature level in the tunnel and the level corresponding to the matrix used.

The reference matrix was established according to measurements at 250 K, and the errors were computed for simple maximum loads, eliminating the outlying figure. For  $T = 150$  K:

$$\Delta X = 1.5 \text{ N, or } -0.0066 \times 10^{-3}/\text{K};$$

$$\Delta L = 5 \text{ mN or } 0.019 \times 10^{-3}/\text{K}.$$

The interaction coefficient variations are negligible, except for a small but significant and unexplained anomaly in Z, which results for example in a  $\Delta M$  under Z of 5.5 mN for  $\Delta T$  of 170 K. This may be a 0.3 mm translation of the force center of reduction. Special attention therefore has to be paid to the expansion effects of the balance and/or of the calibration stand.

The zero variations are very small, e.g. -2.012 N/K for X, or  $6 \times 10^{-6}/\text{K}$  of capacity.

These results confirm that the balance has the contractually required qualities and that its design offers a potential for more economical

use of the tunnel, while conserving the desired precision.

### 3 - TRANSITION

In a modern wind tunnel, it is indispensable to have a tool for calibrating the flow quality throughout the Mach and Reynolds domains (up to  $M = 0.85$  and  $Re = 200 \times 10^6$ ), and also to have processes and instruments capable of localizing the transitions on the model quickly.

#### 3.1 - Flow Qualification

The usual technique for determining the natural transition on a cone with  $10^\circ$  apex angle cannot be used at the ETW because the transition would occur too near the apex, and its abscissa would be too insensitive to the Reynolds number when this number is at very high values.

ONERA CERT/DERA had the idea of creating a body of revolution (Fig. 6) on which a high negative pressure gradient is created upstream, which keeps the transition from climbing upstream. This gradient is then gradually "relaxed" and turns positive, to retain the sensitivity at low Reynolds number.

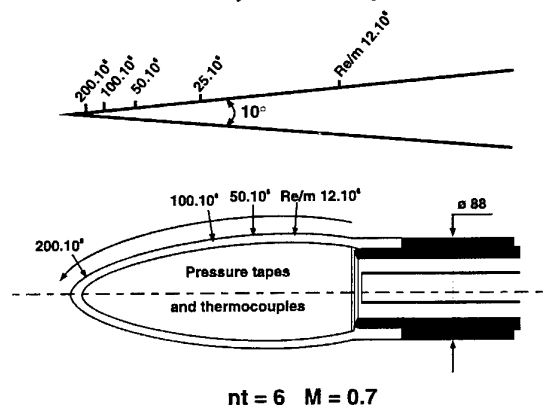


Fig. 6 - Transition Reynolds number on reference model.

The inviscid flow computation was performed in the optimization phase with a panel code with transonic similitude, then a Euler code was used on the optimized shape.

The transition was predicted using a code based on linear instability theory: the frequency most amplified is computed as a function of the abscissa, and the transition corresponds to the unstable amplification

ratio, reaching the critical value  $e^{nt}$ , in which  $nt$  varies from 4 (poor wind tunnel) to 10 (flight).

The body is instrumented around one generatrix with 20 copper-constantan thermocouples, and around the opposite generatrix with 20 pressure holes of 0.2 mm diameter, over a length of 250 mm.

This model, 100 mm in diameter and 400 mm long, was constructed by the IMFL. It consists of a metal skin, 5 mm thick, and the transition position can be observed by an infrared camera viewing an appropriate paint coating.

The predictions will be verified experimentally by preliminary tests in the T2 wind tunnel.

### 3.2 - Transition Triggering

Even in a wind tunnel with very high Reynolds number, it may be necessary to trigger the transition artificially, if only for the sake of cross-referencing at lower Reynolds numbers for comparison with other tunnels.

Various techniques are ordinarily used, the most common being to deposit a strip of Carborundum grains. The reproducibility of this transition is subject to the quality of workmanship. Also, the grains are not always homogeneous, and erosion may even be observed during long test campaigns.

So the CERT looked for some reproducible technique that would have excellent adhesion on a model in cryogenic testing. Of the known techniques (threads, glass balls, Carborundum, cavities, adhesive deposits, and so forth), the following resin stud technique was retained for its hardness, good adhesion, and relative convenience in repetitive applications.

After the black paint is applied for infrared thermographic measurements, we begin by placing a perforated tape and filling the holes with white resin. Once dried, the resin is sanded once. The tape is removed and the studs are sanded again with shims, to the desired thickness.

No bibliographic references exist for the studs (Braslow on flat plates, Von Doenhoff and Dryden). Systematic tests were performed in the T2 tunnel on a 2D airfoil with 250 mm chord. Several configurations were tried, at various Reynolds numbers, and the drag effect was examined (Fig. 7). This solution is an effective one, though it has not turned out to be as convenient as was originally hoped.

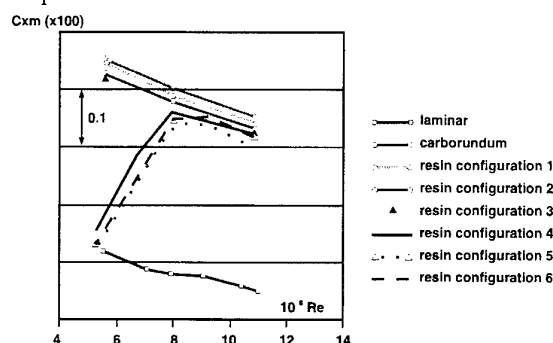


Fig. 7 - Transition tripping.

### 3.3 - Infrared Visualization

This technique is coming into more and more common use in conventional wind tunnels. Compared with visualizations using acenaphthene sublimation, this is a "reversible" technique which allows a sequence of different experimental conditions to be simulated during a given test.

There are two difficulties extending this technique for use in a cryogenic tunnel:

- To avoid the mirror effect, the model's insulating coating has to be emissive; but it must also be as thin as possible (less than 0.1 mm) in order to be applied to an existing model without significantly modifying its shape, and still stand up to cryogenic conditions. The alternative is a thick coating on a "reduced" model.

- The observation camera has to operate at very low temperature, with a sensitivity three times greater than when observing the phenomenon to be detected at room temperatures.

#### - Coating

A number of products were selected on the basis of systematic tests for adhesion, surface



condition, hardness, resistance to immersion in liquid nitrogen, emissivity coefficient for different wavelengths and viewing angles.

A qualification test was then performed on a 2D airfoil in the CERT's T2 tunnel, from 30 to 70 % of chord length, only down to 180 K, because of the available camera (8-12  $\mu\text{m}$ ).

Despite the non-optimum observation conditions, the laminar and turbulent areas were observable, with the model at a slightly higher temperature than that of the flow. As the transfer coefficient is higher under these conditions, the surface temperature is cooler in the turbulent area.

#### - Camera

The ETW performance requirements are the following:

$$M = 0.15 \text{ to } 1.3$$

$$P_i = 1.25 \text{ to } 4.5 \text{ bar}$$

$$T = 90 \text{ to } 313 \text{ K.}$$

A 0.3 K temperature difference has to be observed (Fig. 8).

ETW CONDITIONS			
Temperature	100 K	$\Delta$	300 K
$\Delta T$	0.3 K		1 K
Emissance max	$\lambda$ 30 $\mu\text{m}$		10 $\mu\text{m}$
Maximum contrast	24 $\mu\text{m}$		8 $\mu\text{m}$
PARTICULES SPECIFICATIONS FOR LOW TEMPERATURE			
	100 K		300 K
SiGa detector:	cooling $\leq 20\text{K}$ by liquid helium	HgCdTe detector:	Nitrogen cooling
	observation domain 13-15 $\mu\text{m}$		observation domain 8-10 $\mu\text{m}$
Cooled optics		Ambient optic	
Environnement:	low temperature and pressure		

Fig.8 - Infrared camera requirements for ETW.

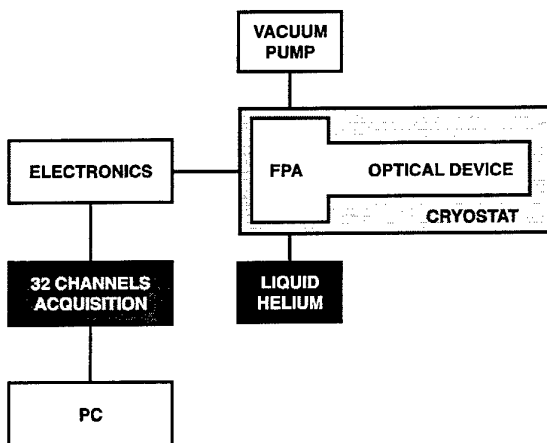


Fig.9 - PETW prototype camera.

A prototype camera was developed by ONERA's Physics Department, and was installed in the PETW in 1994 (Figs. 9 to 11). This is based on a SiGa 64  $\times$  64 Focal

Plan Array (FPA) derived from the 32  $\times$  32 device installed on the ISO satellite. It is cooled to 10 K by liquid helium. The observation optics are also cooled (50 K), as is the cold screen. The camera includes only two cooled aluminum mirrors.

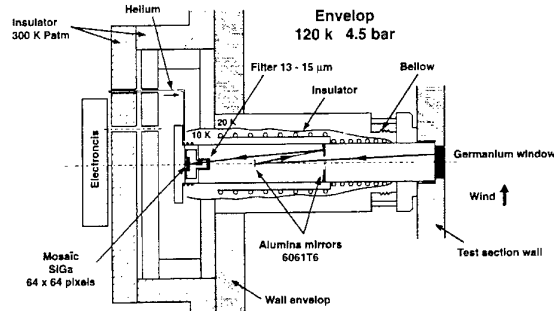


Fig.10 - PETW prototype camera.

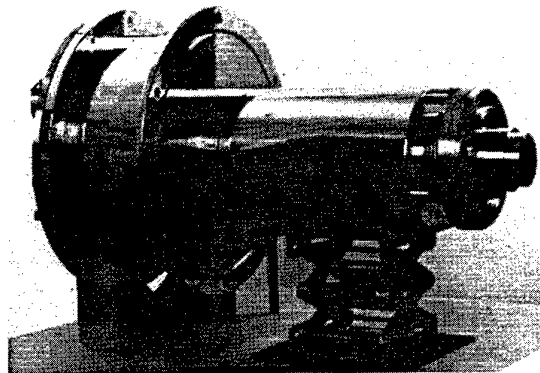


Fig.11 - PETW prototype camera.

This test proved the design feasibility, yielding a processed image of the transition on an airfoil corresponding to better than  $\Delta T = 0.3 \text{ K}$ . Mainly, we have now acquired the necessary thermal protection for the electronics, as well as the image correction technique, the control of spurious images, and window techniques, so that we can begin the ETW's final camera (Crystal project) with confidence (Fig. 12 to 14).

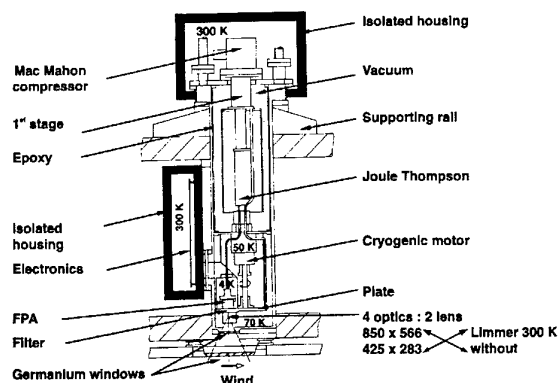


Fig.12 - Crystal camera.

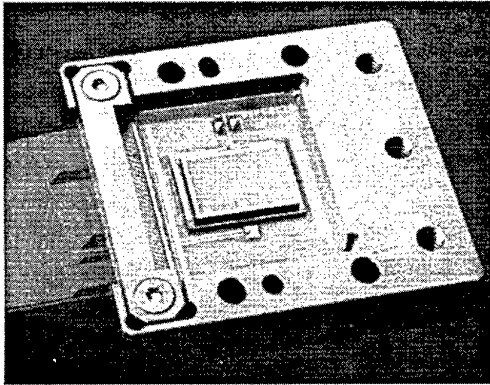


Fig.13 - FPA detector.

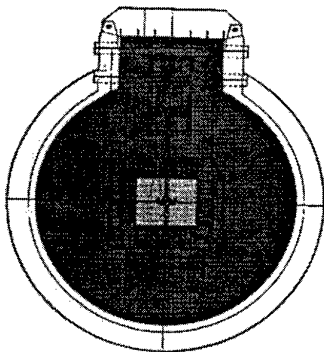
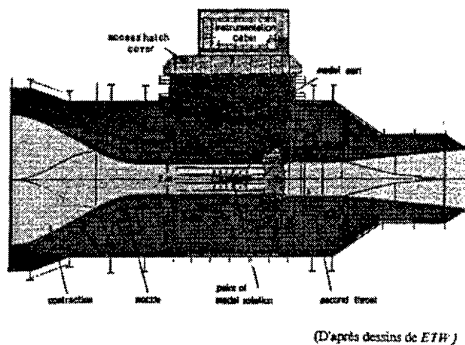


Fig.14 - Installation of Crystal camera in ETW.

This final camera is currently undergoing laboratory acceptance and should be installed at the ETW in the second half of 1996. Its characteristics are the following:

- 128 × 192 SiGa array from the LETI/Lir;
- resolution better than 0.3 K at 120 K;
- cooled optics with two highly aspherical germanium lenses (to reduce dimensions without reducing light flux);
- 850 × 566 mm field (low resolution);
- 425 × 283 mm field (resolution of 2 × 2 mm<sup>2</sup>);
- image refresh frequency > 0.5 Hz;

- cryogenic machine draws 1 W at 4 K for the helium circuit;
- four interchangeable optical systems, to select high resolution, wide field, high flux (attenuator filter for T > 200 K), and low flux, according to experimental requirements.

#### 4 - ATTITUDE MEASUREMENT (Bertin device)

The measurement of an aeroplane model angle of incidence inside a windtunnel test section may require a high precision of 0.01 degree and a high resolution of 0.001 degree, over a  $\pm 10$  degrees angular range. Such a high precision can be fulfilled with either existing inclinometers sensitive to gravity or optical technology instruments. An inclinometer measures the angle between gravity and the model axis and is very sensitive to model accelerations. During wind-on tests the inclinometer measurement could become wrong by 0.2 to 0.3 degree when the model strongly vibrates and the use of an appropriate filter does not remove all possible bias effect. Additionally, an inclinometer is an active device installed inside the model itself, thus requiring electrical connections, causing space availability problems and a heated housing could be necessary in a ETW model. To overcome these drawbacks of the existing technology, ETW GmbH has commissioned BERTIN a French privately owned Research and Development company involved in optics and optoelectronics systems, to design and manufacture a non contact and high bandwidth optical measurement system. This system, the so-called MAMS (Model Attitude Measurement System) has been jointly developed by BERTIN and ETW between 1992 and 1995. It has been widely tested in laboratory and has presented very promising results. It has then been successfully installed and interfaced to the model cart and computer acquisition system at ETW in March 1995 and is currently in a performance evaluation test phase. The very promising laboratory tests results have been confirmed, although some aspects are still to be improved before the MAMS can be considered as fully

operational in the hard environment of the ETW wind tunnel.

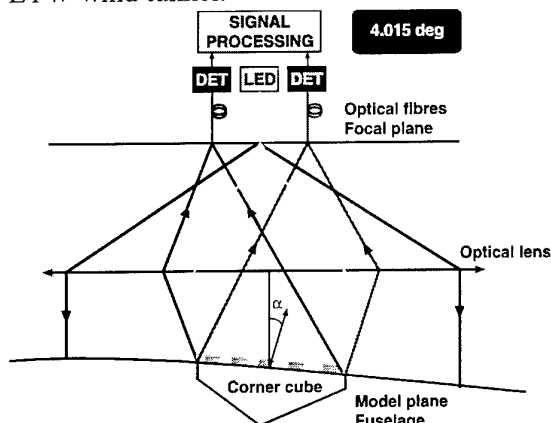


Fig. 15 - MAMS optical arrangement.

#### 4.1 MAMS system description

The MAMS key device, the sensor, consists in a glass corner cube, mounted on the model fuselage, on which is laid a diffraction grating. This device, which is illuminated with an infrared collimated beam (delivered by an LED through a lens), reflects the light in a constant direction whatever the model attitude is. The diffraction grating gives rise to a Moiré effect, which has been proved to deliver +1 and -1 diffraction orders intensities that are (under certain optical configuration) sine modulated with the angle of incidence. When optical fibres are included in the lens focal plane, the +1 and -1 diffraction orders can be easily collected and processed (through an adequate signal processing) to recover the model angle of incidence. Figure 15 describes this arrangement.

#### 4.2 Physical phenomenon description

The light that enters the corner cube under an incidence  $\alpha$ , travels a length  $R$  inside it, equal to twice the corner cube height  $H$ . Then, to ease further theoretical analysis, the corner cube can be considered as a parallel faces plate of thickness  $R=2H$ , of refraction index  $n$ , including on each face a diffraction grating of pitch  $p$ , as represented on figure 16. The light enters the corner cube through the grating first, giving rise to diffraction effect inside the corner cube. If it then travels a length  $R$  inside the corner cube before exiting it through a grating once more, of same pitch  $p$  but shifted from  $R \cdot \tan \theta$  (where  $\theta$  is the angle inside the corner cube, such that :

$\sin \alpha = n \cdot \sin \theta$ ). Using the finite distance diffraction theory, one can calculate the optical wave electric field amplitude distribution (along an axis perpendicular to the grating lines) in the plane of the *second* grating. One can then show that for given planes, the so-called Talbot planes (corresponding to a distance  $R = m \frac{p^2}{\lambda}$ ) this

amplitude distribution is identical to that existing just after the *first* grating. In such a case, the light exit through the *second* grating leads to an amplitude distribution given by the product of the two grating transmission function shapes shifted by the  $R \cdot \tan \theta$ . This gives rise to the Moiré effect that modulates the +1 and -1 diffraction orders. Analysing the diffraction phenomenon at an infinite distance from the grating (in the lens focal plane), one can show that the +1 and -1 diffraction orders are cosine modulated with the angle of incidence and are given by :

$$I(\text{ordre } \pm 1) = \frac{I_0}{2 \cdot \pi^2} \cdot \left[ 1 + \cos \left( 2 \cdot \pi \cdot \frac{\alpha}{T_\alpha} \cdot \mu \cdot k \cdot \pi \right) \right]$$

where  $K$  is a parameter equal to  $\frac{\lambda \cdot R}{n \cdot p^2}$  and  $T_\alpha$

is the phenomenon angular periodicity given

$$\text{by } T_\alpha = \frac{n \cdot p}{R}.$$

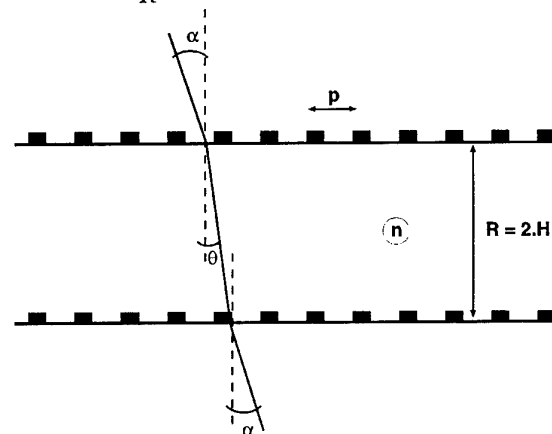


Fig. 16 - Corner cube modelisation.

#### 4.3 Signal processing principle

As one can see from the cosine expression given earlier, the required signal processing to extract the angle of incidence with a constant signal to noise ratio (whatever the angle is) is equivalent to a phase demodulation technic,

where the phase  $\Phi$  to be extracted is  $\Phi = \frac{2\pi\alpha}{T\alpha}$ . The simplest phase

demodulation scheme to implement consists in producing pure sine and cosine shape signals without any DC component and combining them to recover the phase. Choosing the system characteristics such that

$$k = \frac{2m+1}{2},$$

one obtains two antiphase signals  $I_1$  and  $I_2$ , that can be subtracted to keep the modulated cosine shape only. Additionally, using a second emission fibre in the lens focal plane shifted from the first one of a distance  $d$ , two other signals are generated corresponding to an angle  $\alpha$  (such

that  $\alpha \approx \alpha + \frac{d}{F}$  where  $F$  is the lens focal length). Choosing  $d$  such that the generated corresponding phase shift in the  $+1$  or  $-1$  diffraction order signal ( $\Delta\Phi \approx \frac{2\pi}{T\alpha} \cdot \frac{d}{F}$ ) be

$(2m+1)\pi/2$ , one obtains two signals  $I_3$  and  $I_4$  in quadrature with respect to  $I_1$  and  $I_2$ . It is then possible to recover the phase  $\Phi$  (within a  $2\pi$  interval) using the definition relationship :

$$\Phi = \arctg \frac{I_3 - I_4}{I_1 - I_2}.$$

Last of all, considering the rather low angular periodicity of the physical phenomenon (0.3 degree), measuring inside the whole angular range ( $\pm 10$  degrees) requires the removing of the  $2\pi$  ambiguity experienced in all phase measurements. For that purpose, in the MAMS two different wavelengths have been used, such that because of the corner cube glass refraction index chromatic dispersion, two signal sets presenting distinct angular periodicity are obtained, allowing the phase recovery over the whole angular range. Then knowing the angular periodicity  $T\alpha$  one can measure the angle of incidence  $\alpha$  over its whole range  $\pm 10$  degrees.

#### 4.4 Description of the prototype

BERTIN has designed and manufactured in close co-operation with ETW a prototype of such a system. The prototype uses two LEDs (800 nm and 1300nm) as light sources, an optical head integrated in an insulated box to

cope with the test section cryogenic environment ( $-180^\circ\text{C}$ ) and including a lens (which focal length is 220 mm) and a focal plane comprising the optical fibers. This optical head is connected to an optoelectronic signal processing unit through a 20 meters long electro-optical cable designed to cope with the test section pressure and comprising the 12 optical fibers as well as the electrical wires for the box heating. An optoelectronic rack includes all the driving electronics and the signal processing devices as well as the digital interface to the windtunnel data acquisition system.

This MAMS prototype has been carefully tested in laboratory using a model mover simulator, prior to being installed on one of the ETW model carts. This installation took place in March 1995 and the system performance have been investigated since then. Although some improvements are still required before the MAMS can be considered as fully operational at ETW, it is considered right now as being very promising. Figures 17 and 18 show several parts of the MAMS at ETW.

Figure 17 shows the insulated box including the optical head mounted on the ETW test section top wall structure. One can also see the custom airtight electro-optic connector that has been designed for the MAMS and its associated electro-optic cable. Figure 18 shows the mounting of the metal insert comprising the corner cube. The insert top surface is shaped according to the model fuselage shape.

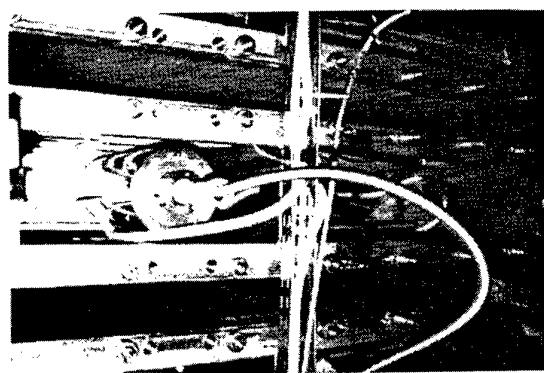


Fig.17 - Optical head in the ETW.

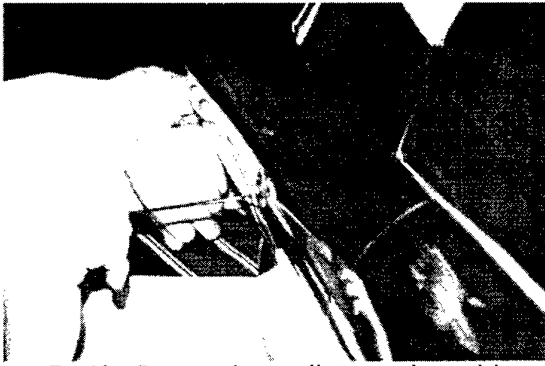


Fig.18 - Corner cube installation in the model.

#### 4.5 Measured performances

The performances that have been measured both in laboratory and in tunnel environment are the following one :

- Resolution : 0,001 degree
- Precision :  $\pm 0,005$  degree over the whole range.
- Range :  $\pm 10$  degrees
- Bandwidth : 200 Hz

The windtunnel tests are not yet 100% completed, but the MAMS has been already tested up to  $-120^{\circ}\text{C}$  and Mach 0,8. Up to these operating conditions the MAMS gave satisfaction.

The figure 19 describes the linearity that have been measured on the MAMS installed on the model cart. The chart corresponds to a  $\pm 9$  degrees sweep in both directions and at two different speeds (0,1 and 0,2 degree/second). It shows the angular difference between a reference inclinometer located inside the model and the MAMS.

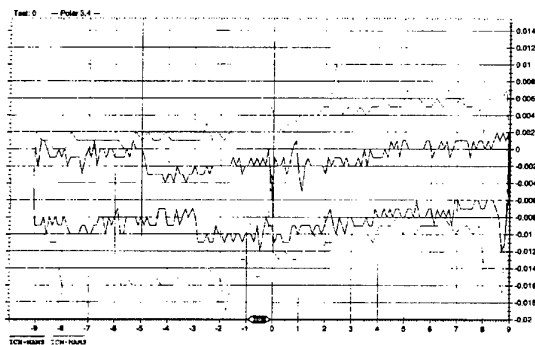


Fig.19 - Inclinometer - MAMS comparison at 0.1 and 0.2 %.

#### 5 -INSTRUMENTED MODEL FOR ETW

The European Wind Tunnel (ETW) operating domain demands specially designed and dimensioned models. Probative technological

development on this subject has been conducted cooperatively by ONERA's *Institut de Mécanique des Fluides de Lille* (I.M.F.L) and *Aérospatiale Toulouse* under the request of the french official services.

#### 5.1 Design constraints

Typically, five types of constraints have to be considered pertaining to:

- dimensioning
- surface finish
- thermal effects
- on-board instrumentation
- model configuration changes.

##### 5.1.1-Dimensioning:

The goal of attaining high Reynolds numbers in order to simulate real aircraft flight conditions for a given Mach number, considering the test section dimensions, demands the lowest possible stagnation temperatures and, simultaneously, the highest possible stagnation pressures. In the specific case of the ETW, this calls for temperatures around 110 K and pressures of up to 4.5 bar. Figure 20 graphs the domain envelope covered by the ETW at Mach 0.78.

It is understandable that under these conditions the models will be severely loaded and the sting lines under extreme stress, which will in certain cases require limiting the flight envelope simulated.

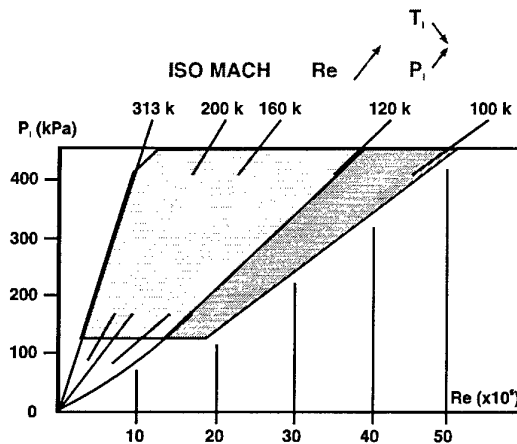


Fig.20 - ETW operational conditions.

Under these temperature conditions (110 K), only aluminum and titanium alloys, stainless

steels, steels with high nickel content, such as the Maraging or even better the Inconel varieties, will do. However, depending on the specified ultimate limits, it becomes necessary to make sure that the material used is not too brittle, which would lead to sudden failure. The ETW has set a lower practical limit of 30 joules (Kv on standard  $10 \times 10$  mm specimen) on material toughness.

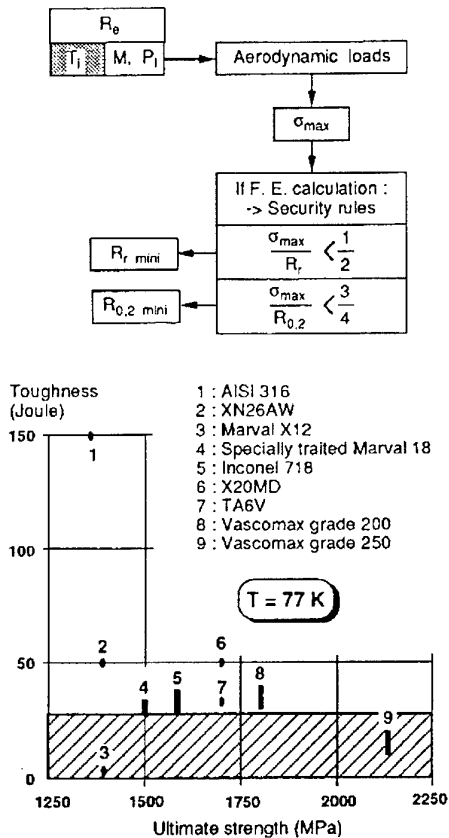


Fig.21 - Ultimate strength for steels.

Figure 21 shows the alloys commonly used for making cryogenic wind tunnel models. It can be seen that, beyond a failure strength of 1500 MPa, the alloys' toughness falls between 50 and 30 joules, and more often between 40 and 30 or even below. At this level, there is practically no plastic range left, and special care must be taken to avoid recesses and other regions of sudden stress variation at the level of the connections, where cracks can initiate and lead to brittle failure.

In practice, the model materials are usually limited to aluminum alloys, AISI 316 stainless steel, European Maraging steels

(Marval 18), specially treated at 1500 MPa, Vascomax grade 200, and titanium alloys.

In light of the level of structural stresses encountered, and the ductility of the materials used, the structures of the model and of the sting line must be dimensioned by a finite element computation.

As the "basic" form of the model must be determined with great precision (for a given flight point, its deformed shape must be the same as that of the aircraft), and as this definition can only be developed by finite-element computations, all that is needed in addition to determine the stresses is an additional mesh generation.

Considering the dynamic vibratory stress due to the bending of the sting line, the rules of thumb are then:

- $\sigma_{\max}/R_t < 0.5$
- $\sigma_{\max}/R_{0.2} < 0.75$

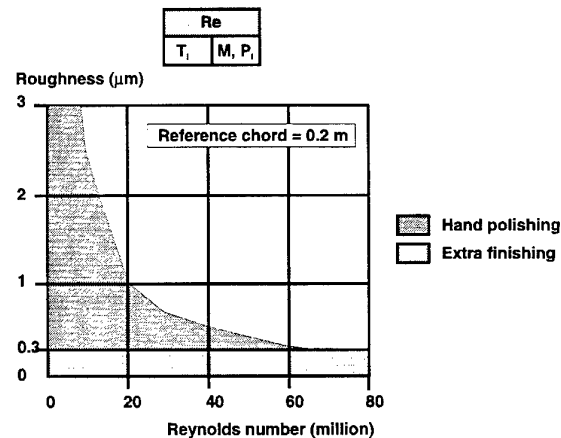


Fig.22 - Surface finish requirement with Reynolds number.

#### 5.1.2. -Surface finish:

To achieve the desired surface finish that will not disturb the boundary layer thickness, which depends on the Reynolds numbers, very high here, the surface must be very carefully manually "mirror"-finished. The typical mean roughness values are  $0.5 \mu\text{m}$ . This is still measurable by ordinary roughness meters. The variation of the surface condition

to be achieved as a function of the Reynolds number is graphed in figure 22. It is readily seen that the needed surface finish has to be fairly improved from that of the conventional models used in non-cryogenic wind tunnels where the Reynolds numbers are limited.

This required surface condition quality has other consequences too, mainly at the level of the connections between the various removable elements of the models, and the assembly techniques used. This practically precludes any apparent screw assemblies, for two reasons. First is the need to mask the screws with some filler product which, since it does not have the same thermal contraction coefficient as the substrate, will create a surface discontinuity dependent on the temperature descent. Secondly, there is the risk that a tool may slip during the assembly process, with the necessary repair that will result.

For the same reasons, surface grooving is also prohibited, unless the groove can be filled with a weld metal of the same type as the grooved metal.

#### 5.1.3. -Thermal stresses:

These stresses appear during the rapid temperature change of  $0.4^\circ/\text{mn}$  when the model is cooled to test section temperature. Computing them is a complex process, because the convection coefficients in the presence of the boundary layer have to be determined first.

Generally, thermal stresses have little effect on the mechanical strength of the model elements. But these absolutely cannot be overlooked and must be calculated in the fuselage-balance and balance-sting assembly regions, which is already very heavily loaded and where exist localized excess stresses due to form factors. Figure 23 gives an example of a full aerodynamic and thermal computation result for the wing of the A340 model used in the ETW.

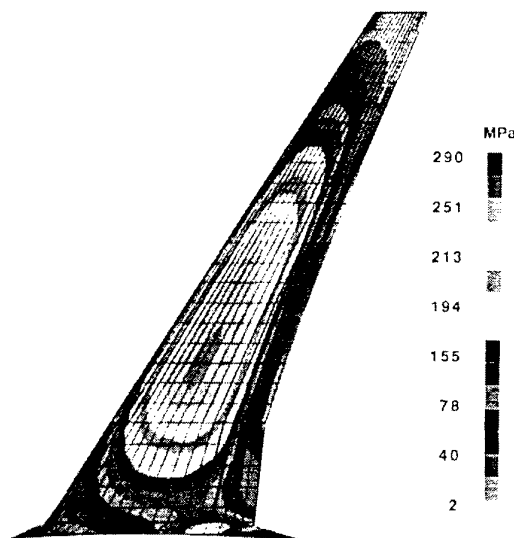


Fig.23 - Calculated wing aerodynamic and thermal strains in ETW.

#### 5.1.4. -On board instrumentation:

There are two classes of onboard instrumentation: those instruments mounted in a warm housing, and those that are not.

The "cold" instrumentation include the static pressure-taps and tubes, nonsteady pressure sensors, accelerometers, thermocouples, strain-gages, linear and angular position transducers, actuators, and the fiber optics for monitoring the geometric position of the model in the test section.

The "warm" instrumentation essentially include the pressure scanners and inclinometer.

The cold instrumentation must have the same precision and reliability characteristics as at room temperature.

The static pressure-taps and tubes pose no particular problem by themselves, except that it is practically impossible to use external grooving, with solid fillers, because the difference in contraction coefficients between the model steel and the various filler products produces a furrowed cold airfoil surface, out of tolerance. Two techniques are commonly used today to instrument the flight surfaces with pressure fittings. The first is to construct them as separate parts, permanently connected together by loss screws. The second is to design a multilayer structure

integrating the pressure transfer channeling. Let us describe this latter technique in greater detail.

Generally, for a channel of given section and length, the time response in the pressure measurement for a given pressure variation is directly proportional [8] to the dynamic viscosity of the fluid, which decreases with temperature (Sutherland formula). This time response will also decrease when lowering the temperature. Since the measurement channel scanning frequency is adjusted according to the response time observed in air at atmospheric temperature, the result will be largely conservative for cold nitrogen.

The nonsteady pressure instrumentation uses transducers specially developed by the makers Endevco® and Kulite® [9]. These transducers are quite comparable in size to those used at atmospheric temperatures, though they are assembled differently to account for the thermal stresses created during the cooling process, by the various components connecting them with the model [9].

#### 5.1.5. -Model configuration changes:

Constraints also occur when the model configuration has to be modified at cryogenic temperatures. If only for the simple question of the time it would take, it is impractical to reheat the model on its sting line, perform the required manipulation, and then return the model to cryogenic temperature and place it back in the test section.

To remedy this situation, the ETW offers users a cold room with breathable dry air down to  $-60^{\circ}\text{C}$ , with the model immersed in a flow of dry air at temperatures down to  $-150^{\circ}\text{C}$ , in an open box. Figure 24 gives a schematic of this model manipulation box. For these cold conditions, the technician wears an isothermal suit and gloves, which somewhat reduces his dexterity; so the removal/installation procedures and the manipulation time have to be reduced to the minimum in this "hostile" environment.

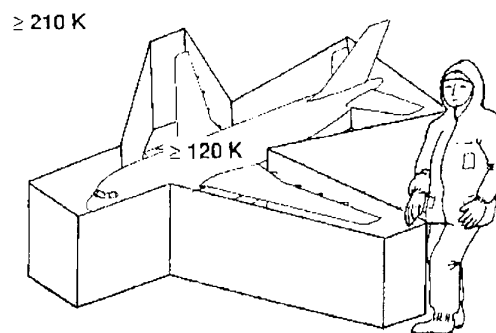


Fig.24 - Cold box for model configuration changes.

A special effort must thus be made in designing the assemblies, and in using motorized actuators whenever possible.

## 5.2 Specific technological developments.

The following is a description of five techniques used in the framework of the probative technological development of cryogenic models for the Airbus A340 in the ETW:

- cam assemblies
- horizontal stabilizer motorization
- joint seal techniques
- "multilayer" technology for flight surfaces densely instrumented with pressure -taps
- geometric checking techniques.

### 5.2.1- Cam assemblies:

These assemblies are designed with two principles in mind. The first is to provide deformation continuity (embedding), and the second is a rapid "quarter-turn" assembly and disassembly process using a wrench with guide nipple to keep the tool from slipping.

To meet these conditions, the assembly is pre-tensioned using the elastic caulking force between the contact faces of the attaching parts. As long as this caulking force exists, there can be no separation between the contact faces, which means there will be the desired deformation continuity between the attached parts.

The second principle, to provide "quarter-turn" assembly, is assured by introducing a



cam, which provides the desired prestressing and irreversibly locks the joint.

The pre-tensioning is easily provided using a spring structure (Figure 25) placed under tension by the elastic deformation created by the cam. This structure has to be computed by finite elements in order to determine the caulking force necessary for the joint continuity, and at the same time exhibit an internal stress distribution such that the spring will remain elastic.

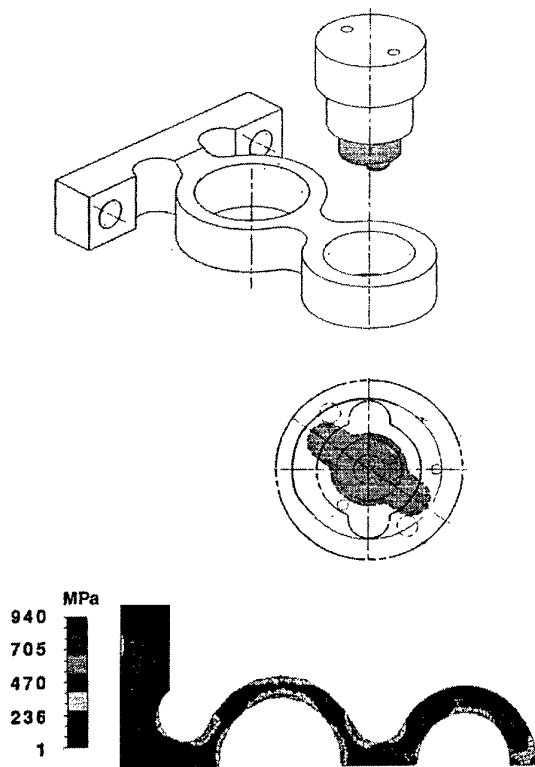


Fig.25 - Cocking cam assembly device for the rear part of the fuselage.

The cam force is such that the applied force passes through its maximum during the rotation, and is slightly reduced at the stop point. If this reduction is correctly estimated, the cam will remain locked in position even under the effect of the vibratory forces on the joint. Moreover, the stresses in the spring will always remain less than those initially introduced in the tightening, since the force applied between the joint faces cannot decrease.

The cam is also secured depthwise by elastic locking, and its installation is perfectly

repetitive, to allow a perfect fit at the skin surface.

The aft fuselage of the A340 "high speed" model was assembled according to this principle (Figure 26). The fuselage elements can be seen to offer excellent continuity, and the cams are perfectly discreet. Assembly/disassembly at the temperature of liquid nitrogen has been demonstrated and validated.

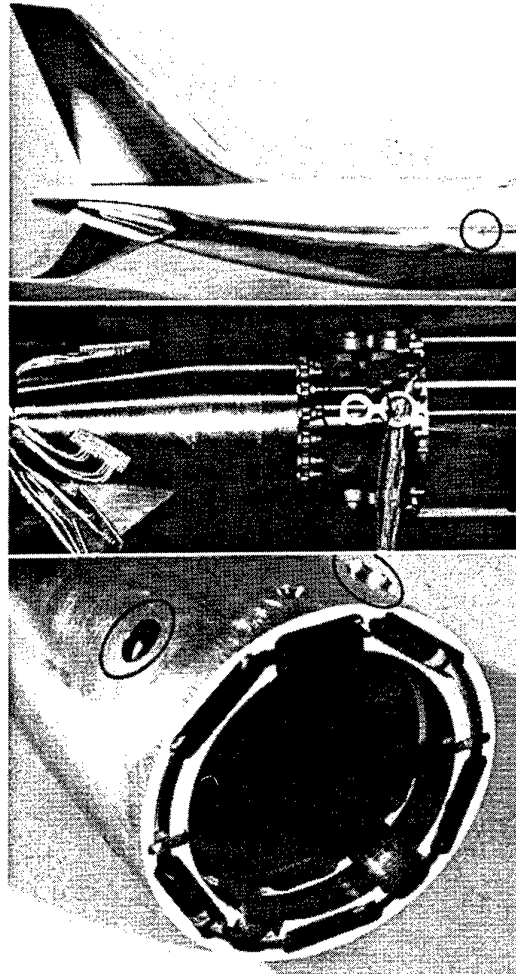


Fig.26 - Rear part assembly.

#### 5.2.2. -Horizontal stabilizer motorization:

To avoid having to set the horizontal stabilizers manually, a motor system was developed for cryogenic environment, using the following principles:

- drive by ball worm screw with an electric brake to prevent system backtracking under the loads applied;
- stepper motor drive;

- rotation shaft mounted on dry-lubricated bearings using a molybdenum bisulfate micro-particle spray and hot polymerization;
- use of standard commercial elements requiring as little possible adaptation for use in a cryogenic environment.

A stepper motor of the Sonceboz® make was chosen with a holding torque of about 1 m-N which, considering the downgear ratio chosen, is sufficient to prevent drive system backtracking.

The cryogenic adaptation needed is to take all the standard elements of this motor, thoroughly degrease them, and dry-lubricate some of them by molybdenum bisulfate polymerization. Once it is reassembled, the motor has to be free from any trace of moisture, grease, or oil, and has to be kept in a perfectly dry atmosphere.

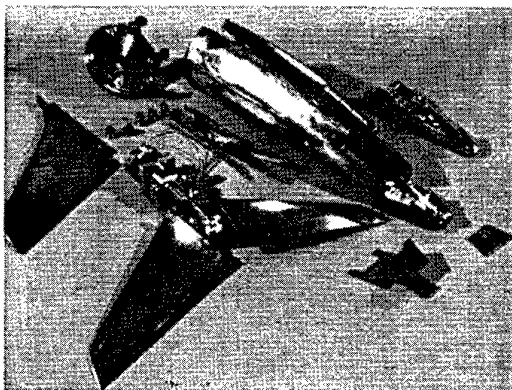


Fig.27 - Pieces for the rear part of the model.

The ball worm screw is of the Transroll® make, entirely of Maraging steel, perfectly degreased, and dry-lubricated.

The bearings consist of dry friction rings with functional elastic play.

Figure 27 shows all the parts used in the aft section drive for the "high-speed" A340 model for the ETW.

A great improvement can be seen (Figure 28) in motor characteristics, especially in the static torque at low temperature. The gain is about 25 % at the temperature of liquid nitrogen. Similarly, with the help of the functional play, the positional precision and repeatability increase with the temperature

decrease, reaching a  $0.01^\circ$  positional precision for the whole horizontal stabilizer block.

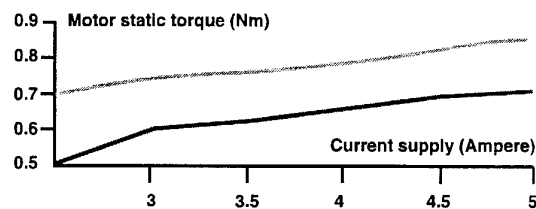
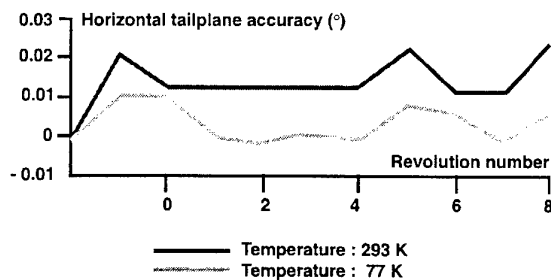


Fig.28 - Motorization for the horizontal stabilizer.

This drive system gives full satisfaction as long as there is no trace of moisture anywhere in the horizontal stabilizer drive mechanics. Machinists' habits of oiling rotating parts and leaving traces of cutting oil commonly found in threaded or drilled holes must be absolutely curtailed.

The molybdenum bisulfate treatment greatly improves the friction characteristics of the assemblies, but offers no guarantee against the risks of seizing in the presence of moisture.

#### 5.2.3. -Joint seals:

Various techniques can be used in a cryogenic medium:

- metal gaskets
- PTFE seals
- indium seals
- pressure drop devices.

#### - Metal Gaskets

Three gasket sections are available on the market: the "C", the "O", and the "V". The C and V type gaskets assure a seal under very high pressure differentials.

The C and O types can be obtained in Inconel, and in the shape desired. The V type gasket, as it requires a great deal of crushing, is commonly made of aluminum.

The C and O types require a surface condition of  $R_a = 0.4 \mu\text{m}$  in the groove seat.

#### - PTFE Seals

Generally, the polytetrafluorethylene matrix is not used in its pure state, because its mechanical characteristics are poor. It can, however, be used at temperatures as low as 3 K.

This matrix is commonly charged with graphite, carbon, or bronze, to achieve the required mechanical and/or thermal characteristics. Their use is then often limited to 120 K. PTFE charged with 60 % bronze has good wear resistance and compressive strength, as well as good thermal conductivity. It makes a good seal.

For all these seals, the surface conditions in the groove seat should be  $R_a = 0.2 \mu\text{m}$  to get a good seal, which is a major drawback to their use.

#### - Indium Seals

These are in common use in cryogenics because they offer excellent seal for low pressure differentials at all temperatures, and require no specific groove seat conditions.

Little closure force is needed to crush the indium seal, even when assembling at low temperatures because the indium remains soft and ductile.

On the other hand, these seals can be used only once, the material is expensive (over 20,000 FF -4000 US \$- per kilogram), and they require compensation for differential contraction. Figure 29 shows how one of these seals is used in a pneumatic link for pressure tubes.

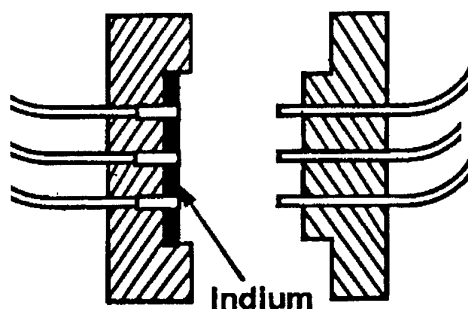


Fig. 29 - Indium seal for pressure tapes connexion.

Due to the toxicity of indium, certain precautions are mandatory in using them:

- Never leave any traces of indium on the hands
- Avoid any contact with a wound or with the eyes (wear glasses)
- Never swallow it. If you do, contact an anti-poson center quickly.
- Protect against vapors, if indium is used as a brazing product (another common use for this metal).
- In case of fire, use powder or  $\text{CO}_2$  extinguishers.

#### - Pressure drop devices

These "seals" are used to reduce the transfers between the inside and outside of the models, at the sting passage. As no more friction can be created in this region, brush bars were used (Figure 30), which press up against the bending sting. This minimizes the contact force to a few Newtons (4 N at the temperature of liquid nitrogen).

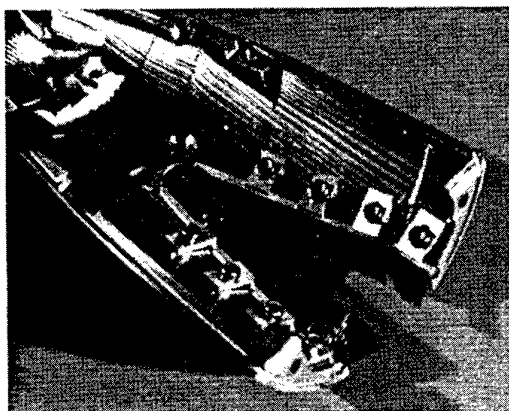


Fig. 30 - Brush seal around the sting penetration.

Only nylon fiber brushes will do.

The leak flow in the A340 Z-sting penetration region was less than a liter per second at atmospheric temperature and fell to 0.3 l/s at 100 K.

#### 5.2.4. -Multi-layer structural concept for model highly instrumented in pressure-taps

Many years ago, it was thought (NASA, Dr Wigley) that this technique would solve the

problem of constructing small scale airfoils for cryogenics, with a very large number of static pressure taps, while maintaining a very pure monoblock structure and very high airfoil precision. As it was practically impossible to build a hollow structure with adequate stiffness and mechanical strength, it was proposed to build the model in multiple layers of metal, printed-circuit fashion. The usually 2D airfoil structure would then consist of an assembly of plates, brazed or diffusion-welded together.

This idea was unshelved for use in the wing of the ETW A340 model, because major advances have been made in titanium alloy diffusion-welding techniques over recent years, and the industrial means now used, with large presses operating at high temperature and pressure under inert gas (Figure 31), are making it possible to handle structures of the size of ETW models. Moreover, assemblies made this way have practically the same mechanical characteristics as the base alloy, especially as concerns their shear strength and fatigue properties.

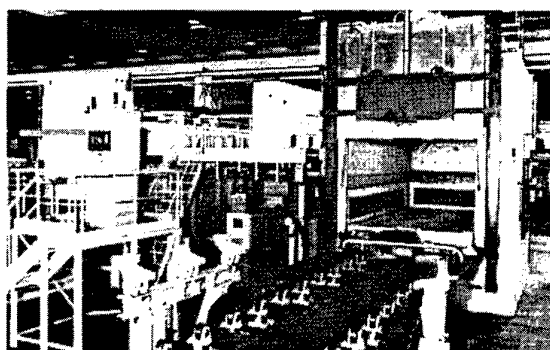


*Fig.31 - Press machine for multilayer structures.*

The wings are thus designed as a stack of TA6V plates of constant thickness. Each plate has its own network of numerically milled pressure channels. The routing is designed using software adapted from electronic multi-layer circuit routing programs. Figure 32 gives an example of this routing. Through-holes are provided to communicate between plates at points where other channels have to be picked up.

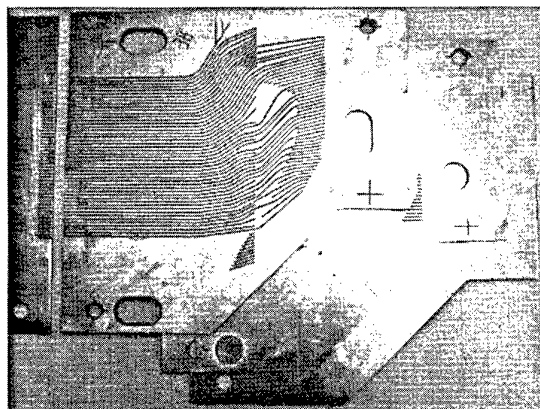


*Fig.32 - Pressure channels in a multilayer structure.*

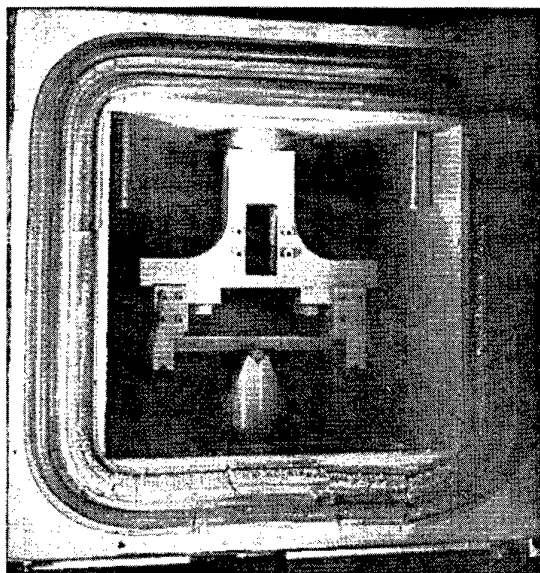


*Fig.33 - Beam fatigue test by 3 points bending method in cryogenic chamber.*

This assembly was tested for fatigue and three-point bending at atmospheric temperature and at 120 K (Figure 33). Behavior is correct, though there is a tendency to crack along the channel edges (Figure 34), without leading to ruin or to intercommunication between channels, even those 0.7 mm apart. This has to be watched, though, and may mean either limiting the model life to a few hundred hours, or monitoring the fatigue cycles actually borne by the structure. At the exit from the wing, the channels are connected with the pressure tubes leading to the pressure scanner by glued steel end fittings (Figure 35).

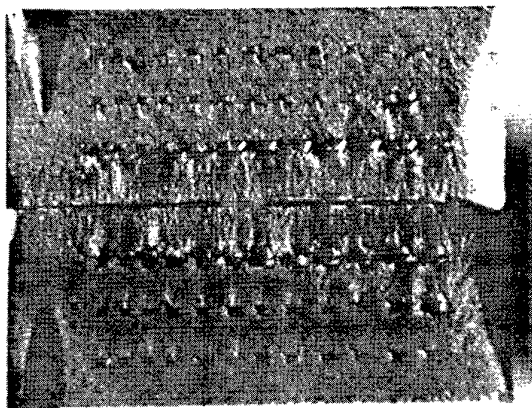


Fig.34 - Fracture topography on 4 layers TAGV beam.

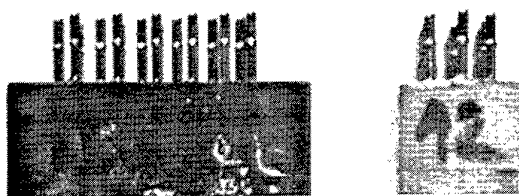


Fig.35 - Steel connecting ends stuck on 4 layers TAGV beam.

#### 5.2.5. - Geometric checking techniques

Two monitoring techniques have been tested on a structure held at a temperature close to that of liquid nitrogen:

- a double-sighting optical method;
- the usual technique using a ceramic feeler.

In a laboratory or shop environment at atmospheric temperature, it is important not to expose personnel to risks pertaining to temperatures close to that of liquid nitrogen. A double-wall open-air box was therefore constructed with its outer wall higher than the inner, so that the gaseous nitrogen would overflow from the inner box to the outer one and then be evacuated by a carefully adjusted vacuum. This way, the air-nitrogen interface is perfectly clear to see (Figure36), and the nitrogen level in the box is regulated so that only the measurement areas are visible. The rest of the protection device consists of a set of stationary and portable oxygen level detection instruments.

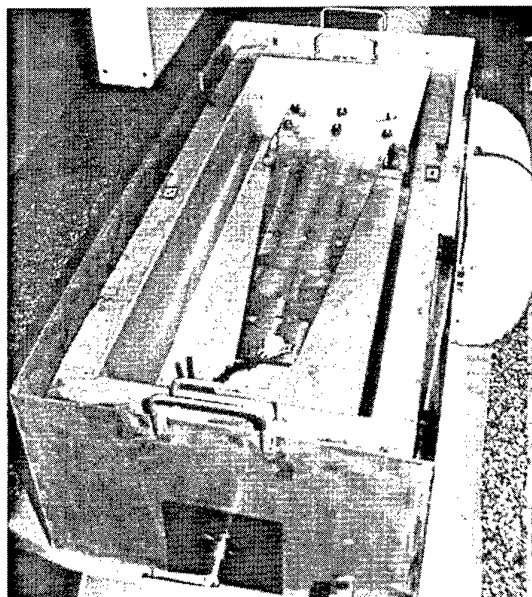


Fig.36 - Double wall container for geometrical checks under cryogenic conditions.

#### - Double-Sighting Optical Method

The optical device (Figure37) consists of two theodolites aimed simultaneously at the point to be measured. The surface is reconstructed in model-referenced coordinates and compared with a reference plane by a small work station. The measurement accuracy depends on the reference plane definition, which must be rectified by machining, and on a numerical definition using eight measurement points.

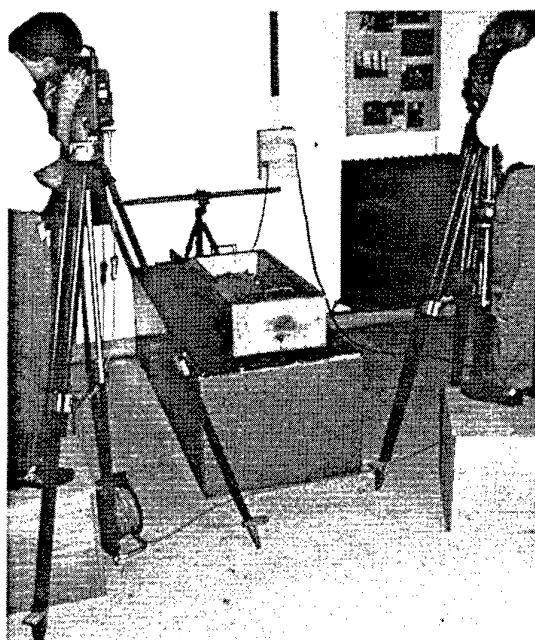


Fig.37 - Optical geometric inspection.

If the model is kept cold, and sightings are made at angles greater than  $30^\circ$ , in order to minimize the errors introduced by the variation of refractive index between air at atmospheric temperature and the gaseous nitrogen at about 85 K, the uncertainty is less than 4/100 mm.

This method is simple, reliable, and contactless; but there are difficulties using it for measuring parts with sharply varying shapes and "shadow" regions. It is suitable for measuring overall model displacements.

#### *- Ordinary Ceramic Feeler*

This method uses all the usual measuring machine apparatus, with the metal feelers replaced by feelers in very rigid ceramic with a very low contraction coefficient and very low heat conductivity (Figure 38). These feelers, however, have to be long enough (about 100 mm) to be able to keep the noble parts of the measuring machine out of the cold. The precision is practically that of the measuring machine, with a correction due to the rod contraction and its "flexibility" under the bumping forces.

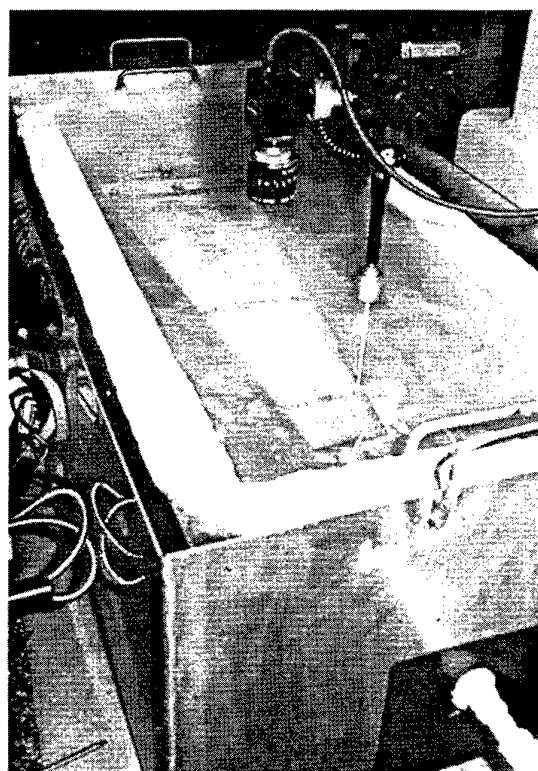


Fig.38 - 2D geometric inspection machine.

This method is to be reserved for checking the airfoils, and can also be applied for measuring the overall deformations.

#### 5.3. Conclusion.

The model for the ETW cryogenic wind tunnel has left the prototype stage and entered that of the commonly used tool, just like models for conventional wind tunnels.

Construction techniques now exist and are transposable, which make the design process easier.

Technological developments are and will continue to be necessary, especially in the immediate future, as concerns motorized drive techniques and the construction of turbine power simulators, as the industry's requirements evolve.

The job from now on is essentially to reduce costs and time requirements, which will involve systematic reviews of model design and construction methods, while staying within the same quality constraints. This work will be done in parallel with that being done to reduce conventional model design and construction times.

In terms of cost, the cryogenic model is currently quite more expensive — by a factor of about 1.25 — than a conventional model of the same size, designed for a wind tunnel operating at the same supply pressure. While the objective is of course to reduce this over-cost, it should be kept in mind that the stresses on the materials, the onboard instrumentation, and the surface condition requirements, make any large reduction unlikely.

The road leading to industrial tests in the ETW has been long but especially interesting. All those who contributed to this end were driven by the challenge.

## 6 REFERENCES

[1] Balance and sting design for cryogenic wind tunnels

M. Bazin et M. Dubois

Symposium on cryogenic wind tunnels  
Southampton 3-5 april 1979

ONERA TP. 1979-40

[2] Construction differences, mechanical interactions, thermal effects and their compensation on load cells and force measuring transducers

M. Dubois

IMEKO 1980

[3] Six component strain gage balances for large wind tunnels

M. Dubois

Experimental mechanics n°11 1981

[4] Sting line feasibility study for force measurements in the european wind tunnel

M. Bazin

Amsterdam 15 september 1982

ONERA TP 1982- 80

[5] Instrumentation for cryogenic wind tunnel

M. Bazin

VKI special course 22-26 april 1985

ONERA TP 1985-29

[6] Instrumentation for cryogenic wind tunnel

M. Bazin

VKI special course 5-9 june 1989

ONERA TP 1989-81

[7] Model attitude measurement system

G. Rivet, M. Lequire BERTIN

2<sup>nd</sup> cryogenic technology review meeting

ETW Köln 28-30 june 1988

[8] *Techniques de l'ingénieur* collection,

article R2111-6.

[9] "Half Transport Aircraft Cryogenic Model for T2 Wind Tunnel", Second Cryogenic Technology Review Meeting, Cologne/Porz, 28-30 June 1988.

# FORCE TESTING WITH INTERNAL STRAIN GAGE BALANCES

**DR.-ING. KLAUS HUFNAGEL**  
**PROF. DIPL.-ING. BERND EWALD**

**TECHNICAL UNIVERSITY OF DARMSTADT, WINDKANAL**  
**FLUGHAFENSTR. 19**  
**64347 GRIESHEIM, GERMANY**

## Summary

The ever rising accuracy requirements in wind tunnel testing for airplane development enforce continuous improvement of force testing technology. The introduction of the cryogenic tunnel is an additional challenge for the force balance, since now the balance accuracy is requested over an operational temperature range of 200 Kelvin.

More than 15 years ago several teams in the world therefore started with investigations in the area of internal balances for cryogenic wind tunnels.

In Germany in 1979 the "Cryogenic Balance Program" was started by the German Ministry for Research and Technology with the target to develop internal balances and calibration technique for the planned cryogenic wind tunnels KKK and ETW.

In the past 17 years of research all aspects of force testing technology have been dealt with and developed to new standards by the Technical University of Darmstadt together with Deutsche Aerospace Airbus GmbH, Bremen.

Within this period 8 balances for cryogenic wind tunnels were built.

Basic research on the aspects of metallic spring materials resulted in new understandings about material selection and material treatment for optimum results.

Principle balance design optimizations are done with finite element analysis. For the routine balance design an interactive computer program was created.

The very successful technique of the Electron Beam Welded Balance was developed. The balance structure is fabricated from parts, which are welded together by electron beam welding. This technique makes it possible to build balances with a complex inner structure to minimize the interferences.

For cryogenic balances the main problems are zero shift and sensitivity shift over the large temperature range and false signals especially in the axial force element due to temperature gradients. The problems were overcome by a very careful strain gage matching process, by use of special gages, by application of numerical corrections and

by a special design of the axial force system with tandem measuring elements in the flexure groups.

For the calibration of the balance a new third order numerical algorithm was developed. The algorithm works with arbitrary load combinations. This was a requirement for the development of a fully automatic balance calibration machine. The machine (the first specimen is already operational at the ETW) performs a six component calibration including all single loads and all combinations of two loads in one working shift. This machine was built in co-operation between Carl Schenck AG, Darmstadt, Deutsche Aerospace Airbus GmbH, Bremen and the Technical University of Darmstadt (TUD)

After the completion of the ETW machine further research was done by TUD to improve the design and the concept for a fully automatic calibration machine. The result of this research is a new design of a small calibration machine for TUD which will be built in the near future.

So all components of the wind tunnel force testing technology have been developed to new standards with the result of considerable accuracy improvements of the wind tunnel results.

## 1. Introduction

The successful design and development of commercial transport aircraft depends (among many other problems!) on excellent aerodynamics. Especially the flight performance reacts very sensitively to aerodynamics. Since flight performance must be guaranteed to the customer long before the first flight of the prototype, the success of the aircraft depends heavily on wind tunnel tests with the utmost accuracy. This ever rising requirement for accuracy in wind tunnel testing and especially the challenge of precise force testing in cryogenic wind tunnels gave a strong impetus for strain gage balance research in the recent past. Since accuracy limits for conventional strain gage balances are set mainly by thermal effects, the target to achieve at least the same or possibly even better accuracy with cryogenic balances in cryogenic tunnels is an extremely difficult



task. For the research work on cryogenic balances a target of one drag count repeatability for transonic transport performance testing was set.

To achieve considerable improvements compared to balances known and used today, a single clever idea respectively a single successful detail improvement is not sufficient. A systematic search through all parts and aspects of balance technology and the improvement of all details of it to the limits of the available technology is necessary. The important parts of this technology are :

- Design philosophy
- Design computation and optimization
- Selection of spring material for the balance body material
- heat treatment
- Balance fabrication methods
- Strain gage selection and wiring method
- Moisture proofing respectively cryogenic environment proofing
- Data acquisition electronics
- Mathematical calibration algorithm
- Calibration equipment
- Strategy of balance use in the wind tunnel

Beside these scientific and engineering aspects some human factors are also very important to get optimum quality:

- Well trained team in mechanical and electrical manufacture
- Intensive communication between wind tunnel operators and balance designers

Seventeen years ago we convinced the German Ministry for Research and Technology, that the force measurement technology is perhaps the most important key technology for the success of the new European Transonic Wind Tunnel (ETW) which was in the early design phase at that time and the Cryogenic Wind tunnel in Cologne (KKK), which was under construction. We were happy to get a long term funding for the development of the Cryogenic Balance. This put us in a position to do concentrated balance research and development in this field. The aim of this research at the Technical University of Darmstadt was to improve each of these partial aspects of balance technology to the scientific limits available today. Due to this research in cryogenic balances many improvements for balances for conventional wind tunnels resulted also. Part of the work was done in close co-operation with the Deutsche Aerospace Airbus GmbH at Bremen with some contributions of the DLR and most of the work was funded by the German Ministry for Research and Technology.

In the USA the TCT was in operation and the NTF was under construction at the same time our program started.

This was the reason for NASA to build a large number of balances (about 12) for the NTF which became operational in 1982. The most experienced team in building internal balances at that time was the team around Alice T. (Judy) Ferris and Tom Moore at Langley. They tried to solve the problems caused by the large temperature range by building balances in a conventional design, special strain gages and the so called "Temporary Gage Matching Technique".

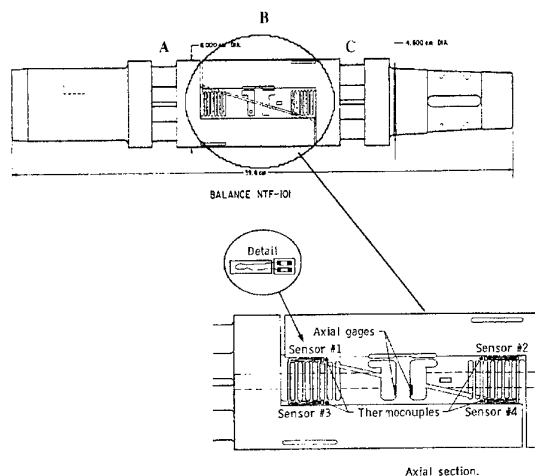


**Fig. 1** Sideview of NTF-Balance 101 B

The gages were especially built by Micro-Measurements (MM). The grid alloy Karma was treated in a way, that the gage factor drift due to temperature is matched to Young's Modulus drift of the spring material (EMC Gages). Additionally the gages should have a very good match in apparent strain to the thermal elongation properties of the spring material, so that the zero drift of the bridges is very low (STC). Usually gage manufacturers only offer gages with one of these properties matched to the spring material (either thermal compensation STC or sensitivity compensation EMC). The whole procedure was very time consuming and expensive and the match in zero drift was not good enough for the balances. Especially at very low temperatures the zero drift of the bridges was in the range of several percent.

To overcome this problem NASA developed the "Temporary Gage Matching Technique". The individual zero drift of each gage is measured on the desired balance material. After the test the strain gages are debonded from the test disk. Gages with nearly the same drift are matched in pairs which could be bonded on the balance. This procedure leads to reasonable good results. The zero drift was now under 1% F.S..

Temperature tests with the balances showed that beside the problem of zero- and sensitivity drift of the bridges there could be large false signals induced by temperature

gradients. This signals depend on the test scenario in the tunnel and the geometry of the model. This problem therefore could not be solved by compensating measures within the strain gage bridges. NASA tried to solve this problem by calibrating the balance under the influence of temperature gradients.

In Europe several other teams started with research on the problems of cryogenic balances.

At the NLR in the Netherlands a small balance of conventional design was built to investigate the problems (Fig. 2). This balance was tested in RAE Test Duct and the TCT at Langley. The major problem with this balance was also the error due to temperature gradients. After the tests with the NLR 771 balance the research at NLR was stopped in the mid eighties.

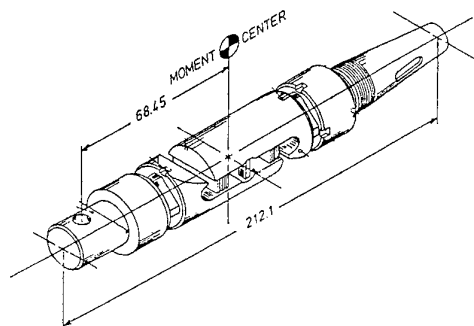


Fig. 2 NLR-Balance 771

At ARA in the United Kingdom a kind of an axial force element with three springs as shown in Fig. 3 was built after the tests with NLR 771 to investigate the effect of temperature gradients on the axial force signal. The result of these tests showed, that the temperature induced signals of the three spring elements are caused by inner distortion of the element. They showed also very clearly that a asymmetrical distribution of stiffness in the balance will lead to an asymmetrical distribution of signals. It could also be shown that the error signal depends very much on the kind of sleeve over the balance representing the model. This means that the temperature gradient induced signal depends on the model material and geometry.

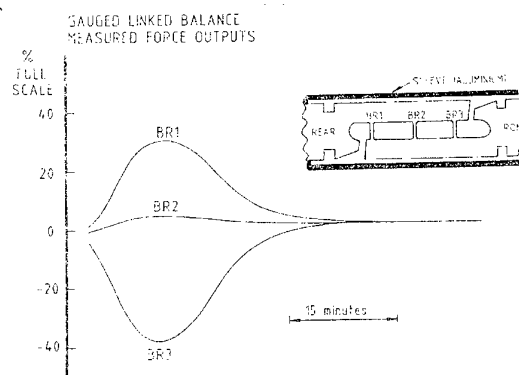


Fig. 3 Signals of RAE -Test Balance due to Temperature Gradients

Most basic research for internal balances in the time between 1963 and 1982 has been done in Europe by ONERA in France. On the field of cryogenic research first the mechanical properties of the possible balance materials were tested. After that strain gages and material combinations were tested to get the best match for a minimum zero drift and sensitivity shift. Several hardware compensation methods for zero drift and sensitivity shift were developed. To solve the temperature gradient problem an additional gaging of the spring in the front and aft parallelogram system as shown in Fig. 4 was proposed.

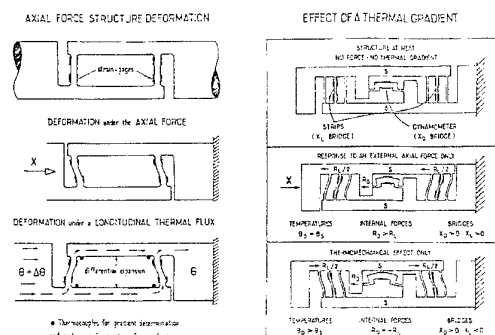


Fig. 4 Compensation of Temperature Gradient Effect

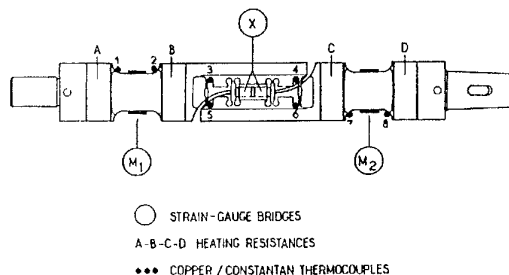


Fig. 5 Three Component Cryogenic Balance of ONERA

After these activities in the United States and Europe, the problems balance designers and engineers were faced with were located as:

- Compensation of zero drift to values below 0.1 %
- Compensation of sensitivity shift
- Elimination of the influence of temperature gradients to axial force

## 2. Balance Development at Technical University Darmstadt

Relative to the other groups the team at Technical University of Darmstadt was inexperienced. That's why the project was launched together with Deutsche Aerospace, Airbus GmbH, Bremen. The people in Bremen built a conventional balance which was gaged with cryogenic proved materials (see Fig. 6).

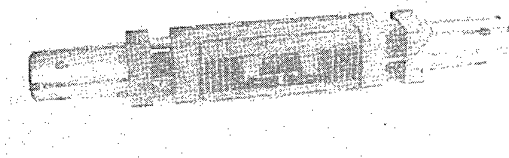


**Fig. 6** Cryogenic Balance W606 of VFW (now Deutsche Airbus Bremen) finished in 1982

The results of the tests with this balance were identical to all the experience of the other groups. Specially the large effect of temperature gradients (see Fig. 7) seemed to be one of the major problems in building a cryogenic balance with the same accuracy as a conventional one.

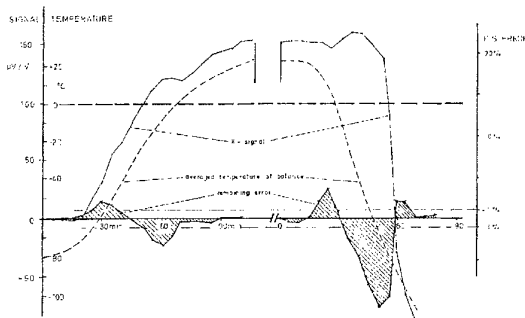


**Fig. 7** Behavior of Axial Force of Balance W606.

After the end of this first research program on cryogenic balances sponsored by German Ministry of Research, Prof. Ewald went to Darmstadt and the program was continued there.

All the six component cryo balances which are described now are designed and manufactured by the University of Darmstadt and Deutsche Airbus. For a complete overview and for the load ranges see the Table in the annex.

The first step in the now beginning evolution in balance design was the so called "Double Bending Beam Axial Force Element". The idea was, to build a balance which is symmetrical to the vertical center line of the balance and so the mechanical effect of the temperature gradient along the balance will result in a symmetrical deformation of the balance (see Fig. 8).

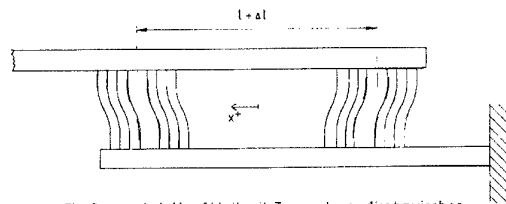


**Fig. 3** Axialkraftteil mit Temperaturgradient zwischen modellfestem - und erdfestem Teil.

**Fig. 8** Deformation of Axial Force Element due to Temperature gradient.

The complete balance and a detail of the axial force element is shown in the next two pictures. This balance is used for many tests in the KKK and for some tests with the TST-Model in the ETW.

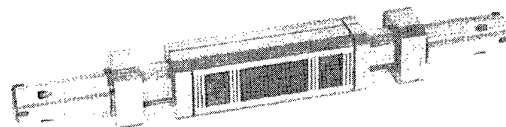


**Fig. 9** Balance W609. First Balance for KKK

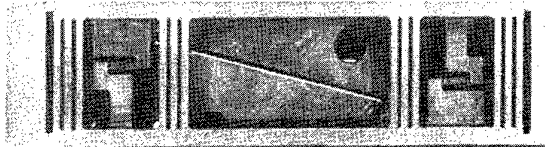


**Fig. 10** Axial Force Element of W609 with double Bending Beam

Both KKK and TUD learned a lot about cryogenic

balances during the tests with this balance and a lot of compensation had to be done after the initial delivery to the KKK.

The comparison of two measured polars in the KKK and the DNW with a model of a transport aircraft is shown in Fig. 11. The differences at high lift condition are caused by Reynolds Number Effects not by the balance.

Wind tunnel measurements are always affected by several sources of errors. To give an imagination of the quality of the balance, Fig. 12 shows the differences of two polars measured under identical conditions to a reference measurement.

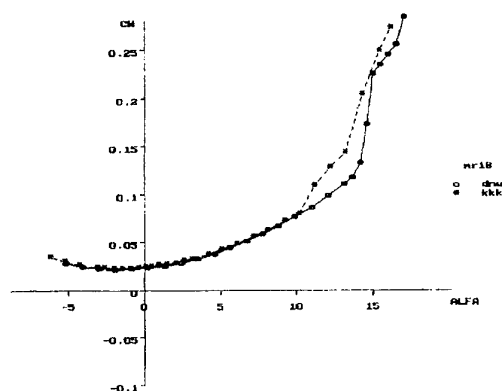


Fig. 11 Comparison of Polars measured in the KKK and the DNW

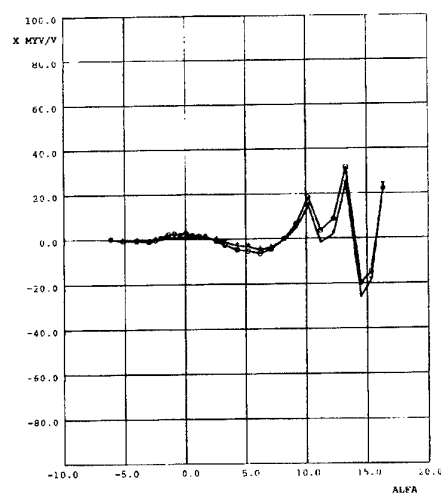


Fig. 12 Repeatability of Balance W609

The little differences between the two plots show, that the repeatability of the balance is good. The differences

at high angle of attack indicate either errors of the balance at high lift, or errors at high lift in the reference measurement.

The intention to compensate the temperature gradient effect with the double bending beam for axial force measuring worked. But, as always, after one gets rid of one problem another one occurred.

The eccentric location of the bending beams causes a high interference of axial force signal due to the pitching moment. This effect is shown in Fig. 13. If the sensitivity of the two axial force beams is identical, the signal due to the pitching moment in axial force will be of a high level but they will have opposite sign. So pitching moment has the same effect on axial force as a temperature gradient has.

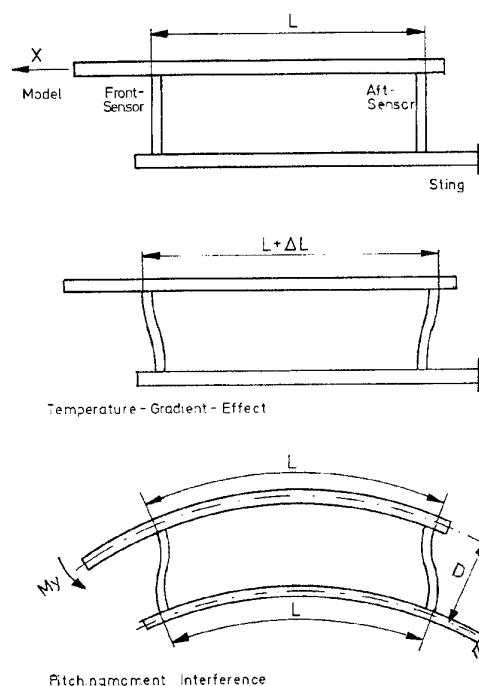
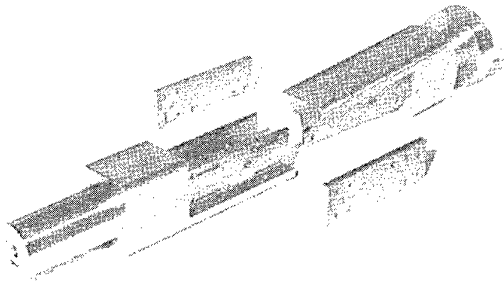


Fig. 13 Pitching Moment Interference on Axial Force

The next step in balance design must be a reduction of the pitching moment interference. We analyzed, that the effect is proportional to the distance ( $D$  in Fig. 13) of the bending lines of the two main beams. The reduction of this distance will reduce the interference significantly. The consequence for the design of the main beam was the interconnected geometry of the main beams of balance W612 (Fig. 14)

With this design the interference could be reduced as expected.



**Fig. 14** Parts of Balance W612 with new Design

The finished balance W612 is shown in the next figure.

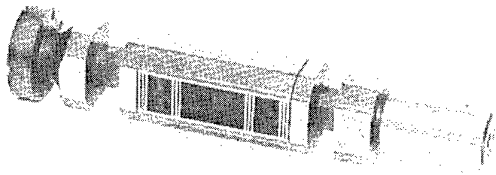


**Fig. 15** Balance W612 for KKK

The axial force measurement beams are identical to that of balance W609 (Fig. 16).

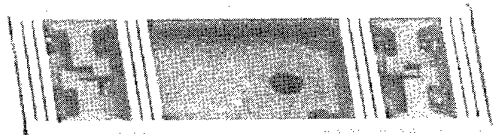


**Fig. 16** Axial Force Element of Balance W612

The complex geometry of these beams has been chosen to minimize the influence of lift on axial force measurement. It was very difficult and time consuming to produce the shape of these beams and to manufacture four beams with identical geometry for equal sensitivity. That was the first reason to change to a more simple shape of the axial force beam. The first balance with which we realized this, was the balance W614 (Fig. 17, Fig. 18).

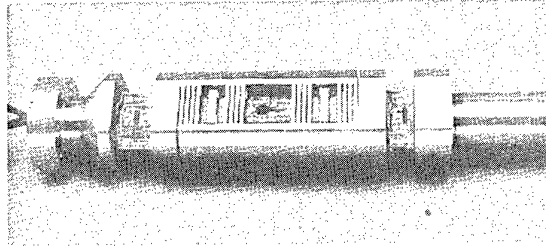


**Fig. 17** Balance W614 for KKK

The axial force beams in this balance were rectangular bars. The second advantage of this design was the good heat transfer from top to bottom. The temperature difference between the gaging areas is lower than in the decoupled version of the entire balances.

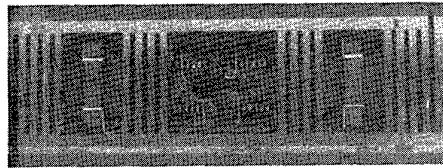


**Fig. 18** New Axial Force Beam Design in Balance W614

The measured effects of this design on temperature and interference were as expected and there was no significant increase in interference of lift on the axial force measurement. But the differences in sensitivity of the axial force beams remained significant.

The reason for this behavior was found in the inaccuracy of the positions of the strain gages. Gaging could not be done with the same precision as the mechanical manufacture.

To overcome this problem the shape of the axial force beam had to be designed in a way, that position errors do not influence the sensitivity of the measurements.

To solve this problem the axial force beams are designed as constant stress beams. This design leads to a constant stress distribution in an area of about 12x10 mm (proved by FE-Calculation). If the strain gages are applied in that area, little position errors do not have any effect on sensitivity. Constant stress beams for axial force measuring were used in the two following balances W617 and W618 (Fig. 20, Fig. 22)

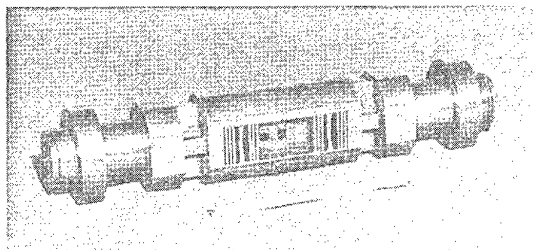


**Fig. 19** Copper-Beryllium-Balance W 617 for ETW ready for gaging



**Fig. 20** Constant Stress Beams for Axial Force Measurement in Balance W617

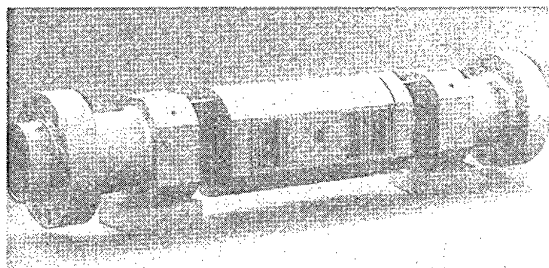


**Fig. 21** ETW-Balance W 618 ready for gaging



**Fig. 22** Constant Stress Axial Force Beam in Balance W618

With this kind of axial force element the compensation of the mechanical effect of temperature gradients was so excellent, that no further hardware or software compensation was necessary.

All the above mentioned balances are not very high loaded and the overall dimensions allow to design a parallelogram-system with one axial force measuring beam in each of the spring packages.

The last balance (W621 see Fig. 23) we designed and built was a very high loaded balance with relatively small dimensions. To keep the overall stress level low and to get a high stiffness, no double bending beam element could be used in this balance. It was the first one we had to redesign after the Finite Element Calculation. The

high loads distort the balance body in a complicated three dimensional way, so that the deformations of the balance body do have a feedback on the stresses in measuring sections. The result of this effect are higher stresses in the areas where they are not expected and higher interferences on axial force.

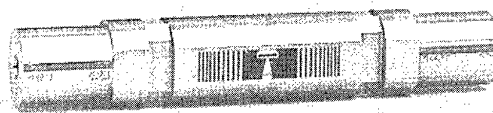


**Fig. 23** ETW Combat Balance W 621

### 3. Balance Design Philosophy

For a successful balance design some essentials must be fulfilled :

1. *Choose the balance ranges as close as possible to the actual measuring task. In defining the ranges include the consideration, that ranges of the balances can be overloaded, if other ranges are not fully used in the tests. This overload capacity of a balance normally is defined by the 'load rhombus'.*
2. *Choose the geometric dimensions of the balance as large as allowed by the available space in the model*
3. *Design the balance structure for maximum stiffness.*

The first point requires the design of dedicated and tailored balances for the different tasks of a wind tunnel. As an example for the same transport configuration model in a transonic wind tunnel at least three different balances are required for high accuracy testing :

- Very sensitive balance for cruise condition L/D optimization work.
- Less sensitive balance for cruise condition work including buffet tests, maximum lift tests and  $M_{DIVE}$  tests.
- Envelope balance for stability and control tests including full control surface deflections and large angles of attack and yaw.

This requirement results in an expensive and numerous balance equipment of a tunnel but improves tunnel accuracy very much.

The maximum load capacity of a balance design within a fixed diameter is limited even if an ultra high tensile strength steel (High Grade Maraging Steel) is used. In

our balance design method we introduced a balance load capacity parameter  $S$ , which is defined as

$$S = \frac{Z \cdot l^* + M_f}{D^3} \quad [N / cm^2]$$

The characteristic length  $l^*$  of the balance is defined as the distance from the reference center to the end of the active part of the balance, see Fig. 24.

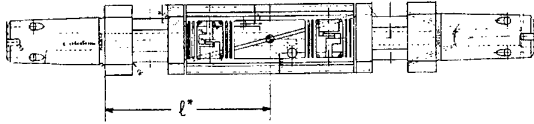


Fig. 24 Characteristic length  $l^*$

So this „Balance Capacity Parameter“ is a simplified measure of the bending stress in the balance body close to the balance connection to model or sting, which may be a cone or a flange. In most balance designs this is the critical position with respect to stress.

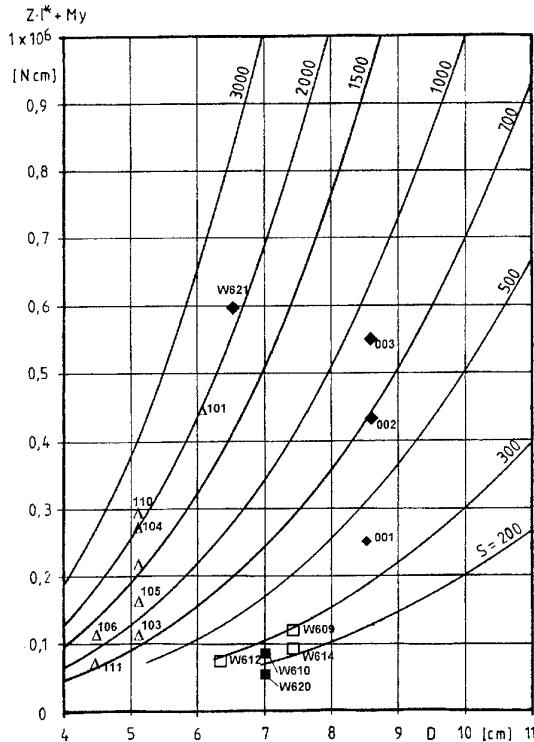


Fig. 25 Load Capacity Parameter  $S$

Fig. 25 shows a range of balances with diameters between 40 and 110 mm. A group of curves of constant load capacity parameter  $S$  is plotted in the diagram. The messages of this figure are :

- Beyond a value of  $S = 2000 \text{ N/cm}^2$  the design of a precise balance including an axial force system is not possible.
- For a transport performance high precision balance the load capacity parameter should not exceed  $S = 500 \text{ N/cm}^2$ .

Even lower load capacity parameters are recommended for optimum precision in drag measurement, if the space in the model allows for the larger diameter.

The third point mentioned above - high stiffness of the balance body - is difficult to achieve with the conventional balance fabrication process by EDM (Electric Discharge Machining). With this method all internal cuts in the balance body must be accessible for the electrode from the outer side of the balance body. This compromises the stiffness requirement. So the fulfillment of the stiffness requirement is mainly a question of the fabrication method.

The ultimate solution of this problem is the **Electron Beam Welded Balance** concept, which was developed by Prof. Ewald at VFW (now Deutsche Airbus) more than fifteen years ago. The balance is fabricated from four pieces, which are prefabricated to the final dimensions of all internal surfaces and welded together by electron beam welding. All external machining including opening of the flexure systems is done after welding. The production steps are clarified by Fig. 26, Fig. 27 and Fig. 28.

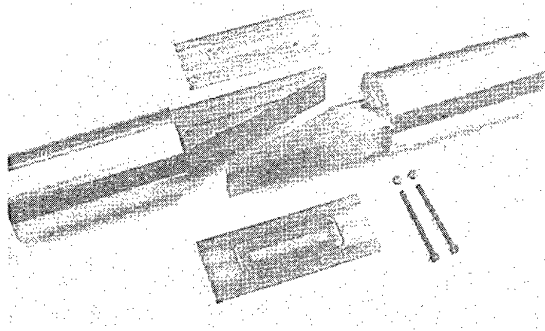
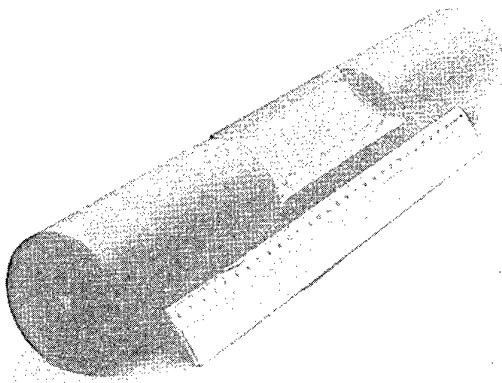


Fig. 26 Prepared Balance Parts



**Fig. 27.** Welded Balance Body



**Fig. 28.** Finished Balance Body

Provided that a proper material is selected and a sophisticated heat treatment after the welding process is done, full material strength is restored in the welding zone and the finished balance is a one piece balance and - with respect to strength and hysteresis - definitively behaves like a one piece balance.

The concept of the Electron Beam Welded Balance turned out to be highly successful and was used since the invention for all balances constructed by the Deutsche Airbus GmbH and by the Technical University of Darmstadt. This fabrication method gives complete freedom in the internal design of the balance structure and allows a much stiffer design of the balance.

#### 4. Balance Design Computation and Optimization

A strain gage balance is a complicated piece of structure with a very large number of dimensions. So the balance design can not be achieved as a closed solution from the external dimensions and the required component ranges.

At the Technical University of Darmstadt the design computation is done with an interactive computer program. With each step the program completely computes the stress situation at all critical positions of the balance body and some additional characteristic parameters. All results are printed. The user checks the results and according to his experience with the design

process he modifies one or several geometric dimensions. Each step is designated as a "RUN". An experienced balance designer needs about 40 to 60 runs for a final satisfying result or for the understanding, that a good balance with the specified ranges can not be designed in the given dimensions. This work can easily be done in some hours. The computation is based on basic stress and strain formula for short bending beams and short torsion beams. Provision is made in the program for notch stress concentration.

The computer program also gives overload diagrams similar to the conventional overload rhombus.

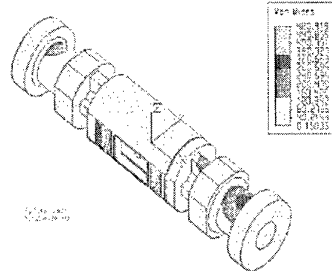


**Fig. 29.** Balance W617, FE Computation

The use of finite element analysis for routine balance design is not possible, since the discretization of the complicated structure with many modifications for the optimized design is too laborious. Nevertheless for principle optimization of strain gage balance designs finite element analysis proved to be an extremely valuable tool, this was demonstrated by the work of Junnai Zhai [22] at the Technical University of Darmstadt. Work on balance optimization with the instrument of finite element analysis is continued at the Technical University of Darmstadt. Fig. 29 shows the stress distribution of the balance W 617 under full combined loads computed by finite element analysis. In a balance optimization study based on this design a minimization of interference effects was achieved by a fully symmetrical design. The constituents of this new design are shown in Fig. 30. and Fig. 31 demonstrate the stress distribution under full combined loads. This study demonstrated, that the finite element analysis allows the valid computation of those balance interference effects, which are caused by the balance deformation under load.

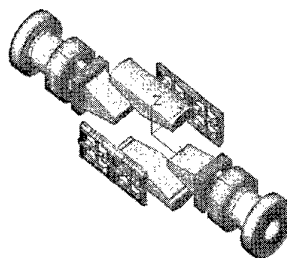


**Fig. 30.** Parts of New Balance Design



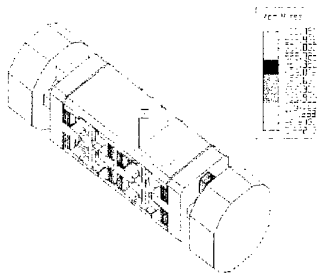


Fig. 31 New Balance FE Computation

## 5. Material Selection

The conventional material for strain gage balances is either maraging steel or precipitation hardening steel like PH 13.8 Mo (1.4534) or 17.4 PH (1.4548). For the welded balance concept we use Maraging 300 (1.6354) for conventional balances resp. Maraging 250 (1.6359) for cryogenic balances. Maraging steel is excellent for electron beam welding; the precipitation hardening steels should be good for welding as well, but no experience was gathered up to now.

A very comprehensive study on force sensor spring materials was performed at the Technical University of Darmstadt. One important result of this study was a general trend of increasing hysteresis with increasing nickel component in the alloy. So the hysteresis quality of the maraging steels is not the best one. The maraging steel hysteresis may be considerably reduced by three provisions:

- Multiple heat treatment for grain refinement as described in [17].
- Deep cooling (77 K, 20 hours) before the aging treatment.
- Underageing, if a lower ultimate strength can be tolerated.

Additionally at the Technical University of Darmstadt a successful method for numerical correction of hysteresis was developed. Nevertheless this method was not applied to strain gage balances up to now.

An excellent material for force sensors may be the titanium alloy Ti Al Mg 4 (3.7164). Hysteresis is almost non existing with this material. Nevertheless more experience especially in electron beam welding and in gage application must be gathered before application of titanium for strain gage balances.

A very promising material for conventional and cryogenic balances is Copper Beryllium (2 % Beryllium), if the load capacity factor allows for the lower tensile

strength of this material compared to maraging steel. Hysteresis is extremely low and electron beam weldability is good. The excellent heat conductivity of copper beryllium will considerably reduce the temperature gradient problems with cryogenic balances. A cryogenic balance for the ETW from copper beryllium was designed and constructed at the Technical University of Darmstadt (see Fig. 19).

The low corrosion resistance of maraging steel is troublesome for balances especially in the case of cryogenic balances. Nickel plating proved to be an efficient counter-measure. In this case the strain gage positions are covered with a protecting coating before the nickel plating process. So the gages are bonded on the uncovered maraging steel.

## 6. Strain Gage Wiring methods.

Up to now we used strain gages exclusively from Micro Measurement (Vishay). From the available range of gages types can be selected, which are well suited for the cryogenic range. For the extreme temperature range of cryogenic balances misadaptation of the STC-Factor is recommended. We use STC-Factors of 11 or 13 for balances constructed from maraging steel.

A more complicated problem is the primary correction of Young's modulus over the extreme temperature range of cryogenic balances. Normal KARMA-alloy is not satisfactory. For a special cryogenic balance production MM has demonstrated, that a special tuning of KARMA gages for extreme temperature range compensation of Young's modulus is possible. Gages of this special type were used for the ETW balance constructed by the Technical University of Darmstadt and Deutsche Airbus.

For a very low zero drift over the temperature range of cryogenic balances misadaptation of STC-factor, close coupled arrangement of the gages of one bridge etc. is not sufficient. Even the gages from one pack of five show considerable scatter in thermal behavior. Gage matching improves this situation very much and was first proposed by Judy Ferris (NASA Langley). Since the thermal behavior of gages can be evaluated only from the applied gage, each individual gage is applied to a common maraging steel sample by cyano cryalate bond. After a measurement of the zero drift of each gage in the cryogenic chamber the arrangement is heated beyond the stability of the cyanocryalate bond and the gages are carefully cleaned. From the results of this process the gages for each bridge are individually selected for minimum bridge zero drift. This procedure is time consuming but reduces bridge zero drift very much.

For final gage application on strain gage balances epoxy hot bonding is used exclusively. Preparing the surfaces, preparing the gages and the bonding procedure must be

done with the utmost care, patience and perfect observance of the manufacturers instructions. Even the utmost care is not sufficient, it must be combined with years of experience in the art of strain gage application.

For conventional balances temperature correction copper wires are integrated in the bridge wiring. For cryogenic balances this procedure is not very successful, since the strong non-linear behavior of the apparent strain can not be compensated by the copper behavior with a different non-linearity. If for special temperature correction methods the measurement of temperatures on the balance is necessary, a number of temperature sensors (6-10) is installed on the balance. PT 100 sensors are used for the temperature measurement. For very high precision the PT 100 sensors are individually calibrated.

The internal wiring of the bridge circuits is carefully designed for symmetric length and symmetric temperature on all internal bridge wire connections. All bridges are wired separately for excitation lines, excitation voltage sensing lines and signal lines. All circuits are connected to the tunnel data system via a high quality miniature connector mounted at the sting end of the balance. Normally 85 pin connectors are used.

Very often in wind tunnel testing practice it is necessary to bridge the balance with other electrical signal and power lines as well as pneumatic lines. These lines may deteriorate the balance accuracy due to their stiffness to an extent, that force testing and testing with the use of balance bridging lines must be done separately. So the wind tunnel productivity is reduced very much.

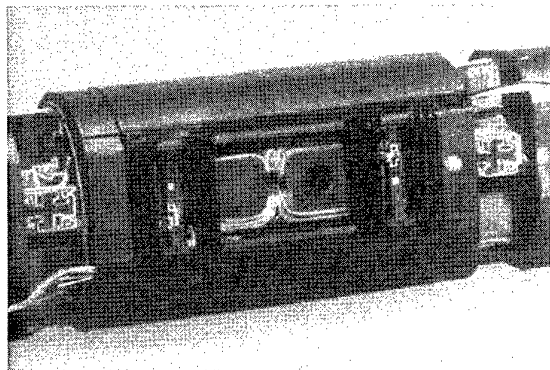


**Fig. 32** Balance W617 with Electrical and Pneumatic Lines for Model Instrumentation

At the Technical University of Darmstadt a concept was developed to integrate these bridging lines into the design of the balance. With such an integrated electric or pneumatic line bridging the balance has connectors at the sting and the model end for the lines. Thus any hysteresis due to the bridging is avoided.

## 7. Moisture Proofing resp. Proofing for Cryogenic Environment

To achieve excellent zero point stability, moisture proofing is most important. For conventional balances a careful observance of strain gage manufacturers instructions may be sufficient. For cryogenic balances moisture proofing is perhaps the most difficult detail of balance construction. Strain gage manufacturers give no sufficient instructions and offer no sufficient materials for these environmental conditions. A very careful application of multiple thin layers of nitril rubber is the best conventional moisture proofing method we found up to now.

## 8. Data Acquisition Equipment

It stands to reason, that for balance signal acquisition top quality equipment is used only. Nevertheless there is a certain disagreement on the basic type of equipment. In most tunnels DC measuring techniques are used in form of specially designed signal conditioning and digitizing units or in form of high quality digital multimeters.

In recent years some commercial developments, especially the DMC data acquisition unit (600 Hz carrier frequency) of the German company Hottinger has brought the AC measuring technique back into the field again. This AC equipment is equivalent and in some cases even superior to the best of DC equipment and has the big advantage of blocking any thermal voltage signals. In the case of cryogenic tunnels with their large temperature differences in the test region this may be essential. The disadvantage of the AC measuring method is the limited frequency range, which may cause concern, if dynamic balance stresses shall be monitored. Nevertheless dynamic signals up to 200 Hz can be monitored with this equipment satisfactorily.

The Hottinger measuring system DMC 9012 resp. its successor DMCplus is used successfully in the Aerodynamics Lab and the Wind Tunnel of the Technical University of Darmstadt, the Aerodynamic Department and Wind Tunnel Department of Deutsche Airbus, the Cologne Cryogenic Tunnel (KKK) and the ETW Calibration Machine. The system can be equipped with up to 28 data channels. The maximum speed of this system is 100 000 measurements per second and the resolution is up to 300 000 parts. The system is fully computer controlled; several systems may be managed in parallel by one PC. The system provides also the excitation for the strain gage bridges.

As a general rule identical electronic measurement hardware or even better the same equipment should be used for balance calibration and for balance use in the wind tunnel.

## 9. Mathematical Method of Calibration

The field of calibration perhaps includes the largest improvement potential of the balance technology. The first item in this field is the mathematical description of the balance behavior. The generally used method is the so called second order calibration. Since many years we extended this to a third order approximation of the balance behavior :

$$S_i = R0_j + \sum_{j=1}^6 A_{ij} F_j + \sum_{j=1}^6 \sum_{k=j}^6 B_{ijk} F_j F_k + \sum_{j=1}^6 C_{ij} F_j^3$$

In this description for the direct component calibration terms a third order term is taken into account. The advantage of this description compared to the conventional second order calibration was often questioned by other experts, nevertheless the use of the third order approximation is simply logical.

Certainly there are physical reasons for a non-linearity of the characteristic line of one component of a strain gage balance (or other Force Sensor) as shown in the positive quadrant of Fig. 33. Since a strain gage balance is a symmetrical structure, almost certainly in the third quadrant the non-linearity of the characteristic line should be mirror inverted to the line in the positive quadrant as shown in Fig. 33 by the continuous line. There is no reason to expect a monotone curvature like shown by the dotted line.

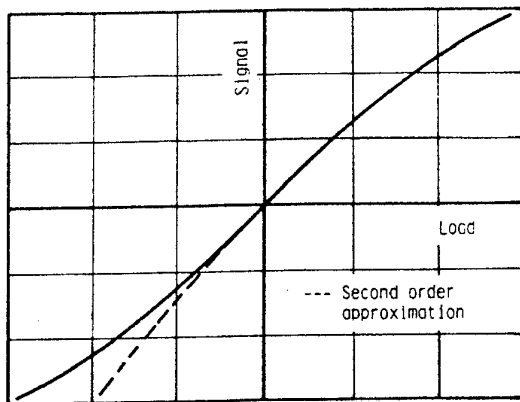


Fig. 33 Second/Third Order Approximation.

The non-linearity of the continuous line in Fig. 33 can be described in a polynomial by the third order term only. This is the only reason why we use the third order description of the balance behavior. Applied to actual calibration data the comparison of second and third order calibrations shows that in the case of the third order approximation the third order coefficients have a considerable size and the second order terms come out

smaller than in the case of a second order approximation. Nevertheless the quadratic terms should not be neglected. Very often a strain gage force sensor has a slightly different sensitivity in the positive and the negative quadrant. This behavior is approximated by the quadratic term. Since all the work is done very fast by the computer, the higher mathematical complexity of the third order approximation is no argument against this algorithm.

The conventional evaluation of the calibration data is based on the method to apply pure single loads stepwise to the balance plus combinations of two pure single loads. In the latter case one load is constant and the other load is applied stepwise. So a simple evaluation of each loading sequence in the sense of a least square error second order polynomial approximation is possible. The complete coefficient matrix is successively compiled from such evaluations of loading sequences. This results in an system of equations

### Component Signal = Function (Loads)

which must be converted to a different set of equations

### Loads = Function (Signals)

for use in the wind tunnel. This conversion is not possible in a mathematical sense since a conversion matrix only exists for a linear matrix. So more or less accurate or questionable approximate solutions must be used for the conversion.

The automatic calibration machine (see chapter 9) invented at the University of Darmstadt produces calibration data, where the desired loads (normally a single component or a combination of two single components) are superimposed by small interfering loads in the other balance components. Though the interfering loads are known precisely, the evaluation of a calibration matrix from such "mixed" loading conditions is not possible with the conventional method. So at the University of Darmstadt we use a different mathematical algorithm, where a system of equations

### Loads = Function (Signals)

is extracted in one step from the complete calibration data set (ca 1000 different loading conditions) as a closed solution in the sense of least square errors. So the questionable conversion of the matrix is no longer necessary and the result is the absolutely best evaluation of the calibration data in a mathematical sense. For more details see [18], [19] and [20].

## 10. Calibration Equipment

With the first balances designed and constructed for the DNW ,VFW made the experience, that the man power

consumed for calibration on a conventional calibration rig caused more than 30 % of the total balance manufacturing expenses. The large amount of man power required for the calibration procedure gave rise to considerations about an automatic calibration machine. Such a machine is necessary even more in the case of cryogenic balances, where the temperature is an additional parameter and the total amount of calibration work may be 4 - 6 times higher than in the conventional case. Obviously this problem is a common problem in the wind tunnel community, since at a number of places all over the world research in automatic calibration started during the last decade.

A concept of an automatic calibration machine was developed by Prof. Ewald at the Technical University of Darmstadt. In this concept the balance is clamped with its model end to a device - called 'measuring machine' - which is very similar to an external wind tunnel balance. Fig. 34 shows the system of the machine and this measuring platform is hatched for clarity.

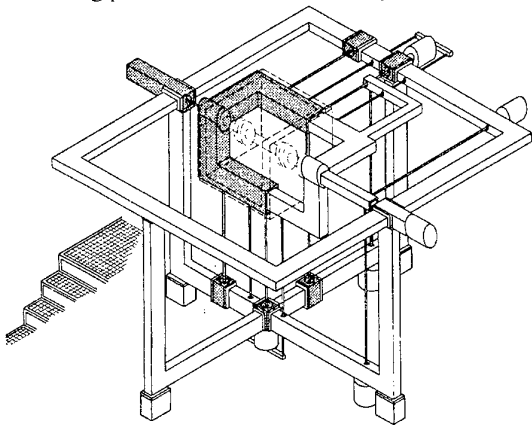


Fig. 34 Calibration Machine, Measurement Platform

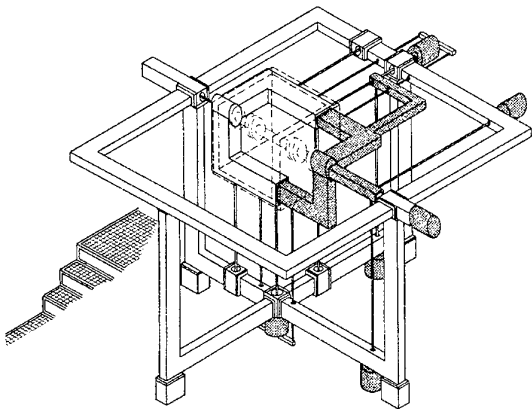


Fig. 35 Calibration Machine, Load Generation System

The master calibration of the 'measuring machine' is done with reference to the reference center of the balance and in the axis system of the measuring platforms flange, so this is a correct measurement of the calibration loads applied to the balance. The 'master calibration matrix' of the measuring machine makes provision for the elasticity of the connecting parts between measuring machine and model end of the balance.

The balance is flanged with the sting end to a loading tree, which is hatched for clearance in Fig. 35. Loads are applied to the loading tree by push-pull acting pneumatic force generators with rolling diaphragms. There is **no realignment** of the force generators and connecting rods to the loading tree. So due to the distortion of the balance the system becomes misaligned and the small interference loads mentioned in chapter 8 occur.

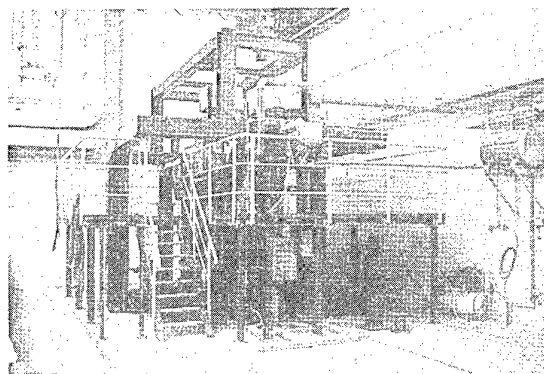


Fig. 36 ETW Calibration Machine

All functions of the machine are controlled by a network of simple PC computers. This network consists of a network server, a supervisory computer and of one controller each for the measuring machine, the balance signal acquisition and the load generation. In the case of a calibration machine for cryogenic balances there is an additional controller for the cryogenic climate conditioning chamber. A sophisticated safeguarding system prevents the demolition of a balance by overloading due to malfunction (or mal-programming) of the load generation. The management of the machine by a computer-network was necessary to guarantee the desired speed of the machine and to guarantee for safeguarding at the same time. With a present-day Pentium PC the control of the Calibration machine can be managed by a single PC. The target was to perform one full six component calibration including application of all single loads and of all combinations of pairs of single loads in one working shift, i.e. in 8 hours. This results in 20-25 seconds time for one loading condition.

A first prototype of the machine was designed and constructed by the Schenck Company at Darmstadt for the European Transonic Wind Tunnel with subcontracts to

the Technical University of Darmstadt (Cryogenic Chamber and Load Generator System) and to Deutsche Airbus (Computer-System and Software). Since spring 1993 the machine is operational at ETW and fulfills the specifications. Fig. 36 shows this machine in the calibration room of ETW.

The big improvement that this machine gives to wind tunnel force measurement is not only the improved accuracy of calibration. The fast operation of the machine reduces manpower for calibration so much, that wind tunnel operators can afford frequent recalibrations of the balances; this improves accuracy and reliability of the wind tunnel tests considerably.

Based on the good experience with the ETW machine the concept was further improved and developed by the University of Darmstadt. This development led to some improvements of the machine and to a simplified design. A prototype of the improved design with a Normal Force Range of  $\pm 6000$  N is under construction at the Technical University of Darmstadt. Fig. 37 demonstrates the design of this machine in principle.

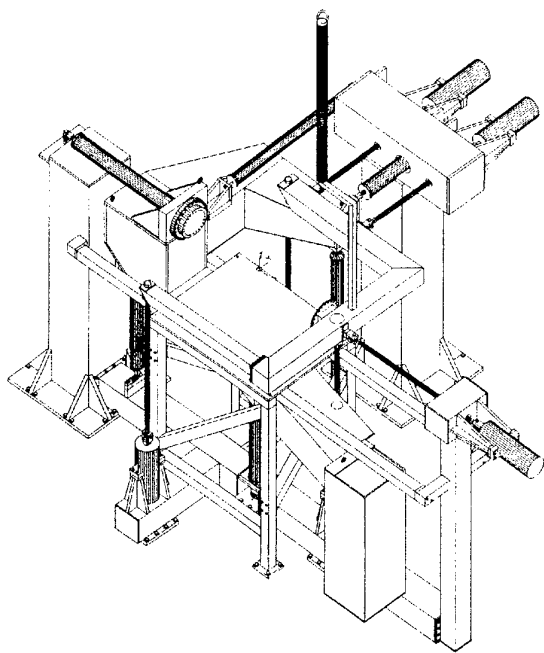


Fig. 37 Calibration Machine of Darmstadt University

## 11. Cryogenic Balance Design

A standard design philosophy for cryogenic balances is not yet established, among the cryogenic community there is even no agreement if unheated or heated

balances are to be preferred. The majority of cryogenic balances is unheated up to now but the promoters of heated balances argue, that this type will not develop spatial temperature gradients in the body and will not require stabilization times if tunnel temperature is changed. This is a strong argument, since the stabilization time will deteriorate the productivity of the tunnel.

Nevertheless we are pessimistic with respect to the heated balance. The massive joints on model and sting end of the balance will cause considerably large heat flows, so a lot of heating power will be required to condition the balance to ambient room temperature. The result most probably will be even worse temperature gradients in some regions of the balance body. From our point of view the more promising solution is a special balance design which tolerates temperature gradients without unacceptable deterioration of the accuracy especially in the axial force measurement.

This was achieved successfully with the concept of the tandem axial force elements, which are integrated in the front and aft flexure groups of the axial force system (see Fig. 38 for example). The predominant part of temperature gradient generated axial force errors is generated by the mean temperature difference in the upper and lower cantilever beam of the axial force system. With the conventional central position of the axial force bending beam the error signals are a function of the arbitrary temperature distribution in the cantilever beams.

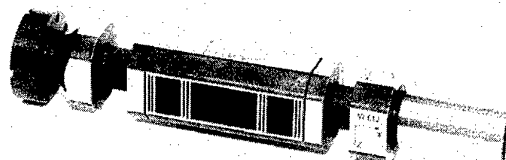


Fig. 38 Cryogenic Balance W 612 (KKK) with tandem axial force elements

With the tandem axial force system the error signals due to temperature gradients in the front and in the aft bending beam element have the same magnitude and opposite signs. By adding the signals of the front and the aft sensor the signals due to temperature gradients are canceled. The unavoidable tolerances in bending beam dimensions and gage position result in small residual error signals due to temperature gradients. Nevertheless these residual errors may be removed by a simple numerical correction.

The concept of the tandem axial force elements is successful. For temperature gradients of 5 degrees centigrade along the balance length the gradient induced error

of the axial force signal without additional numerical correction is only 1  $\mu\text{V/Volt}$  in the case of the ETW balance W 618.

The advantage of using copper beryllium as a material for cryogenic balances was mentioned already in chapter 5.

## 12. The Black Box Balance Principle

A distinguished balance expert well known to the author once said : *"You should never hand out a good strain gage balance to the wind tunnel people, they make everything wrong and they will demolish this delicate instrument"*. Obviously this aphorism is not quite correct since also a lot of good measurements have been performed by the "wind tunnel people" using strain gage balances !

Nevertheless there is some truth in it. The use of a balance in the tunnel, that means connecting it to the data acquisition system, adjusting amplifiers, adjusting excitation voltage, programming the signal evaluation (evaluation matrix, numerical corrections etc.), programming axis system transformation etc. offers so many opportunities for human errors, that an actually acting aerodynamic positive yawing moment may well be printed out by the computer as a negative rolling moment multiplied by  $xx$  plus a constant  $yy$ . To avoid these sources of human errors we invented the 'Black Box Balance' concept.

With this concept a standard electronic hardware for the balance signal conditioning, signal read out and force evaluation for the calibration of the balance and for the use of the balance in the tunnel is specified between client and manufacturer of the balance or is even delivered by the balance manufacturer. The operating parameters of this balance data acquisition hardware must be fully computer controllable. The balance is delivered by the manufacturer together with a floppy disk, which contains the standard balance evaluation program, which sets all parameters of the signal acquisition electronics and converts the balance signals into interference free and corrected forces and moments in physical dimensions.

In the balance itself a miniature memory chip is integrated. This memory chip contains a balance identification code and the calibration matrix.

For the use of the balance in the wind tunnel simply the disk is fed into the balance measurement controller (Standard PC) of the wind tunnel computer system and the balance itself is plugged to the measurement system. So always the standard evaluation software is used without the possibility of introducing errors. The balance controller automatically checks the balance identification code and compares it with the identification code of the

calibration data. With today's miniature memory chips the calibration data are an integrated part of the balance body at least for conventional tunnel balances. So the balance itself tells the wind tunnels balance computer her calibration data without any additional error source. The calibration data are automatically burned into the memory chip (EEPROM) on the balance by the data evaluation system of the Automatic Calibration Machine. The data are refreshed by each recalibration. In the case of a recalibration the calibration software checks for substantial differences between the old calibration matrix and the new one. Such differences may indicate a faulty balance.

Although the Black Box Balance Concept will simplify the use of the balance very much and will exclude nearly all possible human errors, it was not realized so far. The main argument of possible clients against the concept was, that a wind tunnel operator is bound to one balance manufacturer with this concept. Nevertheless, if the balance manufacturer is well qualified, this commitment may be not to bad.

## 13. Future Developments

Some plans for future developments of the balance technology were already indicated in the previous pages. Our most important plans for future developments are :

- Black Box Balance Concept
- Evaluation of Copper-Beryllium Balance Concept
- Evaluation of Titanium Balance Concept
- Integrated Balance Bridge for signal lines, power lines and pneumatic lines
- On Board Measurement for pressure distribution with light transmission of data into the earth system
- Further optimization of balance design by finite element analysis
- Further development of the Automatic Calibration Machine

## 14. Summary

The extensive research on strain gage balances done at the University of Darmstadt in co-operation with Deutsche Airbus demonstrated, that a substantial improvement of the wind tunnel force testing technology requires engineering progresses in any detail of balance design concepts, actual balance designs, material selection, balance fabrication method, gaging methods and calibration equipment and algorithms. So all these

details were included into our balance research efforts and any detail was improved to the technological limits available today. The outcome is a balance technology, which leads to much improved balances for conventional tunnels and to cryogenic balances which up to now (this development is not yet finally finished) bring the target of less than one drag count repeatability for transport configuration performance measurements within reach. Beside all technical improvements, high sophisticated balance technology is always a product of a team of engineers and a well experienced workshop staff. The success of this team even depends on a good cooperation and communication with the wind tunnel people.

### Acknowledgments

The author started balance design and fabrication 12 years ago as an assistant of Prof. Ewald at the Technical University of Darmstadt. He has to thank especially Prof. B. Ewald and Dipl.-Ing. E. Graewe for being good teachers having always a helping hand during the period of learning and the useful discussions.

Valuable contributions to the balance technology also originated from the co-operation with the Cologne Cryogenic Tunnel KKK. A most creative co-operation with the Carl Schenck AG, ETW and Deutsche Airbus made the Balance Calibration Machine possible. Some contracts with ETW allowed further research on cryogenic balances. Without this creative teamwork the substantial improvement of the balance technology and especially the cryogenic balance development could not have been possible.

Most of the work was funded by the German Ministry for Research and Technology.

### References

- [1] E. Graewe, "Development of a Six-Component Balance for Cryogenic Range". Forschungsbericht W 84-022 BMFT 1984
- [2] Prof. B. Ewald, "Grundsatzuntersuchung zum Temperatur-Verhalten von DMS-Axial-Kraftteilen", BMFT LVW 8420 10, Nr. 10/85 1985
- [3] B. Ewald, "Development of Electron Beam Welded Strain-Gage Wind Tunnel Balances", Journal of Aircraft Volume 16, May 1979
- [4] Prof. B. Ewald, G. Krenz, "The Accuracy Problem of Airplane Development Force Testing in Cryogenic Wind Tunnels", AIAA Paper 86-0776, Aerodynamic Testing Conference, March 1986
- [5] Prof. B. Ewald, E. Graewe, "Entwicklung einer 6-Komponenten-Waage für den Kryo-Bereich", 3. BMFT-Status-Seminar, Hamburg, May 1983,
- [6] Prof. B. Ewald, E. Graewe, "Development of Internal Balances for Cryogenic Wind Tunnels", 12th ICIASF, Williamsburg, VA, June 1987,
- [7] Prof. B. Ewald, "Balance Accuracy and Repeatability as a Limiting Parameter in Aircraft Development Force Measurements in Conventional and Cryogenic Wind Tunnels", AGARD FDP Symposium, Neapel, September 1987
- [8] Prof. B. Ewald, P. Giesecke, E. Graewe, T. Balden, "Feasibility Study of the Balance Calibration Methods for the European Transonic Wind Tunnel" Report TH Darmstadt A 37/88, January 1988
- [9] Prof. B. Ewald, Th. Balden, "Balance Calibration and Evaluation Software", Proc. Second Cryogenic Wind Tunnel Technology Meeting, ETW, Cologne, June 1988
- [10] Prof. B. Ewald, T. Preusser, L. Polanski, P. Giesecke, "Fully Automatic Calibration Machine for Internal Six Component Wind Tunnel Balances Including Cryogenic Balances", ISA 35th International Instrumentation Symposium, Orlando, Florida, May 1989
- [11] Prof. B. Ewald, P. Giesecke, E. Graewe, Th. Balden, "Automatic Calibration Machine for Internal Cryogenic Balances", Proc. Second Cryogenic Wind Tunnel Technology Meeting, ETW, Cologne, June 1988
- [12] Prof. B. Ewald, T. Preusser, L. Polanski, P. Giesecke, "Fully Automatic Calibration Machine for Internal Six Component Wind Tunnel Balances Including Cryogenic Balances", ICIASF Congress, September 1989, Göttingen
- [13] Alice T. Ferris, "Cryogenic Strain Gage Techniques used in Force Balance Design for the National Transonic Facility", NASA TM 87712, May 1986
- [14] Prof. B. Ewald, L. Polanski, E. Graewe, "The Cryogenic Balance Design and Balance Calibration Methods", AIAA "Ground Testing Conference" July 1992, Nashville, Bericht A 99/92
- [15] Prof. B. Ewald, K. Hufnagel, E. Graewe, "Internal Strain Gage Balances for Cryogenic Wind Tunnels", ICAS-Congress, Sept. 92, Peking

- [16] Prof. B. Ewald, E. Graewe, *"The Development of a Range of Internal Wind Tunnel Balances for Conventional and Cryogenic Tunnels"*, European Forum on Wind Tunnels and Wind Tunnel Test Techniques, Sept. 92, Southampton
- [17] H.F. Rush, *"Grain Refining Heat Treatment To Improve Cryogenic Toughness of High-Strength Steels"*, NASA TM 85816, 1984
- [18] Schnabl, *"Entwicklung eines numerischen Algorithmus und eines Rechnerprogramms zur Auswertung der Eichversuche an 6-Komponenten-DMS-Waagen."*, Technical University of Darmstadt, Diploma-Thesis A-D-69/87
- [19] Dipl.Ing. T. Balden, *"Ein neues Konzept zur Kalibration von Kryo-Windkanal-Waagen"*, Deutsche Airbus Bremen, Proceedings of DGLR Jahrestagung 1993, Göttingen
- [20] B. Ewald, *"Theory and Praxis of Internal Strain Gage Balance Calibration for Conventional and Cryogenic Tunnels"*, 18 AIAA Ground Testing Conference, June 1984, Colorado Springs
- [21] G. Viehweger, B. Ewald, *"Half Model Testing in the Cologne Cryogenic Tunnel (KKK)"*, 18th AIAA Ground Testing Conference, June 1984, Colorado Springs
- [22] Junnai Zhai, Bernd Ewald, Klaus Hufnagel, *"An Investigation on the Interference of Internal Six-Component Wind Tunnel Balances with FEM"*, ICIASF '95, Dayton, Ohio
- [23] Bernd Ewald, *"Advanced Force Testing Technology for Cryogenic and Conventional Wind Tunnels"*, ICAS Congress 1994, Anaheim, California
- [24] Alice T. Ferris, *"Status Report on Cryogenic Balances for the U.S. NTF"* AGARD Report No.774, Brüssel, Juni 1989

## Annex

<u>List of Existing Balances</u>						
Balance Name and Purpose	Simultaneous Component Ranges					
	X [N]	Y [N]	Z [N]	Mx [Nm]	My [Nm]	Mz [Nm]
W 64 Spin and Roll Balance Constructed for DLR		200	1 500	80	150	100
W 605 General Purpose Balance fabricated for DNW	12 500	12 500	30 000	9 000	11 500	9 000
W 606 First Cryogenic Balance fabricated for KKK	200	500	2 000	120	160	140
W 607 Missile Balance fabricated for AEDC	700	2300	2300	70	460	460
W 608 General Purpose Balance fabricated for DNW	20 000	6 250	50 000	4 500	15 000	4 500
W 609 Second Cryogenic Balance fabricated for KKK	1 400	1 700	4 000	400	500	400
W 610 Darmstadt University Low Speed Tunnel. Gen. Purpose	800	1 000	2 700	400	450	300
W 611 Tech. Univ. of Braunschweig Low Speed Tunnel	120	100	500	10	30	10
W 612 Third Cryogenic Balance fabricated for KKK	900	400	3 000	200	240	70
W 614						



<b>List of Existing Balances</b>						
<b>Balance Name and Purpose</b>	<b>Simultaneous Component Ranges</b>					
Cryogenic KKK - Balance Contract of DLR	1 400	1 700	4 000	400	400	300
W 615 Life Dummy Balance for ETW Calibration Machine	-	3 000	20 000	2 000	1 200	1 000
W 616 Transport Performance Balance for DNW	6 500	10 000	20 000	4 500	7 500	3 000
W 617 ETW advanced Research Balance. Copper-Beryllium	2 000	1 500	20 000	350	1 250	180
W 618 ETW Transport Performance Balance. Contract ETW	1 000	1 000	12 000	100	700	80
W 519 KKK Half Model Balance Contract from DLR	650	-	3 500	2850	350	515
<i>W 620 Project for Deutsche Airbus Low Speed Wind Tunnel</i>	<i>700</i>	<i>700</i>	<i>2 000</i>	<i>200</i>	<i>200</i>	<i>200</i>
W 621 ETW High Capacity Balance. ETW Contract	3 500	5 500	30 000	800	2 500	800

*Balances described in italics are still in the planning phase*

# FUNDAMENTAL CONSIDERATIONS FOR TESTING IN CRYOGENIC TUNNELS

André MIGNOSI

CERT/ONERA

Department of Aerothermodynamics

2 avenue E. Belin - 31055 TOULOUSE Cedex (FRANCE)

## ABSTRACT

This paper summarizes a number of aerodynamic phenomena mainly related to cryogenic pressurized testing. The goal of the analysis effort has been to address aerodynamic difficulties associated with the severe environment of this cryogenic wind tunnel.

The first part describes some of the various flow parameters important to respect the achievement of the best similarity between an aircraft in flight and the model in the wind tunnel. The second part covers the different effects of these factors from simple 2D cases to complex 3D flows : effects of the Reynolds number on laminar and turbulent flows, boundary layer transition, influence of non adiabatic model wall.

Theoretical and experimental points of view are presented and illustrated with practical examples. Efforts to obtain reliable and accurate results have been done in the past and need to be continued to provide the scientists and manufacturers with results leading to a better optimization and prediction of the aircraft performances

## List of symbols

a	: speed of sound
c, C	: model chord, heat capacity
C <sub>d</sub> , C <sub>l</sub>	: drag and lift coefficients
C <sub>f</sub> =τ <sub>p</sub> /q <sub>e</sub>	: skin friction coefficient
C <sub>h</sub> =Φ/ρ <sub>e</sub> U <sub>e</sub> C <sub>p</sub> (T <sub>w</sub> -T <sub>aw</sub> )	: Stanton number
C <sub>p</sub>	: specific heat at constant pressure
C <sub>v</sub>	: specific heat at constant volume
K <sub>p</sub>	: pressure coefficient
L	: reference length
M	: Mach number
n=ln(A/A0)	: amplification factor
P	: static pressure
P <sub>t</sub>	: stagnation pressure
Pr=C <sub>p</sub> μ/λ <sub>c</sub>	: Prandtl number
q=1/2 ρ U <sup>2</sup>	: dynamic pressure
r	: recovery factor
R/m	: Reynolds number per meter
Re <sub>L</sub> =ρUL/μ	: Reynolds number based on L
s	: curvilinear coordinate
t	: time
T	: static temperature
T <sub>aw</sub>	: adiabatic wall temperature
T <sub>t</sub>	: stagnation temperature
T <sub>w</sub>	: wall temperature

$T_u = \frac{\sqrt{u'^2}}{U}$	: Turbulence intensity
U, V, W	: velocity
X, Y	: longitudinal , transverse axis
$\bar{X}$	: X/X <sub>aw</sub> or X/X(R <sub>0</sub> ) ratio to adiabatic wall or to a reference case.

α	: model angle of incidence (°)
δ	: boundary layer thickness

$$\delta_1 = \int_0^\delta \left(1 - \frac{\rho u}{\rho_e u_e}\right) dy \quad \text{: displacement thickness}$$

$$\theta_1 = \int_0^\delta \frac{\rho u}{\rho_e u_e} \left(1 - \frac{u}{u_e}\right) dy \quad \text{: momentum thickness}$$

H=δ<sub>1</sub>/θ<sub>1</sub> : B.L. shape factor

λ<sub>c</sub> : thermal conduction

γ=C<sub>p</sub>/C<sub>v</sub> : ratio of specific heats

$$\gamma_{\text{effective}} = \left( \frac{\partial(\ln(p))}{\partial(\ln(\rho))} \right)_s \quad \text{: derivative at constant}$$

entropy

Φ	: wall heat fluxes (W/m <sup>2</sup> )
μ	: viscosity
ρ	: density
τ <sub>p</sub>	: Skin friction stress

## Subscripts

cr	: critical
t	: stagnation (pressure or temperature)
T	: transition
e	: external (at y=δ)
w	: wall
aw	: adiabatic wall
∞	: freestream conditions (at infinity)

## Abbreviations

2D	: two-dimensional flow
3D	: three-dimensional flow
B.L.	: Boundary layer
GN2	: Gaseous nitrogen
LN2	: Liquid nitrogen

## INTRODUCTION

The use of cryogenic technology has produced real progress in wind tunnel testing, permitting to reach high Reynolds numbers and precise replication of aerodynamic phenomena existing on aircraft in flight.

In parallel to large industrial wind tunnels, the use of research cryogenic wind tunnels with a large Reynolds number capability is also of interest to verify new concepts or built data bases for experimental / theoretical correlation. The development of Navier Stokes and Euler codes also provides another way to improve the predictions and the optimization of aircraft performances (Fig. 1). However the airflow around the complexities of aircraft defied the mathematical and computational analysis, wind tunnel aerodynamic will remain essential to predict aircraft performances.

Cryogenic wind tunnels /1,2,4,5,15,17,18/ offer also the unique advantage of an independent variation of the dynamic pressure  $q = 1/2 \rho U^2$  and of the Reynolds number  $R_C = \rho U c / \mu$  by varying the gas temperature or pressure. Parameters often coupled, such as aeroelastic model deformation and Reynolds effects, can be separated. An important aspect is to analyse how the development of the boundary layer affects the performances. The boundary layer growth is non linear, in addition the boundary layer can be laminar or turbulent, each type of flow leading to very different features.

In open commercial competition small differences of performance are now important, so research centers as well as aircraft industry need reliable and accurate results. Difficulties related to cryogenic and often to aerodynamic complexity must be taken into account. Preparation and analysis of cryogenic tests need a critical mind. The "wind tunnel system" includes a complex set of elements : model, instrumentation, wind tunnel hardware and software, etc., which must be homogeneous and of the best quality.

Beside the experimental aspects, the theoretical and computational fields have achieved important progresses. Experimental data can often be compared to numerical results.

On the opposite, experimental tests can be dedicated to improve the mathematical modelling, to validate a method or to take into account a phenomenon (example an unsteady flow structure) which was ignored at the beginning of theoretical approach.

## 1. AERODYNAMIC PROBLEMS RELATED TO CRYOGENIC TESTING

### 1.1 Review of sensitive parameters involved in a cryogenic tunnel

The respect of the two main parameters of similarity, i.e. the Mach number and the Reynolds number is not enough to reach the expected high quality level. (Fig. 2). First it appears necessary to analyse the real gas effect as well as the low temperature limitations. A

number of parameters (Fig. 2) must be taken into account such as wall and sting interference, model deformation, flow qualities, surface roughness, non adiabatic wall effects, etc...

### 1.2 Real gas effect

The first problem concerns the thermodynamic proprieties of the working fluid which can be pure nitrogen or a mixture of air and nitrogen. Can we assume that it behaves as a perfect gas at low temperature ?

The main critic concerns the large variation of the ratio  $\gamma = C_p / C_v$  of the specific heats at low temperature,  $\gamma$  can increase up to 1.6.

The answer was given by different works conducted at NASA by Kilgore, Adcock and Hall and in Europe /1,5,7/. The conclusion from these studies was that for isentropic expansions as well as for normal shock real gas effects are very small (maximum deviation of about 0.2%) even very close to saturation. If the real gas is studied, for an isentropic expansion by using the best equations (nitrogen characteristics by Jaconsen or the equation of state by Beattie-Bridgman), it is observed that the isentropic expansion coefficient  $\gamma_{\text{effective}}$  remains very close to 1.4 for a wide range of pressure and temperature :  $P_t < 6 \text{ atm.}$  and  $T_t > T_{\text{saturation}}$ . For a real gas many  $\gamma$  can be defined, the ratio of the specific heats is of a small interest compared to isentropic expansion coefficient  $\gamma_{\text{effective}}$  which remains nearly constant.

Many tests conducted at NASA-LANGLEY in the T.C.T (Fig. 3), at Southampton University, at DLR Germany and at ONERA France, etc. have shown the excellent correlation of the results for the same Reynolds number obtained by increasing the pressure or decreasing the temperature.

A real gas effect for a viscous flow will be presented in the section 2.2.2 dealing with transition.

### 1.3 Minimum operating temperature limit

The minimum temperature limit has also been studied mainly because the increase in Reynolds number is large when the temperature decreases near to the saturation limit /1,5,6,7/. From wind tunnel analysis, the minimum temperature is limited by the appearance of the liquid phase in the test section. The liquid phase can appear upstream of the model by heterogeneous condensation if the local Mach numbers around the model are small, or in supersonic pockets due to isentropic expansion created by the model. One explanation is that small particles are present in the flow (probably ice crystals as observed by a laser measurement under the dew point /19/) which initiate the creation and the growth of the droplets without any significant delay. The liquid nitrogen vaporisation downstream of the injector can also be a problem because liquid nitrogen can accumulate in the lower parts of the circuit. Another consideration concerns the flow quality particularly the temperature transverse

gradients and fluctuations which tends to increase at low temperatures due to the increase of the liquid nitrogen mass flow. A sufficient margin is necessary to be sure of the data quality results. I recommend to be over  $T_t=120$  K for a transonic test at  $P_t=4$  bar. By comparison the theoretical limit corresponding to saturation by an isentropic expansion from stagnation conditions to a local Mach number of 1.4 is 115 K

#### 1.4 Flow quality requirements

A lot of aerodynamic phenomena like transition or aeroelastic unsteadiness (buffeting, flutter, etc.) are sensitive to the freestream fluctuations. The longitudinal and transverse gradients (angle of the flow, temperature, Mach number, etc.) are also important to qualify the wind tunnel flow quality.

The fluctuation level in flight is very low and wind tunnel always try to reduce as much as possible the fluctuations and gradients.

Concerning the fluctuations, the main factors to measure are the velocity or  $(\rho U)$ , the static pressure and temperature. It seems necessary to qualify these fluctuations in terms of spectra and R.M.S. (for a given frequency bandwidth). Today laser velocimetry has difficulties to measure a turbulence intensity lower than 0.5%.

The hot wires or hot films (which are more reliable at transonic velocity), are able to measure the  $(\rho u)'$  and  $T'$ . Small unsteady pressure transducers of small size can be mounted at the wall or in static probes to qualify the pressure fluctuations /19/.

Recent qualification tests at ETW have been done with U. Michel from DLR/Berlin, the analysis needs to be completed.

#### 1.5 Moisture problem

Several sources can provide moisture to the tunnel flow : internal insulation material, liquid nitrogen, leaks of the wind tunnel, (drive air for T2 wind tunnel), ...

Ice crystals appears in the flow when the temperature becomes lower than the dew point /19/. The minimum value of this dew point obtained in the T2 wind tunnel after hours or days of purge is about 200 K. The corresponding mass of water is small  $1 \text{ mg/m}^3$  but is enough to produce some ice crystals (diameter  $> 10 \mu\text{m}$ ) able to trip the transition on few points near the leading edge of a laminar model.

#### 1.6 Wall interferences

The wall interference is not a particular problem of cryogenic wind tunnel but some aspects can be noted :

- The wall interference can be an important source of errors for flight test comparisons. The sting support is also important and must be taken into account.

- Solid flexible adaptive walls is a good solution to provide small interference level and good flow qualities /12,13/.

- For ventilated walls, the wall interferences can depend on the flow conditions, the viscous turbulent flow near to the wall depending on the Reynolds number. Furthermore, if the flow is injected from the plenum into the test section, its temperature can be very different due to heat exchanges with the metallic internals (the high thermal capacity of the internals leads to a very long time to reach the adiabatic conditions).

## 2. EXPECTED REYNOLDS NUMBER EFFECTS WITH ADIABATIC WALL

### 2.1 Basic examples of Reynolds number effects

At the beginning of wind tunnel tests, the Reynolds numbers were often rather low compared with full scale flight test. However the data agreed not too bad to first flight measurements. Today the Reynolds numbers of cryogenic wind tunnels can be as high as flight ones and the main difference is connected to the development of the boundary layer. At low Reynolds number the flow is often laminar and evolves to turbulent with the Reynolds number increase. The displacement of the transition location can be a very sensitive parameter. For each type of boundary layer the growth is non-linear and very different between laminar and turbulent flows. For a fixed type of boundary layer an increase of the Reynolds number decreases the boundary layer thickness, effect which often improves continuously the aerodynamic performances. Nevertheless this conclusion is not general.

#### 2.1.1 - Drag of a cylinder at $M=0$

A simple example concerns the evolution of the drag of a cylinder at low velocity (Fig. 4) plotted versus  $R_D$  ( $D$  diameter of the circle). In this case the lift is zero and the drag is mainly produced by pressure forces connected to the separation zone on the backward part of the cylinder. At low Reynolds number, the boundary layer developing on the accelerated forward part is laminar and separates very early ( $\phi=80^\circ$ ) when the pressure gradient changes of sign. This separation produces a large wake and is responsible of main part of the drag (there is a deficit of recompression on the rearward part). This type of flow is suddenly modified if the boundary layer upstream of the separation point is turbulent (around  $R_D=3 \cdot 10^5$ ). In this case the turbulent boundary layer is much more separation resistant and the separation point moves backward ( $\phi=120^\circ$ ). The wake is reduced, the recompression more efficient and suddenly the drag is reduced by a factor of three. The drag after this point increases smoothly.

In conclusion the evolution of an aerodynamic parameter like drag can be continuous or discontinuous, increase or decrease versus Reynolds number. The comprehension of aerodynamic phenomena is vital to assess the data result quality from variable Reynolds number wind tunnel and to suspect flow conditions

which can lead to non linear, inverse or discontinuous evolution of performances.

### 2.1.2 - Adiabatic flat plate boundary layer

The flow developing along a flat plate (Fig. 5) is also a simple case important to understand some basic aerodynamic phenomena. On a flat plate the flow can be divided in two parts : the viscous layer near to the wall, called boundary layer (height  $\delta$ ) with large viscosity effects and the external part considered as an inviscid flow.

The external part is supposed to be at a constant velocity  $U_e = U_\infty$ . The velocity profile of the boundary layer starts at the wall with a velocity  $U(y=0)=0$  and reaches the external flow at a high  $\delta$  with  $U(y=\delta)=0.99 U_e$ . For a given Mach number the main parameter for this flow is the Reynolds number  $R_x = \rho U_e x / \mu$ .

Near to the leading edge, the boundary layer is very thin and stable producing a steady laminar flow. Any small perturbation will be damped up to a critical abscissa  $X_c$  defined by the Reynolds number  $R_c$ . Downstream of this point some of the perturbations are amplified. These disturbance waves, called "Tollmien-Schlichting waves", progressively increase in amplitude for a well defined frequency domain and degenerate into turbulence after a complex, non-linear transient phase called transition. The initial amplitude  $A_0$  of the fluctuations inside the boundary layer are very difficult to estimate (receptivity problem). The causes can be : the external velocity or temperature turbulence, the acoustic noise, the wall roughness, etc. These amplitudes are very small and need to be amplified by a factor of more than thousands to generate the turbulent regime.

The main differences between laminar and turbulent can be sum up as follow :

- The thickness of a laminar B.L. is smaller than a turbulent B.L..

- Velocity profiles are very different. The tangent at the origin indicates a higher skin friction coefficient for a turbulent flow.

- The adiabatic wall temperature is lower for a laminar B.L. than for a turbulent. An estimation of the adiabatic wall temperature is:

$T_{aw} / T_t = (1 + 0.2 r M_e^2) / (1 + 0.2 M_e^2)$  where  $r$  is the recovery factor ( $r=0.85$  for laminar,  $r=0.9$  for turbulent). This phenomenon can be used to detect the transition by using surface temperature measurements (infrared camera).

The skin friction as well as the Stanton coefficients evolve along the plate. For the laminar part they decrease to a very low level and then increase strongly in the transition region. Downstream of transition the turbulent level is high and decreases slowly versus  $x$ .

#### Remarks:

Characteristic parameters can be defined versus  $x$  for any type of boundary layer :

- The displacement or momentum thickness  $\delta_1$  and  $\theta$  related to the loss of mass or momentum of the viscous flow (compared to a complete inviscid flow).

The displacement thickness for a 2D flow can be interpreted as a thickness which has to be added to the model to simulate an inviscid flow around this new shape. A consequence is that a pressure drag can be created by this shape modification. The pressure drag is zero for a flat plate.

- The skin friction coefficient responsible of the other part of the drag. This is the only part of the drag for a flat plate flow.

### 2.1.3 - Reynolds number effects for a fixed decelerated Mach number distribution.

#### Laminar boundary layer

In order to analyse the Reynolds number effect on a laminar boundary layer, two simple cases have been computed with the same fixed Mach number distribution (see figure 6). The lower Reynolds number based on a chord of 0.3 m is about  $2 \cdot 10^6$  ( $P_t=1$  b  $T_t=300$  K), and the three boundary layer parameters  $\delta_1$ ,  $\theta$  and  $C_f$  are plotted. After the first "classical evolution" corresponding to a flat plate boundary layer ( $0 < x < 0.15$  m), the decrease of the external flow velocity produces the decrease of  $C_f$  toward the separation point and the increase of  $\delta_1$  and  $\theta$  (particularly of  $\delta_1$ ). The important conclusion came from the Reynolds number increase (it was multiplied by about 10 at the bottom of figure 6). All the three boundary layer parameters are reduced but the separation point is always at the same location.

Remarks : In practice the Mach number distribution can slightly be modified by the coupling between the inviscid flow and the viscous flow leading to a slight displacement of the separation point. After this separation point, most of the time, the boundary layer reattaches with turbulent character.

#### Turbulent boundary layer

The same type of computational analysis has been achieved for a turbulent boundary layer and the same two Reynolds numbers in figure 7. The fixed Mach number distribution is slightly different in the downstream part (more decelerated flow) to lead to separation, because a turbulent flow is more resistant to separation. The main conclusion is that the separation point moves downstream with the Reynolds increase. The previous remark on the coupling effect is the same.

Because most of the aircrafts develop complete turbulent flow, it can be concluded that without a strong coupling the Reynolds increase is favourable on aircraft performances (drag reduction, increase of the maximum lift, etc.).

## 2.2 - Theoretical approach to predict transition for a 2D flow.

### 2.2.1 The linear stability theory

A theoretical approach of this phenomenon can be made by the linear stability theory. The principle is to introduce sinusoidal small disturbances into the linearized Navier Stokes equations in order to compute the range of unstable frequencies and their amplification /9,10,16/. This method computes versus  $x$  the most amplified frequency (see example in figures 8 and 9). The transition will start when the amplification ratio  $A_{\max}/A_0$  reaches a fixed value  $e^{nT}$ . The value of  $nT$  (between 6 and 10) is supposed to depend on the flow quality of the wind tunnel. The model surface finish is supposed to be perfect. This code needs the external Mach number distribution and the wall temperature (or fluxes) as inputs. The value of  $nT = \ln(A/A_0)$  at the beginning of transition can be correlated to the turbulence level  $Tu$  of the flow by  $nT = -8.43 - 2.4 \ln(Tu)$  as Mack suggested /9/. Some flight tests indicate that values higher than 12 can be reached.

### 2.2.2 - Real gas effects for laminar boundary layer

A recent theoretical study on transition /16/ of the real gas effect at low temperature was achieved with a laminar boundary layer stability code.

A comparison between perfect and real gas has been achieved for the simple case of a flat plate at Mach 1.1  $T_e = 110$  K ( $T_t = 137$  K). The real gas was computed by using the Beattie-Brigden equations.

First the laminar boundary layer was computed, differences due to real gas on the boundary layer characteristics like  $\delta$ ,  $\delta_1$ ,  $C_f$  and velocity profiles were very small..

Figure 8 shows the evolution of the amplification coefficient  $n = \ln(A/A_0)$  versus  $x$  for some unstable frequencies. The comparison between the two numerical results is obtained in the following conditions :

- solid line :  $T_e = 130$  K, constant Prandtl number, perfect gas equation of state;
- dashed line  $T_e = 130$  K, variable Prandtl number, Beattie-Brigden equation.

It is clear that the real gas effects are unimportant not only on the behaviour of the mean laminar flow but also on the unsteady properties. Usual boundary layer and stability codes can be used in cryogenic conditions.

### 2.2.3 Example for a 2D airfoil

Figure 9 illustrates this method for the CAST10 airfoil in T2 wind tunnel : Free transition, ambient temperature  $M = 0.73$   $\alpha = -0.25^\circ$  and  $R_e = 4 \cdot 10^6$ . The upper surface Mach number distribution is quite flat at  $M_1 \approx 1$ . A free transition near 45% of chord was observed by oil visualization and corresponds also to a small bump on the Mach number distribution curve. Computation reproduces correctly this location when  $n = 8$  corresponding to a turbulence intensity  $Tu = 0.1\%$  with the Mack law. On the lower surface, the laminar boundary layer separates at 60% of chord and the transition is fixed by a separation bubble.

At the bottom of figure 9 the displacement thickness  $\delta_1$  is plotted versus  $x$ , in order to explain the bump on Mach number distribution. This bump is related to the large decrease of the displacement thickness in the transition zone, changing the slope of the flow seen by the inviscid fluid near to the surface.

**Remarks :** The boundary layer transition process presented is the "classical type" for 2D flow, it can be by-passed if the initial perturbing amplitude is large, caused by a wall roughness (tripping devices / particles) or by flow vortices.

Transition can also occur for 3D flows, by transverse instabilities or for a swept wing by a leading edge contamination produced by the fuselage turbulent boundary layer (see section 2.4).

### 2.2.4 - Application of the transition prediction method to design new axisymmetrical laminar reference model for cryogenic tunnels.

It appears very important to qualify the flow quality of a modern transonic cryogenic wind tunnel by a simple reference laminar model. As far as transition phenomenon is concerned, the flow quality of a pressurized cryogenic wind tunnel is quite impossible to be checked with a classical  $10^\circ$  cone because the transition occurs very near to the apex of the cone (10 to 20 mm). ONERA proposes to ETW to study a simple axisymmetrical model at  $0^\circ$  of incidence, achieving on the forward part a negative pressure gradient relaxing progressively (Fig. 10).

The shape of this model has been optimized by computation. The wind tunnel flow quality is represented by a constant value of  $n = n_T = \ln(A_T/A_0)$  at the beginning of the transition. The value of  $n_T$  can be linked to the turbulence intensity, the acoustic noise or temperature fluctuations of the wind tunnel flow ( $Tu = 0.6\%$  for  $n_T = 4$  and  $Tu = 0.05\%$  for  $n_T = 10$ ).

For a fixed Mach number (bottom of Fig. 10), four curves with constant amplification coefficients  $n_T = 4, 6, 8, 10$  are plotted versus the unit Reynolds number. On this body the transition will move smoothly between 50 and 200 mm from the stagnation point, depending on the Reynolds number and on the flow quality level. For a fixed Reynolds number the transition location depends significantly on  $n_T$  and moves of about 50 mm for the studied cases. The most forward location is obtained for the maximum unit Reynolds number (example : ETW  $R/m$  (max.) =  $200 \cdot 10^6/m$  for  $P_t = 4.5$  atmos.  $T_t = 120$  K).

This model is constituted by a thin metallic skin of 5 mm in thickness. It will be painted and polished in order to obtain a good surface finish and a good emissivity necessary to measure the wall temperature by an infrared camera.

The instrumentation of the model is based on two types of measurements : the pressure distribution (measured by pressure holes) and wall temperature measurements by using an infrared camera or thermocouples.

The measured pressure and temperature distribution will be used after the tests as an input of the boundary layer code. For each test case, a boundary layer code can compute the maximum amplification coefficient  $n(x) = \ln(A/A_0)$  and from the measured transition location the value of  $n$  at the beginning of the transition zone can be deduced.

Experience has to be gained on this type of model. It will be soon tested in T2 and after in ETW in order to constitute an experimental data base. Such a model could be used for comparative tests in different high Reynolds number wind tunnels such as Cryo Ludwig Tube (Germany), KKK, NTF (U.S.), etc..

### 2.3 Two-dimensional approach for sudden transition on a flat plate.

In order to gain a good understanding of the role played by transition location on the drag of a flat plate of chord  $c$ , the figure 11 shows the variation of  $C_d$  versus Reynolds number for two configurations.

The first configuration consists to fix the transition location at a given percentage of the plate chord. A decrease of drag with the Reynolds number is then observed, the increase in Reynolds number decreases the friction coefficient and therefore the momentum thickness.

However, if the location of the transition, assumed sudden, varies preserving a constant transition Reynolds number  $R_{XT}$  ( $R_{XT}$  is related to the turbulence level), the following phenomena are observed:

- If  $R_C < R_{XT}$ , the entire boundary layer is laminar and the evolution follows the 100% lower laminar curve.

- If  $R_C > R_{XT}$ , there is first an increase in drag, due to the rapid displacement of the transition toward the leading edge, which overrides the gain expected from the Reynolds effect. The increase stops when the transition reaches 20% of chord and then a decrease tending asymptotically to the 100% turbulent curve is observed. It can also be observed that the maximum drag takes place for  $R_C$  between 10 and 40  $10^6$  when  $R_{XT}$  is close to the classical value of 3 to 5  $10^6$ .

The figure 11 presents also the difficulties to simulate a flow at  $R_C = 20 \cdot 10^6$  with a free transition at  $R_{XT} = 5 \cdot 10^6$  in a wind tunnel providing a maximum Reynolds number of 6  $10^6$ .

If the transition location is tripped at  $x/c = 25\%$ , corresponding to the real location at  $20 \cdot 10^6$ , the resulting drag is too high.

If the transition is kept free, the drag will be too low, corresponding to a long laminar flow up to 80% of chord.

To respect the drag the only solution is to trip the transition at  $x/c = 47\%$  but, this location has to be changed with the test conditions ! For an airfoil study, this location, which respects the same drag, has to move with the Mach number, the angle of attack, the chord Reynolds number, and it is impossible to respect at the same time the other coefficients like lift or

momentum. Furthermore the transition location is very difficult to predict, the transition prediction methods depends on too many sensitive parameters.

## 2.4 - Different other types of transition process

### 2.4.1 Leading edge transition

By using the linear stability theory, the transition can be predicted on the attachment line for a swept wing. From theory, the transition occurs when  $R_\theta > 250$ , but in practice, an other phenomenon can decrease this value : the leading edge contamination.

If the disturbances became large, as in the case of the wing root which is in contact with the turbulent boundary layer of the fuselage, the transition occurred for  $R_\theta > 120$ . In this case, spots of turbulence propagate along the attachment line in a non linear mode /10/ inducing a turbulent boundary layer along the entire wing.

#### Important remark:

For almost all the transonic transport aircrafts flying with a swept wing, the Reynolds number is large enough and the flow is turbulent on all the wing due to fuselage contamination or to surface roughness on the attachment line.

### 2.4.2 Transition due to crossflow instability 3D flows

If the flow remains laminar on the leading edge of a wing, another transition mode can exist due to the crossflow instability of the boundary layer velocity profile (figure 12).

An illustration of crossflow instability is presented in figure 13 to study a laminar wing designed by ONERA and Aerospatiale. An AS100 laminar model (swept angle  $15^\circ$ ) represents a part of the wing modified near the side walls to simulate the real 3D flow. For the presented experiments at T2 wind tunnel ( $M = 0.74$ ,  $\alpha = -2.3^\circ$ ) a strong negative pressure gradient on the forward part creates crossflow instability at high Reynolds number. The transition location was measured for a chord Reynolds number range from 4 to 15  $10^6$ . After analysis, the transition at low Reynolds number ( $X_{TR} \approx 70\%$ ) is produced by the backward positive pressure gradient giving streamwise instability. When the Reynolds increases the crossflow instability produces a transition which moves forward when the Reynolds exceeds 10  $10^6$ .

### 2.4.3 Surface roughness effects

The influence of the model surface roughness is capital for the transition phenomenon, all the more because cryogenic wind tunnels achieve high Reynolds numbers decreasing the boundary layer thickness.

Essential points are summarized below:

- For a sphere of a diameter  $k$ , it is considered that the transition occurs suddenly on it when  $R_k = U_k k / \nu$  reaches 500 to 600 ( $U_k$  is the velocity at a height  $k$  in the laminar B.L.).

- If the roughness is an overthickness with height  $k$ , perpendicular to the flow (cylindrical wire, strip of carborundum, plots /19/, etc.) the main parameter is  $k/\delta_1$ . The diagram in figure 14 shows the tripping limit. Near to the leading edge  $\delta_1$  is often in the neighbourhood of 0.01 to 0.02 mm and the value of  $k$  is roughly equal to it.

- For a distributed roughness of grains of sand type (mean height  $k$ ), the transition location is modified when,  $U_k k / \nu$  reaches 100 to 120. Applied to cryogenic flows at  $M=1.2$   $P_t=2$  b  $T_t=120$  K ( $Re/m=110 \cdot 10^6$ ), the critical roughness is  $1 \mu m$ .

- For pressure tap the risk of tripping occurs when  $d/\delta_1 > 20$  where  $d$  is the hole diameter.

Nevertheless the transition location can be modified far downstream from leading edge taps or wall defects even if all those conditions are satisfied.

### 3. NON-ADIABATIC MODEL WALL

#### 3.1 Laminar boundary layer on a flat plate - Wall temperature effect

Analysing the computed development of a laminar boundary layer of very small initial thickness on a flat plate at  $M_e=1.2$ , makes it possible to observe the following phenomena when the ratio  $T_w/T_{aw}$  of the wall temperature to the adiabatic wall temperature is varied (figure 15):

- The variation of the displacement thickness  $\delta_1$  is parabolic as function of the abscissa. In addition, this thickness increases when the wall is heated.

- The variation versus  $x$  of the momentum thickness  $\theta$  is identical to that of  $\delta_1$  but is not particularly sensitive to the wall temperature.

- There is a decrease of the local skin friction coefficient  $C_f$  and a low sensitivity of this coefficient as a function of  $T_w/T_{aw}$ . This result is also in agreement with the momentum equation  $C_f/2 = d\theta/dx$ .

The wall temperature effect is also illustrated in the figure 16. The variation of the integral boundary layer parameters  $\delta_1$ ,  $\theta$ ,  $C_f$  as well as the shape parameter  $H = \delta_1/\theta$  are plotted for two fixed locations corresponding to  $R_x=2$  and 10 million. The results are quite the same for the two locations. In this figure the various values have been divided by the adiabatic reference values noted  $AW$ :  $\bar{X} = g/g_{AW}$ .

For a hot wall, a substantial increase of  $H$  and  $\delta_1$  is observed, on the other hand,  $\theta$  and  $C_f$  decrease very slightly, by approximately 0.5% for  $T_w/T_{aw}=1.1$ .

The wall temperature effect can be compared to the Reynolds number effect for an adiabatic wall (Fig. 17). According to the boundary layer equations, all variables

$\delta_1$ ,  $\theta$ ,  $C_f$  varie as  $1/\sqrt{R_x}$ , which means that  $H$  remains constant.

We can observe an enormous variation of the integral thicknesses and of the skin friction coefficient. All these parameters are divided by  $\sqrt{2} = 1.41$ , when the Reynolds number is doubled.

#### 3.2 Turbulent boundary layer on a flat plate - Wall temperature effect

A turbulent case computation, corresponding to  $M=1.2$   $T_t=120$  K  $P_t=2$  bar, is illustrated in the figure 18 where the variation of  $\delta_1$ ,  $\theta$ ,  $C_f$  is plotted versus  $x$  for three wall temperature values.

The finite volume method uses a mixing length concept developed at CERT/DERAT.

A much more linear variation of  $\delta_1$  and  $\theta$  versus  $x$ , is noticed immediately as well as the low decrease of the friction coefficient. The value of the turbulent skin friction coefficient is substantially above that of the laminar case. If the wall is heated, all parameters are affected:  $\delta_1$  increases,  $\theta$  and  $C_f$  decreases.

The wall temperature effect on the boundary layer parameters is illustrated in figure 19.

As for the laminar case, all the values are divided by the adiabatic reference values. Two locations corresponding to  $R_x=20$  and 100 million were chosen and give approximately the same result. For a hot wall, a considerable increase of  $H$  and  $\delta_1$  ( $\approx 7\%$ ) is observed for  $T_w/T_{aw}=1.1$ , whereas  $\theta$  and  $C_f$  decrease by approximately 3.5%.

The wall temperature can be compared to the Reynolds number effect for an adiabatic wall (Fig. 20). In this case if the Reynolds number is doubled, the decrease of the shape factor  $H$  is very small approximately 1% with a decrease of 10% of the other values.

In conclusion, as for the laminar case, a hot wall thickens the boundary layer displacement thickness. As the skin friction is reduced, The boundary layer tends to separate earlier in the areas of negative velocity gradient. Several differences in sensitivity between laminar and turbulent B.L. are also clear, both as function of wall temperature and of the Reynolds number.

#### 3.3 Laminar to turbulent boundary layer transition - Wall temperature effect for 2D flow

As presented in the section on transition, small disturbances develop in the laminar boundary layer and become amplified until the turbulence occurs. Wall heating leads to earlier transition. Experiments as well as linearized stability theory give clear informations about the great sensitivity of the wall temperature on the transition location in the case of a constant Mach number distribution. The figure 21 from /8/, illustrates this effect on a  $10^\circ$  cone in flight and in wind tunnel. In this figure the authors also plotted the theoretical curve for  $M_\infty=0.85$ . In conclusion the transition location is



very sensitive to wall temperature at constant Mach number since an increase of 1% in the wall temperature is equivalent to a decrease of 4 to 7% of the transition Reynolds number  $R_{XT}$ .

#### 4. EXAMPLES OF WIND TUNNEL REYNOLDS NUMBER EFFECTS

##### 4.1 The CAST10 airfoil - fixed transition

The Reynolds number effects on lift and drag of the transonic CAST10 airfoil are extracted from tests which have been performed at T.C.T. and T2 wind tunnels with adaptive walls (Fig. 22). This figure shows experimental data with a fixed transition at  $x/c=5\%$  for two Reynolds numbers at  $M=0.76$ . Lift and drag coefficients are plotted as function of incidence. When the Reynolds number increases from  $3.3 \cdot 10^6$  to  $20 \cdot 10^6$ , the evolution of the polar curve is very large. For a constant incidence, the lift coefficient is always increased. The drag coefficient can be reduced at low lift ( $\alpha < 0.8^\circ$ ) or increased ( $\alpha = 1.3^\circ$ ). The increase in lift can be explained by the thickening of the boundary layer.

It is more difficult to understand the drag evolution. The drag can be divided in two parts : pressure and skin friction drags. When the Reynolds number increases the skin friction part decreases but the pressure drag can decrease at low lift (no shock) or increase because the shock became stronger.

##### 4.2 The laminar OALT25 airfoil

The effect of the Reynolds number on the transition location has been studied for a sensitive case presented in figure 23. For the lower surface, the transition was fixed at 5% of chord and for the upper surface the transition is free. The upper surface Mach number distribution is quite flat with a small negative pressure gradient between 2% and 20% of the chord.

A Reynolds number range from 5 to 16 million was studied by using pressure or temperature. The transition location on the upper surface located at about  $x/c=70\%$  for the lowest Reynolds number moved forward to the leading edge when Reynolds number increased. To find the transition location in the experiments the temperature distribution and the heat fluxes coefficients were used. Two other ways have confirmed the estimated transition location : the displacement of a "bump" on the Mach number distribution and the variation of the drag coefficient.

In this configuration many runs were carried out by using different combinations of pressure and temperature. No significant deviation of the transition location or of the drag due to the flow temperature level was observed see figure 23.

##### 4.3 Example of an Airbus type half model - fixed transition at $x/c=5\%$

In order to study the Reynolds number effect on a wing, a cryogenic transport type half-model has been designed and manufactured /14/. Pure Reynolds number effect have been achieved by varying the stagnation temperature at constant pressure. The control of the wing tip displacement was made by two optic fibers observed with a video camera (Fig. 24). At constant pressure, the displacement depends mainly on the incidence but not very much on the temperature level.

Reynolds number effect on the pressure coefficient  $K_p$  is presented in figure 24 for two wing sections. The main effects are the downstream displacement of the shock wave and the increase in lift as observed for 2D flows. At the bottom of this figure, this Reynolds effect is compared to the deformation effect produced by the elasticity of the model., if the stagnation pressure is changed. In this case the displacement of the wing tip seems proportional to the pressure and the wing is twisted. In this case, the deformation effect seems to be of the same order of magnitude than the Reynolds number effects.

#### CONCLUSIONS

After an initial phase mainly devoted to the design and development of cryogenic wind tunnel, many facilities are now in use throughout the world. An important question is to know how to make the best possible use of the enormous possibilities offered by cryogenic tunnels. The user should be warned that the Reynolds number is not the miracle parameter guaranteeing validity of the results. It is necessary to preserve a critical attitude and to consider the wind tunnel as a tool, used to analyze and to understand phenomena, to validate new concept and to assist manufacturers and researchers in developing and optimizing aircraft. The effect of the Reynolds number is often complex and gives results which, although unexpected, have a physical explanation, with the guidance from CFD. This paper has tried to describe the importance of many factors, including non adiabatic wall effects, as well as flow quality, and surface roughness which can directly affect the transition location and aircraft performances. The cryogenic wind tunnel technique must also provide reliable and accurate results which can be used to improve prediction and optimization of the aircraft performances.

To be efficient, the cryogenic wind tunnel must offer maximum of flexibility and a low cost, in spite of the complexity of the tests which can be achieved in it. It is by the conjunction of many efforts in those areas that cryogenic wind tunnel testing will occupy a major place in the future.

#### REFERENCES

- /1/ R.A. Kilgore "Model design and instrumentation experiments with continuous wind tunnels". AGARD LS-111 (1980)

- /2/ Cryogenic Wind Tunnels, a selected, Annotated bibliography - Marie H. Tuttle, Robert A. Kilgore, and Karen L. Cole NASA TM 4013
- /3/ Carriere P., 1972, "The injector driven tunnel." AGARD LS 1972-AGARD Report R-600-72. (1980)
- /4/ R.Michel "The development of a cryogenic wind tunnel driven by induction". AGARD LS-111 (1980)
- /5/ M.J. Goodyear " The principles and applications of cryogenic wind tunnels". AGARD LS-111 (1980)
- /6/ M.J. Goodyear Prog. Aerospace Sci. Vol. 29, pp. 193-220 1992, "The Cryogenic Wind Tunnel"
- /7/ R.M. Hall "Real gas effects". AGARD LS-111
- /8/ D.F. Fisher N.S. Dougherty Jr. "In-flight transition measurement on a 10° cone at Mach numbers from 0.5 to 2.0". NASA TP 1571 (1982)
- /9/ L.M. Mack "Boundary layer linear stability theory" AGARD R-709
- /10/ D.Arnal "Boundary Layer Transition : predictions, application to drag reduction" AGARD FDP/VKI Special Course AGARD Report 786 (1992).
- /11/ Blanchard A, Dor J B, Séraudie A, Breil J F. June, 1988, "Flow quality in the T2 cryogenic wind tunnel-problems and solutions." Second cryogenic technology review meeting Köln Germany
- /12/ Archambaud J.P., Mignosi A., May 18-20, 1988, "Two-dimensional and three-dimensional adaptation at T2 transonic wind tunnel of O.N.E.R.A./C.E.R.T." A.I.A.A., 15<sup>th</sup> Aerodynamic Testing Conference, San Diego, California (U.S.A.).
- /13/ Chevallier J.P., Mignosi A., Archambaud J.P., Séraudie A., 1983-4, "T2 wind tunnel adaptive walls design, construction and some typical results." *La recherche Aéronautique*.
- /14/ Dupriez F., Geoffroy P., Outtier G., June 28-30, 1988, "Half transport aircraft cryogenic model for T2 wind tunnel." *Second Cryogenic Technology Review Meeting*, Köln/Porz (Germany).
- /15/ " First International Symposium on "Cryogenic Wind Tunnels", University of Southampton (U.K.). April 1979
- /16/ First European Forum on Laminar Flow Technologie DLGR-Bericht 92-06 - Hambourg Germany March 16-18 1992
- /17/ Special Course on Cryogenic Technology for Wind Tunnel Testing AGARD\_FDP\_VKI April 23-27 1985
- /18/ Advances in Cryogenic Wind Tunnel Technology Special course AGARD\_FDP\_VKI June 5-9 1989
- /19/ A. Séraudie ; J.P. Archambaud "T2 Transonic Cryogenic Tunnel at Toulouse" AGARD\_FDP\_VKI Mai 20-22 1996

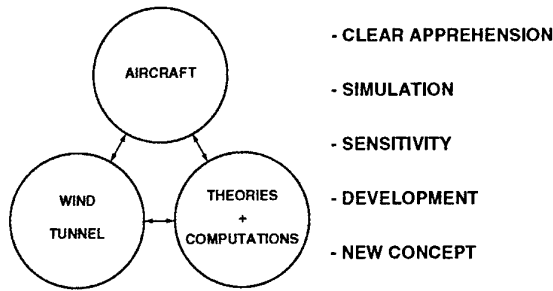


Fig. 1 : General scheme - Wind tunnel part.

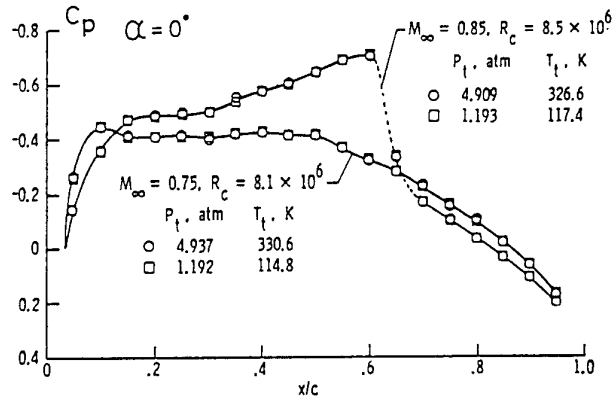
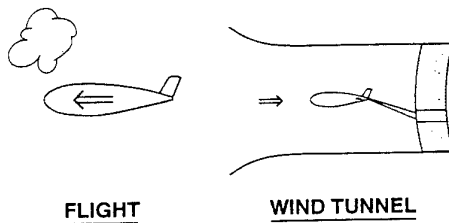


Fig. 3 : 2D symmetrical airfoil at T.C.T. Nasa Langley : pressure distribution at ambient and cryogenic conditions.



## I) STATIONARY (3D OR 2D)

$$Re = \frac{[\text{INERTIA FORCES}]}{[\text{VISCOUS FORCES}]} = \frac{\rho u L}{\mu} \quad Re_F = Re_{WT}$$

$$M^2 = \frac{[\text{INERTIA FORCES}]}{[\text{ELASTIC FORCES}]} = \left(\frac{u}{a}\right)^2 \quad M_F = M_{WT}$$

- REAL GAS EFFECT + CONDENSATION BOUNDARY
- WALL EFFECTS
- STING INTERFERENCE
- MODEL DISTORTION AND SURFACE ROUGHNESS
- NON ADIABATIC WALL EFFECTS
- MISCELLANEOUS : DUST, REPETABILITY, DISCREPANCY, NON LINEARITY, ...

## II) TIME

- FLUTTER, BUFFETING, ...
- TRANSIENTS : TEMPERATURE, MACH NUMBER, PRESSURE, PITCH ANGLE, ...

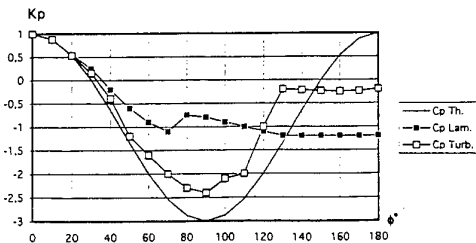
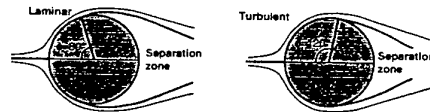
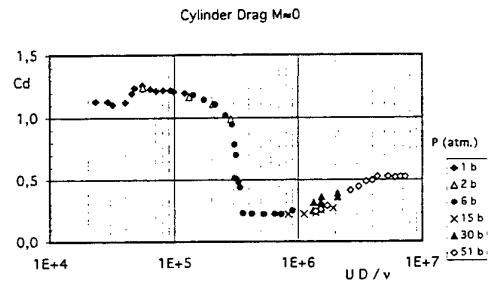


Fig. 2 : Problems involved in cryogenic testing.

Fig. 4 : Drag of a cylinder versus Reynolds number at  $M=0$

## Flat Plate Boundary layer

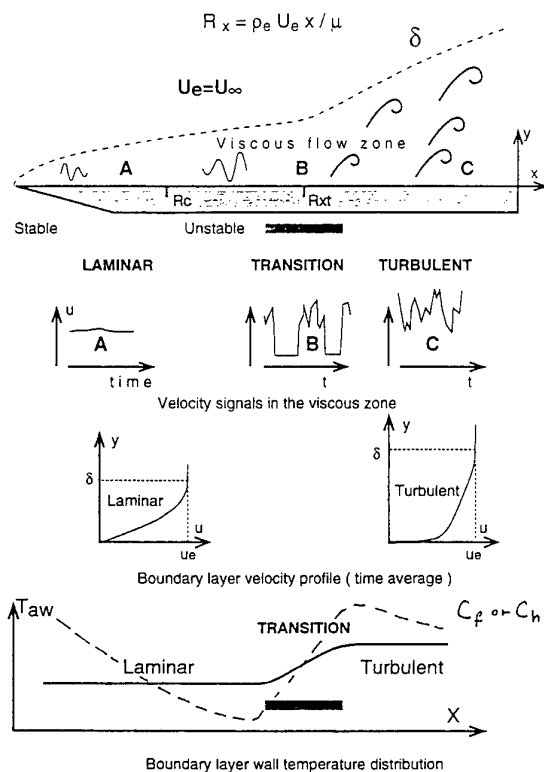


Fig. 5 : Flat plate boundary layer

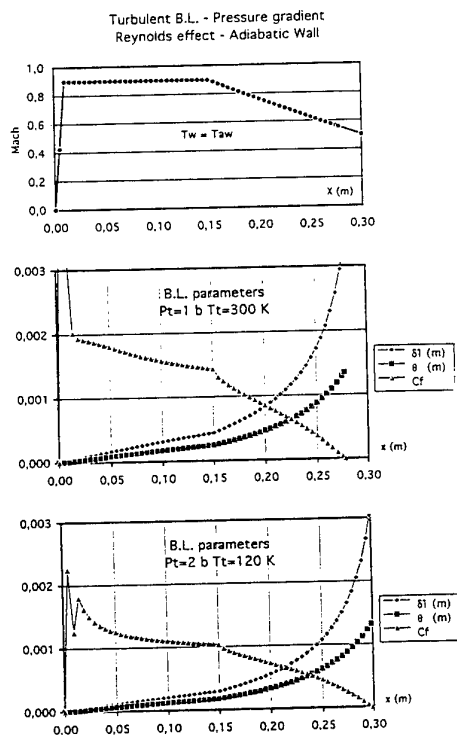


Fig. 7 : Reynolds effects for a fixed positive pressure gradient on a turbulent boundary layer - adiabatic wall

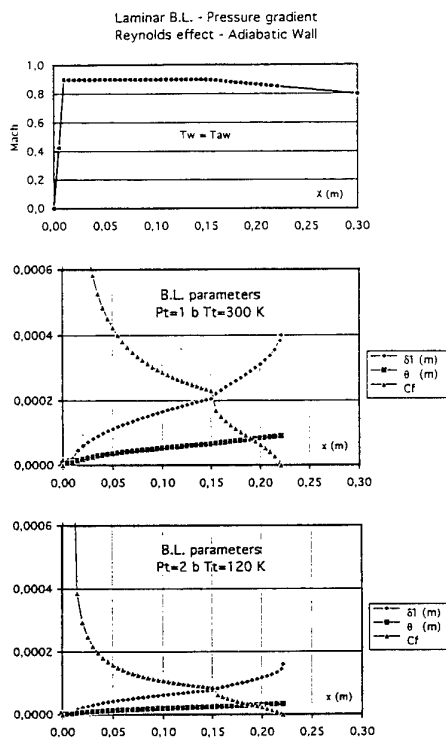


Fig. 6 : Reynolds effects for a fixed positive pressure gradient on a laminar boundary layer - adiabatic wall

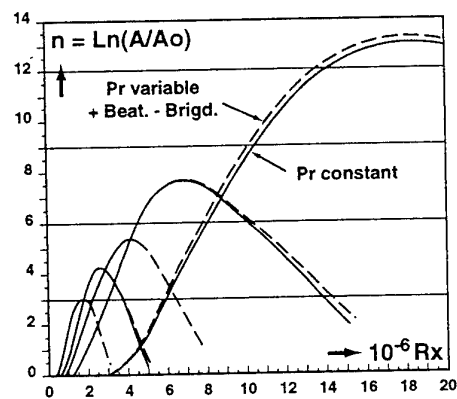
REAL GAS EFFECT on the Amplification coefficient  
Flat plate at  $M = 1.1$   $T_e = 130$  K

Fig. 8 : Real gas effects on the amplification coefficient for a flat plate

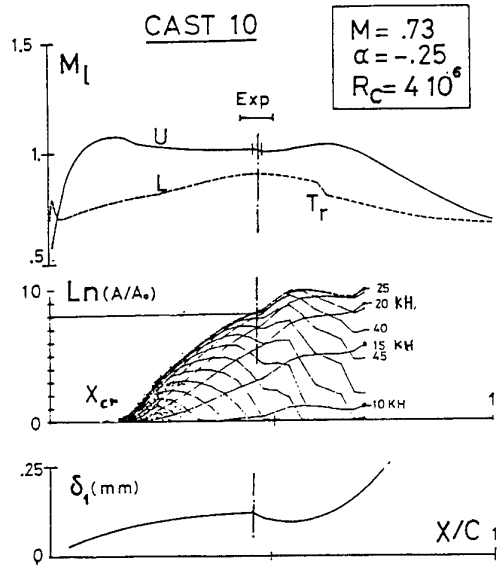


Fig. 9 : Streamwise transition on a CAST 10 airfoil : experimental and theoretical correlations.

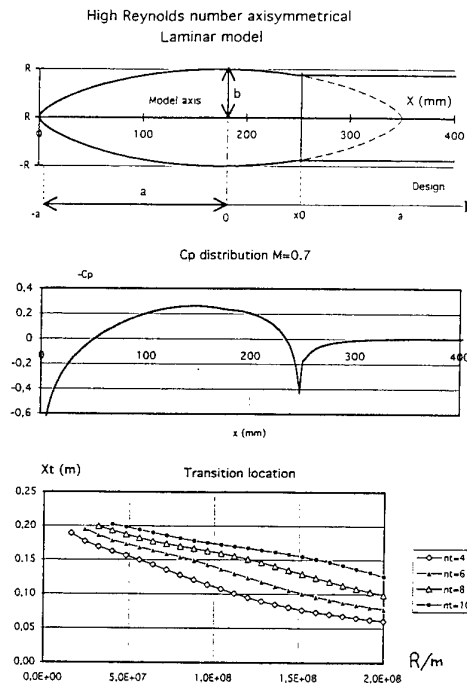


Fig. 10 : High Reynolds number axisymmetrical laminar model for cryogenic tunnels.

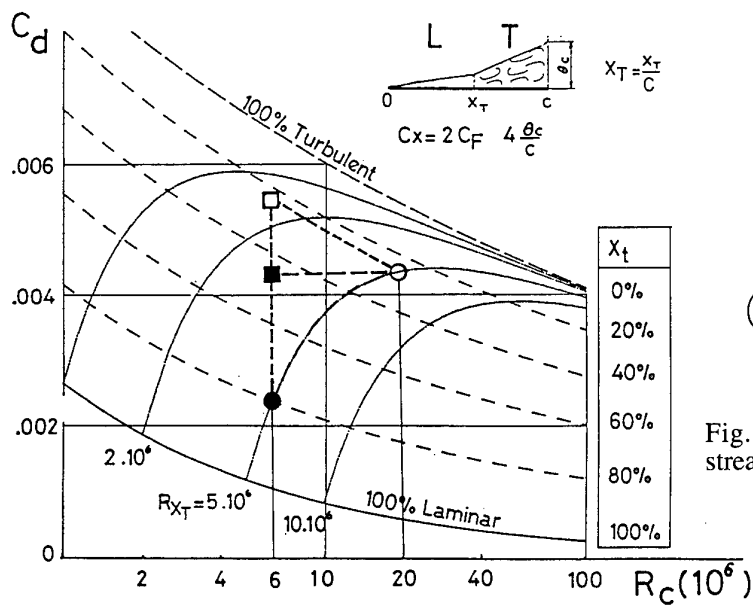


Fig. 11 : Basic Reynolds number effects on a flat plate with fixed or free transition. Problems to simulate high Reynolds numbers.

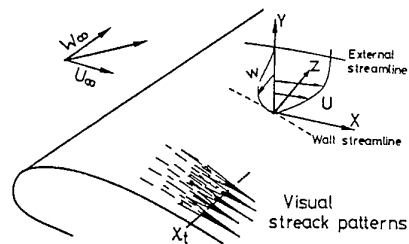


Fig. 12 Cross-flow instability on a wing streak pattern.

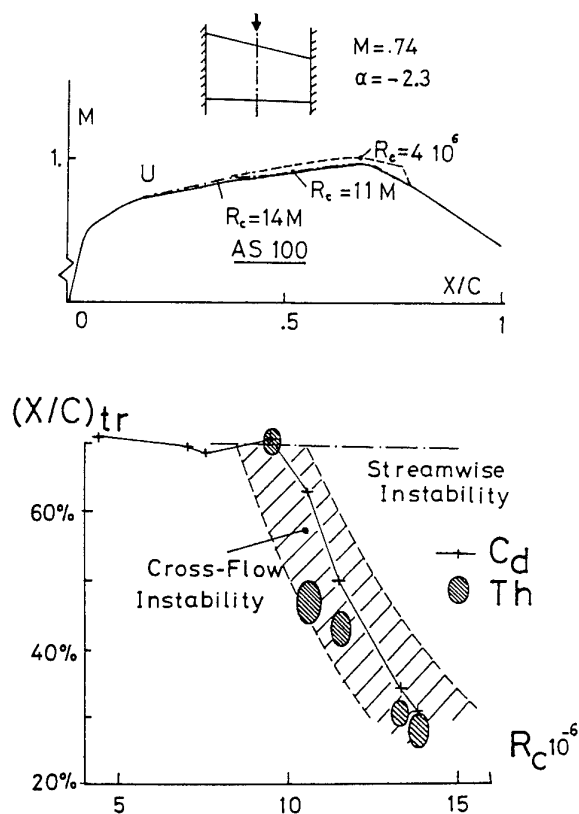


Fig. 13 : Experimental results from T2 with cross-flow instability on a AS100 swept wing :  $M=0.74$   $\alpha=-2.3^\circ$   $T_t = T_{amb.}$  to 124 K.

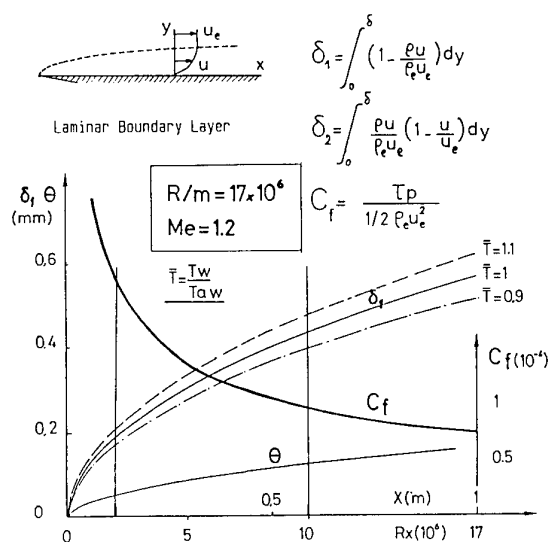


Fig. 15 : Laminar boundary layer development on a flat plate at  $M = 1.2$ .

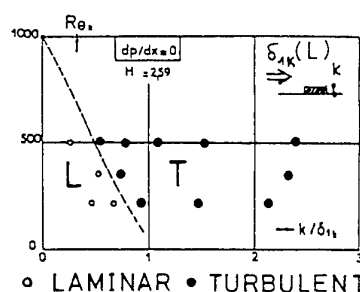


Fig. 14 : Effects of a 2D wall roughness : critical size fixing the transition.

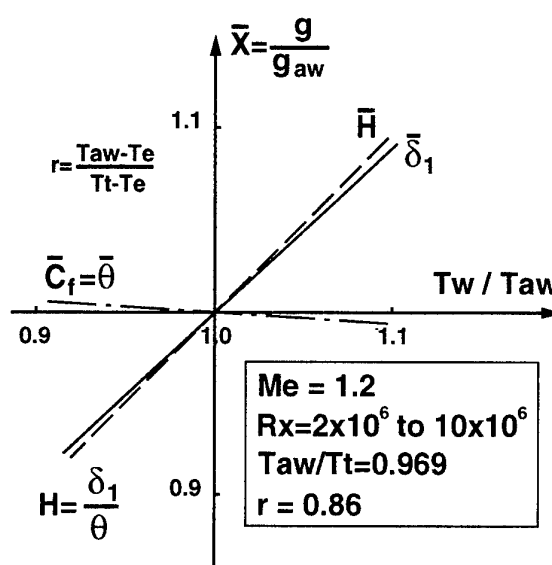


Fig. 16 : Wall temperature effects on a laminar boundary layer at  $M = 1.2$ .

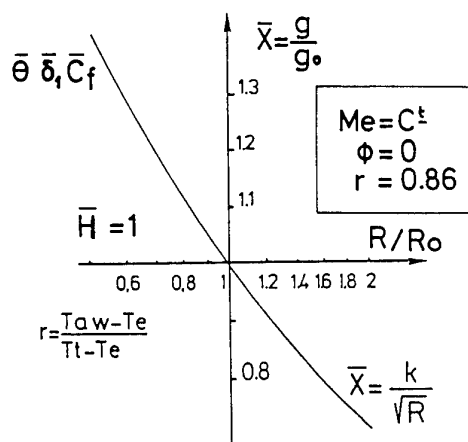


Fig. 17 : Reynolds number effects on a laminar boundary layer with an adiabatic wall.

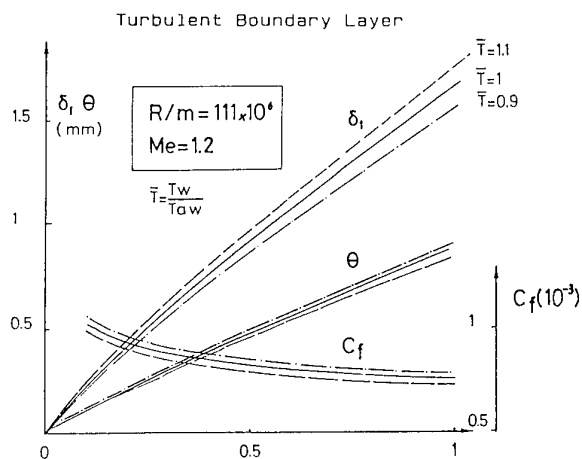


Fig. 18 : Turbulent boundary layer development on a flat plate at  $M = 1.2$ ,  $R/m = 110 \times 10^6$ .

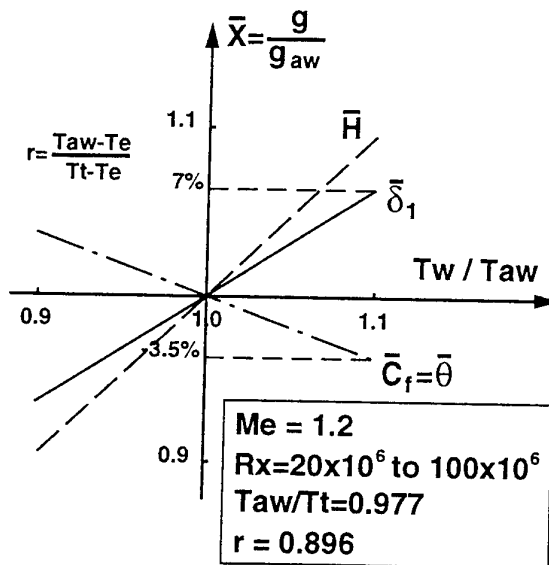


Fig. 19 : Wall temperature effects on a turbulent boundary layer at  $M = 1.2$ .

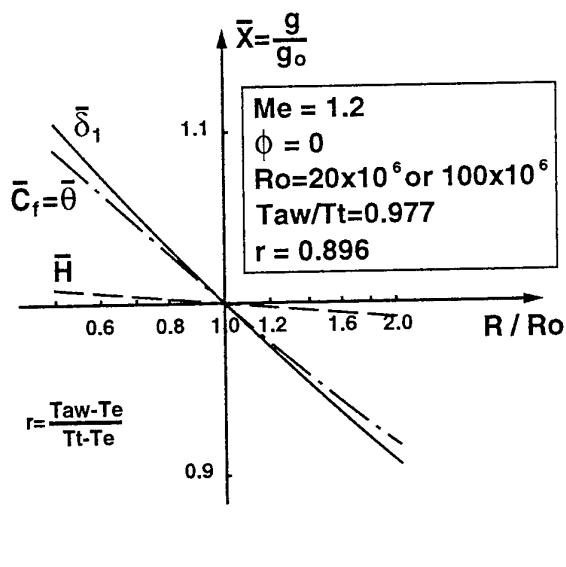


Fig. 20 : Reynolds number effects on a turbulent boundary layer at  $M = 1.2$  with an adiabatic wall.

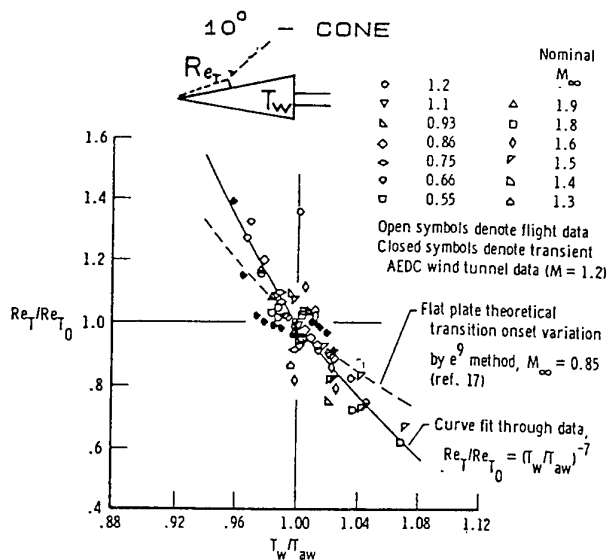


Fig. 21 : Wall temperature effects on the transition Reynolds number on a  $10^\circ$  cone : experimental and theoretical results.

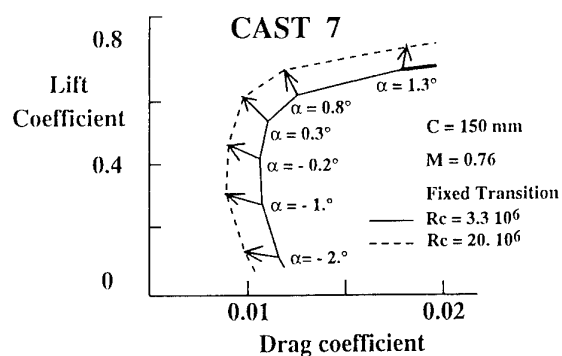


Fig. 22 Polars showing Reynolds effects on lift and drag.

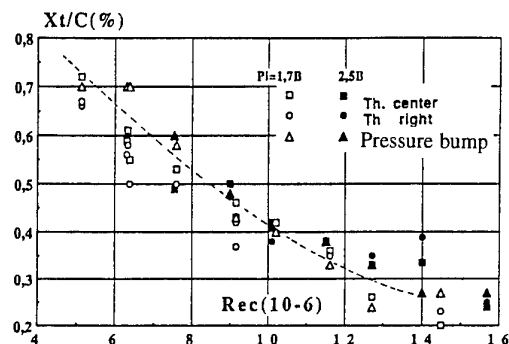
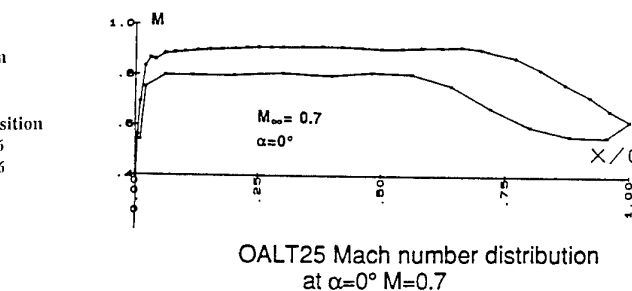
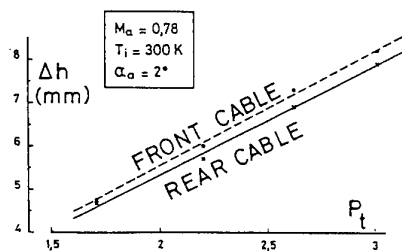
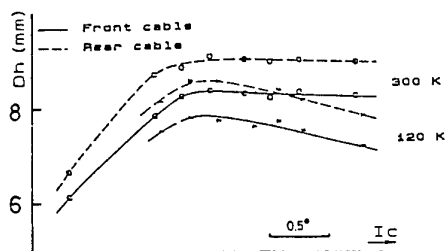
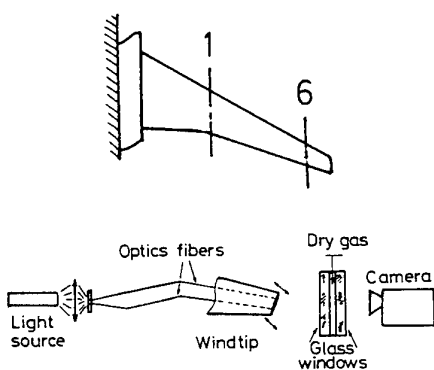


Fig. 23 OALT25 Experimental transition location at  $M=0.7$   $\alpha=0^\circ$  versus Reynolds number.

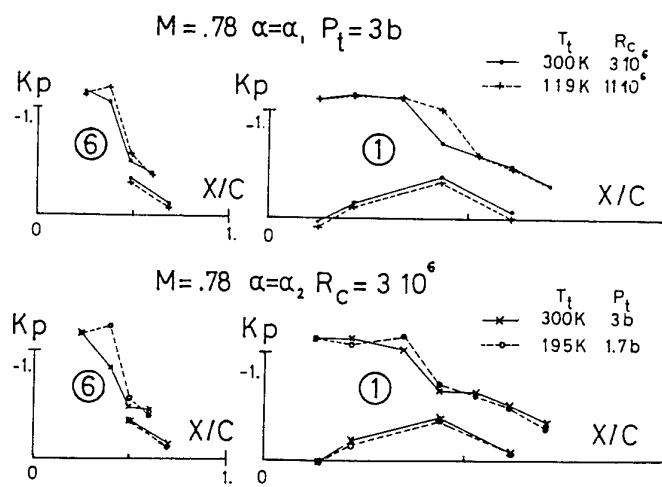


Fig. 24 : Airbus type half model : wing tip displacement measured by an optic system.



# THE CRYOGENIC LUDWIG-TUBE TUNNEL AT GÖTTINGEN

H. Rosemann  
 Institut für Strömungsmechanik  
 Deutsche Forschungsanstalt für Luft- und Raumfahrt e. V.  
 Bunsenstraße 10  
 D-37073 Göttingen  
 Germany

## 1 SUMMARY

The Cryogenic Ludwig-Tube of DLR at Göttingen (KRG) is a blow-down wind tunnel designed for high Reynolds number research in transonic flow. Temperatures down to 100 K and stagnation pressures up to 1 MPa are applied to achieve Reynolds numbers of up to  $60 \cdot 10^6$  (2-D) based on a model chord of 150 mm.

In 1994, a new test section with 2-D adaptive walls was installed, after the performance of the KRG had been evaluated with a relatively simple slotted wall test section.

This paper gives an overview over the Ludwig-Tube concept and describes the design and operation of the facility as well as the main components with special emphasis on the new 2-D adaptive wall test section and the adaptation method.

Two techniques to determine transition under cryogenic conditions have been tested and will be presented. Finally, results of the calibration program and some comparative airfoil testing including a Reynolds number study on a laminar-type airfoil will be shown.

## 2 LIST OF SYMBOLS

### Symbols

$C$	Integration path
$c$	Chord length
$c_p$	Pressure coefficient
$c_D$	Drag coefficient
$c_L$	Lift coefficient
$E$	Voltage
$e$	Fluctuating voltage
$\Delta H$	Wall deflection
$L$	Storage tube length
$l$	Test section length
$M$	Mach number
$p$	Pressure
$Re$	Reynolds number
$T$	Temperature
$t$	Time
$U, V$	Velocity components
$x$	Streamwise coordinate
$y$	Wall distance
$z$	Complex coordinates

### Greek Symbols

$\alpha$	Model angle of attack
$\beta$	Prandtl factor $\beta = \sqrt{1 - M_\infty^2}$
$\xi, \eta$	Coordinates
$\zeta$	Complex coordinates

### Indices

0	Stagnation condition
---	----------------------

1	Condition in the storage tube
$c$	Charge condition
$C$	Condition on the integration path $C$
$\infty$	Free stream condition

## 3 INTRODUCTION

When it was decided to build a new transonic high Reynolds number facility at DLR in Göttingen, the Ludwig-Tube concept, published by Ludwig in 1955 (Ref. 1), was chosen for a number of reasons. The simple design of a Ludwig-Tube, as will be seen below, keeps capital costs low and promises at the same time good flow quality, because many of the components causing disturbances in conventional wind tunnels, like the fan, turning vanes *etc.*, are simply not present.

Because of the intermittent working principle, the costs for cryogenic operation, mostly determined by the consumption of liquid nitrogen, can also be kept small compared to continuously running wind tunnels.

A drawback of a Ludwig-Tube tunnel is certainly the short testing time, posing problems to some measurement techniques. Also, the boundary layer developing in the storage tube can have an adverse effect on the flow quality in the test section.

The KRG was first equipped with a slotted wall test section. Tests and calibration runs were carried out to verify the concept and evaluate the performance of the KRG in the full range of operating temperatures. Some comparative airfoil measurements were also performed. In the following, a second test section with 2-D adaptive walls was designed and manufactured to enhance the quality of experimental results by eliminating interferences from the top and bottom wall. The adaptive wall test section also allows to test larger models, further increasing the Reynolds number and adding some supersonic capability to the facility, as will be explained in Sec. 4.3.5. The installation was finished in summer 1994.

The operation of the adaptive wall test section with the corresponding adaptation method and results from the calibration experiments and from some airfoil tests will be shown in Sec. 5.3 and 8.2.

## 4 DESIGN AND OPERATIONAL CHARACTERISTICS OF THE KRG

### 4.1 Operating Principles of a Ludwig-Tube Tunnel

A Ludwig-Tube consists basically of a long storage tube, a converging nozzle followed by the test section, a valve, and a dump tank. The gas dynamic process of the facility is explained in Fig. 1 by means of an  $x, t$ -diagram. Before the run, the storage tube including all components upstream of the valve are charged to the desired pressure  $p_c$ , whereas the dump tank is kept at atmospheric or lower pressure. Upon opening the valve an expansion fan travels upstream into the tube accelerating the gas to a Mach number  $M_1$  which is determined by the area ratio of the tube to the

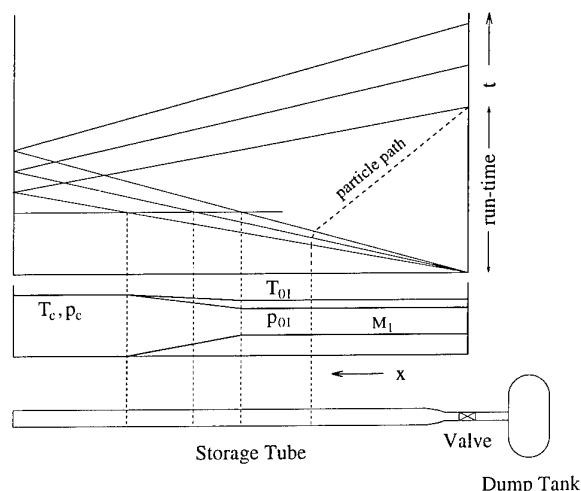


Figure 1: x,t-diagram of a Ludwieg-Tube

sonic throat in the valve. Equally, the Mach number in the test section is given by the area ratio of the test section to the sonic throat. The usable run time is terminated by the time the expansion fan, after being reflected at the end of the tube, returns to the test section and the valve is closed again. Between these two passages of the fan, all flow parameters in the test section remain constant as long as viscosity effects can be neglected.

During the passage of the expansion waves, the stagnation temperature  $T_{01}$  and pressure  $p_{01}$  drop below the pre-test charge values (denoted by the index c), see Fig. 1. Fig. 2 shows the ratios  $p_{01}/p_c$ ,  $T_{01}/T_c$ , the Mach number in the tube,  $M_1$ , and the length  $\Delta L/L$  of the gas column passing through the test section as functions of the test section Mach number  $M$  for a nozzle contraction ratio of 3.6 which applies to the KRG.

## 4.2 Specifications

The basic requirement for the design of the wind tunnel was to obtain a Reynolds number of at least  $50 \cdot 10^6$  on an airfoil model of 150 mm chord at transonic speeds. For an adaptive wall test section with flexible top and bottom walls the chord may be increased to 200 mm. From this, the main dimensions of the test section have been determined to be 400 mm width, 350 mm

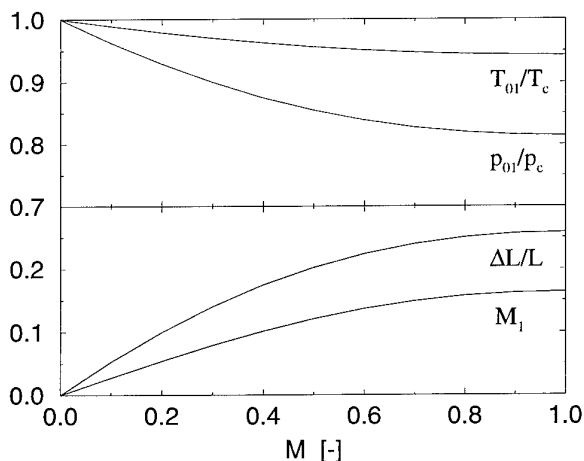


Figure 2: Characteristic flow parameters as function of the test section Mach number

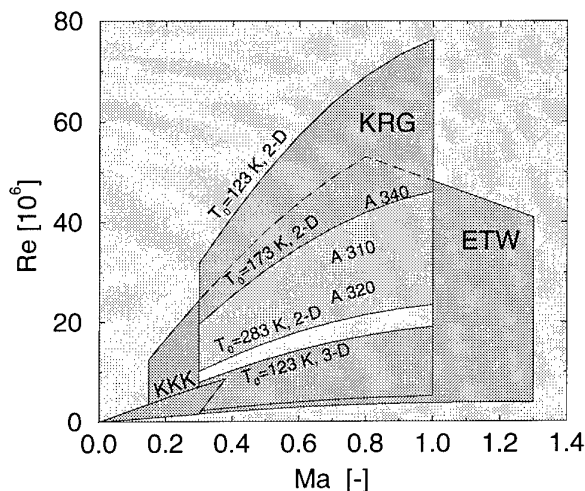


Figure 3: M,Re-diagram of the KRG

height and 2000 mm length. For wall mounted models a relatively high maximum stagnation pressure of 1 MPa is possible yielding the desired Reynolds numbers at a stagnation temperature of 120 K. In Fig. 3 the M,Re-envelope is given for 2-D and 3-D models in comparison with the envelope of the ETW (3-D) and KKK (3-D).

The design goal of a 1 s run time at cryogenic temperatures resulted in a charge tube length of about 130 m. The instationary boundary layer developing behind the expansion wave in the tube influences the flow quality in the test section. To keep this effect, which also depends on the length of the tube (*i.e.* run time), sufficiently low, the contraction ratio has been chosen to be 3.6, yielding a tube diameter of 0.8 m and a boundary layer displacement thickness at cryogenic temperatures of less than 4% of the tube radius.

## 4.3 The Present Ludwieg-Tube Design

### 4.3.1 General Description

A sketch of the general tunnel arrangement is given in Fig. 4. All components are mounted on rolls or sliding supports to account for the thermal contraction due to the cooling. The reaction forces are taken by two thrust stands located upstream of the gate valve and downstream of the bellows, the latter compensating for changes in length between these two points.

The entire wind tunnel has been manufactured of stainless steel (German standard X 10 CrNiTi 189) except the nozzle and the part downstream of the test section, which have been made of cast steel.

The external insulation of the tube consists of an inner layer of mineral wool and an outer layer of polystyrene covered by a vapor barrier with a total thickness of 200 mm and an aluminum sheeting. A nitrogen purge system maintains the entire insulation at a low over-pressure to preclude entry of air or moisture. Figure 5 shows a photograph of the various layers of the tube insulation. All tunnel components are mounted on insulating wooden connections.

The cool-down of the facility upstream of the control and fast-acting valve is carried out by circulating cold nitrogen by means of a blower using three feeding location and a return tube as indicated in Fig. 4. The gas is cooled before it enters the wind tunnel by spraying liquid nitrogen into the circulation tubings. The speed in the main tube is high enough to achieve a uniform cir-

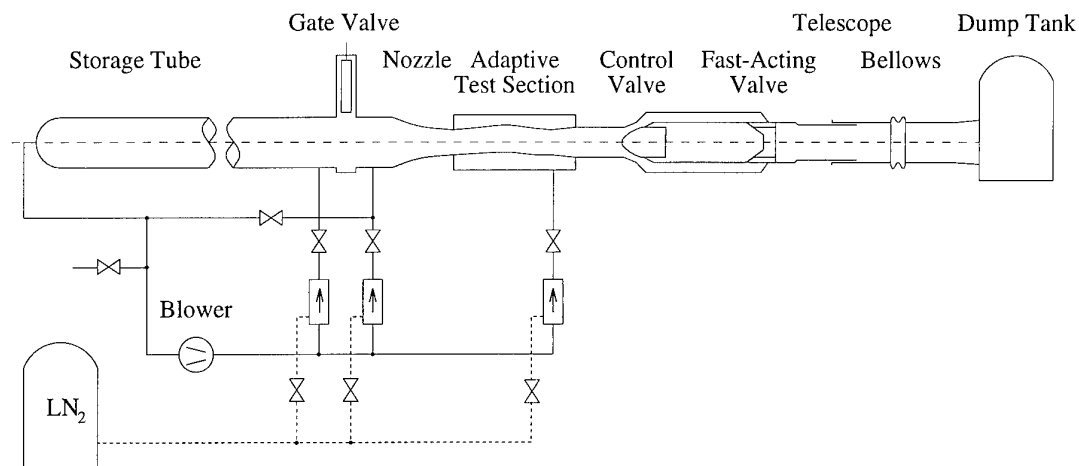


Figure 4: General arrangement of the Cryogenic Ludwig-Tube (KRG)

cumferential and longitudinal temperature distribution. Hence, a vertical temperature stratification is avoided and the temperature is constant during a run. The pressure is adjusted by an exhaust valve.

#### 4.3.2 Gate Valve and Nozzle with Boundary Layer Bleed System

The gate valve upstream of the nozzle separates two charging and temperature conditioning loops: tube and test section (*i.e.* model) temperature can be adjusted independently offering the possibility of preconditioning the model to the correct temperature (or any other desired value). In addition, the gate valve prevents air from entering the tube when the test section is opened or removed.

To compensate for the effects of the instationary boundary layer in the tube on the flow quality in the test section, a boundary layer bleed system has been installed at the entrance of the nozzle, Fig. 6.

A sliding cylinder, moving from the annular space surrounding the nozzle in upstream direction and thereby covering the openings left by the gate and the feeding ring, opens an annular gap which allows the boundary layer to enter the low pressure annulus. The bleed mass flow rate can be controlled by adjusting the gap width according to the boundary layer displacement thick-

ness.

The fixed contour nozzle is made of austenitic cast steel. The cross section changes from a circle at the lip of the bleeding system to a rectangle of 400 mm by 350 mm at the exit.

#### 4.3.3 Control Valve and Fast-Acting Valve

The run of a Ludwig-Tube wind tunnel is controlled by the quick-opening valve which starts the flow and the sonic-throat diffuser which determines the Mach number in the test section. Both functions have been combined in the fast-acting control valve sketched in Fig. 7.

The valve assembly consists of an enlarged tube with a center body which contains two hydraulic actuators operating the control cone and the sleeve valve. The control cone can reproducibly be positioned with an accuracy of 0.01 mm in order to adjust the test section Mach number with an accuracy of better than 0.001. The sliding cylinder at the rear of the valve starts the flow. The opening time can be adjusted to be less than 0.1 s.

The center-body is ventilated to the atmosphere and insulated on the inside; the temperature is controlled by electric heating. Figure 8 shows the hydraulic actuator of the fast-acting valve in the center body.

#### 4.3.4 The Slotted Wall Test Section

This first test section was mostly built for the verification of the tunnel concept, calibration and some comparative airfoil meas-

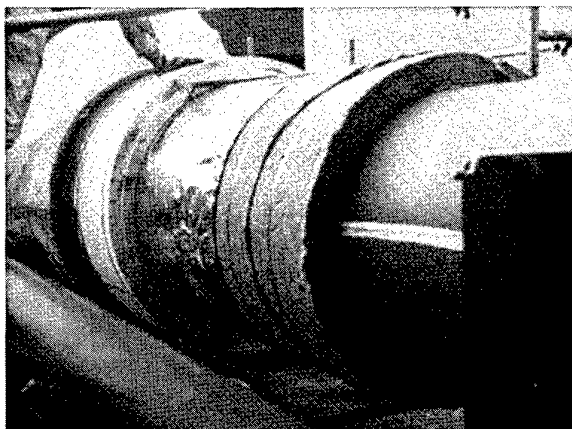


Figure 5: Insulation of the storage tube

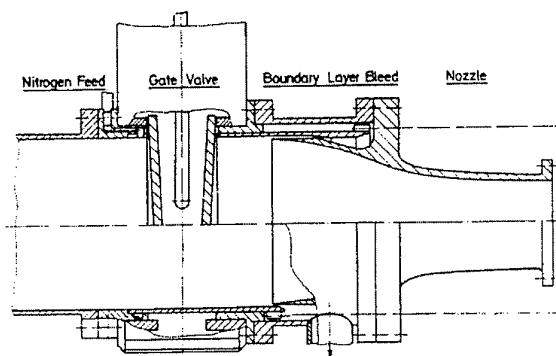


Figure 6: Gate valve and nozzle with boundary layer bleed system

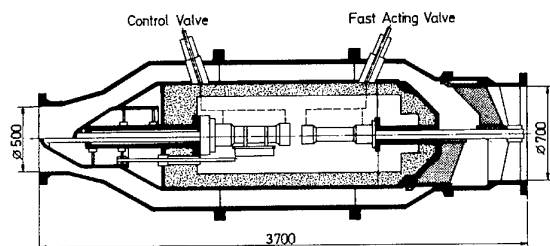


Figure 7: Fast-acting control valve

urements. The cross section is  $0.4 \times 0.35 \text{ m}^2$  and the length 2 m. Top and bottom walls are slotted with an open area ratio of 3% based on top and bottom wall area, the solid side walls are equipped with turntables for 2-D model support. Figure 9 shows the simple design with a circular pressure shell and openings for the installation of the model and movable probes. To reduce the time necessary for pressure equalization during start-up, the empty space between the inner test section walls and the circular pressure shell has been filled with wood, indicated by the dotted areas in Fig. 9. Slots in the rear part of the side walls provide the necessary openings for this equalization process. Pressure tabs are installed along the center lines of each wall.

#### 4.3.5 The Adaptive Wall Test Section

The new adaptive wall test section can be easily exchanged with the slotted wall test section *via* quick locking devices since the main dimensions were kept identical and no other modifications to the tunnel are necessary.

The pressure shell of the adaptive wall test section is again circular, but here it consists of four sectors to be clamped together, thus alleviating the assembly of the flexible walls. A longitudinal section and a cross sectional view is sketched in Fig. 10. The flexible walls are made of glass and carbon fiber epoxy with a thermal expansion coefficient matched to steel and can be adjusted by means of 19 jacks each operated by stepper motors outside the wind tunnel shell under ambient conditions. The jacks

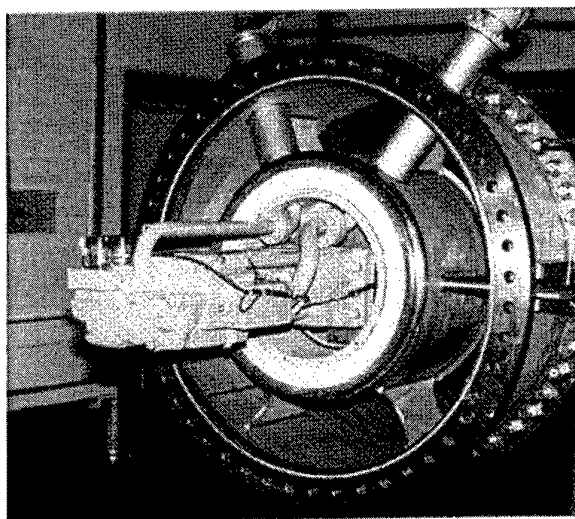


Figure 8: Hydraulic actuator of the fast-acting valve

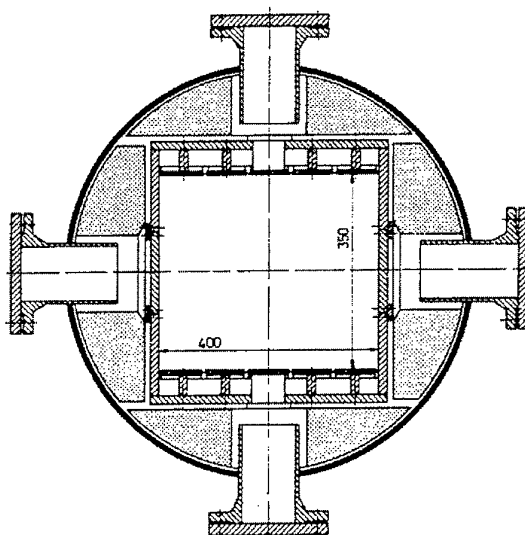


Figure 9: Sectional view of the slotted wall test section

are electrically heated to avoid damage to the seals due to ice building up on the moving parts. The maximum deflection of the flexible walls is  $\pm 45 \text{ mm}$ . This allows also to use the upstream part of the wall as an extension of the nozzle with a convergent and a divergent section, so that the Mach number range of the facility can be extended to about  $M_\infty \approx 1.5$ . In this case the model will be installed at a second mounting position 45 cm further downstream of the usual position, which is at approximately  $x/l = 0.5$  in the test section. A photograph of the interior of the test section with the walls and the drive system is given in Fig. 11.

The stepper motors are connected to the flexible walls through an additional gear box with a 10:1 gear ratio and self-locking spindles. Thereby all motors can be switched off during the experiment to eliminate the chance of disturbing other sensor signals by the very noisy electronic stepper motor power supplies.

The control of the adaptive walls and the adaptation scheme is described below in Sec. 5.2 and 5.3.

## 5 WIND TUNNEL CONTROL AND DATA ACQUISITION/EVALUATION

### 5.1 Operating and Control of the Facility

All functions that are necessary to run the wind tunnel and vital to the safety of the facility are monitored and controlled by a special process control computer. This includes the hydraulic

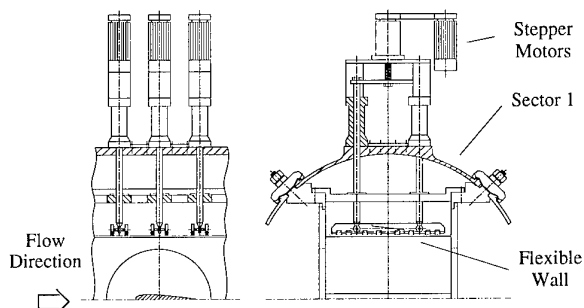


Figure 10: Sketch of the adaptive wall test section

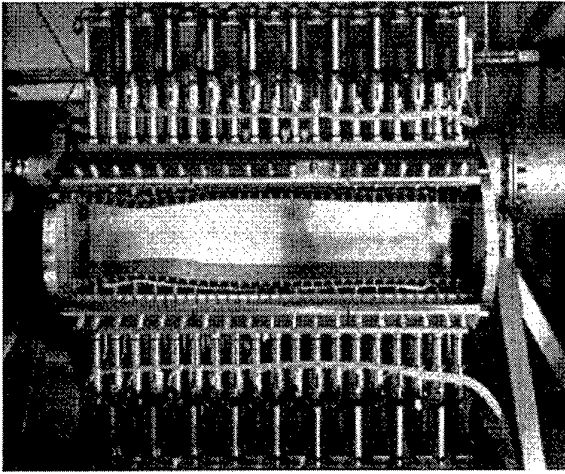


Figure 11: Adaptive wall test section

and pressurized air supply stations, the blower, temperature and pressure in the facility, the supply with gaseous and liquid nitrogen, and the various valves shown in Fig. 4. The oxygen level at a number of stations in the building is also measured. Figure 12 shows the display panel, the monitors and the control panel connected to the control computer. The facility is mostly operated by manual inputs to the computer using the control panel. Pressure can be regulated automatically, but the cool-down process and the temperature is controlled by the tunnel operator. The run is performed by opening the fast-acting valve for the specified duration. Currently no control is carried out during the run.

The data acquisition is performed separately from, but synchronized with the control computer by PC-based systems for pressure measurements and analog voltage inputs. The raw data are transferred over the network to a unix system where the final data analysis is carried out. For the evaluation of the model data as well as for the computation of the adapted wall contours the software package "dark" (Datenauswertung für Rohrwindkanäle) was written for the KRG. The test results are obtained within a few minutes after the run and are typically presented on the screen as shown in Fig. 13.

## 5.2 Instrumentation and Control of the Adaptive Wall Test Section

The layout of the control of the flexible walls was guided by the fact that during the short test time no adjustment of the walls would be necessary (and possible). Therefore multiplexers are used both to connect the stepper motors to one electronic power unit for each wall and also to measure the outputs from the pos-

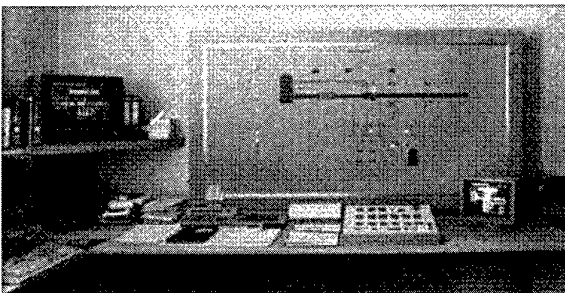


Figure 12: Display and input panels of the control computer

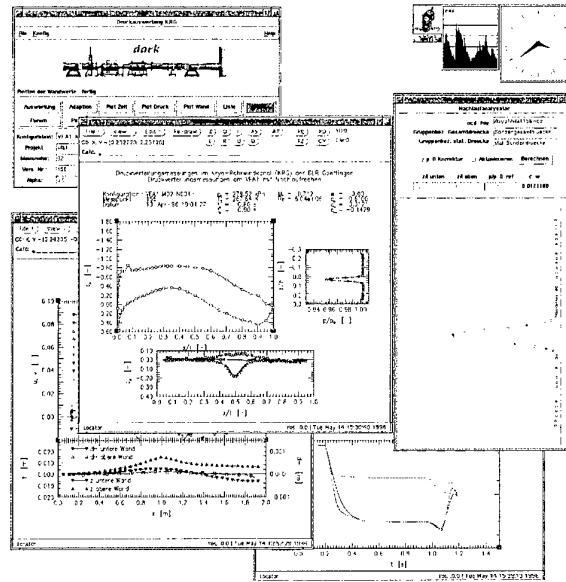


Figure 13: On-line data analysis software "dark"

itional sensors, thereby reducing costs considerably. The instrumentation and control of the flexible walls is shown schematically in Fig. 14.

Since the accurate information about the position of a stepper motor is lost when it is disconnected from the power supply, a completely independent position sensing system was provided. The position of the wall is measured by a combination of a linear and an angular sensor mounted to each of the 19 jacks so that deviations occurring during the switching can be corrected. Even after a complete power failure the position of the flexible wall can be determined without having to perform calibration runs of the stepper motors.

The nominal resolution of the stepper motors setting the position of the wall is  $0.2 \mu\text{m}$ , the theoretical accuracy of the combined sensors  $2 \mu\text{m}$ . However, in reality the resolution is limited by the mechanical construction, designed to set and determine the position with an accuracy of about  $0.1 \text{ mm}$ .

For the adaptation scheme described in the next section the wall contour and the wall pressure distribution have to be known.

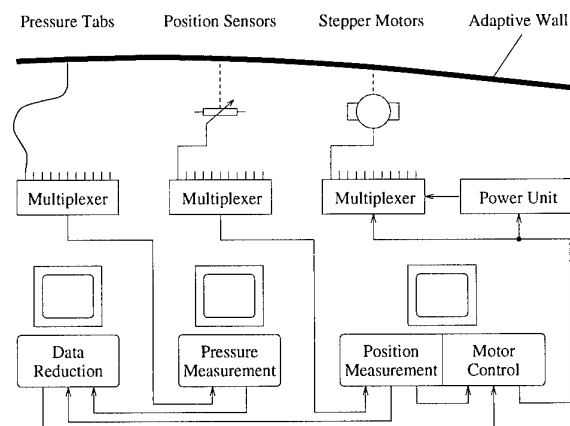


Figure 14: Instrumentation and positioning of the flexible wall

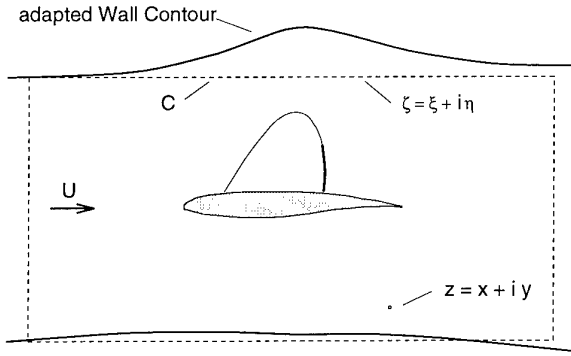


Figure 15: Wall adaptation based on Cauchy's integral formula

Therefore, both top and bottom wall are equipped with three stream-wise rows of 42 pressure tabs in each row. The three parallel rows provide also the spanwise information necessary for 3-D adaptation schemes, which are planned to be used in the future.

### 5.3 The Adaptation Procedure

Since the flexible walls of the KRG can not be adjusted during the short run time, using an iterative adaptation procedure would require a large number of runs to produce one interference-free result. Therefore, a single step method based on the Cauchy's integral formula:

$$f(z) = \frac{1}{2\pi i} \oint_C \frac{f(\zeta)}{\zeta - z} d\zeta \quad (1)$$

with:

$$\zeta = \xi + i\eta; \quad f(\zeta) = U_C - iV_C \quad (2)$$

and:

$$z = x + iy; \quad f(z) = U - iV \quad (3)$$

is applied for 2-D adaptation (Ref. 2). Equation (1) allows the computation of the velocity components  $U$  and  $V$  at any point  $(x, y)$  inside a closed curve  $C(\xi, \eta)$  by integrating the velocity components  $U_C$  and  $V_C$  along  $C$ , see Fig. 15. For adaptation purposes, the integration path  $C$  is chosen to consist of the upper and lower wall as well as of the inlet and outlet cross section of the test section, enclosing the model. Furthermore, it is assumed that the flow in the test section can be described as a superposition of the velocity field induced by singularities representing the model and of singularities representing the wall interferences. Then Eq.(1) can be used to compute the wall induced velocities inside the test section because it can be shown (cf. Ref. 3), that singularities within  $C$  do not contribute to the value of the integral. So the result of Eq.(1) is only determined by those singularities located outside of  $C$ , representing the wall influence.

For an adaptation process first the velocity components  $U_C$  and  $V_C$  are determined from wall pressure measurements and the slope of the walls. For the in- and outflow conditions appropriate assumptions have to be made. Then, the wall-induced velocities at the position of the walls can be computed using Eq.(1). The wall influence is canceled by deflecting the wall by an angle of the same size as given by the wall-induced velocity components, but with opposite sign. The next run with the adjusted wall contours should give the interference-free results.

This method is limited to flows that can be described by the linearized potential equations, at least in the proximity of the walls.

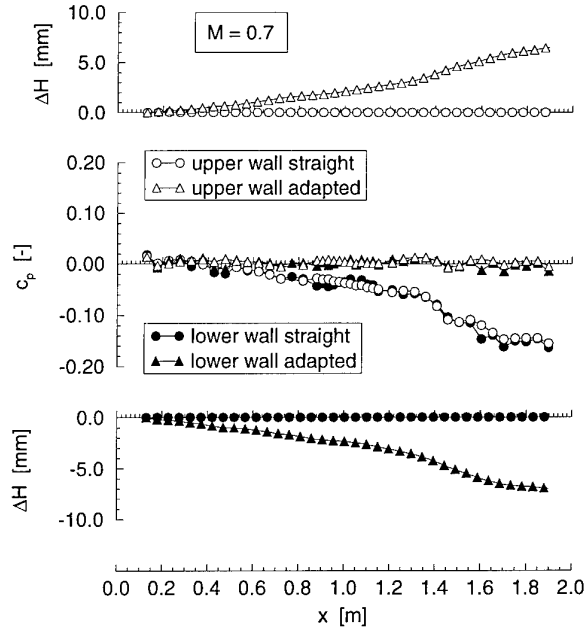


Figure 16: Adaptation of the empty test section

Compressibility effects are taken into account by the Prandtl-Glauert rule. It is therefore to be expected, that for flows with separated regions or large supersonic flow regimes and strong shocks the results will become less accurate. However, it was found that even though an interference-free wall contour is not achieved in a single step under all circumstances, the algorithm still converges, so that interference-free results can be obtained for the prize of some additional runs.

The adaptation procedure was first tested out in the empty test section, only equipped with a wake rake. Figure 16 shows the wall contours and wall pressure distributions before and after the adaptation. The first run with straight walls shows the acceleration of the flow due to the boundary layer development at the test section walls. At about  $x = 1.4$  m the displacement effect of the wake rake mounted on a sting on the test section axis becomes visible. Using the pressure distribution as input for Eq.(1), the wall displacement shown in Fig. 16 was computed and the wall adjusted accordingly. The second run resulted in a nearly constant pressure distribution along the walls.

It might be surprising, that although no correction for the boundary layer displacement thickness had been applied, a constant pressure distribution was obtained. This is obviously the case because the influence of the boundary layer is mostly noticeable in the flow acceleration. Using the slope of the real wall instead of the one corrected with the boundary layer displacement thickness to compute the velocity components  $U_C$  and  $V_C$  for Eq.(1) from the pressure distribution is nearly exact for  $U_C$  and only leads to small errors in  $V_C$ , since the boundary layer is growing only slowly. Recent tests show, that taking into account a reasonably estimated boundary layer displacement thickness changes the computed wall contour only by about 0.2 mm at the position of the model at  $x = 1$  m.

An example for a wall adaptation with model is shown in Fig. 17. The pressure distributions at the model and at the walls show large differences between the first run carried out with straight walls and the fully adapted case, achieved with the second iteration. Very obvious is the velocity increase at the suction side of the model and the upper test section wall due to the straight

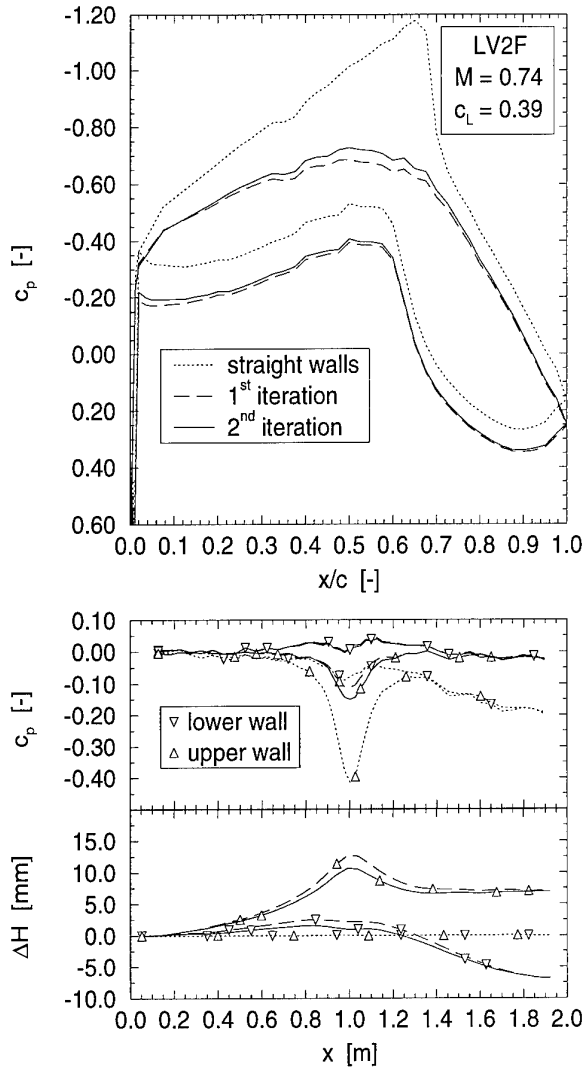


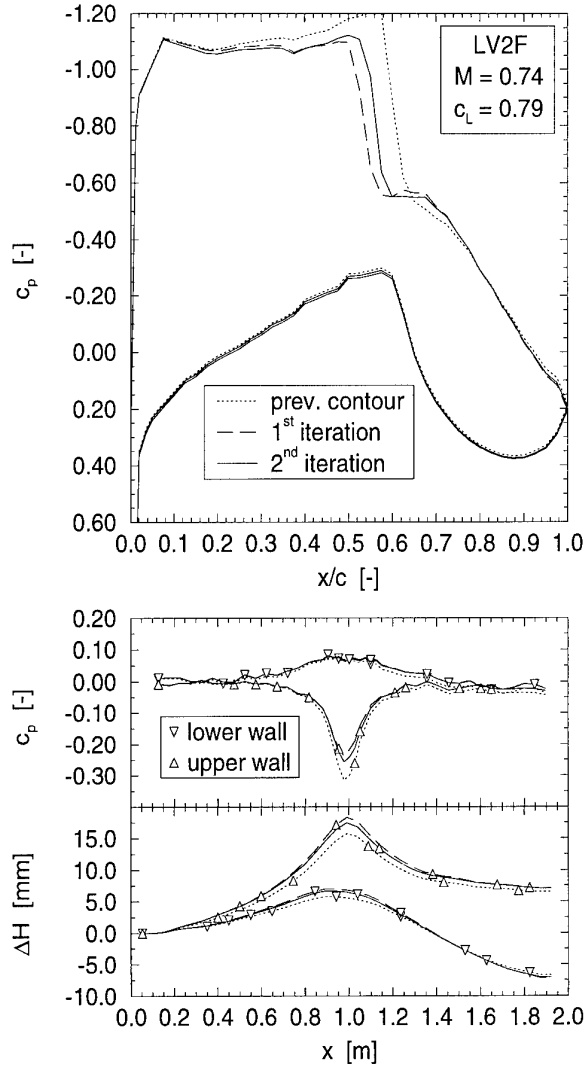
Figure 17: Adaptation starting from straight walls

channel, but, the flow at the walls is still sub-sonic ( $c_p^* = -0.63$  for  $M = 0.74$ ). The pressure distributions at the walls also show the acceleration of the flow before adaptation because of the growth of the wall boundary layers. Again, no boundary layer displacement effect was considered.

For these large wall displacements, adaptation is not achieved in one step. The first iteration brings the wall already close to the final contour, but a slight overshoot has to be corrected in a second step. A third iteration would require wall adjustments of less than 0.2 mm, so that the adaptation is considered to be complete after the second step. Lift changes by  $\Delta c_L = 0.007$  and drag by  $\Delta c_D = 0.0001$  from the first to the second iteration.

Typically, one would of course not start each run with straight walls. More representative for wind tunnel practice is the second example shown in Fig. 18. Here, an  $\alpha$ -sweep was carried out at constant Mach number with  $\Delta\alpha = 0.5^\circ$ . Only small adjustments of the wall contour are necessary from one point of the polar to the next and at these Mach numbers full adaptation is achieved in one step up to moderate lift conditions.

However, Fig. 18 shows a high lift case, where again two iterations are necessary to reach a converged solution for the wall contour. Further adjustments would be less than 0.2 mm. It can

Figure 18: Adaptation starting from the previous point of an  $\alpha$ -sweep

be seen, that the position of the shock is very sensitive to small changes of the wall contour, whereas the other regions of the pressure distribution remain nearly unchanged between the first and the second step.

The iteration is usually performed until further wall adjustments are within the mechanical tolerances of wall construction, or the changes of the results, *e.g.* the force coefficients are within the limits of the required accuracy given by Ref. 4.

For the adaptation of the 2-D flexible wall for 3-D flow experiments other methods (*e.g.* Ref. 5) are available and will be applied in the future.

## 6 CALIBRATION AND FLOW QUALITY

An extensive calibration and validation program was carried out in the slotted test section. First pressure measurements revealed a streamwise pressure gradient in the empty test section. Adjusting the divergence of the upper and lower walls appropriately resulted in a constant streamwise Mach number distribution, Fig. 19. A typical airfoil model (150 mm chord length) would extend from  $x/l = 0.469$  to  $x/l = 0.563$ . Towards the end of the straight section at  $x/l = 1$  the Mach number

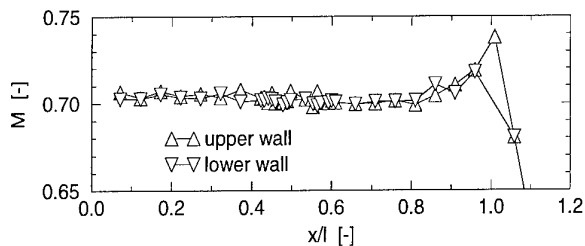


Figure 19: Streamwise Mach number distribution in the slotted wall test section

increases somewhat due to boundary layer growth and inflow from the plenum, before the flow is decelerated in the diffuser at  $x/l > 1$ .

The influence of Mach and Reynolds number on the Mach number at the model position at  $x/l \approx 0.516$  is shown in Fig. 20. There seems to be a slight decrease in Mach number with increasing reference Mach number. For the Reynolds numbers that could be realized with different temperature/pressure combinations no systematic influence of the temperature is visible. The bandwidth of  $\pm 1.5\%$  of the curves in Fig. 20 results in a Mach number deviation of  $\Delta M = \pm 0.001$  at  $M = 0.7$  satisfying the requirements given by Ref. 4. In the meantime, the general accuracy of the pressure measurements could be further enhanced, so that a repeat of these measurements would very likely result in even smaller deviations.

A number of hot-wire measurements have been performed in the test section to determine the turbulence level in the flow. However, calibrating hot wires under the experimental conditions of the KRG is a very difficult task. So far, hot wire signals could be obtained down to cryogenic temperatures, but only a qualitative evaluation was possible, yielding already an interesting result. Figure 21 shows time traces of hot-wire signals measured in the test section at the streamwise model position and various distances from the side wall. Depending on the wall distance, a sudden occurrence of larger fluctuations is observed at different times.

In Fig. 22 the wall distance is plotted against the time of the onset of these fluctuations measured at different Mach numbers in the range of  $0.3 \leq M \leq 0.8$  and charging pressures between 300 kPa and 600 kPa. All points fall, more or less, onto a single straight line with its origin at about the time of the start of the flow. Because of the difficulties mentioned above the magnitude and structure of these fluctuations could not yet be determined. However, it seems reasonable to assume that they stem from the

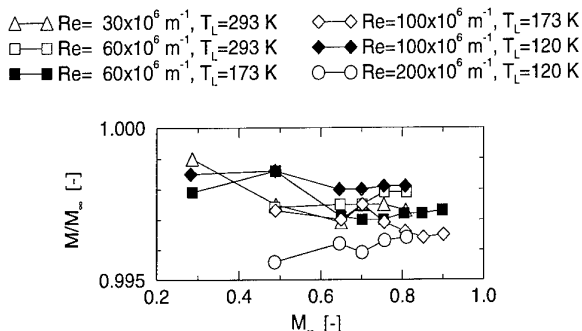


Figure 20: Mach number variation at the model position in the slotted wall test section

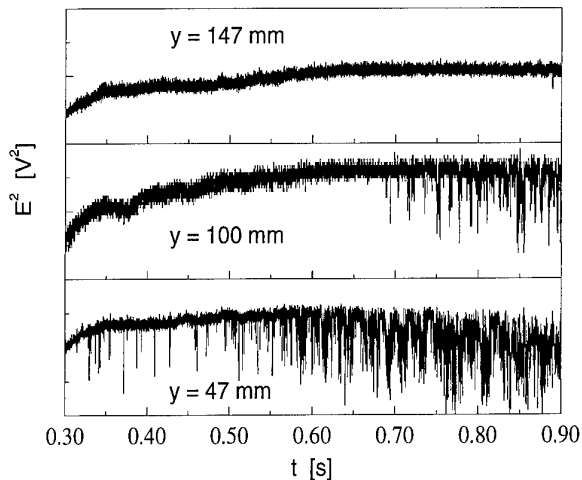


Figure 21: Hot-wire signals at different wall distances

instationary turbulent boundary layer that develops in the storage tube behind the expansion wave.

The boundary layer thickness at the tube exit grows from zero at the start of the run to at least about 50% of the tube radius at the end of the run. Even though it decreases to virtually zero in the nozzle, as calculations and experiments show, some of the flow material now forming the inviscid region in the test section was part of the turbulent boundary layer in the tube and may still have conserved a larger turbulence level. As the interface, which represented the boundary layer edge in the tube, moves across the hot-wire probe, the increase of fluctuations is observed. For these tests, the boundary layer bleed system was not operating.

It has to be mentioned that so far an effect on surface pressure measurements has not been observed. Further experiments, also involving the hot-film technique described in the next section will be carried out in the adaptive wall test section to investigate this phenomenon.

## 7 MEASUREMENT TECHNIQUES FOR TRANSITION DETECTION UNDER CRYOGENIC CONDITIONS

For the correct interpretation of test results, information about the location of the laminar/turbulent boundary transition is very important, especially for laminar-type airfoils. Since well known conventional techniques for transition detection, as thermal imaging and surface mounted hot-films, glued onto the model, are not applicable for low temperatures, two different techniques will be described that have been tested in the KRG.

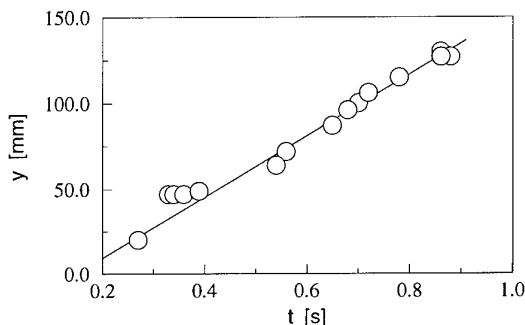


Figure 22: Wall distance over time of intermittency onset in the slotted test section



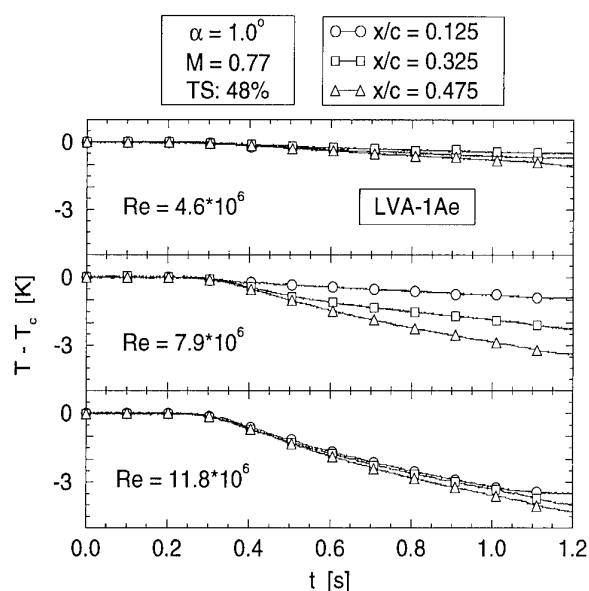


Figure 23: Transition detection by wall temperature measurement

### 7.1 Wall Temperature Measurements by Thermocouples

This technique exploits the difference in the heat transfer from the flow to the model between laminar and turbulent boundary layers. When the flow in a Ludwig-Tube is started, the total temperature drops by a certain amount (cf. Fig. 1 and 2) and the wall underneath a turbulent boundary layer will adjust faster to the new flow temperature because of the higher heat flux yielding a measurable difference in the temperature gradient to the laminar region. This method was already applied in the T2 wind tunnel at ONERA, Toulouse, but had to be adapted to the short run time of the KRG.

For a first test, three thermocouples had been mounted 0.5 mm underneath the skin in the wall with a thickness of 3 mm of the laminar type airfoil model DA-LVA 1Ae designed and built by DASA.

Figure 23 shows the temperature traces of the sensors located at 12.5%, 32.5% and 47.5% chord, respectively, for three different Reynolds numbers. Transition was tripped at 48% chord, just downstream of the third sensor. When the flow starts at about  $t \approx 0.2$  s, very little temperature change over the run time is measured for  $Re = 4.6 \times 10^6$ . At higher Reynolds numbers, larger gradients are observed starting at the most downstream sensor, until at  $Re = 11.8 \times 10^6$  all three sensors indicate a stronger heat flux. This development is an indication for the forward movement of the transition point in this Reynolds number range.

In Fig. 24 the lift and drag coefficients are plotted along with the temperature gradients versus Reynolds number, showing the correlation between the forward movement of the transition and the increase of the drag coefficient between  $Re = 8 \times 10^6$  and  $Re = 10 \times 10^6$ . Obviously, for real measurements the chord-wise resolution has to be improved by placing more sensors in the model than it was possible for these first tests.

### 7.2 Surface Hot-Films Directly Deposited on the Model

Surface hot-films, manufactured on a plastic carrier and then glued on the model surface, are used in conventional wind tunnels to measure wall shear stress and determine transition. However, the sensor types commercially available are not well

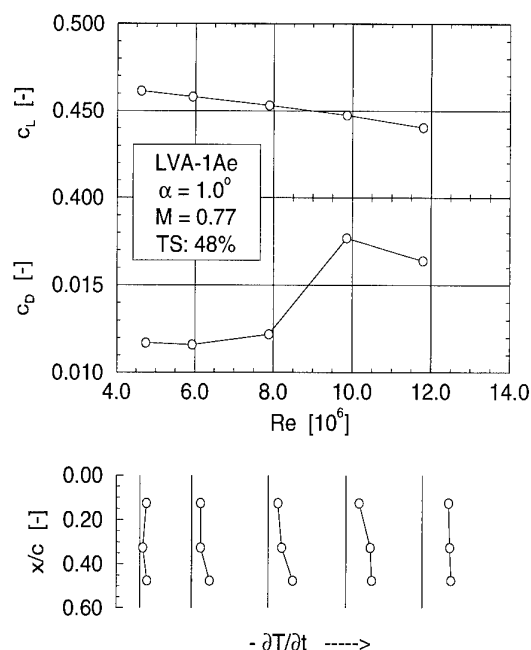


Figure 24: Lift, drag and heat-transfer as function of Reynolds number

suited for an application in a high Reynolds number cryogenic facility since the roughness of the hot-film itself is too high and the gluing poses problems in terms of surface quality, connection of the wires and reliability at low temperatures.

Therefore a technique to directly deposit the hot-film onto the model was developed following the approach of Johnson *et al.* (Ref. 6). Before the sensor itself can be deposited, the steel model has to be coated first with Parylene C, a relatively soft plastic material, providing thermal and electric insulation and compensating for thermal stresses between the model and the following layer of  $SiO_2$  which serves as stable base for the copper leads and nickel sensors. Figure 25 shows the different layers with their approximate thicknesses. All deposition processes have been carried out in vacuum chambers under very low pressure.

After a number of samples had been manufactured and success-

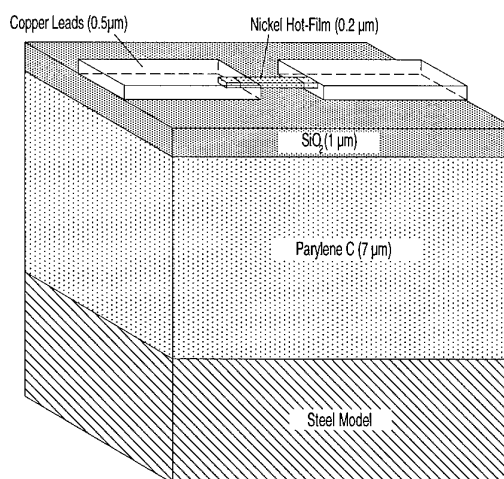


Figure 25: Hot-film sensor with insulation layers

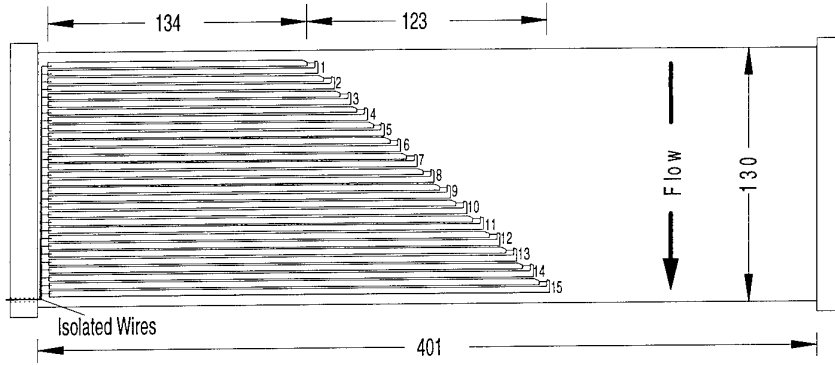


Figure 26: LF2F airfoil model with hot-film array

fully tested, a model of the laminar-type airfoil LV2F had been equipped with an array of 15 sensors as shown in Fig. 26.

However, it turned out to be much more difficult to achieve the same good deposition quality on the model as on the small samples. Because of problems mostly related to surface contamination and uniformness of the deposition only six out of the 15 sensors were working. Results from these sensors were obtained at temperatures down to 120 K, but, for reasons that could not be completely explained during this first investigation, transition was not detected.

Another flow phenomenon could be investigated, though. Figure 27 shows the signals of three sensors located in the shock region at buffet conditions. The fluctuations are the result of the  $\lambda$ -shock oscillating across the sensors. Oscillation frequencies and phase relations could be derived from these signals.

Further experiments with an enhanced deposition technique are planned to finally proof the applicability of these sensors for transition detection and also to investigate the influence of the boundary layer in the storage tube described above in Sec. 6 on the flow at the model.

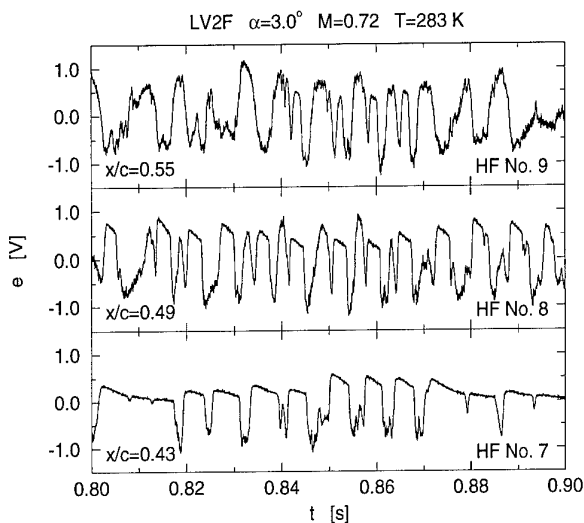


Figure 27: Time-traces of hot-film sensors underneath an oscillating shock

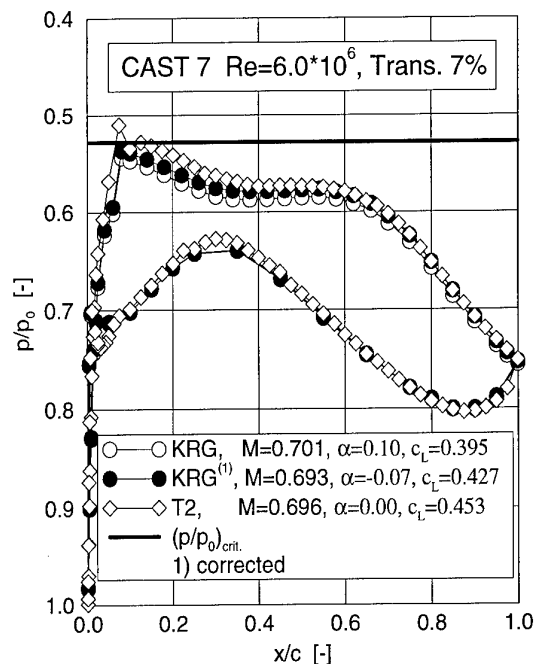
## 8 COMPARATIVE AIRFOIL MEASUREMENTS

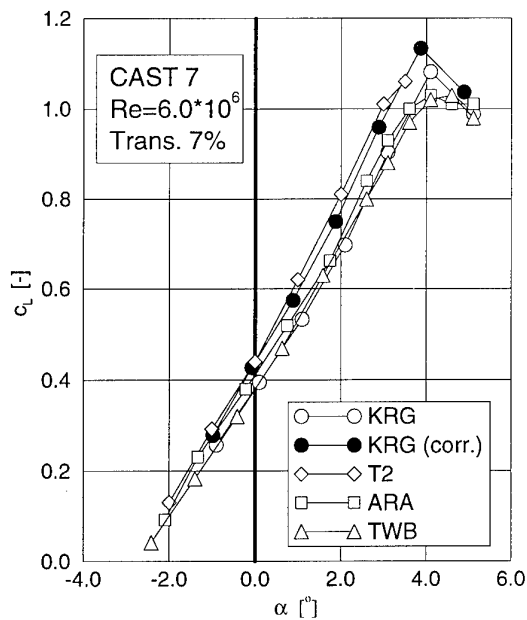
### 8.1 Results from the Slotted Wall Test Section

#### 8.1.1 Pressure Distribution Measurements

For the first pressure measurement tests the CAST 7 airfoil was chosen because of its use in the GARTEur Action Group AD(AG-02) (Ref. 7) for a comparative study of the performance of a number of European wind tunnels and their correction methods. Tests were performed in the KRG at a nominal Reynolds number of  $Re = 6 \cdot 10^6$  with fixed transition at various Mach numbers and angles of attack.

Figure 28 shows as an example a pressure distribution obtained at  $M = 0.70$  compared with interference free results from the T2 wind tunnel (ONERA). Also plotted are the values corrected for wall interference by a correction method for slotted walls based on wall pressure measurements and a model representation (Ref. 8). The corrected results come close to the values obtained in the T2. Remaining differences might be due to the relatively small ratio of model chord to tunnel height of

Figure 28: Pressure distribution in different wind tunnels at  $M = 0.70$

Figure 29: Lift versus angle of attack at  $M = 0.70$ 

150 mm/350 mm in the KRG, which can result in wall interferences not correctable by the present method and due to sidewall interference, which is partially reduced by the wall adaptation process of the T2, but not taken into account by the correction method applied here.

The resulting lift versus angle of attack curve for  $M = 0.70$  is given in Fig. 29 together with results from other wind tunnels. The overall agreement is relatively good and again, the correction for wall effects results in a closer agreement with the T2 curve. In the region of maximum lift, the correction method can not give accurate results, since it is based on a linear treatment of the flow close to the walls and does not account for separated flow on the model.

In Fig. 30 the shock position depending on Mach number is shown for an angle of attack that yields the design lift coefficient of  $c_L = 0.52$  at a Mach number of  $M = 0.76$  in the different wind tunnels. The overall agreement is good.

### 8.1.2 Reynolds Number Effects

For a first investigation of Reynolds number effects, the laminar-type airfoil LV2F (Ref. 9) was selected due to its possibly high sensitivity to Reynolds number changes and flow quality.

The investigation was carried out over a selected Mach number and angle of attack range; however, only some results obtained at the design Mach number of the airfoil, i.e.  $M_\infty = 0.740$  are discussed here.

The flow development with Reynolds number at otherwise constant free-stream conditions ( $M_\infty = 0.740$  and  $\alpha = 0.6^\circ$ ) is demonstrated in Fig. 31: With increasing Reynolds number the lift coefficient initially increases due to improving flow conditions at the trailing edge of the airfoil and a corresponding improvement of circulation. In the range of  $8 \cdot 10^5 < Re < 20 \cdot 10^6$  lift drops rapidly due to the forward movement of the transition point and a corresponding deterioration of trailing edge conditions. As the transition point reaches the leading edge, a reversal in the Reynolds number dependence can be seen for reasons outlined above.

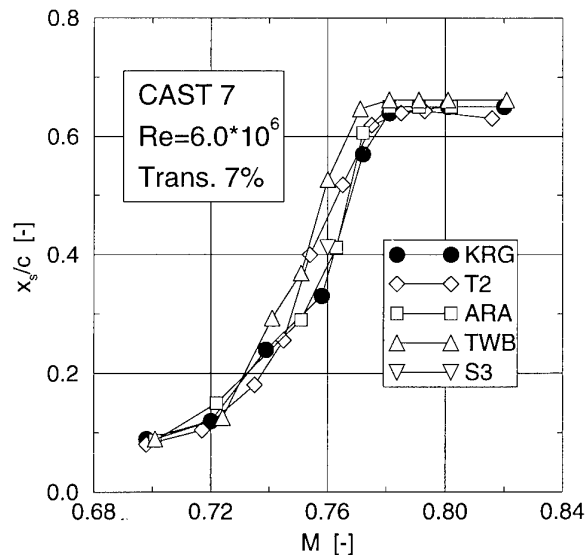
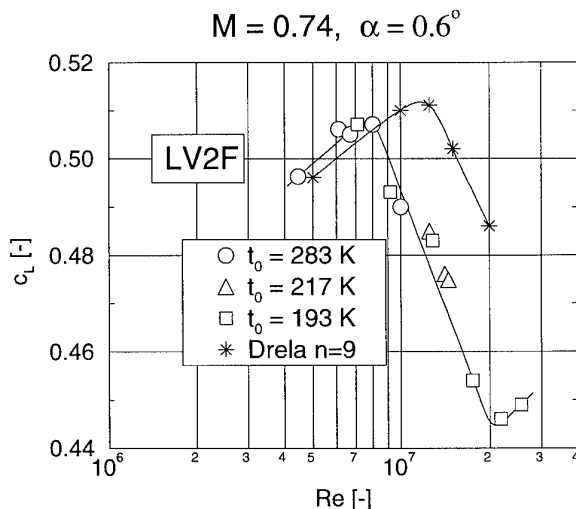


Figure 30: Shock position versus Mach number for different wind tunnels

Also studied was the effect of temperature on the flow development since there was some indication that the wind tunnel flow quality might deteriorate with decreasing temperature (Ref. 10). This was accomplished by producing identical Reynolds numbers at different temperatures by adjusting total pressure accordingly. It is shown in Fig. 31 that there is no obvious effect of temperature on the transition point location, hence flow quality, since the behavior of the lift coefficient with Reynolds number is independent of temperature, at least in the temperature range investigated.

Numerical results from the viscous-inviscid interaction method of Drela based on an Euler solver coupled with a boundary layer code (Ref. 11) exhibit the same Reynolds number dependence as the experimental data. An  $n$ -factor of 9, given by Drela as being representative of free-flight conditions, was used to determine transition locations. The results confirm, that the drop of the lift coefficient is indeed caused by the forward movement of the transition point. However, since some factors effecting trans-

Figure 31: Reynolds number dependence of lift for  $\alpha = 0.6^\circ$

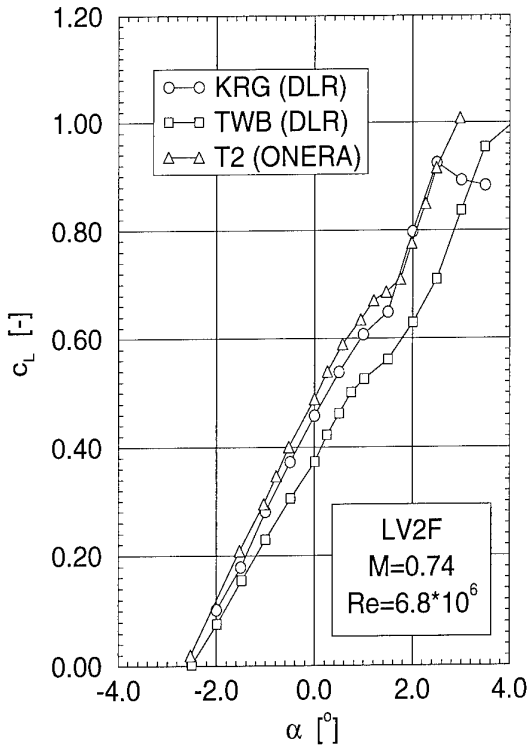


Figure 32: Lift polars for the LV2F airfoil in different wind tunnels

ition, such as model surface quality, are not modeled in the computational method, final conclusions with respect to flow quality of the wind tunnel cannot be drawn from this comparison.

## 8.2 Results from the Adaptive Wall Test Section

The first airfoil measurements in the adaptive wall test section were again carried out with the laminar-type airfoil LV2F (Ref. 9) with free transition at  $Re \approx 6.8 \times 10^6$  for three differ-

ent Mach numbers,  $M_\infty = 0.72, 0.74$  and  $0.76$ .

The lift curve for  $M_\infty = 0.74$  is plotted in Fig. 32 together with corresponding results from the cryogenic wind tunnel with adaptive walls T2 of ONERA (Ref. 9) and from the conventional wind tunnel with a slotted wall test section TWB of DLR (Ref. 12).

The curves show a decrease in the slope between  $\alpha = 0.5^\circ$  and  $\alpha = 1.5^\circ$ . This behavior is usually connected with the forward movement of the transition point leading to a loss of circulation and thereby lift following the same mechanism as described above for Reynolds number variations in Sec. 8.1.2. At larger angles of attack, when the supersonic flow region on the upper surface of the airfoil becomes more dominant, lift increases progressively.

The agreement of the lift polars between KRG and T2 is very good, with only slight deviations for smaller angles of attack and nearly perfect match for large angles. The maximum lift at T2 seems to be higher. The slope of the curve for the TWB is smaller than that of the other two curves, suggesting larger wall interferences.

The loss of lift occurs for the KRG at about the same angles of attack as for the T2, indicating a similar transition point behavior. A more detailed discussion of the T2 results can be found in Ref. 9.

The same difference in the lift polar between KRG and TWB can be found in the test results for a turbulent type airfoil, measured with free transition at a Reynolds number of  $Re = 6 \cdot 10^6$  yielding laminar flow for low lift coefficients, see Fig. 33. The slightly smaller maximum lift coefficient in the KRG is probably due to a difference in the effective Mach number between the two facilities.

Comparing the drag polars, very good agreement is found except for a small range of angle of attacks, where obviously the boundary layer becomes turbulent in the TWB, suddenly increasing the drag coefficient. This increase is not visible in the KRG curve, which indicates a somewhat better flow quality, resulting in a

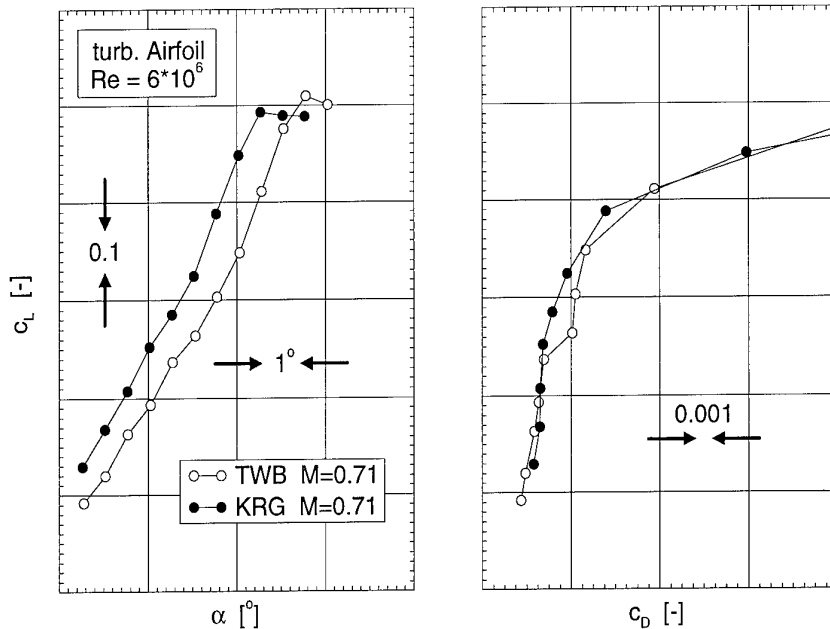


Figure 33: Lift-drag polar for a turbulent-type airfoil with free transition

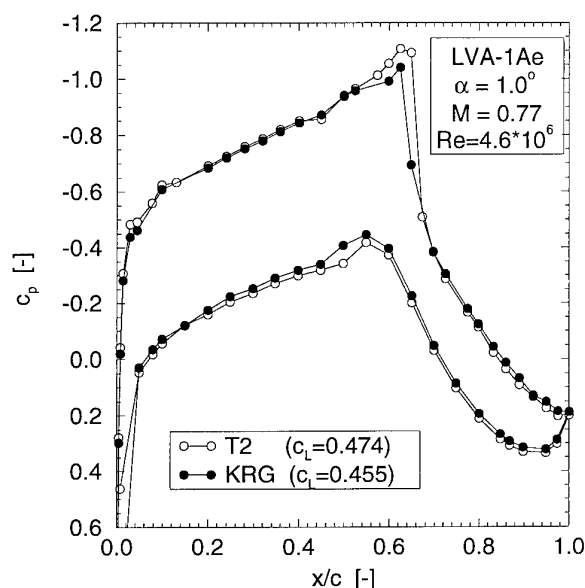


Figure 34: Pressure distribution of the DASA LVA-1Ae for T2 and KRG

later laminar-turbulent transition.

Finally, Fig. 34 shows a comparison between pressure distributions measured with a laminar-type Airfoil DASA LVA-1Ae in the KRG and in the T2 wind tunnel. The results were obtained at the same nominal Mach numbers and angles of attack. Besides a small difference in the shock position of about 2%, the overall agreement is very good. The disturbances around  $x/c \approx 0.5$  are coming from a transition strip, which was located at 48% chord. In the rear part of the model, pressure was measured to be slightly lower in the KRG.

## 9 CONCLUSIONS

The experiments carried out so far in the Cryogenic Ludwig-Tube with the slotted wall test section at temperatures down to the minimum operating temperature and at chord based Reynolds numbers of up to  $Re_c = 25 \cdot 10^6$  have demonstrated the suitability of this wind tunnel concept for high Reynolds number research.

The adaptive wall test section has been built and taken into operation successfully. The calibration runs and the first airfoil tests have shown that, in the Mach number range investigated, complete wall adaptation can be achieved in a single step under most conditions. In those cases, where adaptation could not be obtained in one step, the algorithm was found to converge rather fast.

Comparing results from different airfoils investigated in the adaptive wall test section, good agreement was found with interference-free data from the T2 wind tunnel of ONERA regarding lift polars and pressure distributions. A larger range of laminar flow in the drag polar compared to results obtained in the TWB is taken as indication for a good flow quality.

Further investigations will be carried out to determine the flow quality and the effect on the model boundary layer in the KRG in more detail applying new measurement techniques.

Side wall effects will be studied and, if possible, integrated into the wall adaptation procedure.

## REFERENCES

1. H. Ludwig. Der Rohrwindkanal. *Z. Flugwiss. Weltraumforsch.*, 3:206–216, 1955.
2. J. Amecke. Direkte Berechnung von Wandinterferenzen und Wandadaptation bei zweidimensionaler Strömung in Windkanälen mit geschlossenen Wänden. DFVLR Forschungsbericht FB 85-62, DFVLR, 1985.
3. A. Hurwitz and R. Courant. *Allgemeine Funktionentheorie und elliptische Funktionen*. Springer-Verlag, Berlin, Göttingen, Heidelberg, New York, 1964.
4. F. Steinle and E. Stanewsky. Wind tunnel flow quality and data accuracy requirements. AGARD AR-184, AGARD, 1982.
5. H. Holst. Procedure for determination of three-dimensional wind tunnel wall interferences and wall adaptation in compressible subsonic flow using measured wall pressures. DLR Forschungsbericht FB 91-09, DLR, 1991.
6. C. B. Johnson, D. L. Carraway, P. Hopson, Jr., and S. Q. Tran. Status of a specialized boundary layer transition detection system for use in the U. S. National Transonic Facility. In *Proceedings of the ICIASF Record - International Congress on Instrumentation in Aerospace Simulation Facilities*, (Williamsburg, VA), 22–25 June 1987.
7. Garteur Action Group AD(AG-02): Two-dimensional transonic testing methods. NLR TR 83086 L, GARTEur TP-011, 1981.
8. W. Schröder. 2D-Wall Interferences of the Transonic Wind Tunnel (TWB) of DLR Braunschweig (TWB). Interner Bericht IB 129-89/24, DLR, 1989.
9. G. Redeker, R. Müller, A. Blanchard, and J. Reneaux. Evaluation of transonic laminar airfoil tests under cryogenic conditions including stability analysis and computational results. In *Proceedings of the DGLR/AAAF/RAeS 1<sup>st</sup> European Forum on Laminar Flow Technology*, pages 141–151, (Hamburg, Germany), 16–18 March 1992.
10. G. Viehweger, R. Rebstock, B. Stahl, K. Wichmann, W. Becker, R. Kronen, and D. Distelrath. Der Kryo-kanal Köln (KKK) der DLR (Stand 1992). DLR-Mitt. 93-10, DLR, 1993.
11. M. Drela. *A User's Guide to MSES V2.1*. MIT Computational Fluid Dynamics Laboratory, Cambridge (USA), 1992.
12. Personal communication.

## T2 TRANSONIC CRYOGENIC WIND TUNNEL AT TOULOUSE

Alain SERAUDIE - Jean Pierre ARCHAMBAUD

CERT/ONERA

Department of Aerothermodynamics

2 avenue E. Belin - 31055 TOULOUSE Cedex (FRANCE)

### ABSTRACT

T2 is an induction driven wind tunnel (fig. 1) in which Reynolds number variations are obtained by increasing the total pressure ( $P_t = 1,4$  to 3bar) and reducing the total temperature ( $T_t = 300$  to 110K). The flow is driven by an injection of dry air at ambient temperature and cooled by another injection of liquid nitrogen (fig. 2).

This paper presents the evolution of T2 wind tunnel, mainly in cryogenic condition since 1981, and the aerodynamic cryogenic developments we performed around the wind tunnel activity.

Firstly it gives the wind tunnel main characteristics, it describes the flow control system, and the hollow model technique developed for cryogenic runs. The flow quality measurements are presented, with pressure, temperature, and mass flow fluctuation levels. Moisture contamination is a great problem for flow quality, and we present some solutions to perform good tests on laminar models at high Reynolds numbers. Finally this paper presents some typical results obtained in cryogenic condition : velocity measurements with a laser Doppler anemometer, transition qualification at variable Reynolds number and buffeting investigation with unsteady measurements.

### NOMENCLATURE

#### Symbols:

C : model chord  
 $C_d$  : total drag coefficient  
 $C_h$  : Stanton number  
 $C_p$  : specific heat at constant pressure  
 $f$  : frequency (Hz)  
 $F$  : STROUHAL number ( $f l/U$ )  
 $H$  : test section height at the entrance  
 $M_l$  : local Mach number  
 $M_v$  : freestream Mach number  
 $P$  : static pressure (bar)  
 $P_t$  : total pressure (bar)  
 $(p)'$  : static pressure fluctuations  
 $Q_j$  : injected air mass flow (Kg/s)  
 $Q_{LN2}$  : injected nitrogen mass flow (Kg/s)

$Q_{TS}$  : test section mass flow (Kg/s)  
 $R_c$  : Reynolds number based on model chord length  
 $t$  : time (seconds)  
 $T$  : static temperature (K)  
 $T_{aw}$  : adiabatic wall temperature (K)  
 $T_t$  : total temperature (K)  
 $T_{tj}$  : total temperature of the injected air mass(K)  
 $T_w$  : wall temperature (K)  
 $(T)'$  : stagnation temperature fluctuation  
 $T.D.$  : tripped transition  
 $T.N.$  : natural transition  
 $U_e$  : velocity (external flow to the boundary layer)  
 $X$  : longitudinal axis measurement  
 $\alpha$  : model angle of attack ( $^\circ$ )  
 $\delta_1$  : boundary layer displacement thickness  
 $(pu)'$  : mass flow fluctuations

### INTRODUCTION

The use of cryogenic technology has produced real progress in wind tunnel testings, permitting the attainment in high Reynolds numbers and so the good simulation of aerodynamic phenomena existing on aircraft in flight.

In the T2 wind tunnel, an induction system using ambient temperature air and driving the flow in the circuit at pressure up to 3 bar is combined to a cryogenic operation, cooling the flow by liquid nitrogen injection. The T2 wind tunnel operated at ambient temperature under pressurized conditions from 1975 until its cryogenic adaptation in 1981. The increase in Reynolds number provided more aerodynamic studies in a wide range of transonic flows for basic research and industrial applications. During the same time period, instrumentation and new models, well adapted to low temperatures, were developed to analyse the flow characteristics connected with Reynolds number variations.

After a brief presentation of the main features of the wind tunnel we will describe the control system for the short runs and the different kinds of models in the test section at low temperatures. We will discuss the flow qualities and finally present some typical recent results at high Reynolds numbers.

## 1. DESCRIPTION OF THE T2 WIND TUNNEL

### 1.1. Different Parts of the Circuit

The diagram presented in figure 2 gives a good idea of the main parts of the pressurized transonic cryogenic wind tunnel T2 (Ref. 1).

The settling chamber of square section ( $1,8 \times 1,8 \text{ m}^2$ ) is fitted with a dust filter, a honeycomb and screens. The following duct is convergent with a contraction ratio of 21. The test section is 0,39m wide, 0,37m high and 1,32m long and is equipped with 2-D adaptive walls to avoid transonic blockage and to reduce wall interference effects. In the downstream section, a sonic throat regulates the test Mach number between 0,6 and 1. T2 is an induction driven wind tunnel. Flow is produced by the high pressure dry air injected through the trailing edges of the turning vanes in the first corner downstream of the test section (fig. 3) (Ref. 2). The liquid nitrogen injection, necessary to cool the flow, is located in the driven air mixing chamber, which is immediately after the injector corner. The exhaust of the air-nitrogen mixture takes place in the first diffuser between the test section and the injector corner. The mixed gas goes out through the porous walls of a rectangular channel, removing the sidewall boundary layers, and reducing pressure losses. A return leg with several diffusers and corners closes the wind tunnel. A compressor supplies, at a pressure of 80 bar, a  $45 \text{ m}^3$  tank with the injection compressed air. The cooling liquid nitrogen is moved from the  $20 \text{ m}^3$  storage tank to the pressurized test tank, for the run.

### 1.2. Cryogenic Adaptation

The cryogenic transformation of the original wind tunnel has two main aspects (Ref. 3):

- the liquid nitrogen injection ,
- the internal thermal insulation

#### 1.2.1. Nitrogen Injection and Exhaust System

The nitrogen injection is distributed, in two circular patterns, by 32 spray nozzles of different sizes, separately supplied by their own electrovalves to allow digital regulation of the liquid nitrogen mass flow. This peripheral injection system is located upstream, as far as possible from the test section to improve the flow qualities. The liquid nitrogen is injected perpendicular to the flow in a high velocity and turbulent stream area. This leads to good vaporisation and mixing of the small nitrogen droplets.

Figure 4 shows the diagram of the liquid nitrogen supply system for the injectors. It includes a storage tank of  $20 \text{ m}^3$  from which the test tank of  $2 \text{ m}^3$  is filled and pressurized to 15 bar for a run. The maximum injected liquid nitrogen flow rate is  $Q_{LN2} = 20 \text{ Kg/s}$ ;

the accuracy of this injection regulation is about 0,02 Kg/s.

The exhaust flow, which goes out the circuit through the porous walls of the first diffuser, is regulated with an analog valve positioned before the test, and digital electrovalves driven during the run. This flow is rejected to the atmosphere through a 14 m high chimney equipped with a ventilator.

#### 1.2.2. Internal Thermal Insulation

The internal insulation selected for the T2 wind tunnel is composed of two main parts:

- in the low velocity part, the return leg and the settling chamber (fig. 5), a 10mm thick polyurethane foam was selected, reinforced by a thin skin of *Kevlar* glued between the two 5mm polyurethane layers. Polyurethane is a celled material with very low conductivity and low heat capacity, but with a rough surface,

- in the high velocity part, a 5 mm thick layer of agglomerated cork of Norcoat has been chosen for the air induction corner and the convergent part. A wood layer (5 mm thick) has been glued in the nitrogen injector region and on the test section sidewalls to replace the initial cork (fig 5). The heat insulation quality of these materials is not as good as the polyurethane quality, but they have a good surface finish. More informations about the insulation materials can be found in reference (Ref. 4).

The advantage of internal insulation is that it minimizes the cooled mass, permitting rapid attainment of internal skin temperature close to the adiabatic wall condition.

During the short time of a cryogenic run, the metallic structure remains at ambient temperature; one hundred thermocouples have been mounted to measure the temperature of the flow and of the carbon steel wall.

### 1.3. Test Section

Sidewalls of the test section are the two doors allowing access into the high speed part of the circuit. They are equipped with round and rectangular windows. Some of them are made of a special glass and are used for optic measurements in the test section (infrared, laser). The other windows are round metallic ones and are necessary for the connection between the different models and the tunnel.

The T2 test section is equipped with flexible top and bottom walls made of *INVAR* plates, 1.3 mm thick, each one controlled by 16 hydraulic jacks (fig. 6). This is the 2-D adaptive wall part of the tunnel (Ref. 5 and 6). The movement of each jack is transmitted to the flexible walls by transverse stiffeners welded on the *INVAR* plate. The displacement mechanism and the movement control system are located in the plenum chamber under the wall. Two *TEFLON* seals are fixed on each side of the flexible plates to avoid communication between the flow and the plenum (fig. 6).

To reduce the thermal losses, a combination of slots is made in the stiffeners, 1 mm under the flexible plates,

ensuring a thermal barrier between the *INVAR* plates and the displacement system (fig. 6).

The displacement mechanism is kept close to ambient temperature naturally while the top and bottom walls reach quickly a temperature close to the adiabatic wall temperature during cryogenic testings.

The figure 7 presents variations of the stagnation temperature and the wall temperature versus time during a typical run ( $M_v = 0.7$ ,  $P_t = 2$  bar,  $T_t = 150$  K). The wall temperatures (*INVAR* top and bottom flexible walls) decrease slowly during the cooldown of the fluid ( $M_v=0.3$ ) and then drop more rapidly ( $M_v=0.7$ ) until the stabilisation occurring after 50 seconds. The operating mode to cool down the flow will be described in § 2.

Wall adaptation is performed in real time by an iterative strategy which converges in about 3 or 4 iterations (4 seconds/iteration) (Ref. 15). For 2D flows, a 2D adaptation method allows to cancel wall interferences around 2D airfoils with chord from 0.15 m ( $C/H=0.40$ ) to 0.25 m ( $C/H=0.68$ ). For 3D flows, a 3D adaptation method designed for 2D wall deformations minimizes wall interferences around various types of 3D models (bodies of revolution, aircrafts, half fuselage-wing).

## 2. OPERATING MODE FOR CRYOGENIC RUNS

From the beginning, it has been necessary to equip the T2 wind tunnel with a high performance automatic control system, in order to start the flow and to stabilize the parameters  $M_v$ ,  $P_t$  and  $T_t$  during the short duration of the run.

Good conditions are now obtained through the use of two mini computers which are respectively used for the wind tunnel control (Ref. 7), the adaptation of the walls and the measurements (fig. 8). The first computer is devoted to the control of the parameters ( $M_v$ ,  $P_t$ ,  $T_t$ ) by the regulation of the injected driving-air, the liquid nitrogen, the exhaust gas, and by the adjustment of the sonic throat, giving the desired Mach number in the test section. To improve the performance of the automatic control, the first computer uses simple mathematical models of the wind tunnel, and optimal control laws to anticipate the evolution of the parameters of the run. The second computer handles the control of the measurements and exploring system, data acquisition and wall adaptation. A third computer is mainly used for calculation and program developments.

We present, on figure 9, a typical run at  $M_v = 0.750$ ,  $T_t = 120$  K,  $P_t = 3$  bar, with the evolution of the main flow parameters versus time. There are three separated parts in the run:

- a cooling phase at low pressure and low Mach number (0.3) in the test section. There is an overshoot of injected nitrogen mass flow to reduce the time for temperature stabilization. When the temperature of the model reaches the prescribed point, we enter into the regulation loop, the second phase of the run,

- an intermediate phase, where are increased the Mach number and the stagnation pressure to reach the nominal values fixed for the stabilized part of the run.

During these two phases the model is protected by a metallic rod placed upstream of it (see § 5.2.1).

- a regulation phase, where the regulation process maintains constant parameters for the run ( $M_v$ ,  $P_t$ ,  $T_t$ ). When parameters are stabilized, the data acquisition computer carries out wall adaptation (3 to 5 iterations in 12 to 20 seconds) and then performs wake or boundary layer probings, steady or unsteady measurements on the model, temperature acquisition, etc... In this phase, the accuracy of the regulation is  $\pm 0.5$  K for temperatures,  $\pm 0.001$  for freestream Mach number and  $\pm 2$  mb for pressure.

The run is stopped by closing the nitrogen injection valves, and decreasing the injected driving-air when  $T_t$  approaches ambient temperature.

## 3. CRYOGENIC OPERATING PERFORMANCE

After the wind tunnel conversion, a series of runs at various temperatures, has been performed to determine the characteristics of the cryogenic operating mode.

For the tests at  $M_v = 0.8$  and  $P_t = 1.8$  bar, the variations of the ratios  $Q_j/Q_{TS}$  and  $Q_{LN2}/Q_{TS}$  are shown in the figures 10 and 11. It is observed that  $Q_j/Q_{TS}$  decreases as the operating temperature decreases, which confirms the increase in the induction efficiency predicted by the injector theory, as the temperature ratio between the driving and driven fluids  $T_{tj}/T_t$  increases. The black spot in figure 10 at ambient condition represents the test performance before conversion of the circuit; the small difference is coming from the moderate increase in the pressure losses of the circuit due to the internal thermal insulation.

The ratio of liquid nitrogen flow rate to the test section flow rate is obviously zero at room temperature (fig. 11). It increases practically linearly as the operating temperature decreases. At level  $T_t = 120$  K, the liquid nitrogen flow rate represents approximately 8% of the flow rate in the test section. The full line represents the computed estimation of the ratio of liquid nitrogen necessary to cool only the flow. The difference between the experimental curve and the computed curve gives the order of magnitude of the thermal losses of the circuit : from zero at room temperature, they increase as the temperature decreases and represent approximately 15 % of the total liquid nitrogen flow rate for  $T_t = 120$  K, which confirms the efficiency of the internal insulation. It should also be noted that at low operating temperatures, the driving-air and liquid nitrogen flow rates are of the same order of magnitude (8 to 10% of  $Q_{TS}$ ), i.e. approximately 10 Kg/s for a flow rate in the test section  $Q_{TS} = 100$  Kg/s ( $M_v = 0.8$   $P_t = 2$  bar,  $T_t = 120$  K).

The operating chart of the T2 wind tunnel is presented in figure 12. Two constant stagnation temperature envelopes ( $T_t = 290$  K and 120 K) are drawn, bounded by the capabilities of T2 in terms of Mach number and pressure. The usual operating domain of T2 covers the range of Mach number from 0.3 to 1, stagnation pressure from 1 to 3 bar, temperature from 120 to



300 K, Reynolds number from 3 to 29 million (chord  $\approx 0.18$  m) and testing time from 30 to 120 s.

#### 4. THIN SKIN MODELS

Since 1981, we have got a certain knowledge about the model conception adapted to cryogenic runs. The two following paragraphs describe the development of this evolution.

##### 4.1. First Model Design for Cryogenic Condition

The first solution, adopted in 1982 for the T2 wind tunnel 2-D profiles, was a bulky CAST7 airfoil, with a 150mm chord (Ref. 8). The entirely metallic model was constructed with four thick parts that were electron beam welded together. Due to the short runtime, it was difficult to satisfy the thermal equilibrium requirements with this CAST7 airfoil. It was necessary to pre-cool the model with a cold gaseous nitrogen flow in an ancillary system, which was added to the test section door; after pre-cooling, the model was automatically introduced into the cryogenic flow during the initial phase of the run.

A number of improvements for the T2 models have been implemented since the CAST7 conception in 1982. These improvements are based on progressive exploration of the idea of a low thermal inertia model cooled down directly by the flow in the test section. This will eliminate the complexity of a pre-cooling device for swept wing or half model (Ref. 9, 10 and 11). A summary of model evolution is as follows:

- 1982 CAST7 : bulky
- 1984 CAST10 : bulky except a small chamber  
( $e=3\text{mm}$ )
- 1985 OAT15A : partly hollowed model
- 
- 1986 Fx/AMD-BA : thin skin model (2-D)
- 1987 Transport Aircraft : thin skin model (3-D)
- 1988 AS409 : thin skin model (3-D-laminar)
- 1990 OALT25 : thin skin model (2-D-laminar)

##### 4.2. Realisations of Thin Skin Models

The different features of thin skin models are presented in the figure 13 and a typical example is given in figure 14. They have quite the same main characteristics : thin skin structure, locally reinforced, equipped for cryogenic tests with pressure taps and thermocouples ; pressure transducers can also be fixed under the skin for unsteady measurements. The different manufactured parts of the model can be screwed or welded together ; the assembly by screwing, allows to check the internal equipment before the last mounting phase.

These thin skin models have a low thermal inertia and are cooled down directly by the flow, in the test section, during the beginning of the run.

One of the first models manufactured with this technique was the swept 3-D model, AS409, presented

in figure 15. The model is a wing part that is twisted to maintain a constant spanwise load, designed with a OAS100 profile by AEROSPATIALE. The model is composed of two thin skin parts (3mm) screwed together without welding. The trailing edge and the leading edge are machined as integral parts of the upper side. The upper and lower sides are attached with small cylinders which brace the two sides, avoiding deformations of the model due to pressure efforts. During the last finishing phase, the screw heads are flushed at the level of the lower side. The main interest in this technique is to avoid model deformation due to the welding of the different parts. If it is necessary, we can also open the model to modify or to repair a part of the instrumentation. The model is equipped with three rows of pressure taps and five rows of thermocouples glued under the skin. In the trailing edge part, this model contains a tiny pressure transducer, fixed on a small removable metallic piece, to measure pressure fluctuations on the upper surface (fig. 15).

Another typical model, manufactured by the O.N.E.R.A. center in Lille, is the first cryogenic half model designed for the T2 wind tunnel (A320, fig. 16). The thin skin technology, used for the design of profiles, has been applied to this model, an assembly consisting of a hollow wing and a fuselage (Ref. 12). This half model was fixed on the left door of test section with a thermal joint to compensate the thermal displacement due to the temperature difference between the wing and its heel, which remains at ambient conditions. The fuselage was fixed on this joint without contact with the wing and the lateral door. This model was designed and manufactured with a computed wing deformation, in order to obtain the same attitude in the tunnel under test conditions ( $M_V=0.78$ ,  $P_t=3.3\text{b}$ ,  $T_t=120\text{K}$ ) as in flight.

A wall balance, working at room temperature, gave the aerodynamic loads on the wing and the fuselage.

Another feature of this model is its instrumentation (fig. 17). It has 44 conventional static pressure holes, 12 *ENDEVCO* cryogenic pressure transducers, 1 *ENDEVCO* accelerometer, 1 strain gage, 2 optical fibers in the wing tip, and 3 thermocouples. Outside of the test section, a video camera recorded the wing tip deformation by observing the displacement of the light points from the two optical fibers, during the different parts of the run.

## 5. FLOW QUALITIES

### 5.1. Flow Quality Measurements

The wind tunnel turbulence level  $Tu$ , is an important parameter for the laminar studies. When the transition location is freely moving with the test conditions (the Mach number, the angle of attack, the Reynolds number, the wall temperature,...) the  $Tu$  parameter becomes very influential (Ref. 13); so it has to be known in all the range of the wind tunnel conditions.

### 5.1.1. Instrumentation to Measure Flow Quality

To qualify the flow disturbances in T2, an unsteady type instrumentation was developed measuring the static pressure ( $p'$ ), the mass flow ( $\rho u'$ ), and the stagnation temperature ( $T_t'$ ) in the test section at transonic speeds (Ref. 13).

A probe, equipped with a small cryogenic pressure transducer, measured the static pressure fluctuations. This transducer (Kulite XCQL-7A-093-4D) was calibrated at different temperature levels; the frequency range was from 0 to 10 kHz.

The mass flow fluctuations were measured with a hot film probe (Dantec 55R71), likewise calibrated with temperature; its frequency range is from 0 to 10 kHz. A new probe (Dantec 55R31) recently calibrated in T2 test section comparatively to a wire probe, has been used in ETW, to measure the flow qualities in the test section.

The total temperature fluctuations are more difficult to measure; a special stagnation temperature probe has been designed around a cold wire of 2.5  $\mu\text{m}$  diameter (Ref. 14). This probe measures the temperature of the flow at a constant speed of 50 m/s, fixed by a sonic throat located just upstream of a vacuum pump. The temperature of the wire is nearly equal to the total temperature of the flow, its bandwidth is 0 to 600 Hz. After a calibration using the time response of the wire to a heating pulse produced by a laser, the measures are corrected up to 3 kHz by the experimental transfer function.

### 5.1.2. Experimental Results in T2

The fluctuation measurements are presented on figures 18, 19 and 20 in a dimensionless form versus the total temperature of the flow, from 140 K to 300 K. Several Mach numbers (from 0.7 to 0.77), were experimented here for different temperature levels; these conditions correspond to a laminar airfoil test.

The static pressure is reduced by the total pressure  $P_t$  of the flow. The rms level of  $p'/P_t$  seems quite constant with temperature (fig. 18), the 0.28% value is nearly independent of the flow conditions, only a small change is observed with the bandwidth analysis.

The relative mass flow fluctuations versus test section Mach number, measured at different stagnation temperatures, are presented in the figure 19. They are roughly constant around an average value of  $1.10^{-3}$ .

The relative temperature fluctuations ( $T'/T$ ) increase when the temperature decreases: from 0.02% ( $T'$  rms = 0.06K) at ambient temperature to 0.12% ( $T'$  rms = 0.17K) at 140K (fig. 20). Most of the energy corresponds to the low frequencies; the fluctuations are attributed to the temperature regulation process, the liquid nitrogen spraying, the imperfect mixing of the driving-air (at room temperature) with the driven cryogenic flow, and the wall heat fluxes.

## 5.2. Moisture Contamination

As the unit Reynolds number increases, it becomes more and more difficult to keep laminar boundary layers on the model. The model imperfections trip the transition almost at the same condition. Because the instrumentation indicates local tripping locations depending on test conditions, wind tunnel flow qualities have been suspected. For 2-D airfoil, it has been shown that the freestream fluctuations cannot explain the observed limitation, the trouble comes from the moisture contamination.

Several sources can provide moisture in the tunnel: the driving-air, the internal insulation material, the leaks of the wind tunnel, the liquid nitrogen,.... This moisture can appear in two ways, when the flow temperature goes down the dew point:

- frost on the model (when it becomes colder than the flow),
- ice particles in test section flow.

Usually the model should never be colder than the flow: we stop the cooling phase of the run few degrees above the nominal temperature of the flow, as described previously.

The dew point measured in the test section is included between 205 K and 230 K depending on the purge time of the circuit (Fig 21). The amount of water is 100 times greater at 230 K than at 205 K. On the water equilibrium diagram, we can observe the low water content of the driving-air and gas nitrogen (1mg/m<sup>3</sup>), corresponding to a 195 K dew point.

These low water contents are enough to produce ice crystals with a diameter greater than 0.01mm able to trip the transition on a few points near the leading edge of the model.

In figure 21 are shown two wake probings, obtained with a single pressure probe moving at a constant speed through the wake: one is perfectly laminar, the other admits some broken lines due to intermittent boundary layer. This problem is certainly connected with some ice particles which trip the transition on the upper surface, then vanish to the contact of the profile, a few degrees warmer than the flow.

### 5.2.1. What we have Done to Reduce the Particles Effect on the Model

The circuit must be purged very carefully (fig. 22):

- a control test at ambient temperature is performed before to a series of cryogenic tests,
- the wind tunnel is kept in pressure before and after each test,
- during 10 min before the test, we inject manually a low mass flow of the dry driving-air,
- then there is an automatic purge of 30 seconds at the beginning of the run.

Laminar flows can systematically be obtained for temperatures higher than 200 K, but for lower temperatures, runs can be good or partly turbulent on random points (detected by the spanwise thermocouples or by the wake probes).

The device, used for accelerating the model cooling phase (§6.2.1), was modified to protect the leading edge of the model until the measurements. A rod with a triangular cross section is pushed into the test section, one or two centimetres upstream of the leading edge, at the start of the run (Fig 23). Then it is pulled out just at the beginning of the stabilized phase. At the end of the data acquisition, and before the warming up of the flow, this device is again pushed into the test section to avoid moisture on the model which becomes the coldest point of the circuit.

This protection, mainly efficient around the dew point, is a complementary device of the purge technique to reduce the number of ice particles on the model. Figure 24 shows an example of ice particle tripping effect on drag measurements (critical  $Re=7$  million) which can be avoided with the use of this device (critical  $Re=11.5$  million) (Ref. 9).

Unfortunately, all these precautions are not sufficient, we found again a temperature limitation for the laminar tests even if the critical Reynolds number has been increased up to 11.5 Million.

### 5.2.2. *What we have Done to Reduce the Dew Point of the Flow*

To obtain a dryer flow, tests were performed first with pure nitrogen : the GN2 was injected at ambient temperature in the first corner with a high pressure to drive the wind tunnel flow (Fig 2). Liquid nitrogen is sprayed into the circuit to cool down the flow as usual. We measure a 10 K less dew point, which delays the artificial transition trippings down to 165K (Fig 25). But for systematic tests the real limitation is very close to 180K : all the tests are laminar above this value, some turbulent cones can appear below.

The gain of 10K on the dew point with the complete nitrogen functioning, shows us that the driving-air produces a limit for the laminar conditions with a dew point of  $-70^{\circ}\text{C}$  in the test section. So to improve this limitation, we replace the dryer system of the T2 air supply by a new one, more efficient, to reach a lower dew point of driving-air. The dew point measured at the exit of the old dryer was about  $-82^{\circ}\text{C}$  for a pressure of 1bar; the new one gives dryer air :  $-96^{\circ}\text{C}$  at same pressure. In that new conditions, the best dew point reached in the test section is about 160K, but for systematic tests in laminar condition the temperature limit is very close to 170K. We present on figure 26 the total drag measured half a chord downstream of a OALT25 2D model in laminar condition : drag is measured at 15 positions along the span, the probe 8 being located on the test section axis. On the right hand side of the model we can see the Reynolds number effect on the drag level which decreases with the temperature level. On the left hand side the boundary layer is disturbed by the static pressure holes located close to the leading edge. At low Reynolds number, the level of the drag in this part seems to be a little bit higher than on the right part; when the Reynolds number increases, the

boundary layer becomes thinner and so more sensitive to the geometrical perturbations. Above  $Re=13$  Million, the transition goes ahead, near the leading edge pressure taps, and consequently the local drag coefficient grows very much.

In conclusion, operating mode with pure nitrogen is an improvement in terms of dew point, compared to the previous operating mode with mixture air (old dryer) + GN2. But the new air dryer combined with GN2 seems to give the best result, still reducing dew point temperature of about 10K.

## 6. TYPICAL MEASUREMENTS IN CRYOGENIC CONDITION

### 6.1. Flow Measurements

#### 6.1.1. *Laser Doppler Anemometer*

The last important device developed for T2 wind tunnel is the 3D laser Doppler anemometer; it is used since 1990 at ambient condition for aerodynamic 2D or 3D measurements : to qualify the lateral boundary layer effect, the shock wave - boundary layer interaction on a 2D model, or the 3D flow downstream of the model of a modern transport aircraft, in the T2 test section. The different main parts of the bench are (fig. 27) : the three displacement axis with computer controlled motors, the laser source and optical couplers, 2 emitting optics and their monomode optical fibers, the 2 receiving optics and the 3 real time Doppler F.F.T. processors (B.S.A.). The flow is seeded with oil droplets of  $1\text{ }\mu\text{m}$  in average diameter in the return leg of the circuit (Ref. 16, 17 and 18).

The key points of laser velocimetry in cryogenic condition are the glass window well defined for important temperature gradients (without frosting of the external surface and allowing a good transmission of the beams into the test section) and the seeding of the flow. The first point was studied by the use of 2 thick (60mm) silica windows (fig. 28). The important thickness, solves the problem of pressure (mechanical behaviour) and temperature during the short T2 run time. A computation of the temperature front propagation in the silica material have been done for the definition of the window size (fig. 28). The result is in good agreement with the temperature measurement on the external surface of the window : during the run this part of the glass remains at ambient temperature. In addition the expansion coefficient of the silica material is very low and this kind of material accepts a great temperature gradient without breaking the glass.

The 2D velocity measurements have been performed in the centre of the empty T2 test section at  $M_v = 0.77$ ,  $P_t = 1.7b$  for different temperature levels, with and without seeding. The forward scattering configuration was chosen with a yaw angle ( $20^{\circ}$ ) to simulate future 3D measurements (fig. 29).

When  $T_t$  is decreasing, it achieves successively the H<sub>2</sub>O dew point (210K) and the CO<sub>2</sub> condensation point(135K) of the flow; for these two levels a lot of

small icicles appear in the flow and the frequency detection of the velocimeter becomes greater than at ambient temperature (fig. 30). So below the dew point it's not necessary to inject oil particles in the wind tunnel, ice particles of the flow are sufficient to measure correctly the velocity. Below the flow dew point, with and without seeding there is a good agreement between the velocimeter information and the velocity coming from the pressure measurements (fig. 31).

This investigation is encouraging for future tests concerning laser aerodynamic measurements in cryogenic condition.

### 6.1.2. Wake Pressure Rake

Other very useful tools used during cryogenic tests are the pressure rakes equipped with several pitot and static tubes for the wake probing. These rakes equipped with 1 to 21 pitot tubes and with 1 to 7 static tubes are used to measure the total drag of 2D or 3D models, generally half a chord downstream of the trailing edge (Ref. 18); a typical one is presented in figure 32. The rake probes the flow, moving in a vertical plane, and indicates the model drag in different sections in the spanwise direction. On 2D condition this device can be used for laminar tests at high Reynolds numbers, to see if artificial trippings (turbulent cones) appear on the model, or to determine the model performance (polar evolution). We present a typical drag evolution, measured in the wake of OALT25 laminar profile, in the spanwise direction (fig. 26). In laminar regions (right part) we can observe the Reynolds number effect reducing the drag value. In addition, as mentioned in paragraph 5.2.2, the multiprobes wake rake allows to detect artificial tripping as indicated by the large increase in drag on the left part of the figure 26 for the highest Reynolds number.

The CAST10 airfoil has been tested in T2 in cryogenic condition. The figure 33 presents results for free and fixed ( $X/C=5\%$ ) transitions and for two Reynolds numbers ( $Rc=4$  Million, ambient temperature;  $Rc=21$  Million,  $Tt=120$  K). Free transition polar at low Reynolds number shows a large drag reduction. At high Reynolds the two polars are very close, the free transition going upstream with the increase in Reynolds number. Variation of the fixed transition polar underlines a simple Reynolds effect.

## 6.2. Model Surface Measurements

### 6.2.1. Temperature Measurements

The temperature measurements with thermocouples glued under the thin skin of the model are used during two main parts of the run :

- during the cooling phase of the model,
- for the measurement phase in the stabilised part of the run.

The duration of the first phase of the run, at low Mach number and low pressure, depends on the time necessary to cool down the model. The evolution of temperatures versus time is measured on the upper and lower sides of

the profile during the first phase of the run (fig. 34). With laminar conditions on the model, heat fluxes between the boundary layer and the profile wall are very low and the time necessary to reach a good temperature equilibrium is about 3 minutes (Ref. 11).

During the cooling phase, we introduce a cylinder upstream of the leading edge to generate turbulent flow on this laminar model. The heat fluxes are greater, and the cooling duration is reduced; just one minute is now sufficient to reach a good temperature equilibrium on the model (fig. 34).

The thermocouples are also used during the stabilised phase of the run to measure the temperature level of the model and determine the nature of the boundary layer. The technique is based on a small temperature step of the flow; the observation of how the model comes back to the equilibrium indicates the nature of the boundary layer. The easiest way, found in T2, is to stop the cooling phase of the model few degrees before reaching the nominal temperature. In this case the model is 6 K to 2 K warmer than the flow; each thermocouple measures a time dependent temperature, from which the heat flux is calculated considering a monodimensional sheet of metal; in fact the thin skin of the model is used as a flux meter. The strong difference in the Stanton number evolution along the chord indicates clearly the transition location. Figure 35 shows distributions of Mach number, measured temperature and Stanton coefficient along the model chord for a typical test : the transition location is well defined in this configuration (Ref. 19, 20 and 21).

### 6.2.2. Infrared Visualisations

The infrared technique has been successfully used from the ambient temperature down to about 170 K. We use a high wave length camera INFRAMETRICS (8-12 $\mu$ m), which observes the model coated with a black paint through a lateral ZnSe window. No special model have been used for these visualisations, the perfect hand polishing maraging steel have been simply paint with a polyurethane aeronautical paint (Ref. 27).

This device can be used by two different ways :

- for global visualisations of the model in order to oversee the boundary layer state; often we observe the infrared image during the test to know the condition of the model upper side (Ref. 20 and 21)
- to determine more accurately the transition front location. Before the tests some reference marks are put on the model and we perform some pictures without wind to have good references of the model. After the tests there is a treatment of the infrared file and we can achieve temperature distributions along the model chord to determine the transition front location.

Figure 36 shows a typical visualisation with a natural transition from laminar (clear region) to turbulent (dark region). Because the temperature equilibrium is not yet reached (model warmer than flow), heat fluxes are greater on turbulent region than on laminar one. So the temperature on turbulent region is lower than on laminar one as indicated by the infrared visualisation

which is an instantaneous temperature map of the model surface. At high Reynolds number the inspection of the infrared image give information about the possible appearance of turbulent cones during the test around critical temperature condition ( $T_t \approx$  dew point temperature) or behind local roughness like in the background of the figure 36 (control artificial roughness). In addition temperature distribution along a model chord can be drawn from the infrared image file. This temperature distribution, giving continuous information, is close to those measured with the thermocouples and the transition location can be determined by the estimation of local heat fluxes.

### 6.2.3. Longitudinal Pitot Probing : Jones Criterion

A flat total pressure probe displaced along the chord, on the model surface, can give the total pressure evolution in the boundary layer at a constant height from the wall. This pressure information can be combined with the local static pressure measured on the model to give the local Mach number; this Mach number is different in laminar and turbulent conditions and the probing exhibits an "S" curve through the transition of the boundary layer (Ref. 23). This device determines accurately the transition location under cryogenic condition and gives a continuous information on the line probing : we can determine the beginning, the end and the length of transition (Ref. 22).

We present on figure 37 a Reynolds number effect on the 2D OALT25 laminar model transition location : local Mach number distributions are showing a very small unfavourable pressure gradient on the upper side; pitot probings show clearly the typical "S" curve of the Mach number evolution through the transition front. In this sensitive configuration, we can see the transition motion when the Reynolds number increases.

With the same accurate device we have also followed the model equilibrium effect on the transition location in cryogenic condition (fig 38). In this configuration with decreasing velocity on the upper side, the model is warmer than the flow and the temperature gap between the flow and the model has been changed. The warm wall has an unfavourable effect for the boundary layer transition : the more the model is warm, the more the transition front is located upstream.

A lot of fundamental considerations connected with tests at high Reynolds numbers like non adiabatic wall effects, boundary layer transition problems are given by A. Mignosi (Ref. 23)

### 6.3. Shock-Boundary Layer Interaction

In transonic configuration, when there is a strong interaction between the shock wave and the boundary layer of the upper side it appears instabilities produced by the separation of the boundary layer, between the foot of the shock and the trailing edge. A lot of studies have been yet performed in this field at T2 wind tunnel in 2D and 3D configurations (Ref. 24 and 25). A new one was conducted in 1995 on two 2D models to

compare the Reynolds number effect and the suction of the boundary layer effect (Ref. 26) with fixed transition. We have compared the Mach number distributions on the rear part of the model (fig 39) : when the Reynolds number increases from 6 to 20 million the boundary layer thickness decreases and the shock wave moves downstream; the boundary layer suction on the upstream part of the model produces a comparable effect ( $v_p = -3.6$  m/s). Some boundary layer calculations have been performed in the different configurations, with the experimental conditions. We have drawn the displacement thickness  $\delta_1$  of the upper side boundary layer along the model chord (fig 40). The suction produces a step on the boundary layer thickness evolution, even though the Reynolds effect is more regular. We can observe that the boundary layer thickness is quite the same just upstream of the shock wave location ( $X = 0.16m$ ). The static pressure fluctuations have been analysed with the signals of KULITE pressure transducers located under the thin skin of the rear part of the model. The data rate acquisition was 2000 pts/s; we present the 2 configurations spectra on figure 41 for the transducer located at  $X/C = 87.5\%$ . The levels are quite the same but the low frequency peak occurs at different frequencies : at high Reynolds number the frequency of the peak is lower (60Hz) than at ambient condition (83Hz) due to the temperature effect. The real parameter which remains constant is the reduced frequency called Strouhal  $F = f/U$  ( $f$  frequency,  $l$  characteristic dimension,  $U$  flow velocity at infinity). The measured frequency is shifted with the temperature ratio of the two configurations  $f_{150} = f_{290} (150/290)^{0.5}$ . The R.M.S. values of the pressure fluctuations decreases a bit with the Reynolds or the suction effects; so the flow separation size is decreasing also.

### 6.4. Artificial Tripping of Boundary Layer

A lot of tests in transonic conditions require the use of artificial tripping of the model boundary layer, usually close to the leading edge (to get proper turbulent condition (see § 6.3), to simulate Reynolds number effect, ...). So it is necessary to well adjust the height of the tripping device in connection with the local boundary layer characteristics. A special study has been performed about this purpose in the T2 wind tunnel, using 3D cylindrical roughness elements made of resin (Ref. 28). A variety of roughness heights and arrangements have been tested in a wide range of Reynolds number, measuring the total drag by the wake probing (fig. 42). A laminar curve is get without roughness and a turbulent one with carborundum grains of suitable size. When Reynolds number is increased, the boundary layer thickness is reduced and the used roughness element becomes more and more perturbing and efficient to trip the transition, inducing an increase of the total drag until a fully turbulent behaviour.

## CONCLUSION

T2 is an induction, pressurized, transonic wind tunnel, converted since 1981 for cryogenic operation. It is an

internal insulated facility, equipped with a high performance automatic control system and a test section with a 2D adaptive wall system.

T2 has a low turbulence level at ambient condition and for cryogenic operation ( $((\rho u)'/\rho u = 0.1 \%)$ ) and allows to perform laminar studies at high Reynolds numbers; a limitation remains for laminar tests under the dew point of the flow.

We have developed a lot of thin skin model, well adapted to the T2 short runs, cooled down directly by the flow during the first part of the run to reach a good temperature equilibrium before the measurements. We have improved the dew point level of the flow by replacing the heater system of T2 supply and now we can perform systematic tests in laminar condition down to 170K.

The last device developed around T2 is the 3D laser velocimeter, very useful at ambient condition and now able to measure in cryogenic condition.

The association of research and industrial activities allowed to analyse various subjects in an extended Reynolds number range : model performances, transition, laminar flow, buffeting and 2D or 3D wall adaptation performances, drag reduction technique.

## REFERENCES

- /1/ Michel R., Quemard C., Mignosi A., March 1979, "The induction driven tunnel T2 of O.N.E.R.A./C.E.R.T." *Journal of Aircraft*, Vol. 16, n° 3.
- /2/ Carriere P., 1972, "The injector driven tunnel." AGARD LS 1972-AGARD Report R-600-72.
- /3/ Michel R., Mignosi A., 1982, "Adaptation and first cryogenic operation of T2 O.N.E.R.A./C.E.R.T. Wind Tunnel." *La Recherche Aéronautique-2-1982*.
- /4/ François G., September 1982, "Thermal behaviour and insulation of a cryogenic wind tunnel." *E.T.W. Meeting*, Amsterdam (Netherlands).
- /5/ Chevallier J.P., Mignosi A., Archambaud J.P., Séraudie A., 1983-4, "T2 wind tunnel adaptive walls design, construction and some typical results." *La recherche Aéronautique*.
- /6/ Archambaud J.P., Mignosi A., May 18-20, 1988, "Two-dimensional and three-dimensional adaptation at T2 transonic wind tunnel of O.N.E.R.A./C.E.R.T." A.I.A.A., 15<sup>th</sup> Aerodynamic Testing Conference, San Diego, California (U.S.A.).
- /7/ Gobert J.L., Mignosi A., September 15-17, 1982, "Studies of the cryogenic induction driven wind tunnel T2." *E.T.W. Cryogenic Technology Review Meeting*, N.L.R., Amsterdam (Netherlands).
- /8/ Paci P., September 15-17, 1982, "Practical problems of design and manufacture of 2-D model and of the device for its cooling and introduction into the T2 pressurized cryogenic intermittent tunnel." *E.T.W. Meeting*, Amsterdam (Netherlands).
- /9/ Archambaud J.P., June 5-9, 1989, "The cryogenic induction tunnel T2 at Toulouse" *Special course on advances in cryogenic wind tunnel technology*, V.K.I., Rhode St Genèse (Belgium).
- /10/ Mignosi A., Archambaud J.P., Prudhomme S., Plazanet M., Payry M.J., June 28-30, 1988, "T2 ability concerning model design and instrumentation in short run processing." *Second Cryogenic Technology Review Meeting*, Köln/Porz (R.F.A.).
- /11/ Séraudie A., Blanchard A., Dor J.B. November 12-14, 1986, "Qualification d'essais en ambiance cryogénique à la soufflerie T2." 23<sup>ième</sup> colloque d'aérodynamique appliquée, Modane (France).
- /12/ Dupriez F., Geoffroy P., Outtier G. June 28-30, 1988, "Half transport aircraft cryogenic model for T2 wind tunnel." *Second Cryogenic Technology Review Meeting*, Köln/Porz (R.F.A.).
- /13/ Mignosi A., Arnal D., Prudhomme S., Reneaux J March, 1992, "Problems connected with laminar flows in a cryogenic wind tunnel." First European forum on laminar flow technology. Hamburg
- /14/ Blanchard A, Dor J B, Séraudie A, Breil J F. June, 1988, "Flow quality in the T2 cryogenic wind tunnel-problems and solutions." Second cryogenic technology review meeting Köln Germany
- /15/ Archambaud J.P. September, 1992, "Use of flexible walls to minimize interferences at T2 wind tunnel" European forum on wind tunnels and wind tunnel test techniques. Southampton.
- /16/ Prudhomme S., Séraudie A. September 18-21 1989, "Design of a three-dimensional Laser Doppler anemometer for T2 transonic wind tunnel." ICIASF'89 DLR Göttingen Germany
- /17/ Prudhomme S., Séraudie A, Mignosi A. August 5-9 1991, "A recent three-dimensional Laser Doppler applications at the T2 transonic wind tunnel : optimisation, experimental results, measurement accuracy." 4th international conference on laser anemometry advances and applications Cleveland OHIO (U.S.A.)
- /18/ Séraudie A, Mignosi A, Dor J B , Prudhomme S. October 4-7 1993, "Technique expérimentale de mesure en écoulement transsonique avec un système de vélocimétrie laser tridimensionnel. Application à la détermination de la traînée d'un fuselage." AGARD meeting Brussels (Belgium)
- /19/ Séraudie A, Archambaud J P, Blanchard A, Dor J B, Mignosi A. March 17-22 1991, "T2 cryogenic

transonic wind tunnel. Thermal design and control of the facility including models adapted for short run processing." 3rd ASME-JSME Reno Nevada (U.S.A.)

/20/ Blanchard A, Dor J B, Séraudie A. September 14-17, 1992, "New testing techniques in the T2 cryogenic wind tunnel." European forum on wind tunnels. Southampton university (U.K.)

/21/ Séraudie A, Dor J B, Archambaud J P, Blanchard A. March 16-18 1982, "Laminar flow testing in the T2 cryogenic wind tunnel." 1st European forum on laminar flow technology. Hamburg (Germany)

/22/ Séraudie A, Mignosi A, Dor J B, Payry M J, Barricau Ph, Breil J F. "Analyse fine de la transition en écoulement bidimensionnel : effet des gradients de pression sur le facteur n de début de transition." R.T.S. Derat N° 65/5006.47 Septembre 1994

/23/ Mignosi A May 20-24 1996, "Fundamental considerations for testing in cryogenic tunnels." Lecture 7 AGARD/VKI Special course : Advances in cryogenic wind tunnel technology". DLR KÖLN-PORZ (Germany)

/24/ J B Dor, Mignosi A, Séraudie A, Benoit B. May 24-27 1988, "Wind tunnel studies of natural shock wave separation instabilities for transonic airfoil tests." IUTAM symposium Göttingen (Germany)

/25/ Archambaud J P, Blanchard A, Dor J B, Payry M J. "Procès verbal d'essais de tremblement sur A320 dans la soufflerie T2 (2ieme campagne)". P.V. d'essais OA N°3423 AYD (DERAT N° 13/5017.13) Mars 1988

/26/ Caruana D, Mignosi A, Bulgubure C. September 8-13 1996 "Experimental study on transonic shock wave / turbulent boundary layer interactions and separations instabilities. Suction and Reynolds number effects." ICAS congres Sorrento Napoli (Italy)

/27/ Mignosi A, Bize D, Janvier 1993 "Investigation of the use of model coating materials in conjunction with infrared camera systems at cryogenic temperature. Phase 2 - The selection of coating materials : realization, mechanical, thermal and optic tests." RF DERAT N° 56/5006.37 (ETW contract)

/28/ Caruana D, Dor J.B., Payry M.J., Briel J.F. Etudes liées à la limite de tremblement. Transposition soufflerie - vol. Compléments d'essais RF DERAT N° 68/5006.50 - Octobre 1995

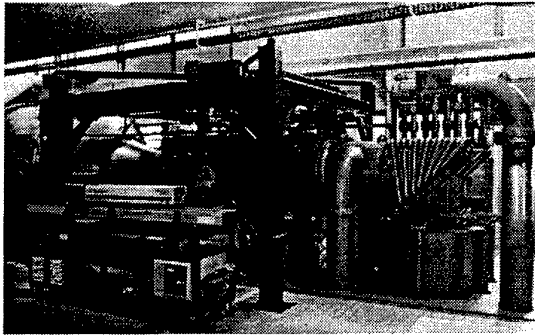


Figure 1 : T2 wind tunnel

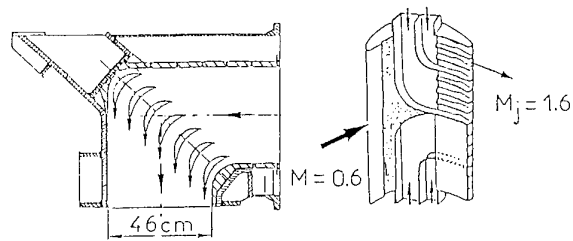


Figure 3 : Air injection corner

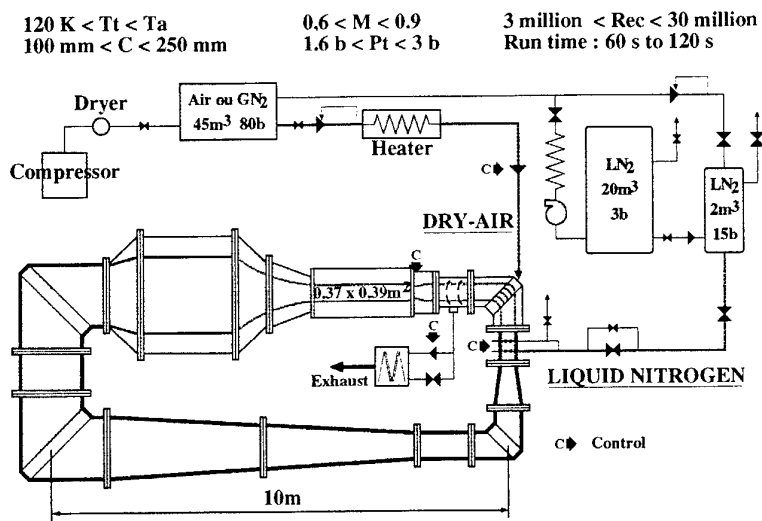


Figure 2 : The T2 wind tunnel layout

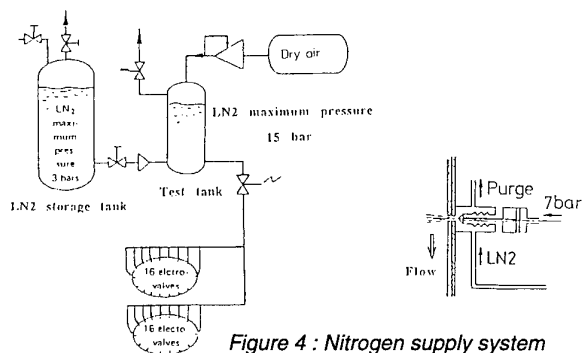


Figure 4 : Nitrogen supply system

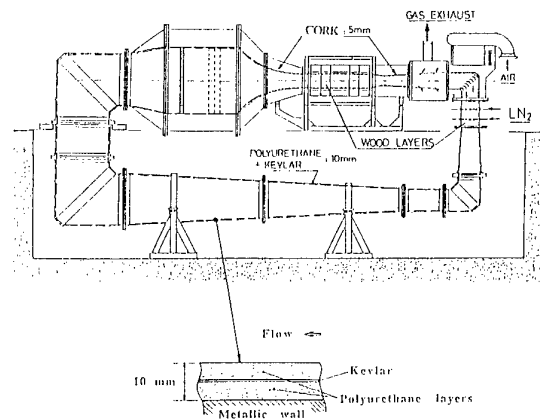


Figure 5 : T2 wind tunnel circuit insulation





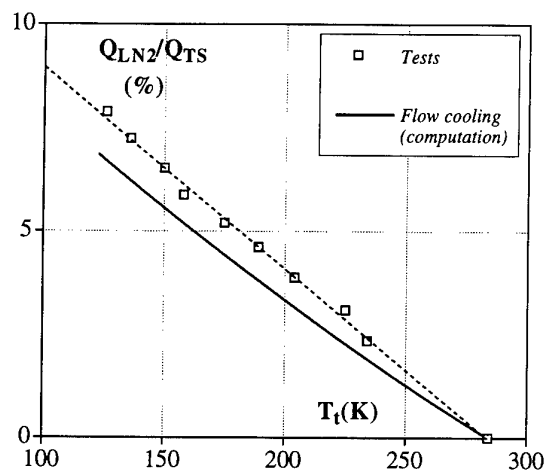


Figure 11 : Liquid nitrogen consumption

Metal	stainless steel ( Marval 18 or Maraging )
Skin	3mm thick
Manufacturing part	4 parts for 2-D models ( Leading edge, Trailing edge, upper and lower surface ) 2 parts for 3-D models: - wings : upper and lower surface - fuselage : right and left
Assembly	soldering ( A320 ) screwing ( AS409 )
Finition	accuracy $\pm 0.02$ mm hand made polishing
Instrumentation	pressure taps ( $\phi 0.1 \rightarrow 0.3$ mm ) foil thermocouples ( RDF ) miniature pressure transducers ( ENDEVCO, KULITE )

Figure 13 : Model general features

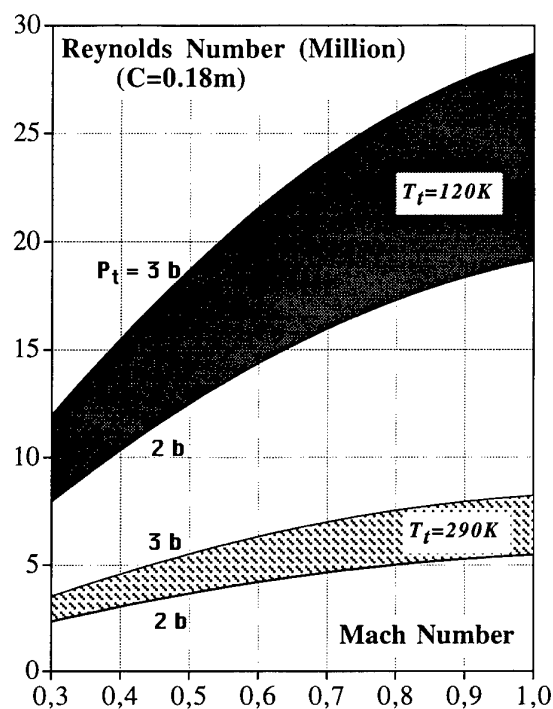


Figure 12 : T2 operating envelope

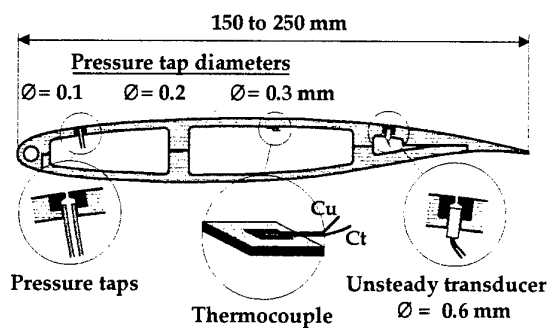


Figure 14 : Typical thin skin model

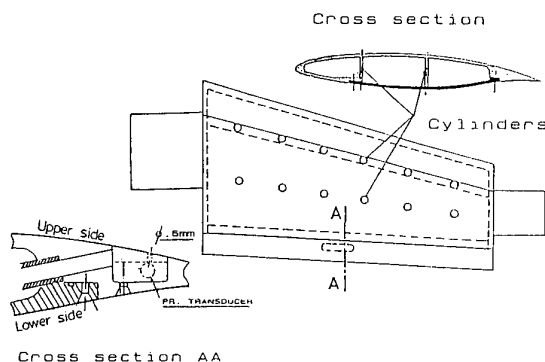


Figure 15 : AS409 model

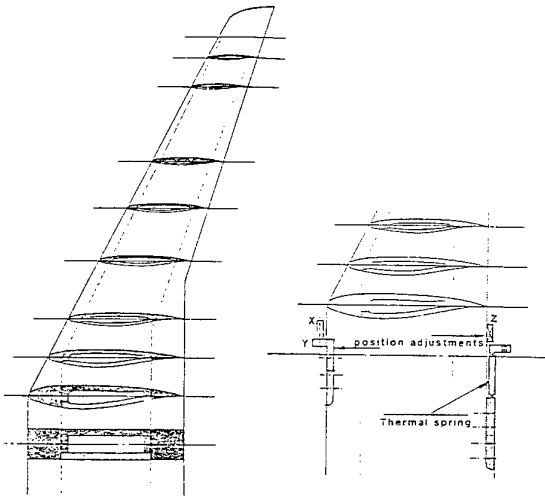


Figure 16 : A320 half model structure

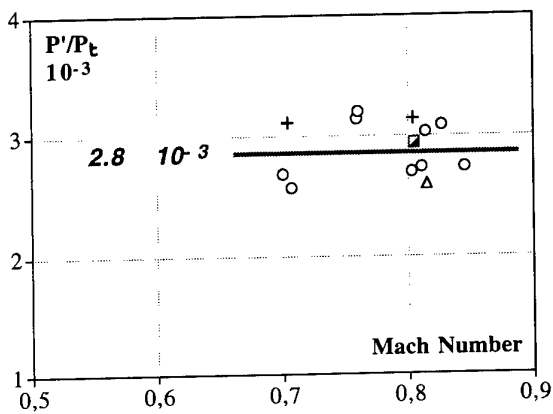


Figure 18 : Pressure fluctuation level at T2

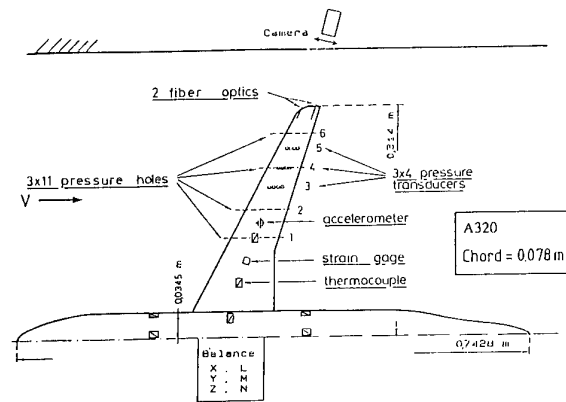


Figure 17 : A320 half model equipment

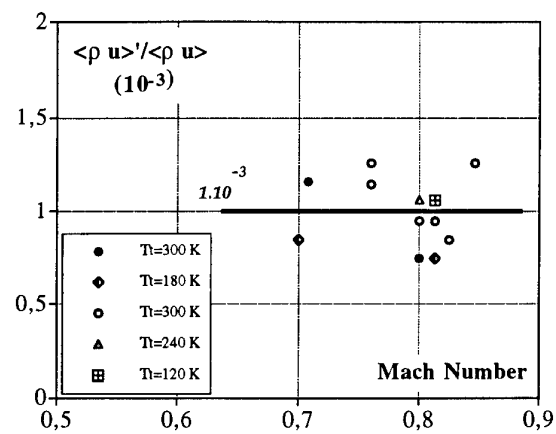


Figure 19 : Massflow fluctuation level at T2

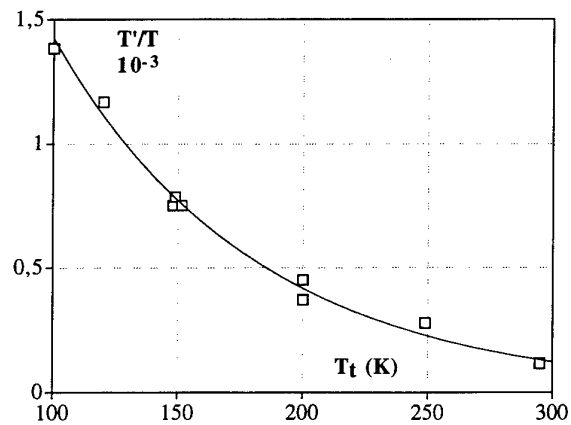


Figure 20 : Temperature fluctuation level at T2

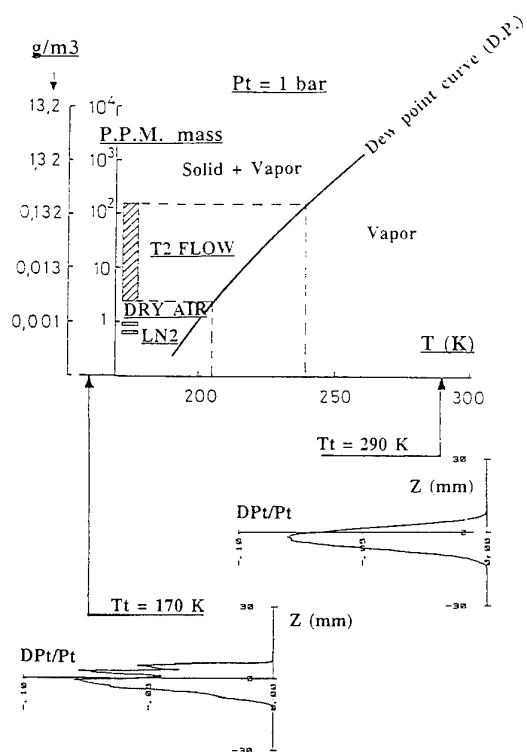


Figure 21 : Dew point in T2 test section

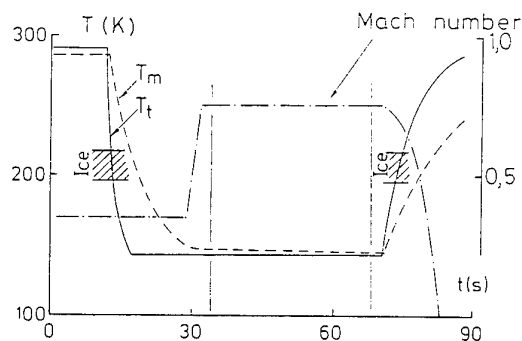


Figure 23 : Leading edge protection

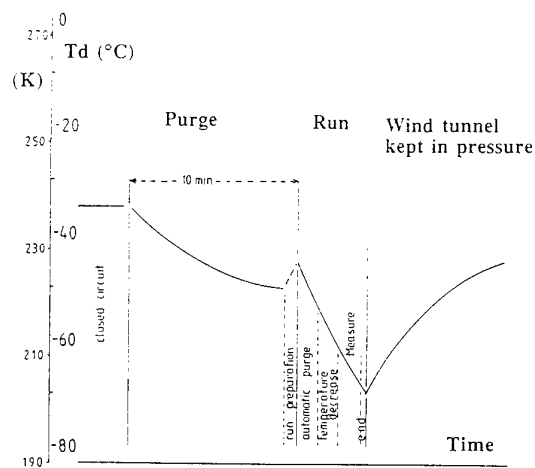
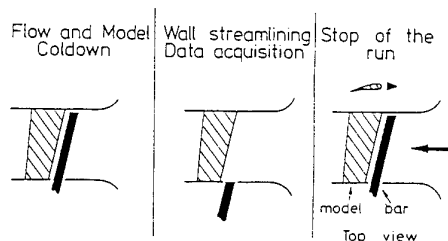


Figure 22 : Purge of the circuit

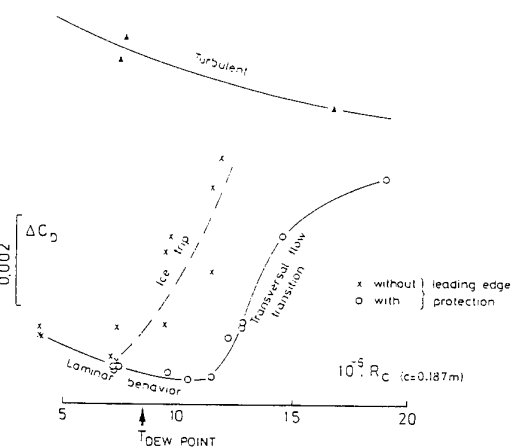


Figure 24 : Efficiency of the leading edge protection

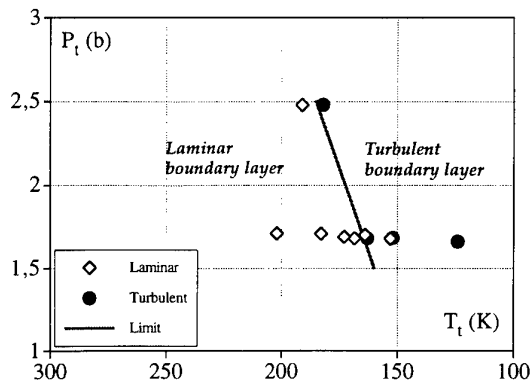


Figure 25 : Limit for laminar tests using LN2

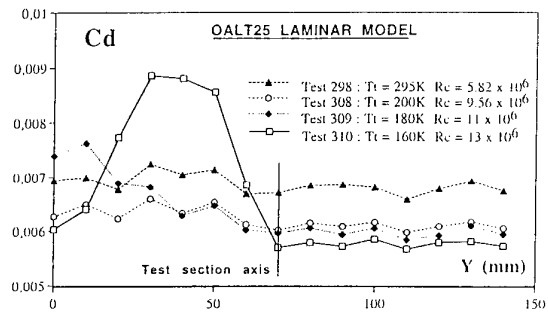


Figure 26 : Drag evolution in spanwise direction with Reynolds number

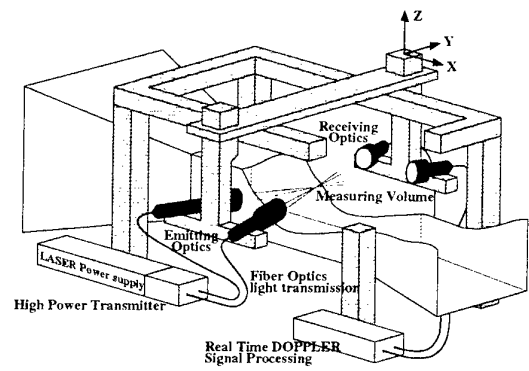


Figure 27 : The 3-D laser doppler anemometer

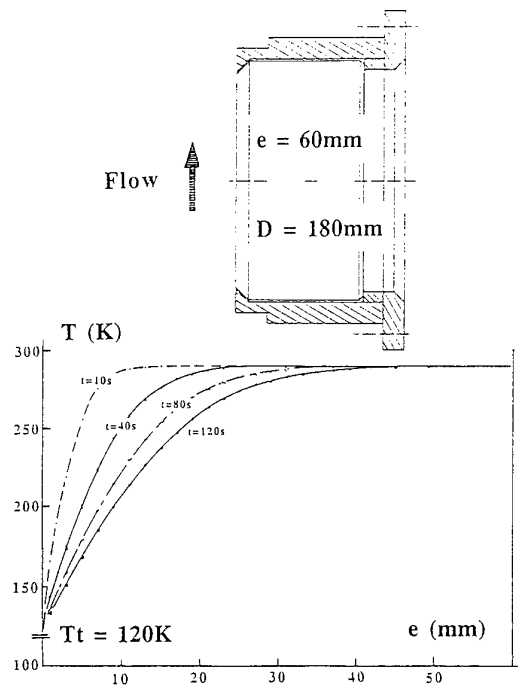


Figure 28 : Silica window design for cryogenic operation

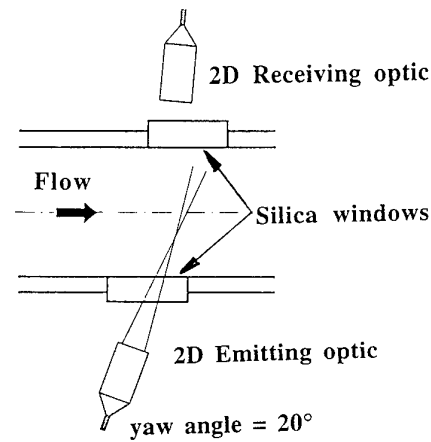


Figure 29 : Laser configuration used for cryogenic tests

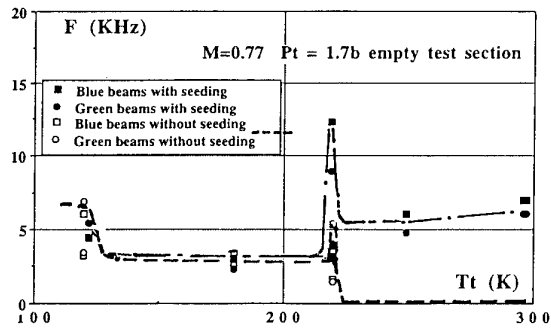


Figure 30 : Data acquisition rate evolution with temperature

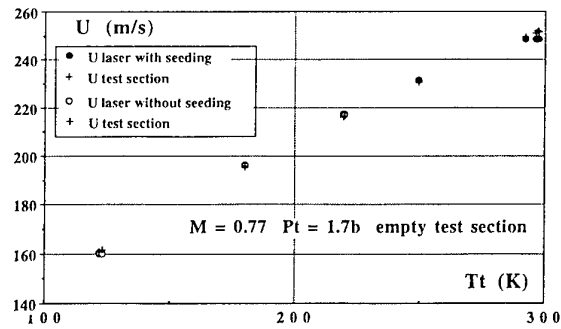


Figure 31 : Velocity measurement results

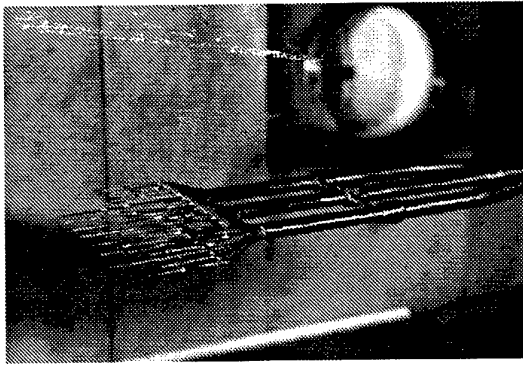


Figure 32 : Pressure wake rake : 21 pitot tubes, 7 static tubes

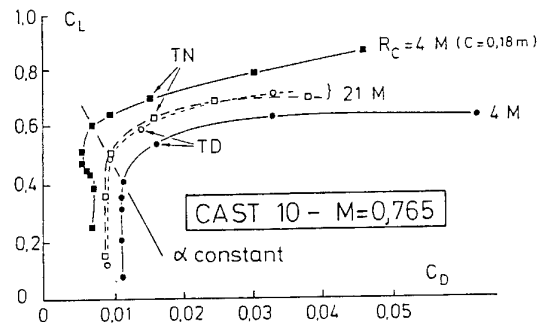


Figure 33 : Results on CAST 10 model

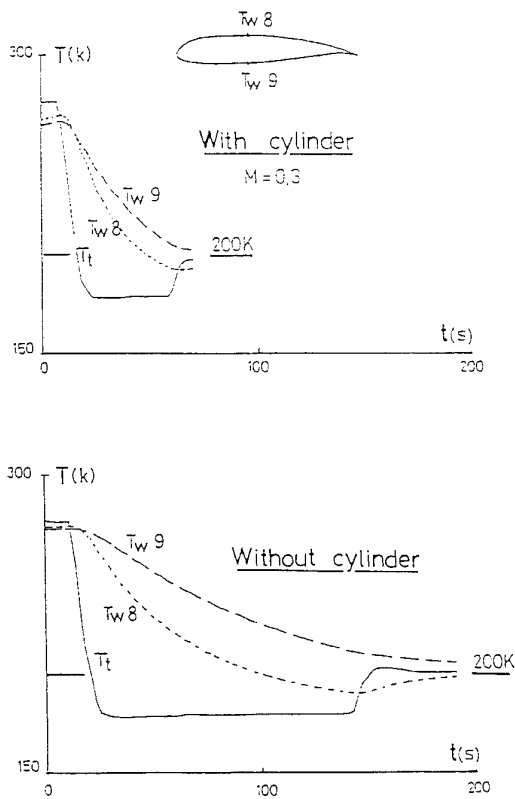


Figure 34 : Cylinder effect on a model cooldown

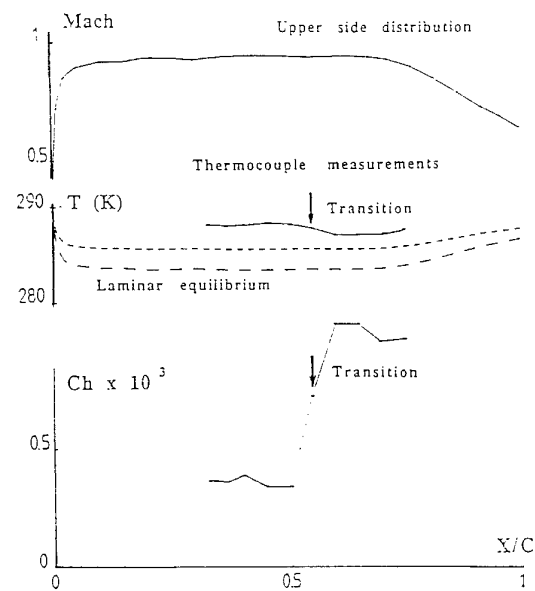


Figure 35 : Transition detection by thermocouples

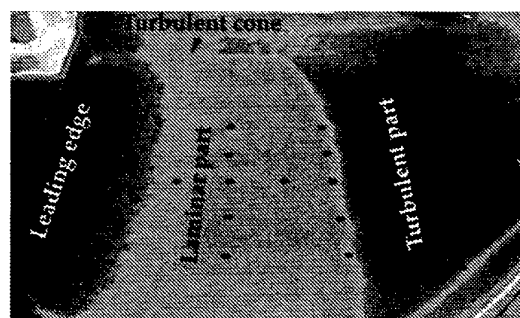
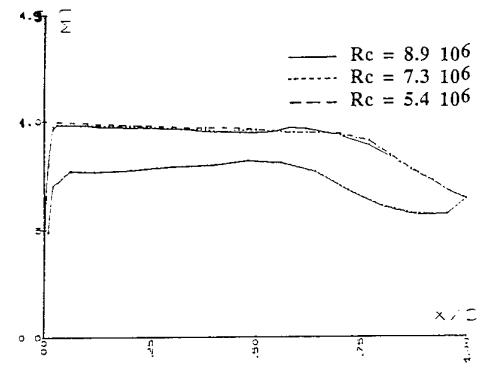


Figure 36 : Infrared imaging



$M = 0.7$

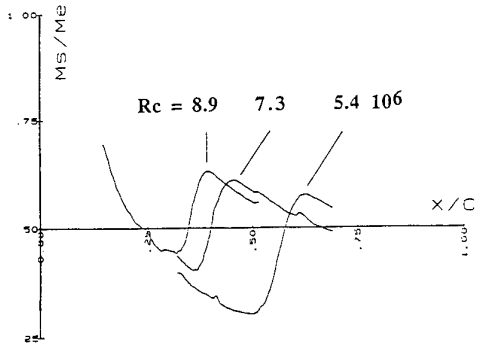
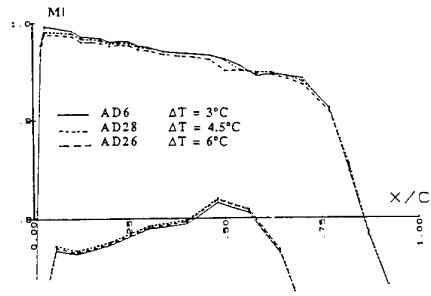


Figure 37 : Total pressure probing : Reynolds number effect on transition location



$M = 0.7$     $Pt = 1.7b$     $Rc = 5.4 \cdot 10^6$

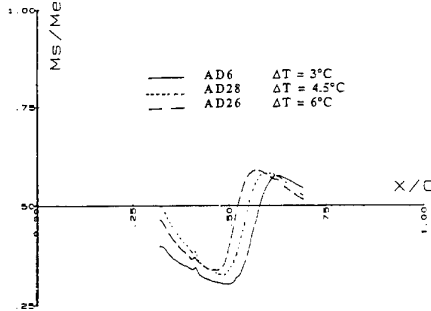
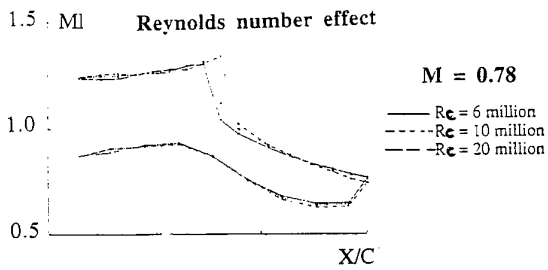
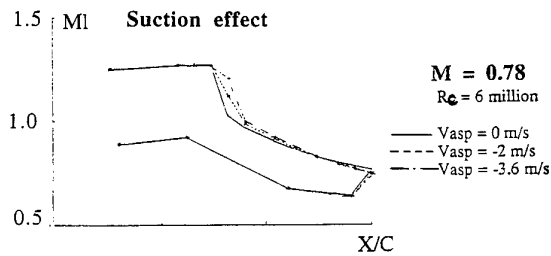


Figure 38 : Total pressure probing : model wall temperature effect on transition location



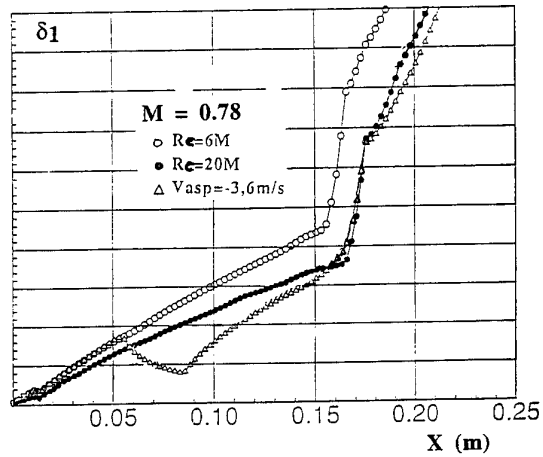
$M = 0.78$



$M = 0.78$

$Rc = 6 \text{ million}$

Figure 39 : Reynolds number and boundary layer suction effects on the shock wave location



$M = 0.78$

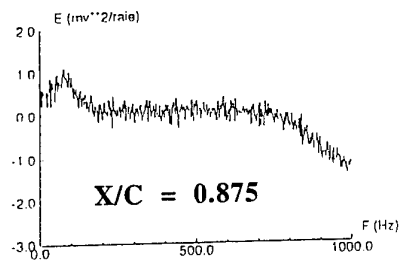
$Rc = 6M$

$Rc = 20M$

$\Delta Vasp = -3.6 \text{ m/s}$

Figure 40 : Reynolds number and boundary layer suction effects on the boundary layer evolution

**$R_c = 6$  million**



**$R_c = 20$  million**

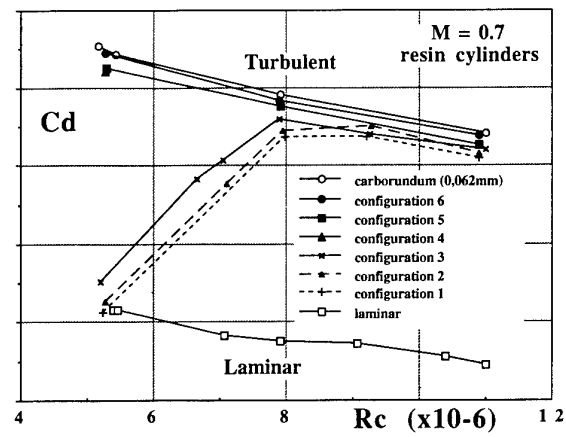
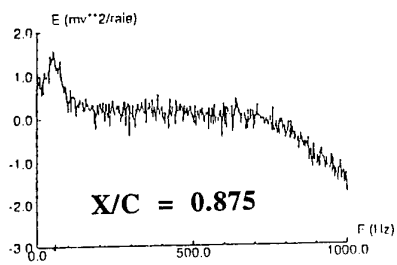


Figure 42 : Reynolds number effect on artificial transition trippings

Figure 41 : Reynolds number effect on pressure fluctuation spectra



# The Concept of the Kryo-Kanal-Köln (KKK)

## Operational Experience, Flow Quality, Model Handling and Half Model Testing Technique

G. Viehweger  
Pulheim, Kryo Kanal Köln  
Postfach 906058  
51140 Köln, Germany

### SUMMARY

The aerodynamic calibration of the KKK at ambient and cryogenic temperatures was completed in 1989. In parallel the control system of the tunnel, which is constructed in a modular basis, was modified and improved to save liquid nitrogen consumption.

During this time operating problems in the circuit and in the subsystems resulting from the cryogenic mode of operation were identified and solved. Basic tests were performed to understand the physics of the desorption of moisture from the internal insulation into the circuit which resulted in a special purging procedure before cryogenic operation.

The aerodynamic tests demonstrated the high flow quality in the test section in the whole operation range.

This paper will give a review on the experimental experience and describes the test equipment of the tunnel.

### LIST OF SYMBOLS

$C_w$	[-]	drag coefficient of the screens
$F_{TS}$	[m <sup>2</sup> ]	cross section of the test section
$m$	[t]	mass
$Ma$	[-]	Mach number
$p$	[mbar]	pressure
$p_{tot}$	[mbar]	total pressure
$p_{stat}$	[mbar]	static pressure
$Re$	[-]	Reynolds number
$t$	[h]	time
$T$	[K]	tunnel temperature
$T^*$	[C°]	gas temperature respectively dew point temperature
$Tu_x$	[-]	longitudinal turbulence
$U, V, W$	[m/s]	velocities

$u', v', w'$	[m/s]	velocity fluctuations
$x, y, z$	[m]	coordinates
$\Theta$	[Grad]	pitch angle
$\Phi$	[Grad]	roll angle
$\nu$	[m <sup>2</sup> /s]	viscosity

### Indices

$G$	gas
$LN_2$	liquid nitrogen
$\infty$	undisturbed

### 1. INTRODUCTION

As is well known, the KKK is the second big cryogenic wind tunnel in operation following the NTF at the NASA Research Center in Langley [1,2].

The tunnel is to be seen in connection with the European Transonic Wind Tunnel ETW. The fact, that KKK and ETW have nearly the same test cross section, turned out to be an essential advantage. In both tunnels the same models can be tested and there is additionally an overlap in the operation range. During the phases of design and construction of the ETW a fruitful transfer of experience and know how flowed from the KKK into this project.

To enable cryogenic test operation the KKK has some additional systems which distinguish the cryogenic tunnel from a conventional tunnel (Fig. 1). These are as follows:

- A closed test section including an access lock and a model conditioning room for handling the model, while the tunnel circuit is held at low temperature,
- a liquid nitrogen injection system to control the gas temperature [3,4],
- an exhaust system to control the tunnel pressure,
- an internal insulation to protect the shell of concrete from the low temperature,
- a control system to control Mach number, temperature and pressure in the required accuracy.

The temperature of the test gas can be varied between 300 K and 100 K by injecting liquid nitrogen into the circuit downstream corner vane 2. In the cooling process the obtained Reynolds number at constant drive power may be increased 5.5 fold. The Reynolds-Mach number capability of the tunnel is shown in Fig. 2. Thus by independent variation of the test parameters the influence of the Mach number, Reynolds number and dynamic pressure (strain) on the model results may be considered separately.

The tunnel has the following technical data:

Test section dimensions	2.4 m x 2.4 m
Length of the test section	5.4 m
Cross section area	5.76 m <sup>2</sup>
Max. model wing span	1.5 m
Static pressure in the test section	atmospheric
Temperature range	100 K to 300 K
Max. Mach number (300 K)	0.325
Max. Mach number (100 K)	0.38
Max. Reynolds number	$9.5 \times 10^6$
Fan power	1 MW
Loss coefficient	0.171

In the case of 2-D-model and half model testing Reynolds numbers of  $15 \cdot 10^6$  resp.  $27 \cdot 10^6$  will be achieved.

This paper will give a short review on the facility components and summarizes the testing experience with regard to cryogenic operating considerations. Also presented are the results of the aerodynamic and cryogenic calibrations and of the status of the test equipment.

## 2. TEST SECTION AREA

The test section area consists of the contraction, the test section itself, and the transition section to the 1st. diffuser as well as lock and model conditioning room (Fig. 3).

In the nozzle with the contraction of 1:10.3 the cross-sectional modification from the octagonal settling chamber to the square test section takes place. The top and bottom walls of the test section run parallel to each other; the two side walls diverge under a fixed angle of  $0.12^\circ$  per wall to compensate the displacement effect of the wall boundary layer. The aperture angle was defined for a mean tunnel temperature in view of the large Reynolds range of the tunnel.

The side walls are equipped with four windows (500 mm  $\varnothing$ ) of schlieren quality, to allow the model to be observed and to allow the use of optical measurement techniques. Furthermore there are two strips with pressure holes located along each wall to enable measurement of the static pressure required for the wall pressure correction process.

In the test section floor there is an opening measuring 1.5 m in width and 3.1 m in length corresponding to the dimensions of the model carts. The upper cover of the cart serves as test section floor for the duration of the tests.

Below the test section are the access lock and the model conditioning room. Both rooms serve to carry out alterations on the model at ambient temperature while the tunnel is held at low temperature. This ensures economical operation of the tunnel. As the lock and the model conditioning room have individual temperature systems for cooling down and warming up they can be employed as independent cryo-test facilities.

## 3. MODEL HANDLING UNDER CRYOGENIC CONDITIONS

If changes need to be made to the model during low-temperature operations, a lift system is used to lower the model cart into the lock, which is at the same temperature as the tunnel. The hole in the floor of the test section is then sealed with a vapor-tight cover, the horizontal door (Fig. 4), to isolate the lock from the low-temperature tunnel. If major conversions are to be made to the model, or if the model is to be changed, the model cart remains parked in the lock. Then the inside of the lock is gradually warmed up by circulating warmed nitrogen gas. The complete operation takes almost four hours, owing to the great mass of the steel model support and the lift system. Finally, before human entry dry air is blown in.

For model handling the riggers at first will enter the entrance lock, which has been installed in front of the gate of the lock as an improvement in 1995. After this inside this separated room the dewpoint will be lowered to the level of the lock by an individual purge system, before the door to the lock will be opened.

The model riggers are equipped with special air breathers in a closed circuit, which allow an operation time of one hour. Thus the penetration of humidity from breath to partly colder parts of the model will be avoided.

Before the model is moved back into the test section, it first has to be cooled back down to the prevailing tunnel temperature. This is done in the lock by injecting liquid nitrogen after the purging operation. Circulating blowers run during the injection phase in order to ensure largely homogeneous cooling of the model, the model cart and the room.

The above mentioned Model Conditioning Room is normally used for check out of model and instrumentation.

All movements of the lift system and monitoring of the warm-up and cool-down processes are controlled from a console in the test hall.

Cool down and warm-up times for lock and model conditioning room:

Cool-down		Warm-up
(300 K $\rightarrow$ 100 K)		(100 K $\rightarrow$ 300 K)
Lock	3 h	4 h
MCR	1 h	1 h

#### 4. MODEL CARTS

##### 4.1 Support System for Complete Models

For measurements on complete models, the model cart illustrated in Fig. 5 is used. It has a universal connecting flange for tail stings on the torpedo head.

In cryogenic operation, the structure of model cart and support take over the temperature prevailing in the tunnel. Several blowers installed in the model cart ensure rapid temperature adaptation of the parts of the structure and, consequently, reliable functioning of the adjusting and traversing devices. The drive motors themselves are installed in heated chambers. Heated connector boxes are installed in the model cart for the plug-and-socket connections of the power cables and measuring lines.

The technical data of the model support are as follows:

- Angular adjustment ranges
  - angle of attack  $-10^\circ \leq \Theta \leq +30^\circ$
  - roll angle  $-90^\circ \leq \Phi \leq +90^\circ$
- Adjustment speeds
  - angle of attack  $\dot{\Theta} = 0.3^\circ/\text{s}$
  - roll angle  $\dot{\Phi} = 0.5^\circ/\text{s}$

Sideslip angles are obtained by combination of pitch and roll.

##### 4.2 Model Cart for 2-D and Half Models

The model cart shown in Fig. 6 is extensive adjustable. It can be equipped with a special turning device for 2D-models up to a wing chord of 1 m, by which Reynolds numbers of 27 mill. can be achieved.

In this figure the bringing in the model in test position is shown in detail. Because of the great span width of the model of 2.4 m it has to be turned at first before the model cart is moved into the lock. After this the model is turned upright, lifted into the test section and connected to the adjustment mechanism for the angle of attack in the ceiling of the test section.

At present time this cart is equipped with a special device for half model testing.

#### 5. HALF MODEL TESTING TECHNIQUE

The half model testing technique, which results in a remarkable increase of the Reynolds number has been developed and installed in the KKK during 92 to 95. The provision of a half model mounting and balance in the KKK qualify the tunnel for highly efficient use in the Airbus aerodynamic development program and in fundamental research on high lift systems [5]. The balance was designed, fabricated and calibrated by the University of Darmstadt [6].

Because of the big masses of half model balance and as a result of extensive experiences on cold tail sting internal balances, the heated balance option was chosen. Thus the long time waiting period necessary for sufficient temperature uniformity in the balance is avoided.

The half model will be mounted in the test section floor on a turntable, which represents the symmetry plane of the model and allows to set angle of attack. The turntable is mounted on the structure of the 2-D model cart and is connected to the earth frame. The model itself is mounted on the rotating balance (Fig. 7).

During the tests the upper and the lower side of the wing can be observed from both sides of the test section, using special methods for surface flow visualization. Windows in the ceiling of the test section will allow additional flow field measurements in the slots of high lift configuration elements to investigate the influence of Reynolds number effects.

The balance is integrated in a temperature conditioning system of special design (Fig. 8).

Above and below the balance flanges an insulation layer of high strength, low heat conductivity and very small extension coefficient is arranged, so a stable connection between model, balance and earth is guaranteed.

Heated metal plates interrupt the heat flux to the balance, which is already reduced by the insulation layers. Finally equalizing layers result in a uniform temperature distribution at both flanges of the balance. The thickness of the insulation layer between the half model and the heated plate was dimensioned in such a way, that it still results in a small heat flux to the model. The turntable bearing and the angle of attack drive are conditioned to ambient temperature as well.

Circumferentially the balance is protected from the cold environment by a cylindrical superinsulation, which also encloses the structural connections between the angle of attack drive and the turntable in the bottom of the test section.

To heat the different components of the temperature conditioning system with the required accuracy in total 5 temperature controllers are needed, which get their signals from a number of temperature sensors installed in selected locations of the balance respectively of the insulation plates.

## 6. INSTRUMENT BOX FOR FLIGHT ATTITUDE MEASUREMENT

To be able to measure the angle of attack and the roll angle of the model with the necessary accuracy of  $\leq 0.02^\circ$ , regardless of the tunnel temperature, the angles are therefore recorded directly in the aircraft model and thus measured in isolation from all deformations which may occur in the support system. The angle of attack and the roll angle are each determined by one inclinometer. The zero position of the model in relation to the angle of attack and roll angle is recorded by two "bubbles" which can be used in a measuring range of  $\pm 5^\circ$  and have an accuracy of  $< 0.01^\circ$ .

As neither the inclinometers nor the bubbles are suitable for cryogenic conditions, they are located in a superinsulated, heated box, in which the temperature can be maintained at a constant level  $\pm 0.1^\circ$ . Using a superinsulation, the heat power could be restricted to 28 Watt. The inner structure consists of aluminium, a material with high heat conductivity, to ensure a well balanced temperature field around the inclinometers and bubbles (Fig. 9). The instrument box is installed in the tip of the fuselage and bolted directly to the balance adapter. As flange material carbon fiber is used.

## 7. MODELING AND CONTROL OF THE TUNNEL

A critical factor in the efficient operation of a cryogenic tunnel is the minimization of the nitrogen consumption and thus the operation costs. This can only be achieved through rapid and precise change in the flow parameters Mach number, pressure and temperature.

Whereas on the one hand the cryogenic tunnels allow parameters to be controlled independently of each other, on the other hand every input change influences all tunnel variables simultaneously and lead thus to spacial and time interactions in the tunnel circuit.

This process was mathematically modeled and takes into account the model altitude [7,8]. During the calibration phase of the tunnel the control system was modified and improved and now the KKK can be run up using a preset temporal ramp function.

Figure 10 shows one of the results for one test set point. The Mach number in the test section is

$Ma = 0.2$  and will be achieved after a time of 120 sec. The fluctuation of the Mach number during the testing phase is  $\Delta Ma \leq \pm 0.001$ . The static pressure fluctuates about  $\pm 0.05$  mbar. The third curve shows that the test gas temperature in the test section only fluctuate in a small range of  $\Delta T \leq 0.1$  K.

## 8. RESULTS OF FLOW QUALITY MEASUREMENTS

To measure the flow quality in the test section of the KKK the 2-D-Model Cart has been equipped with rakes of total pressure tubes and thermocouples. Furthermore hot wire probes were used to measure the turbulence level.

The temperature distribution in the test section at the location of the model ( $x = 0$ ) is shown in Fig. 11. The tunnel velocity is 50 m/s. The non-uniformity of the temperature is  $\pm 0.5$  K at the lowest operating temperature of the tunnel of 100 K.

Figure 12 shows the longitudinal velocity fluctuations as a function of the Reynolds number at ambient temperature and at 200 K. The longitudinal turbulence at ambient temperature in the Reynolds number range between  $0.6 \cdot 10^6 \leq Re \leq 1.9 \cdot 10^6$  is between  $Tu_x = 0.035\%$  and  $0.11\%$ . It is thus virtually identical to the values measured in the German-Dutch Wind Tunnel (DNW). The curve above illustrates the increase in the axial velocity fluctuations resulting from lowering the gas temperature to 200 K. The higher turbulence levels measured at 200 K may possibly be attributable to temperature spots upstream of the test section. Downstream of the last screen of the settling chamber, they unavoidably generate vorticity owing to the acceleration of the flow in the contraction. In addition, the  $c_w$  value of the screens drops at decreasing temperatures, i.e. there is less damping of the turbulence.

The mentioned data for the temperature distribution and the turbulence level in the test section of the KKK are in accordance with the requirements for a modern wind tunnel.

## 9. PURGE AND COOL-DOWN PROCEDURE IN THE KKK

The KKK is equipped with an internal insulation in contact with the tunnel flow [9]. During the purge process, water diffuses from the insulation into the dry purge gas. The moisture contained in the tunnel gas can be eliminated fairly rapidly, whereas moisture transport from the insulating material is a lengthy process.

To investigate the transport mechanisms of moisture from the insulation into the tunnel, a representative  $1 \text{ m} \times 1 \text{ m}$  section of the insulation was installed in a

special purge chamber. To prevent horizontal vapor diffusion from the test sample, its vertical cut surfaces, were sealed with vapor-tight aluminium foil [10,11].

The transport of water vapor from the wooden liner and from the polyurethane foam was investigated separately in order to establish which component of the insulation makes the dominant contribution to the moisture concentration.

The first diagram in Fig. 13 shows the dew point temperatures measured in the exhaust gas from the purge chamber as a function of purging time. It can be seen that far more water vapor diffuses from the wooden liner than from the polyurethane foam. Therefore, the moisture content of the tunnel flow is decisively determined by the diffusion of water vapor from the wooden liner.

To determine the transport of water vapor from the wooden sample as a function of temperature as well additional tests were performed.

In Fig. 13 is to be seen the dew point temperature measured at various wood temperatures during purging and the recovery phase without purging. It can be seen that, as a result of the cooling of the wood, there is a decisive reduction in water vapor transport into the warm  $\text{GN}_2$  purge gas. This means that low dew point temperatures are obtained in a much shorter purging time. These test results lead to a special purge procedure which now is used in the KKK in the cooling-down process.

Figure 14 shows the gas and dew point temperatures measured in the KKK test section during a cool-down procedure as a function of time. At the start of purging, the dew point temperature was  $6^\circ\text{C}$ , i.e. the volume of gas in the tunnel ( $4.600\text{ m}^3$ ) contains a mass of 32 kg water at  $T = 290\text{ K}$ . To eliminate the greater part of the water, the tunnel is purged with about 6 kg/s dry air for 2 hours. The dew point temperature is then  $-18^\circ\text{C}$  and the tunnel gas still contains 4.3 kg water. Subsequently, 3 kg  $\text{LN}_2$  are injected at the same time as the 6 kg/s dry air. The gas temperature falls rapidly at the start and is kept above the dew point temperature at all times by reducing the rate of  $\text{LN}_2$  injection to about 1 kg/s. The gas and dew point temperatures were caused to intersect at  $-48^\circ\text{C}$ . The  $4.600\text{ m}^3$  tunnel gas then contain only 0.223 kg water. Below this point of intersection, the tunnel can be cooled down without problems. It should be noted that the fan operates constantly during the cool-down procedure in order to ensure effective mixing of the moist and dry air.

## 10. TESTING SEQUENCES

In Fig. 15 the Reynolds-Mach number area of a model, like it is practiced in the KKK, is shown. In this

case the tests were performed at a number of different temperature levels.

A typical scenario during a cryogenic test series is to be seen in Fig. 16. The cooling-down phase of the tunnel will start with the purge procedure before described down to the critical dew point of  $-48^\circ\text{C}$ . Included is a change of the model configuration in the lock below the test section at ambient temperature.

## 11. CONCLUSION

The calibration tests under ambient and cryogenic conditions have shown the high flow quality of the tunnel over the whole operating range.

The computer-controlled control system regulates the test parameters Mach number, Reynolds number and temperature with the required accuracy. A special procedure has been developed for purging the tunnel before the cool-down process, ensuring that the temperature drops below the critical dew point in a save way. Extensive experiments with several complete models and a 2-D model were successfully performed. The shortly installed half model testing technique is now in undergoing tests.

## 12. REFERENCES

1. Viehweger, G., "Kryogenisierung des Niedergeschwindigkeits-Windkanals Köln-Porz - Spezifikationsphase -", DFVLR WKT 11/80, Köln-Porz, 1980.
2. Viehweger, G., "The Kryo-Kanal Köln (KKK): Description of the Tunnel Conversion, Thermal Insulation, Instrumentation, Operational Experience, Test Results and Operating Costs", AGARD CP-774, Paper 4, June 1989.
3. Distelrath, D., "Experimentelle Untersuchungen zum Stickstoff-Einspritzsystem des Kryo-Kanal Köln", DFVLR IB 157-80C30, Köln-Porz, 1980.
4. Distelrath, D., "Die Stickstoffanlage des KKK, Teil 1: Das  $\text{LN}_2$ -System", DFVLR IB 39151-83A13, Köln-Porz, 1983.
5. Viehweger, G., Ewald, B., "Half model testing in the Cologne Cryogenic Tunnel (KKK)", AIAA-94-2511.
6. Ewald, B., Hufnagel, K. and Graewe, E., "Grundsatzuntersuchungen zum Temperaturverhalten von DMS-Waagen-Axialkraftteilen", Ergebnisbericht Nr. 1, A10/85, TH Darmstadt, 1985.
7. Palancz, B. and Kronen, R., "Mathematische Modellierung, Simulation und Regelung eines kry-

ogenen Windkanals", DFVLR IB 29100-A03, Köln-Porz, 1982.

8. Kronen, R., "Automatical Control of KKK, Requirements, Sensors, Actuators and Control Performance Results", AGARD CP-774, Paper 5, June 1989.
9. Palancz, B. and Schäfer, B., "Unsteady Thermal Stress Analysis of a Cryogenic Foam Insulation Element", DFVLR FB 81-17, 1981.
10. Stahl, B., Becker, W. and Viehweger, G., "Untersuchungen zum Phänomen der Eiskristallbildung in Kryo-Windkanälen mit Innendämmung am Beispiel des KKK", DLR IB 39114-90A07, Köln-Porz, 1990
11. Stahl, B., "Investigations on the Formation of Ice Crystals the Cryogenic Wind Tunnel Cologne", Royal Aeronautical Society, Paper 24, Sept. 1992.

### 13. FIGURES

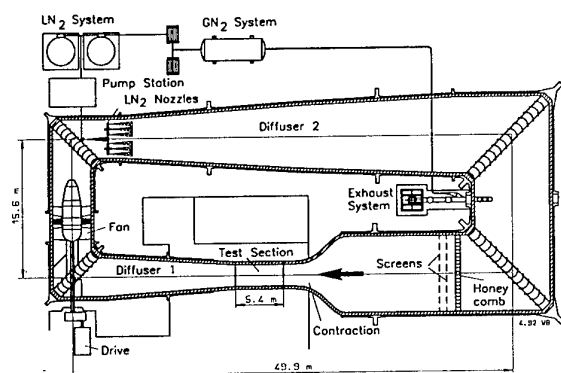


Figure 1. KKK circuit and cryogenic features

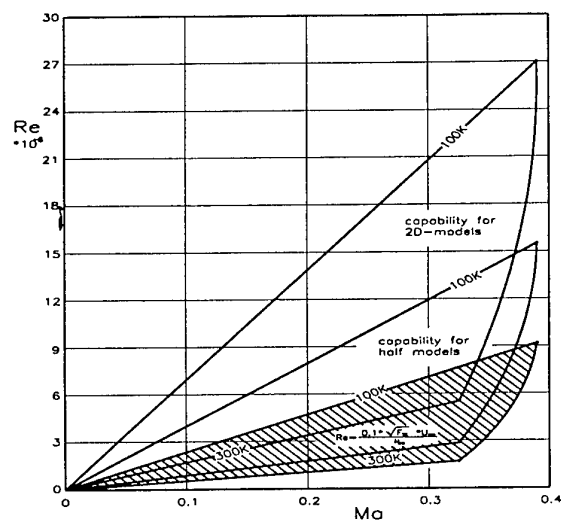


Figure 2. The Reynolds-Mach-capability of KKK

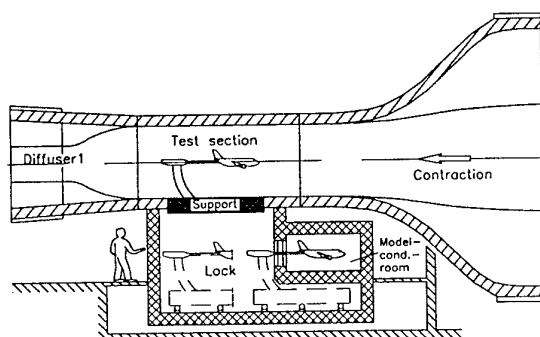


Figure 3. Test section area of the KKK

Test section:	2.4 x 2.4 x 5.4 m
Contraction length:	7,0 m
Contraction ratio:	1:10.3

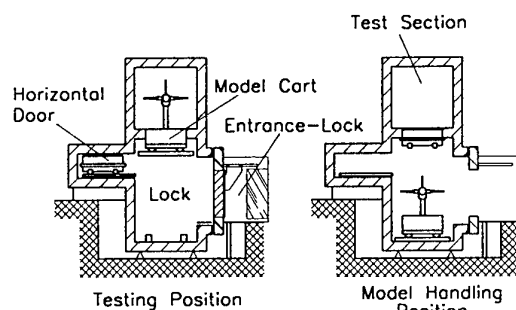


Figure 4. Model cart in test position and in model handling position

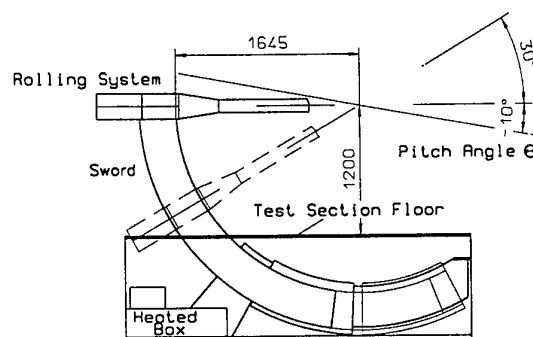


Figure 5. Model cart and model support for complete model testing

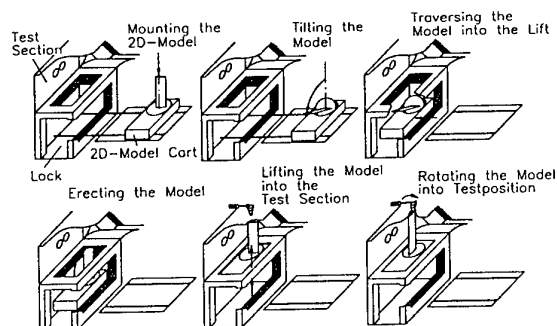


Figure 6. Proceed the 2-D model into test position

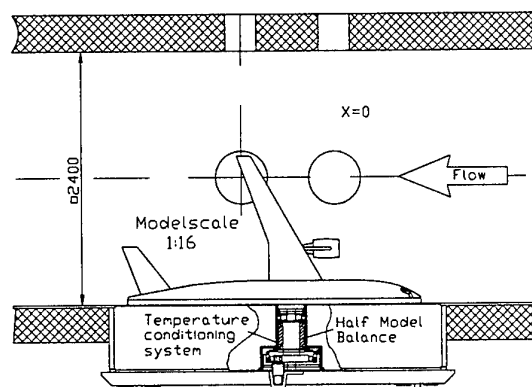


Figure 7. Half model arrangement in the test section of KKK

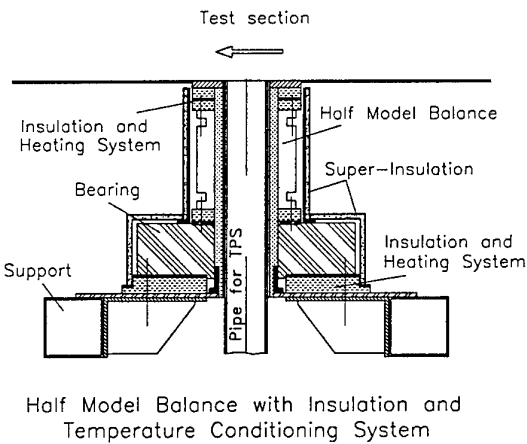


Figure 8. Half model balance with insulation and temperature conditioning system

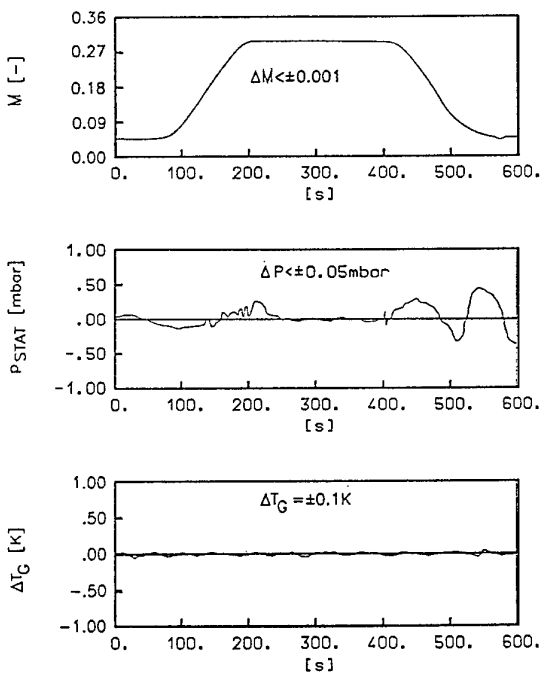


Figure 10. Controller action of KKK during testing phase at  $T = 200 \text{ K}$

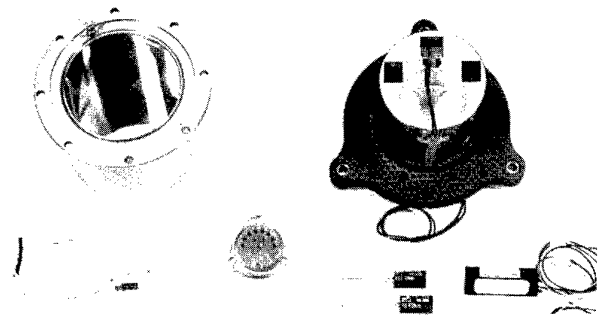


Figure 9. Instrument box for flight attitude measurement

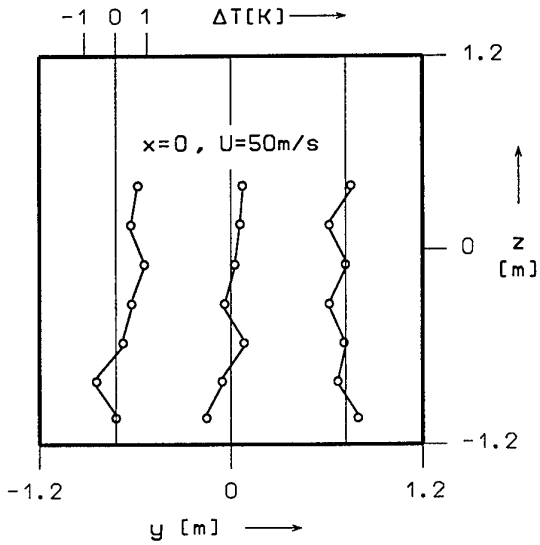


Figure 11. Distribution of the temperature in the test section at  $T = 100 \text{ K}$



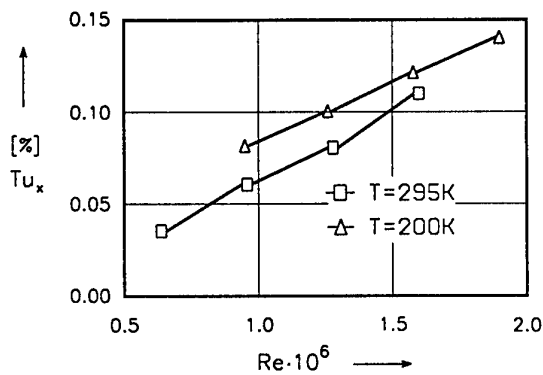


Figure 12. Longitudinal turbulence level in the test section as a function of the Reynolds number at various gas temperatures

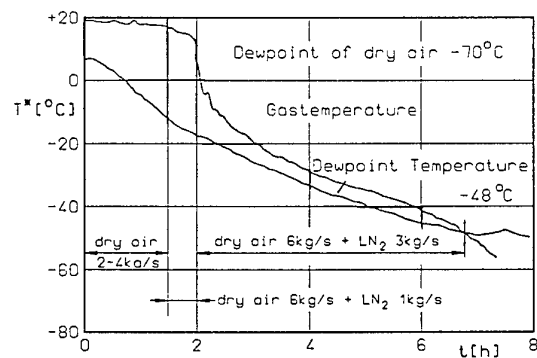


Figure 14. Dew point temperature and gas temperature during purging and cooling procedure of KKK

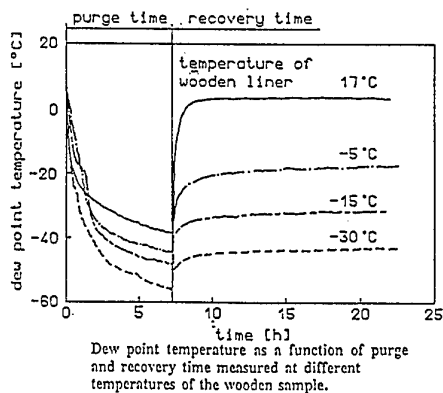
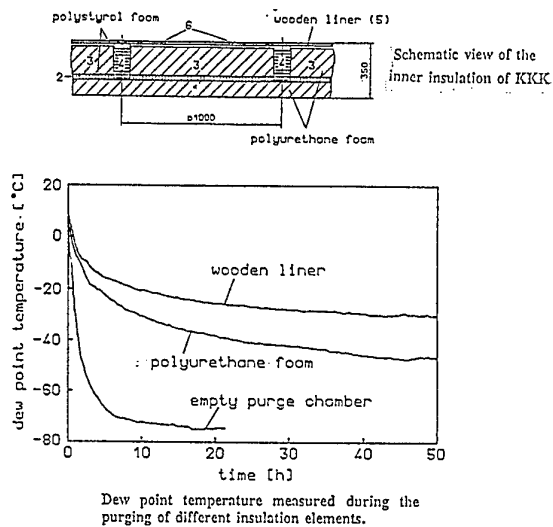


Figure 13. Basic tests at an insulation element of KKK

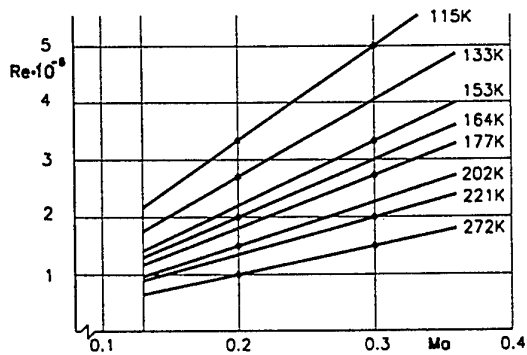


Figure 15. Typical test program for independent variation of Mach number and Reynolds number

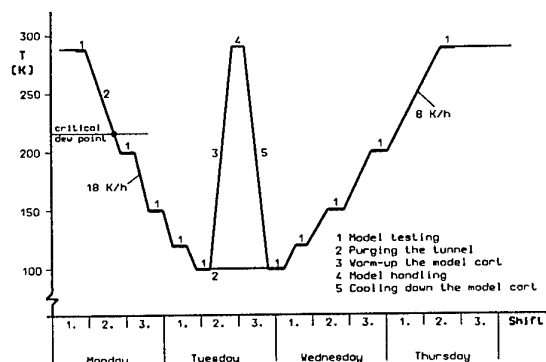


Figure 16. Typical scenario of a cryogenic test series

## Development of Correction Procedure for Signals of cryogenic Balances

R. Rebstock  
DLR Porz-Wahn  
Linder Höhe  
51147 Köln  
Germany

### 1. SUMMARY

Requirements in accuracy and repeatability of test results given by aircraft industry are increasing more and more. Therefore, it is essential to recognize in time all influence on cryogenic balances like model weight and geometric and influence of moisture and temperature gradients top be able to make corrections with suitable procedures. A special attention is paid on diffusion of moisture into carrier material of the strain gauges, which into be avoided by convenient coatings.

### 2. LIST OF SYMBOLS

#### Geometric Values

$F_{TS}$	[m <sup>2</sup> ]	test section area
$l_u$	[m]	design wing cord
$x, y, z$	[m]	coordinates

#### Aerodynamical Values

$C_l$	[-]	lift coefficient
$C_{lmax}$	[-]	maximum lift coefficient
$C_D$	[-]	drag coefficient
$C_M$	[-]	pitching moment coefficient
$C_{Do}$	[-]	minimal drag coefficient $C_{Do}$ at $C_l = 0$
$Ma$	[-]	Mach number
$p$	[mbar]	pressure
$p_{tot}$	[mbar]	total pressure
$p_{stat}$	[mbar]	static pressure
$Re$	[-]	Reynolds number
$T$	[K]	temperature
$t$	[h]	time
$u, v, w$	[m/s]	velocity
$\alpha$	[°]	angle of attack
$\mu$	[m <sup>2</sup> /s]	kinematical viscosity
$T_t$	[K]	temperature of testsection

#### Forces and Moments

$X$	[N]	axial force
$Y$	[N]	side force
$Z$	[N]	normal force
$M_x$	[Nm]	roll moment
$M_y$	[Nm]	pitching moment
$M_z$	[Nm]	yawing moment

### 3. INTRODUCTION

At KKK force measurements are made by use of strain gauge balances.

Irrespective of performing 3 component or 6 component force measurements, we always use the six components  $X$ ,  $Y$ ,  $Z$ ,  $M_x$ ,  $M_y$ ,  $M_z$  to be able to determine interference on all force signals.

All balances are made of vascomax 250 steel (NR. 1.6359) and are applied with strain gauges.

Fig. 1 shows the 6 component balance W 614 of KKK which was constructed and calculated by TH-Darmstadt like all balances of KKK [1]. Attachment of strain gauges and calibration of this balance was made by MMT in Newport News, Virginia.

The internal balances are no single peace balances. They consist of several parts which are electron beam welded.

The balances carry 7 full bridges with strain gauges, which are measured with a carrier wave amplifier. We prefer the carrier wave system opposite to DC-systems for we so can eliminate thermo-effects during temperature variation of the test gas.

The disadvantage of the carrier wave system is to maintain the high resistance between balance body and the strain gauges including the wires.

The internal balances of KKK are constructed as 'cold' balances, which means they follow the tunnel temperature down to  $T = 100$  K.

Fig.2 shows the load limits of the internal balances of KKK. The balance KKK 101 is the development of balance W 609. Opposite to balance W 612, designed for measurement of 3 components at reduced load ranges, the two others a designed for measuring 6 components.

To be able to measure the exact balance temperature of each force component PT 100 thermometer probes are mounted on the corresponding structure parts and are able to measure the temperature with an accuracy of 0.02 K. This significant accuracy is only possible if the probes are especially calibrated.

Since the internal balances of KKK are calibrated at ambient temperature, all effects depending on variation of tunnel gas temperature have to be corrected.

- correction of zero shift
- correction of sensitivity shift
- correction of an existing temperature gradient

Additionally to this corrections the penetration of humidity into the carrier material of the strain gauges has to be avoided.

### 3.1 Avoidance of humidity in strain gauges

Humidity which on special circumstances may penetrate into the carrier material of the strain gauges has a special influence on debasement of repeatability. Especially at warming up of the tunnel gas after a cool down this effect occurs. At this time model temperature and tunnel gas temperature are necessarily higher as the balance temperature and therefore the humidity of the tunnel gas condenses on the still colder balance after tunnel gas temperature rises above the dew-point temperature. Cooling down the next time the penetrated humidity causes incalculable non reproducible additional voltages on the strain gauges.

**Fig. 3** shows the typical shape of the zero shift of a moist strain gauge during a cool down and warm up phase. You can see clearly the jump in the current curve at  $T \sim 0^\circ \text{C}$ . An additional effect is the poor repeatability of the start value at the end of the test.

At KKK simple transverse beams were applied with strain gauge fullbridges and covered with various coating layers. As coatings were used:

- Silicon glue
- strain gauge glue
- calcium fluoride
- silicium nitride at several layer thickness
- silicium nitride as insulator with a covering of nickel.

These coatings were partially added by a sputter- or CVD-methode [2].

The following requirements were given for the coatings:

- absolutely vapor tight
- no detectable transmission of forces
- no impairment of repeatability
- high fatigue strength at maximum force and interchanging temperatures

**Fig. 4** shows a metal disc of vascomax 250 steel applied with 8 strain gauge half bridges. These bridges are coated with silicium nitride layers with various thickness between  $1.5 \mu\text{m}$  and  $6 \mu\text{m}$ .

The effectiveness of the coating (against moisture) was proved by depositing the applied transverse beam probes in distilled water 12 hours before testing.

To investigate effectiveness of various coating thickness the metal disc was used as shown in **Fig. 4**.

The influence of the layer thickness in sensitivity of the strain gauge was investigated by means of a transverse beam as shown in **Fig. 5**. This transverse beam was cooled down to 100 K in steps and loaded with weights at certain temperature levels. Maximum elongation of the beam was calculated previously and the loads were applied accordingly. The fatigue strength of the coatings was proved like shown in **Fig. 5**. The transverse beam was connected with an eccentric drive via spring previously calculated. The amount of rotations of the eccentric disc indicates the fatigue strength.

Before starting tests the covered strain gauges were investigated on cracks or damages by means of an electron scan microscope.

**Fig. 6** shows the scanned plot of a non coated strain gauge at a scale of 1:406. The visible structure is the fibers of the carrier material of the strain gauges.

In **Fig. 7** you can see a strain gauge coated with  $\text{Si}_3\text{O}_2$ . Unmistakable can be seen the formation of oxide crystals with their sharp grain boundaries.

After the cooling cycles and the bending fatigue tests the probes again were examined by electron scan microscope and changes were registered. Among the various coatings a  $3 \mu\text{m}$  layer of silicon nitride was found optimal for it showed no damages after high loads at the bending fatigue tests.

Also the shape of the curve of the voltage value from the strain gauges of this bending probe shows opposite to a dry non coated strain gauge no strange behavior **Fig. 8**.

### 3.2 Calculation and correction of the forces of a cryogenic balance

The calibration of cryogenic balances is made with single loads and with the additional load combinations which allows exactly determination of the interference. Of special interest here is the interference of the load combinations of normal force and pitching moment in the axial force.

To determine the force signals strain gauge bridges are applied at the model side and also at the stingside of the balance on to the adequate structure parts. The balances are equipped with seven full bridges, whereas axial force is measured stingsides and modelsides. The addition of the bridge signals produces the moments and the differential signals the forces.

A non linear calibration matrix results from the needed load combinations to determine the interference during calibration. Therefore, the erection of an evaluation matrix is not possible by solution of a simple single linear equation system but by iteration.

The calculation of forces and moments from the voltage levels of the balance components is made as described now.

Before the basic data are handled by the balance matrix they are corrected on temperature sensitivity. Therefore, the data of 10 PT 100 are available

#### a. Correction of zero shift

$$\begin{aligned} R_{SDj} &= e_{0j} + e_{ij} \cdot T_i + e_{2j} \cdot T_i^2 \\ U_{kj} &= U_j - R_{SDj} \end{aligned}$$

$j = 1, \dots, 7$  strain gauge bridges

$i = 1, \dots, 10$  temperature probes

$U_{Kj}$  = corrected voltages

$U_j$  = non corrected voltages

$R_{SDj}$  = correction for zero shift

#### b. Concentration of single signals into components

$$U_x = U_{XS} + U_{XM}$$

$$U_y = U_{YS} + U_{YM}$$

$$U_z = U_{ZS} + U_{ZM}$$

$\vdots$

$U$  = Balance signals

$S$  = stingside of balance

$M$  = modelside of balance

## c. Correction of sensitivity

$$P_{iT} = P_{i23} \cdot [1 + P_{ii} \cdot \Delta T]$$

$$i = 1, \dots, 6$$

$P_{ii}$  = correction coefficients

$P_{i23}$  = direct coefficients at 23°C

$P_{iT}$  = corrected direct coefficients

## d. Correction of temperature gradients (only X-bridges)

$$R_{vx} = B_1 + \Delta T_m$$

$$B_1 = b_0 + b_1 \cdot T + b_2 \cdot T^2$$

$T_m$  = average temperature

$b_1, b_2$  = correction coefficients

## e. Evaluation via matrix

## e.1 direct coefficients

$$K_i = P_{iT} \cdot U_i$$

$$i = 1, \dots, 6$$

## e.2 linear coefficients

$$L_i = \sum (-B_{ij} \cdot K_j)$$

$$i, j = 1, \dots, 6$$

## e.3 multiplication coefficients

$$M_i = L_i + \sum (-C_{ijk} \cdot L_i \cdot L_j)$$

$$i, j, k = 1, \dots, 6$$

The linear matrix which includes the coefficients for correction of linear interference is named  $b_{ij}$ . The matrix  $c_{ijk}$  includes the coefficients for calculation of quadratic interference.

Opposite to calibration by means of a DC-measuring system where strain gauge bridges were set to zero before calibration, the zero levels at calibration with carrier wave amplifier were considered in the evaluation matrix.

Within an extreme non linear matrix this behavior requires no changes in zero levels of the balance after calibration.

To correct the zero shift the balance was cooled down to 100 K in steps of 20 K during a laboratory test improving a homogeneous temperature distribution at each step. A polynomial of 2nd degree was obtained by the voltage level changes at each temperature, which is used for the temperature correction of zero shift.

The change in sensitivity at lower temperatures was considered by a linear polynomial, whose coefficients were found out via calibration of main loads at temperature steps down to 100 K.

Producing a temperature gradient at the middle of the balance by means of a heating device a correction for temperature gradients could be formed.

But during tests in the wind tunnel it was found, that the temperature gradient across the balance was different and, therefore, was not correctable with correction factors given by laboratory tests. The corresponding temperature gradient results from the idea, to bring the balance in line to test temperature level as soon as possible. Therefore, the given temperature set point was run 20 K below to accelerate the cool down of the balance. Subsequently the tunnel gas temperature again was increased 20 K. By this procedure a temperature gradient occurs like in **Fig. 9**.

The temperature gradient across the balance can be defined by the fact, that during cool down phase a stationary temperature distribution with a stationary temperature gradient is given, whereas the sting temperature is higher than the model temperature. Because of the model with its big surface and its great heat transfer ratio, the modelside of the balance follows the model temperature at the quickest. The model temperature itself is very similar to the tunnel gas temperature. Increasing the tunnel gas temperature now the balance at modelside will be warmed up quickly. The stingside of balance will take no notice of it, for the sting with its big mass causes an inertial system. During the polar, subsequently taken the temperature gradient and resulting stresses decrease and no qualified statement can be given about the axial forces during the polar.

To prevent this problem at KKK no polar curves were taken at non stationary temperature conditions on the balance but after waiting as long as temperature at sting and modelside of balance differs less than 1.5 K.

These days more stringent requirements are given on quality of test results for force measurements in wind tunnels. Small changes on models shall be measured with high accuracy. In view to repeatability of 1 drag count in drag this means a 0.03 % repeatability of balance data for an axial force of 200 N on a transport plane. Next to this all other tunnel parameters like temperature, static and dynamic pressure have to be held at a constant level with adequate accuracy [3]. These requirements are not obtainable with those corrections on zero shift and sensitivity shift given by laboratory tests.

As we learned from tests with transport, fighter and delta wing models sensitivity shift and zero shift don't only depend on tunnel gas temperature but also on model geometry, model weight and mass distribution [4], [5], [6], [7], [8]. Therefore, we had to find a correction process especially made for each model.

To give a feeling for the size of the corrections a temperature corrected polar and a non corrected polar is shown in **Fig.10**. These calculations are basing on data from a test with an ELAC-Model at  $T_i = 110$  K and  $Ma = 0,3$ . Clear can be seen the influence of temperature correction in drag.

**Fig. 11** represents the quota of correction for lift coefficient. The change in slope of the curve without temperature correction results from sensitivity alteration. The influence of zero shift in this case is negligible.

**Fig. 12** characterizes the influence of temperature in signals of the axial force bridges. Opposite to lift coefficient here the influence of zero shifts dominates. The change in sensitivity doesn't take too much effect because of the essential lower forces in axial direction.

The procedure of our temperature correction bases on the acceptance that no corrections are necessary during tests at ambient temperature, i.e. calibration temperature of the balance.

The complication of the correction conforms with an on-line correction to be made at Quick-look, for example, or an off-line correction. At Quick-look only a sensitivity shift correction is made.

As reference values for corrections an average value of several static polar curves (wind-off), which are measured at ambient and stationary circumstances is taken. A variable load results from varying the model angle of attack, for the single loads can be calculated by trigonometrical functions. This procedure is the more precise the more the model weights.

$$U_{i \text{ mitt}} = \frac{1}{n} \sum U_{ik}$$

$$k = 1, \dots, n$$

$$n = \text{number of static polar curves}$$

If it is essential to make a temperature correction of the balance signals the following procedures will take place.

- on-line-correction (Quick-look)  
After the balance temperature fits with test gas temperature and the temperature distribution across balance is acceptable homogeneous, a wind-off polar will be measured.  
For this static polar the components will be calculated from the single signals and the signals of the components will be approximated as a function of the angle of attack.

$$U_{i \text{ stat}}(\alpha, T) = \sum a_{ik}(\alpha, T) \cdot \alpha^k$$

$$k = 0, \dots, 3$$

$$i = 1, \dots, 6$$

Zero shift is calculated via difference between reference polar and static polar at  $T \neq T_{\infty}$ . Comparing the slopes of reference polar (wind-off) and static polar at  $T \neq T_{\infty}$  a change in slope can be calculated, which is equivalent to the change in sensitivity of the components. This correction is adequate for calculating the forces at Quick-look.

- off-line-correction  
After ending of a test series at a certain temperature level a further final static polar is taken. With this polar we assume the temperature distribution across the balance absolutely homogeneous. The difference between the static polar curve taken before wind-on polar curves and the static polar curve after the test series represents the decrease of eventual existing temperature-gradients and as well the zero shift at the amount of almost 2 K. At the first step the zero reading sequence will be corrected with the procedure written under 'on-line-correction' after the test runs are finished. Additionally zero shift will be considered. With the correction calculated by this procedure the static polar taken before test runs (wind-on) will be compared with the reference polar. The zero shifts appearing during wind-on tests can be determined by comparison of the two static polar curves and then will be transmitted into a function versus temperature.

If there is still a slight difference between the weight polar curves after execution of this correction it only can be an effect of a temperature gradient, which will be corrected finally. With this procedure it is possible to execute a temperature correction which is able to correct the temperature effects to  $\leq 1 \mu V/V$ . But it is important to measure the temperature at each bridge with an adequate accuracy and repeatability.

### 3.3 Test Results

Times ago exclusive force measurements were performed at KKK with a cryogenic model of an Airbus A 310 [9]. The target of these tests was to investigate the influence of various transition fixings in boundary layer effects at a wide Reynolds number range. The tests were performed with the cryogenic balance W 609 of KKK.

To reach the requested Reynolds number and Mach number combinations the tunnel temperature was decreased down to 100 K and the Ma-number was varied up to  $Ma = 0.36$ .

Investigation on the behavior of wind tunnel models at low temperatures are described in [7]. These testseries were performed with fixed and free transition. For the tests using transition fixing two types of fixing were investigated.

- 1st test series (TF:A)  
fixing of transition with grain stripes designed for maximum Reynolds number.
- 2nd test series (TF: Free)  
tests with free transition (no fixing)
- 3rd test series (TF:B)  
tests with transition fixing, where fixing grain was 30% larger than used at the first test series.

All these tests were carried out without taleplanes.

**Fig. 13** shows the Mach number and Reynolds number range for the A 310 model. At a tunnel gas temperature of  $T_t = 100 \text{ K}$  and a Mach number of  $Ma = 0.3$  a Reynolds number of  $5.9 \times 10^6$  was obtained. In **Fig. 13** you can see beneath the curve of tunnel gas temperature during the 1st and 2nd test series. After finishing the first test series with TF:A, the model was lowered from the cold tunnel into the model lock of KKK, where it was warmed up and transition fixing was removed (interrupted line). When the model was cooled down again to tunnel gas temperature it was lifted back into the test section, where testing of the 2nd series with free transition was carried out.

The Reynolds number effects with fixed transition by calculated, optimal grain size are to be seen in **Fig. 14** and **Fig. 15**. At a constant Mach number of  $Ma = 0.2$  we can recognize a remarkable increase in maximum lift at rising Reynolds numbers. At the lower part of the polar  $C_L$  versus  $\alpha$  no influence of Reynolds number can be detected. But drag coefficient around  $C_{D0}$  is influenced by Reynolds number effect. With rising Reynolds numbers the drag coefficient is getting smaller.

**Fig. 16** and **Fig. 17** both show the Mach number effect at a constant Reynolds number. With rising Mach numbers the maximum lift coefficient decreases, opposite to the Reynolds

number effects as above. The drag coefficient at this Reynolds number is not influenced by Mach number.

The influence of the various transition fixings in lift and drag coefficient are plotted in **Fig. 18** and **Fig. 19**. The maximum lift coefficient is obtained with free transition. With rising grain size the lift coefficient drifts towards higher angles of attack. The influence of transition fixing in drag coefficient can be detected very clearly. With growing grain size, the drag coefficient increases. The largest difference in drag can be detected between free transition and transition fixing with optimal grain size like fixing TF:A.

The quality of the test results can be read from the reproducibility of the test data. At cryogenic wind tunnels one can characterize three types of repeatability, which differ in the width of time span between two test runs:

- a. Short Term Repeatability  
Two polar curves are successively taken at the same temperature condition
- b. Medium Term Repeatability  
between the corresponding polar curves the balance temperature has been at other levels.
- c. Long Term Repeatability  
The long term repeatability requires long time distance, for example months, between corresponding polar curves and requires as well model removals and erections.

**Fig. 20** and **Fig. 21** show the repeatability at  $Ma = 0.3$  and test temperature of  $T_{at} = 100$  K. In the shape of plots  $C_L$  versus  $\alpha$  there practically is not difference detectable. At the curve  $C_L$  versus  $C_D$ , plotted with a smaller range of angles of attack for obtaining a better resolution, a repeatability of  $\leq 5$  dct is detectable. These two curves are read directly on after the other.

The more remarkable is the plot of the medium term repeatability as shown in **Fig. 22** and **Fig. 23**. The first measurement was carried out during cool down phase at  $T_t = 127$  K at a Mach number of  $Ma = 0.2$ . Later the temperature level was lowered down to  $T_t = 100$  K. After other tests at this level the tunnel gas was warmed up to  $T_t = 127$  K again and the above mentioned test was repeated. The repeatability of this polar is brilliant, i.e.  $\Delta C_D \leq 2$  dct, and, therefore, is a confirmation of the efficient temperature correction.

### 3.4 Conclusion

In cryogenic wind tunnels normally internal cold balances are employed. Due to the temperature dependent drift of signals special correction procedures are required, which also have an influence in the progress of testseries. Against the important problem of moisture on strain gauges a reliable solution was found in form of a special coating. The solution of these problems lead to a high standard of accuracy for test results, which is comparable with those of conventional wind tunnels.

### 3.5 References

- [1] Ewald, B., Hufnagel, K. and Graewe, E., "Grundsatzuntersuchungen zum Temperaturverhalten von DMS-Waagen-Axialkraftteilen", Ergebnisbericht Nr. 1, TH Darmstadt, A10/85, 1985.
- [2] Viehweger, G. and Rebstock, R., "Kraftaufnehmer", Deutsches Patentamt P40/15/666.4-52, 1991.
- [3] Kronen, R., "Automatical Control of KKK Requirements, Sensors, Actuators and Control Performance Results", in AGARD CP-774, June 1989, Paper 5.
- [4] Witte, H., "Auslegung und Konstruktion eines Kryowindkanalmodells für den KKK", DFVLR WKT 29/86, IB 39114-86A22, Köln-Porz, 1986.
- [5] Rebstock, R., "Kraftmessungen mit dem AGARD-Eichmodell, Teil 1", DLR, IB 39114-92A17, Köln-Porz, 1992.
- [6] Wichmann, K., Rebstock, R. and Kronen, R., "Test on the Cryogenic TST Model in the DLR-KKK Wind Tunnel", DLR, IB 39114-92C25, Köln-Porz, 1992.
- [7] Wichmann, K., "Vorversuche zur Windkanal-Messung des Airbus-A310-Modells im Kryo-Kanal-Köln der DLR", DLR IB 39114-93C22, Köln-Porz, 1993.
- [8] Viehweger, G. et al, "Der Kryo-Kanal Köln (KKK) der DLR", DLR Mitteilung, 93-10, Köln-Porz, 1992.
- [9] Rebstock, R. and Wichmann, K., "Tests on the A310 Cryogenic-Model", DLR IB 39114-93C08, Köln-Porz, 1993.

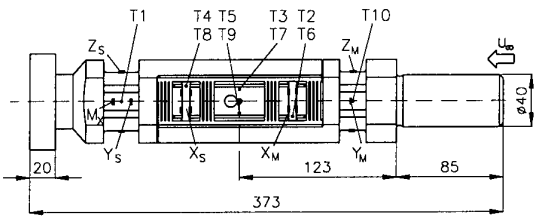


Fig 1 Cryogenic balance KKK 101

	W609	W612	KKK-101
X [N]	1400	900	1400
Y [N]	1700	400	1700
Z [N]	4000	3000	4000
$M_x$ [Nm]	400	200	400
$M_y$ [Nm]	500	240	400
$M_z$ [Nm]	400	70	300

Fig 2 Load limits

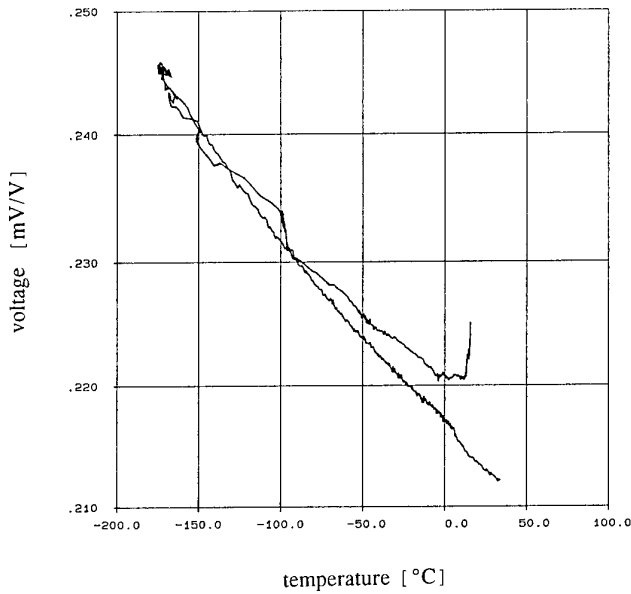


Fig 3 Moistured strain gauge

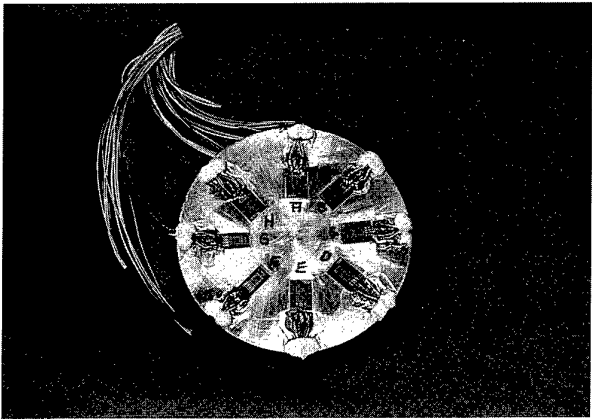


Fig 4 Metal plate with coated strain gauges

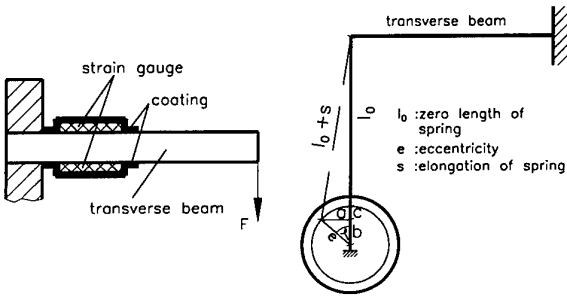


Fig 5 Transverse beam with eccentric drive

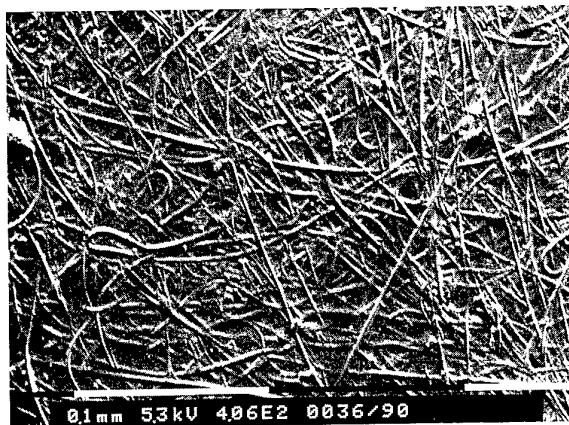
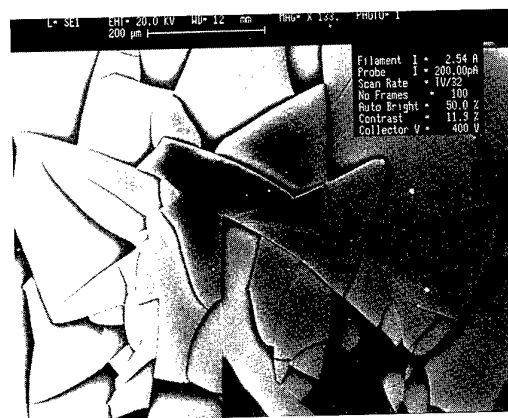
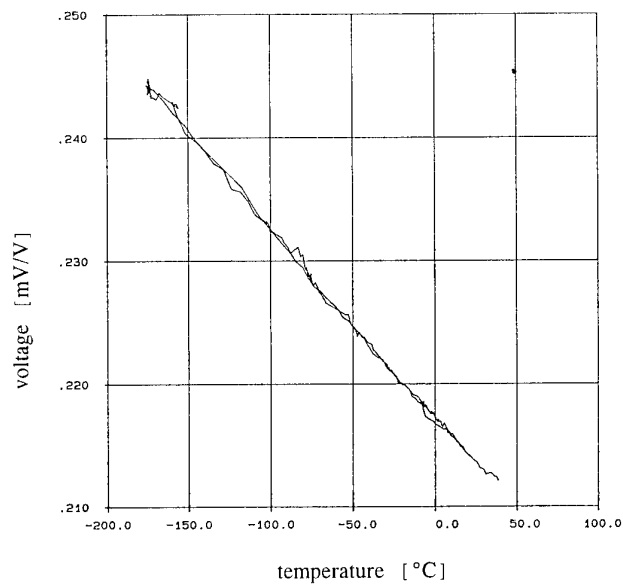
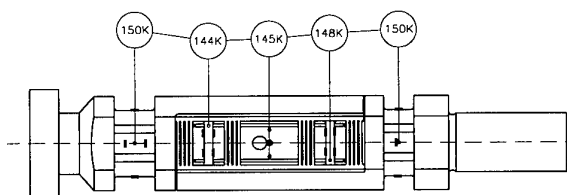


Fig 6 Strain gauge without coating

Fig 7 Strain gauge coated with  $\text{SiO}_2$ Fig 8 Strain gauge coated with  $\text{Si}_3\text{N}_4$ Fig 9 Temperature distribution in the balance  
at  $T_l = 150\text{ K}$



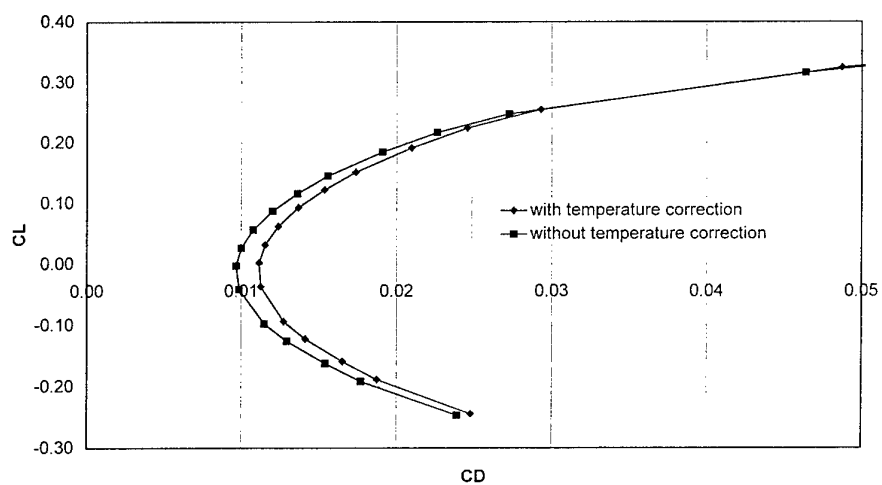


Fig. 10 Influence of temperature correction in polar curve  $C_L$  versus  $C_D$

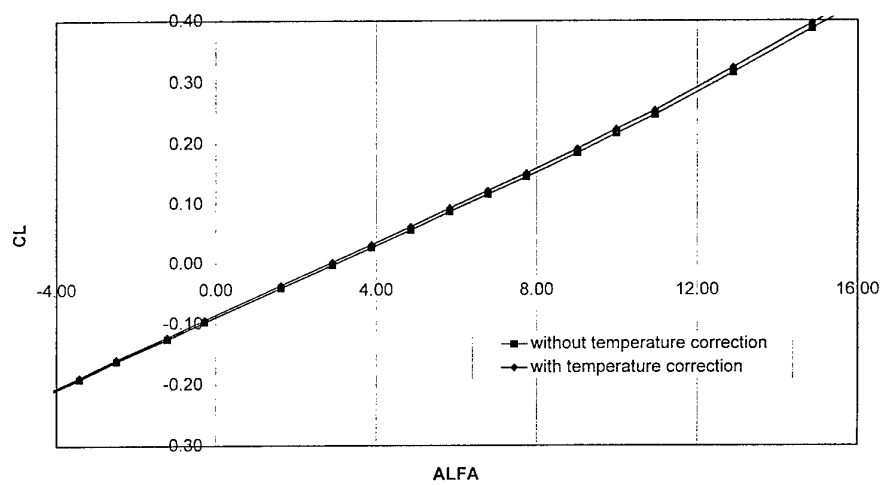


Fig. 11 Quota of correction for  $C_L$

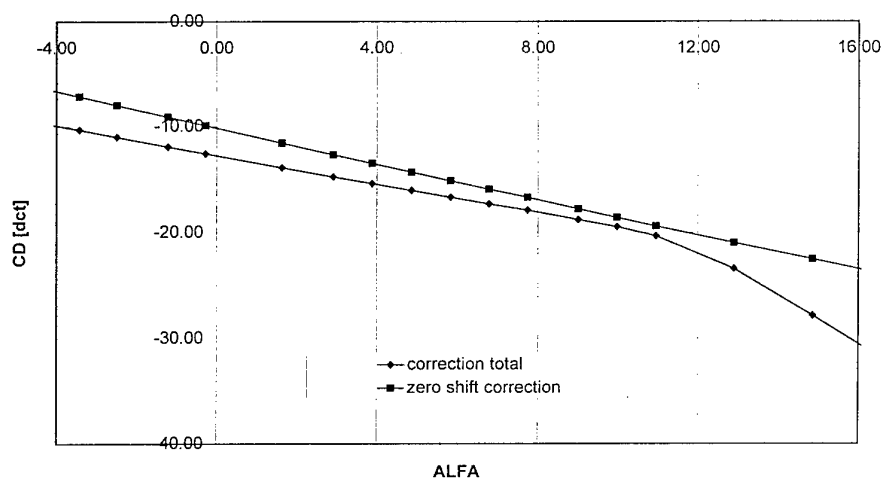
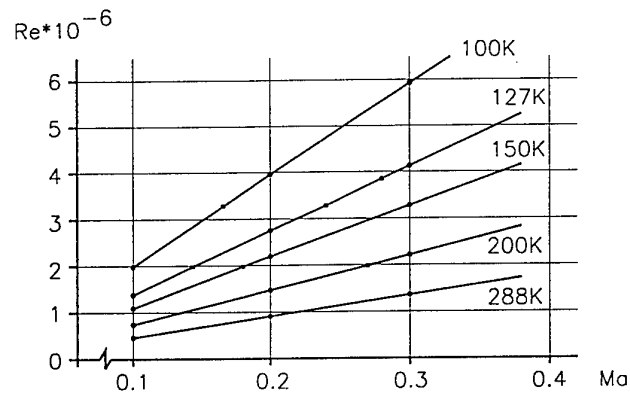


Fig. 12 Quota of correction for  $C_D$



## Cool-Down A310-Model

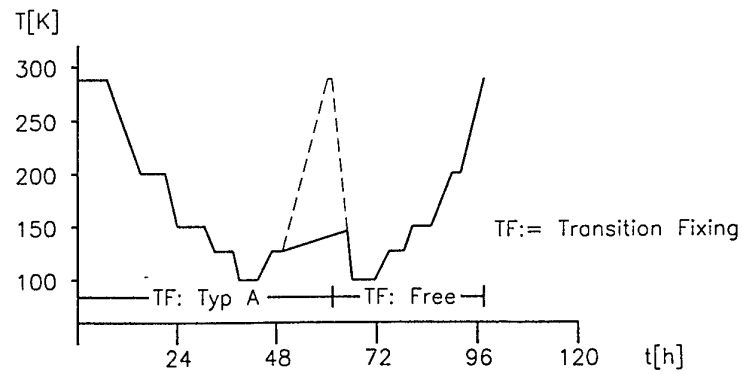
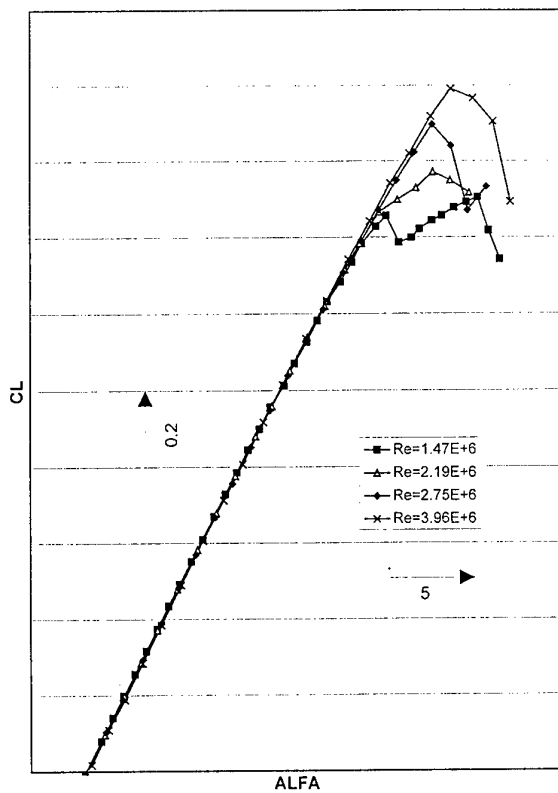
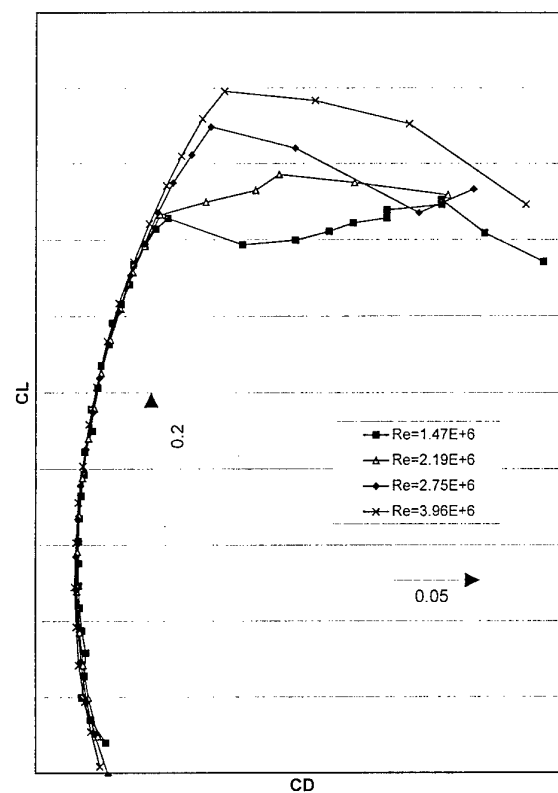
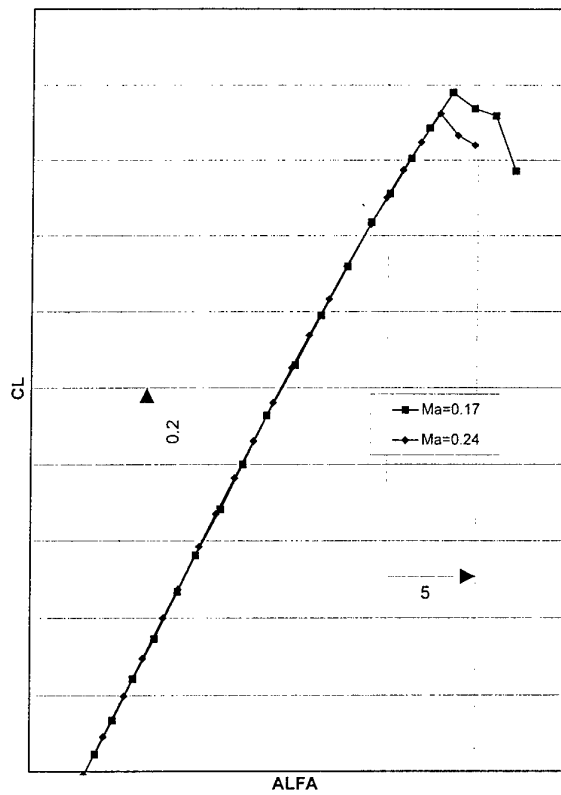
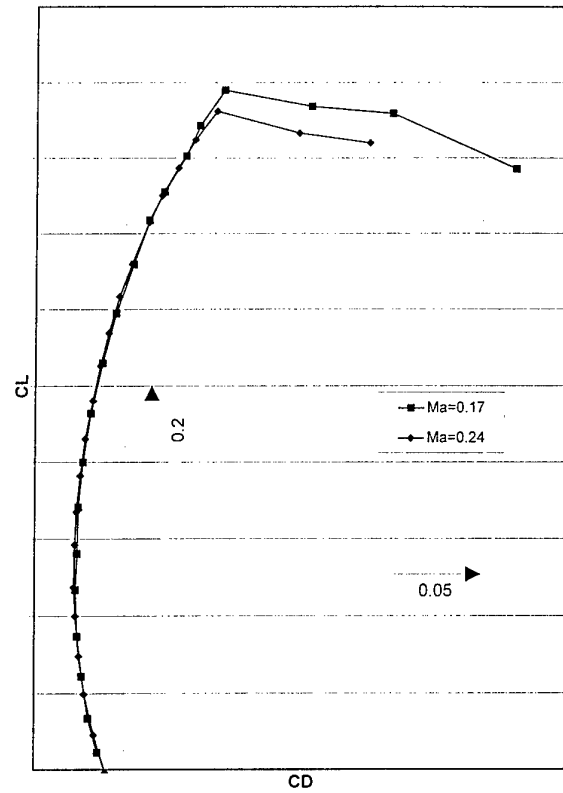
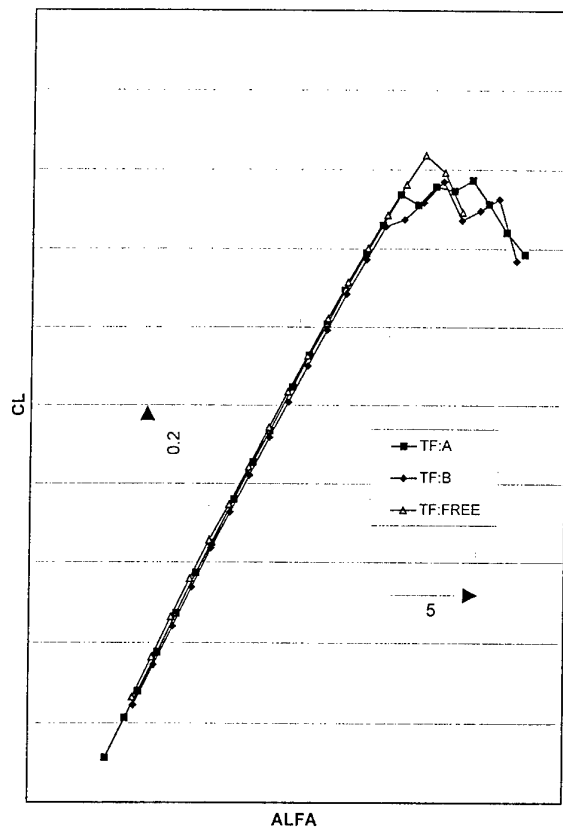
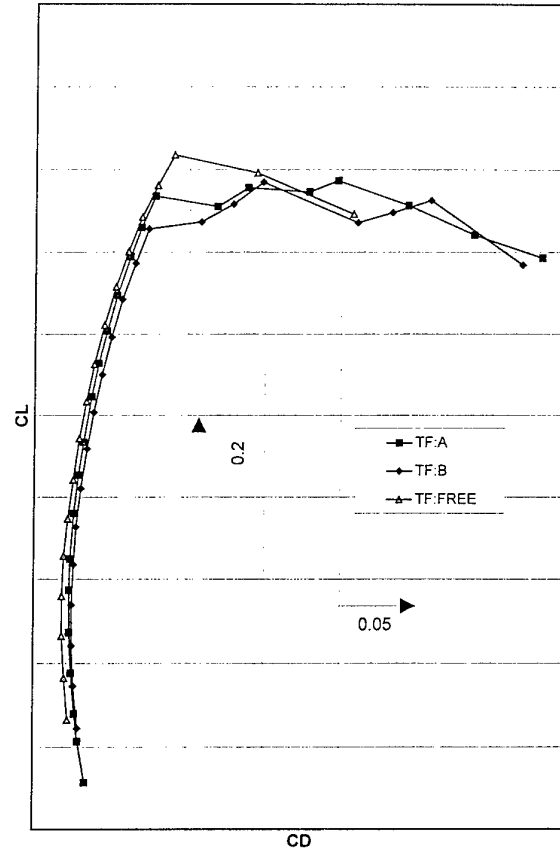


Fig. 13 Mach-Re-Area A 310-Model

Fig. 14 Re-Effect at  $Ma = 0.2$  TF:AFig. 15 Re-Effect at  $Ma = 0.2$  TF:A

Fig. 16 Ma-Effect at  $Re = 3.28 \cdot 10^6$ Fig. 17 Ma-Effect at  $Re = 3.28 \cdot 10^6$ Fig. 18 Fixed transition in comparison with free transition  
 $Ma = 0.2$ ;  $Re = 2.19 \cdot 10^6$ Fig. 19 Fixed transition in comparison with free transition  
 $Ma = 0.2$ ;  $Re = 2.19 \cdot 10^6$

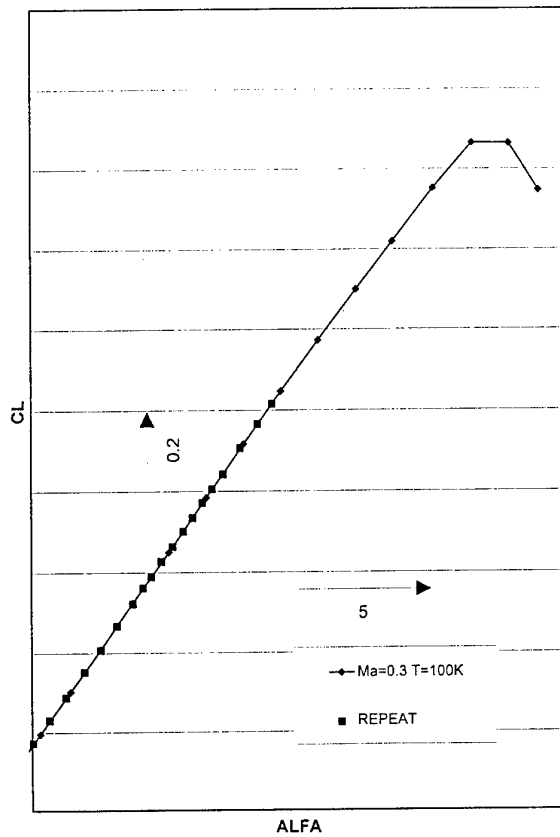
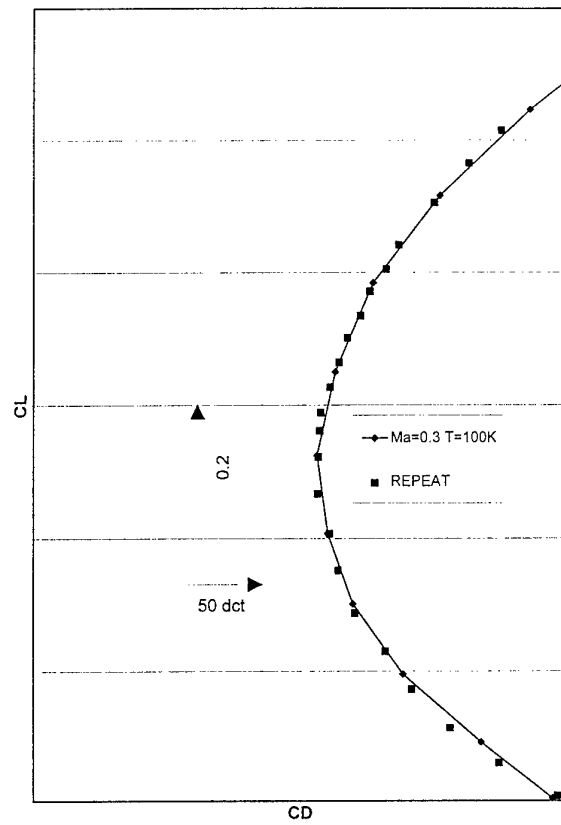
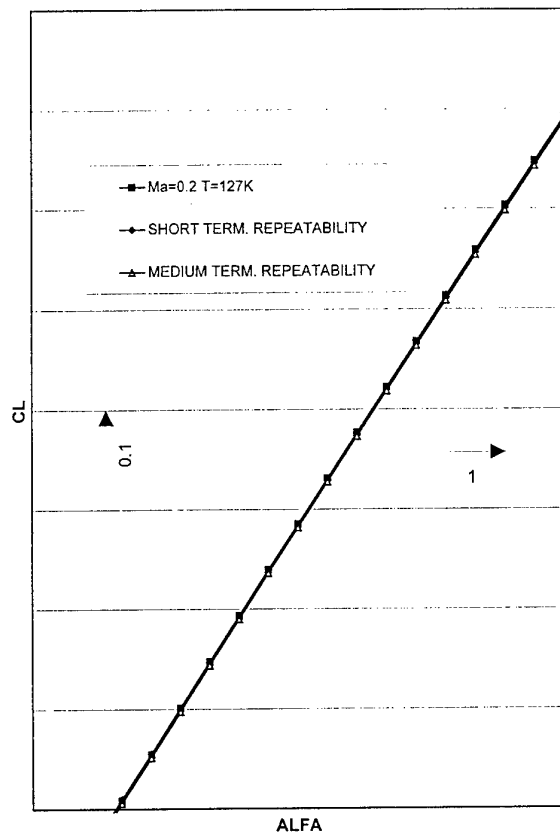
Fig. 20 Repeatability at  $Ma = 0.3$ ;  $T_t = 100$  KFig. 21 Repeatability at  $Ma = 0.3$ ;  $T_t = 100$  K

Fig. 22 Comparison of Medium and Short Term Repeatability

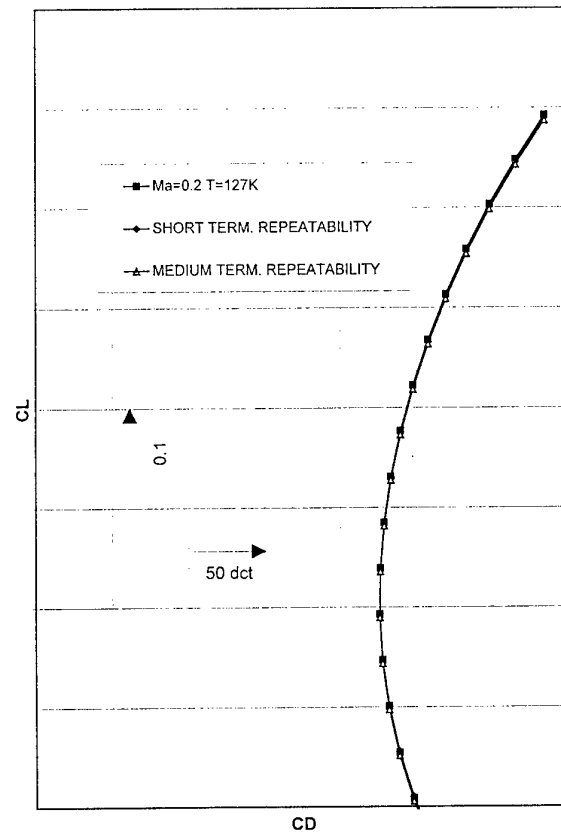


Fig. 23 Comparison of Medium and Short Term Repeatability

## Model Dynamics

Clarence P. Young, Jr.  
ViGYAN, Inc.  
30 Research Drive  
Hampton, VA 23666-1324, USA

### SUMMARY

Model dynamics is a continuing problem when testing in high Reynolds number, high pressure, cryogenic wind tunnels. This lecture describes model and model support vibration problems that have been encountered in the National Transonic Facility located at the NASA Langley Research Center. Test experience and studies related to identification of excitation sources, attenuation of model vibrations, and changes in structural damping at cryogenic temperatures are presented. Results of a successful buffet test conducted in the National Transonic Facility are discussed along with studies of the effects of model vibration on inertial wind-tunnel model attitude measurement devices. Finally, on-line model systems dynamics monitoring systems currently being used in the National Transonic Facility are described.

### LIST OF SYMBOLS

A amplitude  
 $A_i$  acceleration of the  $i^{\text{th}}$  vibration mode measured at the AOA sensor  
 $A_{\text{unf}}$  unfiltered AOA spectrum  
AD analog to digital  
AOA angle of attack  
 $a_x$  axial acceleration  
BDDU Balance Dynamic Display Unit  
CPA Critical Point Analyzer  
FFT Fast Fourier Transform  
 $f_i$  natural frequency of the  $i^{\text{th}}$  vibration mode

G acceleration in g's  
g gravity constant  
 $g_i$  material damping factor for  $i^{\text{th}}$  mode  
HSR High Speed Research  
Hz Hertz  
 $i$  subscript denoting the  $i^{\text{th}}$  vibration mode  
in. inches  
M Mach number  
MPSS Model Protection and Shutdown System  
 $M_y$  yawing moment  
 $n$   $n^{\text{th}}$  vibration mode  
psf pounds per square foot  
 $q$  dynamic pressure  
 $R_e$  Reynolds number  
 $r$  subscript denoting the  $r^{\text{th}}$  vibration mode  
 $r_i$  effective radius of the  $i^{\text{th}}$  vibration mode  
T Temperature  
 $T_t$  Test section temperature  
VG Vortex Generators  
 $V_r$  velocity measurement at the AOA device for the  $r^{\text{th}}$  vibration mode  
 $W_m$  weight of model  
 $\alpha$  angle of attack  
 $\zeta$  structural damping factor  
 $\rho_r$  effective radius for the  $r^{\text{th}}$  mode  
 $\Omega$  mean angular velocity at AOA device  
 $\omega_r$  circular frequency for the  $r^{\text{th}}$  mode

### 1. INTRODUCTION

Model vibrations have been and continue to

be a major problem when testing in high pressure wind tunnels. Such vibrations can jeopardize model structural integrity, overload force balances and support stings, cause models to foul, bias model attitude measurements, affect aerodynamic data accuracy, and oftentimes limit test envelopes. Model/model support vibrations have been a major problem for the high Reynolds number cryogenic National Transonic Facility (NTF) since becoming operational in 1984. The facility is located at the NASA Langley Research Center (LaRC) in Hampton, VA., U.S.A. See reference 1 for a description of the wind tunnel and its capabilities. References 2 and 3 document yaw vibration problems that have been encountered in the NTF. However, severe vibrations have not been limited to the yaw plane. Pitch or stall buffet (oftentimes referred to as limit cycle oscillations) is routinely encountered and can result in high amplitude vibrations when testing at high dynamic pressure. Such vibrations are usually triggered by flow separation with amplitude being generally proportional to dynamic pressure. Roll buffet (buzz), which is sometimes called wing rock, is another vibration phenomenon often encountered in wind tunnel testing which can result in high dynamic loads. These vibrations, although not unique to cryogenic tunnels, are generally more severe in tunnels such as the NTF due to the high dynamic (kinetic) operating pressure in such facilities.

In connection with NTF model/model support vibrations, investigations have been carried out to better understand the possible sources of excitation (e.g., ref. 2 through 5), and to evaluate the effects of vibration on aerodynamic data quality. In particular, experimental and analytical studies have been done to quantify inertial angle-of-attack (AOA) sensor bias due to vibrations (ref. 6)

and develop algorithms for correcting AOA output (references 6 through 8). This problem has also been addressed in Europe as documented in references 9 and 10.

Vibration phenomena experienced with initial testing of a commercial transport in the NTF led to a successful buffet test in the NTF which is documented in reference 11. As a result of continuing model system vibration problems, monitoring systems have been developed and installed in NTF (references 12 and 13) in order to protect the model system(s) from dynamic overload and provide a capability for dynamic testing.

The purpose of this lecture is to describe model vibration problems that are typically encountered in high pressure cryogenic wind tunnels with focus on problems encountered in the National Transonic Facility. The nature of model/model support system vibration problems are described along with investigations that have been conducted (and are continuing) to identify excitation sources and methods for vibration attenuation. In addition, dynamic (buffet) test experience is described and investigations related to affects on aerodynamic data quality are presented. Finally, the current dynamic monitoring systems developed and installed in the NTF are discussed along with dynamic data obtained during actual wind tunnel testing.

## 2. NATIONAL TRANSONIC FACILITY MODEL AND MODEL SUPPORT VIBRATIONS

Since becoming operational in 1984, a number of unexpected model and model support vibration problems have been encountered. The initial problem was vibration of model systems in the yaw plane to the extent that some of the tests had to be limited. In 1986, a concentrated effort was

made to perform theoretical analyses and experimental tests during wind tunnel operation in an attempt to understand the character and source of these oscillations. These investigations are documented in detail in references 2 through 5. The problem background, investigation results (including recent work) and current status of these studies are briefly described in this section.

### 2.1 Model Support System Description

The NTF model support system is shown in figure 1. The movable part of the system is the arc sector (which weighs approximately 35,000 lb.) which is actuated by a hydraulic cylinder to provide pitch attitude, while the sting rotates to provide roll attitude. The arc sector is restrained by five pair of guide pucks (bearings). A section view of two pair of side pucks and one thrust puck is shown in figure 2. The initial puck clearances were very small (0.010 in.) and extremely difficult to set. Currently, the pucks are preloaded to approximately 10,000 lbs. The preloads were applied subsequent to the study documented in reference 3.

An aerodynamic fixed fairing serves as the trailing edge for the arc sector. The fairing has a large hollow section to accommodate instrumentation, and is constructed of 0.75 inch thick aluminum plates that are bolted to a heavy aluminum spar that forms the trailing edge. The fixed fairing is rigidly attached (welded) to the upper wall while the lower edge is free (under the tunnel floor). The arc sector and fixed fairing are coupled structurally in that the fairing plates ride in grooves along the aft surface of the movable arc sector.

### 2.2 Model/Model support Yaw Vibration Experience

Significant yaw vibration problems have been encountered for many different models including commercial and military. Additionally, severe pitch buffet and roll oscillations have been encountered for some models while testing at high dynamic pressure (e.g., see ref. 11). However, yaw vibration has been the limiting factor for most tests.

Model vibration amplitudes have generally been limited due to strain-gage balance loads. Currently, the NTF is equipped with a Critical Point Analyzer (CPA) monitoring system (ref. 12) which monitors balance static plus dynamic loads. The system has both visual displays and audible warnings to indicate exceedance of pre-set load levels and is interlocked to trip the tunnel, if pre-set loads are approached or exceeded. This system is discussed in more detail in a subsequent section of this paper.

### 2.3 System Dynamics and Possible Excitation Sources

Initial dynamic studies of models that have experienced significant yaw vibrations showed dominant frequency response from about 18 to 25 Hz. More recently, severe yaw vibrations have occurred at frequencies up to 30 Hz. Early observations (ref. 2) suggested that the fixed fairing response to the flow field was the principal excitation source. However, other sources such as external mechanical, flow excitation of the model(s), or flutter type instabilities could not be ruled out as possible causes. The following sections describe the analysis and experimental test programs conducted in the

1986-1987 time frame and results of more recent studies of the problem.

## 2.4 Analyses and Experimental Test Programs

This section describes the analyses and experimental test activities beginning in late 1986 along with results of a more recent experimental study conducted in 1993.

### 2.4.1 Aeroelastic Analysis

The initial aeroelastic analysis of the NTF model support system was performed by Strganac (ref. 4). The analysis indicated the potential for an aeroelastic instability to occur within the NTF test envelope capability. This type of instability is commonly referred to as a hump mode type of instability, which is not flutter in the classic sense, but is very much damping dependent, and can be erratic in occurrence. This study suggested that the arc sector and fixed fairing behaved much like a wing and control surface. The analysis indicated that the indicated theoretical aeroelastic stability boundary could be shifted to higher speeds if the center-of-gravity of the fixed fairing were located further upstream, i.e., the location of the heavy spar along the fixed fairing trailing edge could have negative consequences.

Whitlow (ref. 5) subsequently performed an analysis of the model support system using a 3-D aeroelastic code. These analyses also showed a tendency toward a hump mode instability and other lowly damped modes. Whitlow's analysis suggested that there could be a finite range of Mach numbers where model system vibrations would be experienced and above which smoother operations could occur. Also, the close proximity of the wind tunnel side walls to the model support system has adverse

effects. The wind tunnel can interact with the model support structure to possibly cause aerodynamic resonance modes to develop.

Subsequent to the severe yaw vibration problem encountered in 1993 (ref. 3) extensive aerodynamic analyses of the model support structure were carried out at NASA Langley. Various computational fluid dynamics (CFD) codes were used in this analysis activity. Although flow separation over the fixed fairing was predicted, the codes did not predict stable or unstable flow oscillations. However, in the region of the model support, there was evidence from one of the viscous codes which suggested that traveling waves (flow oscillations) triggered by flow separation could propagate upstream. These oscillations were found to be symmetric in character, and at a frequency range near the excitation or natural frequencies of the support system. It should be noted that the fixed fairing trailing edge included angle is greater than originally designed for the tunnel. The trailing edge was modified due to an interference problem with the gate valves. Although the CFD studies suggested that the fixed fairing geometry was conducive to flow separation, no firm conclusions could be drawn. Attenuation options discussed included redesign, attach splitter plates, and drilling holes through the fairing to allow for flow communication across the fairing. An experimental splitter plate was installed in the 1986 study and is discussed in the next section.

### 2.4.2 Operational Testing

Extensive testing began in October 1986 in an attempt to identify potential excitation sources, with the goal of eliminating or attenuating the yaw vibrations. Instrumentation was installed on a generic transport model, the model support and other



structural components as illustrated in figure 3. The effects of test variables such as Mach number, test temperature, cold soak, Reynolds number, angle of attack, and roll attitude were studied. Pre-test activities included a comprehensive vibration modal survey, and measurement of the arc sector pucks (bearings) gaps. The initial series of tests indicated that the source of vibration was not external to the tunnel. The dominant variable affecting yaw vibration turned out to be the tunnel cold soak time, i.e., time after cooldown at which the internal structures were held at or near cryogenic thermal equilibrium for a period of time. Generally, it was observed that high vibration at relatively low Mach numbers (0.5) occurred if the tunnel was held at cryogenic conditions for up to two days. Shorter soak times generally resulted in lower levels of vibration. Also the initial results indicated that the excitation source was at the fixed fairing, and most likely due to flow separation or aeroelastic instabilities. Results of more recent studies suggest that other factors are involved and are discussed in a subsequent section of this paper.

#### 2.4.3 Yaw Vibration Attenuation Studies

Subsequent to the initial tests in the fall of 1986, further tests were conducted in May - August, 1987. Prior to this series of tests the arc sector pucks were reset to tolerances, hot film and pressure transducers added, and vortex generators installed on the fixed fairing.

##### 2.4.3.1 Vortex Generators

Vortex generators were installed on the fixed fairing to alter the flow field and evaluate the effects on the model support system vibrations. The vortex generators design was not optimized but rather used as an

investigative tool. The vortex generator installation is illustrated in figure 4. Initial results showed that the model yaw vibration peak levels were reduced to about half the peak levels for various tests at comparable tunnel conditions.

##### 2.4.3.2 Splitter Plate

Further tests were conducted in the October-November 1987 time frame with both a splitter plate and vortex generators installed. The splitter plate extended 7 inches from the trailing edge and was installed to create a reattachment surface for separated boundary flows over the fixed fairing. The splitter plate installation is illustrated in figure 5. Testing of the combined vortex generator and splitter plates configuration indicated a reduction of approximately 20 percent in yaw vibration levels when compared to data for the same test conditions with only the vortex generators installed on the fairing. Subsequent testing with only the splitter plates installed gave small reductions in vibration amplitude, but was believed to be influenced by re-setting the arc sector guide puck clearances.

##### 2.4.4.3 Flow Visualization

Oil flow visualization studies were conducted with and without the vortex generators installed. The oil patterns showed that with the splitter plate on, the flow reattached with or without the vortex generators.

#### 2.4.4 Results of Yaw Vibration Attenuation Studies

Results of the yaw vibration yaw moment response, normalized to dynamic pressure as a function of temperatures for various combinations of vortex generator and splitter plate installation and various puck clearances

are shown in figure 6. The data of figure 6 indicated that the puck clearance was the major factor that affected the response, but the vortex generators and splitter plate clearly helped. The fact that the vortex generator and splitter plate installations reduced the vibration response seemed to support the conclusion that the fixed fairing was a significant participant in the yaw vibration behavior.

The yaw moment response with pucks loose and reset as a function of tunnel soak time and dynamic pressure is shown in figures 7 and 8. In figure 7 the yaw moment response as a percentage of full scale design limit is shown versus soak time in hours. For the indicated test conditions and pucks reset, the vibration load levels were unchanged (approximately 15 percent of full scale) with soak time, whereas with the pucks loose, the amplitudes tended to increase up to about 35 percent of design limit at around 48 hours soak time before becoming constant. This trend suggested that as the tunnel continues to cool down (soak) the arc sector tends to become loose, or something else occurs which tends to aggravate the problem.

The model yaw moment response as a function of dynamic pressure is given in figure 8 for cryogenic testing between 175°F and -260°F. The data of figure 8 shows that the amplitude of yaw response for pucks loose and reset (tight) increases for both cases as would be expected for a forced dynamic response. The data scatter was quite large for the loose puck condition.

Trends from the experimental data indicated that maintaining the arc sector puck clearance to be tight is important for minimizing yaw vibration. Also, results of these tests suggested that one of the ways to minimize yaw vibration response is to cool the tunnel rapidly and run the test, thereby

reducing the influence of cold soaking on model systems yaw vibration response.

### 3.0 RECENT YAW VIBRATION STUDIES

During recent testing of a high speed research (HSR) model in the NTF, severe model yaw oscillations were encountered during cryogenic operation at high Reynolds number, Mach 1.1, and a dynamic pressure of 2700 lbs/ft<sup>2</sup>. The vibration levels were severe enough to exceed the force balance limit loads which activated the wind tunnel interlocks. Although yaw vibration problems had continued to be a problem after the 1987 investigations, this occurrence was of particular importance. At the time of the severe yaw response no dynamic data were acquired on the model. However, at that time a computer based monitoring system under development for the NTF was in the control room for interface checks. This system is referred to as the Model Reduction and Shutdown System (MPSS) and described in a subsequent section of this paper. The newly developed monitoring system was utilized to obtain dynamic data from the force balance in order to analyze the nature of the yaw vibration response.

During tunnel warmup, (low dynamic pressure); the dynamic response data showed a strong 29-31 Hz mode response on the lateral force components, particularly for the yaw moment component. The lateral force and yaw moment amplitudes were found to be dependent on dynamic pressure irrespective of angle-of-attack. In order to isolate the problem to forcing in the yaw plane, data were acquired for 0° and 90° roll orientations. Frequency spectra showing the pitch and yaw moment peak hold amplitudes for these tests are illustrated in figures 9 and 10. Note that for 0° roll, (fig. 9) the dynamic response is predominately in the

yaw plane with energy at 14 and 28 Hz when the model was rolled 90 degrees the frequency response in the pitch plane (fig. 10) was identical to that in the yaw plane at zero roll angle. The 14 Hz response is the model/sting yaw vibration mode response at high angle of attack while the 28 Hz response (model yawing on the balance) is present at all angles of attack. A subsequent test was run at a dynamic pressure of 1800 lb/ft<sup>2</sup> and cryogenic temperatures (-225°F) in which dynamic data were acquired at 0 and 30 degree roll angle. The frequency spectra from these tests are given in figures 11 and 12. As expected, the high vibration levels (30 Hz) are predominantly yaw at zero roll angle and show both yaw and pitch components at 30° roll. These tests reinforced the initial observation that the origin of the forced response was in the yaw plane, and most likely associated with vibration of the model support structure. However, model yaw dynamic problems had not been experienced at 30 Hz prior to this test, which raised the question as to the origin of the apparent 30 Hz forced response.

### 3.1 Forced Response and Modal Test

In order to better understand the dynamic interaction of the NTF model support system and the HSR model, forced response and modal testing was performed on the combined model/model support system in the test section. The results of a sinusoidal (30 Hz) forced response test are given in figure 13. Note that when exciting the model support structure, the amplitude of vibration at the model is 5 times greater than the reference acceleration. Exciting the model at the same frequency results in low level amplitude at the model support with an attenuation factor of 25. For the random testing with input at the model support structure, the frequency spectra for the force

balance response was found to be virtually identical to the spectra obtained during wind tunnel tests. Clearly, the model vibration was related to vibration of the model support structure responding to the turbulent flow field or some other excitation mechanism. The modal survey (vibration test) of the model/model support system in the test configuration showed significant model support motion, as indicated in the natural vibration mode shapes given in figure 14 through 16. The model/sting were then removed and assembled on the backstop in the model assembly bay. Impact response measurements taken on the arc sector/fixed fairing alone (after model and sting were removed) showed that the natural frequencies were basically unchanged with natural mode frequencies at 19, 23 and 30 Hz. The modal survey in the assembly bay identified a vibration mode at 32 Hz which is the model yawing on the force balance. During tunnel operation the yaw mode coupled with the model support structure yaw mode at 30 Hz which resulted in the severe yaw vibration. Basically, the problem was that of structural resonance, with the model acting very much like a lowly damped vibration absorber tuned to the natural frequency (30 Hz) of the model support structure.

### 3.2 Vibration Attenuation

Various options for attenuating vibrations of the HSR model to acceptable levels were examined. For the model, these included a stiffer force balance in yaw, internal damping mechanism, bump stops, and possible redesign. None of these options were feasible, so attention was focused on reducing the model support structure vibration amplitude. The use of vortex generators and/or splitter plates were discounted for aerodynamic reasons. Installation of some sort of active/passive

damping system or feedback force actuators on the arc sector could not be done in a timely fashion, which left bearing preload as a passive option that could be implemented during the next maintenance shutdown of the tunnel in 1994. It should be noted that earlier experience with setting the pucks snug with the arc sector had resulted in stiction problems when operating at cryogenic conditions. However, a new bearing pad material (vespel) which has a very low friction coefficient was installed on the pucks, and allowed the pucks to be set at zero clearance.

The decision was made to preload each of the side pucks to 10,000 lbs. in an effort to attenuate or suppress the 30 Hz model support structure yaw mode. After preload, a cursory modal test showed that the 30 Hz mode was virtually eliminated, i.e., it no longer showed up in the frequency response spectra. Also, no stiction problems were encountered when pitching the arc sector at cryogenic conditions (-250°F). In February 1995, the HSR model was cryogenic tested successfully at 2700 lb/ft<sup>2</sup> dynamic pressure without encountering significant yaw vibration response. By suppressing the model support yaw vibration mode, the model system yaw mode was no longer in a resonance condition, which solved the problem for this particular HSR model configuration.

This study had revealed that the model support structure natural vibration modes had apparently changed since the 1986-1987 studies, or the 30 Hz yaw mode had not been identified. Review of model system vibrations over the years suggest that many of the model systems had yaw mode frequencies near or within the range of the model support natural vibration frequencies. In retrospect, if the model support structure has been designed such that the lowest

natural frequency had been greater than say 35 Hz, yaw vibration should not have been a significant problem for the NTF.

### 3.3 Structural Damping Studies

The question of material and/or structural damping response of sting-supported systems tested in the NTF at cryogenic temperatures was addressed in a very limited manner in reference 14. Based on testing experience in the NTF over the years, the dynamic response amplitude of models tended to be greater at cryogenic temperatures and particularly during tunnel cool soak, when compared to testing at ambient temperature conditions, i.e., Mach number and dynamic pressure (see reference 2).

Evidence of significant reduction in structural damping was first observed at LaRC during vibration testing of a 2-D flutter model that was successfully tested in the Langley 0.3 Meter Transonic Cryogenic Tunnel (TCT) (see ref. 15). The 2-D model was constructed of 18 Ni Grade 200 maraging steel. Interest in potential changes in structural damping was revived during the NTF vibration problem study reported in reference 3.

Changes in damping at cryogenic temperatures are of paramount importance if aero-elastically scaled models are to be tested in the NTF. In particular, dynamic response amplitude associated with buffeting while testing at cryogenic temperatures can be increased significantly or be potentially unstable, if structural damping is extremely low.

#### 3.3.1 Test Results

The damping data presented in this lecture is given in terms of the damping factor,  $\zeta$ ,

defined as  $\zeta = \frac{1}{2\pi n} \ln \frac{x_0}{x_n}$ , where  $x_0$  is the initial amplitude, the  $x_n$  is the amplitude after  $n$  cycles have elapsed. The damping factor,  $\zeta$  is used for systems assumed to have viscous damping. The solid or material damping factor,  $g$ , is related to the damping ratio by  $\zeta = \frac{g}{2}$ .

Data from reference 15 are displayed in figure 17 for a 2-D flutter model shown in the lower part of the figure. Note the apparent decrease in damping,  $g_3$ , for the first torsion mode, (mode 3) from about .002 to values approaching zero. Interestingly enough damping for mode 1 (first bending) showed a slight increase at -300°F.

A simple experiment was conducted on a high speed civil transport model (HSCT) as illustrated in the sketch of figure 18. Measured damping values for vibration mode 2 (model pitching on balance) are given in figure 19. The data indicated significant decrease in damping factor from about 0.015 at room temperature to .005 at -250°F (approximately 60 percent reduction). The wing bending mode damping gave a similar trend during cooldown as shown in figure 20. It is believed that rapid increase in damping during warmup indicated in figure 20, is due to the thin wing warming up much faster than the force balance (location of temperature sensor).

Laboratory test specimens were also used in reference 14 to evaluate effects of structural joint compliance on damping. Based on these studies it appears that structural damping can decrease significantly at cryogenic temperatures. For dynamic testing or other applications in which structural damping may be important, it is recommended that structural damping be measured at both ambient and cryogenic temperatures. In the absence of measured changes in

damping, a reduction in damping of 50 percent of ambient values (measured or theoretical) is recommended. Natural vibration frequency changes due to

temperature only, can be estimated by changes in Young's modulus.

### 3.4 Current Studies

Over the past year or so additional dynamic studies of NTF dynamics have been conducted. The focus of this study has been on model dynamics, but other aerodynamic and acoustic phenomena have been observed.

Recent analysis of the data of reference 16 as well as additional preliminary dynamic measurement results have indicated the presence of low frequency plenum, diffuser and contraction cavity modes. Also, the high speed diffuser appears to have structural vibration modes at frequencies from 15 to 30 Hz which are in the range of the model support natural mode frequencies. This raises the possibility of a diffuser-test section-model support transmission path. The studies in 1986-1987 did not show a strong correlation between diffuser vibration response and model support vibration response. However, the diffuser could be a participant or contributor to the yaw vibration problem. This work, although preliminary at this point, is ongoing and the implications of the apparent presence of low frequency aerodynamic and acoustic modes have not been determined.

### 4.0 DYNAMIC TESTING IN THE NTF

In the fall of 1988, a transport model being tested at high Reynolds number encountered significant roll (buzz) vibrations between Mach 0.75 and Mach 0.82 at angles of attack between 3 and 5 degrees. The unknown excitation mechanism was postulated to be a

limited amplitude aeroelastic instability involving interaction of the rigid body roll inertia and balance roll spring, driven by alternating flow separation and reattachment induced by variation of the effective angle of attack in rolling motion.

In 1991, a second test was undertaken in order to understand the relation between test variables (Mach number, Reynolds number, and dynamic pressure) and model dynamics; develop dynamic test techniques and procedures to allow safe testing in the buffet regime; and to verify wing vortex generator performance. (The actual airplane is equipped with two sets of vortex generators near the wing mid-span.) Since the NTF does not have any protection (no catcher screen) for the fan blades, and the stability of the buffet response could not be predicted, the re-entry test was judged to be high risk for the facility. NASA Langley agreed to do the re-entry test based on a comprehensive safety analysis review. Highlights of the analyses, tests, instrumentation, monitoring systems, and results of this buffet test are presented in this section. Details of these studies are documented in reference 11.

#### 4.1 Test Description

The commercial transport model employed for the buffet test was supported by a swept strut sting and utilized a NASA Langley 101B force balance. The 0.03 scale model had 48 pressure orifices, a wingspan of 56 inches, was 56 inches in length and weighed approximately 238 lbs.

The model and model support sting was constructed of 18 nickel grade 200 maraging steel. A planform view of the right wing is shown in figure 21. Location of the vortex generators (VG;s) on the wing are illustrated in the figure. The scaled VG's were bonded

to the wings and were extremely small, i.e., .09 in. long, .024 in. high and .004 in. thick.

##### 4.1.1 Test Approach

Prior tests in 1988 showed the roll buffet (buzz) oscillation to be Reynolds number sensitive. The test approach was to obtain data at various Reynolds numbers and dynamic pressures at the cruise Mach number, for the configuration with and without vortex generators. This approach resulted in the test profile shown in figure 22. Initial high Reynolds number runs were to be made with wing vortex generators on, with the expectation that the severity of the roll buffet model dynamics would be reduced or eliminated. The magnitude of the primary test variables Reynolds number and dynamic pressure would then be slowly increased per the test profile of figure 22, with test polars run at small angle-of-attack increments.

##### 4.1.2 Instrumentation

Safety requirements dictated that special instrumentation be installed on the model and swept strut (sting). Three miniature accelerometers were installed in the wings and the swept strut was strain gaged. Miniature PCB quartz accelerometers (0.23 in. diameter by 0.30 in. high) were used. These passive (required no heating) accelerometers were tested extensively at NASA Langley, and sensitivities calibrated over the test temperature range. The accelerometers worked very well. Dropout of accelerometer signals occurred only twice during the tests, and were attributed to wire breakage due to thermal and/or mechanical loading. For more information on the miniature accelerometers see reference 11, (NASA Contractor Report 189595).

## 4.2 Vibration Monitoring and Model Protection

The primary function of the vibration monitoring and model protection system was to protect the model against aeroelastic instability and/or structural failure. Both the customer and NASA Langley employed equipment and test techniques that are used routinely for buffet and flutter testing.

The dynamic measurement systems were used to monitor dynamic response frequency and amplitude using both time and frequency domain data displays. The Balance Dynamic Display Unit (BDDU) and Critical Point Analyzer (CPA) (ref. 12) were used to limit the force balance loads to acceptable levels. The customer and NASA Langley dynamic monitoring and shutdown systems, and CPA were interfaced with the tunnel interlock system for automated shutdown if pre-set load levels and/or peak load cycle count limits were exceeded. Also, manual trip (kill) switches were used by the test engineers. If the tunnel interlock was tripped, the model was automatically pitched to the home position (zero angle-of-attack), the inlet guide vanes (IGV) upstream of the fan were rotated to the fail safe position, thereby unloading the fan, and dropping test section dynamic pressure rapidly. The pitch system interlock provided an angle-of-attack reduction rate of approximately 3 degrees per second. The interlock system worked extremely well in rapidly unloading the model with no operational problems encountered.

## 4.3 Wind-Off Vibration Tests

In order to accurately determine the vibration modes that were involved in the model system aeroelastic response; to validate the structural model; to locate instrumentation; and to set limits on vibra-

tion levels during wind tunnel testing, it was necessary to do a wind-off vibration test or modal survey. The modal test was performed on the model system after installation in the test section. Three of the measured mode shapes of primary interest for the test are illustrated in figure 23.

## 4.4 Test Results

Reynolds number sweeps were conducted with and without the vortex generators installed. The run profile in figure 22 was followed and testing began in January 1991. As the Reynolds number sweep began, it soon became apparent that angle-of-attack would be limited to about 5 degrees due to pitch or stall buffet dynamics. As expected, the test profile of figure 22 was completed with VG's installed without encountering roll buffet. In the second series of test with the vortex generators removed, roll buffet was first observed at Reynolds number of 59 million/ft at Mach 0.80. Subsequent testing at Mach 0.80, 67.5 million/ft Reynolds number and dynamic pressure of approximately 2700 lb/ft<sup>2</sup> resulted in a strong buffet response at angle of attack about 4.5 degrees. The roll buffet or buzz amplitude was about 1 inch peak-to-peak at the wing tips with frequency response at 20 Hz. Fouling between the fuselage and swept strut occurred due to the coupled yaw motion associated with the 20 Hz vibration response.

### 4.4.1 Aeroelastic Stability Trends

An established technique for conducting buffet and flutter tests is to develop inverse amplitude,  $\frac{1}{A}$  plots for the pertinent

A

vibration mode, Fast Fourier Transform (FFT) as tunnel parameters are varied (see ref. 17).

The  $\frac{1}{A}$  plots for the 20 Hz mode response at

A

Mach 0.80 and varying Reynolds number are illustrated in figures 24 and 25. Figure 24 gives the stability trends for the initial series of tests with VG's installed on the model, while figure 25 gives results with VG's off the model. The condition for incipient instability is when  $\frac{1}{A} \rightarrow 0$ . Note from

the figures that the  $\frac{1}{A}$  plots tend to break

over at about 3.5 degrees angle-of-attack. This corresponds to a break in the pitching moment and lift.

The plot in figure 24 shows no sharp trend toward instability with VG's installed. Similar plots are given in figure 25 without VG's installed. The breakover point also occurs around 3.5 degrees angle-of-attack but with a much more rapid build-up in amplitude with increasing angle-of-attack. Note that at 59 and 67 million Reynolds number, buffet onset is encountered and interlocks tripped. Because of fouling problems, attempts to test further into the buffet region were abandoned due to risk of structural damage. Thus, it remained to be determined whether the roll buffet was a limit cycle (amplitude limited) oscillation.

An example of the roll buffet response as seen from a time domain strip chart signal is given in figure 26. When buffet onset and lock-in occurs, the frequency on all channels converges to 20 Hz with rapid increase in amplitude. However, note the rapid decay of the response from peak value to near 0 in approximately 1/4 second. Since the tunnel pitch system moves about 3 degrees/second, the data indicated that only a small change in angle-of-attack attenuates the roll buffet oscillations.

#### 4.4.2 Mach Number Sweep With and Without Vortex Generators

After the roll buffet investigation was completed, the next phase of testing focused on obtaining aerodynamic data at a Reynolds number of 67 million/ft at varying Mach numbers with and without vortex generators installed.

The results with VG's installed are indicated in figure 27. Tests at Mach 0.86, 0.84, 0.82 and 0.80 were limited by pitch buffet. Roll buffet was encountered with VG's on at Mach numbers of 0.75 and 0.70 at angles-of-attack at 5.9° and 6.7° respectively. The test results indicated that the VG's altered the flow over the wing such that roll buffet was not encountered at Mach numbers greater than 0.75., but the pitch buffet boundary was about the same with or without the VG's installed.

During testing without VG's installed at Mach 0.86, violent pitch oscillations were encountered at about 6.25 degrees angle of attack. It should be noted that during the Mach 0.84 run, roll buffet was observed but testing through this condition continued (vibration levels were within limits) to the point where the run was terminated due to pitch buffet. The remaining runs at Mach 0.82, 0.75, and 0.70 were limited by roll buffet as indicated in figure 27.

#### 4.4.3 Aeroelastic Stability Trends for Pitch or Stall Buffett

The pitch buffet boundary is illustrated in figure 27 for tests at full scale Reynolds number, (67 million/ft.). High angle-of-attack buffet is not unique to NTF but at 2800 lb/ft<sup>2</sup> dynamic pressure the loads are extremely high and can result in violent, high amplitude oscillations. During this test at Mach 0.86 and 0.84 violent oscillations



were encountered at angles-of-attack of 6.4 and 6.0 degrees. During the Mach 0.86 run the model oscillations were measured to be approximately 2.5 inches peak-to-peak at a frequency of 10 Hz (1st sting bending mode). At peak amplitude the left wing inboard accelerometer and swept strut strain gage signals were lost due to wire breakage caused by fouling. Although the pitch oscillations were violent, the model and model support (sting) stresses were well within acceptable limits.

#### 4.5 Dynamic Test Results

Buffet testing of a large commercial transport model was successfully completed in the NASA Langley NTF. Test techniques were developed for safely performing dynamic tests in the facility. Testing into the roll buffet regime was limited due to fouling between the model fuselage and support sting. The test marked the first time that scaled vortex generators were successfully employed in the NTF. Good agreement of incremental pitching moment due to vortex generators was shown between NTF and flight data (ref. 18).

#### 5.0 EFFECTS OF VIBRATION ON INERTIAL WIND TUNNEL MODEL ATTITUDE MEASUREMENT DEVICES

During the previously mentioned buffet test, model vibrations influenced aerodynamic data quality and affected the onboard angle-of-attack measurement device. At NASA Langley the predominant instrumentation used to measure model attitude is a servo-accelerometer device that senses model attitude with respect to the local vertical. Under smooth wind tunnel operating conditions, this inertial device can measure model attitude to an accuracy of 0.01 degrees. During wind tunnel tests when the model is responding at high dynamic

amplitudes, the inertial device also senses the centrifugal acceleration associated with model vibration.

This section describes a study of the response of an actual model system to a simulated dynamic environment which shows that significant AOA bias can occur, and is vibration mode and amplitude dependent. Methods for correcting the output of the model attitude inertial sensor in the presence of model dynamics during wind tunnel operation are discussed.

#### 5.1 Experimental Tests and Results

Initial studies conducted to quantify angle-of-attack sensor bias due to model dynamics are documented in reference 6. A follow-up study designed to evaluate the dynamic response of both inertial and optical model attitude measurement devices is documented in reference 7.

##### 5.1.1 Physics of Problem

The physics of model dynamic motion is illustrated in figure 28. It is seen from the figure that the centrifugal acceleration due to model dynamics affects the sensor measurement with respect to the gravity vector. This is true for both pitch and yaw oscillations associated with different modes of vibration. The centrifugal acceleration term  $r\Omega^2$  is the product of the vibration mode effective radius of rotation of the AOA device accelerometer  $r$ , and the angular velocity  $\Omega$ . The output of the AOA device is given symbolically in figure 28 along with an equation for correcting the angle of attack in terms of the  $r_i\Omega_i^2$  contributions.

It should be noted that the AOA bias error due to model dynamics has been a concern for a long time, however the bias was never quantified at NASA Langley. Fuykschot

(ref. 9 and 10) had addressed the problem, and developed first order correction methods as early as 1985.

### 5.1.2 Test Results

The initial test results (ref. 6) clearly showed that AOA bias error can be quite large compared to the desired accuracy of 0.01 degree. Examples of AOA response versus yawing moment for a sinusoidal input at natural frequencies of 10 and 14 Hz for an NTF transport model are shown in figure 29. The 14 Hz yaw mode (model yawing on balances) was excited up to 12000 in-lb. peak to peak, which is approximately 100 percent of the strain-gage force balance full scale design load. Note that the variance of the AOA bias error is quadratic in nature and that a bias error of about -0.15 degrees is measured at 12,000 in-lb (peak to peak). The AOA bias for the 10 Hz mode (1st sting bending in yaw) is more sensitive to yaw moment as 2,000 in-lb (peak-to-peak) or about 16 percent of full scale corresponds to a bias of -0.125 degrees. Although the desired attitude measurement accuracy is 0.01 degree, this level is exceeded at about 3,000 in-lb (peak-to-peak) or about 25 percent of full scale value, which is a relatively low level of model yaw vibration when testing in the NTF at high pressures.

A time trace of the AOA response (static + dynamic) for the 14 Hz mode sinusoidal vibration is given in figure 30. This figure is a snapshot of the MPSS monitoring system display taken near the end of the variable force, constant frequency (14 Hz) forced response of the model/balance yaw vibration mode. Also shown on the figure is the balance yaw moment and pitching moment response. Note that for the yaw moment peak-to-peak amplitude of 12,000 in-lb, the AOA static value is -0.14 degrees which is the mean value of the AOA

dynamic signal (upper graph in the figure). It can be seen from figure 30 that as the yaw moment decreases asymptotically, the AOA static value approaches zero as the yaw moment approaches zero.

### 5.1.3 Correction Methods

Model vibrations are usually unstationary in nature with multiple vibration modes participation. The AOA device, which is rigidly attached to the model, undergoes the same oscillations. Each vibration mode has its own frequency and modal radius characteristics. The experimental work of references 6 and 7 led to a method for estimating the AOA correction due to centrifugal forces acting on the devices. The method requires mounting a biaxial accelerometer on the AOA device that is sensitive to lateral and normal accelerations.

Correction to the AOA signal can be made real time in either the frequency or time domain. The method does, however, require the determination of the effective radius arm,  $r_i$  associated with each mode frequency  $f_i$ , which is obtained by doing a modal survey, preferably with the model installed in the test section. The first order correction for 4 vibration modes is given by:

$$\alpha = \sin^{-1} \left[ \frac{\text{AOA output} + \sum_{i=1}^4 \frac{A_i^2}{f_i^2 \pi^4 r_i}}{g} \right] \quad (1)$$

where  $A_i$  are peak accelerations associated with each mode in "g" units and  $r_i$  is the radius arm associated with each mode,  $f_i$  is in Hertz and  $g$  is the gravitational constant. This method gave very good estimates in laboratory tests. Several other methods have been proposed for correcting the bias error.

One method is to measure the natural frequencies from the frequency spectrum of tangential oscillations, and then determine the bias magnitudes by measuring the magnitude of the second harmonic components of the unfiltered AOA signal spectrum using the following equation:

$$A_{unf}(t) = g \sin \alpha - \frac{V_r^2}{2 \rho_r} (1 + \cos(2\omega_r t)) + a_x(t) \quad (2)$$

where  $a_x(t)$  is the longitudinal component,  $V_r$  is the peak velocity of the  $r^{\text{th}}$  mode, and  $\omega_r$  is the circular frequency of the  $r^{\text{th}}$  mode. The problem with this technique is the participation of multiple vibration modes, and accuracy required to measure small magnitudes of the second harmonic frequency response.

Another correction method was developed by Fuykschot at the National Aerospace Laboratory in the Netherlands. This technique was initially developed for one vibration mode each in the yaw and pitch plane. In the same manner, two accelerometers are used to measure the tangential accelerations due to yaw and pitch motion of the model. The tangential accelerations are integrated to obtain velocity, squared, and divided by a scale factor to compensate for the effective radius of each mode. The mode radius is determined by tuning a potentiometer while manually exciting the model. This method does not address the case where multiple pitch and yaw motions are present.

Buehrle (ref. 8) developed a correction method using measured modal properties of the model system. The method uses the same approach of measuring the tangential

accelerations at the AOA device and determining the effective radius for each vibration mode. Multiple modes are addressed by separating the mode effects by using band-pass filtering, and using a linear superposition of the estimated bias errors for the individual modes as characterized by the following equation:

$$A_{fil} = g \sin \alpha - \sum_{r=1}^m \frac{A_r^2}{2\omega_r^2 \rho_r} \quad (3)$$

where  $A_{fil}$  is the filtered AOA signal and  $A_r$  are the peak accelerations for the  $r^{\text{th}}$  mode. This approach has been validated experimentally using an NTF commercial model. Figure 31 shows the results for random excitation in the pitch plane. Note the excellent agreement between the measured AOA bias and the estimated bias. For these tests, the model correction time domain approach estimated the bias errors to an accuracy within the AOA device accuracy of 0.01. Currently, actual wind tunnel data are being used to further evaluate this approach.

It should be noted that model vibrations may in some cases effect the drag measurements if the axial accelerations are sufficiently high. The drag force correction is given by

$$\text{DRAG FORCE}_{\text{corr.}} = \text{DRAG}_{(\text{meas.})} + W_m \sum_{i=1}^n a_{xi} \quad (4)$$

where  $W_m$  is the model weight and  $a_{xi}$  is the axial acceleration (g's) measured for the  $i^{\text{th}}$  vibration mode.

## 6.0 DYNAMIC MONITORING SYSTEMS IN THE NATIONAL TRANSONIC FACILITY

Since the NTF does not have a catcher screen for fan blade protection, force balance loads and dynamic response monitoring are relied upon to protect against model structural failure.

### 6.1 Force Balance Loads

The force balance loads are monitored by a Balance Dynamic Display Unit (BDDU) and a Critical Point Analyzer (CPU) which provides tunnel interlock protection. These systems are described in reference 12. The dynamic problems encountered initially in the NTF led to development of the BDDU. The system was designed to provide tunnel test engineers with visual and audible warnings when any force or moment component hit full scale design value or 140 percent of full scale. This system proved to be very useful and about 15 of these units are currently in use in wind tunnels at NASA Langley. The BDDU was designed on the assumption that all other force balance components were at full scale when the alarm is triggered. This is a very conservative assumption in that such loadings do not typically occur during testing in the NTF. Subsequently, the CPA was designed and installed in the NTF. The CPA sums the force balance load components algebraically, computes and algebraically sums associated stresses, and compares them to allowable operating values at pre-selected critical points on the force balance. This system allows higher operating dynamic load levels without jeopardizing the force balance structural integrity. The CPA is currently used to trip the NTF interlocks if pre-set load (stress) limits are equaled or exceeded. The BDDU

and CPA units displays are shown in figures 32 and 33, taken from reference 12.

More recently, a very powerful computer based model protection and dynamic response monitoring system has been developed and installed in the NTF control room. The system is described in reference 13. The new system is a computer based, state-of-the-art system designed to protect model systems from dynamic overload and to provide a powerful, on-line dynamic measurements, monitoring and analysis capability. This system is referred to as the Model Protection and Shutdown System (MPSS).

### 6.2 MPSS System

A schematic illustrating how the NTF MPSS works is illustrated in figure 34. A schematic of the system installed in a portable cabinet (rack) and display monitor is given in figure 35, while the signal connections are illustrated in figure 36. The MPSS collects data on tunnel flow conditions, model attitude and model dynamic response data which are analyzed real time in both the time and frequency domain. General specifications are given in reference 13.

#### 6.2.1 MPSS System Operation and Capabilities

The MPSS is designed to monitor dynamic response of the model system using onboard force balance, inertial angle-of-attack sensors, accelerometers and strain gages. A bandwidth of 0-256 Hz was chosen initially to encompass all expected vibration modes of concern for model systems tested in the NTF. Experience with the system suggests that reducing the bandwidth to 0-128 Hz should be sufficient. The sample rate of 4000 Hz per channel simultaneously for 16

channels provides a time domain signal resolution within 5 percent of peak values. However, experience to date suggests that sample rates can be reduced from 4000 to 1000 samples/second without adversely affecting signal quality for 0-128 Hz bandwidth.

Reduction of sample rate and frequency bandwidth is expected to greatly improve graphics speed and provide 4 times as much storage. Fast Fourier transforms are computed for 16 channels simultaneously in 19-20 milliseconds over a 256 Hz bandwidth with a frequency resolution of approximately 1 Hz.

### 6.2.2 Monitoring Dynamic Response

The MPSS displays consist of both time and frequency domain data. Time domain displays are available in 1, 2, 3 and 6 channel configurations for up to 4 seconds of data real time. Frequency domain displays are available in 1, 2 and 4 channel displays. The Fast Fourier Transforms (FFT) are displayed in quasi-real time or in a peak hold mode over the total time of interest. Data storage is available for up to 1.5 hours of continuous operation at the NTF. The graphics displays delay is too long at the present time and can be improved with reduced bandwidth, reduced sample rate, and more efficient graphic driver cards.

### 6.2.3 Safety Trip Algorithms

The MPSS is custom designed to prevent model failure by analyzing data from onboard sensors. The system is designed to generate a trip command which in turn energizes a relay card which in turn commands the NTF logic sequencer to unload the model. The time required to trigger the trip relay is approximately 10

milliseconds (ms). That is, the computation, comparison and trip initiation is accomplished within the 10 ms window.

The NTF relay/sequencer can be configured to pitch the model home (e.g., to zero angle of attack) or unload the inlet guide vanes (IGV) which drops dynamic pressure rapidly in the test section. Both pitch home and IGV unload can be initiated simultaneously.

Several trip algorithms are programmed in the MPSS. These include the following:

(1) Limit Amplitude - Algorithm compares peak values of the response to pre-set limit values. Also, allows number of counts (i.e., number of exceedances before trip) to be pre-set by the operator. Typically 6-9 counts would be chosen.

(2) Rate of Change Limit - This algorithm determines the rate of change for peak amplitudes in the time domain based on the time interval between peaks. Since this algorithm looks at the growth rate (slope) of the signal peaks it can detect potential unstable trends in model vibration.

(3) Time to Double - The time to double algorithm is based on detecting exponential growth of peak amplitudes of the time domain based on harmonic motion. Time to double is a measure of dynamic oscillations which have a divergent time response. This algorithm is best used when guarding against dynamic/aeroelastic instabilities such as divergence and flutter.

### 6.2.4 NTF Applications

The system has been used extensively as a dynamic data acquisition and analysis tool as well as for wind tunnel on-line operation. The system was used to study the effects of vibration on inertial wind-tunnel model

attitude measurement devices (ref. 6). After installation in the NTF control room the system was used to analyze the dynamic interaction between a high speed research model and model support system (ref. 3).

The system has been used extensively to monitor dynamic response of model systems in the NTF. The system provides capability for doing any type of testing including buffet, flutter, etc. Although developed primarily for model protection, interlock connections have not been made. Also, upgrades are needed to enhance and speed up graphic displays and to port real time dynamic data to remote sites.

## 7.0 CONCLUDING REMARKS

Dynamic problems encountered during operation of the National Transonic Facility (NTF) are described. Results of analyses and experimental testing are presented in which the principal variables affecting model dynamics are identified. Experimental laboratory test results indicate that model systems structural damping can decrease significantly at cryogenic temperatures. Yaw vibration of the model/model support system has limited test envelopes for a number of models tested in the NTF. Vibration attenuation has been tried with limited success. Currently, most model systems are limited to about 3000 lb/ft<sup>2</sup> dynamic pressure, however most tests have met high Reynolds number test requirements. In retrospect, the yaw vibration problems probably could have been minimized had appropriate dynamic design criteria been used for design of the model support system.

A highly successful buffet test was conducted safely in the NTF. The test identified buffet boundaries, allowed testing into the buffet regime, and marked the first time that scaled vortex generators were

tested in the NTF which gave excellent correlation with flight data. Test techniques and test approach were developed to establish the NTF capability for conducting dynamic tests.

Studies designed to study the effects of model vibrations on inertial model attitude measurement devices show that significant error in angle-of-attack measurement can be induced by model dynamics. Methods for correcting angle-of-attack measurements have been developed and validated. Finally, the systems currently being used to monitor and limit model vibration amplitudes in the NTF are described. In particular, a new computer based system has been developed and installed in the NTF which provides powerful capability for monitoring, measuring, analyzing and limiting model vibrations in order to reduce the risk of model loss and damage to the facility.

## 8.0 ACKNOWLEDGEMENTS

The author would like to thank Mrs. Doris Vandever for typing the manuscript and layout of the illustrations.

## 9.0 REFERENCES

1. Fuller, D. E.: Guide to Users of the National Transonic Facility. NASA TM 83124, July 1981.
2. Young, C. P., Jr.; Popernack, T. G.; and Gloss, B. B.: National Transonic Facility Model and Model Support Vibration Problems. AIAA Paper 90-1416, 1990.

3. Young, C. P., Jr.; Buehrle, R. D.; Balakrishna, S.; and Kilgore, W. A.: Experimental Study of Dynamic Interaction Between Model Support Structure and a High-Speed Research Model in the National Transonic Facility. AIAA Paper No. 94-1623.
4. Strganac, T. W.: A Study of the Aeroelastic Stability for the Model Support System of the National Transonic Facility. AIAA Paper No. 88-2033, 1988.
5. Whitlow, W., Jr.; Bennett, Robert M.; and Strganac, T. W.: Analysis of Vibrations of the National Transonic Facility Model Support System Using a 3-D Aeroelastic Code. AIAA Paper No. 89-2207, 1989.
6. Young, C. P., Jr.; Buehrle, R. D.; Balakrishna, S. and Kilgore, W. Allen: Effects of Vibration on Inertial Wind-Tunnel Model Attitude Measurement Devices. NASA TM 109083. July 1994.
7. Buehrle, R. D.; Young, C. P., Jr.; Burner, A. W.; Tripp, J. S.; Tchong, P.; Finley, T. D. and Popernack, T. G., Jr.: Dynamic Response Tests of Inertial and Optical Wind-Tunnel Model Attitude Measurement Devices. NASA TM 109182. February 1995.
8. Buehrle, R. D.; and Young, C. P., Jr.: Modal Correction Method for Dynamically Induced Errors in Wind-Tunnel Model Attitude Measurements. 13th International Model Analysis Conference, Feb. 13-15, 1995, Nashville, TN.
9. Fuykschot, Pieter H.: A Correction Technique for Gravity Sensing Inclinometers. NLR Memorandum AF-95-004L. April 1995.
10. Fuykschot, P. H.: A Correction Technique for Gravity Sensing Inclinometers - Phase 2. Proof of Concept. NLR Contract Report CR 95458L.
11. Young, C. P., Jr.; Hergert, Dennis W.; Butler, Thomas W.; and Herring, Fred M.: Buffet Test in the National Transonic Facility. AIAA 92-4032, July 1992. (Also published as NASA Contractor Report 189595).
12. Ferris, Alice T. and White, William C.: Monitoring Dynamic Loads on Wind Tunnel Force Balances. ISA Paper 89-0021, 1989.
13. Young, C. P., Jr.; Balakrishna, S.; and Kilgore, W. Allen: Development of a Model Protection and Dynamic Response Monitoring System for the National Transonic Facility. NASA Contractor Report 195041, February 1995.
14. Young, C. P., Jr. and Buehrle, R. D.: Structural Damping Studies at Cryogenic Temperatures. NASA TM 109073, May 1994.
15. Cole, Stanley R.: Exploratory Test in a Cryogenic Wind Tunnel. Journal of Aircraft, Vol. 23 No. 12, December 1986, pp 904-911.

16. Igoe, William B.: Analysis of Fluctuating Static pressure Measurements In a Large High Reynolds Number Transonic Cryogenic Wind Tunnel. Ph.D. Dissertation to George Washington University.
17. Rublin, C. L.; Watson, J. J.; Ricketts, R. H. and Doggett R. V., Jr.: Evaluation of Four Subcritical Response Methods for On-Line Prediction of Flutter Onset in Wind Tunnel Tests. Journal of Aircraft, Vol. 10, October 1983, pp 835-840.
18. Wahls, Richard P. et al: A High Reynolds Number Investigation of a Commercial Transport Model in the National Transonic Facility. NASA Technical Memorandum 4418. April 1993.



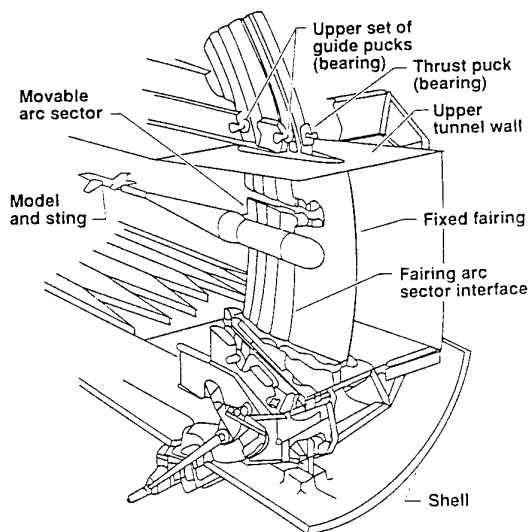


Figure 1. NTF model support system.

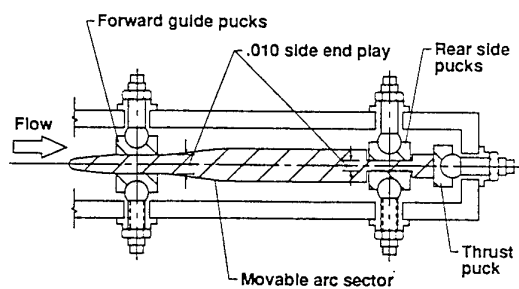


Figure 2. Cross section of movable arc sector illustrating guide pucks.

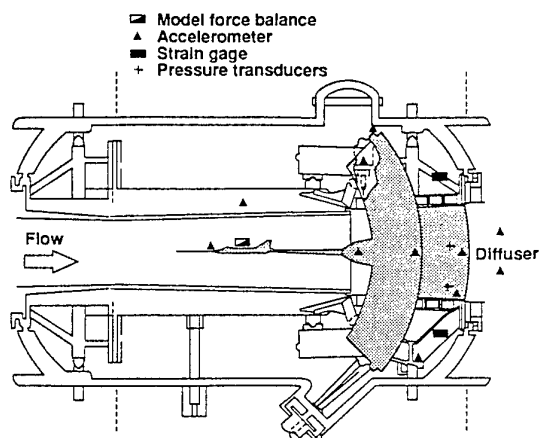


Figure 3. Instrumentation locations for experimental test programs.

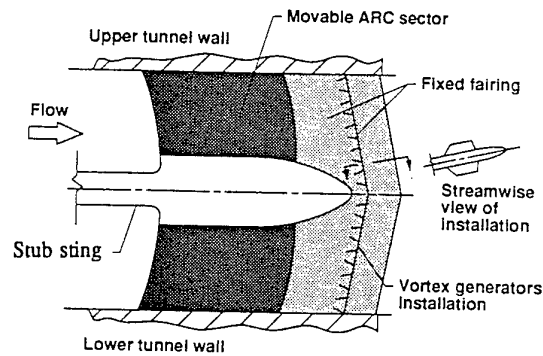


Figure 4. Vortex generators installation on fixed fairing.

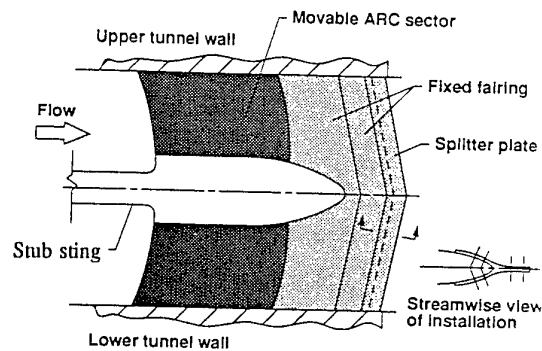


Figure 5. Splitter plate installation on fixed fairing.

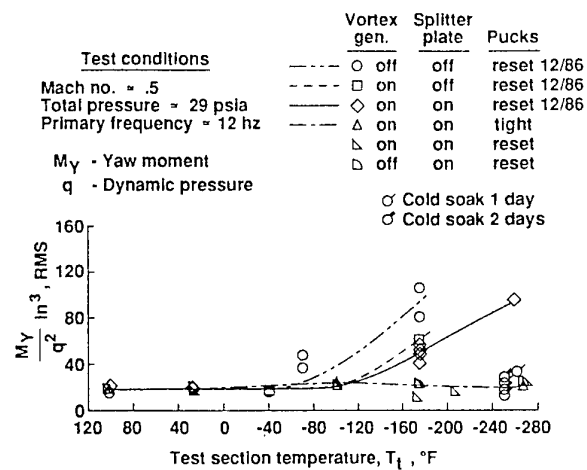


Figure 6. Normalized yaw vibration response versus temperature for various test conditions.

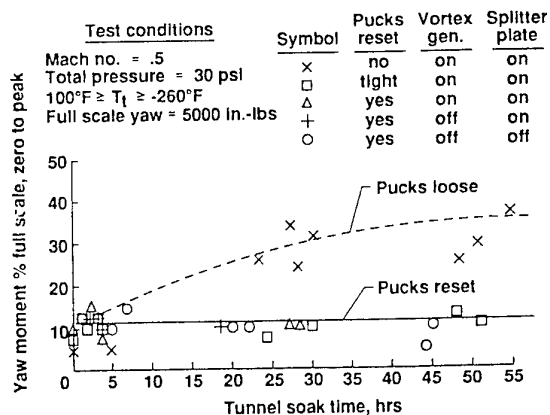


Figure 7. Yaw moment peak response as a function of tunnel soak time for arc sector pucks loose and reset.

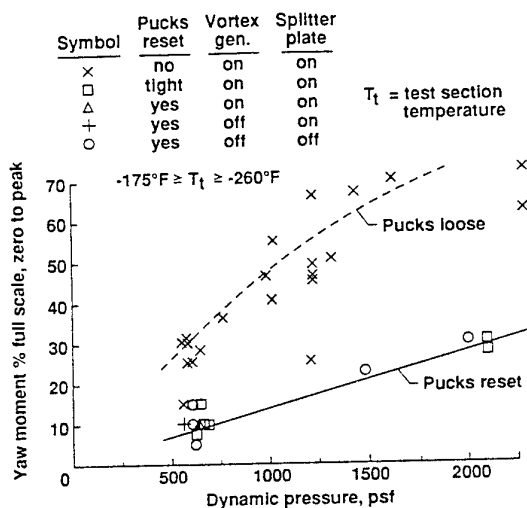


Figure 8. Yaw moment response as a function of dynamic pressure for pucks reset and loose.

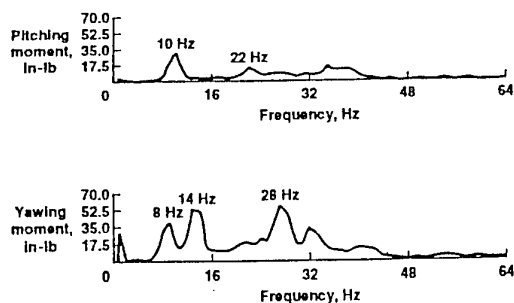


Figure 9. HSR model force balance peak hold spectra during warmup at zero roll angle.

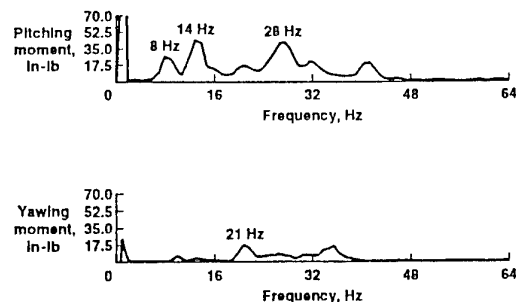


Figure 10. HSR model force balance peak hold spectra during warmup at  $90^\circ$  roll angle.

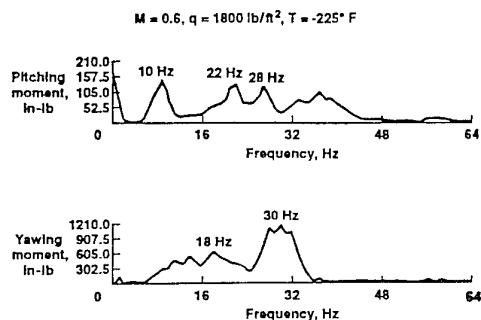


Figure 11. HSR model force balance peak hold spectra at cryogenic run conditions, zero roll angle.

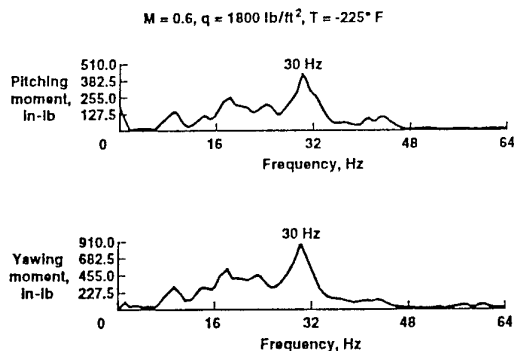


Figure 12. HSR model force balance peak hold spectra at cryogenic run conditions,  $30^\circ$  roll angle.

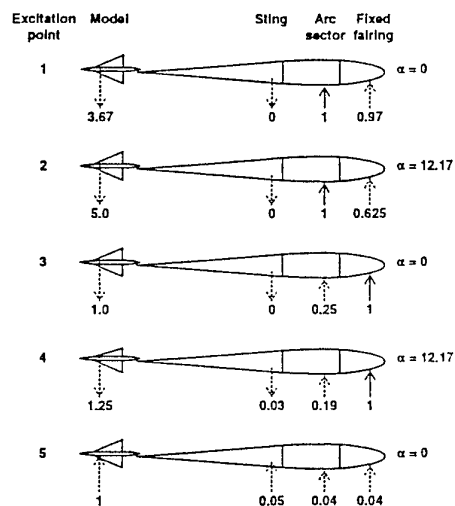
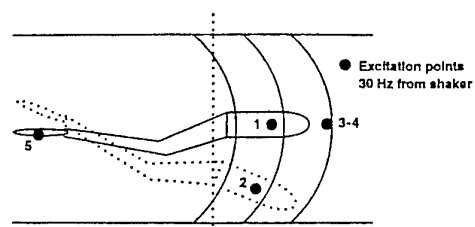


Figure 13. 30 Hz mode forced response of NTF model/sting/arc sector/fixed fairing.

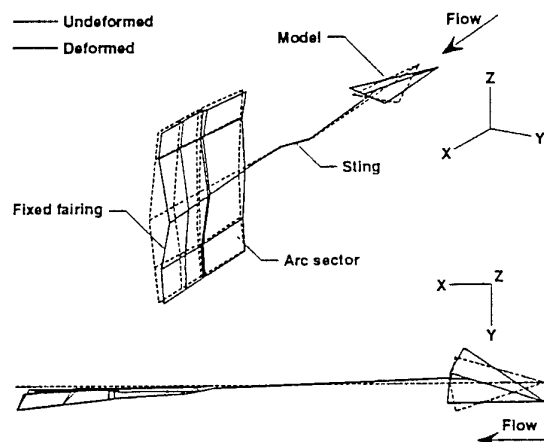


Figure 14. Model/model support structure, 19.2 Hz vibration mode.

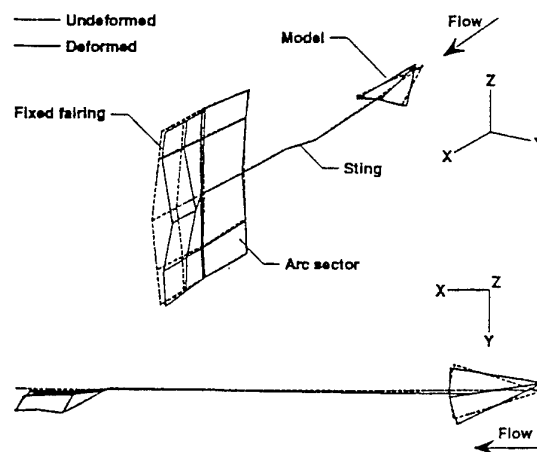


Figure 15. Model/model support structure, 23.8 Hz vibration mode.

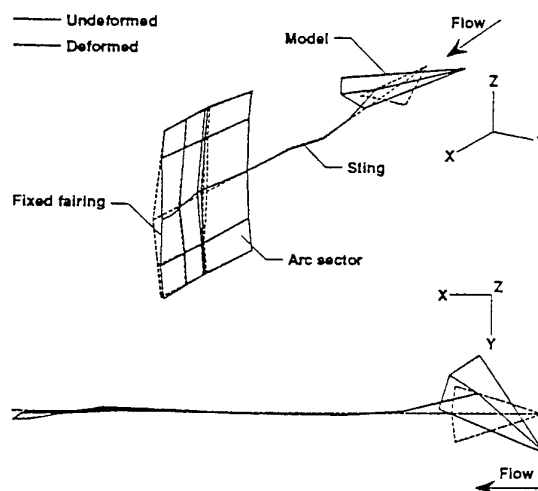


Figure 16. Model/model support structure, 30 Hz vibration mode.

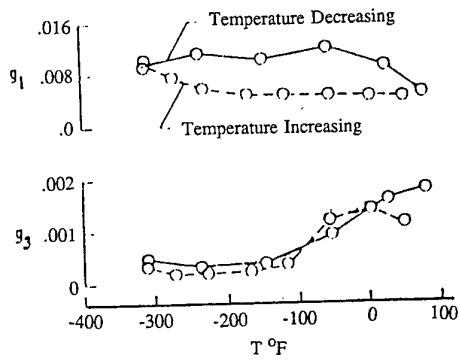


Figure 17. Measured damping values and frequencies for flutter model tested in the 0.3-Meter Cryogenic Tunnel

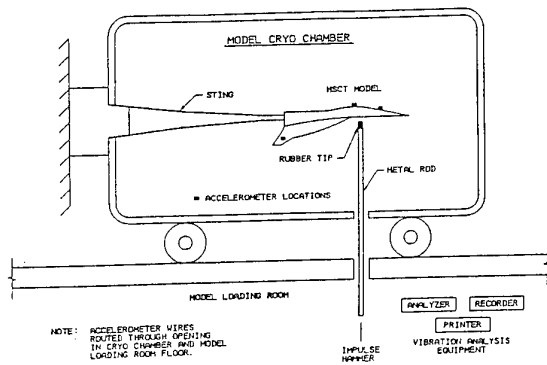


Figure 18. Setup for manually exciting the HSCT model system in the cryo chamber.

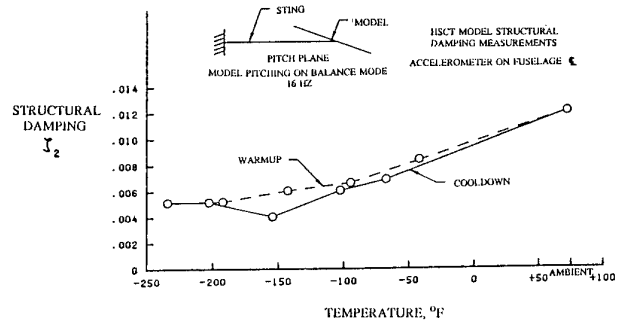


Figure 19. Measured damping values for Mode 2 - HSCT.

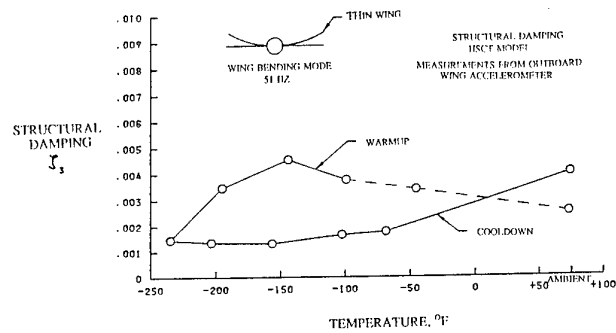


Figure 20. Measured damping values for Mode 3 - HSCT.

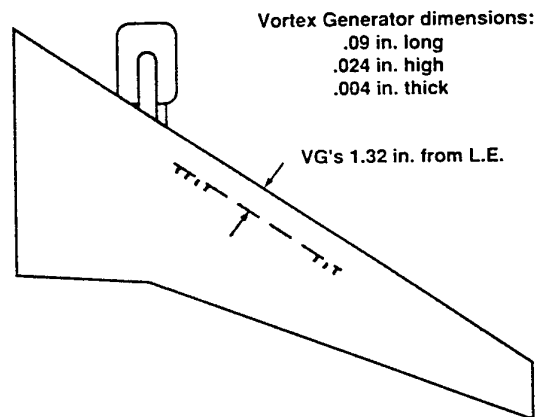


Figure 21. Vortex generator locations on right wing.

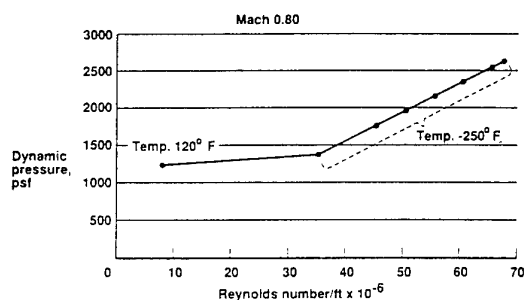


Figure 22. Test profile for investigating Reynolds number effects on buffet.

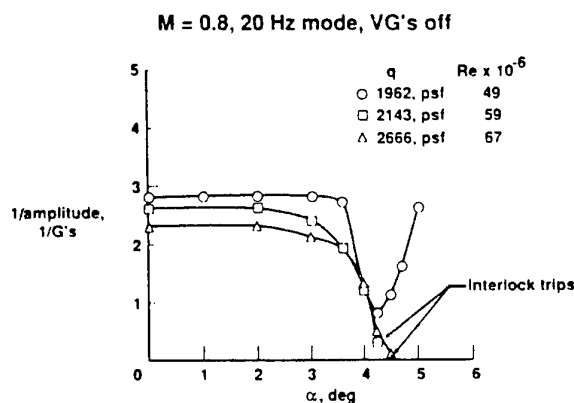


Figure 25. Roll buffet stability index versus angle of attack for variable Reynolds number and with vortex generators removed.

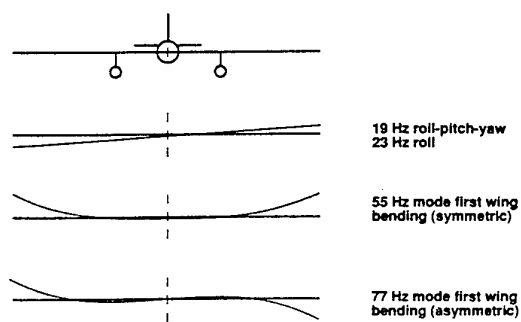


Figure 23. Vibration modes of primary interest for buffet test.

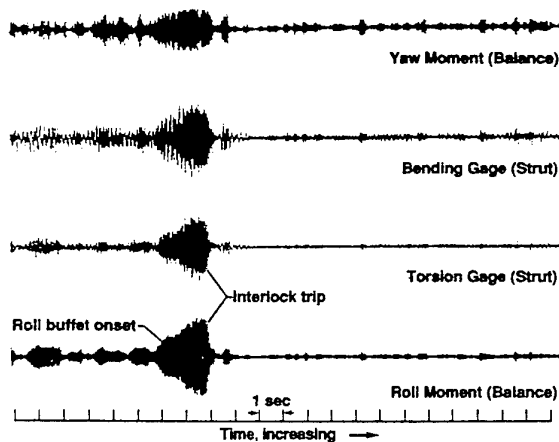


Figure 26. Force balance and swept strut strain gage response due to roll buffet.

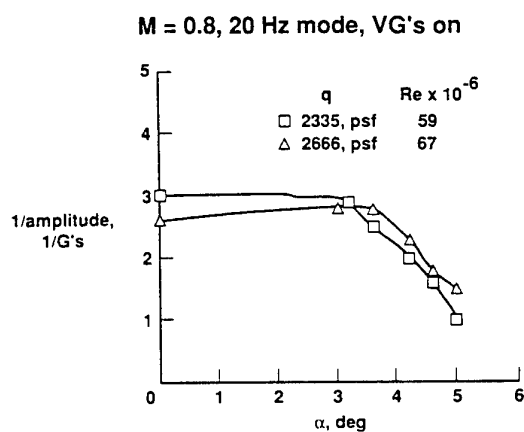


Figure 24. Roll buffet stability index versus angle of attack for variable Reynolds number and with vortex generators installed.

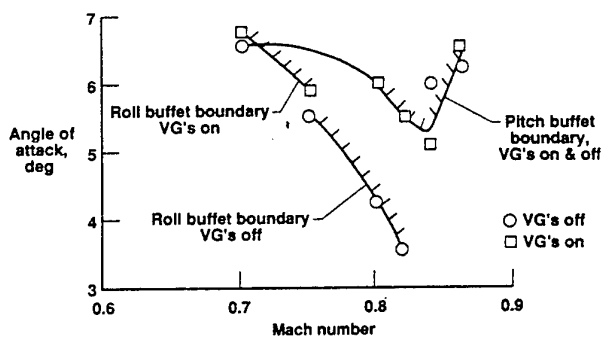


Figure 27. Model dynamic response boundaries at Reynolds number of 67 million/ft.

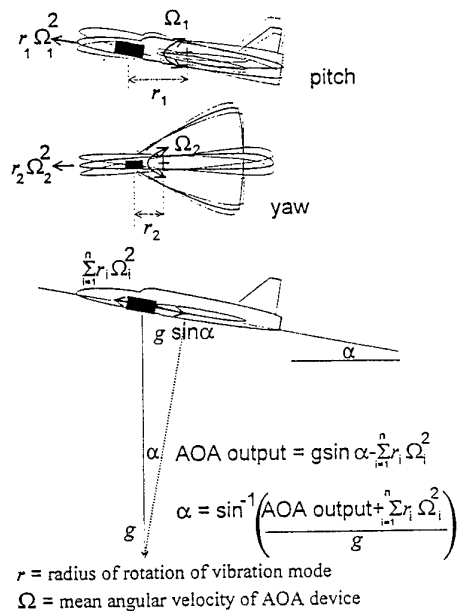


Figure 28. AOA bias error due to model vibration induced centrifugal acceleration.

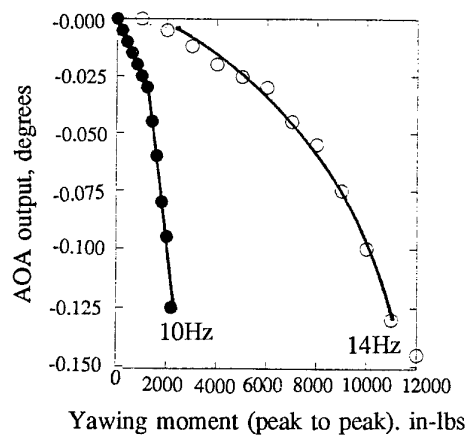


Figure 29. AOA response versus yawing moment for 10 and 14 Hz yaw vibration modes.

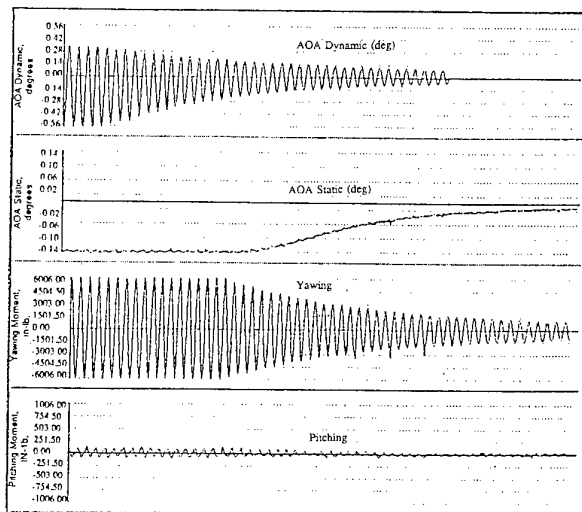


Figure 30. MPSS display illustrating AOA static and dynamic response with yaw moment (due to 14 Hz excitation) as a function of time.

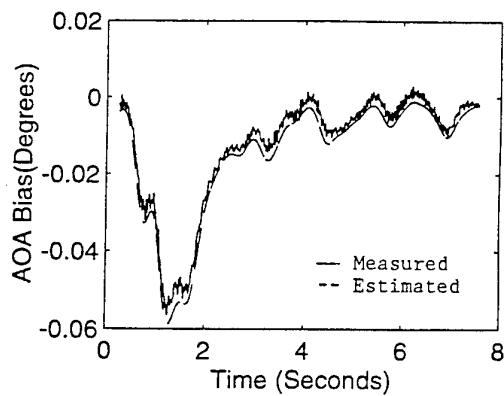


Figure 31. Measured and estimated AOA bias error versus time for random excitation in pitch.

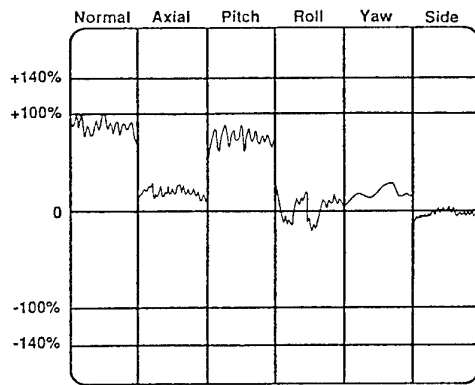


Figure 32. Typical BDDU display.

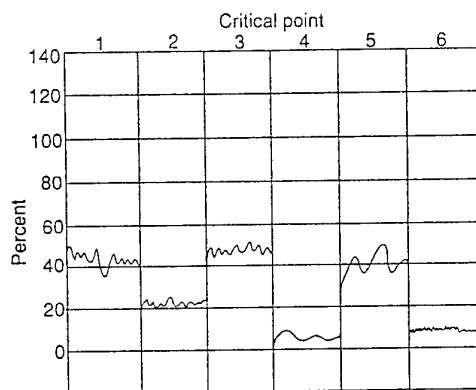


Figure 33. Balance CPA display.

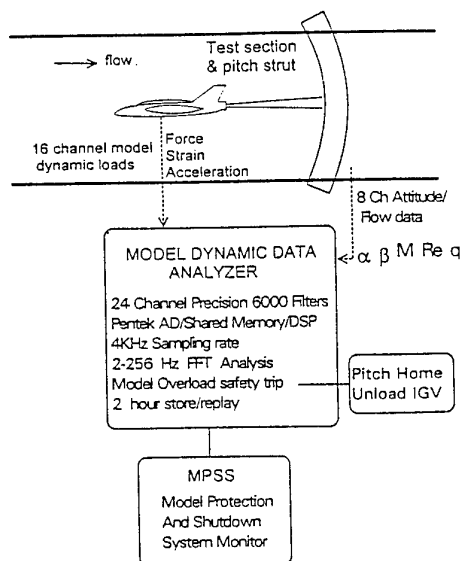


Figure 34. Schematic of the NTF model protection and shutdown system.

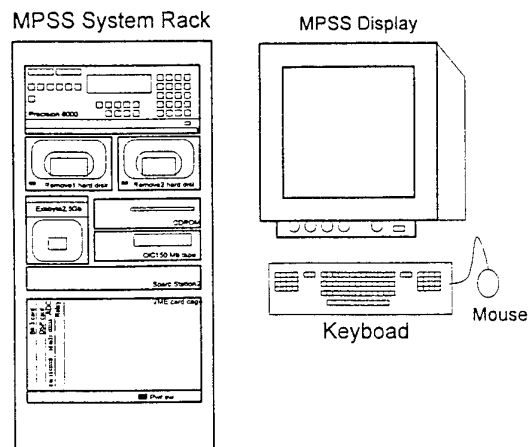


Figure 35. Model protection and shutdown system rack and display.

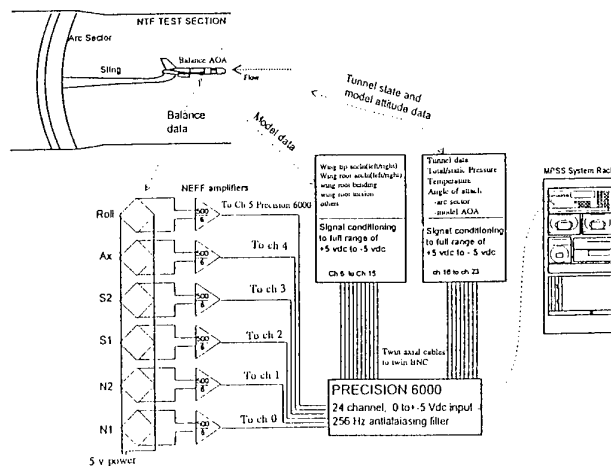


Figure 36. NTF signal connections to MPSS.

# AN OVERVIEW OF TEST CAPABILITIES AT ETW

by  
**Ian Price & Dieter Schimanski**

ETW GmbH  
Ernst Mach Straße  
D-51147 Cologne Germany  
Tel. (0)2203 609134  
Fax. (0)2203 609266

## 1.0 Summary

Throughout the project stages, from the planning and design phases through to the present initial operations phase, it has always been recognized that technical excellence and productivity were fundamental to the success of ETW. In a fiercely competitive market technical excellence must be consistent with state of the art transonic testing especially at high Reynolds numbers. Test techniques have therefore been developed to achieve the high productivity levels required by industrial users for efficient testing.

This paper reviews the major features of the test techniques developed which aim at achieving a high technical quality of testing and a high productivity. Special attention has been paid to ensure that the design for high productivity, has not compromised the technical quality of the final data output.

## 2.0 Facility Description

The ETW facility is a high Reynolds number transonic wind tunnel using nitrogen as the test gas. High Reynolds numbers (of up to 50 million at cruise conditions for full span models of large transport aircraft) are achieved under the combined effects of low temperatures and moderately high pressures. Figure 1 shows the operating envelope of ETW for typical full span models. The symbols indicate the operational envelope covered, during calibration and model test campaigns in the initial operating phase.

ETW is a closed circuit cryogenic wind tunnel driven by a 50 MW variable speed induction motor powering a two stage compressor. It is capable of continuous operation, however, to facilitate model configuration and tunnel temperature changes, it is operated in the intermittent mode with runs of typically 10 to 60 minutes. The high Reynolds number capability is achieved by lowering the test gas temperature, and by raising the pressure. Its operational temperature and pressure ranges are

respectively 90 to 313K and 125 to 450 kPa. Its Mach number range is  $0.15 \leq M \leq 1.3$ . The test medium is gaseous nitrogen which is injected into the circuit in liquid form upstream of the compressor. The liquid nitrogen vaporizes prior to entering the compressor. Between the compressor and the stilling chamber is situated the blow-off station where excess gaseous nitrogen is extracted from the circuit and vented to atmosphere via control valves, silencer, air mixing point, burner, and the exhaust stack. The gas in the circuit then enters the wide angle diffuser where it passes through two filling screens into the stilling chamber and on through a honeycomb flow straightener and two anti-turbulence screens prior to entering the 12 to 1 contraction and the nozzle which can be adjusted for supersonic operation. It then passes through the test section, which houses the model; the second throat area; high speed diffuser; and back to the liquid nitrogen injection station.

The pressure shell is made from austenitic stainless steel and is internally insulated.

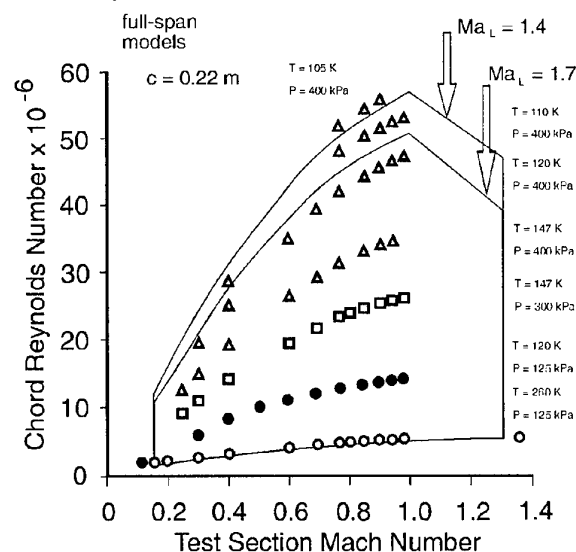


Figure 1 ETW Test Envelope



ETW utilises a removable model cart system to provide both flexibility of operation and high productivity. The initial build of ETW has two model carts with future provision for others as demand dictates. The buildings of ETW provide confidentiality of tests within safe and secure areas for users to prepare their tests, rig and checkout their models, acquire their data and analyse their results.

## 2.0 Test Capabilities

ETW has advantages over conventional wind tunnels other than the increase in Reynolds number, in that the Mach number, Reynolds number and dynamic pressure can all be varied independently. This capability allows the following test trajectories to be accomplished

### 2.1 Pure Reynolds Number Effects

Reynolds number effects can be obtained without varying the aeroelastic distortion of the model. This is achieved by changing only the temperature, while holding Mach number and pressure (and therefore dynamic pressure) constant. This facility enables Reynolds number extrapolation for a model where full scale Reynolds numbers cannot be attained.

### 2.2 Pure Mach Number Effects

Pure Mach number effects can be obtained by varying the stagnation pressure and temperature in order to hold dynamic pressure and Reynolds number constant when Mach number is changed.

### 2.3 Pure Aeroelastic Effects

The effects of aeroelastic deformation of models can be studied by varying the dynamic pressure, whilst holding Mach number and Reynolds number constant.

### 2.4 Flutter Studies

For flutter tests it is desirable to match simultaneously the stiffness and mass density parameters, at a given Mach number. The independent variations of pressure and temperature in ETW allow this matching to be maintained in order to simulate a flight over a range of altitude.

### 2.5 Ambient Temperature Tests

Testing in ETW can also be carried out at ambient temperature as in present day wind tunnels. This has the benefit of giving continuity of data from cryogenic to ambient conditions, and therefore cover the complete range in Reynolds number with

the same model or configuration.

## 2.6 Automated Tunnel Control

A key feature in minimising test cost during the wind on time, has been the successful development of the fully automatic control system. A typical time of 45 seconds is required between polars at different set points to achieve stability within the tightly controlled limits required on Mach, pressure and temperature. Once the tunnel set point is reached, the polar is automatically executed by the model data acquisition system. On completion of the polar the next set point is then requested.

## 3.0 Force and Moment Measurements

As in every transonic wind tunnel the majority of tests in ETW will include the use of a six-component internal strain gauge balance. Based on experience gathered, practical and theoretical considerations, ETW opted for the cold balance concept. This requires multiple calibrations over the complete temperature range. If required, computational corrections for temperature (and temperature gradient) effects on zero, span and possibly interactions can also be applied.

In order to allow an easy exchange and comparison during actual model testing the initial balances were specified to have identical outside dimensions and flanged joints. ETW is currently in the process of procuring a small cross section, high capacity balance with tapered joints for applications with space limitations.

Balances will operate in ETW over a range of more than 200K. Temperature settling times for a balance mounted inside a model have to be minimised, which therefore calls for efficient tunnel operation and accurate measurements to be made during transient conditions after the tunnel flow temperature has been changed. Ten temperature sensors are positioned at strategic locations along each balance to determine any possible gradients.

Basically, accuracy for the main components, is 0.1% of the maximum load over 50 to 100% of the range and 0.05% below 50%. It is acknowledged that realizing these figures requires extensive calibration.

### 3.1 Balance Calibration

The consequence of opting for the cold balance concept is that balances must be calibrated over the complete temperature range. ETW has therefore acquired and developed a novel automatic Balance Calibration Machine(BCM). The BCM can perform a full second or third order calibration at one

temperature level, in one day. A complete calibration in steps of typically 25K can be performed in 9 days. During testing the closest calibration matrix matching the balance temperature is automatically selected. It is envisaged that further developments will incorporate a temperature correction technique between the calibration matrices. Balances showing little sensitivity to temperature effects promise a reduction in the number of calibrations required, and also the level of corrections to be applied. This will result in greater operational flexibility, thus, enhancing productivity and accuracy.

### 3.2 Operational Overview

When testing at cryogenic temperatures the tunnel is first cooled to the set point temperature at a rate of up to 80K per hour. This process is performed at low Mach number with bypass flow being directed through the plenum to fully cool the internal structure. When the set point temperature is reached the cooling process is maintained for a short period to stabilize the tunnel internal structure and minimise any residual thermal gradients and distortions. The bypass flow is then stopped and the tunnel prepared for testing. It should be noted that some additional conditioning may be required to reduce thermal gradients in the balance. However, this is dependent upon the balance/model heat transfer rates and the balance sensitivity to temperature gradients. ETW is at present still refining the test technique to determine the best trade-off between time, Nitrogen/Power consumption, balance thermal stability requirements and data accuracy.

### 3.3 Balance Interchangeability

In recent test campaigns data has been acquired on the ETW Reference Model, with two different balances using identical model and tunnel configurations at both ambient and cryogenic test conditions with low and high dynamic pressures. The data has yet to be fully evaluated, however, early indications show that repeatability levels of 1 drag count can be achieved. These encouraging results give a high level of confidence in the data quality, considering that the results were obtained in two separate test campaigns using different balances with the consequent rebuild of the model. Figure 2 shows a typical comparison between two balances at 180K of CD Vs CL at a Mach number of 0.75 and Reynolds number of 7.6 million. Figure 3 shows the CL Vs alpha plot for the same conditions.

### 3.4 Half Model Development

ETW is also currently acquiring a half model capability. The level of accuracy, repeatability and resolution in force measurement will be consistent with, or exceed that obtained in conventional wind tunnels. It is anticipated that model drag will

be measured to an accuracy of  $CD < 0.00005$  and incidence will be resolved to better than 0.01 degrees.

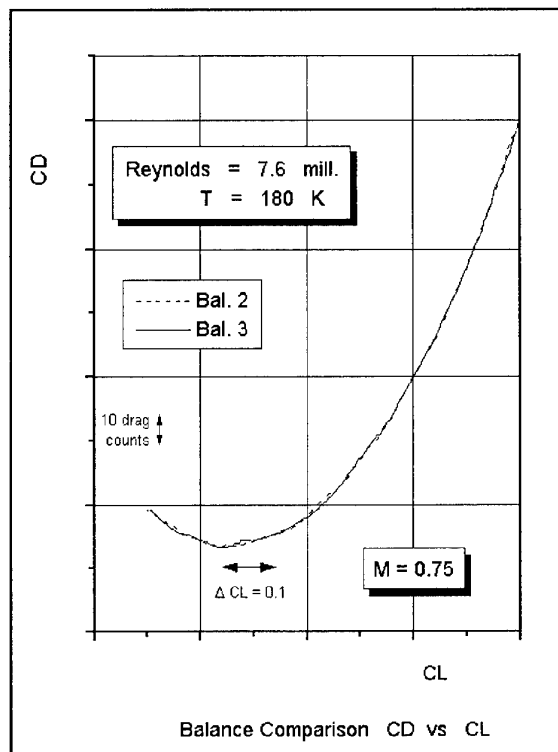


Figure 2 Balance Comparison Cd Vs CL

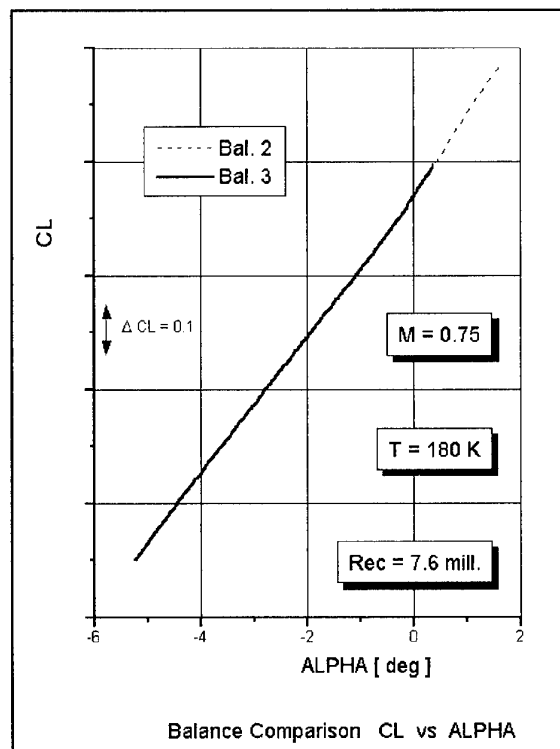


Figure 3 Balance Comparison CL Vs Alpha

#### 4.0 Boundary Layer Transition

The initial polars (low Reynolds number & ambient temperature) of a test programme are often used for inter-facility comparison. In such cases conventional transition bands such as ballotini or carborundum are applied to the model. The effectiveness of the transition fix is then verified by the conventional acenaphthene sublimation method. The removable cart concept at ETW enables the acenaphthene technique to be applied and photographs to be taken in the Variable Temperature Check-out Rooms (VTCR's), prior to and after the test.

ETW has also tested a cylindrical dot method for transition fixing, which is preferred by some clients. In support of this technique, a study was performed for ETW by the T2 group of ONERA. During this study the effectiveness of cylinder diameter, height and pitch, over a large Reynolds number range at transonic conditions, was evaluated.

#### 4.1 Boundary Layer Transition Detection

Being able to simulate full scale flow conditions over a model means that no artificial inducements need to be applied to the model to force the boundary layer to trip from laminar to turbulent conditions at the correct chordwise position. However it is necessary to know the precise location where the transition occurs to understand the results obtained from the model.

ETW has selected the Infrared Camera technique as the preferred method to observe where the transition occurs. This allows remote sensing of infrared radiation which is emitted by heat patterns on the surface of the model and corresponds to actual boundary layer status.

Two different concepts of IR cameras are the basis for measurement of transition in the complete temperature range of the facility :

Concept 1 - a standard IR camera with a detector in the 8 - 12  $\mu\text{m}$  waveband and Concept 2 - a special IR camera with a detector for the waveband above 15  $\mu\text{m}$ .

#### 4.2 Infrared Concept 1

ETW has installed a conventional IR camera, AGEMA Thermovision 1000, in the test section that will detect transition on a model down to flow temperatures of 200K providing on-line results. Provisions are also made for simultaneous operation of a second conventional IR camera.

The detection of transition on model surfaces at temperatures below ambient, requires special provision for the standard

AGEMA camera in the form of a heated housing, a special model coating selected for the temperature range anticipated, and for the testing procedures by optimising a transient temperature step in the facility.

#### 4.1.1 AGEMA Camera Housing

The heated housing for the camera consists of an insulation box open for pressure ventilation during tunnel pressure changes, an actively ventilated, internal heating circuit and a front window of germanium. The housing is installed behind a test section window as presented in figure 4. The camera is attached to a manually movable support structure to optimise the field of view prior to testing.

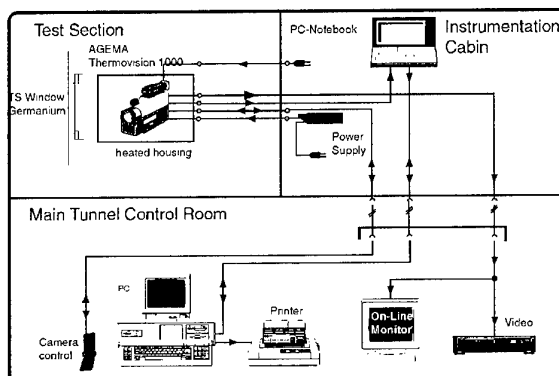


Figure 4 AGEMA Infrared Installation at ETW

#### 4.1.2 Model Coatings

Models need to be coated by a specially selected paint for the low temperature range. After intensive investigations and testing a coating was selected which is compatible with the high standards in surface quality (surface roughness of about 0.4  $\mu\text{m}$ ), and provides the mechanical characteristics for low temperature testing, and also provides all the required thermal and optical characteristics. The paint can be removed easily by chemical paint remover immediately after testing. It also has been applied on models where the wing is used for pressure measurements without blocking any pressure taps.

#### 4.2.3 Tunnel Testing

The testing procedures can be optimised in the facility by using the advantage of quickly induced temperature steps and keeping all other tunnel parameters constant. This increases the effect of transient heat transfer at the model surface significantly, due to the difference of model surface temperature and recovery temperature in the boundary layer. The IR image has to be taken when the temperature difference has reached a maximum.

To establish a wide experience with the AGEMA camera, test campaigns were performed at temperature levels of 300K, 240K, 220K and 200K with different temperature steps. A typical test run showing Temperature Vs time is presented in Figure 5. The shaded areas of the figure show where the best quality results are obtained. As can be seen at the 200K test temperature the temperature step required is greater than at ambient conditions. However, following future development of the image processing methods it is anticipated that this level will be significantly reduced. A black and white version of the colour image achieved during such a run with the ETW Reference Model is presented in figure 6. During these IR trials a transition band was placed between 10 & 40% of the wing span. This provided a good contrast between the inner and outer transition free sections of the wing. The difference between the forced and natural transition point on the wing can clearly be seen.

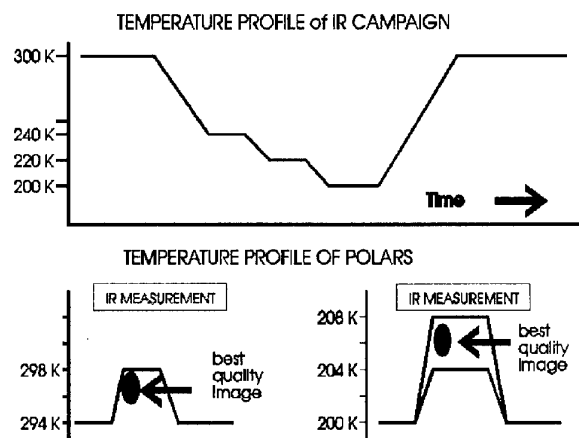
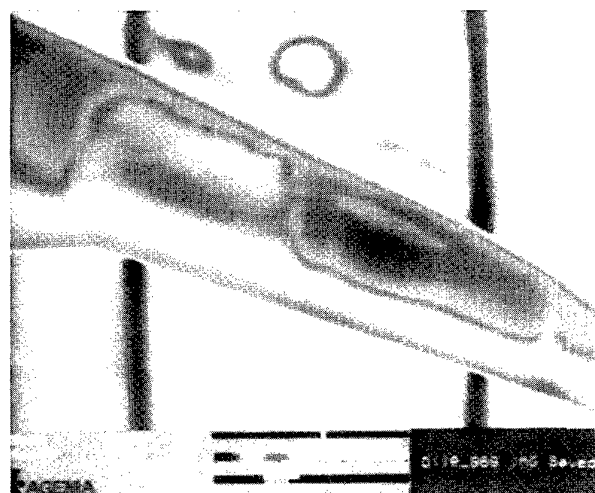


Figure 5 Typical Infrared Test Run



$M = 0.75$ ,  $CL = 0.5$ ,  $T_t = 294K$

Figure 6 Typical Infrared Image

#### 4.3 Infrared Concept 2

A second IR camera system that will detect transition down to temperatures of about 100K is also being procured and should be available by end 1996.

In this case the camera housing itself will be a pressure shell which contains the optical part of the system with an Si:Ga detector cooled down to 15 K during operation. The optical system itself will be below 50 K. Cooling is achieved by a Joule-Thomson closed-cycle system precooled by a Gifford-MacMahon cryomachine. The complete system will be installed in the test section wall similar to the standard AGEMA camera concept.

#### 5.0 Model Deformation Measurement System (MDMS)

Despite the use of very high strength and stiffness alloys, models in ETW will show considerable deformation when subjected to the high dynamic pressures the facility is capable of. It is estimated that for transport type aircraft the wing bending at wing tip location can be up to 40mm, with the added possibility of wing twist. ETW has specified a Model Deformation System based on Moiré techniques which should provide a global overview of the deformation of a complete wing. It should allow quantitative measurement of bending and twist with accuracies of 0.2mm and 0.03 degree respectively over the complete incidence range. The optics will be mounted in the test section top wall.

#### 6.0 Model Attitude Measurement System (MAMS)

When using a balance in the model axis system, as is the case for an internal strain gauge balance, the precise determination of the drag coefficient in the wind axis system requires that the model angle of attack is known with an accuracy of 0.01 degree. ETW will rely on two different and independent systems to establish this crucial parameter. The first system is a classical gravity vector sensing servo accelerometer. ETW typically uses a QFLEX inclinometer, mounted in a heated enclosure inside the model fuselage.

The second system, referred to as MAMS, uses optical techniques to assess the angle between the Test Section top wall and a corner cube mounted in an insert in the model. This insert is typically located in the fuselage directly above or below the centre of rotation of the model, taking into account the kinematics of the ETW model support.

The corner cube has a fine mesh grating on its outer surface. When illuminated with a collimated monochromatic beam the

Moiré pattern created in the focal plane of the collimating lens contains the angle information. By using two wavelengths of monochromatic light and eight detectors, a read-out with a resolution of .001 degree and accuracy of 0.01 degree can be realized over a range of  $\pm 10$  degrees. MAMS is used in conjunction with the classical servo accelerometer inclinometer in the model to calibrate the system under wind-off conditions.

During testing in the tunnel the model may experience vibrations of varying levels. These vibrations are dependent upon the model/sting/balance combinations and the test conditions such as dynamic pressure, Mach and Reynolds number along with buffet onset. It is very difficult, before the test entry (with the exception of buffet) to try to predict the vibration characteristics of a test assembly. When a model experiences such vibrations, errors can be built up in the inclinometer. The MAMS system during commissioning has demonstrated that a high accuracy incidence can be maintained, when the model experiences significant vibrations.

An example of such incidence errors is presented in Figure 7. The plot shows Alpha (inclinometer) - Alpha (MAMS) Vs Alpha (inclinometer). During this particular test the model was traversed from  $-4.7$  to  $+0.7$  Alpha, at a Mach number of 0.75 and temperature of 180K. At the maximum incidence vibrations were experienced by the model, which did not fully reduce until the model was returned to  $-1^\circ$  alpha. This resulted in a maximum error in alpha measured by the inclinometer of  $0.09^\circ$ . In order to illustrate the impact of such errors on the computed drag, the data was processed with both the inclinometer and the MAMS measurements of alpha. Figure 8 shows that the resulting error is greater than 10 drag counts at maximum the incidence.

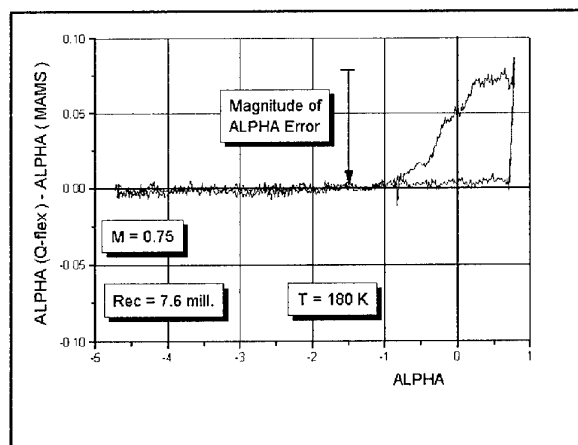


Figure 7 Incidence Error Induced by Model Vibrations .

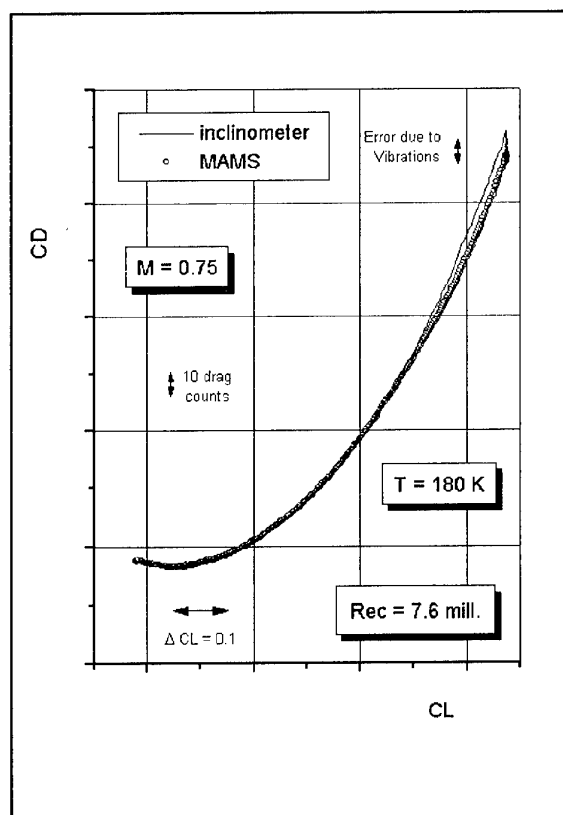


Figure 8 Effect of Model Vibration on Data Quality.

## 7.0 Pressure Testing

ETW makes extensive use of the Electronic Scanned Pressure (ESP) measurement system from Pressure Systems Incorporated (PSI). Prior to ordering these systems from PSI they were carefully evaluated for the demanding requirements of testing in a cryogenic environment (note, the scanners are maintained at elevated temperatures), which resulted in a number of modifications in the interfacing between the Multi-port sensors and the 8400 System Processor. These modifications result in a drastically reduced wire count, longer calibration intervals and improved data quality. The new configuration includes a small (ESP size) Scanner Junction Unit, which is mounted in the vicinity of the sensors. On the System Processor side a new S84-IFC Unit including a power supply has been added.

ETW has developed a series of heated enclosures that are mounted inside the models. Special attention has been paid to thermal stability over the extreme operating conditions of both the upper and lower temperature limits.

Tests to date have shown that it is possible to measure combined forces moments and pressures on heavily pressure

plotted models. With the amount of additional services that the P.S.I. system and the environmental housing required, it was thought that some hysteresis would be apparent on the balance. Detailed checks prior to tunnel testing at both ambient and cryogenic conditions indicate that any such interferences are negligible.

The stated PSI accuracy of  $\pm 0.05\%$  FSD, or better is being achieved by ETW over the complete operating range.

## 8.0 Model Handling

Throughout all phases of ETW's development, from conception through design and construction, great emphasis has been placed on achieving an operational efficiency which is, at least, comparable with that of conventional wind tunnels. A major feature of ETW is its interchangeable model cart system. As well as providing flexibility of operation and increased productivity it also allows models to be prepared and mounted on the cart in more than one location, which therefore offers complete confidentiality to users.

### 8.1 Basic Concept

For ETW to achieve its productivity targets rapid access to the model is required for configuration changes. Therefore, between test runs, the model along with the complete model cart is moved together with the upper test section wall, model support, tunnel pressure door and instrumentation cabin, by means of a special crane, to one of the adjacent Variable Temperature Check-out Rooms (VTCR's). This modular cart system also facilitates the preparation of another model on a second model cart in one of the Cart Rigging Bays (CRB's) in parallel to the test being undertaken in the wind tunnel. Once lifted from the tunnel, the transporter can move and lower the cart assembly into any of the other rooms along the transfer hall. ETW has been designed to accommodate four model carts. Initially, only two cart assemblies have been procured. Model Cart 1 (MC1) has an incidence range of  $-10$  to  $+35$  degrees, the range of Model Cart 2 (MC2) being  $-10$  to  $+20$  degrees. Further developments will allow for half model testing on MC1.

### 8.2 Building Layout

The model carts can be located in any of the three cart rigging bays, where models can be prepared and checked out, or in either of the two variable temperature checkout rooms, where the model and cart can be subjected to any temperature condition for final checkout prior to entering the tunnel. The VTCR's are also used for model configuration changes between tunnel runs. Here model configuration changes can be

undertaken at cryogenic conditions or, if a major change is required, the model can be warmed up to ambient conditions whilst still keeping the model cart cold. Figure 9 shows a section through the transfer hall, which links the CRB's and VTCR's with the tunnel

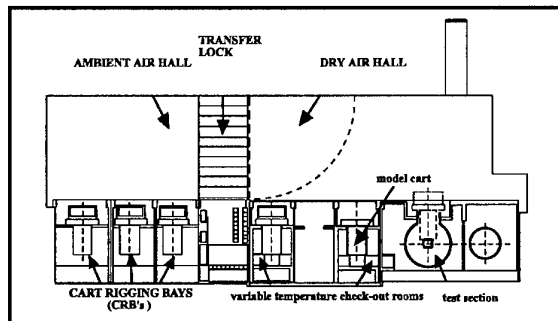


Figure 9 Section Through Transfer Hall

A client, when arriving with his model, is allocated one of the three sets of rooms comprising: a model preparation room, a CRB, and a user analysis room. These rooms are for his sole use during his stay in ETW. Only the client whose model is in the tunnel has access to the control room. Figure 10 shows the plan arrangement of the model handling area.

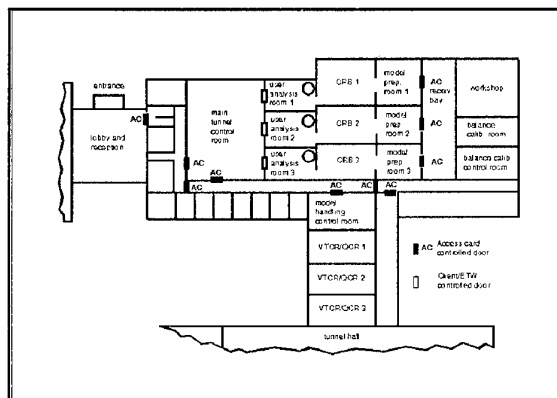


Figure 10 Arrangement of the Model Handling Area.

### 8.3 Test Preparation

"Check it out", this is the basic philosophy adopted by ETW during every stage of model preparation. This procedure ensures that once a model test assembly goes "wind on" the chances of model systems failure are significantly reduced. Once a model is in the tunnel using the very valuable commodities of time, liquid nitrogen and power, minor problems become major issues that impact the whole facility. Below are outlined some of the procedures used.

### 8.3.1 Trial Assembly

All model components are built up on a live balance and sting. The initial checks are to prove that all mechanical and electrical interfaces and space envelopes are correct, including the checking for component fouling.

### 8.3.2 Balance Check-out

The first stage of the final model build is performed on the Model Build Jig or, if available, the Model Cart. The sting and balance are fitted and connected up to a full instrumentation chain. Certified high precision weights can then be applied in all balance axes (see fig. 11). The applied forces and moments can then be compared to the calculated forces and moments from the final data processing program.

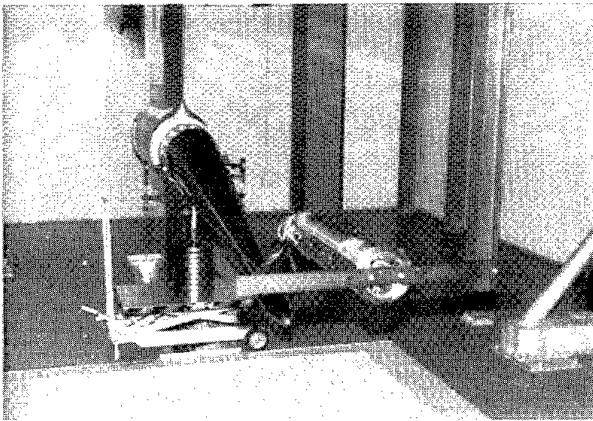


**Figure 11 Check Weight Loading of Balance Prior to Model Assembly**

### 8.3.3 Model Build

The model is now progressively built up with the instrumentation and model reference surfaces being checked at each stage. Finally the sealers, fillers and (if required) transition bands are applied. At this time a final end to end check of all model systems is performed. If the model has been assembled on the Model Building Jig it is now transferred to the Model Cart using a specially designed transporter. Prior to testing, checks are undertaken to determine the dynamic characteristics of the complete test assembly.

### 8.3.4 Environmental Check-out

The model is then transported from the CRB into the dry air lock to dry out the model and model cart prior to its transportation to the VTCR. Once the model is inserted into the VTCR, the complete test assembly is cooled down over the

full temperature range of the test envelope. Again all model systems are checked out during the cooldown. In the past it has proved invaluable to check the performance of balances, heated packages and moveable aerodynamic surfaces.

Wind-off traverses and model weight tare correction loads can be undertaken at cryogenic temperatures with data being computed and evaluated. This gives ETW confidence in the functionality of the model, data acquisition and data processing systems prior to testing. The model can also be loaded at cryogenic temperatures in the VTCR if required. Upon satisfactory completion of all these checks the ETW test engineer along with the client's test director can release the model for test.

### 8.3.5 VTCR Options

The two VTCR's are equipped for different modes of operation, VTCR3 is equipped with the model cold box and will primarily be used for simple model changes under cryogenic conditions. Whilst VTCR1 can be equipped with various items of equipment for model handling and rigging. VTCR1 will primarily be used for larger model changes. It is the normal procedure to maintain the model cart structure at cryogenic temperatures, whilst warming only the model and QCR to ambient conditions. Figure 12 shows the reference model in this VTCR1.

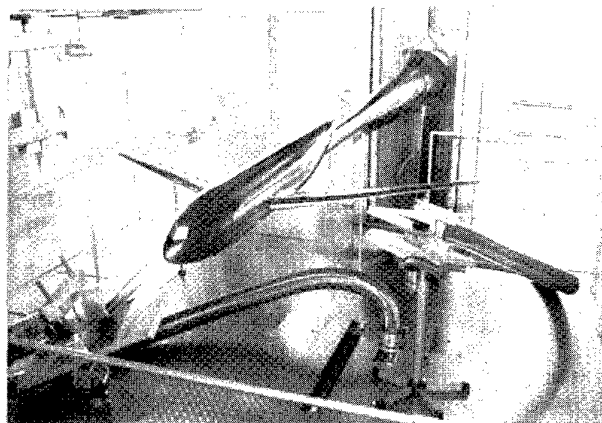


**Figure 12 Reference Model in VTCR1**

## 9.0 Cold Model Handling

To achieve the high productivity capability of ETW it is essential to undertake quick configuration changes on a model between runs. ETW has been designed for the rapid transfer of the complete model cart and test assembly from the cryogenic gaseous nitrogen environment of the tunnel to the dry air environment of the VTCR's. During the transfer, the model and cart are maintained at cryogenic conditions. Once in the

VTCT, the cold model cart is zoned off by a series of doors that isolate the cart and sector assembly from a room in which the model and sting are now contained, the Quick Change Room (QCR). When the doors are closed, the QCR can be warmed up to near ambient temperature conditions. Surrounding the model and sting in QCR3 is a simple, open topped, cold box to which cold dry air at tunnel temperature is continuously supplied. The stratification between the cold air in the model box and the ambient temperature air of the room is so strong that virtually no mixing at the interface takes place. This allows simple rigging work to be carried out on a cold model by operators working at, or close to, normal room temperatures.

Within these areas it is essential to maintain the air at very dry conditions, typically at a dew point lower than  $-60^{\circ}\text{C}$ , to prevent any chance of condensation forming frost on the models. It is for this reason that a positive flow of cold dry air is maintained over the model.

The model riggers entering the QCR are also required to take precautions to reduce the amount of moisture that they normally emit. This can vary dependant on circumstances, from a simple face mask and cold suit, to a full vapour suit.

ETW has also identified, and subsequently developed, techniques to apply fillers at cryogenic temperatures. A number of types of filler materials are being used, the selection of which is dependant upon the test programme.

### 9.1 Model Design

ETW has, where possible, tried to encourage during the early design stages of a model, novel solutions to reduce the amount of external screw holes. The ETW Reference Model for example, in the straight sting configuration, has no external screws in any of the major model components, with the exception of the 2.5 mm screws on the MAMS corner cube insert. However, such models will be the exception, hence fillers will be required on most models following the initial build and during a tunnel test programme where model configuration changes are required. The aim is to regain the surface contour and to present a smooth, continuous aerodynamic surface. For models used in conventional wind tunnels the, gaps, fastener holes etc are typically filled with waxes, plasters, epoxy type resins and usually under normal ambient temperature conditions. For ETW, however, the higher surface quality requirements demanded by the requirements of testing at higher Reynolds numbers must be achieved over the model surfaces generally, and also any filled region. Typical values would be as specified on the ETW Reference Model, of  $\pm 0.02$  to  $0.04$  mm for the surface profile. Figure 13 show the ETW Reference Model in the Z-

sting configuration. Note, in this configuration there are several screw holes on the lower rear filler plates.

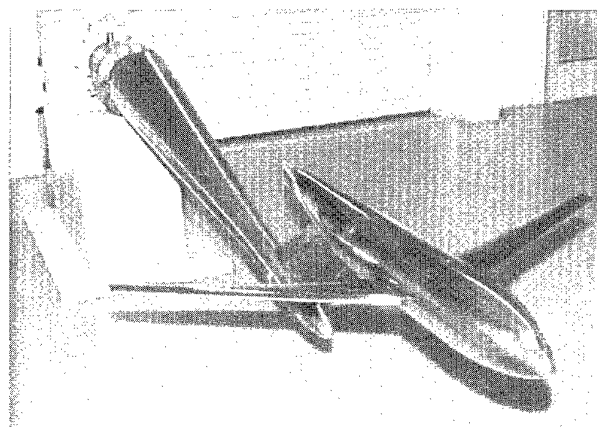


**Figure 13 ETW Reference Model in Z-Sting Configuration**

### 9.2 Development of Model Cold Handling

During the early design phase of ETW, a concept of glove boxes was envisaged for remote configuration changes. There would have been four boxes penetrating each corner of the QCR's. The glove box units would provide an environmental barrier between the operator and the model. The glove box cabin would be fitted with a visor and gloves through which the operator could perform the required tasks on the model. Model riggers would therefore be in ambient conditions during the configuration changes. Following a change from gaseous nitrogen to dry air in the VTCT's, along with a design review on cold model handling, it was decided that a more simple solution could be adopted. This resulted in the idea of a cold box surrounding the model with cold dry air, whilst the model riggers worked in a near ambient environment.

A series of design studies and trials was initiated, supporting the concept of using a cold box for cold model handling, which included the following major tasks:

- Cold Box
  - KKK group of DLR for concept demonstration
  - CMMC of Southampton for detailed design and development
  - ETW commissioning

### 9.3 Cold Box Development

To prove the initial concept of using a simple insulated box around the model, it was decided to build a full scale wooden mock-up of the proposed system. Trials were performed by the KKK group of DLR. The box was insulated and contained a thermal mass at the representative working height of a model.



The cold gas supply was provided by vaporising LN2 in the lower part of the box. The results from these trials demonstrated that a strong stratification between the cold air inside the model box and the surrounding ambient air could be maintained during simple model changes.

ETW then issued a functional specification to create a modular cold box, suitable for a variety of model configurations. The design and manufacture of this cold box was undertaken by CMMC. Figure 14 shows the Reference Model inside the model cold box of QCR 3.

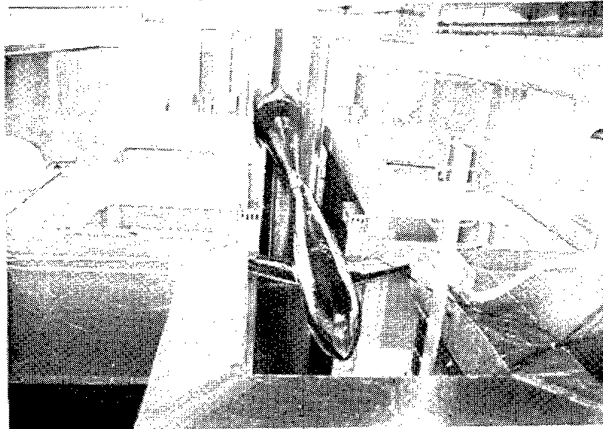


**Figure 14 ETW Reference Model in the Cold Box**

Following delivery and installation of the cold box in QCR3 development trials were performed using a dummy wing mounted on the ETW Commissioning Model. It should be noted that these trials had to be as representative as possible of the operational situation. Therefore a model cart was also required for the cooldowns. Figure 15 shows filler changes being performed on the dummy wing at cryogenic temperatures.



**Figure 15 Filler Development**

It was identified during these trials that the supply of cold air being fed into the box was not enough to prevent the model temperature increasing. Following modifications and further

trials it was decided that the cold gas feed from a bypass line in one of circulation fans was inadequate. Opening the sting doors, initially produces a large flow of cold gas into the box from the cold model cart above. Under these conditions the expected stratification occurs. However, this flow reduces as the pressure equalizes between these Temperature Conditioning Room (TCR) and the QCR. An additional requirement to provide a rapid cooling system for the model, without having to also cool the large thermal mass of a model cart has recently been requested to increase operational efficiency. The cooling requirements for both 'model cold box' and 'rapid cooling' are now undergoing joint development.

#### **9.4 Filler Development**

ETW commissioned studies for model filler development and application techniques with ARA, CMMC and ONERA, covering the following topics:-

- Conventional fillers
- Cold fillers (fusible alloys)
- Cold fillers (alcohol based)
- Special tools
- Technique development
- Shape memory alloys

During the initial studies commissioned by ETW, a range of fillers were identified which performed well under cryogenic conditions and also offered the possibility of being applied to a cold model. These consisted of a number of commercial resins and fusible alloys recommended by ARA and a range of fillers based on a mixture of alcohol, water and talc which were developed by CMMC.

To be able to perform rapid configuration changes on a model and to achieve the full effectiveness of the model handling system that ETW have installed, a means of filling and handworking a model at cold temperatures is essential. The advantage of being able to achieve this without warming a model back to ambient temperature, is that tunnel down time can be minimised and that the thermal stability of the model can be maintained.

To find a solution to the problem of filling holes in a cold model, ETW initiated a further programme of work to develop the techniques of applying fillers to a cold model and for the investigation of methods for handworking the fillers that would not degrade the parent material.

In addition, it was required to extend the range of cryogenic testing to which the fillers had previously been subjected, to

include dynamic (bending and vibration) testing under cryogenic conditions and the measurement of the surface roughness of the fillers at low temperatures.

### 9.5 Filler Types

The candidate filler materials investigated were the polyester resins ISOPON and SOUDAL, a two part epoxy putty, MILLIPUT, a fusible alloy (Cerrobend) and a series of fillers based on a mixture of alcohol, water and talcum powder.

The polyester resins and the epoxy putty are commercial filler materials that are generally cured at normal ambient temperature, although setting can be accelerated by curing at elevated temperatures. It was recognised that these types of filler could only be used during a cold model change if methods for locally heating a recess could be developed that did not result in warming the model significantly.

The fusible alloy Cerrobend is one out of a range of low melting point alloys. It is a relatively soft material, but significantly harder than lead, for example, with a melting point of 343K. It solidifies extremely rapidly, expands upon solidification, and can be remelted if the filled recess still contains some imperfections. The material has minimal adhesive properties and a form of mechanical key is required in the recess. This can be provided by an undercut in the recess or more simply by a trap being machined into the attachment screw.

The fillers based on the alcohol/water/talc mixture set by freezing and when applied to a cold surface will wet the surface and adhere prior to freezing. If the surface is too cold the filler freezes too rapidly and the adhesion is poor. To optimise performance, CMMC developed two recipes that were used in the present study. These were a 60 % isopropyl alcohol + 40 % water mixture for application at temperatures between 180K and 220K and an 80% isopropyl alcohol + 20% water mixture for use between 180K and 140K. Both mixtures are loaded with talc to form a filler with a thin paste consistency. It should be noted that these fillers are only intended for quick model changes, over a limited temperature range.

### 9.6 Filler Test Piece

The test piece used to evaluate the application of the fillers was a model scale inboard wing section in maraging steel. This was chosen to provide a representative thermal mass so that temperature changes due to the application of local heating would be a good indication of what will occur to a complete model. To model the thermal environment the wing section was mounted in an insulated open box lined internally in sheet

stainless steel.

To cool the wing section, liquid nitrogen was sprayed directly over the wing root block and allowed to collect at the bottom of the enclosure. Typically, it took about an hour to cool the wing section from ambient temperatures to 120K.

To assess the performance of the various fillers in service, a bending and vibration rig was developed for use in the small cryogenic chamber at ARA.

## 9.7 Application of Cold Fillers

### 9.7.1 Fusible Alloy

The fusible alloy Cerrobend which has a melting point of 343K, was successfully used to directly fill recesses in the wing section at temperatures down to 120K. Various methods for applying the material were investigated including pouring the molten material from a small crucible, injecting the alloy from a syringe and melting the material directly into the recess with a soldering iron. Using a soldering iron was found to be the best method, as the amount of filler applied could be carefully controlled.

### 9.7.2 Tools And Techniques

The important requirements for handworking the filler materials were to avoid abrading the parent material and to achieve an acceptable level of surface finish. Together with the need to perform the configuration changes to a cold model a secondary requirement was the ability to handwork the materials fairly quickly.

Brass was identified as the most promising material from which to manufacture abrasive tools, being significantly softer than typical cryogenic model materials, but harder than the filler materials under investigation. After some development work with a variety of brass tool forms, a range of practical tools were manufactured. These consisted of a number of files; a multiple bladed shaver; a series of scrapers/knives and a form of brass paper. The files were manufactured using a fly-cutter to produce a sawtooth type profile, with the feed and depth of cut varied to generate files of different fineness. The brass paper was manufactured by gluing 40  $\mu\text{m}$  brass powder to some heavy duty paper using quick setting Araldite.

### 9.7.3 Bending and Vibration Tests

For testing in the ARA small cryogenic chamber the sets of recesses in the specimen plate were filled with the Isopon, Soudal, Milliput and Cerrobend materials. The Cerrobend was

mechanically keyed by simply marking dimples in the sides of the recess. The plate was then pre-loaded to give an initial deflection of 4.2 mm and then dynamically deflected by  $\pm 0.75$  mm at a frequency of 19 Hz. The plate was then thermally conditioned to 120K, held at this temperature for 20 minutes and then warmed back to ambient temperature. Each filler was subjected to a total of 10 thermal cycles down to 120K with the dynamic loading maintained throughout each test. None of the fillers showed any visible signs of degradation, they all remained firmly adhered within the recesses, and the simple technique for mechanically fixing the fusible alloy proved successful.

### 10.0 Concluding Remarks

Measurements to date have shown that the instrumentation and test techniques used by ETW are producing the high level of accuracy required by high Reynolds number testing. During the initial operating phase particular attention has been paid to accuracy and quality under very demanding conditions, with good productivity being achieved. Detailed evaluation of the data and operational procedures is ongoing. Preliminary evaluation has shown that with technique refinement, the productivity can be significantly increased without compromising the data quality.

The Infrared transition detection system and the model attitude measurement system have shown encouraging results during their commissioning phase. Further testing of these systems are planned in the near future, expanding these techniques over the complete tunnel envelope. Other systems are still undergoing development and integration.

All the major items are now in place to perform cold model handling. However, further refinement of the technique and more operational experience on suitable models is still required.

### Acknowledgments

The authors would like to acknowledge the input from the following organisations during the various development periods:-

**ARA** (Aircraft Research Association) Bedford England

**CMMC** (Cryogenic Marine & Materials Consultants Ltd) Southampton England

**KKK** (Kryo Kanal Köln) DLR Germany

**ONERA** (Office National d'Etudes et de Recherches Aérospatiales) CERT & IMFL France

## Cryogenic internal balance calibration at ETW

L. M. Badet  
European Transonic Windtunnel GmbH  
Postfach 90 61 16  
51127 KÖLN  
Germany

### 1 INTRODUCTION

The ETW is a closed circuit, continuous flow transonic windtunnel operating with gaseous nitrogen over a temperature range of 90 K to 313 K and up to 4.5 bar absolute total pressure. For correct simulation of real flight conditions of an aircraft in a windtunnel, the most advanced measurement techniques have to be applied. One important measuring tool is the "Internal Strain Gauge Balance".

The Internal Balance (IB), dynamometric transducer, for a full span aircraft model is mounted between the model and the model support sting. These balances are required to measure, to the highest degree of accuracy, the aerodynamic loads acting on a model during windtunnel testing, whilst operating in the test section in conditions defined as above.

To achieve high accuracies for model load measurements, the basic performance of the balances under all operating conditions and the precision of the balance calibration process prior to the test in the wind tunnel, are of fundamental importance.

The aerodynamic loads acting on the model aerodynamic center during the test are represented by a vector force and a vector moment. These are both split on a reference axis system attached to the above mentioned center, into six aerodynamic components; three forces and three moments.

In order to give a comprehensive aerodynamic analysis of a model under wind, the measuring instrument Internal Balance must be able to measure each of these six degrees of freedom.

### 2 ETW - SIX COMPONENT INTERNAL STRAIN GAUGE BALANCES

ETW ordered four one-piece six component internal strain gauge balances with identical outside dimensions and mechanical interfaces (see Figure No 1) to cover loads associated with test conditions.

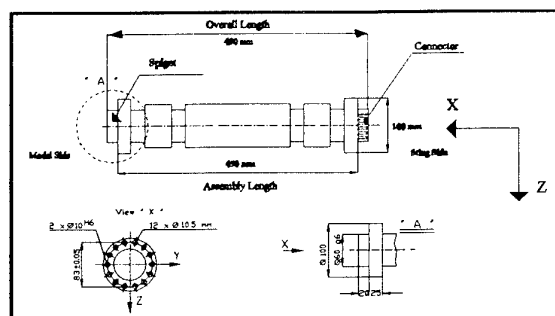


Figure 1: ETW DESIGN SPECIFICATIONS

The balance instrumentation consists of 6 full Wheatstone bridges plus one spare axial force bridge, or 7 in case of a dual drag element, all of them in 6 wire configuration, and 10 temperature sensors of the RTD type (Pt100 in four wire technique). To allow an easy exchange of balances during a test campaign, all the balances are provided with identical 85 pin connectors at the sting joint.

The ETW balance and the alternative balance suppliers opted for a cold concept, i.e. the balances are to operate in ETW within a range of more than 200 K. This implies either computational corrections for temperature and temperature gradient effects on zero, span, and

possibly interactions, or a systematic full force calibration at discrete temperature levels, over the temperature operating range, of the balances with and without gradients.

The actual state of balance calibration at ETW is to calibrate balances every 25 K with stabilized and uniform temperature distribution over the balance body.

### 3 TARGETS AND METHODS OF CALIBRATION

The one degree of freedom dynamometer is a measuring device, which has been designed to be sensitive to one force, acting along a predefined reference axis. The calibration process consists in applying known forces  $F$  (in direction and values) via dead weights. The induced strains in the structure of the dynamometer cause relative length changes, either compressional or extensional, under the gauges bonded on the surface. The order of magnitude of change depends on the design of the structure and on the elasticity coefficients (Young modulus) of the dynamometer material. The stretched gauges undergo a change of their electrical resistance, which, in a Wheastone bridge arrangement, is detected and translated with an output voltage variation of the bridge  $\Delta U$ . The mathematical relations  $\Delta U = \text{function}(F)$  and  $F = \text{function}(\Delta U)$  give the calibrated characteristics of the dynamometer under load.

#### 3.1 Theoretical Background

##### 3.1.1 Reference Axis System of Calibration

The aim of the calibration is to have, within the Internal Balance Axis System, (see Figure No 2) a mathematical model describing with the greatest accuracy, the behaviour and / or characteristics of a balance under load.

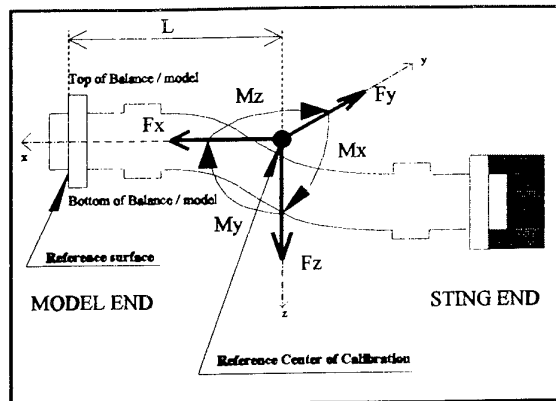


Figure 2: Internal Balance Reference Axis System

The axis system in use at ETW for calibration is a three dimensional, orthogonal and right handed system. It is in accordance with the body axis system defined in the Aviation Standard LN 9300. In this standard the axial force  $F_x$  is defined positive in flight direction, the normal force  $F_z$  positive downwards, and the side force  $F_y$  positive to starboard. The moments about any axis (rolling  $M_x$ , pitching  $M_y$  and yawing  $M_z$ ) are positive clockwise when viewed in the positive direction of that axis. The origin of that system is located at a known distance  $L$  of a reference surface on the longitudinal axis of the balance. The reference surface is, in the case of the flange joint, the interface surface between the model adapter and the balance. The longitudinal axis  $x$  is then defined as the geometrical center line perpendicular to this section. The transversal axis  $y$ , perpendicular to  $x$  axis is imposed solely by the roll fixation mechanism on the model end of the balance. The vertical axis  $z$  is then perpendicular to the so defined plane  $xy$ .

##### 3.1.2 Coefficients of sensitivity

During balance design, a strong emphasis was placed on avoiding interactions, to ensure strict linearity between load applied and dedicated bridge output. In figure 3, a typical bridge arrangement on the Internal Balance structure is shown.

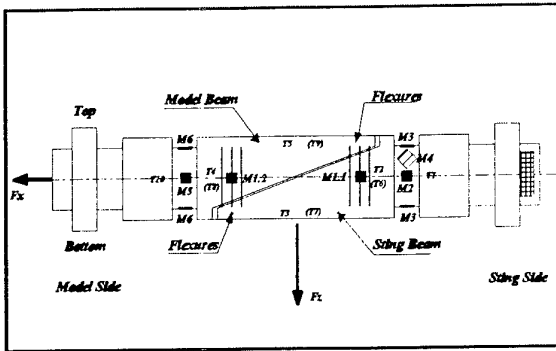


Figure 3: Typical Internal Balance Instrumentation

The bridges M1.1 and M1.2 are sensitive to axial force  $F_x$ , M2 / M5 to side force  $F_y$  and yawing moment  $M_z$ , M3 / M6 to normal force  $F_z$  and pitching moment  $M_y$ , and M4 to rolling moment  $M_x$ .

Unfortunately and particularly true for multi-component one piece balances, the interactions of secondary loads are not negligible, and must therefore be considered, as shown in the mathematical model below. (Equation 1):

$$R_i = R_{0i} + \sum_{j=1}^6 A_{ij} \times F_j + \sum_{j=1}^6 \sum_{k=1}^6 B_{ijk} \times F_j \times F_k + \sum_{j=1}^6 C_{ij} \times F_j^3$$

Equation 1 : Calibration Matrix

with  $i=1$  for  $F_x$  to 6 for  $M_z$ ,

$R_i$  reading of Balance Component "i",

$F_i$  component,

$R_{0i}$  zero readings of  $R_i$ .

Beside the sensitivity of a component reading  $R_i$  to a primary load  $F_i$  described through the principal coefficient  $A_{ii}$  there are:

- Linear interactions of secondary loads (weighted via the coefficients  $A_{ij}$ ,  $j=1$  to 6 and  $j \neq i$ ); Insufficient structural decoupling, induced dissymmetries during machining, errors in location during gauges application...

- Second order interactions; non linear response of component reading  $R_i$  to its primary load  $F_i$  ( $B_{iii}$ ) and interferences of secondary loads due to the elastic deformations of the balance which, under loading, change the balance geometry ( $B_{ijj}$ ,  $i=1$  to 6,  $j=i$  to 6,  $i \neq 1$  and  $j \neq 1$ )...

- Third order interactions: design or machining errors, not precise and repeatable fixation joints, gauges near the joints, symmetrical nonlinearities which can not be described through a 2nd order approximation ( $C_{ijj}$ ,  $j=1$  to 6)...

### 3.1.3 Loading configurations

The above mathematical model implies for a right description and/or evaluation of the different sensitivity coefficients "A", "B" and

	$F_x$	$F_y$	$F_z$	$M_x$	$M_y$	$M_z$
$F_x$	1	1	2	3	4	5
$F_y$		2	6	7	8	9
$F_z$			3	10	11	12
$M_x$				4	13	14
$M_y$					5	15
$M_z$						6

Table 1 : Loading Configurations

"C" (6+21+6=33 per channel with a total of 198 coefficients) that the "relative raw calibration information" is available. This leads to load the balance with the single components (6 off) and all combinations of two components (15 off) as described in Table 1.

### 3.2 Conventional calibration method

In a conventional calibration the internal balance as shown in Figure 4 is mounted with its sting end on to the rig structure. On the model end of the balance a so called calibration sleeve or loading body is attached. With the help of high precision dead weights and the knowledge of the sleeve geometry, desired forces and moments are applied to the Internal Balance. This method requires to retrieve the angular deflections of the model end of the internal balance under load around the three axis in order to bring the model end of the internal balance back to the geodetic axis system, the position in which the introduced loads are based on.

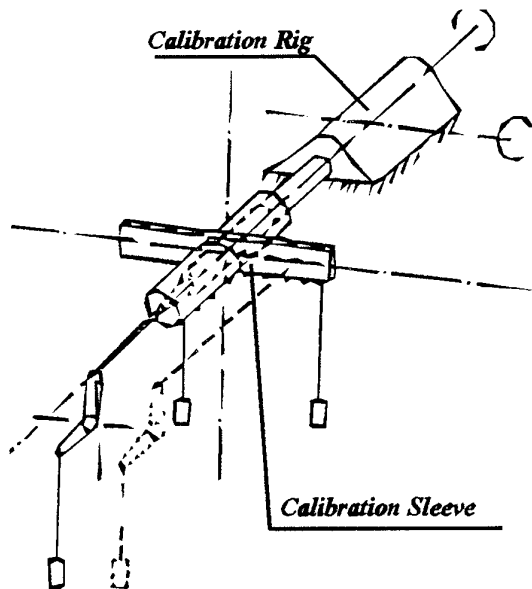


Figure 4: Conventional Calibration Rig

A full dynamometric calibration requires about 1100 different calibration points (see 3.1.3). Depending on the rig capabilities and on the calibration data reduction program, to establish the calibration matrix (Equation 1), this method may involve considerable effort in terms of required man hours.

### 3.3 ETW Balance Calibration Machine

In order to calibrate Internal Strain Gauge Balances over the working temperature range of ETW (90 K to 313 K) it was necessary to develop a machine capable of automatically calibrating Balances (BCM).

The automation covers the setting of the calibration temperature and the desired calibration load(s).

In order to increase the efficiency, productivity during the calibration and flexibility of maintenance and modification, the hardware and software systems have been designed in a modular way, splitting the tasks into four different subsystems as follows: (see Figures 5 and 6):

- 1 the **External Balance** subsystem (EBS),
- 2 the **Internal Balance** subsystem (IBS),
- 3 the **Force Generator** subsystem (FGS) and

4 the **Cryo Chamber** subsystem (CCS).

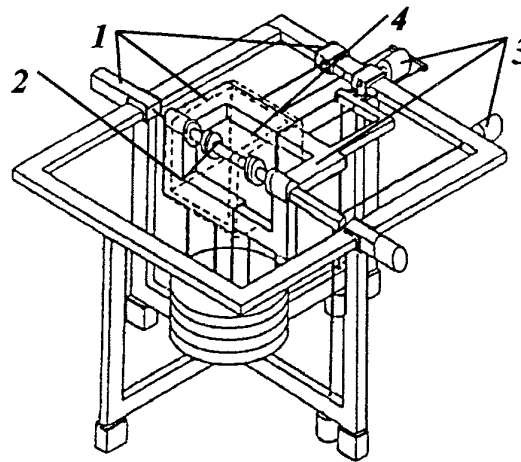


Figure 5: ETW Balance Calibration Machine

These subsystems are controlled by their own PC's, which are in turn connected to a master Supervisor on a local area network. Interfacing to the instrumentation equipment is via an IEEE 488 bus.

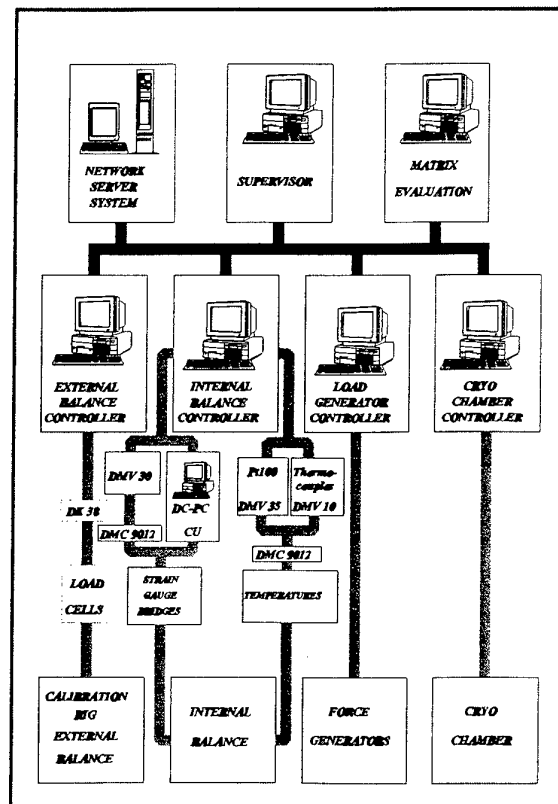


Figure 6 : Data Acquisition System of BCM

Contrary to the conventional method (3.2) the loads are introduced via the Force Generator subsystem and an adequate adapter matching the balance and machine interfaces on the sting side of the balance. Counter weights (not shown in Figure 5) placed on the top of the machine maintain the FGS with virtually no influence on the IB when connected to its sting end.

The model end of the balance is fixed onto the External Balance via an adapter. The EBS, which has been calibrated with the help of high precision dead weights, measures accurately in its calibration reference center and in a geodetic axis system the load vector applied on the IB. With these loads and the measured elasticities of the measuring side up to the reference surface of the IB the calibration loads or True Loads are then transferred into the IB reference axis system (see 3.1.1). Meanwhile, the bridge outputs of the IB connected to the data acquisition system are measured.

Most of the algorithms used to evaluate the calibration matrix from the calibration data set, are not suitable for such a machine. They require at least pure loading configurations as described in Table 1. This is nearly impossible to realize with this system considering that the FGS applies the desired calibration loads not better than 1 % and due to the bending of the measuring side of the BCM under loading, small secondary loads are always superimposed to the primaries.

### 3.4 BCM Evaluation Software

The algorithm developed to cope with the above described loading conditions is based on the minimisation of the sum of the root mean square error (Least Square Error method), over the complete calibration data set. Each calibration data point, with its respective six degrees of freedom, participates in the determination of the sensitivity coefficients (par. 3.1.2) and of the zero readings of the internal balance.

The reverse modelisation called balance

matrix (Equation 2), is from a mathematical point of view, identical to the calibration matrix and treated by the evaluation program in the same way. It means that the balance matrix is not the result of the calibration matrix inversion but computed from the whole data set. This assures at least the same level of accuracy for both modelisations, which is particularly important in the case of the balance matrix used during wind tunnel testing, to determine the model loads.

$$F_i = F_{0i} + \sum_{j=1}^6 a_{ij} \times R_j + \sum_{j=1}^6 \sum_{k=1}^6 b_{ijk} \times R_j \times R_k + \sum_{j=1}^6 c_{ij} \times R_j^2$$

Equation 2: Balance Matrix

with  $i=1$  for  $F_x$  to 6 for  $M_z$ ,  
 $F_i$  component,  
 $R_i$  reading of Balance Component "i",  
 $F_{0i}$  zero load of component  $F_i$ .

## 4 CALIBRATION PROCEDURE

### 4.1 Calibration Setup

#### 4.1.1 Hardware

The determination of the True Loads, which have been applied on the Internal Balance at each Calibration Data Point, requires a reference. This is called the "Zero Readings" of the External Balance and has been measured in the following mechanical configuration (see also Figure 7):

- ▶ Internal Balance model end fixed on to model adapter, sting end free.
- ▶ Model adapter plus balance mounted on to External Balance.
- ▶ Balance cable not connected.



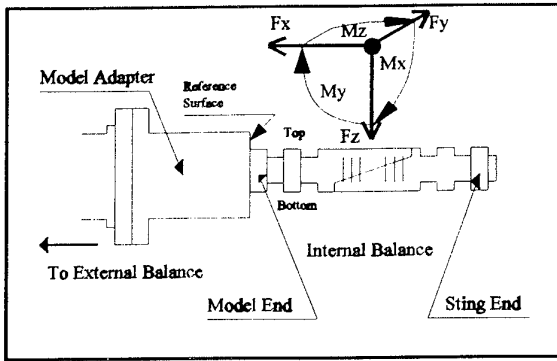


Figure 7: External Balance Zero Readings measurement

For calibration, the sting adapter is mounted on the sting end of the internal balance and on to the loading tree (Figure 8). The internal balance is then connected to the data system via the balance cable. The thick border represents the walls of the cryogenic chamber.

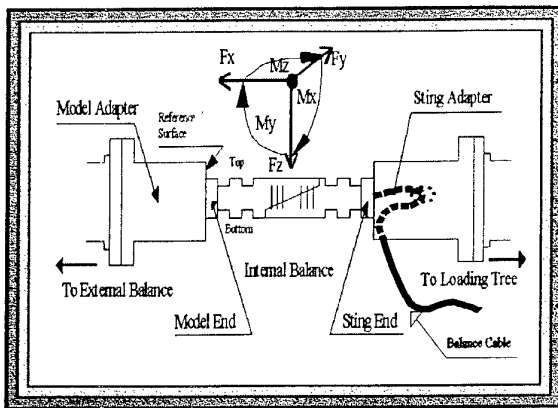


Figure 8: Calibration Assembly Setup

#### 4.1.2 Software

Before starting with the calibration, the machine software has to be configured with some specific parameters of the internal balance.

##### 4.1.2.1 Loading Capacity

###### a Combined design operating loads

These loads are the forces and moments (in N and Nm) which can be applied simultaneously up to their maximum values on the IB during the calibration (or operation).

###### b Nominal loads - Load rhombi / Boundary Equations

The nominal loads give information on the total capacity of the IB and correspond to the maximum values, in N and Nm of each component applied individually.

Some points on the structure of the loaded internal balance are highly stressed. The contribution of each component on these points in terms of strains can be quantified during the design phase of the balance. This analysis, which gives an overview of the balance capabilities, is generally supplied with the balance in graphical form as load rhombis, for some loading combinations only i.e.  $F_z + M_y + F_x$ ;  $F_y + M_z + F_x$ ... A general method, which can be accommodated by the BCM software is to describe the stress level on these points with a so called boundary equation.

$$|F_x| \times K_{1_n} + |F_y| \times K_{2_n} + |F_z| \times K_{3_n} + \\ |M_x| \times K_{4_n} + |M_y| \times K_{5_n} + |M_z| \times K_{6_n} < L_n$$

Equation 3: Boundary Equation

" $L_n$ " is the structural stress limit on the point "n" which should not be exceeded. " $K_m$ " the contribution in terms of stress of the component "i" for this point "n".

#### 4.1.2.2 Balance Instrumentation

###### a Stress Sensors - Output Limits

Up to 7 full Wheatstone bridges in six wires configuration with individual power supply or with common power supply and sensing at the end of the balance cable (four wires configuration) can be accommodated. AC or DC conditioning is for selection.

The entry of bridge output limits in mV / V, which should not be exceeded during the calibration, is for selection too.

## b Temperature Sensors

Up to 12 temperature sensors can be accommodated. Either RTD type temperature sensors i.e. Pt100 or thermocouples, type J,T,K or S can be selected. The calibrated characteristic of these sensors, if available, can be entered into the system via keyboard entries.

### 4.1.2.3 Calibration of the FGS

Although the geometry of the FGS does not change from one balance to another, the differences in sting adapter weight, stiffnesses and load ranges encountered must be taken into account. This calibration process, which requires the combined design operating loads (see par. 4.1.2.1- a) takes approximately 20 minutes. The maximum pressures, necessary for each of the six force actuators to generate the desired loads during the calibration are deduced. This calibration is required to improve the performances of the FGS and is performed at the discretion of the operator. Generally one calibration at ambient temperature and one below 200 K are sufficient.

### 4.1.2.4 Calibration Volume

A rule in the calibration of sensors of any type is to calibrate them in the range in which they will be required to operate. Generally during wind tunnel model testing, the test engineers maintain the model loads within the combined design operating envelope of the internal balance used.

This limitation comes principally from better performances of the balance, and reduced risks of structure failure, which may cause the loss of a balance & model plus tunnel damages.

For this reason the above mentioned loading point is used as basis for the preparation of the different loading configurations of Table 1. Only the BCM itself with the operating range given in Table 2 may limit this intention.

Nota: The accuracy of the External Balance for the loads exceeding their maximum operating

values up to their design range, has been relaxed by a factor two.

Component	Axial Force	Side Force	Normal Force	Rolling Moment	Pitching Moment	Yawing Moment	
Notation [unit]	F <sub>x</sub> [N]	F <sub>y</sub> [N]	F <sub>z</sub> [N]	M <sub>x</sub> [Nm]	M <sub>y</sub> [Nm]	M <sub>z</sub> [Nm]	
± Full Scale	1,500	3,000	20,000	2,000	1,200	1,000	Operating Loads
± Full Scale	2,000	3,000	25,000	2,000	1,500	1,000	Design Loads

Table 2: BCM Operating Load envelope

Although the BCM evaluation routine does not require a systematic distinction between the different loading configuration (see par. 3.1.3 and 3.4), and in order to avoid an incomplete calibration raw data set, all of the 6 single loads and the 15 combinations of two are considered.

Each of these 21 loading configurations are stored in a ASCII file with an appropriate signature, whose content indicates for the system the following information:

- ▶ Desired calibration temperature.
- ▶ Component(s) to be varied and or maintained to a constant value (the components that are not calibrated, are usually maintained at zero).
- ▶ Order and magnitude of the applied loads.
- ▶ Type of loading sequence .

A typical dynamometric calibration consists of around 1,400 loading points. The method of applying the different components on the IB during the calibration is shown in Figure 9. The single loads (6 off) are introduced as described in sequences 1 and 2. Starting point of the loading cycles is either +50 % or +100 % of the full scale value of the considered component. This is then decreased to -50 % or -100 %, and later increased to +50 % or +100 %. The loading variation is performed in regular steps of 10 % of the first point value. The unloaded condition of the balance (see Figure 7), or crossing the zero

is carried out two times. This sequence provides useful information on the IB hysteresis for half and full load ranges. In addition, the amount of the unloaded balance condition is halved. This still gives a sufficient data base for the algorithm to compute the "Zero Readings" or "Zero Loads" of the internal balance (par. 3.4).

The combination of two loads is performed using the sequences 3 and 4, except for the combinations with  $F_z$  where  $F_z$  follows the sequence 6, and the other components the sequence 5. In the case of the loading sequences 4 and 6, the considered components are varied by steps of 50 % of their full scale values, and maintained constant, whilst the other components follow the loading sequences 3 or 5 (steps of 25 % of full scale values).

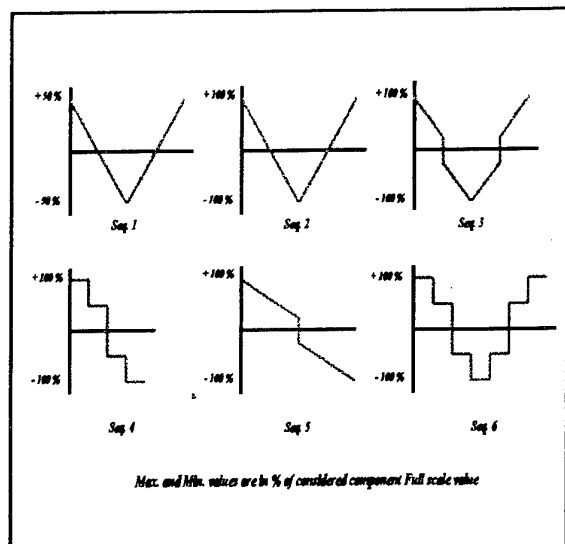


Figure 9: Typical Loading Sequences

## 4.2 Start of Calibration

Once a set of load configurations are defined (in the above case 27 ASCII files), it will be reproduced with an adequate signature for the desired temperature levels. The actual trend is to first calibrate the balances at ambient temperature and then at the following temperatures: 325 K, 315 K, 300 K, 275 K, 250 K, 200 K, 175 K, 150 K, 125 K and 105 K.

### 4.2.1 Temperature Conditioning

By closing the Cryo' Chamber an active purging with gaseous nitrogen and a fan are switched on. It takes approximately 2 hours to reach a dew point of -30 °C. Meanwhile the different features offered for temperature control are filled in.

Three different tests are offered for selection:

*Stability Test:* The Supervisor (see par. 3.3) waits until the CCS reaches the desired temperature and sends its stable flag back. The temperature regulation is performed either with  $LN_2$  to cool down, or with a 1kW heating element located in the chamber, to warm up the environment of the balance.

*Quantity Test:* The Supervisor, which initiates a measurement of the IB temperatures every 10 s, waits until all temperature differences between CGS and IBS are less than a predetermined value.

*Homogeneity Test:* The Supervisor waits until the temperature distribution over the internal balance body is within a defined range. Twelve functions are available as described in Equation 4.

$$T_1 \times K_1 + T_2 \times K_2 + T_3 \times K_3 + \dots \\ + T_{10} \times K_{10} + T_{11} \times K_{11} + T_{12} \times K_{12} < L_n$$

Equation 4: Temperature Boundary Equation

with:  $n = 1$  to 12;

$T_i$ ,  $i = 1$  to 12, internal balance temperatures;

$K_i$  weighting factor to the temperature sensor  $T_i$ ;

$L_n$ ,  $n = 1$  to 12, limit not to be exceeded.

The experience with the BCM and particularly the Cryo' Chamber demonstrates a quasi uniform decrease or increase of the balance temperature. This is due to thermal conduction on both sides of the balance (via the adapters) with the same order of magnitude and forced thermal exchanges per convection over the

complete balance body.

Mostly during a cool down or heating up process the presented temperature tests are used. A 25 K temperature step variation requires for the CCS around 15 minutes to be reached and be stable (stability test).

For the internal balance temperature conditioning the actual strategy is to calibrate it without any spatial and time gradients. The following points by setting the quantity and homogeneity test must be considered:

- ▶ the temperature sensors of the internal balance even calibrated are not necessary stabilising at the same temperature level of the CCS (1.5 K difference in cold conditions i.e. below 175 K is current).
- ▶ the temperature sensors may be sensitive to mechanical strains induced during the loading of the balance. This is the case for Pt100 in foil form.

The CCS at ambient conditions, takes approximately 6 hours to condition the balance within  $\pm 0.5$  K for a 25 K cool down step. This conditioning time may be halved when the CCS is at 125 K. This is due to most of the cooling energy of the injected LN<sub>2</sub>, is absorbed by the chamber itself, in warm conditions.

#### 4.2.2 Force Calibration

As soon as the internal balance is conditioned in temperature, the Supervisor initiates the first loading point of the first loading configuration selected. This sends the desired load information to the FGS, which in turn using its calibration data (see par 4.1.2.3) and the control system of the force generators, introduces the required forces and moments. This is in two steps:

- 1 A coarse setting using the pneumatic part (with GN<sub>2</sub>).
- 2 A fine setting using linear drives, which are also used to maintain the applied loads constant during the sampling of data.

Similarly, on request of the Supervisor, the FGS sends the regulation status. As soon as this status is stable the Supervisor initiates a

measurement of all the subsystems. This data is stored and displayed simultaneously. After the files have been updated the supervisor sends a request to the FGS for the next loading point. This process is repeated until all the loading configurations are completed and all data files are closed.

Throughout the complete loading the balance is continually monitored for overloads, if any are encountered then the system is automatically shut down.

All of the above tasks are performed automatically, and for one temperature level it may take up to 13 hours to complete a full calibration of 1,400 points, as presented in par. 4.1.2.4.

## 5 CALIBRATION DATA REDUCTION

The computation of the 'calibration' or 'balance' matrices is calculated separately for each temperature level.

Firstly the True Loads applied on the internal balance for each test point of the available data set, at the temperature T, are computed in the internal balance axis system. For this task, the calibration matrix of the External Balance, the elasticities of the measuring system up to the reference surface of the internal balance are used. In addition, the relative movement of the reference surface to the reference center of the EB is corrected. This means that independently of the internal balance temperature, the reference center or origin of the axis system is always located at the same fixed distance L (Figure 2) behind the reference surface of the balance, measured at ambient temperature. Therefore the shrinkage or expansion of the balance due to temperature is integrated in to the calibration and balance matrices of the balance.

Meanwhile the raw bridge output signals of the internal balance are combined to build its

component readings. In the case of the balance in Figure 3, with a dual axial force dynamometer it would be:

$R_{F_x} = M1.1 + M1.2$	$R_{M_x} = M4$
$R_{F_y} = M2$	$R_{M_y} = M6$
$R_{F_z} = M3$	$R_{M_z} = M5$

Equation 5: Component Readings

The sum of both axial force bridge output signals is, in this particular design case, necessary

to eliminate the well known thermal distortion due to temperature differences or gradients between the model and the sting beam of the balance, mainly during operation of the balance.

Then the algorithm extracts from this data set of 1,400 test points [True Loads + Component Readings] the calibration and/or balance matrices. 1st, 2nd and 3rd order are for selection. A typical third order balance matrix is given in Figure 10.

The data is stored in 6 columns. Each column represents one balance component. The component readings are defined in equation 5.

Balance Force Components						Signal Combination
$F_x$	$F_y$	$F_z$	$M_x$	$M_y$	$M_z$	
Linear Interference Coefficients [N<m>/( $\mu$ V/V)]:						
0.558954D+00	-0.213593D-05	-0.124165D-02	0.104834D-02	-0.271651D-03	0.235100D-04	RFx
-0.178295D-01	0.488476D+01	0.710207D-01	0.465343D-02	-0.953271D-02	0.551564D+00	RFy
-0.212358D-01	0.337455D-01	-0.883885D+01	-0.124788D+00	0.997644D+00	0.621169D-02	RFz
0.431090D-02	-0.465130D-01	0.101072D+00	0.117097D+01	-0.351956D-01	-0.152405D-02	RMx
0.138862D-01	0.209096D-01	0.883947D+01	-0.251013D-01	0.978444D+00	-0.279317D-02	RMz
-0.204229D-01	-0.484693D+01	-0.446082D-01	0.960585D-02	-0.155407D-02	0.546197D+00	RMz
Product Interference Coefficients [N<m>/( $\mu$ V/V)**2]:						
-0.317198D-07	-0.230928D-07	-0.428445D-07	0.199670D-07	0.282982D-08	0.831828D-08	RFx RFx
-0.272675D-08	-0.813477D-06	0.317781D-07	0.399712D-07	-0.118176D-07	-0.831989D-06	RFx RFy
0.881954D-05	0.580362D-08	0.199322D-05	0.155629D-07	-0.836516D-06	0.489899D-08	RFx RFz
0.138574D-06	-0.456001D-06	-0.703904D-07	-0.388306D-07	0.537705D-07	0.100109D-08	RFx RMx
-0.879323D-05	0.552599D-07	0.180283D-05	-0.141479D-07	0.129740D-07	-0.111900D-07	RFx RMy
0.156780D-06	-0.220764D-05	0.143267D-06	0.626737D-07	-0.128868D-07	-0.195878D-07	RFx RMz
0.513629D-05	-0.519255D-05	0.255316D-05	-0.110828D-05	0.432565D-06	-0.532093D-07	RFy RFx
-0.960561D-05	-0.780513D-05	0.327583D-05	0.238953D-05	-0.266586D-06	-0.811675D-06	RFy RFz
0.856647D-04	0.110806D-05	-0.195403D-04	0.495816D-07	0.204840D-05	-0.293740D-08	RFy RMx
-0.230275D-05	-0.637542D-06	-0.686331D-06	0.200257D-06	-0.149348D-06	-0.617895D-07	RFy RMy
0.151835D-04	0.543356D-05	0.873767D-05	-0.411018D-05	0.122205D-05	0.342736D-07	RFy RMz
0.262705D-04	0.452720D-05	-0.105564D-05	-0.133085D-05	0.251539D-06	0.622215D-06	RFz RFx
-0.200003D-04	-0.461694D-04	-0.230379D-05	0.440308D-05	-0.122548D-06	-0.575819D-05	RFz RFy
0.700803D-04	-0.334288D-05	0.332650D-05	0.650823D-06	-0.313968D-06	-0.244735D-06	RFz RMx
-0.870718D-05	-0.735672D-05	-0.313301D-05	-0.117665D-06	0.232593D-06	-0.686323D-06	RFz RMy
0.860786D-04	0.124154D-06	0.941001D-05	-0.385512D-06	-0.104238D-05	0.108933D-06	RFz RMz
-0.416259D-05	0.420153D-04	-0.746522D-06	-0.174930D-05	0.415626D-06	0.429735D-05	RMx RFx
0.768451D-04	-0.191221D-06	0.258291D-04	0.293655D-06	-0.335322D-05	-0.105756D-06	RMx RFy
-0.372299D-04	-0.144759D-05	-0.245044D-05	-0.657558D-06	0.603219D-07	-0.912180D-07	RMx RFz
-0.839619D-06	-0.655277D-06	-0.605197D-06	0.236792D-06	0.524975D-07	0.353522D-06	RMy RFx
-0.228505D-04	-0.526451D-05	0.389471D-05	-0.636720D-06	0.218895D-06	0.396703D-07	RMy RFy
Cubic Interference Coefficients [N<m>/( $\mu$ V/V)**3]:						
0.498348D-11	0.705700D-11	0.322651D-10	0.139326D-11	-0.689990D-12	-0.140468D-11	RFx <sup>3</sup>
0.372043D-09	-0.278637D-08	-0.833692D-10	0.260806D-09	-0.267016D-09	-0.109787D-08	RFx <sup>2</sup>
-0.158061D-09	0.563587D-10	0.432402D-09	-0.198855D-09	0.604829D-09	0.187396D-11	RFx <sup>2</sup>
-0.462706D-10	-0.280452D-09	0.116512D-08	0.123415D-10	-0.616049D-10	-0.375180D-11	RFy <sup>3</sup>
0.121090D-09	-0.122777D-10	-0.558977D-09	0.167805D-09	-0.901302D-09	0.107127D-10	RFy <sup>2</sup>
-0.400972D-09	-0.733985D-09	0.977932D-10	0.135754D-10	-0.715902D-09	0.336856D-09	RFy <sup>2</sup>
Zero Loads [N<m>]:						
-0.126995D+03	-0.124063D+02	0.615483D+02	-0.483786D+02	-0.886802D+02	0.650075D+02	

Figure 10: Typical Third Order Balance Matrix

The first block of 6 rows shows the linear matrix coefficients "a", with the Component Reading which effects each of the balance components, in the far right column.

The second block of 21 rows shows the product matrix coefficients "b", with the combinations of the two Component Readings responsible for the product coefficients, on the far right.

The third block of 6 rows contains the cubic matrix coefficients "c", with the Component Readings, which, when cubed, are responsible for the coefficients in that row.

The last row shows the zero loads of each balance component.

## 6 RESULTS - INTERPRETATION

### 6.1 Zero Readings / Loads

The constant terms of the evaluated matrices have a real physical meaning.

For the Calibration Matrix, they represent the output of the internal balance when it is in an unloaded condition i.e. all forces and moments which effect the balance are zeroed. In the particular case of the BCM, this state corresponds to that of the internal balance measuring the zero readings of the external balance. It means internal balance sting end free (see Figure 7). This electrical / mechanical condition of the balance is the sum of two contributions:

1 Electrical Offset: this corresponds to the outputs of the balance under zero gravity (temperature dependent) or to the unbalance of the bridges after application.

2 Internal Balance dead weight: in figure 7 nearly half the weight of the balance stretches the bridges (sting beam).

The application at the different temperature levels of a zero load vector on the balance gives those readings back.

The zero loads of the balance matrix are the forces and moments necessary to compensate or annul the above mentioned unbalance of the bridges and the dead weight induced bridge outputs. These (temperature dependent) loads, once applied on the balance at the corresponding temperature, stretch the bridges in such a way that the corresponding component readings are annuled.

### 6.2 Internal Balance shrinkage Linear Coefficient of expansion

With the main sensitivities of the lateral (M2 and M5) and normal (M3 and M6) bridges under their dedicated component  $F_y$ ,  $M_z$  and  $F_z$ ,  $M_y$  it is possible to compute the location on the longitudinal axis of the balance of those bridges to the reference center attached to the calibration matrix (See Figure 11).

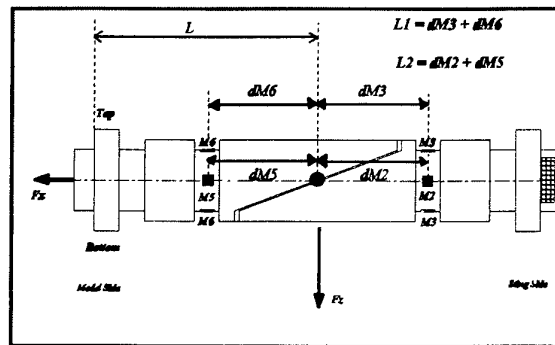
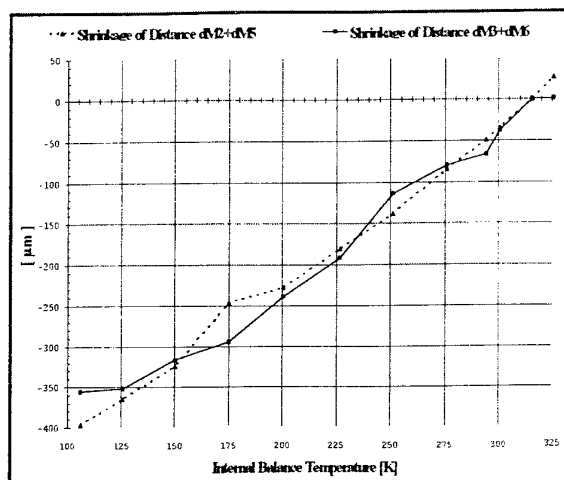


Figure 11: Geometrical location of Side and Normal Force bridges

Considering that this point is at a fixed distance  $L$  (see par. 5) of the reference surface of the balance, and the above computation is at the different temperature levels, it is possible to get an idea of the shrinkage of the balance with the temperature along its longitudinal axis. In the Chart below such a temperature behaviour of an ETW balance calibrated over the range 105 K to 325 K is shown. Cooling down the internal balance the distances  $dM5$  and  $dM6$  increase meanwhile the distances  $dM2$  and  $dM3$  decrease. The lengths  $L1$  and  $L2$  decrease with the temperature.



**Chart 1:** Longitudinal shrinkage of balance with temperature

From this data the linear coefficient of expansion  $\alpha$  (see Equation 6) of the internal balance material can be approached.

$$\alpha = \frac{\frac{\Delta L}{L_{325K}}}{\Delta T} \quad \text{with: } \Delta L = L_T - L_{325K}$$

$$\Delta T = T - 325K$$

**Equation 6:** Definition of Linear Coefficient of expansion

A mean value of the so calculated  $\alpha$ 's for both lengths and at the different temperatures has

the following value:

$$\alpha_{\text{mean}} = 8.90 \cdot 10^{-6} \text{ m / m / K.}$$

At 105 K this becomes:

$$\alpha_{105 \text{ K}} = 7.91 \cdot 10^{-6} \text{ m / m / K.}$$

The value indicated in the literature for the considered Nickel Maraging steel grade 250 is around  $9 \cdot 10^{-6} \text{ m / m / K}$  at ambient temperature, decreasing with temperature.

### 6.3 Calibration Accuracy

Accuracy is defined as the degree of accordance between known loads (True Loads) applied to the balance, and the same loads calculated via the balance bridge outputs and the mathematical model.

The difference between a True Load applied on the Internal Balance and the calculated load is called an error, and is referred to the corresponding component full scale value in per mille.

For both types of matrices, Calibration or Balance an error analysis is performed at each temperature level and each Calibration Data Point, giving approximately 1,400 checked data points per temperature level.

For each of the loading configurations

	Mean value of Mean Squared Error for each component at the different calibration temperatures in [0/00 FS]						Mean value of Standard Deviation for each component at the different calibration temperatures in [0/00 FS]					
	$F_x$	$F_y$	$F_z$	$M_x$	$M_y$	$M_z$	$F_x$	$F_y$	$F_z$	$M_x$	$M_y$	$M_z$
<b>FS [N/Mm]</b>	2000	3200	26000	1000	1500	300	2000	3200	26000	1000	1500	300
106.20 K	0.263	0.157	0.097	0.797	0.196	0.178	0.143	0.095	0.063	0.468	0.127	0.143
125.90 K	0.118	0.113	0.047	0.280	0.146	0.146	0.097	0.082	0.042	0.205	0.111	0.139
150.35 K	0.126	0.106	0.059	0.224	0.130	0.146	0.107	0.079	0.042	0.182	0.110	0.138
175.00 K	0.123	0.132	0.068	0.435	0.134	0.178	0.105	0.102	0.046	0.246	0.113	0.157
200.50 K	0.117	0.104	0.071	0.412	0.139	0.152	0.096	0.079	0.049	0.249	0.107	0.126
226.70 K	0.120	0.095	0.128	0.287	0.150	0.131	0.099	0.072	0.090	0.184	0.106	0.117
251.25 K	0.146	0.126	0.067	0.364	0.149	0.129	0.123	0.081	0.057	0.207	0.105	0.116
275.75 K	0.137	0.084	0.077	0.131	0.128	0.117	0.114	0.063	0.053	0.101	0.096	0.111
294.30 K	0.182	0.107	0.072	0.285	0.135	0.122	0.155	0.076	0.055	0.164	0.102	0.111
300.75 K	0.138	0.119	0.066	0.185	0.137	0.119	0.119	0.087	0.048	0.110	0.104	0.109
315.75 K	0.155	0.081	0.060	0.114	0.124	0.113	0.122	0.058	0.051	0.084	0.099	0.106
325.60 K	0.150	0.093	0.070	0.165	0.118	0.118	0.121	0.063	0.047	0.106	0.097	0.109

**Table 3:** Summary of Error Distribution Statistical Analysis over the Calibration Temperature Range

described in Table 1 and par. 4.1.2.4, the Mean Square Error and its Standard Deviation are extracted, and related per component in per mille of its Full Scale value. In turn, a mean value for the 27 different combinations of both quantities Mean Square Error and Standard Deviation is computed, which initially provides a first impression on the quality of the calibration, as shown for an ETW balance in Table 3.

This statistical approach is not sufficient to release at a particular temperature level the computed calibration and balance matrices. For each of the 27 load combinations a coloured graphical presentation of the following quantities is offered:

- i. The component readings of the internal balance
- ii. The primary True load(s) applied.
- iii. The interactions.
- iv. The error distribution.

These graphical presentations consist of six small figures, each of them dedicated to a component in the sequence below (Figure 12):

<b>Axial Force</b> [X]	<b>Side Force</b> [Y]	<b>Normal Force</b> [Z]
<b>Rolling Moment</b> [Mx]	<b>Pitching Moment</b> [My]	<b>Yawing Moment</b> [Mz]

Figure 12: Plots Layout

For each of these figures, the abscissa represents the checked calibration data points. On the right side, the ordinate represents the % of Full Scale in loading of the considered component (True Loads).

The red colour is for the primary load(s) applied on the balance, the grey one (with scale factor) for the secondary.

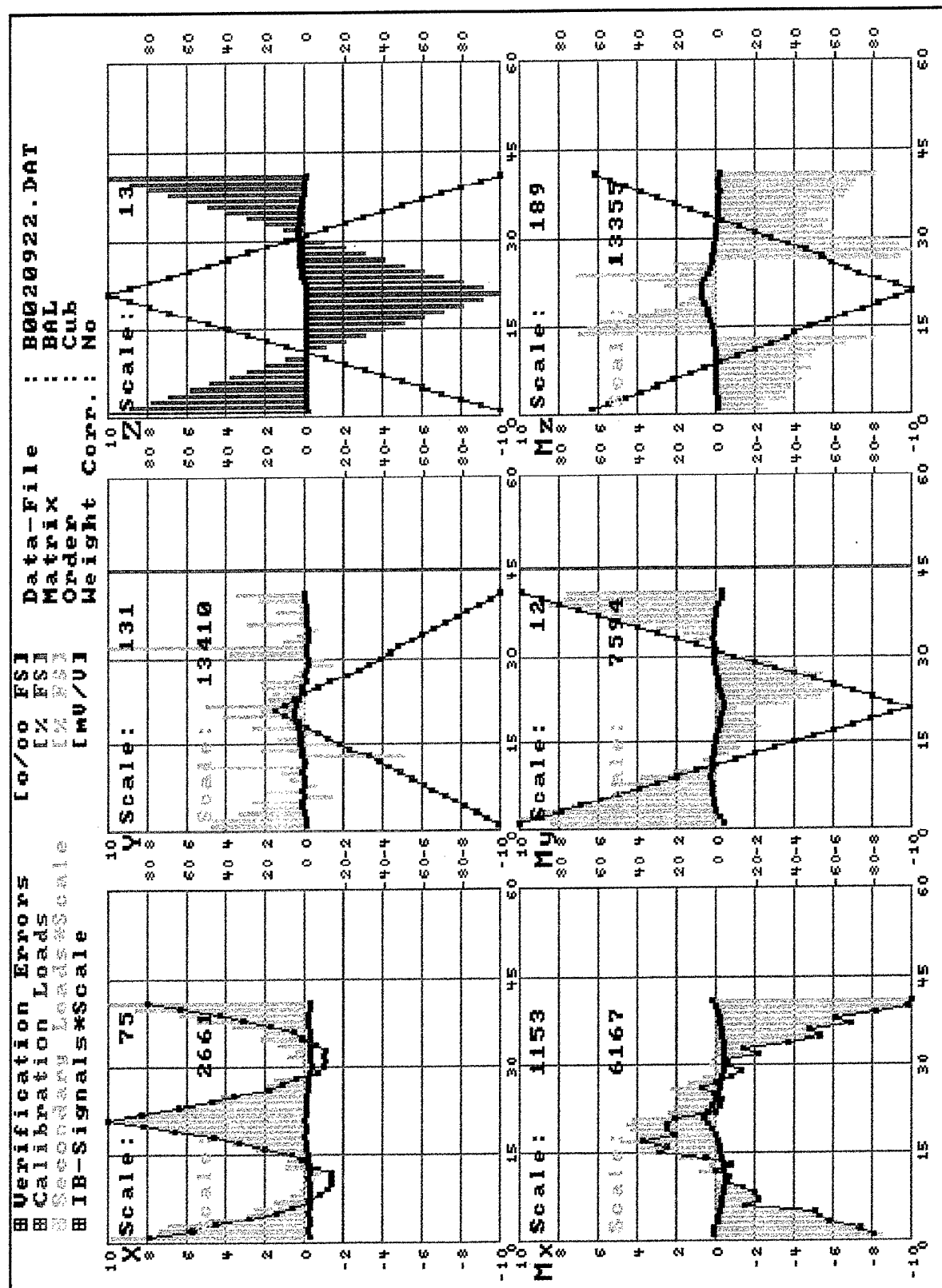
The green curves represent the component readings of the Internal Balance i.e. defined in **Equation 5**.

The blue curve represents the error of the mathematical model to the reference True Loads in per mille Full-Scale of each component.

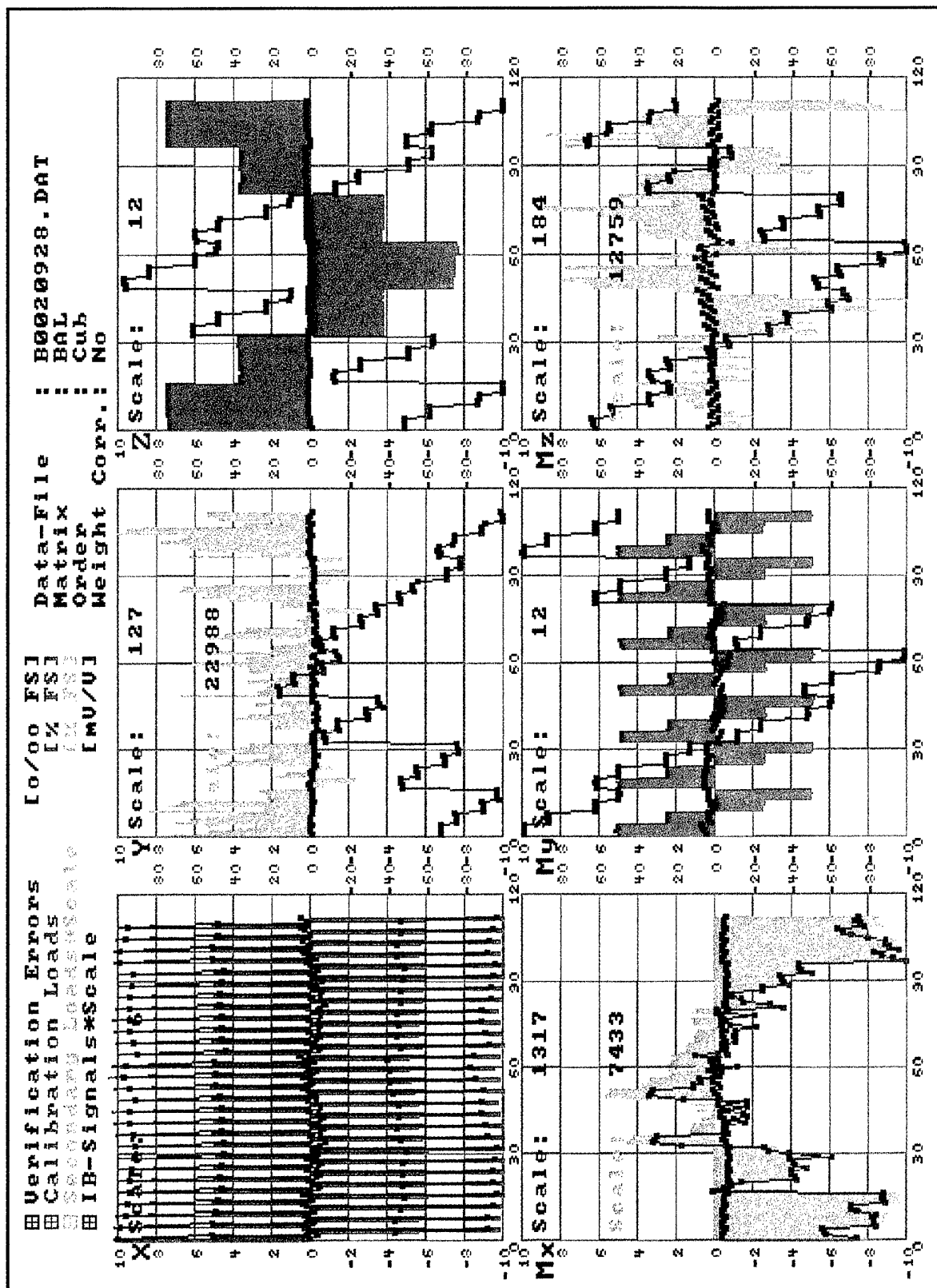
This tool gives the operator a quick view on the matching's level of the mathematical model with the considered load combination. On the next pages two plots have been added. Both are the verification of 104.50 K cold calibration data through the third order balance matrix of the same temperature. The plot 1 represents Normal Force applied singly on the balance. Plot 2, a typical loading configuration of a balance in a Transport Aircraft with simultaneously Fx, Fz and My applied.

A significant difference between both is that the calibration data of plot 2 have not been included in the data set to compute the matrix. Such load combinations (three or more components applied simultaneously) can indicate that a balance has higher order interactions that are present in the mathematical model used. These loadings, often called proof-loadings, are not yet part of a standard force calibration on the ETW BCM.





Plot 1: 104.50 K - Primary Normal Force (F) applied with interactions shown for other channels


 Plot 2: 104.50 K - Verification of a  $F_y$  (100 % FS),  $F_x$  (75 % FS) and  $M_y$  (50 % FS) loading combination

# The National Transonic Facility (NTF) Operational Status

Jeffrey S. Hill  
Facility Manager  
M/S 267  
NASA Langley Research Center  
Hampton, VA 23681-0001

The National Transonic Facility (NTF) is a fully operational, productive and efficient cryogenic wind tunnel currently supporting the Nation's aircraft industry needs providing flight Reynolds number research data for focused development programs as well as investigating the Reynolds number scaling phenomenon. The following presentation is a collection of viewgraphs and notes prepared from previous talks. This material is intended to provide a "general overview" of The National Transonic Facility (NTF) Operational Status as outlined in the following Agenda.

## 1. What is the National Transonic Facility (NTF)?

- The National Transonic Facility provides high quality test data to our customer/users for supporting specific needs for their programs requiring flight Reynolds number test conditions.
- The National Transonic Facility provides services for industry and Department of Defense (DOD) wind tunnel testing
- Research and Development programs
- Subsonic Aircraft Reynolds Number Scaling Research
- Validation of textbook scaling laws
- CFD databases
- The National Transonic Facility is a closed circuit, continuous flow, pressurized, cryogenic wind tunnel

## National Transonic Facility

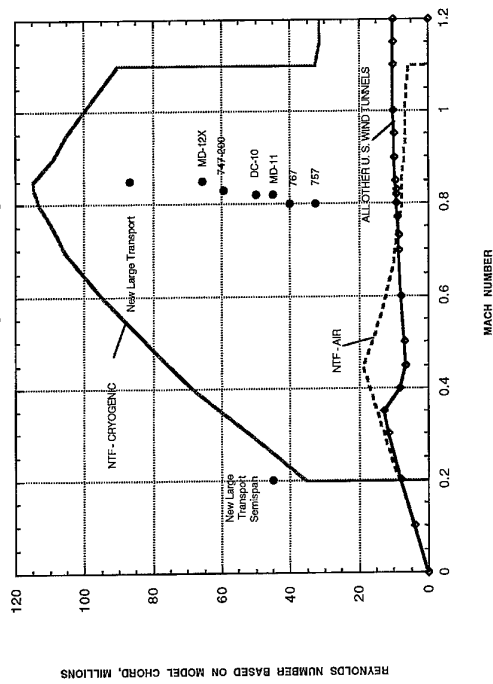
- Continuous Flow, Closed Return, Pressurized, Cryogenic
 

– Dual Mode of Operation	Nitrogen or Air
– Maximum Mach Number	1.2
– Maximum Horsepower	126,000
– Minimum Temperature	-320°F
– Maximum Pressure	130 psia
– ASME Pressure Vessel Code Stamp	
– Internal Volume	230,000 cu.ft.
– Pressure Shell Approx.	5 million lb. Stainless Steel
– Cost	85.6 Million

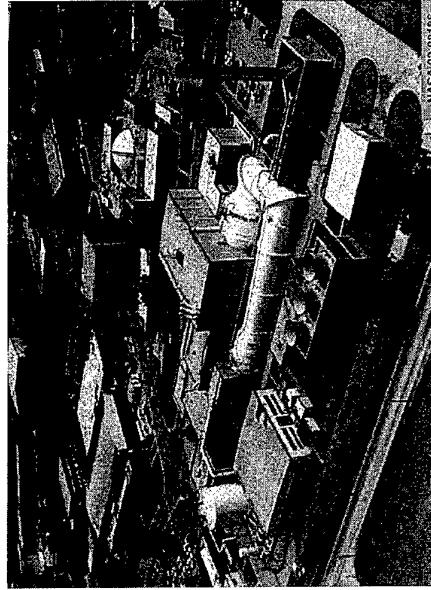
## NTF Operational Characteristics

- Maximum Model Loads
  - Normal 19,000 lb.
  - Axial 9,356 lb.
  - Side 10,000 lb.
- Pitch Range
  - 11 deg to +19 deg
  - Up to 4 deg/sec
- Roll Angle Range
  - $\pm 180$  deg
  - Up to 20 deg/sec
- Access to Model
  - 45 minutes in air mode
  - 4.5 hours in cryo mode
- Cooldown/Warm-up Rate
  - Delta T = 400°F 5 hours complete tunnel
  - Delta T = 70°F no time limit

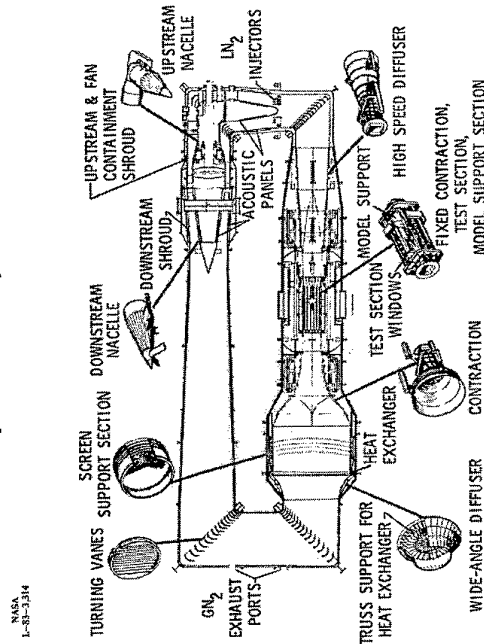
## NTF Capability



## The National Transonic Facility (NTF) Aerial View



## Principal Components



NTF being used for critical experiments to address effects of Reynolds number on a wide range of phenomena including:

- Reynolds number scaling
- Subsonic transports
- Supersonic transport concepts
- High performance military aircraft
- Separation of aerelasticity and Reynolds number effects
- Buffet onset
- Aileron effectiveness
- Nacelle pylon interference
- Performance improvement

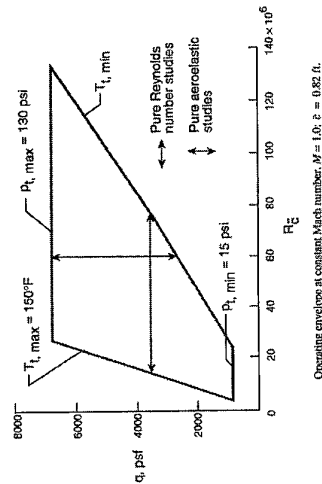
Results from these studies have indicated that some phenomena behave as expected and some do not. Most are configuration dependent.

USAF Advisory Committee 1992

## 2. What is the NTF about?

- High Reynolds number testing techniques / technology
- Problems in Sub-Scale Testing
- Closing the Gap on Scale Effects
- Complex Transonic flows Vary with Reynolds number

## Constant Mach Number



## 3. What does Cryogenic Technology have to do with Reynolds number?

- What's Reynolds number anyway?
- Ways to increase Tunnel Reynolds number
- Benefits of cryogenic high Reynolds number test technique
- Flight and NTF Data at Full Scale Reynolds number

## 4. How does NTF work?

The National Transonic Facility is fundamentally a continuous flow wind tunnel however, because of the limited nitrogen for high Reynolds number cryogenic testing, it is essentially a blowdown wind tunnel. Therefore, it is very imperative to operate the facility as efficiently productively as possible in order to utilize this limited and expensive resource.

- Principal Components of the NTF Circuit
- Nitrogen System
- NTF Drive System
- Vent System
- Model Access
- Model Buildup and Checkout
- Model Transport to Test Section
- Tunnel Control
- Test Cycle

## Plan View of NTF Tunnel Circuit

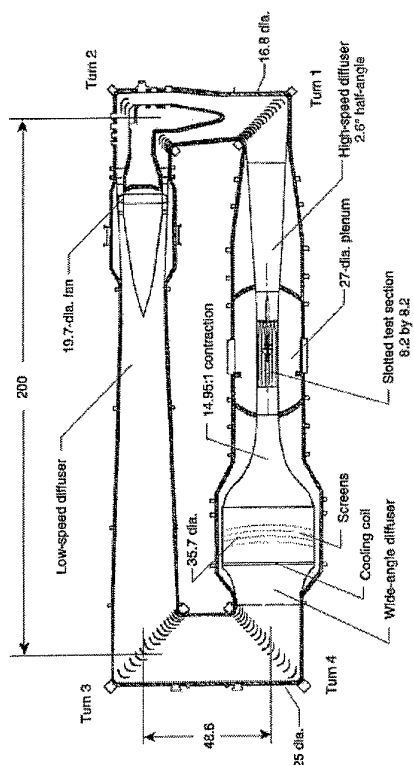
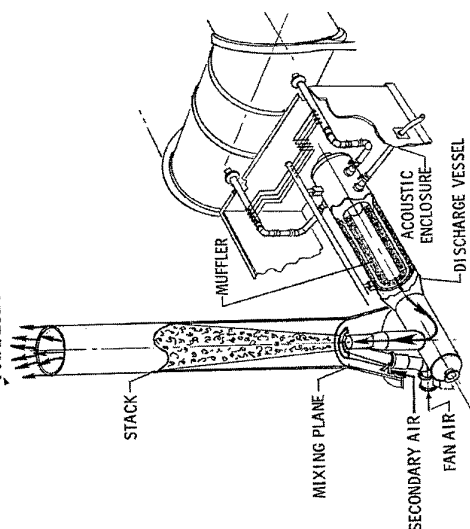
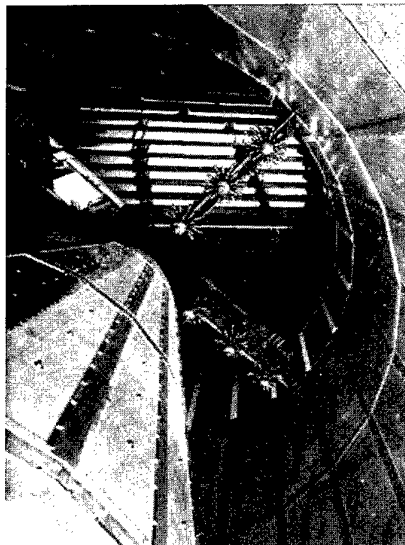


Figure 6. Plan view of NTF tunnel circuit. All linear dimensions are in feet.

## FAN/EJECTOR SYSTEM



## Liquid Nitrogen Injection



## NTF OPERATION CYCLE

Check Instrumentation	
Straighten Shaft	60 min
Calibrate Data System	15 min
Purge O <sub>2</sub> (10 min)	15 min
Purge O <sub>2</sub> (10 min)	15 min
*Cooling (Full Cooldown)	60-90 min
*Conditioning (Full Cooldown)	360 min
*Condition Balance	90 min
To 0 Speed	10 min
Wind-Off Zero	1 min
ESP Calibration	6 min
*From 0 Speed to Test Condition	10 min
Time/Point	22 sec

\*Includes Data Acquisition time plus

\*ESP Zero calibration (1 min)

\*Roll Model 100° (2-4 min)

\*Time between tests (12 min)

\*Main Shafting (10 min)

\*Pitch rate box (1 min/polar)

\*Average Covers

18 polls

4 rolls at 3 min

5 ESPZC at 1 min

From Test Condition To 0 Speed

Access Model (Previous 45 + 90 min for LN2 Ref.)

\*Warm Model

\*Model Change (complex tests)

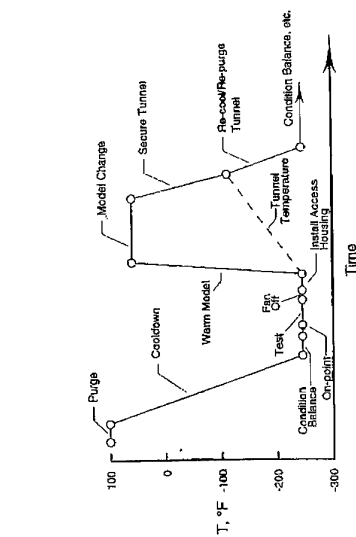
\*Speed Change (Previous 45 + 90 min for LN2 Ref.)

\*Purge Measure (if warm, to get -30°F dewpoint)

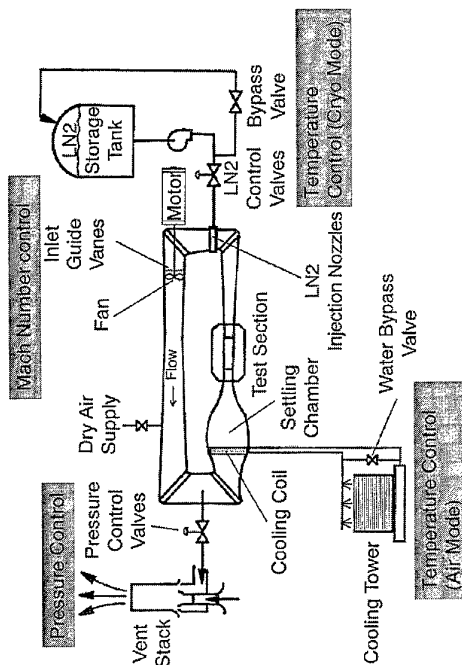
60 min

\*Initial target areas for improvement (Baseline for Computer Simulation Model TM 4664)

## NTF Test Cycle



## NTF Tunnel / Controls Elements



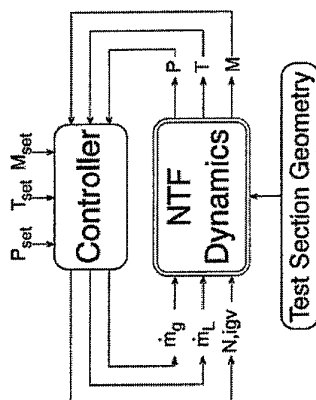
## Tunnel Control

Objective: High productivity in a **safe** and **cost effective** manner.

Approach: Fully automated multivariable control system with capabilities for:

- Programmed test direction with operator intervention
- Real time display and monitoring of control system data
- A microprocessor for each control variable
- A microprocessor based safety interlock system
- Continuously monitoring the working environment for safe oxygen levels

## Cryogenic Tunnel Controls



AIM 17th Aerospace Ground Testing Conference

## Control System Performance

- Automatic Cooldown
  - (structural temperature feedback, fan power)
- Large Set Point Changes
- Regulate the Mach No., Press., and Temp. during test section geometry changes.
- Stability:
  - Mach No. 0.0015
  - Pressure 0.005 atm
  - Temperature 0.2 K

AIM 17th Aerospace Ground Testing Conference

## PRODUCTIVITY ISSUES - PROCEDURES

### Improvements

- Streamlined Procedures
  - Procedures, particularly IOP's, have been reviewed and condensed to improve productivity as a function of:
    - Operating Experience
    - Personnel Training
    - System Enhancement
- Model access has been finalized to allow timely model changes during tunnel cryo conditions.

## SAFETY ISSUES

### Model Safety

- To protect model and support system from overload in case of tunnel process failure/component failure.
  - Dynamic Pressure (Mach Number) overshoot
  - Angle-of-Attack overshoot
- To protect tunnel from model and support system failures
  - Static/Dynamic Overload Conditions
  - Aeroelastic Effects (buffet)
  - Reynolds Number Effects



## MODEL SAFETY PROTECTION SYSTEMS

- Model Protection Microprocessor (Micro B)
  - Dynamic Pressure Limit Input
  - Arc Sector Range Limits Input
  - Violating any Limit will Automatically Fail-safe the Main Drive and Pitch System
- Balance Dynamic Display Unit (BDDU)
  - Monitors Force Balance Loads
  - Facilitates Control Room Monitoring
  - Provides Output for Additional Analysis
- Critical Point Analyzer (CPA)
  - Extends Force Balance Load Limitations
  - Sets Defined Boundaries for Unusual Set-ups
  - Provides Interlock Output
    - Reduces Dynamic Pressure (Mach Number)
    - Reduces Balance Load (Decrease Angle of Attack to a Predetermined "Pitch to Home" Position)
- Manual interlock input from test director and/or test engineer

## **PRODUCTIVITY ISSUES**

### **Model Safety**

- Model constraints: Will always impact research productivity and is part of a good facility operation to identify tradeoffs between Safety and Research. This is a necessary process.
- Model Protection Instrumentation: By enabling model boundaries to be monitored more closely, limitations can be extended with greater confidence, therefore, productivity has improved.
- Catcher Screens: Questionable with respect to model/tunnel safety. However, there is a considerable impact on productivity due to the increased cost of liquid nitrogen usage and reduction in tunnel performance.

## **SAFETY ISSUES**

### **Summary**

- Integrated Operating Procedures will always have a positive impact on productivity. Efforts continue to streamline and modify procedures based on operating experience and system enhancements.
- Model Protection Instrumentation in lieu of mechanical devices (catcher screens) will continue to be used and enhanced to extend limitations based on confidence level and therefore, improve productivity.

**5. Where has NTF been all these years?**

## Milestones in Productivity

Year	Milestone
✓ 1982	Tunnel Operational, First Air Runs
✓ 1983	Tunnel Operational, First Cryo Runs
✓ 1983	Vapor Lock Enclosure, Dry Air Procedures
✓ 1983	LN <sub>2</sub> Plant Operational
✓ 1984	LN <sub>2</sub> Plant Modified for Additional Capacity
✓ 1987	Plenum Doors Operational (Reliable)
✓ 1987	Tunnel Heater Control System Automated, Eliminating 3 <sup>rd</sup> Shift
✓ 1988	Model Access Housings Operational (Reliable)
✓ 1989	Model Heating System Operational
✓ 1991	LN <sub>2</sub> Pumps Operational (Reliable)
✓ 1992	Test Section Sidewalls Operational (Reliable)
✓ 1992	New Micros/Analog Controllers Installed (CoF FY90)
✓ 1992	Drive System Clutch Mechanism Modified/Procedures Changed
✓ 1993	New Data System
✓ 1993	Drive System Equipment Refurbished (Shared with 16" TT)
✓ 1994	Arc Sector Pucks Modified (Capability)
✓ 1995	Identified and Tracked Test Process (Productivity Assessments Studies)

## MODIFICATIONS TO NTF FOR PRODUCTIVITY (FY90)

- Building Addition, 480 Volt Upgrade & Fan Blade Set
- Pitch Hydraulics System Modifications
- Mechanisms
  - Sidewall Model Support System
  - Roll Drive
  - High-Alpha Sting
- Controls Upgrade
  - Analog Loop Controllers
  - Temperature Monitor Scanner
  - Microprocessor Controllers
  - New Mechanisms Controls

## SOFTWARE

- UNIX-Based Software
- Commercially Available Packages
  - Database, Displays, Alerts, etc.
  - User Configured Displays
- Acquisition
  - Modular Routines for Instrumentation
  - Data Storage to Disk Instead of Tape
  - Real-Time Database to Support Displays
- Real-Time Data Reduction
  - Reduce Only Data Necessary for Tunnel
- Operation and Status
  - Provide Both Tunnel and Model Data
- Near Real-Time Data Reduction/Analysis
  - Done at File Server/Workstation level
  - File Server / Networking Used to Make Data Available to Researchers
  - Analysis Done Using Standard Packages

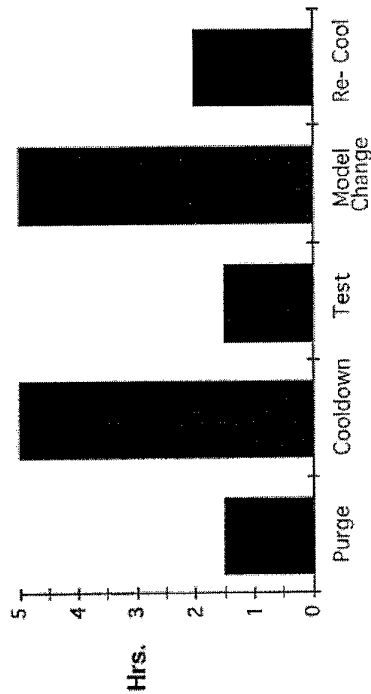
## COMPUTER HARDWARE

- Acquisition
  - Open Architecture
  - Multiprocessors
  - NEFF620's for Analog Data
- Host Machines
  - Open Architecture
  - File Servers
- Tunnel Displays
  - Workstation Technology
- Communications
  - Appropriate Local Area Networks
  - RS-232/IEEE488 as Necessary for Instrumentation

## Study Objectives

- Assess the potential for improving productivity and reducing operating costs in the NTF
- Establish challenging but achievable goals for improvement
- Develop concepts to achieve goals
- Recommend a plan for accomplishment
- Assess ability to meet customer needs/expectations in test techniques
- Assess workforce requirements

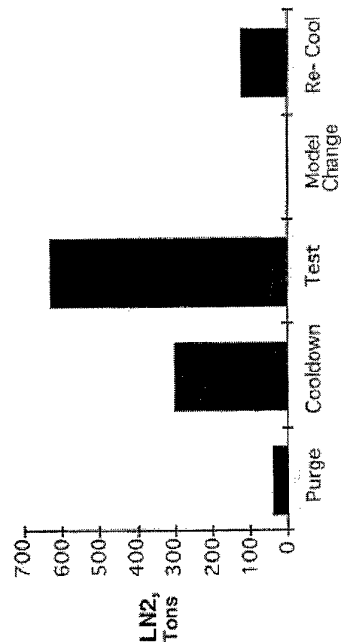
## Example NTF Run Cycle, Hours



## PROJECT ELEMENTS

ITEM	INCREASE POLARS / YEAR	DECREASE LN2 / POLAR	INCREASE RELIABILITY	ADDED CAPABILITY
LN2 Storage	X			
Drive Control System			X	X
Controls Integration and Interlocks		X		
Cooling Coil				X
Model Filing	X	X		
Model Testing	X	X		
Signal Model Access	X			X
Arc Sector		X	X	
Moisture Control	X			
Handling Cart for Semi-Span	X			X
Vent Stack	X		X	
Cryo Chamber				X
Sling Attachments	X			
Increase Cooldown Rate	X			
Upstream Nacelle Heating			X	
Mods				X
Model Attitude Measurement				X

## Example NTF Run Cycle, Tons LN2



## 7. What is NTF doing to establish itself in the aircraft industry?

### Situation

- Times Have Changed
  - Politically
    - Customer focus
    - Dual use
  - Downsizing
    - Workforce
    - Institutional funding
    - R&D Funding
  - NASA is becoming a business
    - Actual cost of research, test, facility,...
    - Direct-charge both internal (and external?)
  - Our product is QUALITY DATA not research

### Goals

- Be customer driven
  - Meet customer expectations 100% of the time
  - Provide customer with data of required uncertainty level  
(no better / no worse)
- Data Quality, Flow Quality, Capability and Productivity
- Operate based on sound business practices
  - Cost Driven
- Provide world class basic instrumentation set (angle of attack, balance, pressure, flow visualization, etc.)
- Lead development of advanced techniques to meet projected customer needs
- Continuously improve test process

### Mission

- To provide reliable, accurate research information to the aeronautics community in a timely manner.
  - To accomplish this requires a focus on increasing productivity, cost effective operations, technical support that adds value, and the development of new facility capability and testing techniques.

## Data Quality Uncertainty Analysis

- Industry has desired a statistical based, quantifiable measure as to the level of uncertainty of data to be expected in the NTF.
- NTF has responded by providing, as part of the pre-test process, a simplified analysis of total uncertainty and repeatability for typical force and moment tests.
- For the simplified analysis historical data is used to predict delivered balance repeatability performance.
- We are striving to achieve, on a routine basis, the repeatability levels desired for test and evaluation.

## Data Quality

- Goals for Repeatability based on Industry needs  
 $\Delta C_L \dots\dots\dots \pm 0.005$   
 $\Delta C_D \dots\dots\dots \pm 0.0001$   
 $\Delta C_m \dots\dots\dots \pm 0.001$
- The repeatability goals for these coefficients are given as confidence intervals about an estimated mean and are stated at the 95-percent confidence level.
- Repeat polar sets are obtained at different times throughout a test to verify these ranges.

TP-3322

## NTF DATA SYSTEM QUALITY

### STATUS

- Drag coefficient confidence interval of 0.0001 demonstrated based on short term and near term repeatability
- Data system noise is very low
- Test section unsteady pressure comparable to best tunnels in the world
- Tunnel upflow is small, approximately 0.13 deg.) but procedures for cooldown and running may effect magnitude - Deformation of tunnel during cool down - Moisture on cooling coils may form frost

### IMPROVEMENTS UNDERWAY

- Maintaining high data quality is a continuous process

## Upcoming NTF Productivity Upgrades

April 1st, 1997 thru January 31st,  
1998

## PERFORMANCE REQUIREMENTS

- Increase cryogenic polars / year (15 data points each) utilizing the existing LN2 plant capacity (100,000 tons per year)
- Technical operator personnel requirements are not to increase on a per shift basis; currently have 10 per shift for tunnel operation
- Reliability, maintainability, and simplicity shall be addressed during the design process

## PERFORMANCE REQUIREMENTS (continued)

- Annual maintenance shall be conducted concurrent with the construction shutdown
- Existing tunnel flow quality shall be maintained (Reference: "Analysis of the Fluctuating Static Pressure Measurements" in the TP-3475 by William B. Igoe)
- Existing control accuracy and response shall be maintained (Reference: SBIR Contract NAS1-19125, May 1993)

Jim A. Osborn 3-27-96  
Part 3 - 4

## Productivity Modeling

- A math model has been developed and utilized to assess the productivity improvement contributed by proposed project elements.
  - Allows insight into productivity barriers
  - Predicts / estimates future productivity
  - Provides quantitative information

## PRODUCTIVITY CONSIDERATIONS

**Productivity:** The ability to perform the intended function within the desired performance criteria. Key issues are those that influence (either directly or indirectly) the ability of the NTF to produce good quality data in the cryogenic mode of operation

<u>Productivity Element</u>	<u>Method of Improvement</u>
Consumables	Use more efficiently Increased availability
Event Frequency/Duration	Eliminate Unnecessary events Reduced time to perform events
Unforeseen Events	Minimize down time - increased reliability Minimize effect of external events - provided additional capacity

## FY 94 CoF PRODUCTIVITY ASSESSMENT

### NTF PRODUCTIVITY CONSTRAINTS

- ONLY 2 Constraints identified - Liquid Nitrogen and Time
- **Liquid Nitrogen**
  - Use of LN2 - Efficiency of Use dictates how much is available
  - Constraint is Average Rate for Process Controls and Data Acquisition
  - Storage of LN2 - LN2 inventory available dictates how long test can run prior to having to wait for LN2
  - Constraint is total LN2 storage capacity
  - Procurement of LN2 - LN2 is required for testing
  - Constraint is operational funds
  - Production of LN2 - Production capacity dictates time for recovering the LN2 system for next cryogenic test
  - Constraint is the instantaneous rate of production (12.5 Tons/hr)

### NTF PRODUCTIVITY CONSTRAINTS

- **Time - Tunnel Operational Time (Occupancy Hours)**
  - Any item that reduces tunnel operational time (if down time is excessive, then time can become dominant constraint)
- **CONCLUSION** - Must solve LN2 constraint first or will not see any improvement in productivity from eliminating time constraints. Modifications to remove time constraints will provide NO additional cryogenic polars until the LN2 constraint is removed.

### OBSERVED CONSTRAINTS

- Cryogenic test profiles exhibit significant Liquid Nitrogen Constraints
- Key to improving productivity and reducing cost per polar is to improve the overall system efficiency.
- Cost per polar reductions are driven by the Liquid Nitrogen consumption during testing. Decreasing time (LN2) per data point reduces cost per polar.
- Increased annual throughput (polars/year) - increasing operational efficiency of Liquid Nitrogen use and reducing time for all activities, including model activities and down time events.
- Large Liquid Nitrogen Storage Tank provides a low risk means to reduce test program duration by eliminating "Out of LN2" events; cost per polar not significantly reduced

## CONCLUSIONS

- Utilizing the Reynold's Number capability of NTF results in a "Nitrogen" constrained test program
- When nitrogen constraints are removed, Model Activity time is next dominant constraint
- Operational reliability is an overriding constraint - if tunnel is down for maintenance or repairs, cannot run. If the tunnel is not maintained, then it will eventually be unable to perform. Therefore, minimize or prevent down times.
- Identified theoretical upper bound on productivity at NTF
- Developed prioritized list of modifications to the NTF for future productivity improvements

## RESEARCH REQUIREMENTS

- Provide a LN2 Storage and Transfer System that:
  - Provides sufficient LN2 storage for uninterrupted testing for a typical test program
  - Affords utilization of the total yearly output of existing PRAXAIR LN2 Plant
- Refill the existing LN2 storage tank in 3 hours maximum
- Provide for increasing NTF sustained run time from 1.5 to 3 hours for a nominal injection rate of 2800 gal / min (560 ton / hr)

## RESULTING DESIGN REQUIREMENTS

- Tank Size: 900,000 gallons (3000 tons)
- Transfer Rates:
  - 1300 Gal / min from new tank to existing tank
  - 250 Gal / min from PRAXAIR Plant to new tank

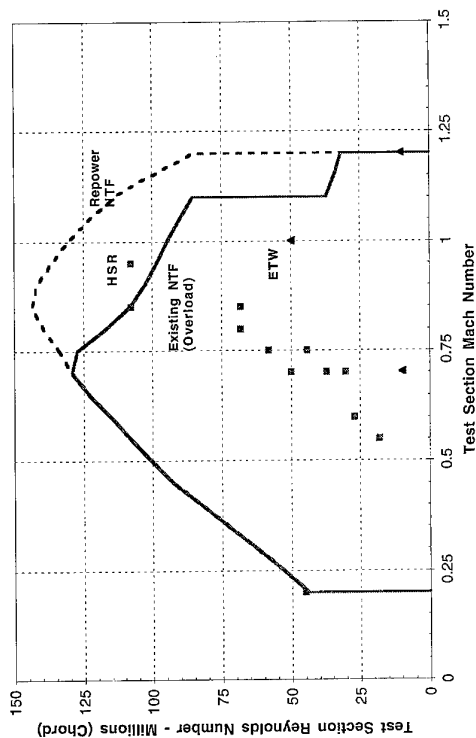
The NTF productivity math model was a key tool for selecting the proper tank size.

## RESEARCH REQUIREMENTS JUSTIFY DRIVE REPLACEMENT

- Productivity enhancements reduce time to Mach # setpoint, and increase data per polar.
- State of the art, commercially available equipment assures most efficient use of tunnel resources - energy, manpower, test time, and maintenance funds.
- Reliability improvements reduce tunnel downtime.
- Independent operation from 16 Foot Transonic Tunnel by eliminating shared Kramer drive control system.
- Simultaneous, full power operation with 16 Foot Transonic Tunnel is possible with new electrical feeder.



## Drive System Performance



## MAINTAINABILITY & RELIABILITY

- Spare parts stock is based on repair time required
- Design reviews, manufacturing inspections, witness testing/shipping supports accurate assessment of equipment performance
- Conservative design margins and duty cycles on subsystem components reduce stress/overload failures
- System MTBF - 40,000 hours, MTTR - 4 hours
- System Design Life - 35 years minimum
- Redundancy of components used where improved design or manufacturing cannot be implemented
- Hardware designed and built for specific functions

## Objectives of Control System Improvements

- Shorter data point cycle time for:
  - Operator to enter new setpoints
  - Pitch / Roll change
  - Data transfers
  - Mach number settling
  - Operator to adjust Mach number
  - Test engineer decision
  - Operator to initiate take-data
- Better data accuracy

Time = \$\$\$

## Process Control System Upgrades

- Scope of Work
  - Communications Upgrade
  - Mach Number Measurement System
  - Mach Number Disturbance Management
  - Alpha / Beta Controls
  - Automated Test Sequencing
  - On-Setpoint Status
  - Performance Monitoring System

## Scope of Work

- Communications Upgrade
  - Provide faster link between microcomputer control systems and research data system(s).
- Mach Number Measurement System
  - Provide feedback signals to micro A control system from PSI 8400 Flow Reference System and calculate Mach number which includes real gas effects.
  - Penetrate tunnel shell and install total and static pressure probes.

## Scope of Work

- Mach Number Disturbance Management
  - Modify Mach number control system to decrease settling time following an angle-of-attack change [by 25%].
- Alpha / Beta Controls
  - Implement optimum pitch and roll strategy within present system mechanical boundaries with the option to close the control loop based on the model angle-of-attack measurement system.

## Scope of Work

- Automated Test Sequencing
  - Sequence tunnel operations from drive start, through data acquisition, to drive stop with interrupt provision using existing control algorithms and research data system.
- On-setpoint Status Indicators
  - Detect and display on-setpoint status; report status to Automated Test Sequencing.
- Performance Monitoring System
  - Capture data and provide displays / reports indicating performance of control systems.

## Benefits

- Communications Upgrade
  - Decreases data transfer time
  - Supports all other improvements
- Mach Number Measurement System
  - Provides single Mach number source
  - Reduces operator decision time
  - Improves data accuracy through newer technology
- Mach Number Disturbance Management
  - Reduces Mach number settling time
  - Improves data quality

## Benefits

- Alpha / Beta controls
  - Minimizes repeat data points
  - Improves data accuracy
  - Addresses new demand from customers
- Automated Test Sequencing
  - Reduces operator interaction **time**

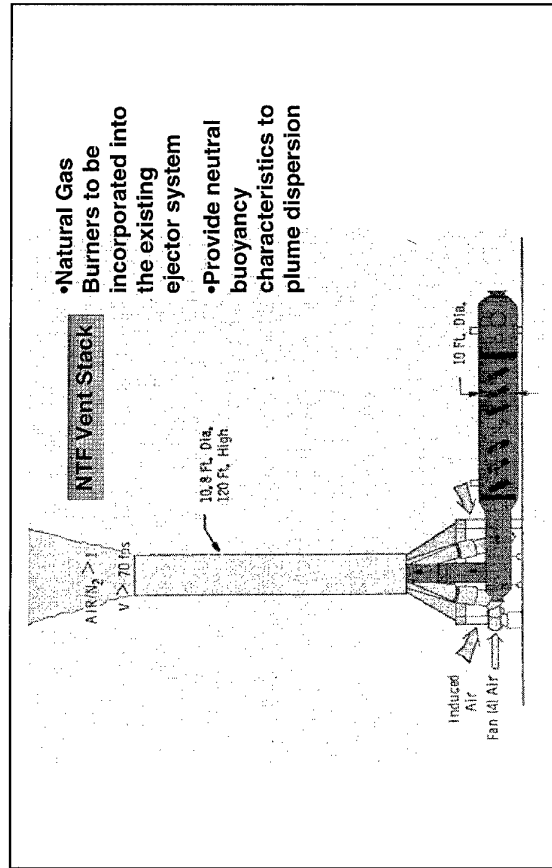
## Benefits

- On-setpoint Status
  - Reduces operator interaction **time**
  - Reduces test engineer decision **time**
- Performance Monitoring System
  - Automates facility performance measurement
  - Enhances facility maintainability

## Summary

Controls improvements shorten time to achieve and maintain test conditions, leading to:

- shorter data collection time
- less energy consumption
- lower cost of operations



## 8. Where is NTF going?

### Continue to Improve

- Focus on the current customer / test
  - All organizations at LaRC supporting wind tunnel testing must work as a single entity reaching the same goal
  - Test Process and Procedure Re-engineering
  - Standardize/Institutionalize procedures

### Wind Tunnel Metrics

#### Customer Expectations

- Test Envelope (Meets)
  - Mach range
  - Reynolds number
  - Test Duration
  - Special test capability
- Data Quality (High)
  - Flow
  - Data accuracy and repeatability
  - Controls accuracy and repeatability
- Productivity (High)
- Test Cost (Low)
- Accessibility (Quick)
- Local staff functions (Excellent)
- Local response to test anomalies (Fast)

## Other Cryogenic Wind Tunnel Projects

Robert A. Kilgore  
CES-Hampton  
359 Marlfield Circle  
Hampton, VA 23669 U.S.A.

### SUMMARY

The first cryogenic tunnel was built at the NASA Langley Research Center in 1972. Since then, many cryogenic wind-tunnel have been built at aeronautical research centers around the world. I describe in this lecture some of the more interesting and significant of these projects that have not been covered by other lecturers at this Special Course.

In this lecture I describe cryogenic wind-tunnel projects at research centers in four countries: **China** (Chinese Aeronautical Research and Development Center); **England** (College of Aeronautics at Cranfield, and Defence Research Agency - Bedford); **Japan** (National Aerospace Laboratory, University of Tsukuba, and National Defense Academy); and **United States** (Douglas Aircraft Co., University of Illinois at Urbana-Champaign, and NASA Langley).

### 1. INTRODUCTION

So far in this Special Course, we have heard about some of the cryogenic wind-tunnel projects in the member countries of AGARD. From Germany, Dr. Rosemann reported on the DLR Cryogenic Ludwig Tube Tunnel at Göttingen. From France, Mr. Seraudie reported on the cryogenic induction tunnel T2 at ONERA-CERT in Toulouse. Dr. Rebstock and Mr. Kronen reported on the DLR Kryo Kanal Köln (KKK). Messrs. Price, Schmanski, and Badet have given us some details on the recently completed European Transonic Tunnel (ETW). Finally, Mr. Hill has told us about the U.S. National Transonic Facility (NTF) located at the NASA Langley Research Center in Hampton, Virginia.

The lectures of this AGARD-FDP/VKI Special Course, taken together, show a high level of cryogenic wind tunnel activity within the AGARD community. It should be no surprise that there have been several other cryogenic tunnel projects, either completed or planned, in both AGARD and non-AGARD countries. My purpose in this lecture is to describe briefly some of the more interesting and significant of these projects.

I do not try to describe all of the cryogenic tunnel projects not otherwise covered in this series of lectures. Rather, I have selected examples of the wide variety of cryogenic tunnel projects which have arisen since we built the first cryogenic wind tunnel 24 years ago.

### 2. CHINA

Starting in 1975, researchers at the Chinese Aerodynamic Research and Development Center (CARD), Mianyang, Sichuan Province, The People's Republic of China, have studied various schemes for high Reynolds number transonic wind tunnels.

From their early studies they concluded that a 2.4 x 2.4 m continuous flow cryogenic nitrogen tunnel would be especially attractive for meeting their high Reynolds number transonic testing requirements. However, the cost of building a continuous-

flow fan-driven tunnel is high. Therefore, researchers at CARD studied alternative intermittent cryogenic wind-tunnel schemes as a way to get high Reynolds numbers at less cost. Reference 1 reports the results of some of the early studies at CARD.

The intermittent cryogenic tunnel scheme proposed by CARD would use precooled high pressure air. The air would be further cooled by throttling before passing through the wind tunnel test section into a storage tank. As noted in Reference 1, using an existing high pressure air storage system considerably reduces the capital cost of the proposed cryogenic tunnel. Reference 2 gives a more complete description of the CARD study related to the 2.4 x 2.4 m high Reynolds number cryogenic transonic wind tunnel.

The large transonic cryogenic tunnel proposed by CARD researchers has not been built. However, interest is still high at CARD for building a large high Reynolds number tunnel.

In 1990, a team of researchers at CARD, led by Dr. Que Ping, put into operation a 0.1 x 0.1 m low-speed fan driven cryogenic tunnel. The low-speed tunnel has been used to gain experience and study some of the problems related to operation of a cryogenic wind tunnel.

During a recent visit to CARD, researchers described to me a new method they were studying to achieve relatively long run times for a large transonic cryogenic wind tunnel. The new drive method is based on using multiple shock tubes to provide a constant supply of cold gas to drive the cryogenic tunnel. It appears that these studies at CARD related to intermittent tunnels are being made in parallel with studies of a more conventional fan-driven cryogenic tunnel.

### 3. ENGLAND

#### 3.1 College of Aeronautics, Cranfield

Schultz and his coworkers at Oxford University proposed and built an isentropic light piston tunnel (ILPT). The purpose of the ILPT was to measure heat transfer rate on gas turbine blades in a short duration, hot, low-Reynolds-number flow (Ref 3). Figure 1 shows a schematic of the ILPT.

In this tunnel concept, compressed air drives a light piston into a charge tube, compressing and heating the gas in the tube almost isentropically. The piston acts as a barrier between the compressed air expanding into the charge tube and the gas it is compressing. Compression continues until the gas in the charge tube reaches the desired pressure and temperature. A fast-acting valve (or diaphragm) at the end of the charge tube then opens to allow the hot test gas to pass through the test section. By properly designing the tunnel, the volumetric flow of compressed air from the reservoir into the charge tube exactly matches the flow of gas from the charge tube through the test section. By matching the flows in this way, it is possible to maintain constant test conditions.

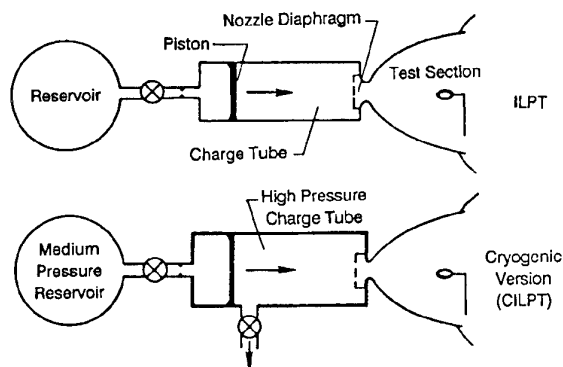


Fig. 1 Cryogenic ILPT compared with standard ILPT. [Ref 4]

At the College of Aeronautics, Cranfield Institute of Technology, Bedford, Stollery and Murthy suggested the Oxford type of light piston tunnel could operate in reverse. This arrangement would generate intermittent low-temperature, high-Reynolds-number flows (Ref 6). Figure 1 shows the simplest form for the cryogenic isentropic light piston tunnel (CILPT) in which high pressure gas in the charge tube vents to the atmosphere.

Opening the vent valve causes the pressure and temperature in the charge tube to expand isentropically. The vent valve is closed when the pressure and temperature reach the values required for the test. The valve separating the test section from the charge tube is then opened.

Following a predetermined delay of a few milliseconds, the piston is set in motion by opening the valve between the charge tube and the medium pressure reservoir. This pushes the cold gas in the charge tube out through the test section. Again, matching the incoming and outgoing volumetric flows keeps the test conditions constant. Figure 2 shows the idealized pressure and temperature time history for both the ILPT and the cryogenic version of the ILPT.

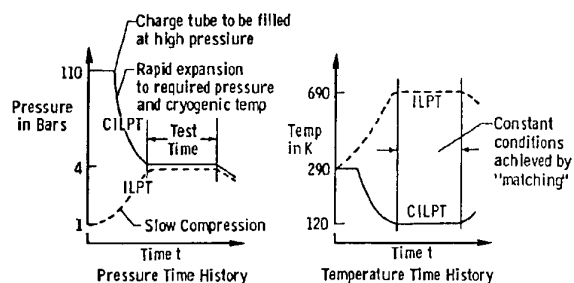


Fig. 2 Pressure and temperature time histories for cryogenic and standard versions. [Ref 5].

Stollery and his coworkers built a pilot intermittent cryogenic wind tunnel based on this light piston concept. Using nitrogen as the test gas, they achieved both the low stagnation temperature and the required matching of volumetric flows.

Reference 7 gives an analysis of the CILPT, the design details of the pilot CILPT, and experimental results from the tunnel. Table 1 lists the major characteristics of the pilot CILPT at Cranfield. Figure 3 shows the general arrangement of the pilot CILPT.

TABLE 1. - Pilot Cryogenic Isentropic Light Piston Tunnel at Cranfield (England)

Type .....	isentropic expansion, light piston
Material of construction .....	stainless steel
Insulation .....	none
Cooling .....	isentropic expansion
Test gas .....	nitrogen
Charge tube pressure .....	up to 3549 kPa
Test section size (h,w,l) .....	2.86 x 2.86 x 15 cm
Mach range .....	transonic
Contraction ratio .....	6:1
Stagnation pressure .....	100 kPa
Stagnation temperature .....	down to 110 K
Running time .....	0.3 s
Max. Reynolds number/m .....	42 million

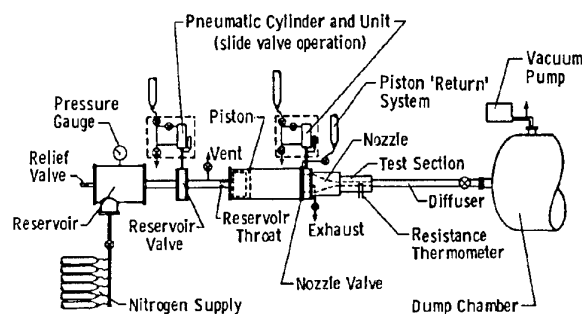


Fig. 3 General arrangement of Pilot CILPT at Cranfield. [Ref 7]

Stollery and his coworkers have made preliminary studies of much larger versions of the CILPT (Ref 6). For example, when they assume the original specifications for the cryogenic version of the European Transonic Windtunnel, that is,  $p_1 = 440$  kPa (4.4 bars),  $T_1 = 120$  K,  $1.95 \times 1.65$  m test section and  $R_c = 40$  million at  $M = 0.9$ , the total test mass required for 10 seconds running time is 53,000 kg. The corresponding charge tube volume is 4060 m<sup>3</sup> which would require, for example, a 4 m diameter cylinder over 300 m long.

To achieve the required temperature during the expansion process, the ideal pressure ratio through which the gas expand is 25:1. Thus, part of the charge tube must be built to accommodate pressures of 11 MPa (110 bars). In fact, departure from the ideal, caused by heat transfer from the walls of the charge tube to the gas, requires expansion of the gas through a considerably larger ratio. To achieve a stagnation temperature of 120 K from an initial temperature of 300 K, requires an expansion ratio of about 35:1 (Ref 4).

If we used the CILPT concept to achieve the maximum design Reynolds number of 120 million of the 2.5 x 2.5 m U.S. NTF at the design maximum stagnation pressure of 880 kPa (8.8 bars), the test mass would be 194,000 kg stored in a 7400 m<sup>3</sup> charge tube at 22 MPa (220 bars).

As noted in Reference 6, CILPT versions of the ETW or the NTF would be very large facilities but would have the virtue of being simple. Reference 6 also notes that concerns remain

over the quality of the flow in such facilities and possible variations in the stagnation temperature during the run because of heat transfer from the charge tube to the gas.

Stollery and his coworkers also studied a more modest use of the CILPT. An example given in Reference 6 assumed an arbitrary structural limit of 600 kPa (6 bars) and a  $0.6 \times 0.6$  m test section designed for  $M=0.9$ . The charge tube volume required for a 1 second run would be a modest  $47 \text{ m}^3$ , that is, a 2 m diameter cylinder 15 m long. Such a facility could achieve a Reynolds number of 19 million compared with 5.2 million for a straight blowdown tunnel operating at  $p_t = 600 \text{ kPa}$  (6 bars) and  $T_t = 300 \text{ K}$ .

### 3.2 Defence Research Agency - Bedford

Law and his colleagues at the Defence Research Agency (DRA) Bedford – formerly the Royal Aerospace Establishment (RAE) – built a closed circuit Cryogenic Test Duct. Although the Test Duct has now been decommissioned, it is a good example of an inexpensive and convenient way to provide cryogenic gas flow for testing wind tunnel balances and model components.

The Test Duct was part of the United Kingdom support for the European Transonic Windtunnel (ETW) program (Ref 8). The maximum gas velocity through the  $0.3 \times 0.3$  m test section was 25 m/s, falling with temperature. By controlling the rate of injection of  $\text{LN}_2$  in the circuit of the Test Duct, the gas temperature could rapidly be reduced and controlled at any level between ambient and 90 K.

Law fitted the Test Duct with external insulation for the early experiments. The external insulation consisted of a plywood shroud containing vermiculite in a 10 cm gap between the plywood and the aluminum Duct. He provided a dry nitrogen purge in the insulation space for dryness and to reduce the chance of oxygen enrichment. In a successful effort to increase the rate at which they could change temperature, Law lined about 75 percent of the inner surface of the Duct with a 3 mm thick layer of either cork or FEP insulation. Table 2 gives the major characteristics of the Cryogenic Test Duct at DRA-Bedford.

TABLE 2. - Cryogenic Test Duct at DRA-Bedford (England)

Type .....	closed circuit, centrifugal fan
Material of construction .....	aluminum
Insulation .....	external and internal
Cooling .....	liquid nitrogen
Test gas .....	nitrogen
Test section size (h,w,l) .....	$0.3 \times 0.3 \times 1.5 \text{ m}$
Speed range .....	up to 25 m/s
Contraction ratio .....	1:1
Stagnation pressure .....	atmospheric
Stagnation temperature .....	90 K - ambient
Running time .....	typically 1 hour
Max. Reynolds number/m .....	11.4 million
Drive motor .....	9 kW
Fan speed .....	up to 2500 rpm
$\text{LN}_2$ tank volume .....	$1.28 \text{ m}^3$

They used a simple calibration device to load small wind tunnel balances mounted in the test section. They were able to observe the behavior of a 3-component balance under transient temperature conditions. In addition, the test section of the Duct

had transparent sides which allowed direct visual observation during tests. Reference 8 gives details of the design and performance characteristics of the DRA Cryogenic Test Duct Facility and some results on the NLR 771 strain gage balance.

## 4. JAPAN

There are many good wind tunnels in Japan. Some of the best are at the National Aerospace Laboratory (NAL) in Chofu, Tokyo. The tunnels at NAL include the 2 m x 2 m Transonic Wind Tunnel and the 5.5 m x 6.0 m Low-speed Wind Tunnel. These are the largest transonic and subsonic tunnels in Japan. However, these tunnels cannot achieve the test Reynolds number needed to develop modern aircraft.

To overcome the problem of low Reynolds number, at least four groups in Japan have developed and are now using cryogenic wind tunnels.

A review article published in 1988 in Cryogenics describes four of the cryogenic tunnels in Japan (Ref 9). Emphasis in the review article is on the cryogenic engineering aspects of their design and operation. In this section I briefly describe some of the cryogenic tunnels in Japan with emphasis on the mechanical, aerodynamic, and operational aspects.

Ishikawajima-Harima Heavy Industries Co., Ltd. (IHI) was the general contractor for the first four cryogenic wind tunnels built in Japan. Sub-contractors did much of the detailed work on the tunnels. However, in Japan the custom is to refer only to the general contractor who assumes full responsibility for the success or failure of the project.

### 4.1 National Aerospace Laboratory (NAL)

#### 4.1.1 NAL 0.1 x 0.1 m Transonic Cryogenic Tunnel

In 1982 IHI designed and built the 0.1 x 0.1 m Transonic Cryogenic Tunnel for NAL (Refs 10,11). Dr. Sawada and his colleagues at NAL have used this relatively small tunnel to gain operational experience. They have also used this tunnel to support design studies for much larger cryogenic tunnels proposed for Japan.

Figure 4 is a sketch of the 0.1 x 0.1 m Transonic Cryogenic Tunnel at NAL. Liquid nitrogen is injected into the tunnel through pipes in the cross-leg at the right. Gaseous nitrogen exhausts from the tunnel from the opposite cross-leg. The plenum moves on a trolley to give access to the perforated-wall test section.

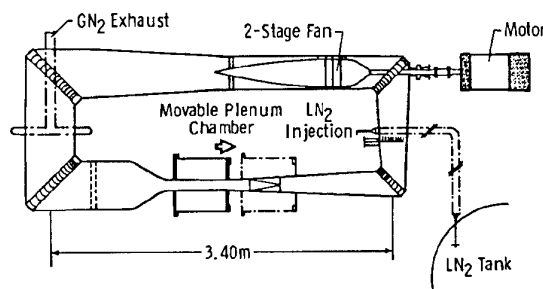


Fig. 4 Sketch of Transonic Cryogenic Tunnel at NAL.

Sawada and his colleagues at NAL have made a wide variety of operational tests in the 0.1 x 0.1 m tunnel. They used the

original manual control systems for the typical purging, cooldown, running, and warm-up operations.

In 1985 they installed automatic controls for nitrogen injection and exhaust and fan speed. Under manual control, changing from one test condition to another took from 5 to 10 minutes. The same changes in test conditions now take only about 1 minute under fully automatic control.

Table 3 gives some of the design and performance details of the 0.1 x 0.1 m Transonic Cryogenic Tunnel. Note the relatively high contraction ratio of 18:1. Such high contraction ratios tend to be a design characteristic of Japanese wind tunnels.

**TABLE 3. - Transonic Cryogenic Tunnel  
at NAL (Japan)**

Type .....	closed circuit, fan
Material of construction .....	A5052 Al-alloy
Insulation .....	external, purged
Cooling .....	liquid nitrogen
Test gas .....	nitrogen
Test section size (h,w,l) .....	0.1 x 0.1 x 0.3 m
Mach range .....	up to 1.02
Contraction ratio .....	18:1
Stagnation pressure .....	up to 2 bars
Stagnation temperature .....	90 K - ambient
Running time .....	more than 2 hrs
Max. Reynolds number/m .....	130 million
Drive motor .....	55 kW
Fan speed .....	600 - 5700 rpm
LN <sub>2</sub> tank volume .....	2.17 m <sup>3</sup>

The 0.1 x 0.1 m tunnel is now under completely automatic control through a small digital computer (Ref 12). The operators make excellent use of computer graphics (in color) to display tunnel conditions during a run. They store the test conditions on a hard disk and can quickly plot them (again, in color) for study after the run. A test run in the 0.1 x 0.1 m tunnel can last for several hours with each run using about 1000 litres of liquid nitrogen.

The 0.1 x 0.1 m tunnel has good visual access to the test section through windows in the plenum. They keep the windows free of frost by using a vacuum between two pieces of glass. However, after several hours of running on a humid day, a hot air gun is often used to remove frost from the outer layer of glass.

#### 4.1.2 NAL 0.2 m Supersonic Wind Tunnel

Dr. Sawada and his colleagues have recently built and put into operation a small supersonic wind tunnel at NAL. The test section is 0.2 m x 0.2 m and 0.4 m long. The new tunnel is initially being operated using ambient temperature air over a supersonic Mach range from 1.5 to 2.5 (using a symmetrical flexible nozzle) and over a subsonic Mach range of 0.55 to 0.8. With air operation the total pressures are from 0.05 to 0.15 MPa and total temperature of 330K.

Sawada and his colleagues have designed this supersonic tunnel for cryogenic operation. (It is the first supersonic cryogenic tunnel.) Once some modifications are made (including installing a larger drive motor), the tunnel can operate at total pressures from 0.05 to 0.3 MPa in air and 0.1 to 0.5 MPa us-

ing cryogenic nitrogen. Using direct injection of liquid nitrogen for cooling, the new supersonic tunnel at NAL will operate at total temperatures from 100 K to 330 K depending on Mach number.

## 4.2 University of Tsukuba

Researchers at the Institute of Engineering Mechanics at the University of Tsukuba, under the leadership of Professor Adachi, have built two low-speed cryogenic wind tunnels. One has a 0.1 x 0.1 m test section and the other a 0.5 x 0.5 m test section.

### 4.2.1 0.1 x 0.1 m Low-Speed Cryogenic Tunnel

The 0.1 x 0.1 m low-speed cryogenic tunnel operated at cryogenic temperatures for the first time in 1980. Graduate students use this closed circuit, fan-driven tunnel for various research projects. In addition, researchers have used it for the calibration of sensors and to gain operational experience with cryogenic tunnels. This tunnel also furnished valuable design information needed for the larger low-speed tunnel at Tsukuba. Because of the relatively small size of this tunnel, researchers will probably not use it for serious aerodynamic research. Table 4 gives the major design and operational characteristics of the 0.1 x 0.1 m low speed tunnel.

**TABLE 4. - 0.1 x 0.1 m Cryogenic Low-Speed  
Tunnel at University of Tsukuba (Japan)**

Type .....	closed circuit, fan
Material of construction .....	stainless steel
Insulation .....	external
Cooling .....	liquid nitrogen
Test gas .....	nitrogen
Test section size (h,w,l) .....	0.1 x 0.1 x 0.3 m
Speed range .....	up to 30 m/s
Contraction ratio .....	3.41:1
Stagnation pressure .....	up to 2 bars
Stagnation temperature .....	100 K - ambient
Running time .....	up to 2 hrs
Max. Reynolds number/m .....	30 million
Drive motor .....	2.2 kW
Fan speed .....	1500 - 4300 rpm
LN <sub>2</sub> tank volume .....	0.175 m <sup>3</sup>

### 4.2.2 0.5 x 0.5 m Low-Speed Cryogenic Tunnel

Figure 5 is a sketch of the 0.5 x 0.5 m low-speed cryogenic wind tunnel at Tsukuba. The tunnel lies in the vertical plane with the test section at the top. The 0.5 x 0.5 m Cryogenic Tunnel is a closed circuit, fan-driven tunnel with internal insulation. It operates at pressures up to 8 bars. Researchers have used this tunnel to make aerodynamic measurements on a circular cylinder over a wide range of Reynolds numbers.

A mostly mild steel (SM-41B) pressure shell makes this tunnel unique among pressurized continuous-flow cryogenic tunnels. Only the contraction, first diffuser and fan portion of the pressure shell are made from stainless steel (SUS 304). The original internal insulation was a non-rigid foam covered with a wooden liner. This system gave problems with moisture and cracking. It was replaced in 1985 with a new system consisting of glass wool, rigid urethane, and a stainless steel liner. Table 5 gives the major characteristics of the 0.5 x 0.5 m low-speed tunnel.



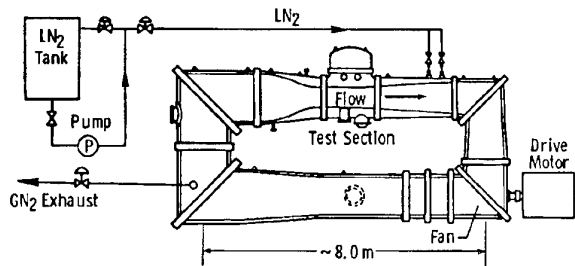


Fig. 5 0.5 x 0.5 m Low-speed Cryogenic Wind Tunnel at University of Tsukuba.

TABLE 5. - 0.5 x 0.5 m Cryogenic Low-Speed Tunnel at University of Tsukuba (Japan)

Type .....	closed circuit, fan
Material of construction .....	mild steel, some stainless
Insulation .....	internal
Cooling .....	liquid nitrogen
Test gas .....	nitrogen
Test section size (h,w,l) .....	0.5 x 0.5 x 1.2 m
Speed range .....	7 - 65 m/s
Mach range .....	up to 0.30
Contraction ratio .....	6.12:1
Stagnation pressure .....	1.22 - 8.10 bars
Stagnation temperature .....	112 K - ambient
Running time .....	30 min. at max R
Max. Reynolds number/m .....	200 million
Drive motor .....	450 kW
Fan speed .....	150 - 1500 rpm
LN <sub>2</sub> tank volume .....	18 m <sup>3</sup>

#### 4.3 National Defense Academy (NDA)

IHI built a cryogenic tunnel for the Department of Aerospace Engineering of the Japanese National Defense Academy, Yokosuka, Japan. They delivered this tunnel, the *NDA High Reynolds Number Flow Facility*, in March of 1985.

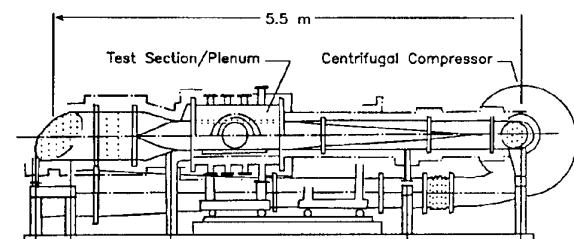


Fig. 6 High Reynolds Number Flow Facility at NDA.

Figure 6 is a sketch of the closed circuit tunnel. Table 6 gives the major characteristics of the cryogenic tunnel at NDA.

The sketch is a side view showing the centrifugal compressor at the right. The plenum mounts on a trolley which moves to the right to allow access to the test section.

The test section has two 30-cm diameter optical observation windows to allow for flow visualization. Professor Yamagu-

chi and his colleagues at NDA completed the initial tunnel calibration in 1985 (Ref 13). Researchers at the Academy use this tunnel for basic fluid mechanics studies.

TABLE 6. - High Reynolds Number Flow Facility at NDA (Japan)

Type .....	closed circuit, centrifugal compressor
Material of construction ..	SUS 304 and SCS 13 stainless
Insulation .....	external
Cooling .....	liquid nitrogen
Test gas .....	nitrogen
Test section size (h,w,l) .....	0.30 x 0.06 x 0.72 m
Speed range .....	up to 157 m/s
Mach range .....	up to 0.83
Contraction ratio .....	14:1
Stagnation pressure .....	up to 1.77 bars
Stagnation temperature .....	108 K - ambient
Running time .....	up to 100 min.
Max. Reynolds number/m .....	93 million
Drive motor .....	75 kW
LN <sub>2</sub> tank volume .....	4.9 m <sup>3</sup>

#### 5. UNITED STATES

##### 5.1 Douglas Aircraft Company

The Douglas Aircraft Company, Long Beach, California, modified two blowdown transonic tunnels for cryogenic operation. The first had a 1-ft test section and the second had a 4-ft test section. Reference 14 gives a description of some of the modifications to the tunnel required for cryogenic operation.

Douglas demonstrated the world's first blowdown cryogenic wind tunnel when their 1-ft tunnel first ran at cryogenic temperatures on May 20, 1977. The success of the 1-ft tunnel led to approval of a program to modify the Douglas 4-ft tunnel for cryogenic operation.

They used the 1-ft tunnel for a series of tests to determine the effect of nonadiabatic model wall conditions on supercritical airfoil characteristics. They found serious effects with only small deviations from adiabatic conditions at test conditions critical to the transonic transport designer (Ref 15).

Figure 7 shows a sketch of the Douglas 4-ft Cryogenic Wind Tunnel (4-CWT).

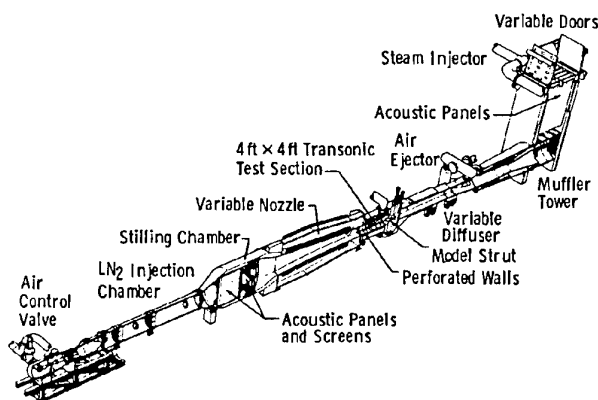


Fig. 7 Sketch of Douglas 4-ft. Cryogenic Wind Tunnel (4-CWT). [Ref. 14]

Table 7 gives the basic specifications for the 4-CWT. They modified the 4-CWT and successfully ran it at cryogenic temperatures in 1980-81.

The 4-CWT was capable of Reynolds numbers greater than 200 million per metre (60 million per foot). However, Douglas dropped the project, primarily because of the high cost of providing a system for model thermal conditioning to the strict tolerances required.

TABLE 7. - 4-ft Cryogenic Wind Tunnel (4-CWT) at Douglas (USA)

Type .....	blowdown
Material of construction .....	mostly mild steel
Insulation .....	internal
Cooling .....	liquid nitrogen
Test gas .....	mixture of air + nitrogen
Test section size (h,w,l) .....	1.2 x 1.2 x 3.7 m
Mach range .....	0.5 - 1.2
Contraction ratio .....	7.8:1
Stagnation pressure .....	170 - 480 kPa
Stagnation temperature .....	100 K - ambient
Running time .....	45 s at R/m = 135 million
.....	30 s at R/m = 200 million
Max. Reynolds number/m .....	200 million
LN <sub>2</sub> tank volume .....	151 m <sup>3</sup>

## 5.2 University of Illinois at Urbana-Champaign (UIUC)

Clausing and coworkers in the Department of Mechanical and Industrial Engineering at UIUC have built a special-purpose low-speed fan-driven cryogenic tunnel. They have used this tunnel to study forced, natural, and combined convective heat transfer at very large values of both Reynolds number and Grashof number.

The need to predict accurately combined convective losses from large, high temperature bodies prompted the building of the cryogenic tunnel at UIUC. Typical of such bodies is the receiver for a solar power tower where both the Grashof and Reynolds numbers are large. Clausing and his coworkers proposed to use a cryogenic heat transfer tunnel as an economical way to get the large Grashof and Reynolds numbers with an appropriate and near constant Prandtl number (Ref 16).

Figure 8 shows the variations of Grashof number and Reynolds number with temperature.

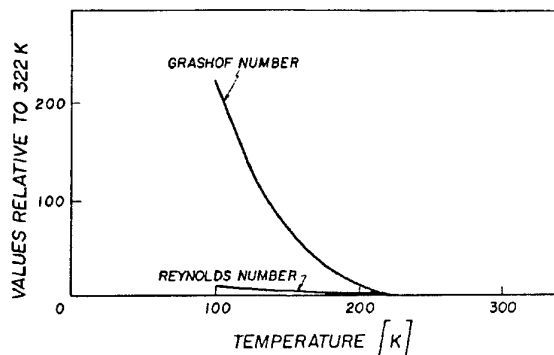


Fig. 8 Effect of temperature on Grashof and Reynolds number. [Ref 16]

As shown in Figure 8, the use of cryogenic temperatures is a good way to get higher Reynolds numbers but an even better way of getting higher Grashof numbers.

Also, the cryogenic environment virtually eliminates the influence of radiative heat transfer. Radiative heat transfer often causes large errors in natural convection data taken in conventional facilities (Ref 17). Clausing and his colleagues have extensively reported both the theory and advantages of the cryogenic heat transfer tunnel (Refs 17,18) and I will not repeat them here. Table 8 gives the basic specifications for the UIUC Cryogenic Facility.

TABLE 8. - Cryogenic Heat Transfer Tunnel at UIUC (USA)

Type .....	closed circuit, fan
Material of construction .....	mostly aluminum
Insulation .....	external, urethane
Cooling .....	LN <sub>2</sub> heat exchanger with GN injection
Test gas .....	nitrogen
.....	air for T > 290 K
Test section size (h,w,l) .....	1.22 x 0.60 x 1.0 m
Speed range .....	0 - 8 m/s
Contraction ratio .....	1:1
Stagnation pressure .....	atmospheric
Stagnation temperature .....	80 - 300 K
Running time .....	several minutes
Max. Reynolds number/m .....	4 million
Drive motor .....	11.2 kW
Fan speed .....	0 - 1750 rpm
LN <sub>2</sub> tank volume .....	1 m <sup>3</sup>

Figure 9 shows a sketch of the UIUC Cryogenic Facility.

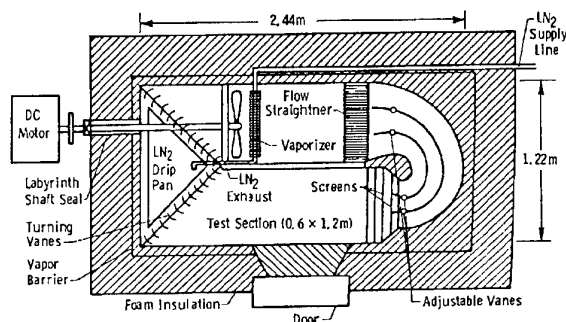


Fig. 9 Cross-sectional view of UIUC Cryogenic Heat Transfer Tunnel. [Ref. 16]

They cool the tunnel by passing liquid nitrogen through a heat exchanger/vaporizer located just downstream of two 0.5 m diameter cast aluminum fans. They vent the resultant gaseous nitrogen from the heat exchanger/vaporizer into the tunnel circuit. In this way, they avoid any problems that might arise from incomplete evaporation of liquid nitrogen using direct injection. During operation they keep a slight overpressure in the tunnel to keep out room air. Reference 19 gives a complete description of the UIUC Cryogenic Facility.

The UIUC Cryogenic Facility has been an extremely successful use of the cryogenic tunnel concept. Since first operated on August 17, 1978, they have used it for a variety of forced,

natural, and combined convective heat transfer research (Refs 20,21).

The receiver for *Solar One* is a right-circular cylinder about 7 metres in diameter and about 13 meters high. The ability to make such measurements in a relatively small cryogenic wind tunnel is a dramatic demonstration of the usefulness of the simulation laws. It also demonstrates the ingenuity of researchers who take advantage of emerging technology to solve long-standing problems.

### 5.3 NASA Langley

The first demonstration of the cryogenic wind tunnel concept came with the building and operation of an atmospheric low-speed tunnel at NASA Langley in January 1972 (Ref 22). The Langley low-speed cryogenic tunnel started its life as an abandoned 1/24-scale model of the Langley V/STOL tunnel. It was therefore typical of modern low speed-wind tunnels in its aerodynamic design. It needed only minor changes for cryogenic operation.

The first true cryogenic operation, that is, stagnation temperature less than about 172K (-150°F), was on January 31, 1972. At 12:05 pm we reached a temperature of 133 K (-220°F).

The 1/24-scale model of the V/STOL tunnel no longer exists as a cryogenic tunnel. We reconverted it to an ambient temperature tunnel. However, I will briefly describe it for several reasons.

First, this low-speed tunnel was typical in both layout and operating principle to the majority of cryogenic tunnels built or proposed.

Secondly, it is a tunnel of considerable historical significance. It proved the validity of the cryogenic wind tunnel concept and served as the test bed for the development of operational procedures and testing techniques.

Finally, I describe the low-speed tunnel to show that not all cryogenic wind tunnels must be expensive and complex. Figure 10 shows a sketch of this historic tunnel. Table 9 gives the basic specifications and operational characteristics for the Langley low-speed cryogenic tunnel.

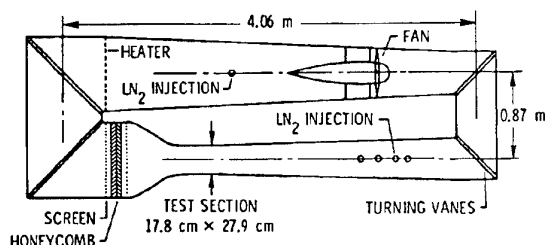


Fig. 10 Sketch of Langley Low-Speed Cryogenic Wind Tunnel. [Ref. 23]

We cooled the low-speed tunnel and removed the heat of compression added by the fan by spraying liquid nitrogen directly into the tunnel circuit. We used simple spray nozzles in either of the two locations shown in Figure 10. The rate of cooling was fairly rapid. For example, we could stabilize a tempera-

ture of 116 K within 10 minutes of the start of cooling from room temperature. During the early part of 1972, we operated the tunnel at temperatures from 333 K to 80 K. Approximately 40 hours of tunnel operation was at cryogenic temperatures, that is, below 172 K.

At a reference station in the test section, we could hold the test temperature to within about  $\pm 1$  K by automatic on-off control of one or more of the injection nozzles. We could hold much closer temperature control using a simple wire-grid electric heater built into the low-speed end of the tunnel. By injecting a slight excess of liquid nitrogen, we could establish temperature equilibrium by manually adjusting the heat input from the heater. Using this technique, we could hold test temperature to within about  $\pm 0.2$  K.

TABLE 9. - The Low-Speed Cryogenic Tunnel at NASA - Langley (USA)

Type .....	closed circuit, fan
Material of construction .....	mostly plywood and plastic
Insulation .....	external
Cooling .....	liquid nitrogen
Test gas .....	nitrogen
Test section size (h,w,l) .....	17.8 x 27.9 x 63.5 cm
Speed range .....	up to 50 m/s
Mach range .....	up to 0.14
Contraction ratio .....	9:1
Stagnation pressure .....	atmospheric
Stagnation temperature .....	80 - 333 K
Running time .....	typically 1 hour
Max. Reynolds number/m .....	20 million
Drive motor .....	7.4 kW
Fan speed .....	up to 3500 rpm
LN <sub>2</sub> tank volume .....	1.14 m <sup>3</sup>

Since we already had the basic tunnel circuit, the low-speed tunnel project was a very low-budget research effort. The cost of materials used to modify and insulate the tunnel was less than \$2000 (1971-1972). Materials of construction included wood, plywood, Plexiglas, mild and stainless steels, aluminum, brass, copper, and fiberglass reinforced plastic. The fan blades were made of laminated wood.

We made simple viewing ports to let us see key areas of the tunnel circuit. These included the test section, spray zones, corner vanes, screen section, and contraction section. We made the viewing ports from either 3 or 4 layers of Plexiglas separated by air gaps. Thermal insulation for the rest of the tunnel circuit was a 7.6 to 10.2 cm layer of expanded polystyrene applied to the outside of the tunnel and covered with a 0.0127 cm polyethylene vapor barrier.

We spent a lot of time measuring the temperature distribution around the tunnel circuit. In the early days of the project, one of our main concerns was finding an efficient yet simple way to cool the tunnel and still have temperature uniformity, in both time and space, in the test section.

Once we worked out adequate operating procedures, we used the low-speed cryogenic tunnel to verify, as far as possible, the validity and practicality of the cryogenic tunnel concept (Ref 23).

We made two simple *proof-of-concept* tests in the low-speed cryogenic tunnel. The first used a flat plate with a laminar boundary layer. It showed that the true aerodynamic effects of Reynolds number increases are indeed provided when temperatures are reduced to the cryogenic range. The second used a sharp leading edge delta wing model. It showed we could use ordinary strain-gage balance techniques to measure forces and moments at cryogenic temperatures.

In addition to the two proof-of-concept tests, we made other studies in the low-speed cryogenic tunnel. These were related mainly to developing acceptable cooling techniques and operating procedures (Ref 23).

## 6. CONCLUDING REMARKS

Following the development of the cryogenic wind tunnel at the NASA Langley Research Center in 1972, a large number of cryogenic wind-tunnel projects have been undertaken at various research establishments around the world. The purpose of this lecture has been to describe briefly some of the more significant cryogenic wind-tunnel projects not covered by other lecturers at this Special Course.

## 7. ACKNOWLEDGMENTS

I am indebted to the following people for providing information and material for this lecture: Prof. Han, Mr. Pan, and Professor He of the Chinese Aeronautical Research and Development Center (CARDIC), Mr. Takashima and Dr. Sawada of the Japanese National Aerospace Laboratory (NAL), Prof. Adachi of the University of Tsukuba, Professor Yamaguchi of the Japanese National Defense Academy (NDA), Prof. Stollery of the College of Aeronautics at Cranfield, Mr. Law of the Defence Research Agency - Bedford, Mr. Fancher of the Douglas Company, and Professor Clausen of the University of Illinois at Urbana-Champaign (UIUC).

## 8. REFERENCES

1. Pan Ruikang: *A Cryogenic High-Reynolds Number Transonic Wind Tunnel With Pre-Cooled and Restricted Flow*. Acta Aerodynamica Sinica, No. 2, 1984. pp. 87-92.
2. Kilgore, R.A.: *Other Cryogenic Wind Tunnel Projects*. Paper 9, AGARD Report No. 774, 1989. pp. 12.
3. Schultz, D.L.; Jones, T.V.; Oldfield, M.L.G.; and Daniels, L.C.: *A New Transient Cascade Facility for the Measurement of Heat Transfer Rates*. Oxford Univ. Eng. Lab. Report 1207/77, 1977.
4. Stollery, J.L.; and Stalker, R.J.: *The development and use of Free Piston Wind Tunnels*. Proceedings of the 14th International Symposium on Shock Tubes and Waves, Sydney, 1983, pp. 41-50.
5. Mohan, S.R.; and Stollery, J.L.: *A Study of the Temperature Achievable by Expansion of High Pressure Gas*. Aeronautical Journal, vol. 84, Aug. 1980, pp. 253-255.
6. Stollery, J.L.; and Murthy, A.V.: *An Intermittent High-Reynolds-Number Wind Tunnel*. Aeronautical Quarterly, vol. 28, Nov. 1977, pp. 259-264.
7. Mohan, S.R.: *Cryogenic Wind Tunnels High Reynolds Number Testing*. Ph.D. Thesis. College of Aeronautics, Cranfield Institute of Technology, U.K., June 1983.
8. Law, R.D.: *Early Experiments In Using the Cryogenic Test Facility at RAE Bedford, England*. Paper 8, ETW Cryogenic Technology Review Meeting, NLR-Amsterdam, 1982.
9. Dress, D. A.; and Kilgore, R. A.: *Cryogenic Wind Tunnel Research: A Global Perspective*. Cryogenics, vol. 28, January 1988, pp. 10-21.
10. Takashima, K.; Sawada, H.; Aoki, T.; and Kayaba, S.: *Trial Manufacture of NAL 0.1m x 0.1m Transonic Cryogenic Wind Tunnel*. NAL TR-910, 1986, 58 pp.
11. Sawada, H.: *NAL TCWT Status - Cryogenic Operation*. NAL News, 1984-3, No. 299, pp. 2-4.
12. Sawada, H.: *Automatic Operation of the NAL Cryogenic Wind Tunnel*. NAL News, 1986-1, No. 321, pp. 2-4.
13. Yamaguchi, Y.; Kuribayashi, N.; and Kaba, H.: *Characteristics for Ambient Conditions of NDA Cryotunnel and an Attempt on its Automatic Cryogenic Operation*. Proceedings of the 1988th Annual Meeting of JSASS, April 5-6, 1988, pp. 73-74.
14. Cadwell, J.D.: *Progress Report on the Douglas Aircraft Company Four-Foot Cryogenic Wind Tunnel*. Paper 18, AGARD LS 111, 1980. pp. 7.
15. Lynch, F.T.; et al.: *Nonadiabatic Model Wall Effects on Transonic Airfoil Performance in a Cryogenic Wind Tunnel*. Paper 14, AGARD CP-348, 1983.
16. Clausen, A.M.; Clark, G.L.; and Mueller, M.H.: *The Cryogenic Heat Transfer Tunnel - A New Tool for Convective Research*. Presented at the Winter Annual Meeting, ASME, San Francisco, Calif., 1978. pp. 73-78.
17. Clausen, A.M.: *Experimental Studies of Forced, Natural and Combined Convective Heat Transfer at Cryogenic Temperatures*. Paper 24, 1st Int. Symp. on Cryogenic Wind Tunnels, Southampton, U.K., 1979.
18. Clausen, A.M.: *Advantages of a Cryogenic Environment for Experimental Investigations of Convective Heat Transfer*. Int. J. of Heat and Mass Transfer, vol. 25, no. 8, 1982, pp. 1255-1257.
19. Mueller, M.H.; et al.: *Description of UIUC Cryogenic Wind Tunnel Including Pressure Distributions, Turbulence Measurements and Heat Transfer Data*. Univ. of Ill. Tech. Rept. ME-TN-79-9180-1, 1979. 82 pp.
20. Clausen, A.M.; Wagner, K.C.; and Skarda, R.J.: *An Experimental Investigation of Combined Convection from a Vertical Cylinder in Cross-flow*. ASME J. of Heat Transfer, vol. 106, no. 3, 1984, pp. 558-562.
21. Clausen, A.M.: *Natural Convection Correlations for Vertical Surfaces, Including Influences of Variable Properties*. ASME J. of Heat Transfer, vol. 105, no. 1, 1983, pp. 138-143.
22. Goodyer, M.J.; and Kilgore, R.A.: *The High Reynolds Number Cryogenic Wind Tunnel*. AIAA Paper 72-995, 1972. Also, AIAA Journal, vol. 11, no. 5, 1973, pp. 613-619.
23. Kilgore, Robert A.; et al.: *The Cryogenic Wind Tunnel for High Reynolds Number Testing*. NASA-TN-D-7762, 1974, 96 pp.

## REPORT DOCUMENTATION PAGE

<b>1. Recipient's Reference</b>	<b>2. Originator's Reference</b> AGARD-R-812	<b>3. Further Reference</b> ISBN 92-836-1047-4	<b>4. Security Classification of Document</b> UNCLASSIFIED/ UNLIMITED																		
<b>5. Originator</b> Advisory Group for Aerospace Research and Development North Atlantic Treaty Organization 7 rue Ancelle, 92200 Neuilly-sur-Seine, France																					
<b>6. Title</b> Advances in Cryogenic Wind Tunnel Technology																					
<b>7. Presented at/sponsored by</b> The AGARD Fluid Dynamics Panel, the Consultant and Exchange Program of AGARD, and the von Kármán Institute (VKI) for Fluid Dynamics.																					
<b>8. Author(s)/Editor(s)</b> Multiple			<b>9. Date</b> February 1997																		
<b>10. Author's/Editor's Address</b> Multiple			<b>11. Pages</b> 276																		
<b>12. Distribution Statement</b> There are no restrictions on the distribution of this document. Information about the availability of this and other AGARD unclassified publications is given on the back cover.																					
<b>13. Keywords/Descriptors</b> <table><tbody><tr><td>Wind tunnels</td><td>Strain gages</td></tr><tr><td>Cryogenics</td><td>Flow visualization</td></tr><tr><td>Aerodynamics</td><td>Instruments</td></tr><tr><td>Reynolds number</td><td>Accuracy</td></tr><tr><td>Aeroelasticity</td><td>Safety</td></tr><tr><td>Mach number</td><td>Productivity</td></tr><tr><td>Test facilities</td><td>Pressure measurement</td></tr><tr><td>Reviews</td><td>Wind tunnel models</td></tr><tr><td>Thermal insulation</td><td>Design</td></tr></tbody></table>				Wind tunnels	Strain gages	Cryogenics	Flow visualization	Aerodynamics	Instruments	Reynolds number	Accuracy	Aeroelasticity	Safety	Mach number	Productivity	Test facilities	Pressure measurement	Reviews	Wind tunnel models	Thermal insulation	Design
Wind tunnels	Strain gages																				
Cryogenics	Flow visualization																				
Aerodynamics	Instruments																				
Reynolds number	Accuracy																				
Aeroelasticity	Safety																				
Mach number	Productivity																				
Test facilities	Pressure measurement																				
Reviews	Wind tunnel models																				
Thermal insulation	Design																				
<b>14. Abstract</b> <p>Lecture notes for the AGARD Fluid Dynamics Panel (FDP) Special Course on "Advances in Cryogenic Wind Tunnel Technology" have been assembled in this report. Subjects included cryogenic systems, thermal insulation, facility and model design and construction, strain-gage balances, pressure instrumentation, flow visualization, data accuracy, safety, and productivity. In addition, there were reports on various operational cryogenic facilities.</p> <p>The material assembled in this report was prepared under the combined sponsorship of the AGARD Fluid Dynamics Panel, the Consultant and Exchange Program of AGARD, and the von Kármán Institute (VKI) for Fluid Dynamics.</p>																					

Aucun stock de publications n'a existé à AGARD. A partir de 1993, AGARD détiendra un stock limité des publications associées aux cycles de conférences et cours spéciaux ainsi que les AGARDographies et les rapports des groupes de travail, organisés et publiés à partir de 1993 inclus. Les demandes de renseignements doivent être adressées à AGARD par lettre ou par fax à l'adresse indiquée ci-dessus. *Veuillez ne pas téléphoner.* La diffusion initiale de toutes les publications de l'AGARD est effectuée auprès des pays membres de l'OTAN par l'intermédiaire des centres de distribution nationaux indiqués ci-dessous. Des exemplaires supplémentaires peuvent parfois être obtenus auprès de ces centres (à l'exception des Etats-Unis). Si vous souhaitez recevoir toutes les publications de l'AGARD, ou simplement celles qui concernent certains Panels, vous pouvez demander à être inclu sur la liste d'envoi de l'un de ces centres. Les publications de l'AGARD sont en vente auprès des agences indiquées ci-dessous, sous forme de photocopie ou de microfiche.

CENTRES DE DIFFUSION NATIONAUX

## ALLEMAGNE

Fachinformationszentrum Karlsruhe  
D-76344 Eggenstein-Leopoldshafen 2

## BELGIQUE

Coordonnateur AGARD-VSL  
Etat-major de la Force aérienne  
Quartier Reine Elisabeth  
Rue d'Evere, 1140 Bruxelles

## CANADA

Directeur - Gestion de l'information  
(Recherche et développement) - DRDGI 3  
Ministère de la Défense nationale  
Ottawa, Ontario K1A 0K2

## DANEMARK

Danish Defence Research Establishment  
Ryvangs Allé 1  
P.O. Box 2715  
DK-2100 Copenhagen Ø

## ESPAGNE

INTA (AGARD Publications)  
Carretera de Torrejón a Ajalvir, Pk.4  
28850 Torrejón de Ardoz - Madrid

## ETATS-UNIS

NASA Goddard Space Flight Center  
Code 230  
Greenbelt, Maryland 20771

## FRANCE

O.N.E.R.A. (Direction)  
29, Avenue de la Division Leclerc  
92322 Châtillon Cedex

## GRECE

Hellenic Air Force  
Air War College  
Scientific and Technical Library  
Dekelia Air Force Base  
Dekelia, Athens TGA 1010

## ISLANDE

Director of Aviation  
c/o Flugrad  
Reykjavik

## ITALIE

Aeronautica Militare  
Ufficio del Delegato Nazionale all'AGARD  
Aeroporto Pratica di Mare  
00040 Pomezia (Roma)

## LUXEMBOURG

Voir Belgique

## NORVEGE

Norwegian Defence Research Establishment  
Attn: Biblioteket  
P.O. Box 25  
N-2007 Kjeller

## PAYS-BAS

Netherlands Delegation to AGARD  
National Aerospace Laboratory NLR  
P.O. Box 90502  
1006 BM Amsterdam

## PORTUGAL

Estado Maior da Força Aérea  
SDFA - Centro de Documentação  
Alfragide  
2700 Amadora

## ROYAUME-UNI

Defence Research Information Centre  
Kentigern House  
65 Brown Street  
Glasgow G2 8EX

## TURQUIE

Millî Savunma Başkanlığı (MSB)  
ARGE Dairesi Başkanlığı (MSB)  
06650 Bakanlıklar-Ankara

**Le centre de distribution national des Etats-Unis ne détient PAS de stocks des publications de l'AGARD.**

D'éventuelles demandes de photocopies doivent être formulées directement auprès du NASA Center for AeroSpace Information (CASI) à l'adresse ci-dessous. Toute notification de changement d'adresse doit être fait également auprès de CASI.

AGENCES DE VENTE

NASA Center for AeroSpace Information  
(CASI)  
800 Elkridge Landing Road  
Linthicum Heights, MD 21090-2934  
Etats-Unis

The British Library  
Document Supply Division  
Boston Spa, Wetherby  
West Yorkshire LS23 7BQ  
Royaume-Uni

Les demandes de microfiches ou de photocopies de documents AGARD (y compris les demandes faites auprès du CASI) doivent comporter la dénomination AGARD, ainsi que le numéro de série d'AGARD (par exemple AGARD-AG-315). Des informations analogues, telles que le titre et la date de publication sont souhaitables. Veuillez noter qu'il y a lieu de spécifier AGARD-R-nnn et AGARD-AR-nnn lors de la commande des rapports AGARD et des rapports consultatifs AGARD respectivement. Des références bibliographiques complètes ainsi que des résumés des publications AGARD figurent dans les journaux suivants:

Scientific and Technical Aerospace Reports (STAR)  
publié par la NASA Scientific and Technical  
Information Division  
NASA Langley Research Center  
Hampton, Virginia 23681-0001  
Etats-Unis

Government Reports Announcements and Index (GRA&I)  
publié par le National Technical Information Service  
Springfield  
Virginia 22161  
Etats-Unis  
(accessible également en mode interactif dans la base de  
données bibliographiques en ligne du NTIS, et sur CD-ROM)



AGARD holds limited quantities of the publications that accompanied Lecture Series and Special Courses held in 1993 or later, and of AGARDographs and Working Group reports published from 1993 onward. For details, write or send a telefax to the address given above. *Please do not telephone.*

AGARD does not hold stocks of publications that accompanied earlier Lecture Series or Courses or of any other publications. Initial distribution of all AGARD publications is made to NATO nations through the National Distribution Centres listed below. Further copies are sometimes available from these centres (except in the United States). If you have a need to receive all AGARD publications, or just those relating to one or more specific AGARD Panels, they may be willing to include you (or your organisation) on their distribution list. AGARD publications may be purchased from the Sales Agencies listed below, in photocopy or microfiche form.

NATIONAL DISTRIBUTION CENTRES

## BELGIUM

Coordonnateur AGARD — VSL  
Etat-major de la Force aérienne  
Quartier Reine Elisabeth  
Rue d'Evere, 1140 Bruxelles

## CANADA

Director Research & Development  
Information Management - DRDIM 3  
Dept of National Defence  
Ottawa, Ontario K1A 0K2

## DENMARK

Danish Defence Research Establishment  
Ryvangs Allé 1  
P.O. Box 2715  
DK-2100 Copenhagen Ø

## FRANCE

O.N.E.R.A. (Direction)  
29 Avenue de la Division Leclerc  
92322 Châtillon Cedex

## GERMANY

Fachinformationszentrum Karlsruhe  
D-76344 Eggenstein-Leopoldshafen 2

## GREECE

Hellenic Air Force  
Air War College  
Scientific and Technical Library  
Dekelia Air Force Base  
Dekelia, Athens TGA 1010

## ICELAND

Director of Aviation  
c/o Flugrad  
Reykjavik

## ITALY

Aeronautica Militare  
Ufficio del Delegato Nazionale all'AGARD  
Aeroporto Pratica di Mare  
00040 Pomezia (Roma)

## LUXEMBOURG

See Belgium

## NETHERLANDS

Netherlands Delegation to AGARD  
National Aerospace Laboratory, NLR  
P.O. Box 90502  
1006 BM Amsterdam

## NORWAY

Norwegian Defence Research Establishment  
Attn: Biblioteket  
P.O. Box 25  
N-2007 Kjeller

## PORTUGAL

Estado Maior da Força Aérea  
SDFA - Centro de Documentação  
Alfragide  
2700 Amadora

## SPAIN

INTA (AGARD Publications)  
Carretera de Torrejón a Ajalvir, Pk.4  
28850 Torrejón de Ardoz - Madrid

## TURKEY

Millî Savunma Başkanlığı (MSB)  
ARGE Dairesi Başkanlığı (MSB)  
06650 Bakanlıklar-Ankara

## UNITED KINGDOM

Defence Research Information Centre  
Kentigern House  
65 Brown Street  
Glasgow G2 8EX

## UNITED STATES

NASA Goddard Space Flight Center  
Code 230  
Greenbelt, Maryland 20771

**The United States National Distribution Centre does NOT hold stocks of AGARD publications.**

Applications for copies should be made direct to the NASA Center for AeroSpace Information (CASI) at the address below.

Change of address requests should also go to CASI.

SALES AGENCIES

NASA Center for AeroSpace Information  
(CASI)  
800 Elkridge Landing Road  
Linthicum Heights, MD 21090-2934  
United States

The British Library  
Document Supply Centre  
Boston Spa, Wetherby  
West Yorkshire LS23 7BQ  
United Kingdom

Requests for microfiches or photocopies of AGARD documents (including requests to CASI) should include the word 'AGARD' and the AGARD serial number (for example AGARD-AG-315). Collateral information such as title and publication date is desirable. Note that AGARD Reports and Advisory Reports should be specified as AGARD-R-nnn and AGARD-AR-nnn, respectively. Full bibliographical references and abstracts of AGARD publications are given in the following journals:

Scientific and Technical Aerospace Reports (STAR)  
published by NASA Scientific and Technical  
Information Division  
NASA Langley Research Center  
Hampton, Virginia 23681-0001  
United States

Government Reports Announcements and Index (GRA&I)  
published by the National Technical Information Service  
Springfield  
Virginia 22161  
United States  
(also available online in the NTIS Bibliographic  
Database or on CD-ROM)

